

Springer Proceedings in Energy

Mohan Lal Kolhe
S. B. Jaju
P. M. Diagavane *Editors*

Smart Technologies for Energy, Environment and Sustainable Development, Vol 2

Select Proceedings of ICSTEESD 2020

 Springer

Springer Proceedings in Energy

The series Springer Proceedings in Energy covers a broad range of multidisciplinary subjects in those research fields closely related to present and future forms of energy as a resource for human societies. Typically based on material presented at conferences, workshops and similar scientific meetings, volumes published in this series will constitute comprehensive state-of-the-art references on energy-related science and technology studies. The subjects of these conferences will fall typically within these broad categories:

- Energy Efficiency
- Fossil Fuels
- Nuclear Energy
- Policy, Economics, Management & Transport
- Renewable and Green Energy
- Systems, Storage and Harvesting
- Materials for Energy

eBook Volumes in the Springer Proceedings in Energy will be available online in the world's most extensive eBook collection, as part of the Springer Energy eBook Collection. To submit a proposal or for further inquiries, please contact the Springer Editor in your region:

Kamiya Khatter (India)

Email: kamiya.khatter@springer.com

Loyola D'Silva (All other countries)

Email: loyola.dsilva@springer.com

More information about this series at <https://link.springer.com/bookseries/13370>

Mohan Lal Kolhe · S. B. Jaju · P. M. Diagavane
Editors

Smart Technologies for Energy, Environment and Sustainable Development, Vol 2

Select Proceedings of ICSTEESD 2020

 Springer

Editors

Mohan Lal Kolhe
Faculty of Engineering and Science
University of Agder
Kristiansand, Norway

S. B. Jaju
Department of Mechanical Engineering
G. H. Raisoni College of Engineering
Nagpur, Maharashtra, India

P. M. Diagavane
Department of Electrical Engineering
G. H. Raisoni College of Engineering
Nagpur, Maharashtra, India

ISSN 2352-2534

ISSN 2352-2542 (electronic)

Springer Proceedings in Energy

ISBN 978-981-16-6878-4

ISBN 978-981-16-6879-1 (eBook)

<https://doi.org/10.1007/978-981-16-6879-1>

© The Editor(s) (if applicable) and The Author(s), under exclusive license to Springer Nature Singapore Pte Ltd. 2022, corrected publication 2023

This work is subject to copyright. All rights are solely and exclusively licensed by the Publisher, whether the whole or part of the material is concerned, specifically the rights of translation, reprinting, reuse of illustrations, recitation, broadcasting, reproduction on microfilms or in any other physical way, and transmission or information storage and retrieval, electronic adaptation, computer software, or by similar or dissimilar methodology now known or hereafter developed.

The use of general descriptive names, registered names, trademarks, service marks, etc. in this publication does not imply, even in the absence of a specific statement, that such names are exempt from the relevant protective laws and regulations and therefore free for general use.

The publisher, the authors and the editors are safe to assume that the advice and information in this book are believed to be true and accurate at the date of publication. Neither the publisher nor the authors or the editors give a warranty, expressed or implied, with respect to the material contained herein or for any errors or omissions that may have been made. The publisher remains neutral with regard to jurisdictional claims in published maps and institutional affiliations.

This Springer imprint is published by the registered company Springer Nature Singapore Pte Ltd. The registered company address is: 152 Beach Road, #21-01/04 Gateway East, Singapore 189721, Singapore

Preface

Smart Technologies for Energy, Environment & Sustainable Development are going to facilitate low-carbon society, and expedite local socio-economic development.

Substantial amounts of smart technologies are going to be integrated in the near future for development of environmental friendly infrastructure. They will be important part of the electricity, heat, gas, transport, building sectors, etc. However, energy security, greenhouse gas emissions, sustainable buildings, cleaner transportation, and resilience are key challenges, and they need to be solved for a low-carbon economy through focused and integrated efforts with the use of smart technologies.

Smart Grid performs an important role in the ‘Energy Transition’ to integrate environmental friendly energy systems within the distributed network infrastructure (e.g. electricity, heat, gas, transport, etc.) for the sustainable development. The necessity for ‘Energy Transition’ is broadly understood and shared, as the world starts to embrace a transition towards sustainable energy systems by shifting from fossil fuel-based energy production to decentralized renewable energy and energy efficient systems.

As the Editors of the Select Proceeding of ICSTEESD-2020, ‘Smart Technologies for Energy, Environment and Sustainable Development’, Special Volume of Springer Proceedings in Energy (ISSN: 2352-2534), we wish to express sincere gratitude to the authors for diligent research dissemination as well as to the reviewers for providing constructive and critical comments in improving the quality of the selected articles. The objective of this special volume is to present advancements in smart technologies for environment friendly energy systems and their management, policies for making an energy transition towards sustainable societies. The selected peer-reviewed articles are classified in the categories of (i) Sustainable Electrical Energy Systems, (ii) Environmental Management, and (iii) Industrial Engineering with focus on sustainable development. The ICSTEESD-2020 is a major multidisciplinary sustainable engineering conference organized with the objective of bringing together academia, industry practitioners and engineering graduates to analyze scientific studies focusing on both clean energy technologies, environmental sustainability and smart network concepts to integrate the relationship among them. The ICSTEESD 2020 is envisioned to analyze the increasing penetration of environment friendly technologies with energy efficiency and management as central topics with effective participation

from the academicians, industry practitioners, governmental policy makers, as well as of community service providers. The ICSTEESD-2020 has been organized at G. H. Rasoni College of Engineering (GHRCE), Nagpur, India on 04-05 Dec 2020.

As editor(s) of this special issue of the Springer's proceeding of ICSTEESD-2020, we want to tribute deep sense of appreciations to the international academic partners (e.g. University of Agder, Norway; University of Ruhuna, Sri Lanka; Kyushu Sangyo University, Japan; University of Dundee, UK; Mie University, Japan) for academically assisting the ICSTEESD-2020. We wish to express our sincere appreciation to the authors, plenary speakers, presenters, participants, supporters, reviewers, technical committee members as well as the entire team of G. H. Rasoni College of Engineering, Nagpur (India). We are very grateful to Shri Sunil Rasoni, Chairperson of the Rasoni Group of Institutions; Dr. Sachin Untawale, Director, GHRCE, Nagpur; Dr. Rupesh Shelke, Dr. Bhalchandra Khode and the ICSTEESD 2020 organizing committee members for contributing effectively in making the Springer's ICSTEESD-2020 and publication of the special volume successful.

We strongly believe that the ICSTEESD 2020 has provided an effective platform to integrate academia, industry practitioners and engineering graduates to share their research and innovations for the sustainable development of the society.

Kristiansand, Norway
Nagpur, Maharashtra, India
Nagpur, Maharashtra, India
December 2020

Prof. Dr. Mohan Lal Kolhe
Prof. S. B. Jaju
Prof. P. M. Diagavane

Contents

Quality Enhancement of Bituminous Concrete Using Cenosphere Fillers	1
Maitri Mallick, Bhabanisankar Sahani, Mohini Priya Padhi, Jyoti Prasad Ganthia, Nihar Ranjan Mohanta, and Dhanada Kanta Mishra	
Analysis of Liquid Storage Concrete Containers Partially Restraint at the Base	9
Rameshwar J. Vishwakarma and Ramakant K. Ingle	
A Study on Behavior of Reinforced Concrete Exterior Beam-Column Joint: A Literature Review	17
Yogesh Narayan Sonawane and Shailendrakumar D. Dubey	
Encouragement of Magnetic Treated Grey Water in High-Strength Concrete	27
E. Prabakaran, M. Nithya, Jessy Rooby, and A. Vijayakumar	
Spiritual Elixir: Application of Ganga Water in Treatment of Wastewater	33
Monika Negi, Ayushi Maithani, and Sakshi Gupta	
Seismic Response of Base Isolated Elevated Circular Water Tank	43
Tanuja Khati, Smita Kaloni, Shashi Narayan, and Chetana	
Analysis of Pauri Garhwal Forest Fire Burned Area for the Years 2015–2019—A Case Study	51
Pooja Dobhal, Rishi Prakash, Nitin Mishra, and B. V. Khode	
Enhancement of Seismic Properties of Reinforced Concrete Beam–Column joints—A Review	69
P. Nikita and V. M. Preethi	
Geotextile Filters in Earthen Dam—A Review Study on Construction and Rehabilitation	79
Hridayesh Kumar Trivedi, Nikita Choudhari, and Sumit Gandhi	

Seismic Response Control of RCC Building Using Dampers	95
Chinmay Gurmule, S. S. Sanghai, and P. Y. Pawade	
Utilization of Sugarcane Bagasse Ash for the Stabilization of Pavement Subgrade: A Probabilistic Approach	103
Monalisa Priyadarshini and Jyoti Prakash Giri	
Experimental and Analytical Study of Negative Stiffness Device for Protection of Structures Against Earthquake—A Review	113
Vaishali Kishan and Priyanka Jadhav	
Laboratory Study of Permeability for Sub-Base Using Flyash and Fibre	127
Dharampal Singh Kandari, Deepak Kumar Singh, and Shashank Kothari	
Comparative Analysis of CFST Columns and RC Columns Under Uniaxial Compressive Loads	135
Shashank Kothari, Deepak K. Singh, and Pankaj Chamoli	
Use of Bagasse Ash as a Filler Material in Soils	145
Rahul Vaishnava, Ajit Kumar, and Sanjeev Kumar	
Assessing the Accuracy of Open Source Altitude Data for the Hilly Area in Tehri Garhwal District of Uttarakhand, India	153
Kishan Singh Rawat, Sanjeev Kumar, Anil Kumar Mishra, and Sudhir Kumar Singh	
Crop-Type Classification Using Sentinel-2A and in Situ Data: Case Study of Shri Dungargarh Taluk of Rajasthan, India	179
Pritam K. Meshram, Kishan Singh Rawat, Sanjeev Kumar, and Sudhir Kumar Singh	
Evaluation of Total Dissolved Solids and Quality Zones of Groundwater Using Vertical Electrical Soundings and GIS Method	189
Kishan Singh Rawat, Sanjeev Kumar, and Sudhir Kumar Singh	
Monitoring Drought of Maharashtra, India by Using Standardized Precipitation Index	201
Smruti Ranjan Sahu, Kishan Singh Rawat, Sanjeev Kumar, Anil Kumar Mishra, and Sudhir Kumar Singh	
Precipitation Trends Along the Himalayan and Pir Panjal Mountains of Jammu and Kashmir	209
Mohammad Rafiq, Kishan Singh Rawat, Sarish Mukhtar, Anil Kumar Mishra, Sanjeev Kumar, and K. K. Gupta	
Evaluation of Critical Performance Parameter for Tube Settlers	217
M. P. Bhorkar and P. B. Nagarnaik	

Climate Change: Understanding the Frail Associations Between Scientific Evidence and Public Perception 227
 A. Arun Kumar, Sanjeev Kumar, Ramesh Krishnamurthy, and Vandana Rani

Comparative Analysis of MIVAN Formwork and Conventional Formwork 239
 Prakash Patil and Palash Mundhada

Study of Indirect Traffic Parameters Along Metro Construction Route 247
 Smita Pataskar and Sunil Pimplikar

Performance Investigation of Desiccant Wheels for Air Dehumidification 257
 Kishor Rambhad, Manoj Kumbhalkar, Vednath Kalbande, Rahul Jibhakate, Nikhil Jumde, and Pramod Walke

Corruption and Its Mitigation Strategy Using Lean Philosophy 265
 Brajesh Kumar Kanchan, Guddakesh Kumar Chandan, Roma Kumari, and Ojaswi Gautom

A New Approach for the Prediction of the Stability of Lotka-Volterra Model as a Biological Reaction 275
 Pragati Dethe and Arvind Bodhe

Review of Investigation in Performance of Magnetic Refrigeration System 285
 Aniket R. Ingale, Pranay D. Kumbhare, Ram G. Sanodiya, Ravindra A. Ravane, and Ashish S. Raut

A Comparative Study on the Effect of Nanoparticles in Vapour Compression Refrigeration System 291
 Saroj Chavhan Borkar and Sanjeo Choudhary

An Experimental Evaluation of FEA-Based Helical Compression Spring to Design a Shock Absorber 299
 Amol Vikas Joshi, Devanand Tayade, and Wasim Patel

Laboratory Investigation of Composite Made of Alumina Dispersed Aluminium Prepared by UTM Pressed Powder Metallurgy Method 309
 M. K. Manik, Mani Bhushan Singh, and Vishal Vhagat

A Computational Study of a Dump Combustor with and Without Swirler 331
 Rohan R. Pande and Mohd Zeeshan

Effect of Aspect Ratio on Fatigue Behaviour of Steel Shear Wall 351
 R. K. Chethan Gowda, K. Ashwini, and H. M. Rajashekaraswamy

Life Cycle Analysis for Biodiesel Fuels—A Holistic Approach	359
Anurag Mishra, R. Arjun Thangaraj, and Pramod S. Mehta	
The Role of 3D Printing in the Biomedical Application: A Review	371
Ujwal Sontakke and Santosh Jaju	
Microsurfacing Machines: A Review	383
Kratika Ravekar and Santosh B. Jaju	
Shape Memory Alloy as a Smart Material: A Review	395
Shrutika Dahake, Nilesh Awate, Rupesh Shelke, and Abhay Khalatkar	
Influence of Room Temperature Rolling Process on Mechanical and Corrosion Behaviors of Al 6061alloy	403
Alok Singh Verma and Anuj Jain	
Enhancement of Activated Flux Tungsten Inert Gas Welding Using SiO₂ Flux for Joining 304L Stainless Steel Sheets	413
Dattatray Chopade, Prashant Lugade, Nitish Sinha, Avinash Panchal, and Shivji Kumar	
An Overview on the Microstructure and Mechanical Properties of Vibrated Magnesium Alloy During Solidification	423
Vatsala Chaturvedi and Trinath Talapaneni	
CFD Analysis of Waste Heat Recovery (WHR) System of Diesel Generator Set	433
Tejas Shankhpal, Vikrant Haribhakta, and Santosh Trimbake	
Optimization of Solar Hot Water Storage Tank Performance During Charging Process Using Buckingham’s Theorem	451
Mahesh V. Kulkarni, Dheeraj S. Deshmukh, S. P. Shekhawat, and M. S. Deshmukh	
Performance Analysis of Photovoltaic Module Using Microchannels and Nanofluids	469
S. M. Lawankar, Shoeb J. Inamdar, and Shubham K. Changole	
Thermal Analysis of Salinity Gradient Solar Pond in Nagpur City	487
Shyamal G. Chakrabarty, Uday S. Wankhede, and Rupesh S. Shelke	
Mathematical and Thermal Modeling for Solar Drying of Tomato Slices	493
Rajendra C. Patil and Yogesh S. Kulkarni	
Efficiency Improvement of Concentrated Photovoltaic (CPV) System by Way of Various Active and Passive Cooling Techniques—A Review	507
Yogesh Nandurkar, Vivek Korde, and Narendra Giradkar	

Experimental Study of Vacuum Tube Heat Pipe-Based Solar Collector for Cooking Application 517
 Asim Kumar Joshi, Sachin Gupta, Arunendra Kumar Tiwari, Falgun Raval, and Milan Sojitra

Reliability Assessment of Smart Grid with Renewable Energy Sources, Storage Devices, and Cyber Intrusion 525
 Lalit Tak, Atul Kumar Yadav, Neeraj Kumar Singh, and Vasundhara Mahajan

Distance Relaying with Power Swing Detection in the Presence of Distributed Resources 543
 Pankaj Ramtekkar, Suraj Dudhe, Ankur Gupta, and Munishwar Meshram

Modeling and Simulation of FPGA-Based Vector-Controlled Induction Motor Drive Using Simulink 549
 Sumit Kumar Gupta

Design of Sine Filter for GTO-Based Auxiliary Converter for Electric Locomotive Using MATLAB Simulink 561
 Rutuja S. Hiware, Shradha K. Umathe, and Shridhika Bire

Analysis of Control Techniques and Filter Design of Multilevel Inverter 571
 Vaidehi Korde, Neha Sute, V. B. Borghate, and V. M. Korde

Increasing the Accuracy and Reducing the Installation Cost of Automatic Power Factor Correction System Using TRIAC 589
 Mohammad Khalid Saifullah, Md. Sajedul Rahman, Md. Masum Miah, Md. Rubaiyat Rahman Shibly, Nasim Mia, Md. Salman Rahman, Saikat Das, and K. M. Ahsan-uz-Zaman

Testing Topologies to Overcome Fault in Micro-Grid Connected System 599
 Ankur Kumar Gupta, Rishi Kumar Singh, and Shradha Umathe

Improving Reactive Power Compensation by Using Hybrid-STATCOM 607
 Ramchandra Adware and V. K. Chandrakar

Electric Vehicle Technology: Trends and Challenges 621
 Nadeem Akhtar and Vijay Patil

Solar Micro-Inverter with Phase Shift Power Modulation and Half Wave Cyclo-Converter 639
 Amit L. Nehete, Gururaj Talewad, and Chetan B. Khadse

Load Flow Analysis of 5 Bus Power System for Three Phase Symmetrical Fault Using MATLAB 647
 Prajakta Vikas Dhole and Sahebrao Narsingrao Patil

MIL, SIL, and PIL Simulations of a Grid-Tied Inverter	657
Piyush Pandey, Saurabh Mani Tripathi, Utkrisht Goswami, Hemant Kumar Verma, and Aman Kumar Sriwastava	
Performance Investigation on Vector Controlled IPMSM Drive Using MIL, SIL, and PIL Simulations	667
Utkrisht Goswami, Saurabh Mani Tripathi, Piyush Pandey, Saumya Jain, and Govind Saroj	
Artificial Intelligence Based State of Charge Estimation of Electric Vehicle Battery	679
S. P. Nanigrani and Ishaan S. Nanigrani	
Accelerometer-Based Hand Gesture Control Robot Using Arduino and 3-Axis Accelerometer	687
Ankit and Shweta Agarwal	
Artificial Intelligence-Based State of Charge Estimation of Electric Vehicle Battery	699
Samruddhi Dewalkar and S. P. Nanigrani	
Wattages Optimization of Small Hydro Power Station to Build up Energy	707
Prachi Dashrath Mohite, Shweta Abhay Khalatkar, and Abhay M. Khalatkar	
A Review on the Development of Solar Power Automatic Biodegradable Waste Sorter and Composter	715
Amit S. Borole and A. R. Phadke	
Correction to: Spiritual Elixir: Application of Ganga Water in Treatment of Wastewater	C1
Monika Negi, Ayushi Maithani, and Sakshi Gupta	

About the Editors

Prof. Dr. Mohan Lal Kolhe is a full professor in smart grid and renewable energy at the Faculty of Engineering and Science of the University of Agder (Norway). He is a leading renewable energy technologist with three decades of academic experience at the international level and previously held academic positions at the world's prestigious universities, e.g., University College London (UK/Australia), University of Dundee (UK); University of Jyväskylä (Finland); Hydrogen Research Institute, QC (Canada); etc. In addition, he was a member of the Government of South Australia's first Renewable Energy Board (2009–2011) and worked on developing renewable energy policies. Due to his enormous academic contributions to sustainable energy systems, he has been offered the posts of Vice-Chancellor of Homi Bhabha State University Mumbai (Cluster University of Maharashtra Government, India), full professorship(s)/chair(s) in 'sustainable engineering technologies/systems' and 'smart grid' from the Teesside University (UK) and Norwegian University of Science and Technology (NTNU) respectively. He is Series Editor of Springer Proceedings in Energy. His research works in energy systems have been recognized within the top 2% of scientists globally by Stanford University's 2020, 2021 matrix. He is an internationally recognized pioneer in energy field, whose top 10 published works have an average of over 175 citations each.

Prof. Dr. S. B. Jaju obtained his master's degree in Industrial Engineering from VRCE (Now known to be VNIT), Nagpur, and received PhD from Rashtrasant Tukadoji Maharaj Nagpur University. He has completed Master of Business Administration from IGNOU, New Delhi. He is presently working as Dean (Research & Development) and Professor in the Department of Mechanical Engineering of G. H. Raisoni College of Engineering. He has more than 23 years of teaching experience. He has to his credit more than 100 research papers published in national and international journals and conferences, 01 book and 06 book chapters. He has attended more than 50 symposiums, short-term courses, training, and workshops. He has delivered more than 50 expert lectures in short-term training programmes and workshops. He served as convener of series of All India Seminar Quality Progress, general chair of International conference on advances in mechanical engineering, and program chair

in IEEE International Conference on Emerging Trends in Engineering & Technology. He is serving as member on editorial board, reviewer of international journal, chaired number of technical sessions in conferences. He is associated with many prestigious professional societies like Institution of Engineers (India); ISTE New Delhi; Indian Institution of Industrial Engineering, Mumbai; Indian Society of Mechanical Engineers (ISME), New Delhi; IEEE-Robotics and Automation Society and ASME. He is a certified Lead Auditor of ISO 9001: 2008 QMS by IRCA UK. He has guided more than 20 PG dissertations, 05 PhDs awarded, 01 PhD student have submitted thesis. He has filed 6 patents, 1 copyright, completed research project of AICTE. He has visited National University of Singapore; Multimedia University, Malaysia; University of Technology, Mauritius; and various universities in Dubai. He received BEST TEACHER AWARD given by G. H. Raisoni College of Engineering for the year 2003-2004. He has also received BEST CASE STUDY AWARD (non-traditional area) in the form of Silver Medal by National Council of Indian Institution of Industrial Engineering, Navi Mumbai, for the year 2004–2005. He has received 07 Best Paper Awards. His research area includes quality cost, total quality management, supply chain management, service quality, lean manufacturing, productivity improvement techniques and industrial engineering areas.

Prof. Dr. P. M. Diagavane is currently professor at the Department of Electrical Engineering, G. H. Raisoni College of Engineering, Nagpur. She obtained her B.E. (Electrical) from Government college of Engineering Amravati and M.S. (Electronics & Control) from BITS Pilani and PhD from Rashtrasant Tukadoji Maharaj Nagpur University, Nagpur. Her major areas of research interests include control engineering, soft computing tools, optimization techniques, renewable energy in electrical engineering. She has more than 30 years of teaching experience. He has to her credit more than 65 research papers published in national and international journals and conferences, 02 book chapters. She has attended more than 50 symposiums, short-term courses, training, and workshops. She received Best Teacher Award given by G. H. Raisoni College of Engineering for the year 2014–2015. She had organized and was general chair of International conference published by IEEE and Springer. She is serving as reviewer of international journal and chaired number of technical sessions in conferences. She is associated to many prestigious professional societies like Institution of Engineers (India), ISTE New Delhi and IEEE.

Quality Enhancement of Bituminous Concrete Using Cenosphere Fillers



Maitri Mallick, Bhabanisankar Sahani, Mohini Priya Padhi,
Jyoti Prasad Ganthia, Nihar Ranjan Mohanta, and Dhanada Kanta Mishra

1 Introduction

A highway pavement is usually a design that has prepared materials on top of a healthy soil sub-grade. The primary purpose of which is to transfer loads of the used vehicle to the sub-grade. Pavement is a real travel surface, especially made long-lasting as well as practical to withstand the traffic load commuting on it. Pavement offers friction for vehicles, thereby providing an acceptable operating quality surface, adequate skid resistance, optimal reflective lighting and low noise pollution. The essential objective is to ensure that the stresses transmitted due to the load of the wheel are sufficiently minimized so that they do not exceed the load capacity of the sub-grade.

2 Bituminous Mix Design

The design of a bituminous mixture is intended to decide the proportion of bitumen, filler, fine aggregates and coarse aggregates to produce a mixture that is workable, solid, durable and economical. Generally, the construction of the highway pavement required a large cost of money. Reasonable architecture, therefore, saves detailed speculation. Appropriate pavement design includes structural design and mixing

M. Mallick (✉) · B. Sahani · M. P. Padhi
Department of Civil Engineering, KMBB College of Engineering and Technology, Khordha,
Bhubaneswar, Odisha 752056, India

J. P. Ganthia · N. R. Mohanta
Department of Civil Engineering, GIET University, Gunupur, Odisha, India

D. K. Mishra
Department of Civil Engineering, Hong Kong University of Science and Technology, Kowloon
Bay, Hong Kong, China

design. The objective of structural intent is the thickness design of the paving material, and the mixing design consists of a dry mix design and a wet mix design.

2.1 Coarse Aggregate

The aggregates retained on a 4.75 mm sieve are called coarse aggregates. Coarse aggregates of crushed rock, angular in form, free from dust particles, mud, vegetation and organic matter, offering compressive and shear strength and strong interlocking properties, should be screened. For the preparation of bituminous mixtures (SMA, DBM, BC) aggregates as per MORTH grade of a specific form of binder in the appropriate quantity are mixed as per Marshall Procedure. The coarse aggregate is chosen on the basis of the necessity and suitability of the mixing design and should be as defined. Specifications shall include physical specifications as set out in the MORTH standards.

2.2 Fine Aggregate

Clean sifted quarry dusts should be fine aggregate and free from clay, loam, vegetation or organic matter. A local crusher with fractions of 4.75 mm has been collected and retained on 0.075 mm IS sieve, which consists of fine aggregates consisting of stone crushing material. The vacuum is filled in the grower and the binder is steeped.

2.3 Filler

The sieve is called a filler machine that passes through 0.075 mm. The vacuum is completed, the bond is reinforced and permitting. The mineral filler must consist of finely divided materials such as rock dust, broken slag, cement, ash-flying content, hydrated lime, etc. Stone dust for preparing the control mix is used as standard filler for this analysis, while stone dust and cenosphere are used for substitution purposes as fillers both. In Figs. 1 and 2 the cenospheric materials are shown.

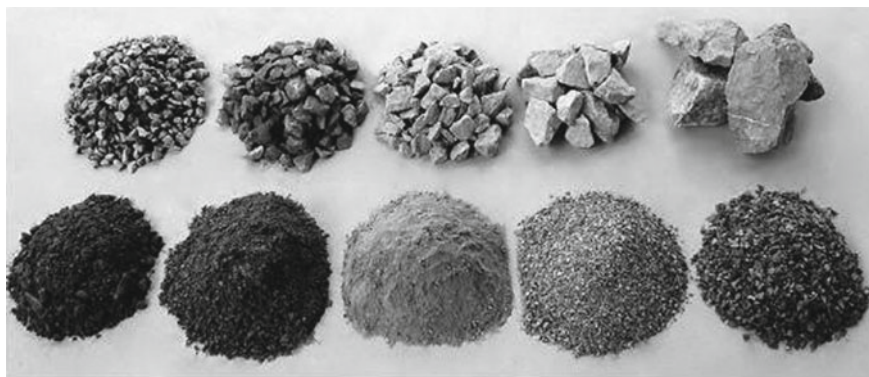


Fig. 1 Different size of aggregates



Fig. 2 Different size of aggregates of cenosphere materials

3 Cenosphere

The division of carbon fly powder with an empty circular structure is one of the most critical considerations. Cenosphere, because of its specific characteristics, such as low mass thickness, high warm opposition, high workability and high efficiency, can be related in many applications. During the carbon combustion process, the general cenosphere and other particles are produced. A cenosphere has a lightweight, idle, hollow sphere of vast quantities of silica and alumina, filled with air or inactive gas, which is normally processed in warm power plants as a result of coal burning. The cenosphere varies from almost black to nearly white and its real gravity is between 0.4 and 0.8 g/cm³, offering exceptional lightness. The cenosphere components are SiO₂ (quartz), Al₂O₃ (alumina), Fe₂O₃ (haematite), CaO (calcium oxide), TiO₂, MgO (periclase) and H₃PO₄ (phosphoric acid). The cenosphere's spherical nature allows for a low volume surface area that needs less resin, binder and water, and is therefore an adjustable tool for polymers and various polymer composites. Cenosphere is the only part of the surface. Cenospheres can be used as a lightweight concrete filler with a decreased water release for building applications. This is ideal for sturdy bridge desks, paves and highways.

4 Marshall Test Experimental Program

Marshall test is a standard laboratory method that is used worldwide to define bitumen-coating paving mixtures' strength and flow characteristics. The way to describe bituminous mixes is very common in India. Because of its ease and low cost, this test method is well known. Since the Marshall method has numerous benefits, the best binder content (OBC) method has been determined to use this method (Fig. 3).

5 Experimental Results

Experimental analysis is categorized into four contents:

- Initial deals with characteristics and parameters
- Second deals with control mix and calculation using Marshal test
- Third deals with result analysis and compositional contents
- Fourth deals with the strength of the tensile test.

Result analysis of control mix results is shown in Table 1 and (Table 2).

Fig. 3 Marshal test of material mix**Table 1** Characteristics of control mix for BC

Bitumen mix content (%)	Strength stability (KN) at 60°C	Content flow (mm)	Mix bulk density(gm/cc)	Mix air voids (%)	VMA content (%)	VFB content (%)
6	10.87	2.8	2.85	5.2	15.62	72.6
6.5	12.58	3.0	2.65	4.2	15.34	80.6
7	13.21	3.5	2.64	3.25	15.55	81.6
7.5	11.07	4.0	2.52	3.05	15.20	82.2

The changes are occurring that the mixture's stability is closely correlated to the density and versatility of the mix. That is if the consistency of the mix is longer, either the mix density should be greater or the mix versatility should be greater, or both. With excess filler, consistency also improves, but the combination gets unstable and sudden cracking. In cases of filler failure, but the mixture is soft, stability decreases. The stability of the mix and the volume density are identical in nature here. Here it is found that the stability decreases from the combination of 60–100% cenosphere. The decrease in density can be induced. Density is a compaction and material type feature. Compaction depends on the compactive effort, the form of material and the quality of bitumen.

Table 2 Result analysis of Mix

S. No	Bitumen mix content (%)	FC (% by vol.)	Strength stability (KN) at 60°	Content flow (mm)	Mix bulk density (gm/cc)	Mix air voids (%)	VMA content (%)
1	6.012	95 SD + 10 C	12.20	2.64	3.463	4.64	70.20
2	6.012	85 SD + 20 C	12.01	2.74	3.464	4.54	71.18
3	6.012	75 SD + 30 C	13.12	2.72	3.465	4.12	71.56
4	6.012	65 SD + 40 C	13.46	2.92	3.469	4.24	72.12
5	6.012	55 SD + 50 C	14.10	2.95	3.566	4.46	74.46

6 Conclusion

From the above experimental study, it is found that cenosphere mix content enhances the filler by 70%. Furthermore, it has become more breakable. Hence using the bitumen mix reduces the brittleness and increases the tensile strength of the material mix. This research helps the other researcher to use the material percentage with the use of advanced testing techniques to get better material for roads and pavements. The tensile strength increases by 94.2% with optimum analysis and satisfies the minimum necessary of 80% of strength and stability.

References

1. C.A. Carpenter, A comparative study of fillers in asphaltic concrete. *Public Roads* **27**, 101–110 (1952)
2. W.B. Warden, S.B. Hudson, H.C. Howell, Evaluation of mineral filler in terms of practical pavement performance. *Proc. Assoc. Asphalt Pav. Technol.* **27**, 101–110 (1952)
3. F.V. Zimmer, “Fly ash as bituminous filler”, in *Proceedings of the 2nd Ash Utilization Symposium, Pittsburgh, PA, 10–11 March 1970*. (United States Department of Interior, Bureau of Mines, Washington, DC, 1970)
4. K.S. Sankaran, D.R. Rao, The influence of the quality of filler in asphaltic paving mixtures. *Indian Roads Cong* **35**, 141–151 (1973)
5. N.E. Henning, Evaluation of lignite fly ash as a mineral filler in asphaltic concrete. Report No. 2(73) (Twin city testing and engineering laboratory, St. Paul, Minn., 1974)
6. J.C. Rosner, J.G. Chehovits, G.R. Morris, “Fly ash as a mineral filler and anti- strip agent for asphalt concrete”, in *Proceedings of the 6th International Ash Utilization Symposium. Vol. 1. United States Department of Energy, Morgantown, W.Va. Report No. DOE/METC/82/2* (1982)
7. E. Tons, R.O. Goetz, M. Razi, Fly ash as asphalt reducer in bituminous base courses. Project Report. (University of Michigan, the Board of Water and Light, Consumer Power Co., and Detroit Edison Co., Detroit, Mich, 1983)

8. ARS Suheibani, The use of fly ash as an asphalt extender. Ph.D. thesis, University of Michigan, Ann Arbor, Mich. 1986
9. N. Ali, J.S. Chan, S. Simms, R. Bushman, A.T. Bergan, Mechanistic evaluation of fly ash asphalt concrete mixtures. *J. Mater. Civil Eng.* **8**(1): 19–25 (1996) doi:[https://doi.org/10.1061/\(ASCE\)0899-1561\(1996\)8:1\(19\)](https://doi.org/10.1061/(ASCE)0899-1561(1996)8:1(19))
10. I. Asi, A. Assa'ad, Effect of jordanian oil shale fly ash on asphalt mixes *J. Mater. Civ. Eng.* **17**(5), 553–559 (2005). doi:[https://doi.org/10.1061/\(ASCE\)08991561\(2005\)17:5\(553\)](https://doi.org/10.1061/(ASCE)08991561(2005)17:5(553))

Analysis of Liquid Storage Concrete Containers Partially Restraint at the Base



Rameshwar J. Vishwakarma and Ramakant K. Ingle

1 Introduction

The design of concrete circular containers is largely affected by the type of restraint at the base. Widely used guidelines like IS: 3370 (Part IV) 1967 (Reaffirmed 1999) [1] and PCA (1993) [2] provided coefficients for the analysis of circular containers with different restraint conditions at the base. However, analysis due to loss of restraint is not specified in these guidelines. Practically, the base of the container is not completely restraint; some yielding occurs at the base and hence outward deflection of the container wall at the base will not be zero. If the site consists of very soft ground overlying a much harder stratum, the tank will normally be supported on piles. In general, the piles will all be vertical. The floor stretches (radial deformations) and the bottom of the wall may move outwards reducing the restraint. Practically in such cases, the bottom of the wall should not be considered as fixed (fully restraint). Loss of restraint should be accounted for while determining the internal forces developed.

The continuity analysis method gives exact results considering the restraint/end conditions at the base of the wall.

R. J. Vishwakarma (✉)

Department of Civil Engineering, Malaviya National Institute of Technology, Jaipur, India
e-mail: rameshwar.ce@mnit.ac.in

R. K. Ingle

Department of Applied Mechanics, Visvesvaraya National Institute of Technology, Nagpur, India
e-mail: rkingle@apm.vnit.ac.in

2 Analysis Procedure

Pure membrane state of stress is not possible in actual practice and the edge displacements are actually restrained. This gives rise to secondary stresses in the form of moments and hoop stresses.

In practice, the base of a tank is not always rigid and may undergo angular deformations at the edges. In some cases, even radial deformations are possible. The same is the case with the roof of the tank. The extent of angular and radial deformations occurring at the ends of the wall will influence the hoop tensions and moments in the wall at various levels.

Analysis of the container can be done using methods like membrane analysis, IS code method, finite element method and continuity analysis. In this paper continuity analysis and finite element analysis are done to obtain the response of the container for hydrostatic pressure.

If T is the hoop force per unit height of the wall, caused at any depth ' h ' below the top, it will give rise to horizontal radial inward forces on the wall equal to T/R [3]. Let $P_h = T/R$ and y be the net outward deflection at any point at a depth ' h '.

Where, t is the uniform thickness of the wall, E is the modulus of elasticity of concrete, R is the radius of the tank wall, H is the total height of the wall, and w is the density of water.

$$T = \frac{yE}{R}t$$

$$P_h = \frac{T}{R} = \frac{yEt}{R^2}$$

In the beam, the relation between load and its deflection is given by

$$\frac{yEt}{R^2} + EI \frac{d^4y}{dh^4} = wh$$

$$\text{If } \mu^4 = \frac{t}{4R^2I}$$

$$\frac{d^4y}{dh^4} + 4\mu^4y = \frac{wh}{EI}$$

This is a differential equation whose general solution can be obtained by finding the complementary function and particular integral.

$$y = \frac{wh}{4EI\mu^4} + \{e^{\mu h}[A\sin\mu h + B\cos\mu h] + e^{-\mu h}[C\sin\mu h + D\cos\mu h]\} \quad (1)$$

For complete restraint, we know the deflection of the wall at the base $y = 0$, i.e., at $h = H$

$$\frac{wH}{4EI\mu^4} + \{e^{\mu H}[Asin\mu H + Bcos\mu H] + e^{-\mu H}[Csin\mu H + Dcos\mu H]\} = 0 \quad (2)$$

$$\frac{wH}{4EI\mu^4} = \frac{wHR^2}{Et}as\mu^4 = \frac{t}{4R^2I}$$

wHR^2/Et is the amount by which the base of the wall would move outwards if it had a frictionless sliding joint. The term $wh/4EI\mu^4$ in Eq. (1) is the equation of the 'free stretch' line and the term in the curly brackets is the amount by which the shape curve of the wall departs from the free stretch line.

In this case, it is assumed that the upper end of the wall is free and the base of the wall is not completely restraint (i.e., there is no 100% fixity).

As the top of the wall is free, the bending moment and shear force will be zero.

Hence at $h = 0$, $(d^2y)/(dh^2) = 0$ and $(d^3y)/(dh^3) = 0$.

We get $C = A$ and $D = B - 2A$.

Here 'C' and 'D' are eliminated in terms of A and B. Now, apply the boundary conditions at the base of the wall to find the values of A and B.

At bottom of the wall, the slope will be zero and there will be some outward deflection at the base of the container wall. The effective restraint is P%.

Hence yielding at the base will be $y = \frac{(100-P)wh}{100 \times 4EI\mu^4}$ at $h = H$

$$y = \frac{(100-P)wH}{100 \times 4EI\mu^4} = \frac{wH}{4EI\mu^4} + A(e^{\mu H} \sin \mu H + e^{-\mu H} \sin \mu H - 2e^{-\mu H} \cos \mu H) + B(e^{\mu H} \cos \mu H + e^{-\mu H} \cos \mu H) \quad (3)$$

$$0 = \frac{PwH}{400EI\mu^4} + A(e^{\mu H} \sin \mu H + e^{-\mu H} \sin \mu H - 2e^{-\mu H} \cos \mu H) + B(e^{\mu H} \cos \mu H + e^{-\mu H} \cos \mu H) \quad (4)$$

As slope at the base is zero at $h = H$, $\frac{dy}{dh} = 0$

$$\frac{dy}{dh} = 0 = \frac{w}{4EI\mu^4} + A[\mu e^{\mu H}(\sin \mu H + \cos \mu H) + \mu e^{-\mu H}(\sin \mu H + 3 \cos \mu H)] + B[\mu e^{\mu H}(\cos \mu H - \sin \mu H) - \mu e^{-\mu H}(\sin \mu H + \cos \mu H)] \quad (5)$$

Now, Eqs. 4 and 5 are two linear simultaneous equations with A and B unknown only. Solving these equations, we get all the constants of the equation and can calculate hoop tension, vertical moment and shear force throughout the height of the wall using the following equations:

$$\text{Hoop Tension } (N_{\theta}) = \frac{yEt}{R}$$

$$\text{Vertical Moment } (M) = -EI \frac{d^2y}{dh^2}$$

$$\text{Shear Force } (V) = EI \frac{d^3y}{dh^3}$$

3 Validation of Analysis Results

A finite element model is developed to obtain internal forces. Shell element [4–9] is used to model container walls in SAP 2000 software. Hydrostatic pressure is applied as a surface load from inside of the container wall. Results obtained from continuity analysis are verified using finite element results for different restraint conditions at the base of the wall. Figures 1 and 2 show that the results obtained by continuity analysis are in good agreement with the results obtained from the finite element model with the same conditions.

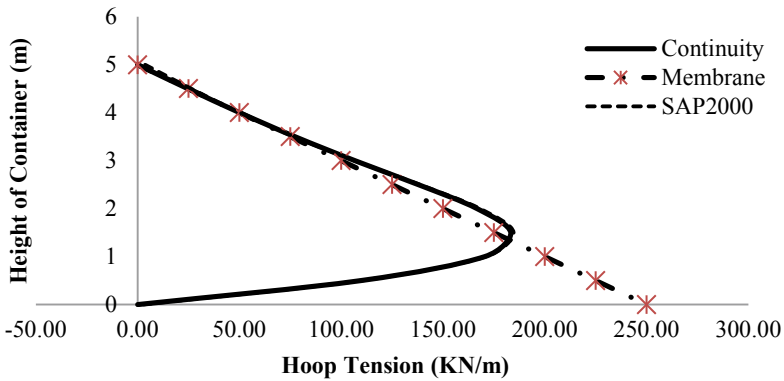


Fig. 1 Hoop tension developed in the container wall

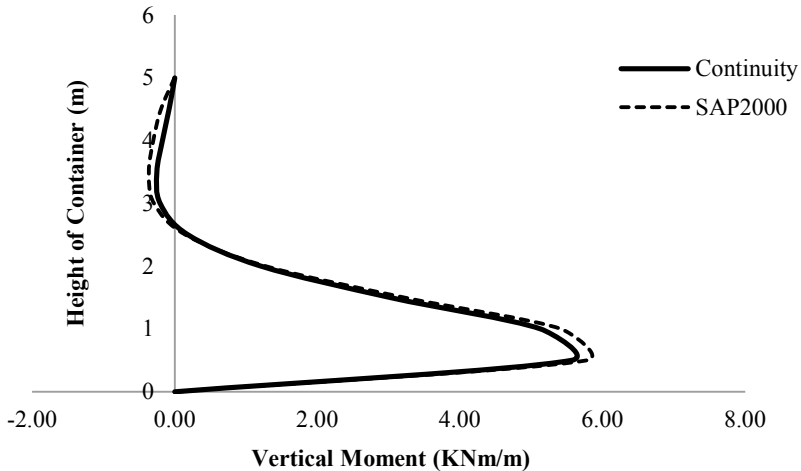


Fig. 2 Vertical moment developed in the container wall

4 Results and Discussion

To study the effect of the release of restraint in the cylindrical container, different containers are considered and the results obtained are compared.

A cylindrical container having 10 m diameter, 2 m height, 0.2 m thickness with only 75% effective lateral restraint is considered. The results obtained are given in Table 1.

Here we have $H^2/Dt = 2$ with the lateral restraint as only 75% effective; the deformed shape of the wall is as shown in Fig. 3 and the base displaces outward

Table 1 Analysis results for container with complete and 75% effective restraint

Height from the base	Complete restraint			75% Effective restraint		
	y (m)	H.T. (kN/m)	Mmt (kNm/m)	y (m)	H.T. (kN/m)	Mmt (kNm/m)
2	0.000023	22.59	0.00	0.000016	16.44	0.00
1.8	0.000025	25.00	0.08	0.000021	21.37	0.06
1.6	0.000027	27.20	0.28	0.000026	26.13	0.21
1.4	0.000029	28.72	0.54	0.000030	30.39	0.41
1.2	0.000029	28.95	0.78	0.000034	33.67	0.61
1	0.000027	27.31	0.94	0.000035	35.50	0.76
0.8	0.000023	23.45	0.91	0.000036	35.53	0.79
0.6	0.000017	17.46	0.59	0.000034	33.71	0.63
0.4	0.000010	10.12	-0.15	0.000030	30.44	0.17
0.2	0.000003	3.26	-1.45	0.000027	26.85	-0.68
0	0.000000	0.00	-3.44	0.000025	25.00	-2.04

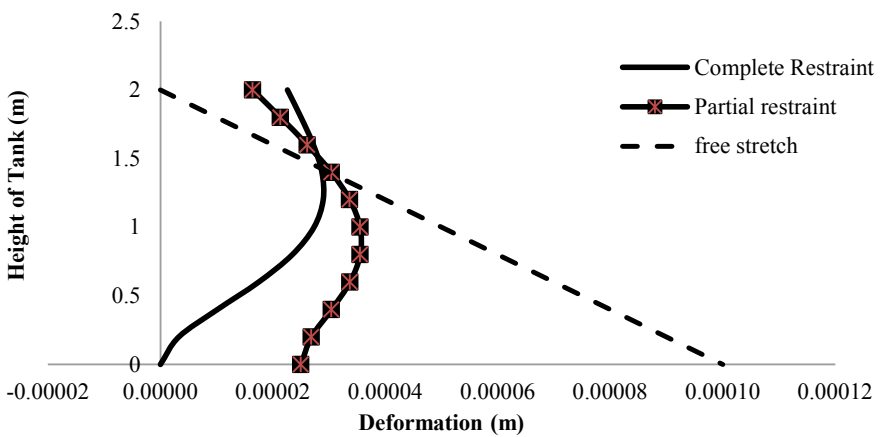


Fig. 3 Deformation in the wall for complete and 75% restraint condition

by 25%. Figure 3 also shows the shape if the restraint is complete; hence the base displacement is zero for 100% effective restraint. Figure 4 shows that reducing the effective restraint will increase the hoop tension. Figure 5 shows the corresponding vertical moments developed in the wall for both restraint conditions.

The moment at the base of the wall falls from -3.4397 kNm/m to -2.0407 kNm/m (a reduction of 40% in the moment for a loss of 25% of the restraint) and the restraint shear falls from 11.88 to 8.21 kN (a reduction of 30%).

To understand clearly the effect of the release of restraint on hoop tension and moments, one more example is considered and given below.

Cylindrical container having 10 m diameter, 5 m height, 0.25 m thickness. $H^2/Dt = 10$ for this case.

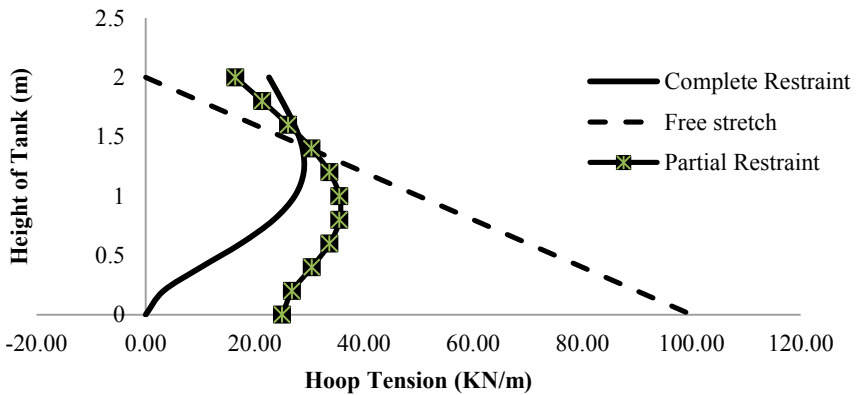


Fig. 4 Hoop tension in wall for complete and 75% restraint condition

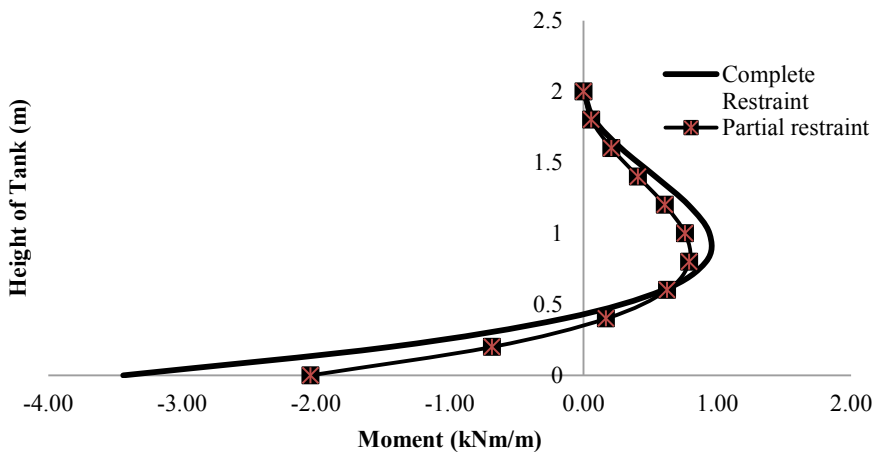


Fig. 5 Vertical moment in the wall for complete and 75% restraint condition

From Figs. 6 and 7 it can be seen that hoop tension in the middle and bottom sections of the wall increases and decreases at the top with the reduction in restraint, while vertical moment decreases with the reduction in the restraint.

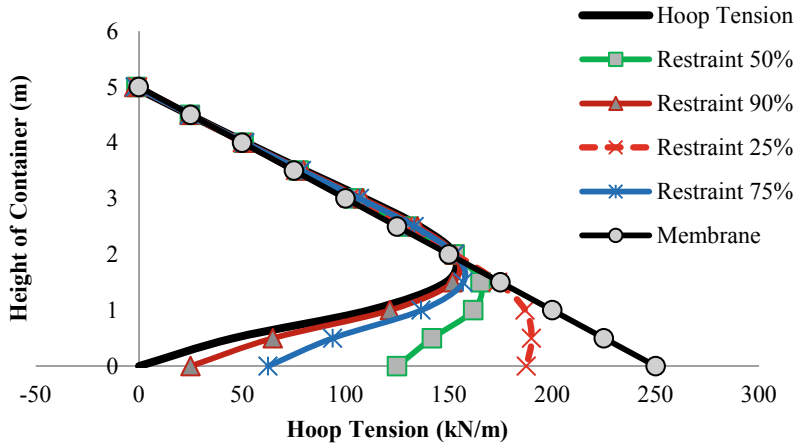


Fig. 6 Hoop tension in the wall for different restraint conditions

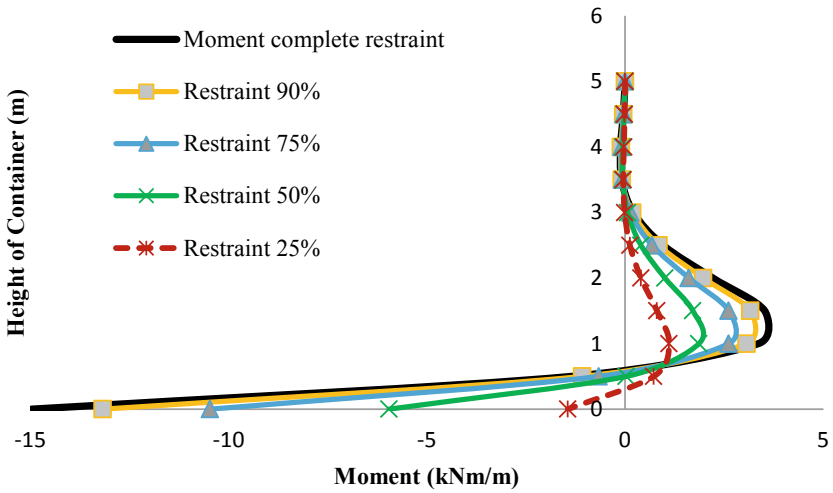


Fig. 7 Vertical moment in the wall for different restraint conditions

5 Conclusion and Recommendation

This study represents the analysis results for containers with uniform wall thickness subjected to water pressure with loss of restraint at the base. The following broad conclusions and recommendations are made:

- Loss of restraint should be taken into account while designing the container because a large amount of variation in hoop tension as well as in vertical moments can be seen.
- Exact analysis will also help to provide the correct amount of reinforcement at the appropriate location. This will ensure the economy as well as the safety of the structure.
- Membrane analysis does not take into account the effect of restraint, therefore should not be used where continuity analysis or finite element analysis is possible.

References

1. IS 3370 Part IV, Code of practice for concrete structures for the storage of liquids. (Bureau of Indian Standards, New Delhi, 1967)
2. W. Domel, A.B. Gogate, Circular concrete tanks without prestressing. (Portland Cement Association, Skokie, Illinois, 1993)
3. J. Krishna, O.P. Jain, Plain and reinforced concrete, vol. 2. (Nem Chand and Bros, Roorkee, India, 1980)
4. R.J. Vishwakarma, R.K. Ingle, Effect of panel size and radius of relative stiffness on critical stresses in concrete pavement. Arab J Sci Eng **43**(10), 5677–5687 (2018). <https://doi.org/10.1007/s13369-018-3308-x>
5. R.J. Vishwakarma, R.K. Ingle, Simplified approach for the evaluation of critical stresses in concrete pavement. Struct. Eng. Mech. **61**(3), 389–396 (2017). <https://doi.org/10.12989/sem.2017.61.3.389>
6. R.J. Vishwakarma, R.K. Ingle, Effect of non-uniform soil subgrade on critical stresses in concrete pavement, in *Transportation Research* (Springer Singapore, 2020), pp. 805–817. doi:https://doi.org/10.1007/978-981-32-9042-6_64
7. R.J. Vishwakarma, R.K. Ingle, Observations on evaluation of flexural stresses in rigid pavement. Indian Highw. Indian Road Cong. **46**(4), 29–37 (2018)
8. S.B. Magade, R.K. Ingle, Influence of clear edge distance and spacing of piles on failure of pile cap. Iran J Sci Technol Trans Civ Eng (2019). <https://doi.org/10.1007/s40996-019-00285-9>
9. S.B. Magade, R.K. Ingle, Numerical method for analysis and design of isolated square footing under concentric loading. Int J Adv Struct Eng **11**, 9–20 (2019). <https://doi.org/10.1007/s40091-018-0211-3>

A Study on Behavior of Reinforced Concrete Exterior Beam-Column Joint: A Literature Review



Yogesh Narayan Sonawane and Shailendrakumar D. Dubey

1 Introduction

1.1 Beam-Column Joint

In the RC frame structure, the beam-column joint is a really complicated and vulnerable zone, where the beam and column elements meet in all three directions [1]. Such a joint always confirms the continuation of structure and transfer various forces that are induced at the end of all structural members. In earthquake-prone regions, buildings are to be designed in such a way that reduces the damages after the earthquake. The structural behavior of RC moment-resisting frame structure in the latest earthquake around the world has emphasized the performance of the beam-column joints [2]. Therefore in the RC framed structure, such beam-column joint should be designed and constructed to resist earthquake effects. Over the last few decades, the research on the reinforced concrete beam-column joints has been focused on their seismic behavior, because such joints are a major source of energy dissipation. So proper design should be required. If not properly designed, they may experience an excessive reduction of both strength and stiffness due to load reversal. In India, traditional separation structural steel and reinforced concrete construction practice does not effectively modify the design guidelines for seismic beam-column joints. The current seismic method is more useful than the capacity design method where the beam-column joint and its associated connecting system are recommended for sustainable performance [3]. During an earthquake, the overall response of the RC

Y. N. Sonawane (✉)
Research Scholar, KBCNMU, Jalgaon, India

S. D. Dubey
SSVPS, Dhule, India

KBCNMU, Jalgaon, India

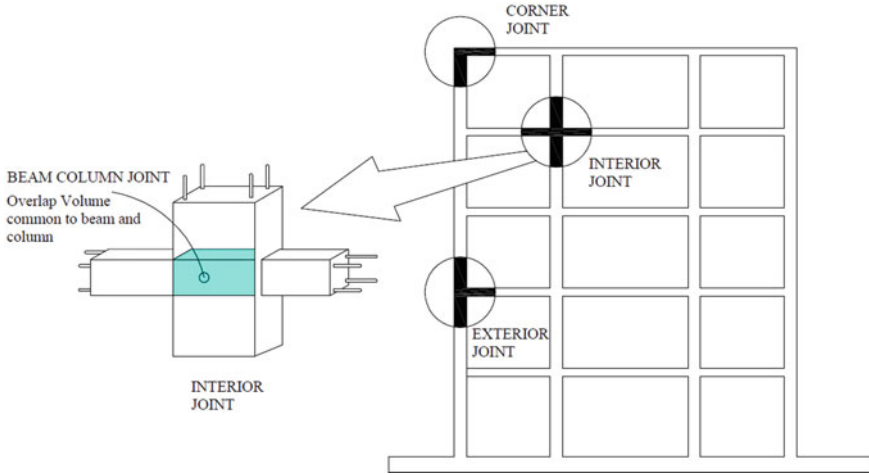


Fig. 1 Beam-column joints are a critical part of a reinforced framed structure

framed structure is mainly controlled by the behavior of its joints. The beam-column joints of a non-seismic detailed structure are weakest in the earthquake as compared to the joints of a seismically detailed RC framed structure. It has been most recognized that the deficiency of these beam-column joints is mainly created by insufficient transverse reinforcement and anchorage capacity in the beam-column joints. As a result of lack of reinforcement details, constituent materials have partial strength, resulting in an inadequate structural performance with joints having limited force-carrying capacity even under moderate earthquake (Fig. 1).

1.2 Classification of RC Beam-Column Joint

In an RC moment-resisting structure, majorly three types of beam-column joint can be recognized, which are exterior, interior, and corner joint, as shown in Fig. 2. According to ACI 352 R-02, the classification of the beam-column joint based on various loading conditions are Type-1 and Type-2. A Type-1 beam-column joint is made of a member designed to satisfy ACI 318-02 strength requirement for a member without significant inelastic deformation, i.e., without considering special ductility requirement. Type-1 design is for resisting gravity load and normal wind load.

In another Type-2 connection, frame members are designed to maintain a constant strength under structural deformation reversal into the inelastic range. This joint is specially designed to resist lateral load due to earthquake, blast, and cyclonic windfall [4].

In RC moment-resisting frames, basically, three joints are classified into: (i) Interior B-C joint, (ii) Exterior B-C joint, and (iii) Corner B-C joint.

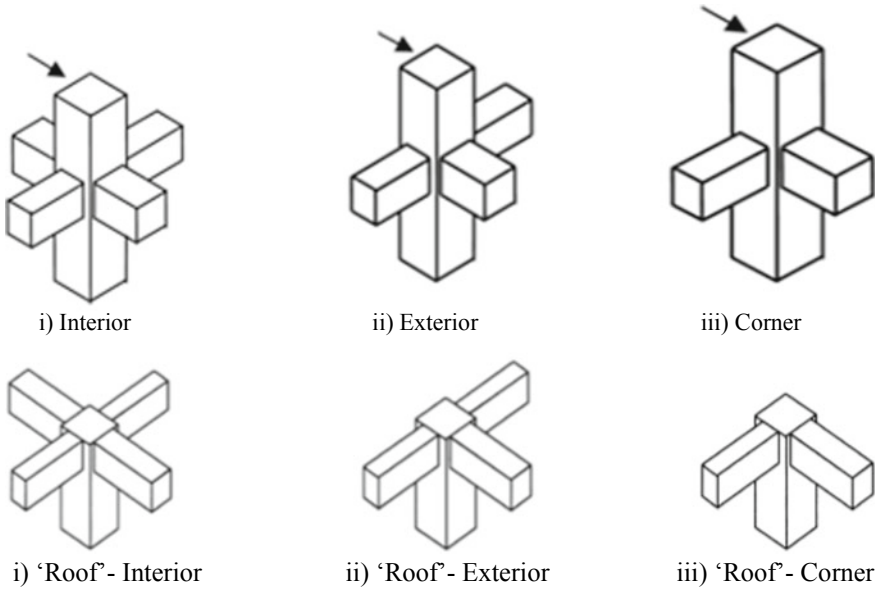


Fig. 2 Classification of joints in moment-resisting frame structure (Source: ACI-352R-02) [4, 5]

The researchers are majorly concerned about the following three things about the behavior of beam-column joints:

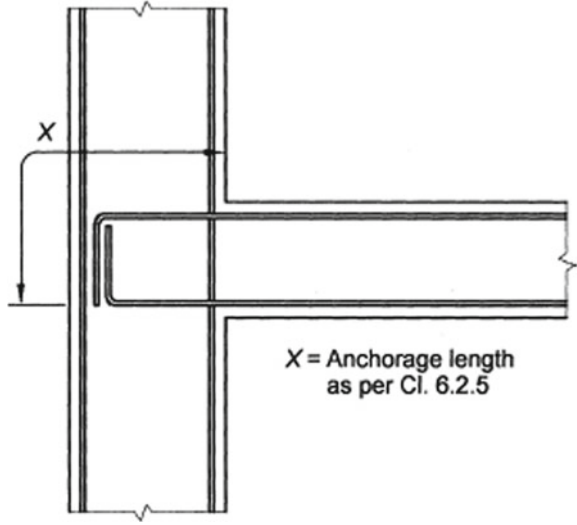
1. Deformation due to joint seismic behavior.
2. Joint shear demand.
3. Joint shear capacity.

To fulfill the above joint requirement, the anchorage mechanism plays a significant role to enhance the performance of the beam-column joint under earthquake. There are many papers related to the behavior of beam-column joints under various loading patterns published in many journals and conferences around the world. Below we will focus the literature review on beam-column joints under various broad sections such as review of codes, the performance of joint under static, seismic loading, various anchorage mechanisms, etc. for easy understanding of the research purpose.

1.3 Review of Codes

In India, the Indian standard code does not include the required recommendations on reinforced beam-column joints. If such a joint is not designed and detailed properly it may cause failure due to the overturning of forces in the beam-column joint throughout an earthquake. The IS 1893: Part 1—5th revision has brought more than

Fig. 3 Anchorage of beam bar at the exterior beam-column joint (IS 13920:2016)



50% of the entire country under moderate and severe zone [6]. Therefore reinforcement detailing of joints assumes more importance. But unfortunately, specific guidelines for designing beam-column joint are not clearly mentioned in the Indian code of practice (i.e. IS 456:2000 and IS 13920:1993). We have many standard codes associated with the beam-column joints, and they are IS 13920:2016, ACI 352–2002, ACI 318.2011, NZS 3101:2006, EN 1998:2003, etc.

Anchorage: At exterior beam-column joints

As per IS 13920:2016, Cl. No 6.2.5, at the exterior beam-column joint, the upper and lower bars of the beam shall be provided with a length of anchorage outside the inner face of the column, which is always equal to the development length tension plus 10d minus the grant for 90° bend (refer Fig. 3).

Design: Beam-column joint for distortional shear

Shear strength of concrete in joint: As per IS 13920:2016, Clause No. 9.1.1, in beam-column joint the nominal shear strength τ_{jc} of concrete shall be taken as.

$$\tau_{jc} = \begin{cases} 1.5 A_{ej} \sqrt{f_{ck}} & \text{For joints confirmed by beams on all four faces} \\ 1.2 A_{ej} \sqrt{f_{ck}} & \text{For joints confirmed by beams on all three faces} \\ 1.0 A_{ej} \sqrt{f_{ck}} & \text{For other joints} \end{cases}$$

where A_{ej} = effective shear area of beam-column joint by $b_j w_j$

b_j = effective breadth of joint perpendicular to the direction of shear force; and

w_j = effective breadth of the joint along the direction of shear force.

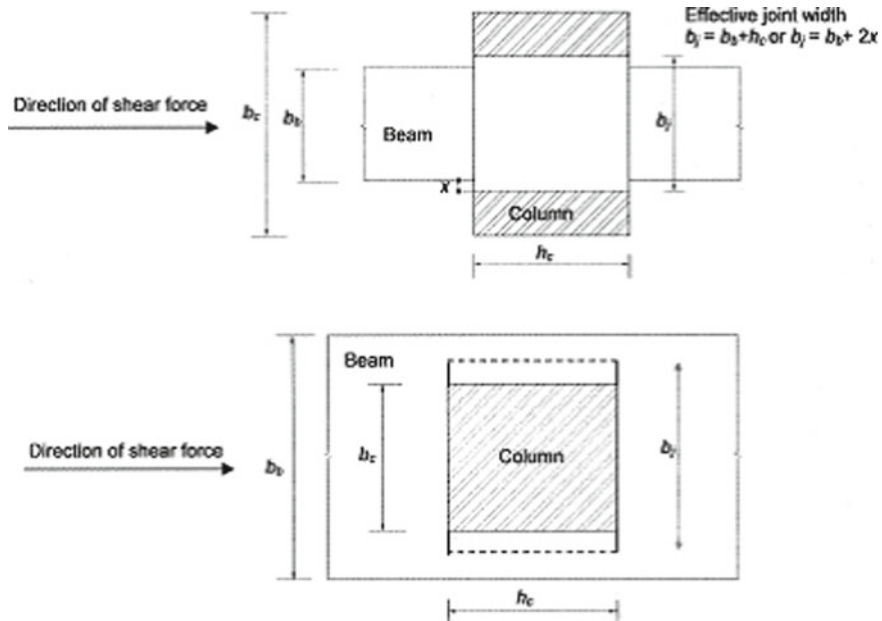


Fig. 4 Plan of effective breadth and width of beam-column joint (IS13920:2016) [7]

The effective depth of joint b_j shall be obtained from the following (refer Fig. 4):
 $\min [b_b : b_c + 0.5 h_c]$ if $b_c < b_b$.

where

b_b = width of the beam

b_c = width of the column and

h_c = depth of column in considered direction.

The width of B-C joint: If the beam tension reinforcement is extended by the beam-column joint, the size of the minimum width parallel to the beam will be 20 times the largest longitudinal beam bar diameter [7] (Fig. 5).

1.4 Exterior Beam-Column Joint

In the exterior beam-column joint, the bond failure is commencing and progresses toward the joint core at the face of the column due to yield penetration and splitting crack after a few cycles of inelastic loading. Due to the gradual loss of bond, the longitudinal reinforcement bar will be pulled out if a straightened bond. Failing to pull out of the longitudinal bars, the bond results in a complete loss due to flexural strength. This type of failure under any circumstances is not acceptable, therefore appropriate anchorage assemblage of beam longitudinal reinforcement bar in a beam-column

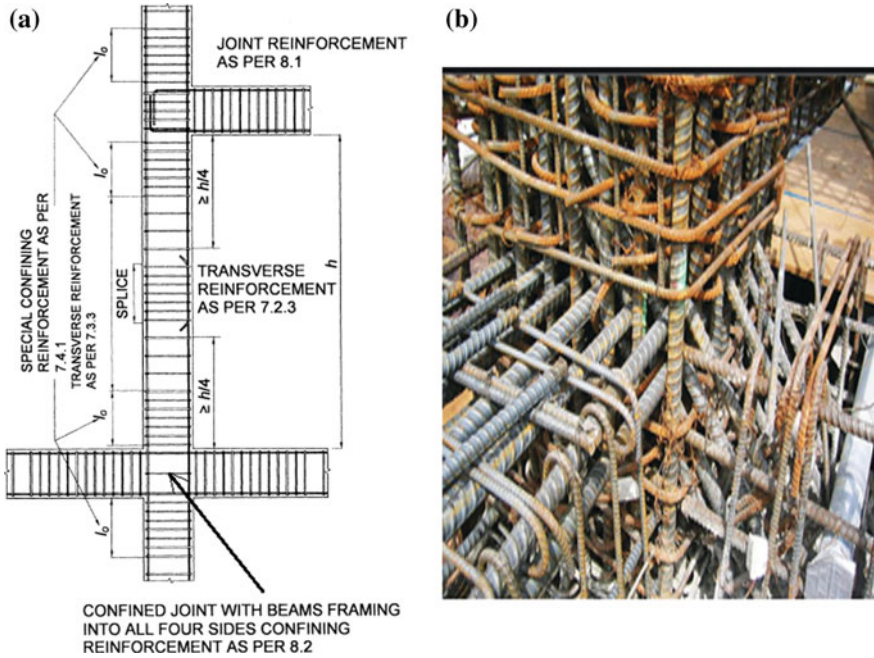


Fig. 5 a Typical ductile detailing IS 13920-2016 [7]. b Reinforcement steel congestion at beam-column joint

joint is of greatest importance. This failure (pull out) of a bar in an exterior beam-column joint can be achieved by making hooks for the bar or by providing beam-column anchorage. Hooks are always required in achieving satisfactory anchorage (Fig. 6).

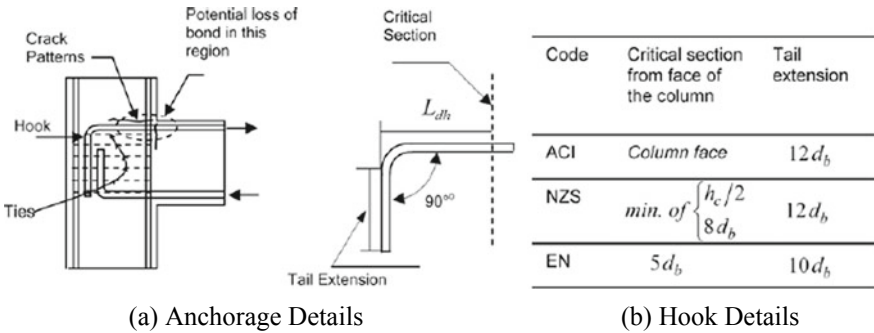


Fig. 6 Details of exterior joint [8]

Forces acting on the exterior beam-column joint. In the beam-column core region, shear and flexural stresses are performed simultaneously. The design of the beam-column joint is frequently controlled by the shear force. At the joint of a building frame structure, moments, and shear forces are generated, and stress resultant at the faces of the beam-column joint core is introduced (Fig. 7). To resist a large amount of lateral loads without occurring severe damages, the building needs strength and energy dissipation capacity. It is very uneconomical to design RC framed structure for the highest probable earthquake ground motion with no damages.

The symbols that refer to stress resultant are:

C_c = Compression in the concrete.

C_s = Compression in the reinforcement.

T = Tension force in reinforcement.

V = Sum of shear stress.

In the panel zone of the above joint (Fig. 8a) from the position of stress resultant, it is obvious that compression stresses (f_c) and diagonal tension (f_t) are induced. The ultimate capacity of adjoining members develops when diagonal stresses can be high and may cause extensive cracks. The intensity of diagonal tension is affected by the magnitude of flexural steel and the axial compression load on the column [10] (Fig. 9).

Failure mechanism of joint. The beam-column joint has several possible failure modes such as:

1. Failure of the beam plastic hinges adjacent to the joint through shear and flexure.
2. Shear failure.
3. Bond failure of the longitudinal reinforcement in beam.

In the seismic design philosophy of RC framed structure, the structural beam-column joint is designed on the concept of a strong column and weak beam. It means that moment in the beam and moment in the column ends, i.e., M_b and M_c , respectively, at the node should satisfy the equation $M_c > M_b$ [11]. The joint behavior shows the composite relation between the bond and the shear [12].

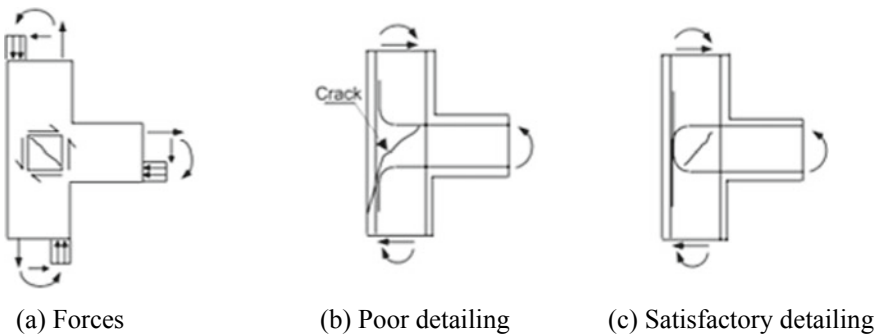
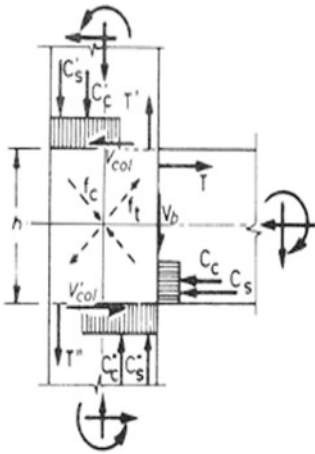
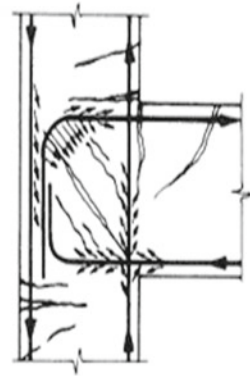


Fig. 7 Reinforcement detail at the exterior joint [9]



(Forces acting on panel zone)
(a) Stress resultants



(Steel and bond forces)
(b) patterns of crack and bond forces

Fig. 8 Forces acting at the exterior B-C joint

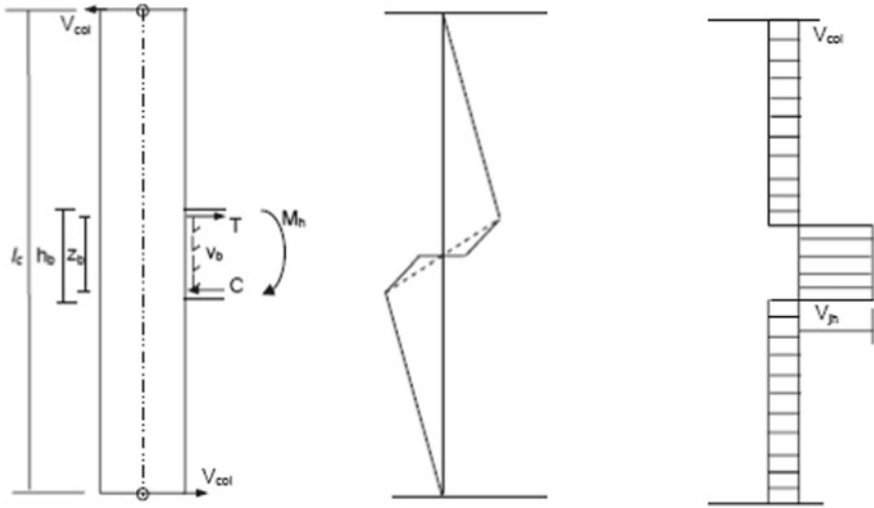


Fig. 9 Horizontal shear in an exterior beam-column joint [11]

Bond strength of beam-column joint. In terms of stability of the whole structure, the least serious of these is a bond failure. This failure mode reduces the strength and stiffness of the beam; therefore the beam may prefer the failure mode. The longitudinal bar of the beam-column joint requires a sufficient length of development. So the overall size of the beam-column joint decides on the requirement of the bond [8].

Shear force on the joint. Due to some external forces which are acting on the face of the B-C joint, high shear stresses are developed within that joint. Wide cracking occurs inside the joint under load reversal conditions, disturbing its stiffness, strength, and overall performance; hence such joint becomes flexible and is sufficient to experience considerable shear deformation. It is essential to determine the shear force in the horizontal and vertical directions.

Shear force is an exterior joint

Figure 8 shows features of the exterior beam-column joint. The horizontal shear force and column shear in the joint can be calculated on the basis of equilibrium principles.

The column shear force is

$$V_{col} = \frac{T_b Z_b + V_b \frac{h_c}{2}}{l_c}$$

and the horizontal shear across the beam-column joint can be expressed as

$$V_{jh} = V_{col} \left(\frac{l_c}{Z_b} - 1 \right) - V_b \left(\frac{h_c}{2Z_b} \right)$$

2 Concluding Remarks

A review of the existing literature shows that beam-column joint needs special attention with respect to its reinforcement detailing with proper anchorage systems. The important source of failure of the beam-column joint is a large amount of shear force experienced at the juncture. Indian standard code IS 13920 is quiet on many crucial concerns related to the essential design of RC beam-column joints under earthquake loading which does not include the required recommendations on reinforced beam-column joints. If such a joint is not designed and detailed properly it may cause failure due to the overturning forces in the joint throughout an earthquake. Although there is a special need for extending research in this area to determine the alterations in the research findings, it is required to incorporate some provisions in the Indian code. The mechanisms in a joint efficiency with respect to shear and bond are also revived.

References

1. A.K. Kaliluthin, Dr.S. Kothandaraman, T.S. Suhail Ahamed, A review on behavior of reinforced concrete beam-column joint. *Int. J. Innov. Res. Sci. Eng. Technol.* 3(4), 11299-11312 (2014)
2. P. Rajaram, A. Murugesan, Experimental study on behaviour of interior RC beam column joints subjected to cyclic loading. *Int. J. Appl. Eng. Res. Didigul* 1(1), 49–59 (2010)

3. K. Padmanabham, Dr. K. Rambabu, Design and improvement aspects of reinforced concrete beam-column joint under seismic condition. *Int. Res. Eng. Technol. (IRJET)* **05**(8), 176–184 (2018)
4. American Concrete Institute (ACI), Building code requirements for structural concrete and commentary. ACI 318–95. (Farmington Hills, Mich, 1985)
5. ACI-ASCE Committee 352R-02, Recommendations for design of beam-column connections in monolithic reinforced concrete structure
6. N. Subramanian, D.S. Parakash Rao, Seismic design of joints in RC structure-A review. *Indian Conc. J.* 883–892 (2003)
7. IS 13290:2016, Ductile Design and detailing of reinforced concrete structures subjected to seismic forces- code of practice (First Revision), BIS 2016
8. S.R. Uma, S.K. Jain, Seismic design of beam–column joints in RC moment resisting fraomes— review of codes. *Struct. Eng. Mech.* **23**(5), 579–597 (2006)
9. Dr.S.R. Uma, Prof. A. Meher Prasad, Seismic behavior of beam column joints in reinforced concrete moment resisting frames, IITK-GSDMA-EQ31-V1.0
10. T. Pauley, R. Park, Reinforced concrete beam-column joint under seismic action. *ACI J.* 585–593 (1978)
11. M.M. Ali Irfani, A Vimala, Collapse mechanism of strong column weak beam buildings of varying height. *Int. J. Eng. Adv. Technol. (IJEAT)* **9**(1) ISSN: 2249–8958 (2019)
12. H. Shiohara, New model for shear failure of RC interior beam-column connections. *J. Struct. Eng.* **127**, 152–160 (2001)
13. K. Bindu, R.P.M. Sukumar, K.P. Jaya, Performance of exterior beam-column joint under seismic type loading. *ISET J. Earthq. Technol.* **46**(02), 47–64 (2009)
14. IS 13290:1993, Ductile design and detailing of reinforced concrete structures subjected to seismic forces- code of practice
15. IS 1893 (Part 1):2016, Criteria for earthquake Resistant design of structures (Sixth Revision)”, BIS 2016
16. P.D. Dhake, H.S. Patil, Y.D. Patil, Role of hoops on seismic performance of reinforced concrete joints. *Struct. Build.* **168**(10), 708–717 (2015)
17. K.R. Siva Chidambaram, Comparative study on behaviour of reinforced concrete beam-column joint with reference to anchorage detailing. *JCER* (2012)

Encouragement of Magnetic Treated Grey Water in High-Strength Concrete



E. Prabakaran, M. Nithya, Jessy Rooby, and A. Vijayakumar

1 Introduction

The number of supplementary materials produced in developing countries increases day by day for energy production and other activities. Infrastructural development becomes important for a nation to ensure its living condition for its citizens. As a part of industrial growth and infrastructural growth in a vertical manner, the need for high-strength concrete comes as a necessary one in urban areas. Concrete utilization per person increases day by day and leads to greenhouse gases. In high-strength concrete making the utilization of super-plasticizer or water reduction agents plays a vital role to give an impact on strength parameters [1]. The rate of urbanization increased 34% in India and 1.82% worldwide, which leads to environmental pollution. The rate of consumption of water for the construction industry increased day by day and the virtual water for construction influenced the GDP of the nation.

E. Prabakaran (✉)

Department of Civil Engineering, Dr. N.G.P Institute of Technology, Coimbatore, India

M. Nithya

Department of Civil Engineering, Kakinada Institute of Technological Sciences,
Ramachandrapuram, Kakinada, India

J. Rooby

Department of Civil Engineering, Hindustan Institute of Science and Technology, Chennai, India

A. Vijayakumar

Department of Civil Engineering, GMR Institute of Technology, Rajam, Andhra Pradesh, India

2 Magnetic Water

The magnetic field can change the ion arrangement in the water and the clustered water molecules become aligned and produce more bond strength. The molecular arrangement of water after magnetization of the hydrogen ions and oxygen ions come in a linear way [2, 3]. The water passed through electromagnetic force (EMF) improves the bond between hydrogen ions, and the relative resistivity is also improved. The EMF value can improve the pH value due to ion rearrangement. The hardness of water is reduced by magnetic treatment [4]. The term magnetization does not mean that water will attract magnetic elements; instead, it is the fact that when water is subject to the magnetic field it produces either a permanent magnet or an electromagnet for a specific duration. The water molecules get reoriented in much more minor size [5]. The water molecules have a bond angle of 104° , bulkier in size, which when magnetized get reduced to a smaller angle and make them more soluble and efficient [6]. The magnetized field will be perpendicular to the orientation of water molecules; thus this helps to de-clutter the large cluster into smaller groups of molecules [7].

3 Materials and Methodology

The high-strength concrete (M50) is produced with and without the use of grey water by using fly ash with various magnetic field intensities. OPC 53 grade cement is used with a specific gravity of 3.14 [8]. M-sand is used as a fine aggregate with a specific gravity of 2.61. Coarse aggregate has a specific gravity of 2.65. The grey water was collected and allowed for aeration taken. The collected normal water and treated grey water properties are shown in Table 1. The magnetic setup is prepared with disk magnets of N40 to produce 1.2 T magnetic strength. The magnetically treated grey water and normal magnetic water properties tested as per [9] are mentioned in Table 1. Class F fly ash from Mettur thermal power plant is collected with a specific gravity of 2.81. Concrete mix design done by using IS10262:2009 [10, 11] and mix for M50 is 0.35:1:1.404:2.90.

The concrete was tested in a fresh and hardened state to determine the variation of properties when using grey water with and without magnetic field influence.

4 Tests and Results

The samples with various proportions as shown in Table 2 are taken for the test.

- CNWa-Concrete with Nominal water.
- CF10Nwa -Fly ash concrete.
- CGWa -Nominal mix with treated water.

Table 1 Properties of grey water and normal water in a magnetic field

Properties	NW	Mag.Wa (1.2 T)	Gr. Wa	Gr.Mag.Wa (1.2 T)	Std. values (As per IS456)	Temp
pH	7.17	7.33	7.41	7.9	6.5–8	29 °C
Chlorides, mg/l	74.97	54.98	104.68	94.69	500 mg/l	
Total solids (mg/l)	0.8	0.8	1.2	0.8	–	
Turbidity (NTU)	8.1	3.6	8.2	3.3	2000 NTU	
Hardness, (mg/l)	25	21	900	85	–	
Sulphates	25	18	125	52	0–150	
Nitrates, mg/l	9.96	9.94	0.07	0.07	45 ppm	
Calcium	96	72	100	76	200 ppm	
Potassium	2.7	2.6	4	3.6	12 ppm	
Sodium	35.6	34.2	45.1	45	45 ppm	

Table 2 Slump values for different samples

Designation of samples	Slump value (mm)
CNWa	38
CF10NWa	34
CGWa	40
F10GWa	34
CF10MNWa	45
CF10MGWaa	49

- CF10GWa -Fly ash concrete with treated water.
- CF10MWa -Fly ash concrete with treated water.
- CF10MGWa -Fly ash concrete with treated magnetic water.

4.1 Fresh Concrete Properties

Slump cone test was carried out to know the plasticity of concrete for placing, and the results are shown in Table 2. The normal conventional concrete is made using super-plasticizer conplastSP430. Slump value is lower than concrete made with magnetic water. Grey water produces an equivalent slump with conplast430. The same grey water produces more slump with magnetic field influence without conplast430.

4.2 Hardened Concrete Properties

The compression test was finished affirming to IS 516–1959. All the solid examples were tried in a 2000 kN limit of the pressure testing machine. Solid 3D squares of size $150 \times 150 \times 150$ mm were tried for compressive quality. The split elasticity of solid example is tried following 7, 14 and 28 days restoring and it is given beneath the table. A cylindrical specimen is utilized to test the split elastic test. The limit of the machine is 2000 kN and the size of the example is 300 mm in stature and 150 mm in dia. The ultrasonic pulse speed test is completed to know the porosity of specimens. Tables 3 and 4 show that the results were determined for various hardened concrete properties.

Concrete with 10% fly ash replacement with normal water provides a 13% increase in compressive strength compared to conventional concrete mix [12, 13]. Concrete with treated grey water provides a 10% increase in strength compared to conventional concrete. Fly ash 10% replaced concrete with treated grey water and provides a 7% increase in strength compared with conventional concrete. Concrete with 10% fly ash replacement with magnetic water (1.2 T) provides 18% increase in compressive strength compared to the conventional concrete mix. Fly ash 10% replaced concrete with treated magnetic grey water (1.2 T) provides 20% increase in strength compared with conventional concrete.

Table 3 Compressive strength

Designation of samples	Compressive strength (MPa)		
	7 days	14 days	28 days
CNWa	37.3	42.63	53.28
CF10NWa	42.15	48.17	60.21
CGWa	41.03	46.89	58.61
F10GWa	39.91	45.61	57.02
CF10MNWa	44.01	50.30	62.88
CF10MGWa	44.76	51.15	63.94

Table 4 Split tensile strength

Designation of samples	Split tensile strength (MPa)		
	7 days	14 days	28 days
CNWa	1.98	2.83	3.16
CF10NWa	2.26	3.11	3.68
CGWa	1.69	2.54	3.39
F10GWa	2.26	2.54	3.11
CF10MNWa	1.98	2.83	3.71
CF10MGWa	1.69	2.56	3.59

Table 5 Ultrasonic pulse velocity

Designation of samples	Ultrasonic pulse velocity, (km/s)	Pulse velocity (km/s)	Approximate compressive strength (MPa)
CNWa	4.6	>4.5	Above 40
CF10NWa	4.4	>4.5	Above 40
CGWa	4.8	>4.5	Above 40
F10GWa	4.7	>4.5	Above 40
CF10MNWa	4.6	>4.5	Above 40
CF10MGWa	4.9	>4.5	Above 40

All specimens with magnetic field show improved tensile capacity of concrete. Grey water specimens show improved strength parameters compared with conventional concrete.

4.3 Quality of Concrete Through UPV

The quality of the solid relies upon the holding quality between concrete glue and total. The denser concrete produces more strength due to the maximum coverage of pores with cement paste hydration particles. Table 5 shows the more CH crystals formation due to magnetic field influence.

5 Conclusion

- The new and solidified properties of cement with attractive typical and grey water alongside fly ash as halfway substitution for concrete were acceptable.
- Higher slump can be attained through the magnetic water due to ionization that takes place in water molecules at higher magnetic intensity. Magnetic water improved the slump values and thus the workability. A 20% increase in slump is observed for 10% fly ash concrete with magnetic water and treated magnetic grey water.
- Magnetic treated water concrete in 1.2 T specimen provides a constant increase in strength behaviour compared to normal water concrete.
- Fly ash replaced concrete attains later age strength, and the maximum strength capacity is due to minimum porosity due to fly ash addition.
- Treated grey water (GW) specimen provides equal strength compared to normal water in all ages and concrete made with magnetic grey water provide the maximum strength at the 1.2 T magnetic strength.

- Porosity has reduced 35% in F20GWC with 1.2 T when compared with control concrete.

References

1. P.K. Mehta, P.M. Monteiro, Concrete: structure, properties, and materials. (Prentice Hall, 1993)
2. H. Afshin, M. Gholizadeh, N. Khorshidi, Improving mechanical properties of high strength concrete by magnetic water technology. *Sci. Iran.* **17**(1), 74–79 (2010)
3. S. Bharath, S. Subraja, P. Arun Kumar, Influence of magnetized water on concrete by replacing cement partially with copper slag. *J. Chem. Pharm. Sci.* **9**(4), 2791–2795 (2016)
4. H. Banejad, E. Abdosalehi, The effect of magnetic field on water hardness reducing, in *Thirteenth International Water Technology Conference, IWTC 13*, (Hurghada, Egypt, 2009), pp. 117–128
5. M. Gholizadeh, H. Arabshahi, The effect of magnetic water on strength parameters of concrete. *J Eng Technol Res* **3**(3), 77–81 (2011)
6. K. Laxminarayana, M. Subhan., Experimental studies on durability of magnetic water concrete. *Int. J. Res.* **04**(10), 703–717 (2017)
7. N. Su, Y.H. Wu, C.Y. Mar, Effect of magnetic water on the engineering properties of concrete containing granulated blast-furnace slag. *Cem. Concr. Res.* **30**, 599–605 (2000)
8. IS:12269–1987 Specification for 53 grade ordinary Portland cement
9. IS:3025–1986, Methods of sampling and test (physical and chemical) for water and waste water
10. IS: 456:2000, Indian Standard Code for Plain and reinforced concrete-code of practice
11. IS:10262–2009, Recommended Guidelines for concrete mix proportioning
12. E. Prbakaran, J. Robby, Experimental investigation on concrete using flyash as a partial replacement for cement with grey water in magnetic field. *Int. J. Rec. Technol. Eng. (IJRTE)* **7** (2019)
13. E. Prbakaran, J. Robby, Analysis of magnetic treatment water usage in concrete. *J. Adv. Res. Dyn. Con. Syst.* **11**(01) (2019)

Spiritual Elixir: Application of Ganga Water in Treatment of Wastewater



Monika Negi, Ayushi Maithani, and Sakshi Gupta

1 Introduction

Ganga river is known to be the firm backbone of our Indian culture and its distinctiveness. Basically, it's a junction of Mandakini, Alaknanda and Bhagirathi rivers visible in Devprayag of Uttarakhand. It originates from the Gangotri glacier in the Garhwal region of the Himalayas and ends up into the Bay of Bengal after moving through entire North India thoroughly. The Holy Ganga waters are known for the holy dip into it setting the devotees not only free from common skin diseases but also giving them long extended life [1] but the interpretations done earlier on the divinity of river also throws light on this bacteriophage's anti-microbial properties being unresponsive to a number of analytic agents [4]. These not only nullify the bacteria but also many other pathogens causing disorder in the human body functioning. This is the reason that owing to these healing properties of Ganga water it is often considered 'Spiritual Elixir', meaning giving life forever. Referring to this property of bacteriophage to remove even toxic bacteria like *Escherichia coli*, therefore, it can be even concluded that it has found applications not only for medical purposes but also in aquaculture, agricultural field and in food industries. Microbes contaminating potable water result in causing a large number of water-borne diseases, which require proper control as an initiative to enhance public health. In this work, the use of Ganga water sample containing these bacteriophages finds application in the treatment of water for improving its drinking standards due to the capability of Ganga waters to enhance the wastewater treatment in a positive way, thereby reducing the disease-causing as well as undesirable microbes present in water [3]. The Ganges water comprises the

The original version of this chapter was revised: The author group has been changed. The correction to this chapter is available at https://doi.org/10.1007/978-981-16-6879-1_70

M. Negi · A. Maithani · S. Gupta (✉)
Graphic Era (Deemed To Be University), Dehradun 248001, India
e-mail: sakshilibran@gmail.com

© The Author(s), under exclusive license to Springer Nature Singapore Pte Ltd. 2022, corrected publication 2023

M. L. Kolhe et al. (eds.), *Smart Technologies for Energy, Environment and Sustainable Development, Vol 2*, Springer Proceedings in Energy,
https://doi.org/10.1007/978-981-16-6879-1_5

largest river water body structure covering over more than five state boundaries in India, backing a population of more than 500 million and also sufficing various needs of people like industrial requirements, domestic needs, irrigation water for crops etc. But despite being a life-providing asset, certain breaking of laws led to disposal and discharge of contaminated as well as untreated industrial and municipal effluent discharges resulting not only in polluting river water system but deteriorating the quality of water. Unfortunately, these surface sources including rivers and streams are only treated as the most easily available and accessible disposal sites to dump all kinds of effluent discharges without even measuring proper disposal standards of the effluent and depreciating overall health and quality of these surface sources and as an outcome risking the sustainability of entire ecosystem [5]. Therefore today, this Holy Ganga has sadly become a highly polluted water body having not only human waste but also contaminants from effluents of wastewater treatment plants pushing the existing government authorities to initiate extensively high-budgeted projects for cleaning this Holy Ganges water, including Ganga Mahasabha and Ganga Action Plan (GAP), National River Ganga Basin Authority (NRGBA), Ganga Manthan, Ganga Programme etc. So with experimentation, we are looking into the perspective of this pathogen-resistant property of Ganga water and if it can be used as a treatment methodology further.

2 Research Done in This Field

The word 'Bacteriophage' comes from the word 'bacteria' and the Greek word 'phage' which means to feed on. Biologically bacteriophage is a kind of virus that feeds on bacteria and even has the ability to reproduce itself with time. This plays an important role and this is the main attribute of these viruses to be used for the wastewater treatment process. This treatment actually works on the dreadful actions caused by these bacteria and this has been worked upon experimentally long back in 1896 by a British bacteriologist [2]. He actually studied the microbiological properties of Ganga waters and reached the conclusion that the bacteria which are usually present in tap water causes most of the common water-borne diseases like cholera that usually die out in Ganga water. He further went on with his research and even studied the antibacterial effects of Ganga waters and even concluded that these bacteriophages cannot survive the hot temperatures as he conducted similar experiments with boiled Ganga water as well but ended into negative results. Today, this particular property of bacteriophage has taken up much popularity, and researchers across the globe are working upon it and it can be expected to provide a promising future for wastewater treatment, for sure. Also during the entire mechanism of these viruses on bacteria present in wastewater, there is absolutely zero harm to the ecosystem around [7].

During current times these bacteriophages have been put into use for uprooting these harmful contaminants and the results are highly appreciable and positive.

Removal of pests in the agricultural sector, food sectors, biotechnology, pharmaceuticals industries is all using this treatment efficiently including even treatment of infections happening due to lung diseases or any surgical wound. It has already been successfully used for treating patients suffering from dysentery as well as staphylococcal septicemia due to the anti-staphylococcal nature of these bacteriophages and therefore injecting administration is used for this treatment very effectively, thereby reducing its severity as well as in the elimination of the species of these *Staphylococcal aureus* ones from cerebrospinal fluid. Other uses include DNA transportation as well as for delivering vaccines [6].

3 Methodology Used

There has been vast and draining research done on this subject so far but what our work aimed was on looking over the use of this Ganga water as a liquid to be injected in a sample to be tested for treatment having certain colonies of bacteria for the same. For this streaking technique is used, wherein a sample of microorganism species is taken from a pure sample plate and microbiological culture is grown on a new plate along with the traces of Ganga water and study the resultant effect on colonies formed for further studies. For carrying out the experiment various samples were collected categorized as dairy wastewater from the dairy farm of Graphic Era Deemed to be University, Dehradun campus, domestic wastewater from kitchen outlets, Ganga water sample as well as municipal wastewater sample from Rispana River, Dehradun. Out of all these samples of wastewater microbiological culture was made to grow on different new plates to study the growth pattern and changes in the colonies of bacteria if any. We have used the serial dilution method which usually involves diluting a sample with a solution of different dilution factors usually in a logarithmic progression to have a good range of results. It involves developing colonies by using agar media which acts as food for bacteria on a petri plate and after colonies are grown, then a certain portion is used by using the serial dilution method to observe the nature and density of the colonies formed.

3.1 Instruments, Apparatus and Salts Used

- (a) Nutrient agar media (NAM)
- (b) EMU agar media
- (c) Autoclave
- (d) Laminar airflow
- (e) BOD incubator
- (f) Petri plates and test tubes
- (g) Micrometer and tips
- (h) Bunsen burner

- (i) Samples (domestic wastewater), (dairy wastewater), (municipal wastewater)
- (j) Ethanol

3.2 Procedure

3.2.1 Labeling of a Petri Plate for Testing

- (a) Petri plates are usually labeled on the underside.
- (b) Labeling needs to be done very carefully along the margins only so as to give enough space to observe the dish after the incubation period.
- (c) Labeling includes the date of sampling and the name of the organism.
- (d) It is very important to eradicate any water drops present in or around the petri dish by using ethanol through sterile swabs of cotton.

3.2.2 Preparation of Nutrient Agar and EMB Agar

- (a) Suspend 2.8 g of nutrient agar powder and 3.596 g of EMB agar in 100 ml of distilled water each, respectively.
- (b) This mixture is to be heated properly with proper mixing so that all the components get dissolved properly.
- (c) It is also important to preheat the autoclave before using it.
- (d) The mixture of this nutrient agar is kept in the autoclave for about 15 min at 121 °C.
- (e) After 15 min it is allowed to cool but it should be noted that it does not get solidify.
- (f) The nutrient agar is put into each dish and then these dishes are left till agar gets solidified on the same sterile surface.
- (g) The laminar airflow is switched on for about 15 min before streaking is carried out.
- (h) Before the immediate start of streaking switch off UV light.

3.2.3 Streak

- (a) Make sure your hands should be cleaned with ethanol once they enter the laminar airflow chamber.
- (b) Also note, open all autoclaved plates inside the airflow chamber only.
- (c) The wire loop is to be sterilized.
- (d) It is equally important to cool it by brushing on the corners of the sterile (agar) dish.
- (e) After that, the loop is touched one by one to the culture formed having the entire bacteria mixture.

- (f) The next process includes moving the loop on the upper one-third portion of the petri dish back and forth in a zig-zag format but the lid of the dish should be opened only sufficient for inserting of the loop.
- (g) By doing so, the loop will be having a large number of bacteria obtained from the agar's surface.
- (h) The loop has to be sterilized in the flame.
- (i) Now the petri dish having the agar is to be turned at 90° and the loop is to be dragged in a zig-zag way in the remaining half of the petri dish so that the area is the same where we have streaked earlier top one-third but without touching the earlier streaks.
- (j) Again the loop is to be sterilized in the flame.
- (k) Petri plate is again turned at 90° and the same procedure is repeated for the remaining portion of the petri dish (in a zig-zag pattern) but none of the areas which has to be streaked earlier has to be touched.
- (l) Finally, the plate is incubated for around 24 h, and after that, the isolated colonies formed can be seen on the petri dish if streaking is done properly.
- (m) Count the number of colonies over the digital colony counter.

4 Results

Table 1 showcases the bacterial colony count of samples consisting of equal volumes (5 ml each) of the original raw wastewater sample and old Ganga water sample. The mix samples were diluted for better and countable results, dilutions being performed up to 10^{-6} and thereafter incubation for 24 h was provided with these results (Fig. 1).

Here, we followed the quadrant method to count the colonies manually, by counting one quadrant colony and then multiplying it by 4. Also, it may be noted that a big colony comprises more number of bacteria than smaller ones, hence the count can be only counter-checked with a pictorial representation of experimental results obtained. Figures 2, 3, 4, 5 and 6 show the same scenario. There are two dish plates in every figure one with a raw sample of municipal discharge, dairy wastewater and domestic wastewater on the left side of the figures, respectively, and the other dish plates having raw samples and old Ganga water samples on the right side of the figures. It can be clearly observed that the dishes having old Ganga water show less number of colonies formed after the experimentation and hence a low count of bacteria. Hence it justifies the fact very well that the bacteriophage present in Ganga water has the ability to treat the bacteria present in contaminated water. It may also be noted that the results that didn't follow may be wrong due to human error pertaining to contamination in spreading of the sample over media or may be due to the inability of bacteria to thrive properly within 24 h pertaining to cold wintertime during the time of experimentation (Fig. 1). As we followed a practical approach, we assume that 83.3% turnout proves to be favoring our theoretical claim. Though the optimum results were obtained at a dilution of 10^{-5} , therefore, the figures that follow symbolize

Table 1 Bacterial count of different samples on agar and NAM (nutrient agar media) media

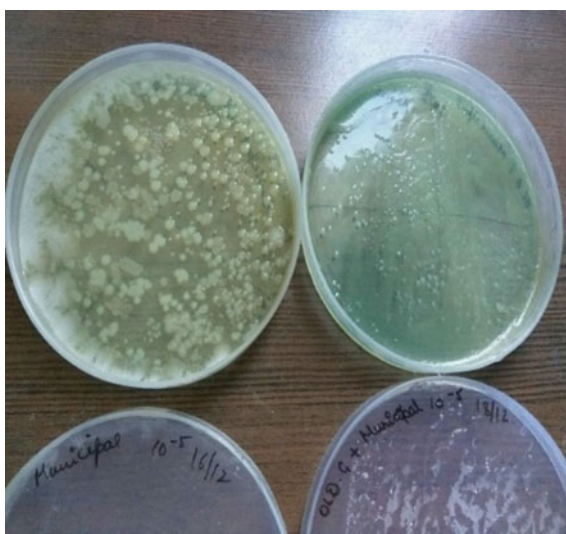
S. no	Agar Media			Common for both media		Nutrient Agar Media		
	Original sample (10 ml)	Old Ganga sample (5 ml) + Original sample (5 ml)	Remarks (follows theoretical approach)	Dilutions	Sample type	Original sample (10 ml)	Old Ganga sample (5 ml) + Original sample (5 ml)	Remarks (follows theoretical approach)
1	(63*4) + 1 Big colony	(79*4)	Follows	10 ⁻⁴	Domestic sample	(62*4)	(101*4)	Doesn't follow
2	(35*4) + Big colonies	(82*4)	Follows	10 ⁻⁵		(61*4)	(52*4)	Follows
3	(107*4)	14 + 1 Big Colony	Follows	10 ⁻⁶		(52*4)	(25*4)	Follows
4	35 + Big Colonies	(76*4)	Follows	10 ⁻⁴	Dairy sample	35	(100*4)	Doesn't follow
5	(25*4) + Big colonies	(83*4)	Follows	10 ⁻⁵		(25*4)	(17*4)	Follows
6	(30*4) + Big colonies	(70*4)	Follows	10 ⁻⁶		(30*4)	(54*4)	Follows; as smaller colonies were seen in place of original larger ones
7	99 + Big colony	(56*4)	Follows	10 ⁻⁴	Municipal sample	45 + Big colony	(62*4)	Follows
8	(107*4)	(82*4)	Follows	10 ⁻⁵		107 + Big colony	(78*4)	Follows
9	(98*4)	(81*4)	Follows	10 ⁻⁶		(17	(100*4)	Doesn't follow

robust differentiation between archaic samples and the amalgamated ones (after the addition of old Ganga water).

Fig. 1 Old Ganga +
Municipal (NAM)



Fig. 2 Old Ganga +
Municipal (Agar media)



5 Conclusion

The Ganges and many such freshwater streams which exhibit self-healing properties open up the scope for liquid filtration rather than opting for separation of bacteriophage first and then putting it to use infiltration mechanism.

With our experiments we were able to gather that out of 18 samples (nine for agar media and nine for nutrient agar media), 15 outcomes, i.e., 83.3% favored our

Fig. 3 Old Ganga + Dairy
(NAM)



Fig. 4 Old Ganga + Dairy
(Agar media)



theoretical concept which was mixing of bacteriophage-supporting Ganges waters with the selected wastewaters (from domestic, municipal and dairy sources) to get rid of hazardous *E. coli* and alike bacteria, thus enabling cogent filtration technique.

6 Suggestions for Further Scope

A varied range of opportunities could be witnessed in this field as in our research, we worked upon stale Ganga water samples which were approximately 2 years old for all tests. Therefore, tests with fresh Ganga water sample is left for exploring.

Fig. 5 Old Ganga + Domestic (NAM)



Fig. 6 Old Ganga + Domestic (Agar media)



Also, further studies could be carried out on the specifics of types of bacteria so that a higher level of filtration could be attained.

References

1. S.G. Darian, *The Ganges in myth and history*. Motilal Banarsidass Publication (2001)
2. F. D'Herelle, G.H. Smith, *The Bacteriophage, Its Role in Immunity* (Williams & Wilkins, 1922)
3. K.D. Alley, *On the banks of the Gaṅgā: when wastewater meets a sacred river*. (University of Michigan Press, 2002)
4. J. Reiss, C. Abbott, S.F. Gold, SACRED WATERS: A pilgrimage up the Ganges river to the source of Hindu culture (Book Review). *Publishers Weekly* **248**(42), 68–68 (2001)

5. D. Berwick, A walk along the Ganges. (Dennison Berwick, 1986)
6. K.P. Flint, The long-term survival of *Escherichia coli* in river water. *J. Appl. Bacteriol.* **63**(3), 261–270 (1987)
7. C.J. Beauchamp, A.M. Simao-Beaunoir, C. Beaulieu, F.P. Chalifour, Confirmation of *E. coli* among other thermotolerant coliform bacteria in paper mill effluents, wood chips screening rejects and paper sludges. *Water Res.* **40**(12), 2452–2462 (2006)

Seismic Response of Base Isolated Elevated Circular Water Tank



Tanuja Khati, Smita Kaloni, Shashi Narayan, and Chetana

1 Introduction

Water tanks are very common in India for supplying water as the water demand is not constant throughout the day. In elevated circular water tank, as the water is at certain height, the chances of failure of tank become more. The main causes of failure of water tank are shear failure in beams, column fails axially, sloshing. Sloshing is the free water movement inside the tank (Fig. 1).

In earthquake prone areas, structure can be resisted from earthquake either by increasing the mass of the structure or by decreasing the forces to be transmitted in the structure. Increasing the mass of the structure also makes the structure uneconomic. Rather than increasing the mass of the structure, base isolation takes a different approach. The purpose of base isolation technique is to decouple the structure from the ground and mitigate the acceleration transmitted to the ground. Base isolation technique makes the structure more flexible, which results in more time period than the rigid one.

Housner [5] inspected a partially filled tank as 2DOF's and empty or full tank as SDOFS. Furthermore, the water mass in the tank was divided into two parts as convective and impulsive mass.

Jadhav and Jangid [8] investigated the seismic response of water tank with and without base isolators by selecting real earthquakes. Newmark's step-by-step method was used to solve coupled differential equation. A convenient model was introduced to study the effect of base isolation technique. From the results, it was concluded that lead rubber elastomeric bearing is more effective than sliding systems in reducing the seismic responses.

Omidinasab and Shakib [10] modeled an elevated intze water tank and presented the study of dynamic behavior of tank and the effect of staging height on the analysis.

T. Khati (✉) · S. Kaloni · S. Narayan · Chetana
National Institute of Technology Uttarakhand, Srinagar 246174, India



Fig. 1 Failure of water tank

The author adopted the seven real ground motion for the linear and nonlinear time history analysis of tank. The author concluded that for nonlinear analysis as the height of staging increases, structure becomes more vulnerable to earthquake. For linear analysis, lower height is more susceptible to earthquake.

Kakkerla et al. (2016) studied the various spring-mass parameters for a circular water tank elevated by different staging heights. Hydrodynamic parameters were calculated using guidelines given by IIK-GSDMA. The nonlinear static analysis was executed so study the ductility characteristics for different staging heights.

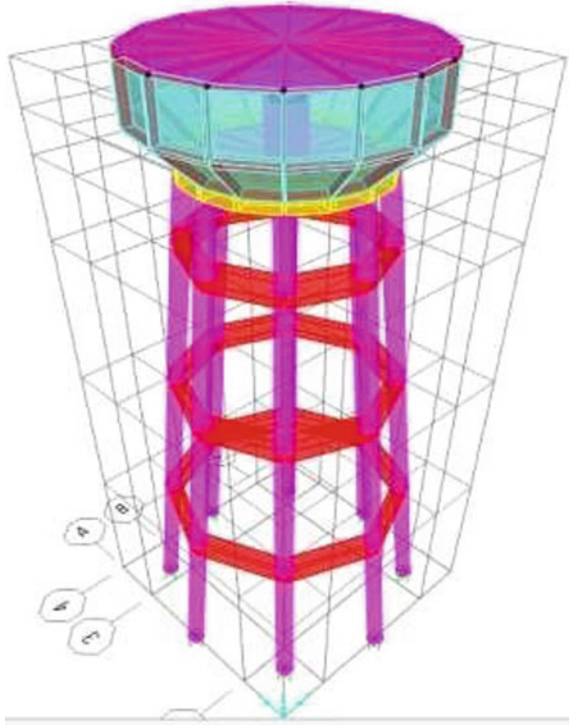
Jivani (2017) made an attempt to understand the dynamics of the elevated water tank with the variation of the height of staging for a number of different ground motions. Fluid–structure interaction has been considered. The analysis is done using SAP2000.

Nayak and Thakare [9] studied the performance of staging of the elevated water tank. The effect of bracing was considered in the study for the full and empty condition of the water tank. A nonlinear time history analysis was carried out using SAP 2000 under Uttarkashi earthquake. Results show that retrofitting technique was found to be effective in reducing the seismic response.

Hashemi and Aghashiri [4] presented the study of rectangular tank and compared the effect of two lead rubber bearings and friction pendulum bearing to isolate the tank. The author concluded that with increasing the flexibility of base isolation, base isolators perform better in reducing the seismic response.

The presented work consists of the study of dynamic analysis of elevated circular water tank, isolated by elastomeric bearing and friction pendulum bearing. The base isolators are placed at the top of staging and at the bottom of the staging. The main objectives of the study are to (a) compare the seismic response of fixed end support condition with base isolators and (b) reduce seismic response transmitted to both water tanks (Fig. 2).

Fig. 2 Elevated water tank using finite element software



2 Materials and Methods

A time history (nonlinear) analysis is performed on the elevated circular water tank. A real ground motion, Northridge earthquake 1994, is used for the dynamic analysis of water tank recorded at Simmi Valley Station of PGA (g) 0.41, of magnitude (Richter scale) 6.70. The first 24.99 s is used in the analysis. The analysis is done for empty and full tank conditions. Time period and frequency are analyzed for the water tank using modal analysis for different modes. The analysis of the water tank is done using finite element software.

3 Results and Discussions

See Table 1.

Tables 2 and 3 show the time period of fixed support conditions and base isolators at different placing of staging. Table 2 shows the decrease of time period as the mode number increases. Table 3 shows the results that time period of the water tank increases after the implementation of base isolators. Rubber isolator is found to be

Table 1 Specification of water tank

S. no.	Components	Size (mm)
1	Roof slab	120
2	Wall	250
3	Floor slab	150
4	Floor beams	400 * 600
5	Internal diameter	6000
6	Circular column (8)	450
7	Shaft	250
8	Bottom cone	300

Table 2 Elevated circular water tank with fixed support condition

Support condition	Mode1	Mode2	Mode3
Fixed	Time period (s)	Time period (s)	Time period (s)
	1.8612	1.8521	1.7512

Table 3 Elevated circular water tank with base isolators at different placing of staging

Mode no.	Base isolator	At bottom of staging	At top of staging
Mode 1	Rubber isolator	Time period (s)	Time period (s)
		2.7944	1.6302
	Friction pendulum bearing	2.0251	1.2026
Mode 2	Rubber isolator	2.7864	1.6163
	Friction pendulum bearing	2.2041	1.1274
Mode 3	Rubber isolator	2.269	1.6163
	Friction pendulum bearing	1.8412	1.0930

more effective at increasing the time period at the bottom of the staging rather than at the top of the staging. Analysis shows the residual displacement of 0.0046. Figures 3 and 4 show the comparison of base shear of elevated circular water tank with different base isolators placed at the top and bottom of staging with fixed support end condition. Results show that base isolator performs better at reducing the base shear when placed

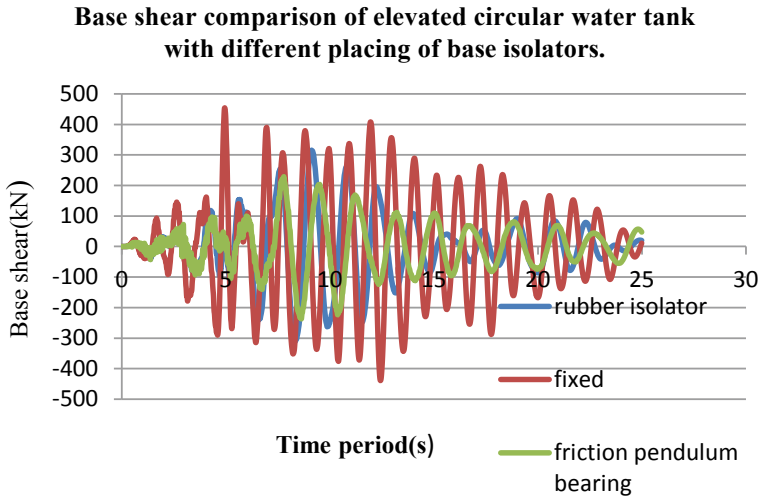


Fig. 3 Base isolators placed at top of staging

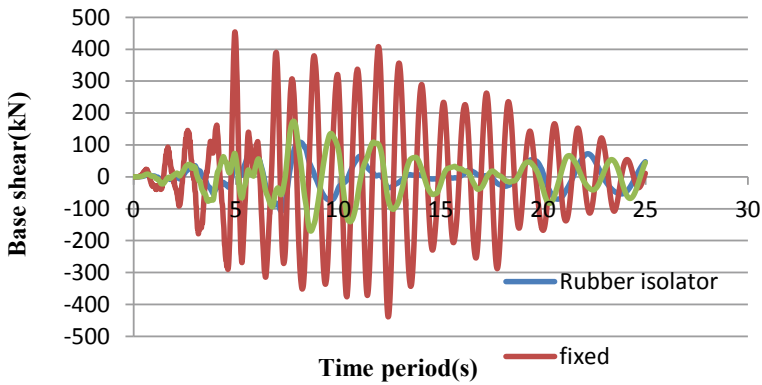


Fig. 4 Base isolators placed at bottom of staging

at the bottom of the staging rather than at top of the staging. Figures 5 and 6 show the comparison of roof displacement of different base isolators at elevated circular water tank at the top and bottom of staging with fixed support end condition. Both base isolation systems perform better at reducing the roof displacement at the top of the staging rather than at bottom of the staging. Out of the two base isolation system, friction pendulum bearing gives a better result than rubber isolator at reducing the roof displacement (Table 4).

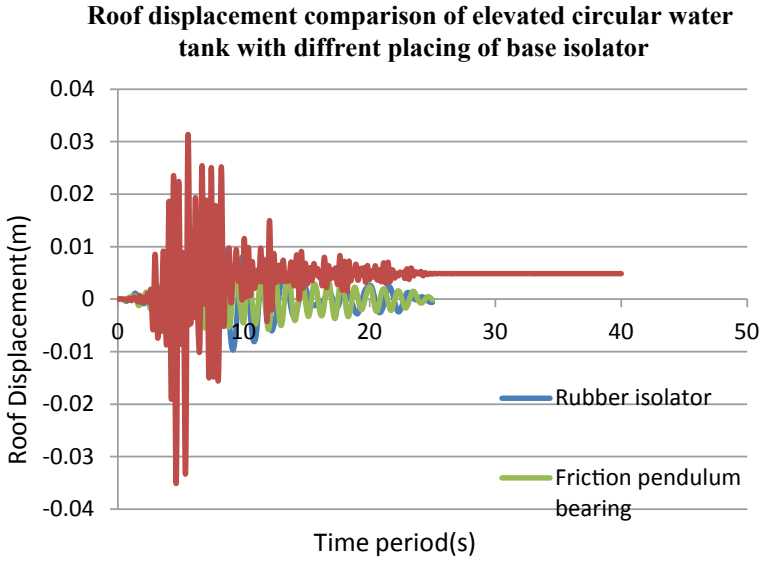


Fig. 5 Base isolators placed at top of staging

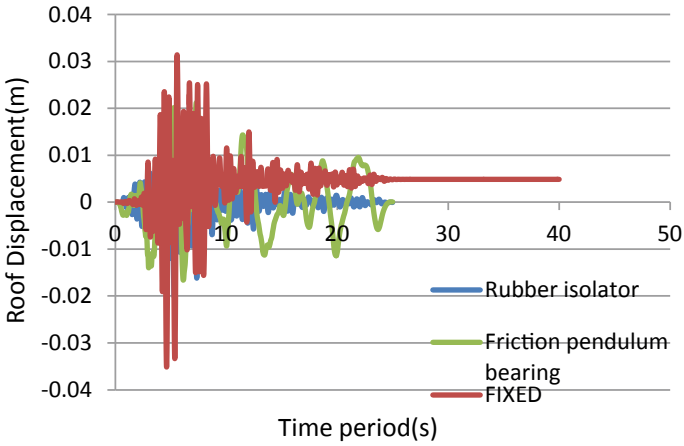


Fig. 6 Base isolators placed at bottom of staging

4 Conclusion

The following conclusion can be drawn from the results:

1. The seismic response of elevated circular water tank seems to be reduced after the implementation of base isolators. However, the effect of base isolators at

Table 4 Comparison of seismic response of different base isolators

Seismic response	At top of staging		At bottom of staging		Fixed end support
	Rubber isolator	Friction pendulum bearing	Rubber isolator	Friction pendulum bearing	
Maximum base shear (kN)	315.4521	228.6367	103.4998	179.2956	454.0278
Maximum roof displacement (m)	0.0095	0.0067	0.0181	0.0211	0.0312
Residual displacement (m)	0	0	0	0	0.0046

reduction of seismic response depends on the placing of base isolators at the water tank.

- At the bottom of staging, rubber isolator reduces the base shear 77.2%, friction pendulum bearing reduces 60.5% and at the top of the staging base isolator reduces the base shear 30.52%, friction pendulum bearing reduces 49.64%.
- At the bottom of staging, rubber isolator reduces the roof displacement 70.2%, friction pendulum bearing reduces 79.4.5% and at the top of the staging base isolator reduces the roof displacement 40.5%, friction pendulum bearing reduces 30.2%.
- Time period decreases as the mode number increases and frequency increases as the mode number increases.
- The analysis shows the residual displacement of tank for fixed support conditions.

References

- ACI 350.3, *Seismic design of liquid containing concrete structures*. (American Concrete Institute, Farmington Hill, MI, USA, 2001)
- A.C. Chougule, P.A. Chougule, S.A. Patil, Study of seismic analysis of water tank at ground level. *Int. Res. J. Eng. Technol.* **4**(7), 2895–2900 (2017)
- M.A. Gate'a, A. Atalla, Dynamic analysis of elevated tanks having various supporting frame configurations. *J. Univ. Thi-Qar* **10**(2), 1–13 (2015)
- S. Hashemi, M.H. Aghashiri, Seismic responses of base-isolated flexible rectangular fluid containers under horizontal ground motion. *Soil Dyn. Earthq. Eng.* **100**, 159–168 (2017)
- G.W. Housner, Dynamic behavior of water tanks. *Bull. Seismol. Soc. American* **53**, 381–387 (1963)
- IITK-GSDMA Guidelines for Seismic Design of Liquid Storage Tanks Provision with commentary and explanatory examples (NICEE, IIT Kanpur, 2007)
- IS 1893–2002 (Part-I) Criteria for Earthquake Resistant Design of Structure—Part-1, General Provisions and buildings, Bureau of Indian Standards, New Delhi
- M.B. Jadhav, R.S. Jangid, Response of base-isolated liquid storage tanks. *Shock. Vib.* **11**(1), 33–45 (2004)

9. C.B. Nayak, S.B. Thakare, *Investigation of corrosion status in elevated water tank by using nondestructive techniques in Baramati region. In International conference on construction real estate, infrastructure and project management* (NICMAR, Pune, 2017), pp. 1–17
10. F. Omidinasab, H. Shakib, Seismic response evaluation of the RC elevated water tank with fluid-structure interaction and earthquake ensemble. *KSCE J. Civ. Eng.* **16**(3), 366–376 (2012)
11. K.S. Sree, D.S.S.P. Reddy, A study on design of water tanks using SAP (2016)

Analysis of Pauri Garhwal Forest Fire Burned Area for the Years 2015–2019—A Case Study



Pooja Dobhal, Rishi Prakash, Nitin Mishra, and B. V. Khode

1 Introduction

Forest fire is a disaster causing a threat to biodiversity. Though it's a vital mediator in many ecosystems by promoting diversity and natural regeneration, but also cause serious natural disturbance to ecosystem [1, 2]. In Uttarakhand, forest fire occurs very frequently due to the existence of highly inflammable Pine-Trees [3]. Though the fire in study region is mainly due to anthropogenic reasons [4], but due to high temperature and less moisture content in the atmosphere during the summer season from April to May, the forest fire becomes predominant in the Uttarakhand region. Due to frequent occurrence of fire, the extinction of various plants, animals, and the reduction of forest regions has been taking place. Moreover, at regional and local levels, fire plays a vital role in socio-economic consequences as well, both affect the lives and property [5].

Therefore, there is an urgent need for fire management system here. For dealing such situations, remote sensing is the solitary method that allows capturing the form of data that humans cannot intellect such as near infrared and thermal electromagnetic spectrum [6]. Recent statistics grounded on Earth observation (EO) satellites estimates that approximately 4 million km² are burned annually all across the globe [7, 8]. Though currently MODIS and SNPP/VIIRS have been used for monitoring the active of forest fire in Uttarakhand and analyzing the burnt area, but due to its coarser resolution, the accuracy is low.

P. Dobhal (✉) · N. Mishra

Department of Civil Engineering, Graphic Era Deemed to be University, Dehradun, India

R. Prakash

Department of Electronics and Communication Engineering, Graphic Era Deemed to be University, Dehradun, India

B. V. Khode

Department of Civil Engineering, G. H. Raisoni College of Engineering, Nagpur, India

Therefore, we have used Landsat-8 data, which has much finer resolution than MODIS and other existing detection systems, but due to its coarser temporal resolution, it cannot be used for monitoring purpose, but can give more accurate statistics of burned area analysis and detect change over time due to the forest fire. Here, we have used Landsat-8 imageries to detect and analyze burned area of Pauri Garhwal Region by using Normalized Burn ratio and classify the area as per severity range proposed by USGS.

2 Study Area

Pauri Garhwal is one of the districts in Uttarakhand. It is one of the regions in the state, which is highly prone to forest fire due to the existence of pine and other extremely inflammable trees. It is situated between the latitude of 29°45'N to 30°15'N and longitude 78°24'E to 79°23'E encompassing an area of 5329 km² with an elevation of 1650 m. Pauri region generally has pleasing in summer and cold in winter with a maximum temperature of 45 °C in June at Kotdwar and drop to a min of 1.3 °C in January at Duthatoli, giving an average temperature from 25 to 30 °C [9].

There are huge variations on the forest type in Pauri Garhwal such as Khair/Sisso and Chir Pine, which grow between 900 and 1500 m elevations while Oak forest grows at ranging from 800 m to the highest elevations in the region. Deodar forests are restricted to higher elevations only and the most alluring types of trees occur in the Himalayan region.

Pauri Garhwal region has hilly terrains with thickly afforested slopes that receives ample amount of rainfall usually begun from mid-June to mid-September. Study area has an average rainfall of 218 cm out of which 90% is generally confined in the monsoon period (Fig. 1).

3 Data Used

In this paper, Landsat-8 satellite imageries of pre- and post-fire season and shape file to clip study area has been used. Landsat-8 Level 1 imageries have been downloaded from USGS-Earth Explorer website. It was developed by National Aeronautics and Space Administration (NASA) carrying two sensors, i.e. the Operational Land Imager (OLI) and Thermal Infrared Sensor (TIRS). Landsat-8 is positioned on a sun-synchronous orbit at the altitude of 705 km with 10:00 am equatorial passing time. Landsat-8 typical terrain corrected Level 1 T from OLI data has been used in this study. It consists of 9 spectral channels and a spatial resolution of 30 m for bands 1–7 and 9 (15 m for Panchromatic Channel 8 and 100 m for TIRS bands) and a scene size of 185 km × 180 km [10]. Temporal resolution of Landsat-8 satellite data is 16 days. The shape file for Uttarakhand state and India has been taken from arcgis.com.

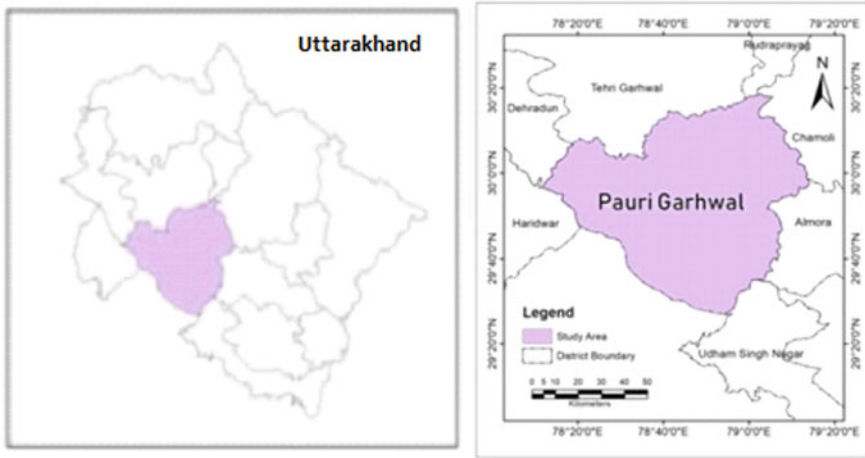


Fig. 1 Location of study area

4 Methodology

The aim of this paper is to calculate the burnt area of a region by using the method of normalized burnt ratio (NBR) and to classify the study area as per its severity range proposed by USGS. This study shows that Landsat-8 can provide more accurate statistics of burnt area using better spatial resolution than the present analyzing sensors. Subsequent steps describe the methodology of extracting and classifying the burnt area pixels in Landsat-8 Level 1 image. Figure 2 demonstrates the flowchart of the methodology adopted to analyze burned area [11].

Step 1: Using shape file of the observed area, the Landsat-8 Level 1 image of pre-fire and post-fire has been extracted.

Step 2: Cloud masking algorithm has been applied to remove the clouds from image for better calculation of burned area.

Step 3: Now calculate the Normalized Burnt Ratio of pre-fire and post-fire scenes.

Step 4: Calculate the difference of pre-fire and post-fire normalized burnt ratio (dNBR).

Step 5: Classify the dNBR on different burn severity class and thresholds as ranges proposed by USGS.

Step 6: Calculate the statistics per class.

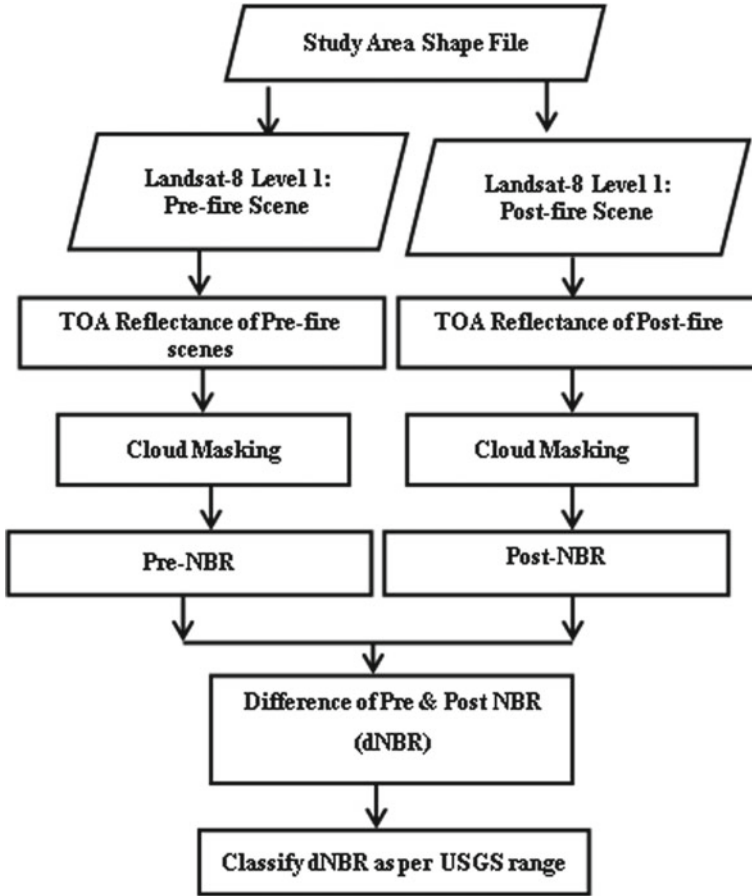


Fig. 2 Flowchart showing methodology adopted for analyzing burned area

5 Results and Discussions

Landsat-8 Level 1 data are in the digital form so it does not show any direct association with physical properties of landcover. To obtain the value of physical properties such as atmospheric temperature, surface temperature and surface moisture, we need to convert these DN into surface reflectance values. Equation (1) has been used to convert DN into surface reflectance (Fig. 3).

$$R = M \times DN + A \quad (1)$$

where

R = Top of atmospheric planetary spectral reflectance,

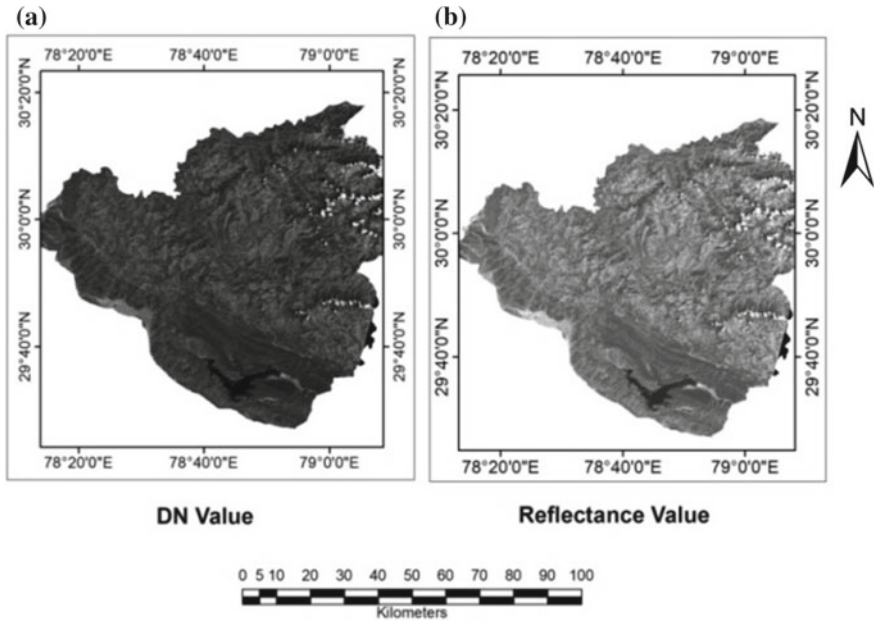


Fig. 3 Conversion from digital number to reflectance. **a** Data in DN. **b** Data in reflectance value

M = Reflectance multiplicative scaling factor for respective band,
 DN = Level 1 pixel value in DN.

Cloud masking has been done to remove clouds, snow and shadows from satellite images so that it cannot disturb the further processing of images. By mosaicking, the composite images with the smallest possible clouds and snow extent are created (Fig. 4).

Normalized Burn Ratio (NBR) uses the near-infrared and shortwave infrared wavelengths, which highlights the burned areas and estimates burn severity (www.Un-spider.org). Healthy vegetation has a very high value of NIR and a low value in SWIR before fire, but after fire vegetation shows low reflectance values in the NIR and high reflectance values in the SWIR. NBR is calculated for pre- and post-fire by using Eq. (2) (Fig. 5).

$$NBR = \frac{\rho_{NIR} - \rho_{SWIR}}{\rho_{NIR} + \rho_{SWIR}} \tag{2}$$

where

NBR = normalized burn ratio

ρ_{NIR} = reflectance of near infrared band, i.e. Band 5

ρ_{SWIR} = reflectance of short-wave infrared band, i.e. Band 7.

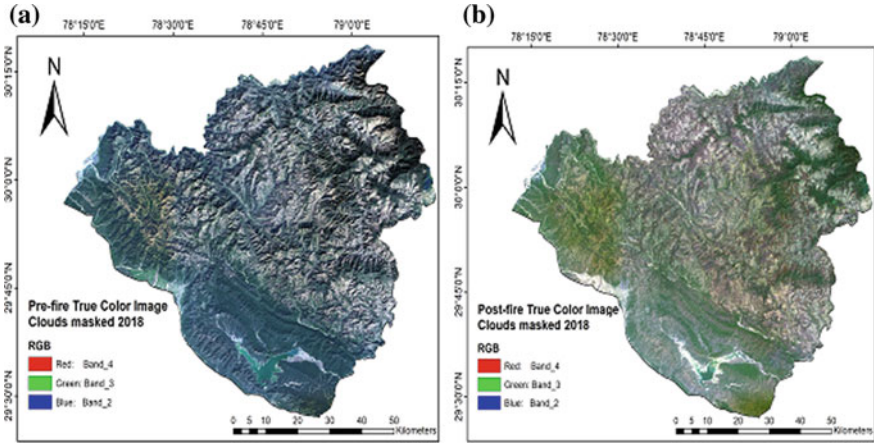


Fig. 4 Cloud masking on reflectance data. **a** Pre-fire data. **b** Post-fire data

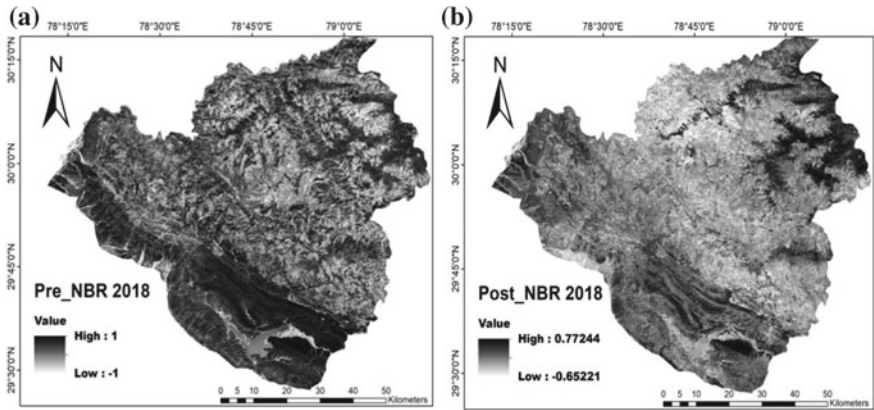


Fig. 5 Normalized burn ratio. **a** Pre-fire data. **b** Post-fire data

Now to detect the burned area, post-fire NBR is subtracted from pre-fire to obtain a difference normalized ratio (dNBR), which can be used for burn severity assessment (Fig. 6).

$$dNBR = NBR_{pre} - NBR_{post} \tag{3}$$

where

- dNBR = difference in normalized burnt ratio
- NBR_{pre} = normalized burnt ratio of pre-fire image
- NBR_{post} = normalized burnt ratio of post-fire image.

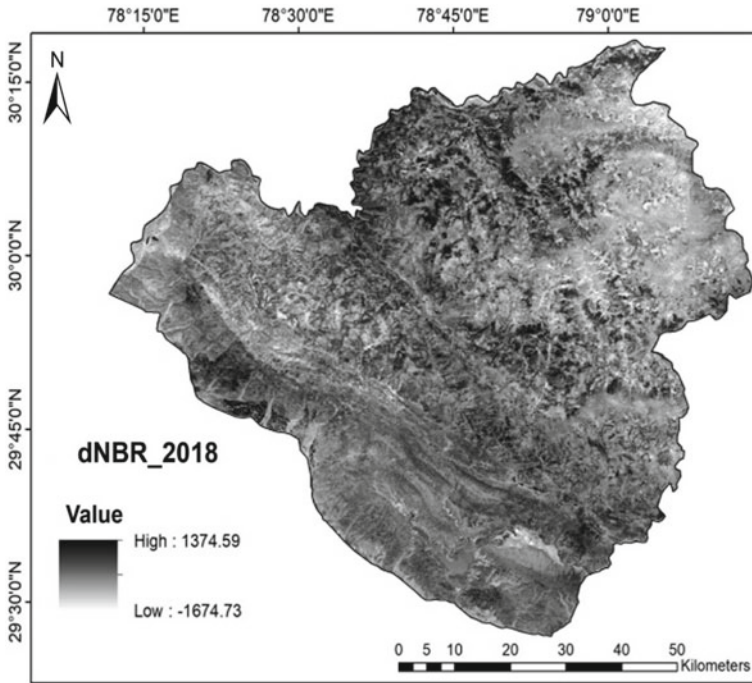


Fig. 6 Difference in Normalized Burn Ratio (dNBR)

The impact of fire on vegetation is not binary like burned and unburned; it is rather having a variety of conditions, dependent on the type of fire and its behavior. It is also affected by the time between the extinction fire and time of image acquisition [12]. On the basis of dNBR calculation, we can state that an area with high dNBR shows more intense damage whereas areas with the values of negative dNBR might show increased vegetation productivity [13]. Classification of dNBR has been done as per burn severity ranges suggested by the United States Geological Survey (Fig. 7).

6 Five-Year Analysis

This study has been carried out from the year 2015–2019 for a detailed study of the burned area of the region. Figures 8, 9, 10, 11, 12, 13, 14, 15, 16 and 17 show the classified dNBR and graph of related values for the years 2015–2019, respectively. Tables 1, 2, 3, 4 and 5 show the statistics of the data.

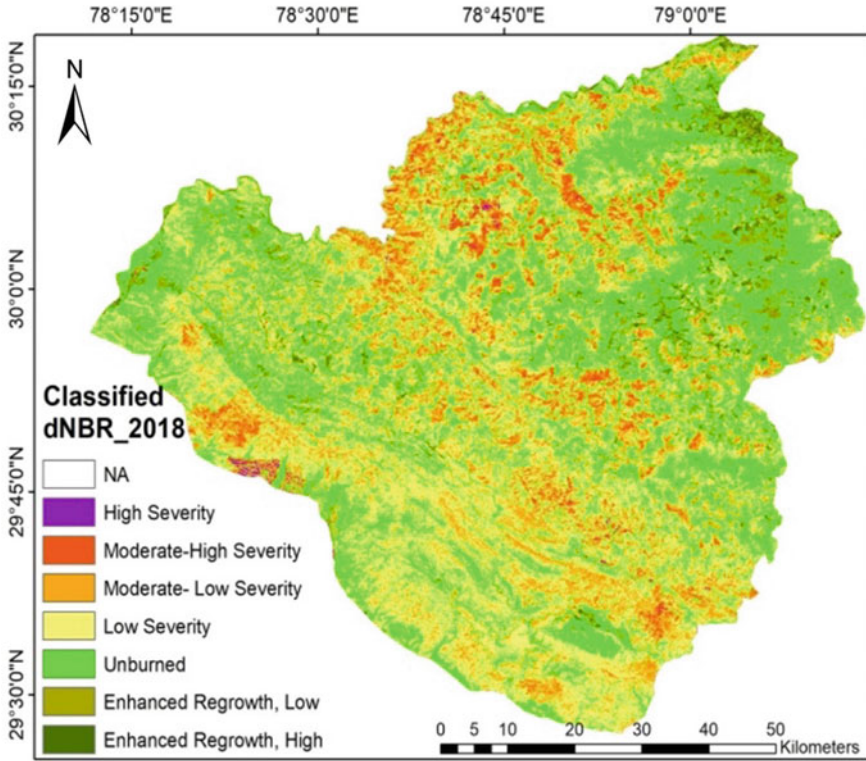


Fig. 7 Difference in normalized burn ratio (dNBR)

7 Conclusion

Landsat-8 has much finer spatial resolution (Band 1–7—30 m, Pan bands—15 m) than MODIS (≥ 1 km) and VIIRS (375 m) due to which it provides accurate details of the burned area and can be highly helpful in applying various techniques to reduce the impact of fire. Burned area analysis provides several details such as change in forest area with time, area more vulnerable for fire area and how fire is impacting our environment (Table 6).

From statistics, it can easily be observed that burned area in the region mostly lies between moderate and low severity. Though high enhanced regrowth has been observed mostly in 2016 and 2018, almost same pattern of burning and regrowth is observed every year (Figs. 18 and 19).

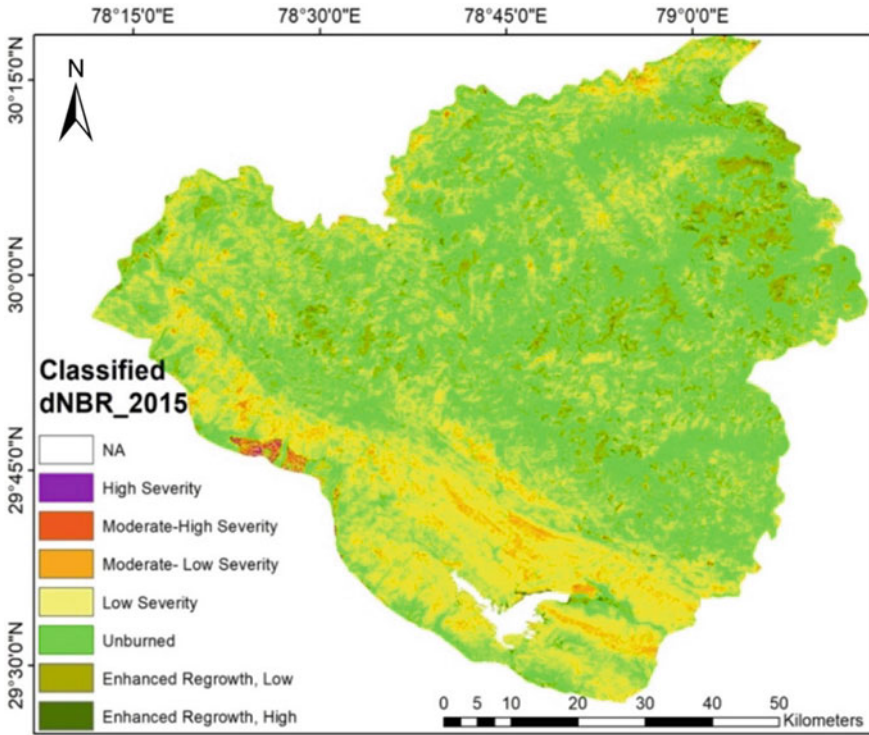


Fig. 8 Statistics of classified dNBR for the year 2015

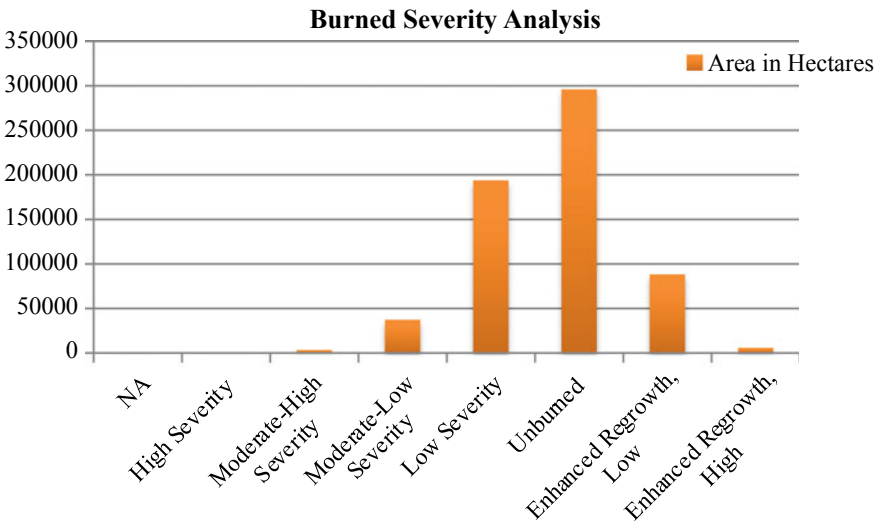


Fig. 9 Graph to represent statistics of classified dNBR 2015

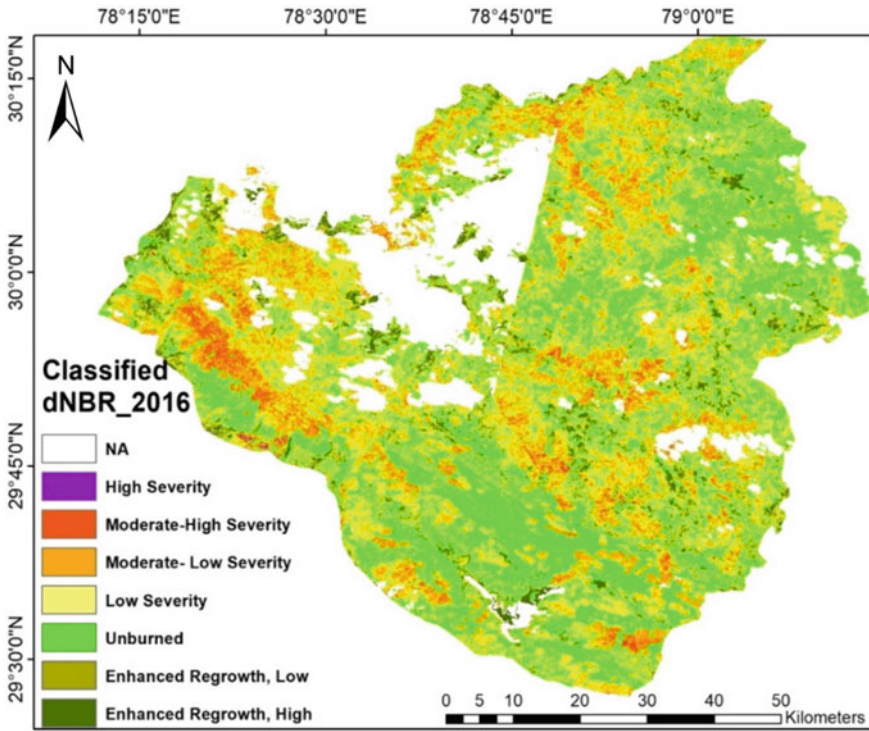


Fig. 10 Classified difference in normalized burn ratio for the year 2016

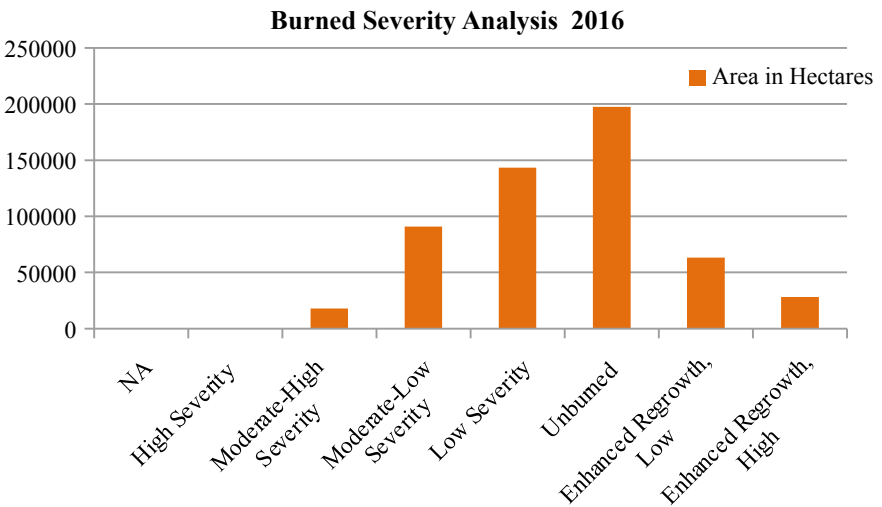


Fig. 11 Graph to represent statistics of classified dNBR 2016

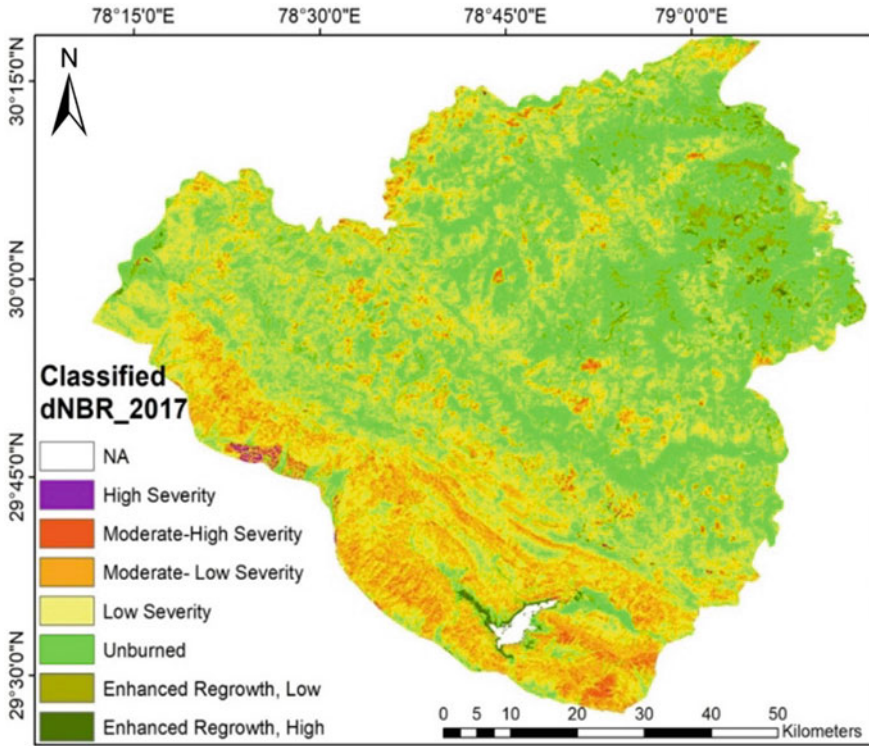


Fig. 12 Classified difference in normalized burn ratio for the year 2017

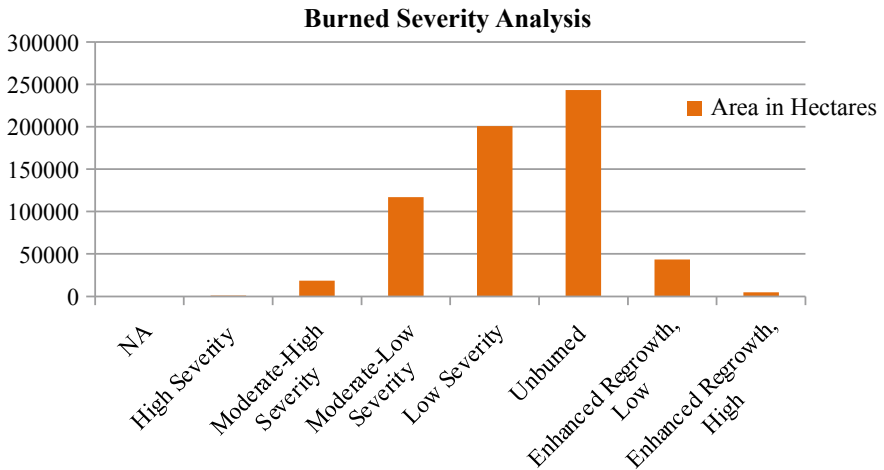


Fig. 13 Graph to represent statistics of classified dNBR 2017

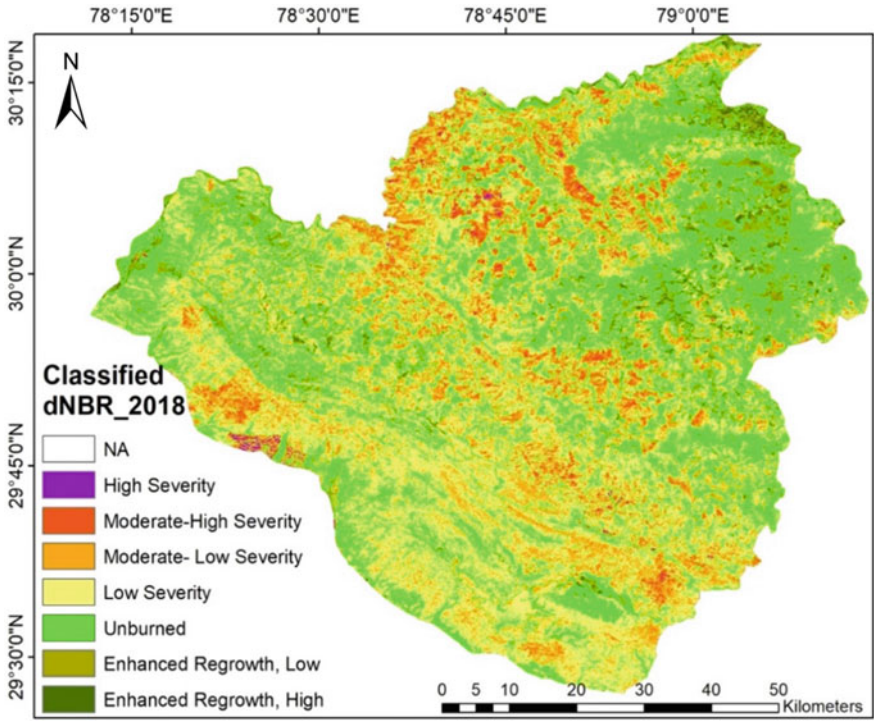


Fig. 14 Classified difference in normalized burn ratio for the year 2018

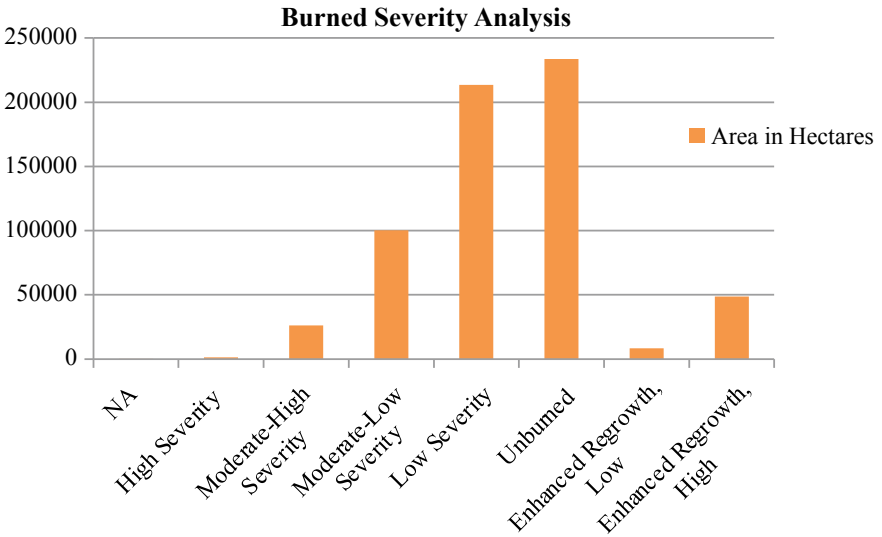


Fig. 15 Graph to represent statistics of classified dNBR 2018

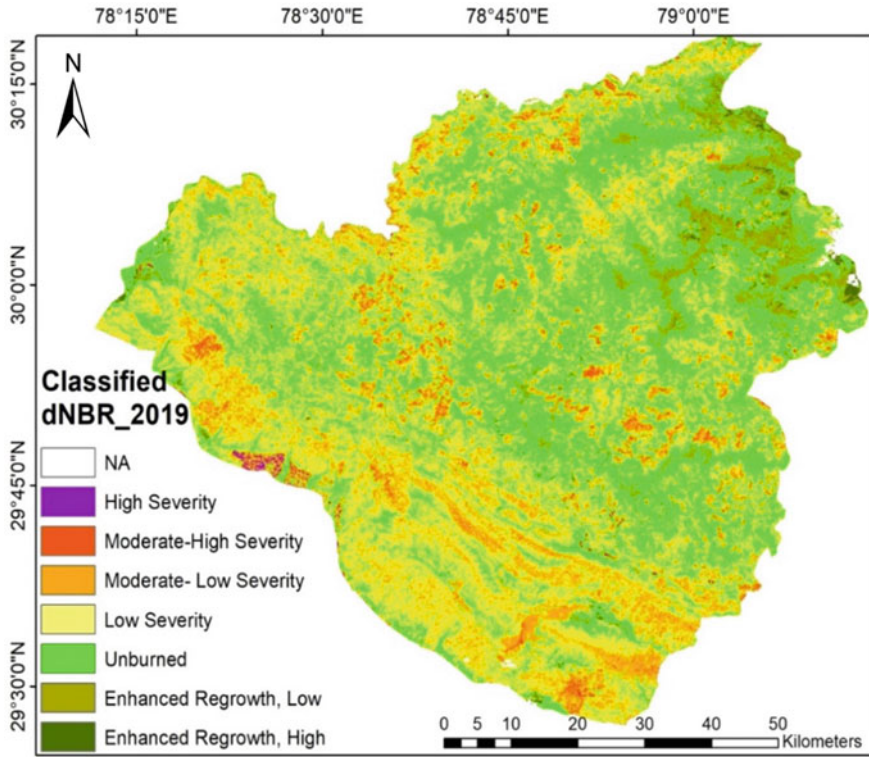


Fig. 16 Classified difference in normalized burn ratio for the year 2019

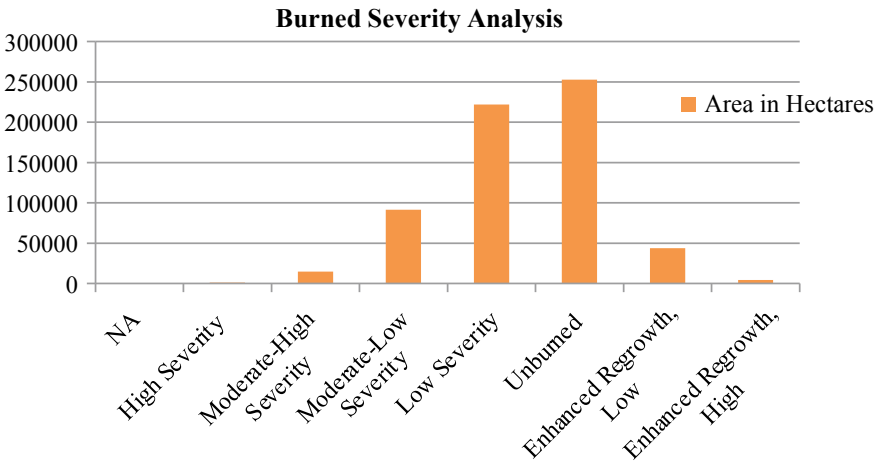


Fig. 17 Graph to represent statistics of classified dNBR 2019

Table 1 Statistics of classified dNBR for the year 2015

Class	Hectares	Percentage	Pixels
NA	0.09	0	1
High severity	658.08	0.1	7312
Moderate–high severity	3577.68	0.57	39,752
Moderate–low severity	37,527.66	5.94	416,974
Low severity	194,068.62	30.72	2,156,318
Unburned	296,065.62	46.87	3,289,618
Enhanced regrowth, low	88,490.88	14.01	983,232
Enhanced regrowth, high	6029.91	0.95	66,999

Table 2 Statistics of classified dNBR for the year 2016

Class	Hectares	Percentage	Pixels
NA	0	0	0
High severity	367.38	0.07	4082
Moderate–high severity	17,919.45	3.29	199,105
Moderate–low severity	90,821.88	16.67	1,009,132
Low severity	143,419.95	26.32	1,593,555
Unburned	197,595.45	36.26	2,195,505
Enhanced regrowth, low	63,105.21	11.58	701,169
Enhanced regrowth, high	28,312.38	5.2	314,582

Table 3 Statistics of classified dNBR for the year 2017

Class	Hectares	Percentage	Pixels
NA	0.9	0	1
High severity	1014.21	0.16	11,269
Moderate–high severity	18,467.19	2.93	205,191
Moderate–low severity	117,098.28	18.56	1,301,092
Low severity	200,657.7	31.8	2,229,530
Unburned	243,474.48	38.59	2,705,272
Enhanced regrowth, low	43,477.11	6.89	483,079
Enhanced regrowth, high	4628.97	0.73	51,433

Table 4 Statistics of classified dNBR for the year 2018

Class	Hectares	Percentage	Pixels
NA	0.09	0	1
High severity	1230.39	0.19	13,671
Moderate–high severity	26,169.12	4.14	290,768
Moderate–low severity	100,346.58	15.88	1,114,962
Low severity	213,556.68	33.79	2,372,852
Unburned	233,645.31	36.97	2,596,059
Enhanced regrowth, low	8357.04	1.32	92,856
Enhanced regrowth, high	48,624.93	7.69	540,277

Table 5 Statistics of classified dNBR for the year 2019

Class	Hectares	Percentage	Pixels
NA	0.9	0	1
High severity	1342.89	0.21	14,921
Moderate–high severity	14,786.01	2.35	164,289
Moderate–low severity	91,650.33	14.54	1,018,337
Low severity	221,776.11	35.18	2,464,179
Unburned	252,615.6	40.07	2,806,840
Enhanced regrowth, low	43,998.3	6.98	488,870
Enhanced regrowth, high	4264.29	0.68	47,381

Table 6 Statistics representing area (in ha) per class for the years 2015–2019

Class	Area (in ha)				
	2019	2018	2017	2016	2015
NA	0.9	0.09	0.9	0	0.09
High severity	1342.89	1230.39	1014.21	367.38	658.08
Moderate–high severity	14,786.01	26,169.12	18,467.19	17,919.45	3577.68
Moderate–low severity	91,650.33	100,346.58	117,098.28	90,821.88	37,527.66
Low severity	221,776.11	213,556.68	200,657.7	143,419.95	194,068.62
Unburned	252,615.6	233,645.31	243,474.48	197,595.45	296,065.62
Enhanced regrowth, low	43,998.3	8357.04	43,477.11	63,105.21	88,490.88
Enhanced regrowth, high	4264.29	48,624.93	4628.97	28,312.38	6029.91

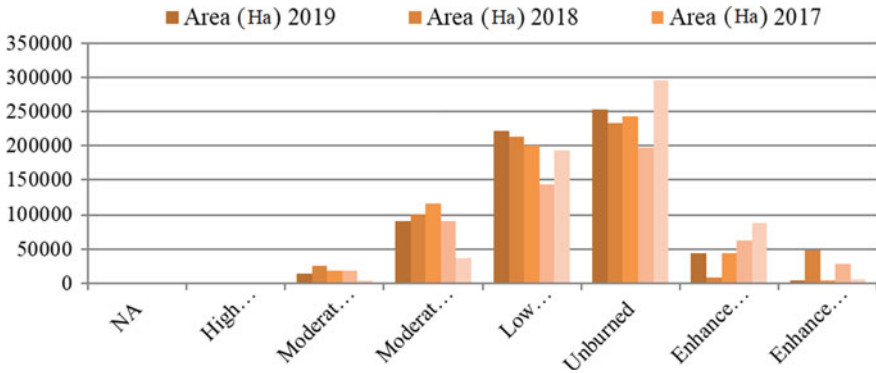


Fig. 18 Graph representing area (in ha) per class for the years 2015–2019

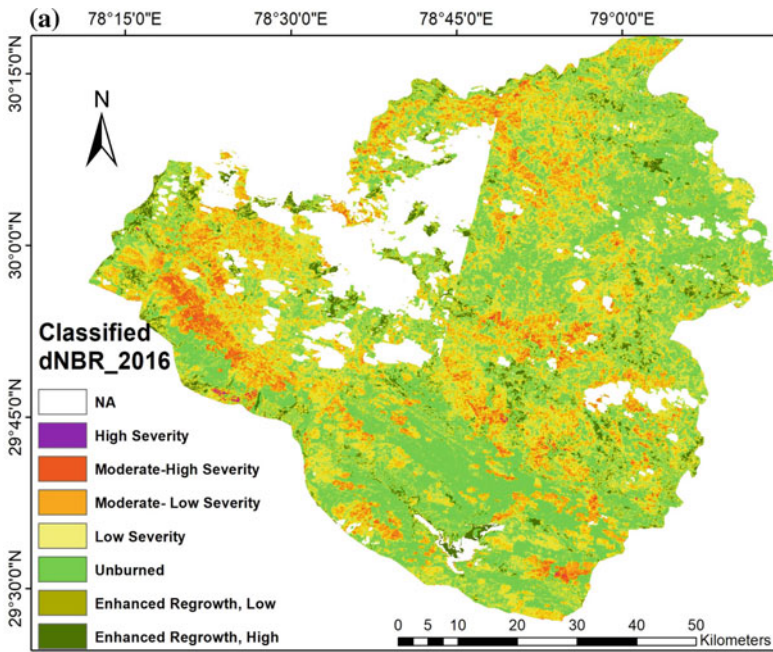


Fig. 19 Map representing the difference in classified dNBR of the year 2016 for the month. **a** January to June and, **b** January to July

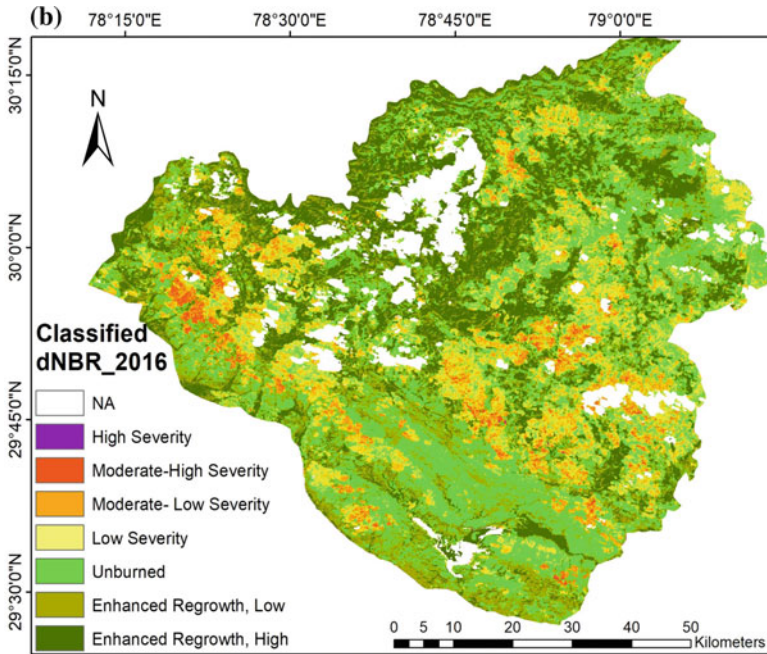


Fig. 19 (continued)

References

1. L. Kelly, L. Brotons, Using fire to promote bio-diversity *Science* **355**, 1264–1265 (2017)
2. E. Chuvieco, F. Mouillot, R. Guido, V.D. Werf, J.S. Migueld, M. Tanasea, N. Koutsias, M. García, M. Yebra, M. Padillag, I. Gitash, A. Heili, T.J. Hawbaker, L. Giglio, Historical background and current developments for mapping burned area from satellite Earth observation. *Remote Sens. Environ.* **225**, 45–64 (2019)
3. C.S. Jha, G. Krishnan, K.C. Thumaty, J. Singhal, Monitoring of Forest Fires from Spae- ISRO's initiative for near- real time monitoring of the recent forest fires in Uttarakhand, India. Article in *Current science* (2016)
4. T.R. Chand, K.V.S. Badrinath, M.S.R. Murthy, G. Rajshekhar, C.D. Elvidge, B.T. Tuttle, Active forest fire monitoring in Uttaranchal State, India using multi-temporal DMSP-OLS and MODIS data. *Int. J. Remote Sens.* Vol. **28**, Issue. 10, 2123–2132
5. E. Chuvieco, I. Aguado, M. Yebra, H. Nieto, J. Salas, P. Martín, L. Vilar, J. Martínez, S. Martín, P. Ibarra, J. de la Riva, J. Baeza, F. Rodríguez, J.R. Molina, M.A. Herrera, R. Zamora, Development of a framework for fire risk assessment using remote sensing and geographic information system technologies. *Ecol. Model.* **221**, 46–58 (2010)
6. E. Chuvieco et al., Application of remote sensing and geographic information systems to forest fire hazard mapping Emilio Chuvieco Russell G. Congalton. *Remote Sens. Environ.* **29**, 147–159 (1989)
7. E. Chuvieco, J. Lizundi_Loiola, M.L. Pettinari, R. Ramo, M. Padilla, K. Tansey, F. Mouillot, P. Laurent, T. Storm, A. Heil, S. Plummer, Generation and analysis of a new global burned area product based on MODIS 250 m reflectance bands and thermal anomalies. *Earth Syst. Sci. Data Discuss.* **2018**, 1–24 (2018)

8. L. Giglio, L. Boschetti, D.P. Roy, M.L. Humber, C.O. Justice, The collection 6 MODIS burned area mapping algorithm and product. *Remote Sens. Environ.* **217**, 72–85 (2018)
9. P. Saklani, Forest fire risk zonation, a case study Pauri Garhwal, Uttarakhand, India
10. W. Schroeder, P. Oliva, L. Giglio, B. Quayle, E. Lorenz, F. Morelli, Active fire detection using Landsat-8/OLI data. *Remote Sens. Environ.* **185**, 210–220 (2016)
11. Step by Step: Burn Severity mapping in Google Earth engine. Unspider Knowledge Portal
12. E. Chuvieco, C. Yue, A. Heil, F. Mouillot, I. AlonsoCanas, M. Padilla, J.M. Pereira, D. Oom, K. Tansey, A new global burned area product for climate assessment of fire impacts. *Glob. Ecol. Biogeogr.* **25**, 619–629 (2016)
13. S. Indratmoko, N. Rizqihandari, Burn area detection using Landsat 8 OLI TIRS. *IOP Conf. Ser.: Earth Environ. Sci.* **338**, 012035 (2019)

Enhancement of Seismic Properties of Reinforced Concrete Beam–Column joints—A Review



P. Nikita and V. M. Preethi

1 Introduction

There has been a substantial increase in structure failure caused due to earthquakes in the past few decades all over the world. The need for improving the seismic resistance of buildings arises in this situation. Numerous research studies have been conducted in this domain in the past few decades. Strengthening of seismic characteristics of structures includes solutions ranging from wrapping FRP sheets externally to the use of different types of concrete.

The beam–column joint is one of the most important zones of an RC structure. These joints are considered as crucial zones for the effective load transfer from the beam to the column. It is prone to heavy forces in times of earthquake excitation. Therefore, its behavior affects the performance of the entire structure. Inadequate splicing of reinforcement, poor compaction, absence of transverse reinforcement are some of the reasons that cause failure. Closely placed steel reinforcement at beam–column joints and insufficient development length further validate the need for analyzing and strengthening the beam–column joints. The seismic behavior of the structure can be analyzed by considering the parameters like failure mode, crack pattern, energy dissipation capacity, ductility, stiffness degradation, load–displacement characteristics, shear strength, and more. The specimens are subjected to reversal cyclic load and pseudo-static load as it gives a similar effect to the earthquake. In practice, structures are not cast monolithically, whereas, in lab, specimens are cast monolithically. Therefore, casting and testing of such specimens are taken into account.

The basic modes failure mode of beam-column joints is beam yielding, joint shear failure after beam yielding, joint shear failure, compressive flexural failure at beam end. Beam yielding occurs when shear strength is greater than joint shear stress. If

P. Nikita (✉) · V. M. Preethi
PSG Institute of Technology and Applied Research, Coimbatore, India

shear stress is greater than the shear strength joint shear failure will occur. The last one occurs due to the crushing of concrete. Structures in the seismic zones should be built by adopting Seismic design. The defected beam–column joints can be rehabilitated by wrapping FRP sheets. The seismic property of the structure can be enhanced by wrapping FRP sheets in the beam–column joints [1–8], using fiber reinforced concrete [9–12], and by using other types of concrete [13–16]. The debonding of FRP sheets is identified as a major issue during the usage of FRP sheets [1, 3, 4, 8], which has been addressed.

A detailed study of the beam–column joints becomes a requisite in the construction field [17]. This literature study consists of the seismic strengthening techniques of beam–column joints used by various researchers, focusing on the external wrapping of polymer sheets and the usage of different types of concrete.

2 Enhancement of Beam–Column Joint by Wrapping Polymer Sheets

The seismic performance of RCC buildings can be enhanced by providing a proper beam–column joint as it is the most vulnerable part of the building when subjected to dynamic loads. One of the commonly used methods to enhance the beam–column joint is the wrapping of polymer sheets. Some of the parameters considered here are failure mode, energy dissipation capacity, stiffness, ductility, shear strength, and hysteresis behavior.

2.1 CFRP Sheets

Kien-Le-Trung and team [1] and Mahmoud et al. [2] studied the strengthening of the beam–column joint by wrapping CFRP (Carbon fiber Reinforced Polymer). Different orientations like T shape, X shape, L shape, U shape were followed also with combination of strips and sheets. When T and L shape sheets were used, the failure was due to the debonding of sheets from the specimen. It was observed that X-shaped sheets produced flexural cracks and an insignificant number of shear cracks. The combination of two layers of T, L sheet along with the beam–column interface along with strips reduced the shear failure. Wrapping CFRP sheets is considered as an important method to improve the load-carrying capacity of beam–column joints. The sheets when aligned in a similar direction to the principal axis of the structure, higher values were obtained [1]. CFRP material added in the form of strips can increase load carrying capacities. However, adding U-shaped strips on columns is found to be more beneficial. The shape of the sheets used can affect the performance to a great extent. X-shaped configuration was found to be appropriate. The load-carrying capacity was maximum when the layer of sheets was increased [1]. The

use of L-shaped CFRP sheets was inferior to X-shaped sheets in the improvement of ductility [2]. Reference-defected specimen and strengthened specimen showed lower ductility when compared with the control specimen. The orientation of the CFRP plays a major role in altering seismic performance. Diagonally overlying sheets were seen to strengthen the specimen with the absence of joint stirrups. The performance of inadequate spliced columns was improved by near-surface mounted CFRP sheets. The vertical deflection was seen to be lower for NSM CFRP sheets. The strengthened specimens had higher stiffness when compared with the control specimen and defected specimen [2]. Debonding was seen at greater drift ratios for specimens with CFRP sheets. Increasing the number of CFRP sheets can improve energy dissipation. In T joints when two layers of CFRP sheets were used, a 30% increase in value was observed concerning the control specimen. The usage for FRP fans can significantly increase energy dissipation and prevent debonding [3].

2.2 EBROG Technique

Ilija and team [4] and Mostofinejad and Hajrasoulihab [5] studied the retrofitting of the RC Strong Beam—Weak Column joint by EBROG (Externally Bonded Reinforcement on Groove) and EBR [Externally Bonded Reinforcement]. The beam–column was wrapped by CFRP sheets in X orientation along with CFRP fans. Brittle shear failure was observed when columns and joints were retrofitted with CFRP sheets. Whereas, when the beam along with the column and joint retrofitted, plastic deformation moved away from the column face. Due to the application of the EBROG technique, CFRP sheets were not de-bonded. The specimen that was retrofitted by the EBR technique was failed by debonding of CFRP sheets [4]. The specimens whose beam, column, and joints retrofitted with CFRP sheets and CFRP fans by EBROG had improved ductile behavior when compared with other specimens, i.e., 81, 139, 111% with control specimen. When the EBR technique was applied the ductility improved but it was lower than the EBROG technique. Strengthening of beam–column joints with FRP fans is an effective method to improve performance. The peak load of 84.6 kN was recorded at a drift ratio of 5.2%, which shows that the grooving method along with FRP fans used has led to a significant enhancement [5]. The specimen with three layers of carbon sheets on top and bottom with four CFRP fans showed the maximum energy dissipation of 60% at a drift ratio of 4.5%. It was also found that the specimens strengthened using the EBROG technique can contribute to the survival of structure under high lateral displacements in the performance. The usage of EBROG also helps to ensure effective bonding. The stiffness value of the specimens retrofitted with CFRP sheets and CFRP fans by EBROG was 91 and 109% (at 4.5% drift) higher than the control specimen [4]. The specimen with seismic design had 59% higher stiffness (at 4.5% drift) than the control specimen. The retrofitted specimen in the beam–column joint had 109% (at 4.5% drift), higher stiffness than the control specimen [5].

2.3 Epoxy Resin Injection

Karayannis [6] studied the rehabilitation of RC beam–column joints. The tested control specimens were repaired with epoxy resins and CFRP sheets and compared with specimens, which were strengthened with CFRP sheets. The specimens with CFRP sheets had damages away from the beam–column joint. CFRP sheets effectively increased the load-carrying capacity of specimens. Epoxy resin injection helps to repair the structure. Specimens with no shear reinforcement and CFRP wrapping displayed an increase of 186% of the maximum observed load in comparison with the control specimen. Specimens repaired with externally bonded U-shaped CFRP sheets showed higher energy absorption than the ones with only epoxy resin injection. The combination of resin injection and CFRP sheets on beam–column joints showed the maximum increase in energy absorption.

2.4 Other Techniques

Roy and Islam Laskar used glass fiber reinforced polymer for retrofitting joint specimens [7]. Specimens were not cast monolithically. Wrapping of GFRP sheets changed the cracking pattern. Delamination of sheets with less number of shear cracks was observed. The ductility of the GFRP retrofitted specimen was higher than the control specimen (57–144%). For different flexural ratios, the load-carrying capacity was maximum for the CFRP sheets. Specimens with GFRP wrapping dissipated a higher amount of energy than the control specimen. (34–118%). GFRP wrapped specimens had higher initial stiffness than the control specimen. The rate of stiffness degradation rate was also reduced. Shaabana and the team studied the behavior of beam–column joint retrofitted with ferrocement layers [8]. Meshes were oriented in 45°, 60°, and 60° with steel bars and tested with single, double, triple layers. Initiation and propagation of cracks were delayed and had less number of shear cracks. The orientation of the mesh and the number of layers played an important role in controlling the crack.

3 Enhancement of Seismic Behavior Internally

To strengthen beam–column joints, wrapping of CFRP sheets was done. Apart from this, the joint can be strengthened by using fiber reinforced concrete. Fiber-reinforced concrete can be prepared by adding steel fibers, polypropylene, nylon fibers, carbon fibers, etc. It improves the tensile strength of the structure as well as enhances the ductility, which is one of the most important parameters in seismic study. Proper reinforcement in the beam–column joint is necessary for seismic resistance. Placing conventional concrete in such cases is quite difficult. This can be avoided by using

self-compacting concrete. The use of self-compacting concrete has also influenced the seismic resistance.

3.1 Fiber Reinforced Concrete

Rather et al. [9] and Jannal Shannang et al. [10] studied the use of hooked steel fibers [HSF], brass-coated steel fibers [BCSF] in reinforced beam–column joints. HSF, BCSF were used in concrete at a proportion of 1.5% [9], 2, 4% [10] of volume of concrete, respectively. The joint had a combination of shear and flexure failure. Specimens with HSF had reduced the propagation of cracks than BCSF, and this was due to good bonding between concrete and HSF. The HSF and BCSF had a good impact in improving the ductility. This was due to better confinement of beam–column joints than the reference specimen. Increasing the percentage of steel fibers improved the loading carrying capacity. The use of HSF and BCSF in the mix had reduced stiffness degradation.

Fine aggregate was replaced with crumb rubber in 10, 15, 20, 25% [11]. Steel fibers with hooked ends of 35, 65 mm were used in the ratio of 0.35 and 1% and used two different sizes of coarse aggregate (10 and 20 mm) in individual specimens. As the crumb rubber percentage was increased, the failure mode shifted from beam yielding (B) to joint shear failure after beam yielding mode (BJ). When steel fibers were used, shear strength of the joints was improved. When 20 mm coarse aggregate was added, the failure mode shifted from BJ to B mode and this was due to interlocking of aggregates. Ductility was improved when 1% of steel fiber and 25% crumb rubber were used. When crumb rubber was increased to 25%, there was a reduction in ductility, and initial stiffness was reduced. When the same proportion of crumb rubber and a different size of coarse aggregate were used, there was a reduction in the ductility as well as in initial stiffness due to the formation of a large interfacial transition zone. In the mixtures with 20 mm aggregate, increasing the percentage of CR (20%) increased the ultimate load and displacement. In the case of 10 mm aggregates, the optimum percentage of CR (15%) showed better performance. The use of steel fiber along with the crumb rubber reduced the stiffness degradation rate.

Coarse aggregate was replaced by polyvinyl alcohol fiber in construction [12]. Specimens with different transverse reinforcement ratios and different design loads were cast. FRC was used only in specified portions of beam–column joint, i.e., to the width of 1 times the depth of beam and column and 1.5 times the depth of beam and column. The specimen failed by shear failure along with yielding of reinforcement in beam and column. Greater axial load ratio resulted in improved load carrying capacity and gave less pinched loops. The compressive strength of the concrete also affected seismic performance. The higher compressive strength of FRC drastically increased the load-carrying capacity and reduced the deformation capacity. Using polyvinyl alcohol (PVA), fiber improved the energy dissipation capacity compared with the control specimen.

3.2 Other Types of Concrete

High Strength Self Compacting Concrete (HSSCC) was used in the core of the joint [13]. The failure was not due to the slippage, and the shear stress was transferred successfully to the joint. When conventional high strength concrete (CHSC) was used, the failure was due to the slippage of reinforcement. The hysteretic loop of the specimen with HSSCC was fatter and showed less pinching loops. At a given drift ratio, specimens with HSSCC will experience fewer cracks in the joint area compared with other concrete specimens.

The addition of flyash as a partial replacement of cement was found to be an effective method to improve seismic properties [14]. Five specimens were prepared with 20, 30% flyash replacement with and without the use of superplasticizers. The specimens failed by the formation of a plastic hinge and which was similar to the control specimen. The ductility of flyash incorporated specimens with superplasticizer was higher than the specimen without superplasticizer. The hysteretic loop was found to be more stable for the specimen, which had 20% fly ash with a superplasticizer. It also showed a higher load carrying capacity compared with the control specimen and other specimens. There was a decrease in initial stiffness of the specimens with flyash but specimens with superplasticizer had higher stiffness than the specimens without superplasticizer.

Electric Arc Furnace slag is used as a replacement for coarse aggregate and its seismic behavior was studied [15]. The specimens had diagonal cracks in the joint. The ductility index of the specimen with EAF concrete was higher than the control specimen. EAF concrete allows the beam–column joints to take higher loads. The specimens with EAF had higher initial stiffness than the control specimen and a slight increase in energy absorption was observed. Valeria Corenaldesi et al studied the use of recycled concrete aggregate as in beam–column joints [16]. The specimen's failure was similar to strong column–weak beam design and was due to flexure stress. Specimens with recycled concrete aggregate had high energy dissipation.

4 Conclusion

The structures will only be able to resist the heavy lateral forces if the beam–column joints are strong enough. Various research activities are going around the world aiming to develop new methodologies to improve the seismic resistance of buildings. Providing high ductility to structures, with enough stiffness allows the structure to dissipate seismic energy. CFRP possesses high superior strength among all polymer sheets and shows higher energy dissipation values. In cases where joint stirrups are not present, diagonally lying sheets are effective.

From Fig. 1, it is concluded that X-shaped sheets have high energy dissipation capacity, and addition of CFRP fans was seen to improve the strength. Brittle shear failure can be precluded by the application of the EBROG technique. Epoxy resin

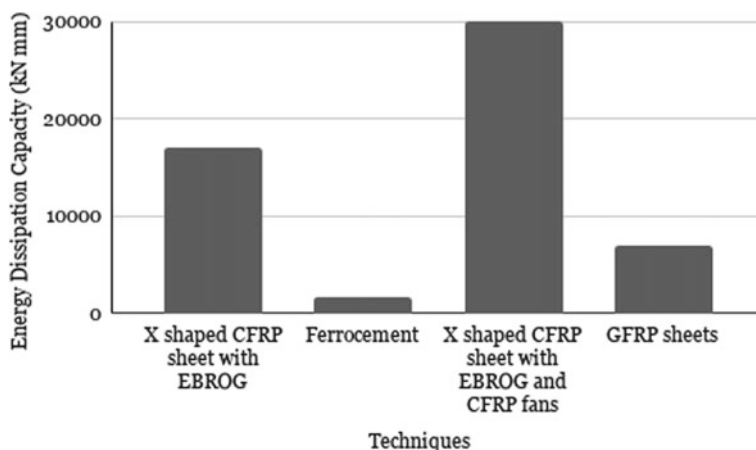


Fig. 1 Energy dissipation of externally strengthened specimens

injection helps to restore structural integrity and improve bonding. It was studied that NSM sheets help to overcome the problem of debonding. However, the bonding of glass fiber reinforced polymer sheets showed lesser energy dissipation compared with CFRP sheets. It was found that the X-shaped CFRP sheet specimens with CFRP fans showed an increase of 43.33% energy dissipation values compared with those without fans.

Beam–column joints can also be enhanced by using fiber-reinforced concrete. The use of fibers in the concrete can reduce the congestion of reinforcement in the joints and simultaneously improve the ductile behavior. It can be inferred that the use of steel fibers can reduce and delay the crack propagation. Energy dissipation values of specimens with polyvinyl alcohol fibers were found to be 95.96% higher than that of specimens with electric arc furnace slag.

From Fig.2, it is concluded that concrete with polyvinyl alcohol fiber is the best method in the internal strengthening techniques. The use of steel fibers helps in improving shear strength as well.

High ductility values ensure that the structure can undergo large deformations without failing. Figure 3 confirms that CFRP sheet is a potent material to increase seismic resistance. X-shaped CFRP sheets show an 84.05% increase in displacement ductility ratio when compared with brass-coated steel fibers. From the comparison results of the graphs, it can be concluded that external wrapping of polymer sheets to beam–column joints can effectively prevent structures from seismic failure.

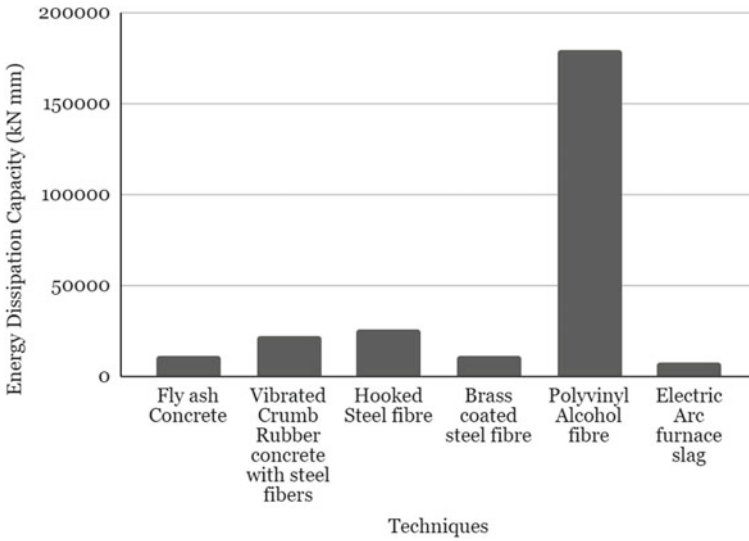


Fig. 2 Energy dissipation of internally strengthened specimens

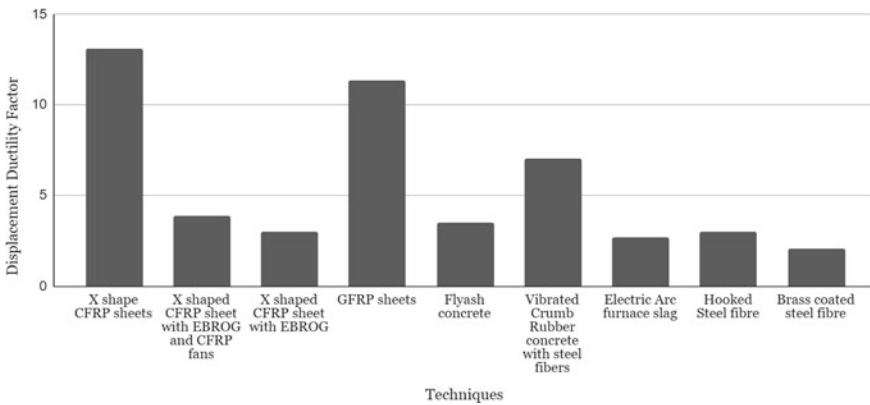


Fig. 3 Displacement ductility factor of various techniques

References

1. A. Kien Le-Trung, K. Lee, J. Lee, D.H. Lee, S. Wooc, Experimental study of RC beam-column joints strengthened using CFRP composites. *Comp.: Part B* (2009)
2. M.H. Mahmoud, H.M. Afefy, N.M. Kassem, T.M. Fawzy, Strengthening of defected beam column joint using CFRP. *J. Adv. Res.* (2013)
3. E. Ciro Del Vecchio, M. Di Ludovico, Experimental investigation of exterior RC beam-column joints retrofitted with FRP systems. *J. Comp. Construct.* **18**(4) (2014)
4. E. Ilia, D. Mostofinejad, Seismic retrofit of RC strong beam weak column joints using EBROG method combined with CFRP anchorage system. *Eng. Struct.* (2019)

5. D. Mostofinejada, M. Hajrasoulihab, 3D beam column corner joints retrofitted with X shaped FRP sheets by EBROG/EBR method. *Eng. Struct.* (2019)
6. C.G. Karayannis, Strengthening and rehabilitation of RC beam column joints using carbon FRP jacketing and epoxy resin injection, *Earthquake engineering and structural dynamics* (2008)
7. B. Roy, A. Islam Laskar, Cyclic performance of beam-column subassemblies with construction joint in column retrofitted with GFRP-structures-published by Elsevier (2018)
8. I.G. Shaabana, O.A. Seoudb, Experimental behaviour of full scale exterior beam column space joints retrofitted by ferrocement layers under cyclic behaviour, 9 November 2017 Published by Elsevier Ltd.
9. A.I. Rather, A.R. Dar, A.F. Ghowsi, Improved performance of steel fiber reinforced beam-column joint—an experimental study, in *3rd International Conference on Innovative Technologies for Clean and Sustainable Development* (2020)
10. M. Jamal Shannag, N. Abu-Dyya, G. Abu-Farsakh, Lateral load response of high performance fiber reinforced concrete beam–column joints
11. B.H. AbdelAleem, A.A.A. Hassan, Effect of combining steel fibers with crumb rubber on enhancing the behavior of beam-column joints under cyclic loading. *Eng. Struct.* (2018)
12. X.-W. Liang, Y.-J. Wang, Y. Tao, M.-K. Deng, Seismic performance of fiber-reinforced concrete interior beam-column joints. *Eng. Struct.* **126** (1 November 2016)
13. M.S. Ashtiani, R.P. Dhakal, A.N. Scott, Seismic performance of high-strength self-compacting concrete in reinforced concrete beam-column joints. *J. Struct. Eng.* **140**(5) (May 2014)
14. S.K. Shaw, A. Sil, *Experimental Study on Cyclic Loading Characteristics of Fly Ash as Partial Replacement of Cement in Beam-Column Joint*. Elsevier Ltd.
15. L. Faleschini, L. Hofer, Ma.A. Zanini, M.D. Benetta, C. Pellegrino, Experimental behavior of beam column joints made with EAF concrete under cyclic loading. *Eng. Struct.* (2017)
16. V. Corinaldesi, V. Letelier, G. Moriconi, Behaviour of beam column joint with recycled aggregate concrete under cyclic loading. *Construct. Build. Mater.* **25**(4) (April 2011)
17. S.R. Uma, S.K. Jain, Seismic design of beam-column joints in RC moment resisting frames. Review of codes

Geotextile Filters in Earthen Dam—A Review Study on Construction and Rehabilitation



Hridesh Kumar Trivedi, Nikita Choudhari, and Sumit Gandhi

1 Introduction

In earthen dams, filters play a crucial role in inhibiting the “prolongation” and “development” of erosion. The possibility of piping and internal erosion is reduced by suitable filters. A filter must possess two correlated and essential requirements other than the principal necessity (i.e. retention) as follows.

1.1 Permeability

Filters are meant to provide sufficient passage for water seepage and to restrict the generation of extreme pore water pressure. According to Fell et al. (2004) [5] over narrow filter zone, there is the development of high gradients because of extended cracks causing concentrated leaks. This weakens the properties of filter material due to the formation of suffusion, hydraulic fracture or backward erosion.

1.2 Self-healing and Collapsibility

As per Soroush [28] and Tahmasebipoor et al. [30], filter materials should work as a whole, i.e. filter layer should defy core cracking (caused due to earthquake, hydraulic fracturing, differential settlement, rapid drawdown and so on) or discontinuity. For

H. K. Trivedi (✉) · N. Choudhari · S. Gandhi
Department of Civil Engineering, JUET, Guna, MP, India

S. Gandhi
e-mail: sumit.gandhi@juet.ac.in

limiting the core cracking filter and drain material should possess collapsibility and self-healing properties. Fell (2005) [7] proposed that filter crack holding capability is affected by fines (amount and plasticity).

According to Mittal et al. [20], filters (like chimney and horizontal) are used for lowering the phreatic level and for safety issues and integrity of the complete dam structure. Projects, where the presence of granular material is not in abundance at the nearby site or where the appropriate sized aggregates cannot be obtained in sufficient amount, make it an uneconomic and tedious task to design and construct a filter. Therefore, it is either difficult or expensive to construct a graded filter. Efficiency of filters can also be affected, hence in order to overcome such situations, geotextile filter can be used and can replace granular filter.

2 Theory

Universally accepted terminology commonly called as “geotextile” was introduced in 1977. Geotextiles are majorly used for separation, filtration, drainage and reinforcement. In earthen dams, geomembrane was introduced as waterproofing element in Italy (during 1959) and as chimney drains in France (during 1973) as suggested by Srivastava et al. [29]. During 1970s, a number of different standards for “filter fabrics” were suggested, some of them influenced by granular filter criteria by Terzaghi. Previously followed criterion (1970s) for filter fabrics is $k_F > k_S$, $0.150 \text{ mm} < O_F < d_{85S}$, $4\% < A_R < 36\%$.

According to US filter criteria, nonwoven fabrics as filters can't be used as they violate the Terzaghi's criteria of filters. Progressively, the basis for the above criteria disappeared for nonwoven fabrics and new criteria that are applicable to all types of fabrics are $k_F > k_S$, $O_F < d_{85S}$, $A_R > 4\%$. For the experimental evaluation of drainage performance of geotextile and soil assembly, the selected test procedure should imitate the genuine soil and geotextile interaction. Haliburton and Wood [12] studied that the estimation of geotextile's drainage performance should be done by gradient ratio tests, and the clogging resistance of a geotextile is somehow related with its 'equivalent opening size' (EOS). Hoare [11] and Sato et al. [27] found that under unidirectional conditions of flow, the filtering mechanism can be obtained via erosion of fine particles toward the filter away from the zones in the soil, bridge formation by coarse particles, formation of self-induced filters.

Robert et al. [25] studied that cross-plane flow involves the fact that geotextile has a porous structure, i.e. the recognition of soil and fabric filtration cases were introduced during the first use of geotextile. However, the in-plane flow characteristic of fabric has received less recognition, but there exist many research areas for geotextiles that are capable of in-plane drainage. It includes

- i. Road drain interceptors,
- ii. For lowering consolidation time (as drain wells),
- iii. For the hydrostatic pressure elimination behind the retaining walls,

- iv. For the seepage force dissipation in earth and slope of rock strata,
- v. In earthen dams (as chimney drain and drainage gallery),
- vi. For pore water pressure dissipation (in embankments and fills, fabric retaining walls and encapsulated soil systems),
- vii. For transmitting water under the railroad ballast,
- viii. In the areas of frost action for leading subsurface water off,
- ix. In frost heave and arid areas for breaking capillary zones,
- x. For the dissipation of gas pressure under the pond liners.

In-plane flowability of most of the woven geotextiles and nonwoven geotextiles (mainly heavy arranged and heat set) is not significant. Conversely, in-plane flow can be observed in nonwoven geotextiles, which are thick needled or resin set because of their very open structures.

For construction of earthen dams, its renewal geotextiles can be used. Usually, the repair and replacement work are done on those dams where the function of geotextile is not crucial for dam's safety. As geotextiles are susceptible to establishment damages and can be clogged possibly, there exists an uncertainty in their reliability and hence the use of geotextiles as deeply buried filters is limited in dams. Recently, the criteria for geotextile filter are re-evaluated and verified the acceptability of geotextiles for large earth dams. The re-evaluation criterion needs permeability criterion, retention criterion, porosity criterion and thickness criterion.

As per Zornberg [34] governing factor for filtration is the filter opening characteristics (i.e. size, shape, density and distribution). Three of the filter opening characteristics (i.e. size, density and distribution) are addressed by the above four criteria. According to Giroud [10], the filter opening shape is of minimum consideration and hence not included in the above criteria. Whereas, for some manmade and woven geotextile filters, shape can be a governing issue. Ultimately, the above-suggested criteria for geotextile filters reasonably allow their safe design.

3 Discussion

3.1 Effect of Properties of Geotextile on Filtration/Drainage

Hydraulic Properties. Several researchers studied that the filtration of a geotextile depends on various hydraulic properties (such as permeability, porosity, viscosity, pore size, Reynold's number, drag coefficient, shape factor, specific gravity of fluid, filter opening size, tortuosity etc.) of the filter, fluid and the base material under the influence of compressive force. Palmeira and Gardoni [22] studied that:

$$k = \frac{g}{\nu} \frac{\pi}{2} \frac{d_f^2}{(1-n)} \frac{1}{C_D R_{E_g}} \quad (1)$$

On the basis of Kozeny [15] and Carman [4], classical approach following equations has been presented by Giroud [9]:

$$k = \frac{\beta \rho_w g}{16 \eta_w} \frac{n^3}{(1-n)^2} d_f^2 \tag{2}$$

$$k = \frac{\rho_w g O_F^2}{32 \eta_w} \tag{3}$$

Based on extended theories anticipated for packed spheres, cylinders or other fluids, the Kozeny-Carman equation for flow through packed spheres [19] for nonwoven geotextiles is:

$$k = \frac{1}{36 k_o T} \frac{\rho_w g}{\eta_w} \frac{n^3}{(1-n)^2} d_{sp}^2 \tag{4}$$

Air flow through porous medium of geotextile is governed by the equation (Lord 1995) [17] :

$$k = \frac{1}{17.72} \frac{\rho_w g}{\eta_w} \frac{n^5}{(1-n)^{1.32}} d_f^2 \tag{5}$$

Miszkowska et al. [18] studied the normal permeability behaviour of geotextile under different loading conditions in the laboratory from the sample of 23 years exploited Bialobrzegi Dam in Poland. Details are mentioned in Table 1 and Fig. 1.

Under the load of 2, 20 and 200 kPa, there is a reduction of 1.2, 2 and 4 times in the permeability coefficient, respectively. This study suggested that even in the worst conditions of clogging and compression, the permeability of geotextile (i.e. under 200 kPa, $k_g = 0.0008$ m/s) is approximately 10 times that of the soil permeability, which was found to be $k_{soil} = 7.65 \times 10^{-5}$ m/s, this result is desirable as Giroud [8] suggested that the permeability of geotextile must be only 10 times greater than soil permeability. After 23 years, the water permeability of nonwoven geotextile becomes 0.00268 when tested which is 1.5 times less than the virgin value. Robert et al. [25] and Rollin et al. [26] presented an empirical formula for permeability of geotextiles (woven and nonwoven) for both in-plane and cross-plane flow as:

Table 1 Permeability coefficient under the different loads for nonwoven geotextile Miszkowska et al. [18]

Load (kPa)	Water permeability coefficient of geotextile k_g (m/s)
Without load	0.0019
2	0.0017
20	0.0013
200	0.0008

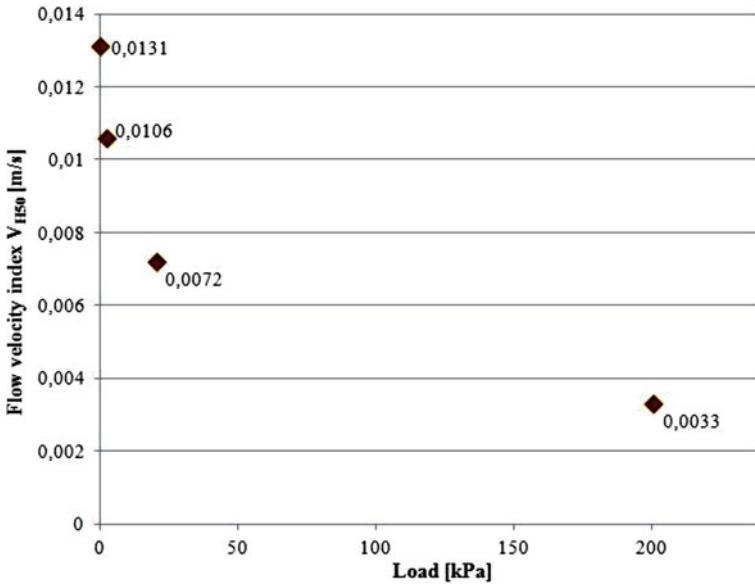


Fig. 1 Variation of load and flow velocity index for tested materials [18]

$$k = 0.00212 \times \gamma^{-1/2} \tag{6}$$

$$\gamma = \frac{2.31(1 - n)}{\pi d_f^2} \tag{7}$$

$$n = 1 - \frac{m}{\rho t} \tag{8}$$

In the above relations, porosity of fabric is critical as it significantly changes under load. Moreover, Rollin et al. [26] studied the fabric properties through image analyzer technique and suggested an analytical relation for permeability calculation of geotextiles.

$$k = \frac{d_f(d_f + \bar{d}_p)n\rho\mu}{A} \tag{9}$$

Strength of Geotextile. Fourie and Addis [6] presented that for the design criteria of a geotextile filter, the filtration opening size must relate with a characteristic diameter of soil to be retained as:

$$\frac{O_{95}}{d_{85}} \leq x \tag{10}$$

Table 2 Properties of geotextiles by Zhang et al. [33]

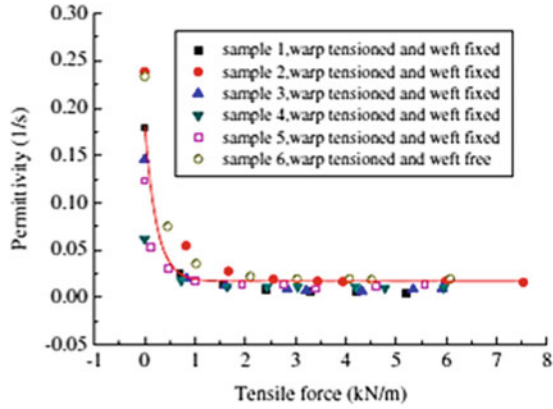
Geotextile	Warp tensile strength (kN/m)	Weft tensile strength (kN/m)	Elongation at break (%)		Apparent opening pore size (mm)	Mass unit area (g/m ²)
			Warp	Weft		
W1	20.5	17.5	18.1	17.4	0.08–0.5	120
W2	26.2	19.9	18.6	18.1	0.08–0.5	160

When the geotextiles are subjected to a tensile load of 2.06 kN/m from an un-tensioned case, FOS reduces to 0.59 mm from approximately 0.82 mm. This results in the 28% decrease in the d_{85} of soil in which geotextile can retain. As equal orthogonal in-plane small tensile load is applied, the small pores start to close and only on increasing the tensile load bigger pores start collapsing and as unequal orthogonal tensile load applied, the shape of woven geotextile openings starts distorting and hence pore spaces decreased. The notable change is the excessive change in woven geotextile behaviour due to small load change, which suggests the importance of the smaller pore size or spaces.

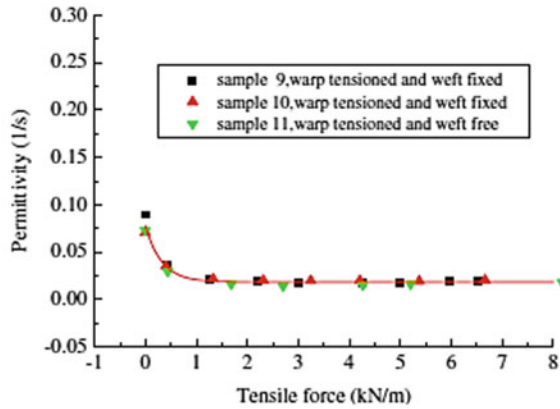
Srivastava et al. [29] studied a 10 m high and 5 m top width homogeneous dam section with 1 V: 2H (u/s) and 1 V: 3H (d/s) slopes, full condition and 2 m freeboard height through FEM analysis (mesh is generated by 15-node triangular elements). This study proved that the use of geosynthetics as seepage barrier manages the seepage losses as well as increases the stability under static and dynamic loading conditions of the dam section. Factor of safety under static loading condition is increased by 1.45 times, and for the deformation of the crest of the dam and acceleration of crest reduces to almost 3 times and 2.5 times, respectively. Zhang et al. [33] studied warp tensile and weft tensile loads effect over permittivity of the geotextile. Two geotextiles (namely W1 and W2) were selected with different properties as shown in Table 2.

This study proves that the increase in warp tensile force causes permittivity to decrease promptly for geotextiles (both W1 and W2); as soon as the tension reaches a value of 1 kN/m the permittivity becomes steady. When warp fibres are in relaxed state, the gaps between adjacent weft fibres and also between weft and warp fibres become larger. Through the gap between warp and weft fibres, water can flow and then reaches adjacent weft fibres. Due to the warp tension, geotextile is stretched, and the gap between weft and warp fibres is reduced continuously that resulting in flow reduction through that gap and ultimately permittivity of geotextile reduced sharply at early stage of loading but as the tension reaches to 1 kN/m, the gap between weft and warp fibres did not decrease further, causes a steady permittivity. In the case of weft tension, the results are opposite from warp tension. As the geotextiles are subjected to weft tension, the permittivity increases because the weft fibres increased in size, get thinner and open up the weave, which allows water to flow uninterrupted. Also, the geotextile having more strength has less permeability because the arrangement of fibres is tight and thick (Fig. 2).

Fig. 2 Permittivity of geotextile with warp tension for **a** W1 and **b** W2



(a)



(b)

There are various mechanisms through which the impervious core of an embankment dam can crack along with differential settlement, seismic activity and desiccation, which leads to a high compressive soil pressure on geotextile, if the embankment crack is in the direction perpendicular to the plane of the geotextile then the geotextile may tear because it will experience stretching over short distance. Failure criteria for embedded fabric, with interface friction top and bottom:

$$P = \frac{T_{ult}}{FS} = 2L\sigma \tan\delta = 2L(K_a\gamma h)\tan\delta \tag{11}$$

Elasticity of the fabric, where there is an effective embedment on both sides of the crack centre:

$$e_{ult} = \frac{c}{2L} \tag{12}$$

Table 3 Properties of geotextiles used by Miszkowska et al. [18]

Geotextiles	Mass per unit area (g/m ²)	Thickness (mm)	Opening size (μm)	Tensile strength CMD	Tensile strength MD
A	420	4.5	83	27.1	26.7
B	280	2.6	80	24	20.3
C	200	2.0	100	14.5	16

Table 4 Results of change in permeability after the test [18]

Type of geotextile	kn for Unworn Nonwoven Geotextile (m/s)	kn for Nonwoven geotextiles after artificial clogging (m/s)	Decrease of kn (%)
A	0.0042	0.0018	57.1
B	0.0013	0.0002	84.6
C	0.0017	0.0006	64.7

Combining above two equations

$$c = \frac{T_{ult} * e_{ult}}{K_a \gamma h \tan(\delta) FS} \quad (13)$$

Compression and Clogging on Geotextile. Miszkowska et al. [18] studied the artificial clogging test at constant compression of 10 kPa for three types of nonwoven geotextiles (as A, B and C) with properties as mentioned in Tables 3 and 4.

Clogging depends on material's physical properties, such as: opening size, thickness and mass. Miszkowska et al. [18] presented the study that protection of bank under cyclic flow condition can be done if wide geotextile with lesser shrinkage is used. Moreover, Palmeira and Tatto [23] proposed that for the slopes under cyclic load and water flow, base soil with geotextile filter of larger width can minimize the values of maximum pore pressure due to damping effects. The CT images were presented by Miszkowska et al. [18], which confirmed that the clogging of geotextile pores was due to soil particles but entrapment of more fines was observed (Fig. 3).

Maheshwari and Gunjagi [16] studied the variation in permittivity of woven and nonwoven geotextiles and presented that there was a little amount of clogging and piping occurs with sand, and there is a development of blinding layer over the nonwoven geotextile with clayey soil, and there was a slight development of piping with the first layer of clay soil but it disappears as these layers increase. But woven geotextiles are moderately clogged and little piping occurs in case of sandy soil whereas, with clayey soil, very heavy clogging takes place because of a smaller number of filter openings and formation of blinding layer over the geotextile.

Aydilek and Edil [2] studied that percent open area (POA) is defined as the ratio of open area to the total area of woven geotextile and compared with the apparent opening size (AOS) of the manufactured woven geotextiles. POA and permittivity

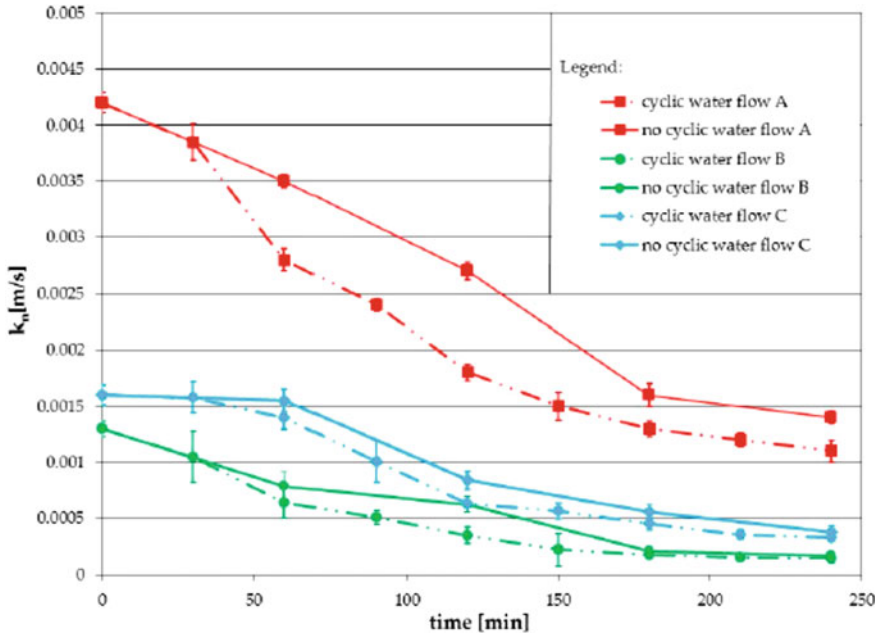


Fig. 3 Variation of permeability with time [18]

are directly related, which affects the geotextiles’ filtration performance. For the calculation of POA, the image analysis technique is suggested by Austin et al. [1], Mlynarek and Lombard [21]. This method includes the counting of white and black pixels in a binary image that corresponds to pore opening and filaments, respectively. Giroud [9] suggested an equation for woven geotextiles (only for monofilament and multifilament) POA calculation. The equation is as follows:

$$POA = \left[\frac{O_F}{(O_F + d_F)} \right]^2 \tag{14}$$

The transmissivity of saturated fabrics was found to be decreased in water flow test as normal stress increased but becomes steady at higher stresses. This result is significant as Zhang et al. [33] presented almost the same result years later.

Furthermore, Robert et al. [25] studied that inlet air pressure influences the transmissivity as well as permeability of geotextile in the air flow tests but remains unaltered by normal stress application. Importantly, the air flow properties are of higher order than water flow properties for the same geotextile. This is mainly due to the lesser density and viscosity of air than water. Result shows that air can also penetrate easily through the saturated geotextiles because of hydrophobicity of polymer and permselectivity of air. Therefore, geotextiles should be designed such that they must have maximum water transmissivity and adequate air escape capability.

Giroud [10] presented mathematical relations for calculations of geotextile filtration opening size based on the coefficient of uniformity and the density of soil as follows:

For $C'_u \leq 3$:

$$\begin{aligned} O_F &\leq (C'_u)^{0.3} d'_{85S} && \text{for a loose soil} \\ O_F &\leq 1.5(C'_u)^{0.3} d'_{85S} && \text{for a medium dense soil} \\ O_F &\leq 2(C'_u)^{0.3} d'_{85S} && \text{for a dense soil} \end{aligned}$$

For $C'_u \geq 3$:

$$\begin{aligned} O_F &\leq \frac{9 d'_{85S}}{(C'_u)^{1.7}} && \text{for a loose soil} \\ O_F &\leq \frac{13.5 d'_{85S}}{(C'_u)^{1.7}} && \text{for a medium dense soil} \\ O_F &\leq \frac{18 d'_{85S}}{(C'_u)^{1.7}} && \text{for a dense soil} \end{aligned}$$

According to Palmeira and Gardoni [22], the normal and in-plane permeability's values of nonwoven geotextiles are mostly varied with the characteristics of the microstructure of geotextile and normal stress acting on it. This result is significant as Giroud [9] presented a satisfactory accuracy for virgin geotextile coefficient of permeability prediction under compression. The permittivity and compressibility of geotextiles reduce when it gets clogged. However, the values of specimens of soil impregnated geotextile are found to be within the range as compared with virgin geotextile whereas glass bead impregnated geotextile specimens showed values above the range. This property suggests that impregnated geotextiles are low compressible.

State of Soil and Geotextile. The unsaturated condition of the materials (soil and geotextiles) affects the overall hydraulic behaviour of the earthen system as there is a chance of redistribution of water content profile. Nonwoven geotextiles behave similarly to coarse soils as having very low air entry values between 0.4 and 0.9 kPa. Bouazza et al. [3] observed that geotextile required low suction below 1.2 kPa to drain or filter, whereas, on increasing suction, the drainage or filter capacity decreases rapidly. Capillary break develops at the interface of unsaturated soil and geosynthetic layer, causing an increase in soil pore pressures, hence soil losses its strength and ultimately structure collapse. The above study supports the work of Iryo et al. (2003) [13], they experimentally observed the water characteristic curve and hydraulic conductivity function of unsaturated geotextiles using van Genuchten's equations and FEM analysis.

Mittal et al. [20] studied that if the small earthen dam has to be made, the local soil can be replaced by fly ash (product of thermal power plant) and bentonite (abundant in India). They examined the base material with geotextile, granular filter, without filter using laboratory analysis and analytical tool SEEP/W. The author's results are mentioned in Table 5.

Table 5 The results drawn from the study are summarized as below [20]

Parameters	Without any filter	With granular filter	With geotextile filter
Time taken by water to appear at downstream slope (hrs)	3.5	2.5	2.75
Seepage rate per unit width (m^3/s)	4.24×10^{-6}	15.87×10^{-6}	11.81×10^{-6}
Failure of downstream slope	Yes	No	No
Seepage rate per unit with obtained from SEEP/W analysis (m^3/s)	4.43×10^{-6}	11.43×10^{-6}	11.42×10^{-6}

3.2 Performance

In the drainage system, there are many factors that affect the durability of geotextile filters but one of the dominating factors is clogging, which is caused by physical, biological and chemical processes. According to Veylon et al. [32] study for a long service, the geotextiles (both woven and nonwoven) function well in terms of mechanical resistance. The filtration performances are affected due to binding by granular cake, internal clogging; chemical clogging by calcite precipitation on the downstream face of the geotextiles, which also decrease its hydraulic performance.

Portelinha et al. [24] observed that nonwoven section has 40% less tensile strength than woven sections as well as unconfined stiffness (at 5% strain) three times lower, even though both type geotextiles show similar behaviour for internal displacement and reinforcement strain. Generally, the maximum displacement and reinforcement strain observed in nonwoven section but serviceability limit state analysis shows that confined tensile properties of non-woven geotextiles gave better field performance. After a certain period, the average suction of soil became constant, which was a positive contribution to the performance of both sections.

According to Zornberg [34] in homogenous earthen dam, the clogging was negligible (only 0.2%) of the pore volume of the geotextile, as tested on the geotextile after 22 years used in the Valcros Dam. This supports the work of Portelinha et al. [24] and Veylon et al. [32] that most of the displacement and deformation of geotextiles soil filtration system/interface take place during construction and its performance is influenced by many factors such as type of soil and geotextiles, field conditions, filtration and hydraulic behaviour.

The rapid pore pressure dissipation resulted in high effective stress in permeable geotextile reinforcement, which enhances its stability than with geogrid reinforcement or without any reinforcement. Hence, it shows that even in case of poorly draining soil, the permeable geotextile satisfies the dual functions of reinforcement and drainage behaviour as suggested by Tan et al. [31].

3.3 Limitations of Using Geotextile Filters

Koerner and Koerner [14] studied 69 cases of geotextiles failure and group them into four categories that are design, atypical soils, atypical permeants and field condition. A summary of the geotextile filters failure is given below in Table 6.

Table 6 Geotextile filters failure

Category	Type	Number of occurrences	Resulting situation
Design	Poor fabric selection	1	Inadequate fabric voids
	Poor fabric design	5	Inadequate fabric voids
	Socked drainage pipe	2	Inadequate fabric voids
	Reversing flow conditions	6	Soil loss and piping
Atypical soils	Cohesionless fines	6	Soil loss and piping
	Gap graded soils	3	Soil loss and piping
	Dispersive days	2	Excessive fabric clogging
	Ochre clogging	6	Excessive fabric clogging
Atypical permeants	Oil and sludges	2	Excessive fabric clogging
	Turbid water	2	Excessive fabric clogging
	High alkalinity water	2	Excessive fabric clogging
	Landfill leachates	10	Excessive fabric clogging
	Wastewater and agricultural	5	Excessive fabric clogging
Field installation	Lack of intimate contact	16	Soil loss and piping
	Glued filter fabric	1	Excessive fabric clogging

4 Conclusion

Geomembranes and geotextiles can be used as filters in earthen dams for seepage control as well as stability. The filtration property is affected by strength of the geotextile and base material, hydraulic characteristics, compression and clogging.

Usually, filtration reduces as compression and clogging increase, hence it reduces the stability of the dam but geotextiles have the property of collapsibility that enables them to widen the pores and recover the filtration rate. At the same time as soon as geotextile comes under the influence of in-plane vertical tension, the filtration increases, as the weave of the geotextile opens up.

It is important to use geotextile filters as it has many advantages over graded granular filter material due to lower risk of contamination and segregation of drainage aggregate during installation. However, the quality of fabric is to be ensured for its design due to atypical soil quality as atypical soil governs many geotextile parameters. This can be overcome easily for its efficient use in all such hydraulic structures.

5 Notations

A	=	$C_D \times R_E$
A_R	=	Relative open area of the filter fabric (area of openings/total area of filter fabric)
C_D	=	Drag coefficient
C	=	Crack aperture (feet)
C'_u	=	Coefficient of uniformity
CMD	=	Cross-machine direction
d'	=	Geotextile thickness
d'_{85}	=	Linear particle size of the soil corresponds to 85% by mass
d_f	=	Geotextile fibre diameter
\bar{d}_p	=	Average fabric pore size
d_{85}	=	Characteristic diameter of the soil to be retained such that 85% particles are smaller than
d_{sp}	=	Diameter of the spheres

(continued)

(continued)

e_{ult}	=	Ultimate strain (at T_{ult}) (%)
FS	=	Factor of safety
G	=	Acceleration due to gravity
H	=	Depth (feet) elasticity of the fabric, where
K	=	Permeability coefficient / hydraulic conductivity
k_o	=	Pore shape factor, generally $k_o = 2.5$
K_a	=	Earth pressure coefficient
L	=	Effective embedment length (feet)
MD	=	Machine direction
O ₉₅	=	FOS, such that 95% of the pores are smaller than this size
O _F	=	Geotextile filtration opening size (FOS)
P	=	Pullout force (lbs)
R_{Eg}/R_E	=	Reynold's number
T	=	Tortuosity factor, generally $T = 2.0$ and $k_o T = 2.22$
T	=	Fabric thickness
T_{ult}	=	Ultimate tensile strength (lbs)
X	=	Experimentally determined value, [generally $x = 1$ or 2 (Carroll,1983; Christopher & Holtz,1985)]
N	=	Kinematic viscosity of the water
N	=	Porosity of the medium
B	=	Shape factor, a function of tortuosity (T) Giroud [9] suggested average value of $\beta = 0.11$
ρ_w	=	Specific gravity of water
η_w/μ	=	Dynamic viscosity of water

(continued)

(continued)

Γ	=	Fibre density of the fabric
Σ	=	Stress normal to plane of geotextile (psf)
Δ	=	Interface friction angle between soil and geotextile
Γ	=	Unit weight of overburden (pcf)

References

1. D. Austin, J. Mylnarek, E. Blond, Expanded anti-clogging criteria for woven filtration geotextiles, in *Proceedings of Geosynthetics '97*, vol. 2 (IFAI, Long Beach, California, USA, 1997), pp. 1123–1144
2. A. Aydilek, T. Edil, Evaluation of woven geotextile pore structure parameters using image analysis. *Geotech. Test J.* **27**(1), 99–110 (2004)
3. A. Bouazza, J.G. Zornberg, J.S. McCartney, H. Nahlawi, Significance of unsaturated behaviour of geotextiles in earthen structures. *Aust. Geomech. J.* **41**(3), 133–142 (2006)
4. P.C. Carman, Fluid flow through granular beds. *Trans. Inst. Chem. Eng.* **15**, 150–167 (1937)
5. R. Fell, C.F. Wan, J. Cyganiewicz, M. Foster, Closure to Time for Development of Internal Erosion and Piping in Embankment Dams, ed. by R. Fell, C.F. Wan, J. Cyganiewicz, M. Foster. *J. Geotech. Geoenviron. Eng.* **130**(9):980–981 (2004)
6. A.B. Fourie, P.C. Addis, Changes in filtration opening size of woven geotextiles subjected to tensile loads. *Geotext. Geomembr.* **17**(5–6), 331–340 (1999)
7. R. Fell, *Geotechnical engineering of dams*. CRC press, 10 Jan 2005
8. J.P. Giroud, Discussion on filter criteria for geotextiles, in *Proceedings of the Second International Conference on Geotextiles*, Las Vegas, NV, USA, vol. 4 (1982), pp. 36–38
9. J.P. Giroud, Stability of geosynthetic-reinforced soil above a cavity. *Geotext. Geomembr.* **14**(2), 95–109 (1996)
10. J.P. Giroud, Development of criteria for geotextile and granular filter, in *Proceedings of the 9th International Conference on Geosynthetics*, Guarujá, Brazil (2010)
11. D.J. Hoare, Synthetic fabrics as soil filters. *J. Geotech. Eng.* **108**(10), 1230–1245 (1982)
12. T.A. Haliburton, P.D. Wood, Evaluation of US Army Corps of Engineers gradient ratio test for geotextile performance, in *Proceedings of 2nd International Conference on Geotextiles*, Las Vegas (1982), pp. 97–101
13. T. Iryo, R.K. Rowe, On the hydraulic behavior of unsaturated nonwoven geotextiles. *Geotext. Geomembr.* **21**(6), 381–404 (2003)
14. R.M. Koerner, G.R. Koerner, Lessons learned from geotextile filter failures under challenging field conditions. *Geotext. Geomembr.* **43**(3), 272–281 (2015)
15. J. Kozeny, Ueber kapillare Leitung des Wassers im Boden. *Stizungsber Akad Wiss Wien* **136**, 271–306 (1927)
16. B.K. Maheshwari, D.A. Gunjagi, Filtration and clogging behavior of geotextiles with roorkee soils. *Geotech. Geol. Eng.* **26**, 101–107 (2008)
17. A. Lord, T. Soong, R. Koerner, Relaxation behavior of thermally induced stress in HDPE geomembranes. *Geosynthetics. Int.* **2**(3), 626–634 (1995)
18. A. Miszkowska, S. Lenart, E. Koda, Changes of permeability of nonwoven geotextiles due to clogging and cyclic water flow in laboratory conditions. *Water* **9**(9), 660–674 (2017)

19. D.J. Mitchell, P. Richmond, Study of physical adsorption using the mean spherical model. *J. Chem. Soc., Faraday Trans.* **72** (2), 1613–1621(1976)
20. S. Mittal, Anamika, Performance study of geotextile filter in earthen dam with flyash and bentonite as base soil. *J. Indian Water Resour. Soc.* **37**(3), 42–48 (2017)
21. J. Mlynarek, G. Lombard, Significance of percent open area in the design of woven geotextile filters, in *Proceedings of Geosynthetics '97*, vol. 2 (IFAI, Long Beach, California, USA, 1997), pp. 1093–1107
22. E.M. Palmeira, M.G. Gardoni, The influence of partial clogging and pressure on the behaviour of geotextiles in drainage systems. *Geosynth. Int.* **7**(4–6), 403–431 (2000)
23. E.M. Palmeira, J. Totto, Behaviour of geotextile filters in armoured slopes subjected to the action of waves. *Geotext. Geomembr.* **11**(3), 46–55 (2014)
24. F.H.M. Portelinha, J.G. Zornberg, V. Pimentel, Field performance of retaining walls reinforced with woven and nonwoven geotextiles. *Geosynth. Int.* **21**(4), 270–284 (2014)
25. M.K. Robert, A.B. John, P.M. Joseph, Water and air transmissivity of geotextiles. *Geotext. Geomembr.* **1**(1), 57–73 (1984)
26. A.L. Rollin, R. Denis, L. Estaque, J. Masounave, Hydraulic behaviour of synthetic nonwoven filter fabrics. *Proc. Canadian J. Chem. Engrs* **60**, 226–234 (1982)
27. M. Sato, T. Yoshida, M. Futaki, Drainage performance of geotextiles. *Geotext. Geomembr.* **4**(3–4), 223–240 (1986)
28. A. Soroush, P.T. Shourijeh, H.F. Aghajani, A. Mohammadinia, A.H. Aminzadeh, A review of the sand castle test for assessing collapsibility of filters in dams. *Geotech. Test J.* **35**(4), 503–516 (2012)
29. Srivastava A, Babu GLS. Stability analysis of earth dams under static and earthquake loading using geosynthetics as seepage barrier, in *Proceedings of the 18th International Conference on Soil Mechanics and Geotechnical Engineering*, Paris (2013), pp. 1607–1610
30. A. Tahmasebipoor, R. Noorzad, I. Shooshpasha, A. Barari, A parametric study of stability of geotextile-reinforced soil above an underground cavity. *Arab. J. Geosci.* **5**(3), 449–456 (2012)
31. S.A. Tan, S.H. Chew, C.C. Ng, S.L. Loh, G.P. Karunaratne, P. Delmas, K.H. Loke, Large-scale drainage behaviour of composite geotextile and geogrid in residual soil. *Geotext. Geomembr.* **19**(3), 163–176 (2001)
32. G. Veylon, G. Stoltz, P.M. Eriaux, Y.H. Faure, N.T. Foltz, Performance of geotextile filters after 18 years' service in drainage trenches. *Geotext. Geomembr.* **44**(4), 515–533 (2016)
33. Y. Zhang, W. Liu, W. Shao, Y. Yang, Experimental study on water permittivity of woven polypropylene geotextile under tension. *Geotext. Geomembr.* **37**, 10–15 (2013)
34. J.G. Zornberg, Ingenuity in geotechnical design using geosynthetics. *Geotech. Eng. State Art Pract. Geotech.* **226**, 398–419 (2012)

Seismic Response Control of RCC Building Using Dampers



Chinmay Gurmule, S. S. Sanghai , and P. Y. Pawade

1 Introduction

Seismic isolation of a structure can help in reducing the ground motion produced from any earthquake, transfer to the structure. There are various types of system available to reduce these effects. Such devices may increase the cost in any structure, but by optimization, the number and location of damper can be done. Such devices help in reducing the seismic effect on buildings. There are many structures all around the globe where such devices are used in seismic zones for ground forces and wind forces with an aim of reducing vibration in structure. The use of such devices in future can help in limiting damages to structure and life as well.

2 Dampers and Types of Dampers

Various studies [1–3] have shown that buildings are generally designed for vertical loadings, as due to growing population and urbanization, the structures in metro cities are slimmer and taller. When any natural calamity like earthquake occurs, the structures are unable to resist the seismic forces, which causes failure and leads to loss of life. To resist such forces, lateral load resisting mechanism, structural control techniques are formed. These include the use of various types of control system and different types of dampers, which include control systems like, passive control system, active control system and semi-active control system. The passive systems are

C. Gurmule

Structural Engineering, G. H. Raisoni College of Engineering, Nagpur, India

S. S. Sanghai (✉) · P. Y. Pawade

Department of Civil Engineering, G. H. Raisoni College of Engineering, Nagpur, India

e-mail: sanket.sanghai@raisoni.net

further classified as passive strengthening, base isolation, passive energy dissipation, tuned mass damper and tuned liquid dampers. The dampers are classified as friction, metal, viscous, viscoelastic, shape memory alloys, liquid dampers and mass dampers. For new constructions, the cost of lateral strengthening is generally high, whereas, for existing structures, the lateral load strengthening system is technological intensive and is considered to be inconvenient. This type of system not only resists the seismic forces but also wind forces. To achieve satisfactory results for earthquake response as per the study [4], three methods are identified:

- i. Structural isolation method—which is very efficient but expensive and difficult to carry out.
- ii. Active control system—needs to keep the dampers activated all the time, which may be undependable during earthquakes as the power supply may get disrupted.
- iii. The passive energy dissipation systems—are able to resist the seismic energy due to which the demand on structural members is reduced, which reduces the structural damage.

3 Working of Dampers

As per study [2, 4–6] during an earthquake, high energy is developed and is directly applied to the structure. Dampers dissipate this energy into heat energy, which are kinetic energy and potential (strain) energy to structure, and is absorbed or gradually reduced. Dampers help in protecting the building from structural and non-structural damage induced by earthquake and wind loads. If the structure has no damping, the vibration will be continuous and if the structure has material damping then the vibration will be reduced gradually. The increase in dampness reduces structural response damping effect at low frequency and has no effect on spectrum amount at high frequency. Dampers are based on rotational friction concept; they consist of layers of long and short steel plates that are bolted together with a high capacity bolt in each joint, and between the plates, circular friction pads are placed, this regulates the movement of plates during seismic activity. When an external force acts on a frame structure, the top of the structure starts to displace horizontally. The frictional force developed due to this will be resisted by the steel plates, and friction pad will resist the force in horizontal. When the structure moves to and from due to seismic excitation, dissipation of induced energy is done due to tension-compression in dampers. The use of dampers is very popular amongst engineers, as the dampers are easy to assemble and very flexible in arrangement.

4 Structural Analysis Programs

Many studies [7–15] show that the manual procedure of seismic analysis for any structure with dampers will prove to be lengthy and time consuming. It includes the calculation for stiffness and solution of matrix. Mainly used structural analysis programs are ETABS, SAP2000, and ANSYS. The procedure of analyzing structure with the help of such software can be time saver. While modeling and analyzing the structure, specific construction code for the analysis purpose is available in software. The software analysis procedure includes modeling of the model, assigning section and material properties, assigning load patterns and load cases. Selection of code is required for analysis purposes. The analysis type includes static, dynamic, linear, non-linear, response spectrum analysis. Depending on the load cases, the values of maximum base shear, absolute acceleration, absolute displacement, story drift from the analysis obtained can be varying for different stories. The various results obtained can be compared and then the design or data for damping system to be used can be determined. There can be difficulty in assigning a particular analysis type for a particular damping system, to obtain the results. In one of the study [10], it was mentioned that, specific type of analysis should be carried for design and placement of different types of damping system. Which will be used is found out.

5 Targeted Performance

Various studies [16–21] have tried to formulate or put forward the terms, which can affect the performance of controlled systems, their impact due to seismic forces on structure, and how the values of such terms can be maintained so as to keep the structure stable and safe. Adopting incremental dynamic analysis can help to calculate the seismic response of a structure at various earthquake intensities. By developing IDA curve, the collapse of the structure can be determined. Each curve is related to the maximum relative displacement. To avoid failure, the ultimate displacement ratio should be designed [16]. In the study [17–20], damping can influence the response of structure during earthquake, in the first mode 20–25% of total damping is sufficient. Additional damping may lead to increase in acceleration values, which may cause reduction in interstory drift. Utilization of optimal damping can help in minimizing the repair cost caused to a structure by an earthquake. The use of dampers is needed, as it reduces peak acceleration and number of large response cycles and duration of shaking of the building. Displacement-based design can help in minimizing the effect due to ground motion [21]. A five-step procedure starting from target reduction to obtaining the characteristics for reduction purpose, the relation between damping coefficients and target reduction factors was in existence for shear, equal floor mass and lateral stiffness [22].

6 Optimization Techniques

Damper optimization is a new area of research in recent years. As providing dampers at all stories or at a particular spacing will not prove to be economical and will be a very costly affair with the cost of construction taken into account. Various studies [22–28] have been done to find different techniques of optimizing the number of dampers required, by different types of algorithm and equations considering nonlinear analysis to satisfy the required capacity. Dampers dissipate energy in proportion to velocity and not displacement and therefore do not cause a large increase in earthquake forces but estimating damper cost can be uneconomical. Optimizing the properties of dampers can help in minimizing the number of dampers to be used [22]. Spectral analysis, developed and conducted in the frequency domain, is an attractive method, it is found to be flexible with good performance and shows that computational time period is reduced [23]. A new semi-active algorithm is adopted to adjust the damping capacity according to the deformation results. It can be used for different ground excitations and shows uniform distribution of inter-story drift [24]. To minimize the maximum displacement at the top of the structure, inter-story drift and the acceleration at the top of the structure simultaneous optimization using the firefly algorithm are done. It is a function-based algorithm by which performance for preferred function type can be done [25]. The backtracking search optimization algorithm (BSA) is used, recommended as an effective tool for optimum design of friction dampers for optimum and economical design [26]. To reduce the top floor displacement for more than one mode, Differential Evolution (DE) algorithm used for optimization is found to be effective [27]. The analysis of structures installed with seismic control devices must be done by a step-by-step time history analysis, since the devices introduce strong nonlinearities in the system. If some measures of structural response are reduced then, this may lead to an increase in some other response quantities, and therefore, there is no unique way of defining an optimal problem, but a pre-selected design objective can help in obtaining desirable flexibility in the design [28].

7 Location and Number of Dampers

Using dampers in structure is costly. Therefore, the number and proper location of damper in a structure are important. A very less study or research is available on the numbers and placement of dampers for dynamic response of any structure. The change in numbers and placement of dampers can play an important role in behavior in structure for resisting such dynamic forces. Various studies [29–33] have been performed on software, by comparing the results of dampers located at various stories and after using optimization techniques. The placement of dampers seems to play an important role in resisting such forces. A large number of damper placements do not always lead to a good result, the best arrangement for number and placement of damper is one damper per story with the same damping constant

[29]. A new mathematical model of location optimization called as improved weight coefficient method, resulted in to use of a greater number of dampers, while in practical applications, the number of dampers should be confirmed by including cost factor [30]. When dampers and base isolation both are used together, maximum bending moment was reduced. Seismic dampers at proper location can reduce the story drift to a greater extent and thus reduce the bending moment [31]. On the basis of energy dissipation criteria [32], top roof displacement, maximum base shear and percentage energy dissipated were some factors taken for comparison purpose, the number and position of dampers influence the structural response for seismic forces. A large number of dampers do not always give the best result. The placement of damper on bay of floors including ground floor is done, the optimum bay is the first bay in the direction of earthquake, placing dampers at each and every bay is not recommended as it is not effective, placing dampers at ground floor is ineffective [33].

8 Conclusion

The conclusions from the above studies are:

- i. Various types of dampers are used in buildings globally. It can help in reducing the seismic effect on structure. Practical and experimental research approves the use of dampers. A satisfactory response of structure under seismic conditions can be achieved with the help of dampers. The construction and working are found to be easy and very effective.
- ii. Structural analysis of building with damping system using software can help in evaluating the performance and fixing the targeted response values for structure, by modifying those values a better response can be obtained. Story drift, base shear values are reduced in structure with damping system as compared with same structure with no damping system, and the behavior of structure with damping system is a way better than structures with the absence of damping system.
- iii. A number of optimization techniques are available, which can be used to obtain the significant number of dampers required for better performance of structure. The number of dampers required after optimization proves to be economical rather than placing dampers without optimization. The position and number of dampers in a building can affect the cost of construction, and therefore, proper number of dampers per story must be selected after optimization.

References

1. V. Umachagi, K. Venkataramana, G.R. Reddy, R. Verma, Applications of dampers for vibration control of structures: an overview, in *International Journal of Research in Engineering and Technology, IC-RICE Conference Issue November 2013* (2013). <http://www.ijret.org>
2. N. K. Rai, G. R. Reddy, S. Ramanujam, V. Venkatraj, P. Agrawal, Seismic response control systems for structures. *Defence Sci. J.* **59**(3) (2009)
3. A. Heysami, Types of dampers and their seismic performance during an earthquake. *Curr. World Environ.* **10**(1), 1002–1015 (2015)
4. J. Marko, D. Thambiratnam, N. Perera, Influence of damping systems on building structures subject to seismic effects. *Eng. Struct.* **26**(13), 1939–1956 (2004)
5. I.H. Mualla, L.O. Nielsen, M. Sugisawa, Y. Suzuki, Large capacity dampers for buildings and structures, in *15th World Conference on Earthquake Engineering*, Lisbon, Portugal (2012)
6. I.H. Mualla, E.D. Jakupsson, L.O. Nielsen, Structural behavior of 5000 kN damper, in *14th European Conference on Earthquake Engineering*, Ohrid, vol. 30 (2010)
7. H. Shad, A. Adnan, Simulation of structure with TLD in Ansys software as modal and harmonic analysis, in *Regional Engineering Postgraduate Conference (EPC)*, University Technology Malaysia Malaysia (2011)
8. S.N. Gowda, Sindgi, Seismic analysis of high-rise building using tuned liquid damper, in *International Journal of Future Generation Communication and Networking*, vol. 13, no. 3 (2020), pp. 2843–2861
9. R. Folić, M. Čosić, B. Folić, Damping models for flow chart based structural analysis, in *The 15th International Science Conference VSU*, Sofia, Bulgaria (2015), pp. 155–164
10. W. Khan, S. Akhtar, A. Hussain, Non-linear time history analysis of tall structure for seismic load using damper. *Int. J. Sci. Res. Publ.* **4**(4), 1–5 (2014)
11. M. Umeshchandra, J. Sandhya Rani, Response reduction of tall buildings subjected to seismic loads by tuned mass damper. *CVR J. Sci. Technol.* **14**, 102–106 (2018)
12. X. Lin, P.J. Moss, A.J. Carr, Seismic analysis and design of building structures with supplemental lead dampers, in *Proceedings of the 12th World Conference on Earthquake Engineering* (2000)
13. P.A. Vikhe, Kawade, Seismic response control of high-rise building by using viscous damper, **2**(5) (2016)
14. N. Prajapati, N. Sorathia, Seismic analysis and performance of high-rise building with damper. *Int. J. Adv. Eng. Res. E-ISSN (O)*, 2348–4470 (2018)
15. P. Sajjan, P. Biradar, Study on the effect of viscous damper for RCC frame structure. *Int. J. Res. Eng. Technol.* **5**(9) (2016)
16. W. Guo, J. Wu, Y. Hu, Y. Li, T.Y. Yang, Seismic performance evaluation of typical dampers designed by Chinese building code. *Earthq. Eng. Eng. Vibr.* **18**(2), 433–446 (2019)
17. A. Occhiuzzi, Additional viscous dampers for civil structures: analysis of design methods based on effective evaluation of modal damping ratios. *Eng. Struct.* **31**(5), 1093–1101 (2009)
18. D. Gobbo, G. Marcantonio, A. Blakeborough, M.S. Williams, Improving total-building seismic performance using linear fluid viscous dampers. *Bull. Earthq. Eng.* **16**(9), 4249–4272 (2018)
19. K. Kasai, Performance of seismic protective systems for supertall buildings and their contents (2016)
20. J. Kim, H. Choi, Displacement-based design of supplemental dampers for seismic retrofit of a framed structure. *J. Struct. Eng.* **132**(6), 873–883 (2006)
21. M. Kargahi, C.G. Ekwueme, Optimization of viscous damper properties for reduction of seismic risk in concrete buildings, in *13th World Conference on Earthquake Engineering, Paper*, no. 1027 (2004), pp. 1–6
22. S. Silvestri, G. Gasparini, T. Trombetti, A five-step procedure for the dimensioning of viscous dampers to be inserted in building structures. *J. Earthquake Eng.* **14**(3), 417–447 (2010)
23. L.F.F. Miguel, L.F.F. Miguel, R.H. Lopez, Methodology for the simultaneous optimization of location and parameters of friction dampers in the frequency domain. *Eng. Optim.* **50**(12), 2108–2122 (2018)

24. H. Quintana, Caudana, M. Petkovski, Optimum performance of structural control with friction dampers. *Eng. Struct.* **172**, 154–162 (2018)
25. S.P. Ontiveros-Pérez, L.F.F. Miguel, L.F.F. Miguel, A new assessment in the simultaneous optimization of friction dampers in plane and spatial civil structures. *Math. Prob. Eng.* 2017 (2017)
26. L.F.F. Miguel, L.F.F. Miguel, R.H. Lopez, Simultaneous optimization of force and placement of friction dampers under seismic loading. *Eng. Optim.* **48**(4), 582–602
27. H. Cetin, E. Aydin, B. Ozturk, Optimal design and distribution of viscous dampers for shear building structures under seismic excitations. *Front. Built Environ.* **5**(90), 1–13 (2019)
28. L.M. Moreschi, M.P. Singh, Design of yielding metallic and friction dampers for optimal seismic performance. *Earthq. Eng. Struct. Dynam.* **32**(8), 1291–1311 (2003)
29. C. Tovar, O.A. López, Effect of the position and number of dampers on the seismic response of frame structures, in *13th World Conference of Earthquake Engineering*, Vancouver, BC, Canada, vol. 10 (2004)
30. J.-T. Qu, H.-N. Li, Study on optimal placement and reasonable number of viscoelastic dampers by improved weight coefficient method. *Math. Prob. Eng.* 2013 (2013)
31. A. Shakibabarough, M. Valinejadshoubi, A. Bagchi, Effects of damper locations and base isolators on seismic response of a building frame. *Int. Scholarly Sci. Res. Innov.* **10**(6), 739–744 (2016)
32. I.-S. Oance, S. Gelmambet, Effect of number and position of rotational friction dampers on seismic response of steel frame. *Ovidius Univ. Ann. Constanta-Ser. Civil Eng.* **21**(1), 99–104 (2019)
33. O.S. Hussien, M.I. Elamy, Optimal placement of dampers on multistorey frames using dynamic analysis. *Strength Mater.* **52**(3), 470–479 (2020)

Utilization of Sugarcane Bagasse Ash for the Stabilization of Pavement Subgrade: A Probabilistic Approach



Monalisa Priyadarshini and Jyoti Prakash Giri

1 Introduction

Subgrade is mainly functioning to possess adequate support to pavement, and it should offer good resistance of load carrying capacity, better drainage quality under adverse climate with loading conditions. Generally, the subgrade soil sometimes might be not having enough strength to support the traffic loading coming over it. The soil that comprises clay particles expresses substantial mark of distress due to loss of strength during wet seasons and shrinkage during dry conditions. Black cotton soil is one of such type of soils, which lose its strength during the rainy season due to their expansive behaviour, and this type of soil is found in maximum part of our country. Due to its poor properties, this type of soil becomes unsuitable for engineering construction purposes like road construction. To counteract this issue, stabilization of soil is required [1, 2]. Soil stabilization is referred to the improvement of the soil stability or load carrying capacity of the pavement layer by the controlled compaction; proportioning and/or addition of suitable admixture or stabilizers [2, 3]. In the past few decades, number of researchers were tried to improve the properties of black cotton soil with different types of solid wastes and the results are also a promising one [4]. Based on the same trend, the aim of the study is focused on to stabilize the subgrade layer made with black cotton soil incorporating waste materials named as sugarcane bagasse. The utilization of this waste that may result in reduction

M. Priyadarshini (✉)

Department of Civil Engineering, Government College of Engineering Kalahandi, Bhawanipatna, Odisha 766002, India

e-mail: monalisa@gcekbpatna.ac.in

J. P. Giri

Department of Civil Engineering, GMR Institute of Technology, Rajam, Andhra Pradesh 532127, India

e-mail: jyotiprakash.g@gmrit.edu.in

in wastage also makes the environment sustainable. In addition, a probabilistic study has also been done to confirm its suitability for soil stabilization in the construction of pavement.

2 Experimental Programme

2.1 Materials

In the present study, the soil (black cotton) was collected from the local source at Rajam (Fig. 1), Andhra Pradesh, and the different physical properties were tested in the laboratory as shown in Table 1. Similarly, cement and sugarcane bagasse (Fig. 2) were collected from local distributor and nearby sugar factory respectively. The specific gravity of cement and sugarcane bagasse found in the laboratory was 3.01 and 2.18, respectively.

Fig. 1 Black cotton soil



Table 1 Basic properties of used soil sample

Black cotton soil	Results
Liquid limit	68%
Plasticity limit	34.2%
Shrinkage limit	21%
Plasticity index	35.4
Consistency index	1.26
Liquidity index	0.08
Specific gravity	2.61

Fig. 2 Sugarcane bagasse ash



2.2 Test Performed

2.2.1 California Bearing Ratio Test

The California Bearing Ratio (CBR) is the measurement of the resistance to penetration of standard plunger under controlled density and moisture conditions according to IS 2720-16 (1987) [5] of a material. The controlled density (maximum dry density, MDD) and moisture contents (Optimum Moisture Content, OMC) were observed from the standard proctor test [6] as shown in Table 2.

The CBR values for unsoaked and soaked specimens are calculated and mentioned in Table 3. From the table, it was observed that the higher CBR value was offered when the soil was stabilized with 5% of cement. However, the black cotton soil stabilized with bagasse ash offered a higher soaked and unsoaked value at 10% by weight of soil mass.

Table 2 MDD and OMC of stabilized soil

Material	MDD (kN/m ³)	OMC (%)
Black cotton soil	1.671	16
Soil + 5% cement	1.964	20
Soil + 5% bagasse ash	1.665	16
Soil + 10% bagasse ash	1.590	18
Soil + 15% bagasse ash	1.465	20
Soil + 20% bagasse ash	1.313	22
Soil + 25% bagasse ash	1.253	24
Soil + 30% bagasse ash	1.117	26

Table 3 CBR and UCS values for the different subgrade specimens

Material	CBR (Unsoaked)	CBR (Soaked)	UCS (KN/M ²)
Black cotton soil	6.8	2.9	104.8
Soil + 5% cement	23.2	13.5	312.4
Soil + 5% bagasse ash	12.4	4.5	187.5
soil + 10% bagasse ash	15.5	8.3	257.8
Soil + 15% bagasse ash	13.8	7.2	234.2
Soil + 20% Bagasse Ash	11.9	5.8	173.2
Soil + 25% bagasse ash	10.7	4.9	155.6
Soil + 30% bagasse ash	8.5	4.2	146.9

2.2.2 Unconfined Compression Strength Test (UCS)

The UCS test is generally used to determine the compressive strength of a material, which is calculating the unconsolidated and undrained shear strength under unconfined conditions according to IS 2720–10 [7]. The UCS test results observed for all the combinations of stabilized subgrade soli are presented in Table 3. From this, it was found that the sample prepared mixed with cement offered higher strength compared with others followed by soil with 10% sugarcane bagasse. As general, when the percentage of waste was increased in the mixed the strength also decreased. This may be due to a lack of bonding between soil and waste material like bagasse ash.

3 Probabilistic Studies

For getting a model that can find the proper regularities in the distribution models, statistical study is done in this present study. 100 samples were prepared with the fixed composition for the probability study. 25 selected probability distribution functions were chosen having two to three and four parametric distributions. The parameters for generating distribution curves were evaluated as shown in Table 4 at 0.05 of significance level of that follow the acceptance criteria by the goodness of fit test as Kolmogorov–Smirnov (K-S), Kolmogorov- Smirnov-Lilliefors (K-S-L), and Anderson–Darling (A-D) and chi-squared tests, by which the remaining distributions cannot be considered for the analysis as shown in Table 5. The A-D test is a modified version of the K-S test and is found to be more sensitive to deviations in the tails

Table 4 Parameters used in various probability distribution functions

	Distribution type	Parameters
1	Beta (4P)	$\alpha_1 = 6.8457, \alpha_2 = 3.2152, a = 4.3679, b = 6.2353$
2	Burr (3P)	$k = 9.0259, \alpha = 26.768, \beta = 6.2322$
3	Burr (4P)	$k = 102.79, \alpha = 7.167, \beta = 3.1947, \gamma = 4.0717$
4	Erlang (2P)	$m = 461, \beta = 0.01221$
5	Erlang (3P)	$m = 241, \beta = 0.01728, \gamma = 1.4685$
6	Fatigue Life (2P)	$\alpha = 0.0469, \beta = 5.6322$
7	Fatigue Life (3P)	$\alpha = 0.00309, \beta = 84.348, \gamma = -78.71$
8	Gamma (2P)	$\alpha = 461.85, \beta = 0.01221$
9	Gamma (3P)	$\alpha = 188.12, \beta = 0.01967, \gamma = 1.9404$
10	Gen. Gamma (4P)	$k = 1.5895, \alpha = 185.06, \beta = 0.21317, \gamma = -0.04892$
11	Gumbel Max(2P)	$\sigma = 0.20457, \mu = 5.5203$
12	Johnson SB (4P)	$\gamma = -1.5094, \delta = 1.9702, \lambda = 2.4616, \xi = 3.9808$
13	Kumaraswamy (4P)	$\alpha_1 = 323.39, \alpha_2 = 81.019, a = -68.394, b = 6.7802$
14	Log-Gamma (2P)	$\alpha = 1345.4, \beta = 0.00128$
15	Log-Logistic (2P)	$\alpha = 36.246, \beta = 5.6273$
16	Log-Logistic (3P)	$\alpha = 1.3159E + 8, \beta = 1.9738E + 7, \gamma = -1.9738E + 7$
17	Lognormal (2P)	$\sigma = 0.04689, \mu = 1.7285$
18	Lognormal (3P)	$\sigma = 0.02875, \mu = 2.2118, \gamma = -3.4989$
19	Nakagami (2P)	$m = 118.22, \Omega = 31.86$
20	Normal (2P)	$\sigma = 0.26237, \mu = 5.6384$
21	Pearson 5 (2P)	$\alpha = 451.01, \beta = 2537.4$
22	Pearson 5 (3P)	$\alpha = 401.8, \beta = 2147.2, \gamma = 0.27588$
23	Pearson 6 (4P)	$\alpha_1 = 51,673.0, \alpha_2 = 34,377.0, \beta = 24.904, \gamma = -31.797$
24	Weibull (2P)	$\alpha = 25.977, \beta = 5.75$
25	Weibull (3P)	$\alpha = 7.0494, \beta = 1.6616, \gamma = 4.0845$

Note $\alpha_1, \alpha_2, \alpha, k, \delta$ and m = continuous shape parameters; β, σ and λ = continuous scale parameters; γ, μ and ξ = continuous location parameters; a and b = boundary parameters; and Ω = continuous parameters

of the distribution than the K-S test [3, 8]. The test (A-D) was also used in many previous studies [9, 10]. From the goodness of fit (GOF) results as tabulated, the JSB distribution ranks the first and that conforms the best distribution among all distribution for the soaked CBR values, which is a bounded distribution to four parameters (4P). These GOF tests are nonparametric and are mostly used for continuous distributions. The GOF tests were conducted to fit out the ranks of each distribution through which one can predict the best suit distribution with the least rank value among all distributions for the CBR value of subgrade are as shown in Table 5.

A comparison graph is drawn for PDF and CDF for all 25 distributions considered in the study, presented in Fig. 3a, b. From the figure, it was observed that the JSB

Table 5 GOF test for compressive strength of data sample

S.n	Distribution	K-S and K-S-L		A-D		Chi-Squared	
1	Beta (4P)	0.03362	2	0.12434	2	0.62016	2
2	Burr(3P)	0.04935	5	0.22558	5	3.0346	15
3	Burr (4P)	0.04079	4	0.15856	4	2.3678	11
4	Erlang (2P)	0.08873	24	0.72101	23	2.4871	13
5	Erlang (3P)	0.08266	21	0.61652	21	2.361	10
6	Fatigue Life (2P)	0.07607	18	0.54101	18	3.578	18
7	Fatigue Life (3P)	0.06847	11	0.41169	9	2.0086	7
8	Gamma (2P)	0.07294	15	0.48817	14	5.8567	24
9	Gamma (3P)	0.0727	14	0.51071	16	2.4489	12
10	Gen. Gamma (4P)	0.07226	13	0.46481	13	4.5714	22
11	Gumbel Max (2P)	0.13719	25	3.5579	25	9.0047	25
12	Johnson SB (4P)	0.03331	1	0.11673	1	0.57657	1
13	Kumaraswamy (4P)	0.06041	8	0.37427	7	3.3651	17
14	Log-Gamma (2P)	0.07956	20	0.61008	20	3.5891	21
15	Log-Logistic (2P)	0.08472	22	0.70931	22	2.7753	14
16	Log-Logistic (3P)	0.05759	7	0.42342	11	2.3352	9
17	Lognormal (2P)	0.076	17	0.54025	17	3.5782	19
18	Lognormal (3P)	0.0746	16	0.50085	15	5.856	23
19	Nakagami (2P)	0.06973	12	0.44607	12	2.0051	4
20	Normal (2P)	0.06675	9	0.38578	8	2.0072	6
21	Pearson 5 (2P)	0.07908	19	0.59989	19	3.5877	20
22	Pearson 5 (3P)	0.08769	23	0.72322	24	2.3253	8
23	Pearson 6 (4P)	0.0681	10	0.4142	10	2.0064	5
24	Weibull (2P)	0.05095	6	0.34093	6	3.1836	16
25	Weibull (3P)	0.03882	3	0.15196	3	0.68292	3

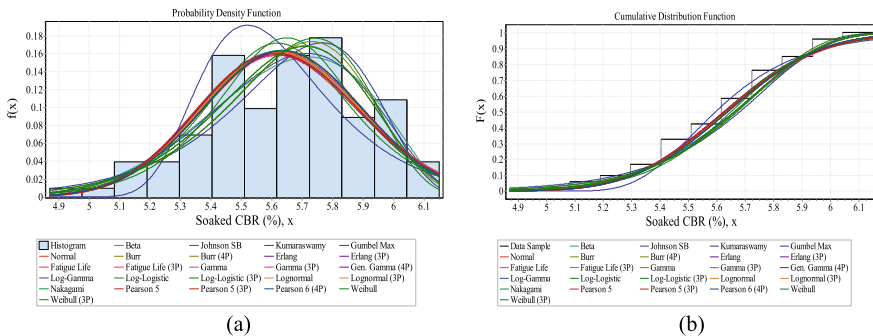


Fig. 3 PDF and CDF plots for all the distributions

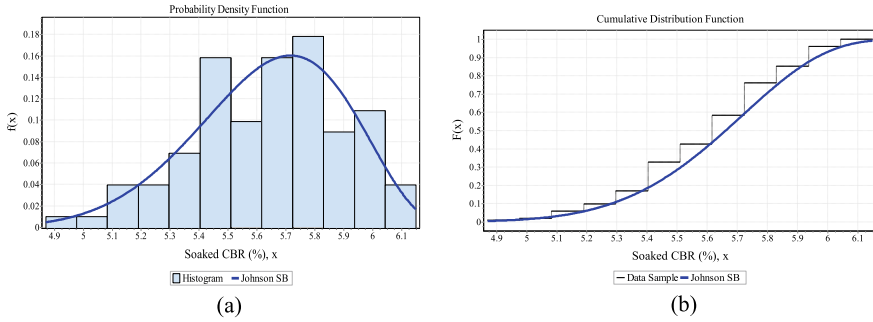


Fig. 4 PDF and CDF plots for the JSB distributions

distribution is found to be the best suit distribution, the PDF and CDF plots for JSB distribution are shown individually in Fig. 4a, b.

The probability density function for JSB distribution

$$f(x) = \frac{\delta\lambda}{\sqrt{2\pi}(x - \xi)(\xi + \lambda - x)} \exp\left\{-\frac{1}{2}\left[\alpha + \delta \ln\left(\frac{x - \xi}{\xi + \lambda - x}\right)\right]^2\right\} \quad (1)$$

$$f(x) = \phi\left(\alpha + \delta \ln\left(\frac{x - \xi}{\xi + \lambda - x}\right)\right) \quad (2)$$

where, ξ = location parameter; δ and α = shape parameters ($\delta > 0$); λ = scale parameter ($\lambda > 0$); and ϕ = Laplace’s integral. The function domain is bounded as $\xi \leq x \leq \xi + \lambda$.

The different performances of JSB distribution are also studied. A probability–probability plot (P-P) is a graph between the observed CDF values that are plotted against the fitted CDF values. The quantile–quantile plot (Q-Q) gives the plot between the observed data against the fitted distribution quantiles. Both the P-P and Q-Q plots were drawn present in Fig. 5a, b to study the suitability between observed data and

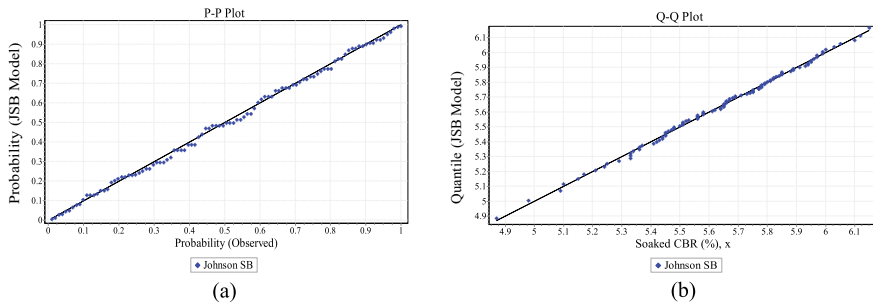


Fig. 5 P-P and Q-Q plots for the JSB distribution

the modelled distribution. From the P-P and Q-Q plots, it can be observed that the data with the JSB function were almost linear along the 45° line, which referred to both predicts the variability of CBR value of soil specimen with significant accuracy.

4 Conclusions

The present research is based on the study of experimental as well as statistical variations of the subgrade properties stabilized with waste material for pavement construction. The different properties are found out by taking various compositions by replacing the sugarcane bagasse. From the experimental study, it was observed that as usual as the soil stabilized with cement offered better results compared with other combinations considered in the study. The minimum value of soaked CBR that satisfies the minimum value according to IRC 37 (2018) is taken for further analysis. However, the black cotton soil stabilized with sugarcane bagasse ash also offered a promising result in terms of CBR (both soaked and unsoked) and UCS test. Furthermore, the same was also validated through probabilistic study for soaked CBR values. For this, 25 distributions were chosen to get the best fit of the probabilistic model that closely represents the soaked CBR value of the stabilized subgrade layer. The best fit probability distribution was found based on the goodness-of-fit tests on the available experimental dataset as Johnson SB (JSB) probability distribution. The P-P and Q-Q plots are also studied that confirmed the appropriateness of Johnson SB (JSB) distribution to model the soaked CBR value as it also satisfies the minimum value according to IRC specification for pavement construction.

References

1. K.Y. Anjani, G. Kumar, K. Roop, S.K. Suman, Stabilization of alluvial soil for subgrade using rice husk ash, sugarcane bagasse ash and cow dung ash for rural roads. *Int. J. Pavement Res. Technol.* **10**, 254–261 (2017)
2. S.K. Amit, K.S. Suhas, D.D. Mahesh, Effective utilization of sugar industry waste bagasse ash in improving properties of black cotton soil. *Int. J. Eng. Res. Technol.* **3**(4) (2014)
3. A.H.S. Ang, W.H. Tang, *Probability Concepts in Engineering: Emphasis on Applications to Civil and Environmental Engineering*, 2nd edn. (Wiley, New York, 2006)
4. H. Hayder, L. Dang et al., Remediation of expansive soils using agricultural waste bagasse ash. *International Conference on Transportation Geotechnics 13* (2016)
5. IS 2720–16, *Methods for Test for Soil: Laboratory Determination of CBR*. Bureau of Indian Standards, New Delhi, India (1987)
6. IS 2720–7, *Methods for Test for Soil: Determination of Water Content-Dry Density Relation Using Light Compaction*. Bureau of Indian Standards, New Delhi, India (1980)
7. IS 2720–10, *Methods for Test for Soil: Determination of Unconfined Compressive Strength*. Bureau of Indian Standards, New Delhi, India (1991)
8. S. Sahu, P. Teja, P. Sarkar, R. Davis, Variability in the compressive strength of fly ash bricks. *J. Mater. Civ. Eng.* **31**(2), 06018024–1–10 (2019)

9. A.K. Chandrappa, K.P. Biligiri, Flexural-fatigue characteristics of pervious concrete: Statistical distributions and model development. *Constr. Build. Mater* **153**, 1–15 (2017)
10. K. Kilinc, A.O. Celik, M. Tuncan, A. Tuncan, G. Arslan, O. Ario, Statistical distributions of in situ microcore concrete strength. *Constr. Build. Mater.* **26**(1), 393–403 (2012)

Experimental and Analytical Study of Negative Stiffness Device for Protection of Structures Against Earthquake—A Review



Vaishali Kishan and Priyanka Jadhav

1 Introduction

Typically structures which are designed as per codes experience considerable irreversible deformations at the time of severe earthquakes, causing degradation in stiffness, deterioration in strength and escalation in inter-storey drift. By making use of systems for passive seismic protection like supplementary damping devices, the inelastic effects obtained could be reduced to some extent. This concept was developed effectively to lower the response and lessen the damage by moving the irreversible energy dissipation from the framing system to the dampers [1–3]. Some of the examples of passive systems are fluid dampers [1, 4], active and semi-active control devices [3], base isolation systems [5, 6, 7, 8, 9], adaptive friction dampers [10], adaptive tuned mass dampers [11], friction dampers [12].

However, the acceleration and total storey forces obtained using these approaches were still on the higher side.

Adaptive systems are more refined compared to the typical passive systems. It is a combination of an adaptive stiffness device and damping device. Depending on the amplitude of displacement, it changes stiffness and damping of the devices [10, 11]. It shows force–displacement behaviour and by adding structural properties it shows better features than the earlier structure.

Recently pseudo-negative-stiffness dampers (PNSD) efficient of creating negative-stiffness hysteretic loops was suggested by Iemura and Pradono [13] It was shown that the total force could be considerably reduced by supplementing negative-stiffness hysteretic loops. This method was successfully validated on structures such

V. Kishan (✉) · P. Jadhav

Department of Civil Engineering, Terna Engineering College, Nerul, Navi Mumbai 400706, India
e-mail: vaishalikishan@ternaengg.ac.in

as cable-stayed bridges, highway bridges and buildings for different kinds of ground motion. These do not assist structure to move in the direction of the motion unlike the NSD.

All the approaches reported above have some or the other limitation. The active control device needs feedback and ample power whereas the semiactive control device needs feedback and nominal power. The passive control device may decrease displacement but cause more base shear. On combining adaptive negative stiffness with a damping device, the base shear and displacement response obtained in the structure is reduced. However, negative stiffness systems have acquired comparatively less attention than the semiactive and pseudo negative stiffness systems and hence show a considerable gap. Thus, it is essential to reduce the inelastic behavior movements in the frames by developing new true negative stiffness devices. NSD can minimise destruction in structural main system by minimizing the base shear, inter-storey drift and inelastic deformation.

To reduce the inertia forces, earthquake-resistant structures are currently designed by reducing the design strength to ensure ductile behavior during seismic activity. At the most, this approach secures safety of life during the design seismic event and prevents failure of structure during the maximum considered event. It is observed there are large story drifts, permanent deformations and subsequently structure loses its functionality following strong seismic events.

To minimise simultaneously accelerations and inter-story drifts in the retrofit of structures, [14, 15] brought in the idea of decreasing the structure's strength and stiffness by adding additional viscous damping. The same objective was achieved for new construction as per the approach specified in ASCE 7, Chapter 18 [16] for structural design with damping [17].

Cimellaro et al. [18] suggested design approach of weakening the structure wherein damping devices were added using control theory to ensure structural stability and the positions and magnitude of the changed structural elements were determined. The procedure suggested was to first find out the new structural parameters with the help of nonlinear active control algorithm, ensuring the stability of the structure. Then by either removing or weakening some structural elements and by adding energy dissipation systems, the characteristics of similar structural parameters of passive system were determined. With the help of optimization algorithm, the design of passive dampers and weakened elements were carried out to acquire a response as close as possible to an actively controlled system.

Nagarajaiah et al. [19, 20] and Pasala et al. [21] have developed an alternative "adaptive weakening" strategy called the adaptive negative stiffness method (ANSS). All reactions such as acceleration, inter-story drift and base-shear of the structure were reduced significantly by using the supplementary damping devices along with the negative stiffness device NSD. The idea regarding apparent yield was proposed where yield could be replicated in the structural system by providing an NSD and moving the yield away from the main structural framework. The original rigidity of the structural framework is not changed unlike the weakening concept which was suggested earlier. The integrated unit assembly acts similar to a structure that is

yielding by engaging the NSD at an adequate displacement. A true negative stiffness system produces forces that help motion and not resist it like positive stiffness system. The NSD is able to produce true negative stiffness and therefore may not require additional power, sensors and controllers to obtain the desired forces. It was observed that NSD greatly decreases base shear and acceleration, and by incorporating a passive damping device with a marginal damping coefficient for the elastic and inelastic structures, the inter-story deformations can be minimized. Numerical findings showing the efficacy and remarkable results of the ANSS /NSD by analysis were also published.

This report introduces the working principle, description, development, operation of NSD and study of the behaviour of NSD.

2 Working Principle

To imagine the effect of true negative stiffness on a structure, viscous damper with damping coefficient C and NSD with stiffness K_n have been added, consider the relations of force–displacement as shown in Fig. 1a (The structure’s force displacement relation is indicated in green, viscous damper is shown in magenta and NSD is shown in red). When NSD is applied to the structure, indicated in Fig. 1b, there is reduction in the stiffness of assembly from K_e to $K_a = K_e - K_n$ for displacement more than x_1 as shown in blue line, Fig. 1b.

For a system which is perfectly linear (shown with green line in Fig. 1b if F_2 is the maximum restoring force and x_2 is the maximum displacement then, for the same load, for assembly of the structure and NSD, the maximum restoring force is F_3 and maximum displacement is x_3 (blue line in Fig. 1b. Stiffness of the NSD, K_n is chosen to obtain the optimal decrease of base shear. Force applied by the NSD is indicated with a red line in Fig. 1b. Even though, decrease in the base shear is obtained for the assembly of structure and NSD, the maximum deformation may increase as compared to the structure without the NSD. Reduction in the deformation of this system can be obtained by incorporating passive dampers in addition to the NSD

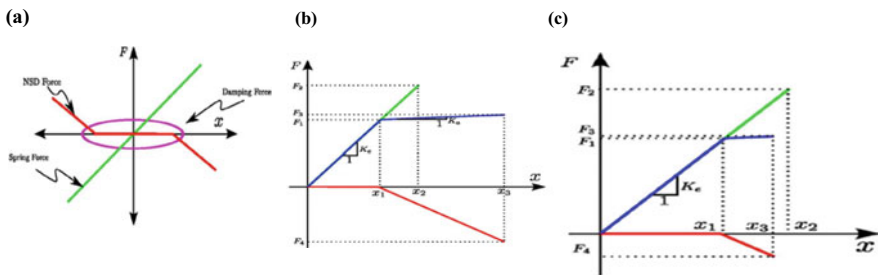


Fig. 1 a Component forces, b Structure + NSD, c Structure + NSD + Damper

(Fig. 1c). If a linear viscous damper is added to an assembly of structure and NSD, there is reduction in the maximum displacement ($x_3 < x_2$).

3 Description and Operation of Negative Stiffness Device

The photograph of Negative Stiffness Device (NSD) (Fig. 2) and schematic diagrams of NSD in un-deformed shape (Fig. 3a) and deformed shape (Fig. 3b) are shown.

The NSD produces a thrust in the similar direction as that of the forced displacement. It can be set up either in an isolated structure between isolation level and ground or in the middle of the storeys. About its level of installation, the NSD causes reduction in the total force. As a consequence of this similar reduction of stiffness and strength is obtained, resulting in the decrease of acceleration and forces due to inertia.

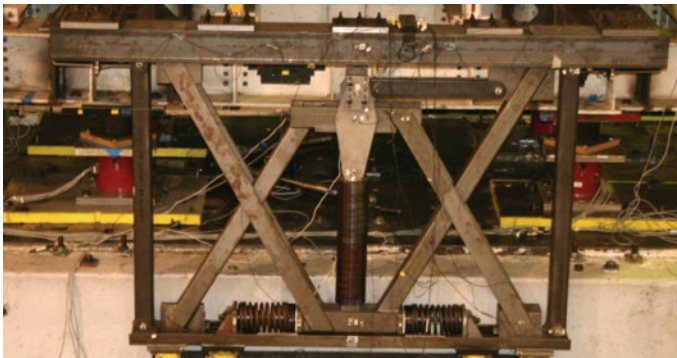


Fig. 2 The photograph of Negative Stiffness Device (NSD)

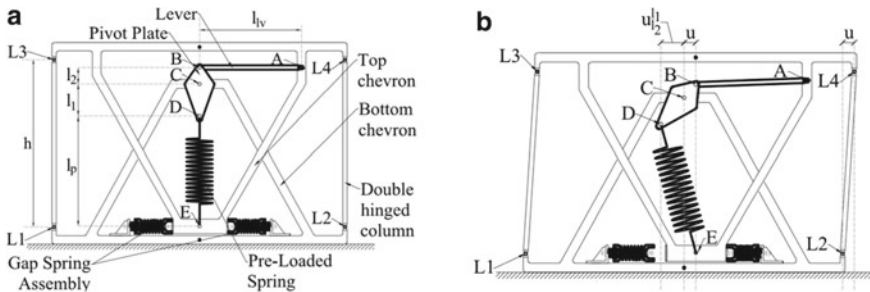


Fig. 3 Schematic diagrams of NSD in **a** un-deformed shape, **b** deformed shape

A Gap Spring Assembly system (GSA) in the NSD ensures a significant effect of positive stiffness for slight displacements and assures requirements of serviceability. The GSA is a group of springs that give stiffness to the NSD for displacements between zero and a predetermined limit. The GSA shows a bilinear elastic behaviour because of which for displacements less than the predetermined limit, the combined system has zero or slight negative or positive stiffness. In case of greater displacements, the system has the negative stiffness of the NSD.

The NSD consists of a precompressed spring, two GSAs, pivot plate, lever, top and bottom chevron braces and two double-hinged columns [22]. Using link mechanism the precompressed spring shifts the horizontal loads to the bottom and top part of the frame. When the device undergoes deformation, the precompressed spring rotates and applies a force along the direction of the displacement thereby creating negative stiffness. For smaller values of displacement, the GSA opposes the NSD function so that the device gives zero or some small negative or positive stiffness up to a displacement of predetermined value. When the displacement increases, the force in the precompressed spring reduces thereby reducing the negative stiffness value for higher displacements. At greater displacement, the NSD provides positive stiffness which is a desirable characteristic during large earthquakes.

The performance of NSD is assessed by the motion of the pivot plate and preloaded spring (motion of points A, B, C, D, E) and also by the properties of spring of stiffness K_s , initial length DE and preload P_{in} . Consider there is displacement of the top of the NSD towards the right by u as shown in Fig. 3b. A displacement is imposed by the lever on (point B) the top edge of the pivot plate thereby causing the plate to rotate about the pivot C. By virtue of the stiffness of the lever and its insignificant rotation, the displacement at point A and point B are basically the same. As when the pivot plate rotates around point C, point D shifts in a direction contrary to the imposed displacement. It should be observed that point E, which is the bottom pin of the precompressed spring is rigidly attached to the upper part of the NSD via the top chevron brace and thus undergoes an equal displacement as that of point A. Due to the kinematics of the spring's top pin Point D and bottom pin Point E, there is rotation in the precompressed spring and as the spring is precompressed and rotated in the direction opposite to the imposed displacement, it assists the motion instead of opposing it. This gives rise to negative stiffness. The spring displays its least span when the NSD is not deformed. When the NSD deforms, the spring expands and there is reduction in precompression force, increase in its angle of inclination because of which there is reduction in the horizontal component of force produced by the NSD. This causes gradual decrease in negative stiffness intensity, which finally leads to positive stiffness. This takes place at greater displacements and it is called stiffening all through this report. This behaviour of NSD with GSA and without GSA is illustrated in the graphs (Fig. 4).

Two GSA are positioned at the bottom of the NSD, each operating in compression. A GSA is joined to one side to the lower part of the NSD via the end plate as indicated in Fig. 3a while the other side is connected to (point E) the head of the top chevron brace of the NSD and therefore it transfers only compressive forces. Thus, both GSA devices function in one direction whereas together, they produce forces along both directions.

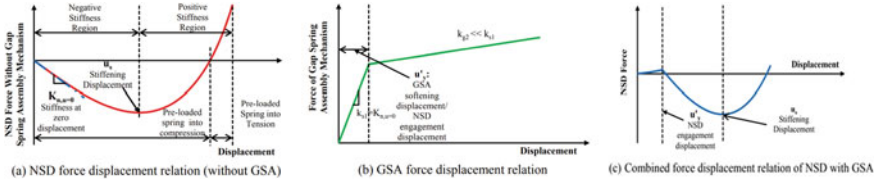


Fig. 4 Behaviour of NSD with GSA and without GSA

The combined force–displacement relation of NSD with GSA (Fig. 4c) is obtained when lateral force–displacement relations of the compressed GSA (Fig. 4b) and NSD (Fig. 4a) are clubbed together.

For the displacements lesser than the apparent-yield displacement $u'y$, the negative stiffness is cancelled. The GSA could be developed to produce a positive stiffness either equivalent to or slightly more than the negative stiffness at zero displacement such that, the total stiffness produced by the NSD for displacements lower than $u'y$ is almost or slightly above zero as shown in Fig. 4c. It is to be observed that the compressive forces in the preloaded spring and the double-hinged columns of the assembly are in equilibrium.

4 Basic Force–Displacement Relations of Negative Stiffness Device

Derivation of the basic relations of force–displacement is shown in this section. The equations so obtained are based on assumptions that members of the frame are rigid, all the elements have no mass and the hysteresis in the joints of NSD is insignificant.

4.1 Analysis of Negative Stiffness Device

For the analysis of the NSD, balance of forces and kinematics in the deformed configuration has to be taken into consideration. Consider an NSD is set up in a structure and is subjected to a lateral displacement of known magnitude u to its top (Fig. 3b). The force generated by the device along the direction of the imposed displacement is derived as follows:

Consider the FBD of the pivot plate shown in Fig. 5a. Forces F_B , F_C and F_S act on the pivot plate while force F_g of the GSA does not act on the pivot plate as shown.

The FBD of the bottom chevron is shown in Fig. 5b.

Also additional assumptions made are as follows:

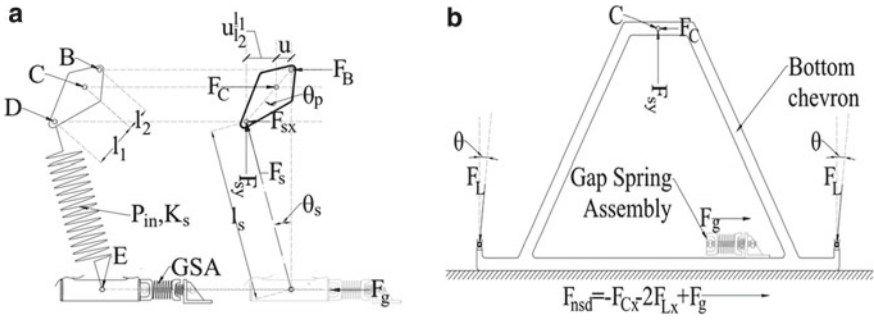


Fig. 5 a Forces acting on pivot plate, b Free body diagram of bottom chevron

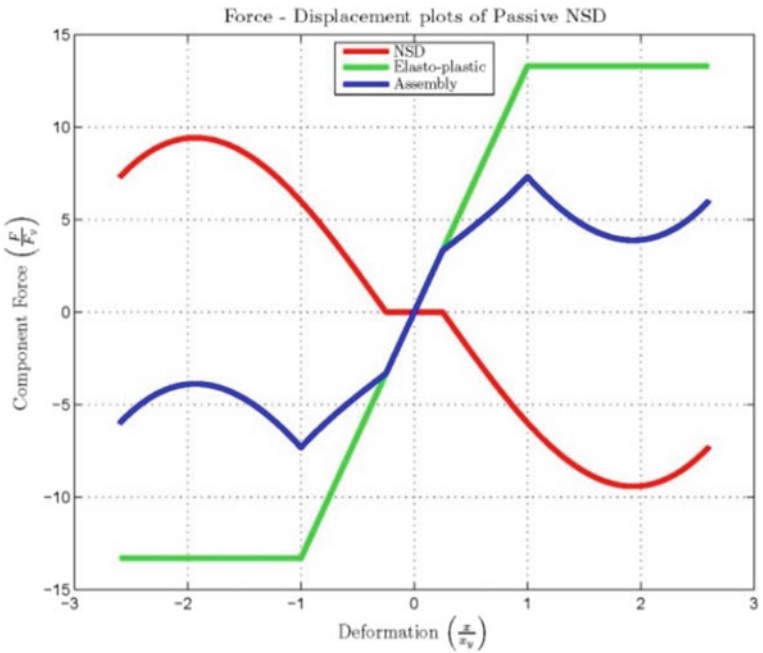


Fig. 6 Force displacement loops of NSD (Green-Base structure, Red-NSD, Blue-Assembly)

- It is assumed that the lever has zero rotation. Hence the lever force will act in the horizontal direction and the points A and B will have the same displacement. Practically the lever rotates; rotation is very small if the lever is long.
- The loss in the height of the NSD because of inverted pendulum motion is neglected. This loss in the height, however little, will cause vertical displacement of point E, minute lever rotation and some loss in the spring preload.

When a displacement of u is imposed on the top of the NSD following actions take place

- (1) The lever induces the pivot plate to rotate and point B moves horizontally by an equal amount as the applied displacement.
- (2) Point E is connected rigidly to the top channel via top chevron and it experiences the applied displacement u .
- (3) Point D moves horizontally in the direction opposite to u .

$$u_B = u, u_E = u, u_D = -u \frac{l_1}{l_2} \quad (1)$$

where l_2 is the distance between point C and point B and l_1 is the distance between point C and point D in Fig. 5a.

Point B moves down and point D moves up by:

$$\begin{aligned} v_B &= l_2 - \sqrt{l_2^2 - u^2} \\ v_D &= l_1 - \sqrt{l_1^2 - \left(u \frac{l_1}{l_2}\right)^2} \end{aligned} \quad (2)$$

The vertical distance between points E and D is:

$$v_{DE} = l_p + v_D = l_p + l_1 - \sqrt{l_1^2 - \left(u \frac{l_1}{l_2}\right)^2} \quad (3)$$

where l_p is the length of the precompressed spring in the un-deformed configuration (Fig. 2a).

The spring length in the deformed configuration is obtained by using Eqs. (1), (2) and (3)

$$l_s = \sqrt{\left(l_p + l_1 - l_1 \sqrt{1 - \left(\frac{u}{l_2}\right)^2}\right)^2 + u^2 \left(1 + \frac{l_1}{l_2}\right)^2} \quad (4)$$

Taking moments about point C of the pivot plate in Fig. 5a, and calculating the axial force in the lever at point B

$$F_B = \frac{F_s}{\sqrt{l_2^2 - u^2}} \left[\cos \theta_s \left(u \frac{l_1}{l_2}\right) + F_s \sin \theta_s \left(\sqrt{1 - \left(\frac{u}{l_2}\right)^2}\right) l_1 \right] \quad (5)$$

where θ_s is the angle of inclination of the spring and F_s is the force of the precompressed spring.

This force varies with displacement and is given by:

$$F_s = P_{in} - K_s(l_s - l_p) \quad (6)$$

where P_{in} is the precompression force of the spring (a positive value) and K_s is the stiffness of the precompressed spring.

It is to be noted that force in the spring increases when the lateral displacement is zero.

The sine and cosine of the spring inclination angle are given by:

$$\begin{aligned} \sin \theta_s &= \frac{u}{l_s} \left(1 + \frac{l_1}{l_2} \right) \\ \cos \theta_s &= \frac{1}{l_s} \left(l_p + l_1 - \sqrt{l_1^2 - \left(u \frac{l_1}{l_2} \right)^2} \right) \end{aligned} \quad (7)$$

The total force generated by the NSD, except for the GSA force, is the resultant of force acting on point C and the horizontal component of forces in the double-hinged columns. From vertical equilibrium in Fig. 5b, the vertical component of the axial load in the double-hinged columns is equal to the vertical component of the spring force.

The component along the horizontal direction of the axial load in the double-hinged columns is given by:

$$F_{Lx} = \frac{1}{2} F_s \cos \theta_s \tan \theta \approx \frac{1}{2} F_s \cos \theta_s \frac{u}{h} \quad (8)$$

where θ is the inclination angle of the double hinged columns.

The total force exerted by the NSD, inclusive of the GSA force, is given by:

$$F_{NSD} = -F_c - 2F_{Lx} + F_g \quad (9)$$

where F_g is the GSA force and F_c is the horizontal force at point C as calculated from horizontal equilibrium of the pivot plate and given by:

$$F_c = F_B + F_s \sin \theta_s \quad (10)$$

Substitutions of Eqs. (5) to (8) and (10) into (9) and after some algebra yields the total NSD force as:

$$F_{NSD} = - \left(\frac{P_{in} + K_s l_p}{l_s} - K_s \right) \left(\frac{l_1}{l_2} \right)$$

$$\left(2 + \frac{l_p + l_1}{\sqrt{l_2^2 - u^2}} + \frac{l_2}{l_1} \frac{h + l_p + l_1 - (l_1/l_2)\sqrt{l_2^2 - u^2}}{h} \right) u + F_g \tag{11}$$

The force–displacement of the gap spring assembly (GSA) is given by:

$$F_g = \begin{cases} k_{s1}u, & 0 \leq u \leq u'_y \\ k_{s1}u'_y + \frac{k_{s2}k_{s1}}{k_{s2} + k_{s1}}(u - u'_y) & u > u'_y \end{cases} \tag{12}$$

where k_{s1} is the stiffness of the inner spring S_1 , k_{s2} is the stiffness of the outer spring S_2 and u'_y is the displacement at which the assembly shows change in stiffness.

4.2 Analytical Model of NSD

It is clear from the above equation that fundamental parameters that define negative stiffness are stiffness of the precompressed spring (K_s) and NSD spring preload (P_{in}) and on optimising them seismic response can be reduced to a large extent. The above Eq. (12) can be solved using Python code, Matlab or excel sheet. Using the nominal properties of the NSD (Table 1), given as an example, calculations are done and results obtained are as shown in Fig. 6.

Using Eq. (11) and putting $F_g = 0$, NSD force–displacement relation without the GSA is obtained and shown in red. Using Eqs. (11) and (13), NSD force–displacement relation with the GSA is obtained and is shown in blue. Using Eq. (13) the force–displacement relation of only GSA is obtained and shown in green.

Table 1 Nominal NSD properties [23]

Quantity	Symbol	Value	Units
Length BC of pivot plate		25.4	cm
Length CD of pivot plate	h	12.7	cm
NSD spring length	h	76.2	cm
NSD spring stiffness	K	1.4	kN/cm
NSD spring preload	Pi,	16.5	kN
Double hinged column height	h	124.5	cm
Lever length	l,v	67.3	cm
NSD engagement displacement		1.65	cm
GSA spring S1 stiffness		4.9	kN/cm
GSA spring S2 stiffness		0.3	kN/cm
GSA spring S2 preload	Pi, 2	8.1	kN

The results obtained by solving the equations could be used in any of the commercial software like capable of modelling nonlinear force–displacement relation of NSD.

The characteristics of bi-linear hysteresis can be captured by the Sivaselvan-Reinhorn model [24].

With an objective of reducing the base shear of the structure and at the simultaneously limiting the maximum displacement of structure, NSD has to be used in addition with a non-linear passive damper.

By adopting optimisation method as proposed by Cimellaro et al. [18, 25], the optimal properties of the damper could be found out such that error between force produced due to passive device and the active control force is minimal. It is shown that a viscous damper with damping ratio of 20% is very effective with the assumed properties of NSD.

Below equation gives the force generated by the passive damper

$$F_{NPD} = 2\xi\sqrt{K_e m} \dot{x} \quad (13)$$

where, F_{NPD} is the force generated by the damper, ξ is damping ratio, K_e and m are the elastic stiffness and mass of the structure respectively.

5 Experimental Outcomes

Performance study of true negative stiffness and an adaptive negative stiffness system on a shear structure having five degrees of freedom was carried out by Gisha et al. [26] and optimum parameter values and number of damping devices were evaluated depending on response of structure under seismic activity. Experimental analysis on a three-storey model, seismically isolated structure equipped with NSD was carried out by Pasala et al. [27] and results obtained both analytically and experimentally were compared to verify the analytical models of NSD. An NSD was incorporated in a Reinforced concrete structural frame consisting chevron bracings by Onkar et al. [28] using SAP 2000. Study on a model of G + 5 RCC building with ANSS was done by Mirza Arif and Chakrabarti [29]. The NSD equations were worked out in MATLAB and data obtained was utilised for analytical modelling in SAP2000. Analysis was carried on 2D and 3D steel buildings with NSD by Jadhav et al. [30] and seismic response was studied for different time history loadings. NSD equations were solved using MATLAB and ETABS 2016 was used for the analytical modelling and optimal placement of NSD was obtained based on the structural response to seismic activity,

6 Conclusions

This paper explained the description, operation and modelling of an innovative Negative Stiffness Device (NSD) having the following features:

- (1) The NSD minimizes the lateral stiffness of the structure after a prescribed displacement. This is carried out by using Gap Spring Assembly which facilitates positive stiffness up to a predetermined displacement. It generates negative stiffness by means of an extremely compressed spring that creates a force along the direction of motion. By using a double negative stiffness magnification, the amount of spring force is amplified and thus NSD can be designed using spring with a realistic stiffness and preload. The NSD has nonlinear elastic behaviour and the magnitude of the negative stiffness decreases with increase in the displacement thereby ensuring stability of the system at considerable displacements.
- (2) NSD causes reduction in stiffness because of which viscous damper's effective damping becomes considerably larger when they are supplemented in parallel to NSD. This results in significant displacement reduction about the level where the NSD is installed.
- (3) NSD is passive as it does not need external power source and structural response feedback.

References

1. M.C. Constantinou, M.D. Symans, Experimental study of seismic response of buildings with supplemental fluid dampers. *Struct Design Tall Build* **2**(2), 93–132 (1993)
2. R.F. Lobo, J.M. Bracci, K.L. Shen, Inelastic response of R/C structures with viscoelastic braces. *Earthq. Spectra* **9**, 419 (1993)
3. B.F. Spencer Jr., S. Nagarajaiah, State of the art of structural control. *J. Struct. Eng.* **129**, 845 (2003)
4. M.D. Symans, M.C. Constantinou, Seismic testing of a building structure with a semi-active fluid damper control system. *Earthq. Eng. Struct. Dynam.* **26**(7), 759–777 (1997)
5. J. Dyck, S. Nagarajaiah, D. Taylor, Variation of supplemental stiffness and damping using adjustable fluid spring and damper. *Proc Eighth US Natl Conf Earthq Eng. EERI, CD-ROM* (2006)
6. S. Nagarajaiah, A.M. Reinhorn, M.C. Constantinou, Nonlinear dynamic analysis of 3D base-isolated structures. *J. Struct. Eng. ASCE* **117**(7), 2035–2054 (1991)
7. S. Narasimhan, S. Nagarajaiah, E.A. Johnson, H.P. Gavin, Smart base-isolated benchmark building. Part I: problem definition. *Struct. Control. Health Monit.* **13**(2–3), 573–588 (2006)
8. S. Sahasrabudhe, S. Nagarajaiah, Experimental study of sliding base isolated buildings with magnetorheological dampers in near-fault earthquakes. *J. Struct. Eng.* **131**, 1025 (2005)
9. S. Nagarajaiah, S. Sahasrabudhe, Seismic response control of smart sliding isolated buildings using variable stiffness systems: an experimental and numerical study. *Earthq. Eng. Struct. Dynam.* **35**(2), 177–197 (2006)
10. D.M. Fenz, M.C. Constantinou, Spherical sliding isolation bearings with adaptive behavior: theory. *Earthq. Eng. Struct. Dynam.* **37**(2), 163–183 (2008)

11. S. Nagarajaiah, Adaptive passive, semiactive, smart tuned mass dampers: identification and control using empirical mode decomposition, hilbert transform, and short-term fourier transform. *Struct. Control. Health Monit.* **16**(7–8), 800–841 (2009)
12. A.V. Bhaskararao, R.S. Jangid, Seismic analysis of structures connected with friction dampers. *Eng. Struct.* **28**, 690–703 (2005)
13. H. Iemura, M.H. Pradono, Advances in the development of pseudonegative-stiffness dampers for seismic response control. *Struct. Control. Health Monit.* **16**(7–8), 784–799 (2009)
14. A.M. Reinhorn, S. Viti, G.P. Cimellaro, Retrofit of structures: strength reduction with damping enhancement. In: *Proceedings of the 37th UJNR panel meeting on wind and seismic effects*, 16–21 (2005)
15. S. Viti, G.P. Cimellaro, A.M. Reinhorn, Retrofit of a hospital through strength reduction and enhanced damping. *Smart Struct. Syst.* **2**(4), 339–355 (2006)
16. American Society of Civil Engineers, Minimum design Loads for buildings and other structures. *Stand. ASCE*. 7–10, Reston, VA (2010)
17. O.M. Ramirez, M.C. Constantinou, C.A. Kircher, A.S. Whittaker, M.W. Johnson, J.D. Gomez, C.Z. Chrysostomou, Development and evaluation of simplified procedures for analysis and design of buildings with passive energy dissipation systems, Report No. MCEER-00-0010, Revision 1. Multidisciplinary Center for Earthquake Engineering Research, Buffalo, NY (2001)
18. G.P. Cimellaro, O. Lavan, A.M. Reinhorn, Design of passive systems for control of inelastic structures. *Earthq. Eng. Struct. Dynam.* **38**(6), 783–804 (2009)
19. S. Nagarajaiah, A.M. Reinhorn, M.C. Constantinou, D. Taylor, D.T.R. Pasala, A.A.S. Sarlis, Adaptive negative stiffness: a new structural modification approach for seismic protection. In: *Proceedings of 5th World Conference on Structural Control and Monitoring*, Tokyo, Japan (2010)
20. A.A.S. Sarlis, D.T.R. Pasala, M.C. Constantinou, A.M. Reinhorn, S. Nagarajaiah, D. Taylor, Negative stiffness device for seismic protection of structures—an analytical and experimental study. In: *3rd Table 1: Description of variables International conference on computational methods in structural dynamics and earthquake engineering*, May 2011 (2010)
21. D.T.R. Pasala, A.A. Sarlis, S. Nagarajaiah, A.M. Reinhorn, M.C. Constantinou, D. Taylor, (2012) Adaptive negative stiffness: a new structural modification approach for seismic protection. *J. Struct. Eng. ASCE*. [https://doi.org/10.1061/\(ASCE\)ST.1943-541X.0000615](https://doi.org/10.1061/(ASCE)ST.1943-541X.0000615), Posted ahead of print, 3 April 2012.
22. S. Nagarajaiah, A. Reinhorn, Applicability of pseudo-force method to highly nonlinear dynamic problems. *ASCE: Proceedings of structures congress*, 165–172 (1994)
23. D.T.R. Pasala, A.A. Sarlis, S. Nagarajaiah, A.M. Reinhorn, M.C. Constantinou, D. Taylor, Negative stiffness device for seismic protection of structures. *J. Struct. Eng. ASCE* **139**(7):1112–1123 (2013)
24. M.V. Sivaselvan, A.M. Reinhorn, Hysteretic models for deteriorating inelastic structures. *J. Eng. Mech.* **126**(6), 633–640 (2000)
25. A.M. Reinhorn, O. Lavan, G.P. Cimellaro, Design of controlled elastic and inelastic structures. *Earthq. Eng. Eng. Vib.* **8**(4), 469–479 (2009)
26. M.M. Gisha, Q. Asim, R.S. Jangid, Optimal placement of negative stiffness damping system, in *Proceedings of ASME 2015 Conference on Smart Materials Adaptive Structures and Intelligent Systems* (Colorado Springs, ASME Press, USA, 2015)
27. D.T.R. Pasala, A.A. Sarlis, S. Nagarajaiah, A.M. Reinhorn, M.C. Constantinou, D. Taylor, Negative stiffness device for seismic protection of structures: shake table testing of a seismically isolated structures. *J. Struct. Eng. ASCE* **152**(5), 04016005-1–04016005-13 (2016)
28. P. Onkar, S.N. Tande, A.B. Kulkarni, Concept of negative stiffness device in RC buildings in seismic areas. *Int. J. Latest Trends Eng. Technol.* **7**(1), 125–132 (2016)
29. B. Mirza Arif, M.A. Chakrabarti, Optimal use of negative stiffness damper for seismic resistant frames. *IOSR J. Mech. Civil Eng.* 14:23–31 (2017)
30. P. Jadhav, S. Shaikh, Optimization of seismic response of steel structure using negative stiffness damper. *Int. J. Adv. Struct. Eng.* **11**, 351–360 (2019)

Laboratory Study of Permeability for Sub-Base Using Flyash and Fibre



Dharampal Singh Kandari, Deepak Kumar Singh, and Shashank Kothari

1 Introduction

Roads are an important mode of transport in India. In India, national highway covers a distance of 142,126 km, state highways stretch across a distance of 176,166 km and rural roads stretch across a distance of 39,35,337 km [1]. There are three causes for the failure of a pavement, one is drainage, two is drainage and three is drainage. Monsoon damage to road surfaces in India is well known. As rain falls, water flows on the road surface, some of the water seeping into the pavement structure. Any surface irregularities present mean stagnation of water [2]. Any cracks present likewise facilitate ingress of water and permit water to act on larger areas of surface courses and other layers. Presence of pot-holes makes matters still worse. As traffic moves on a road surface which is flushed with water both on top and inside, hydrostatic pressures are generated which aggravate the rate of breakup. As breakup gets initiated, it tends to accelerate at such a geometric progression that the road surface becomes unrecognizable in a few days. The infiltration of water into the pavement can be minimized (a) by providing proper roadside drainage (b) by providing sub-surface drainage (c) by providing permeable base or sub-base for rapid removal of water which enters the pavement structure (d) by providing a filter layer such as geotextile to prevent the migration of fines into the permeable base from the subgrade, subbase material. The quality of GSB layer is very important for the useful life of the road. Therefore, the permeability of GSB materials is very important for evaluating the drainage capability. Due to shortage of conventional materials, the use of alternate materials like fly ash, fibres, construction and demolition waste, etc., in road construction would solve this problem. Granular Sub-base (GSB) is the layer just above the compacted soil layer (subgrade soil). It transfers traffic loads to the subgrade while providing

D. S. Kandari (✉) · D. K. Singh · S. Kothari
Graphic Era (Deemed to be University), Dehradun 248001, India

drainage and frost protection [3]. Subbases for flexible pavements must have relatively free drainage and must be free of frost action. Strength is not so important, however, since the course is lower in the pavement structure and therefore withstands much smaller loads. Permeability is one of the important material properties that have to be considered in the design thickness of GSB [4]. The coefficient of permeability, k , is an important value which is used for expressing the drainage capability of soils. The permeability coefficient is the property of the porous material to allow water to pass through it. The coefficient of permeability a soil can be determined in the laboratory by two different methods (a) Constant head method which is suitable for granular materials (b) Falling head method which is used for less permeable soils. The permeability coefficient is dependent on the properties of the permeating liquid as well as the porous medium.

2 Material Selection

2.1 Aggregate

In the present study, Type-I aggregate and Type-II aggregate were collected from Chamoli district, Uttarakhand. Type-III aggregate was collected from local area. The various tests such as specific gravity, water absorption, crushing, L.A. abrasion and impact were conducted on aggregates. The test results for Type-I aggregate are presented in Table 1. The test results for Type-II aggregate are presented in Table 2. The test results for Type-III aggregate are presented in Table 3. The particle size distribution curve for aggregate is shown in Fig. 1. The grading for close graded GSB material is presented in Table 4.

Table 1 Results of tests conducted on Type-I aggregate

Sr. no	Tests on aggregates	Test results
1	Crushing value (%)	15.10
2	L.A. abrasion value (%)	28.61
3	Impact value (%)	15.90
4	Specific gravity	2.65
5	Water absorption (%)	0.70

Table 2 Results of tests conducted on Type-II aggregate

Sr. no	Tests on aggregates	Test results
1	Crushing value (%)	16.1
2	L.A.abrasion value (%)	27.45
3	Impact value (%)	18.55
4	Specific gravity	2.78
5	Water absorption (%)	0.25

Table 3 Results of tests conducted on Type-III aggregate

Sr. no	Tests on aggregates	Test results
1	Crushing value (%)	11.2%
2	L.A.abrasion value (%)	28.96%
3	Impact value (%)	14.60%
4	Specific gravity	2.61
5	Water absorption (%)	0.65

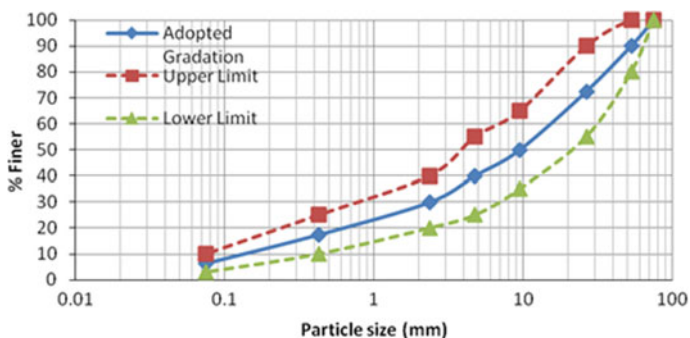


Fig. 1 Particle size distribution curve for aggregate

Table 4 Grading for close graded [5] GSB materials

IS sieve size, mm	Upper limit	Lower limit	Adopted gradation
75	100	100	100
53	100	80	90
26.5	90	55	72.5
9.5	65	35	50
4.75	55	25	40
2.36	40	20	30
0.425	25	10	17.5
0.075	10	3	6.5

2.2 Fibre

In the present study, polypropylene fibre was used. The different percentages of polypropylene fibre (0.5%, 1.0%, 1.5% and 2.0% by dry weight of mix) was mixed in GSB mixtures. Table 5 shows properties of polypropylene fibre.

Table 5 Properties of polypropylene fibre

Sr. no	Particulars	Value
1	Polypropylene formula	(CH ₂ -CH ₂)
2	Average diameter(mm)	0.3
3	Aspect ratio	100
4	Specific gravity	0.9

Table 6 Properties of flyash

Sr. no	Particulars	Test results
1	OMC	23%
2	MDD	1.38 g/cc
3	Liquid Limit	15.3%
4	Specific gravity	2.03

2.3 Flyash

In the present study, specific gravity test and compaction test were conducted on flyash. The different percentages of flyash (22, 25 and 28% by dry weight of mix) was mixed in GSB mixtures. The percentages of flyash were decided by using Routhfutch method. Table 6 shows the properties of flyash.

3 Laboratory Study and Analysis of Results

3.1 Standard Proctor Test

The optimum moisture content(OMC) and maximum dry density(MDD) of various GSB mixtures were obtained by conducting [6] heavy compaction test (Figs. 2 and 3). Figures 2 and Fig. 4 show variation of OMC of GSB mixtures with varying percentage of flyash and fibre, respectively. Figure 3 and Fig. 5 show variation of MDD of GSB mixtures with varying percentage of flyash and fibre, respectively.

As flyash content increases, OMC increases and MDD decreases. The MDD value decreases due to low value of specific gravity of flyash. The OMC increases with increase in flyash content because more water content is required due to their larger surface area. The addition of Polypropylene fibre to GSB mixes with varying percentages reduces MDD and increase OMC. The OMC increases with increase in fibre content. This is due to adsorption of water particles on the surface of polypropylene fibre. The MDD value decreases with fibre content because of the low value of specific gravity of fibre.

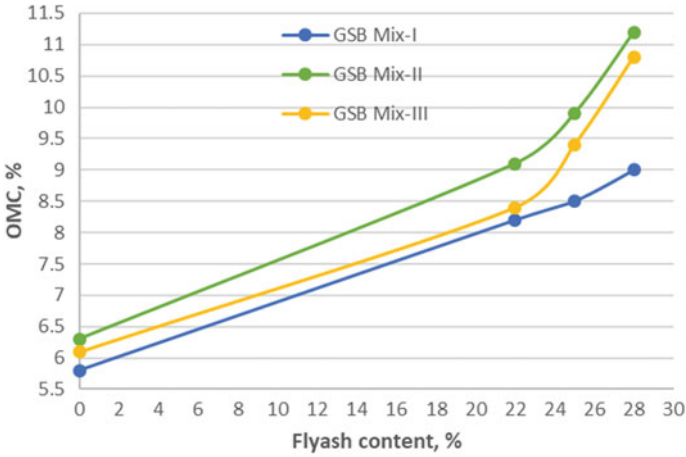


Fig. 2 Variation of OMC of GSB mixtures with varying percentage of flyash

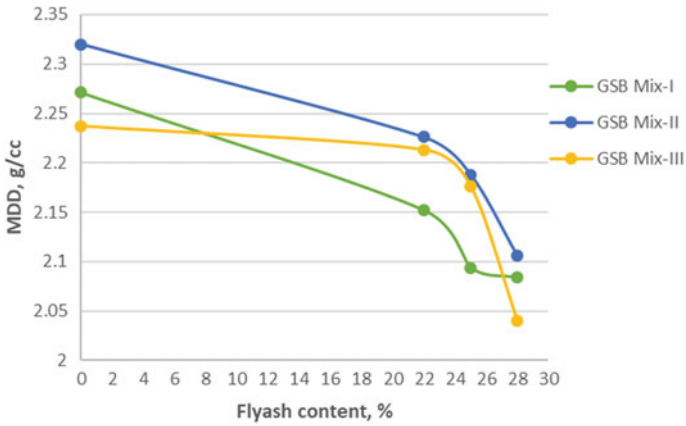


Fig. 3 Variation of MDD of GSB mixtures with varying percentage flyash

3.2 Permeability Test

In the present study [7] the constant head method (suitable for granular materials) was used to determine the coefficient of permeability of various GSB mixtures. The permeability values for GSB mixtures with varying percentage of flyash and fibre are shown in Fig. 6 and Fig. 7, respectively.

It was found that value of permeability of GSB mixtures increases with increase in polypropylene fibre because fibre increases the void content due to absence of cohesiveness and poor distribution of fibres. The permeability value of GSB mix-flyash mixtures decrease with increase in flyash content. This is due to increase

Fig. 4 Variation of OMC of GSB mixtures with varying percentage of fibre

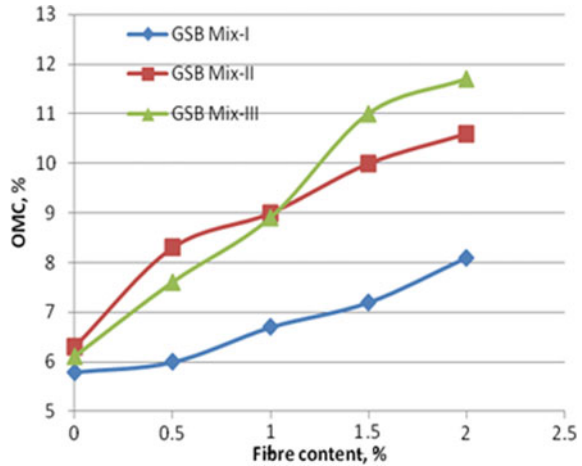
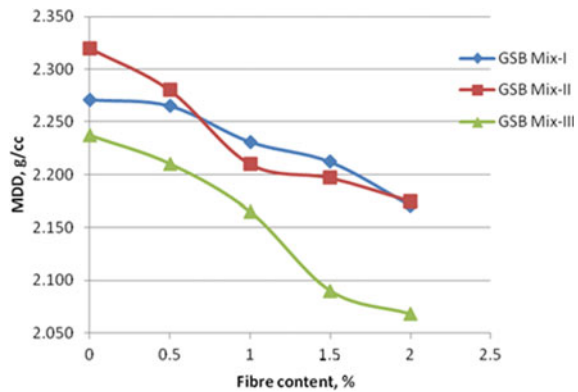


Fig. 5 Variation of MDD of GSB mixtures with varying percentage of fibre



in surface area with the increase in flyash content, generating more resistance to water flow through void between particles. Thus, leading to reduction in the value of permeability.

4 Conclusion

The inclusion of flyash to GSB mixtures increases OMC, decreases MDD and decreases permeability values. The optimum value of flyash is observed to be 22% based on greater CBR value. The inclusion of fibre to GSB mixtures increases OMC, decreases MDD and increases value of permeability. The optimum value of fibre is observed to be 1.5%. Inclusion of fibre beyond 1.5% caused problems in mixing. Also, increase in strength of mix is insignificant. Between fibre and flyash, fibre is

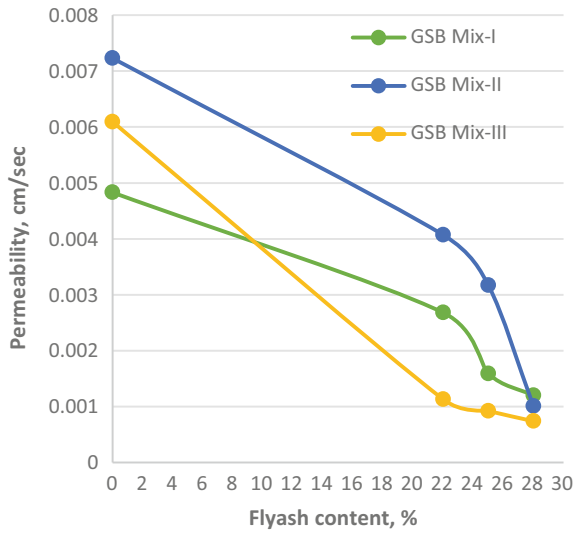


Fig. 6 Permeability value of GSB mixtures with varying percentage of flyash content

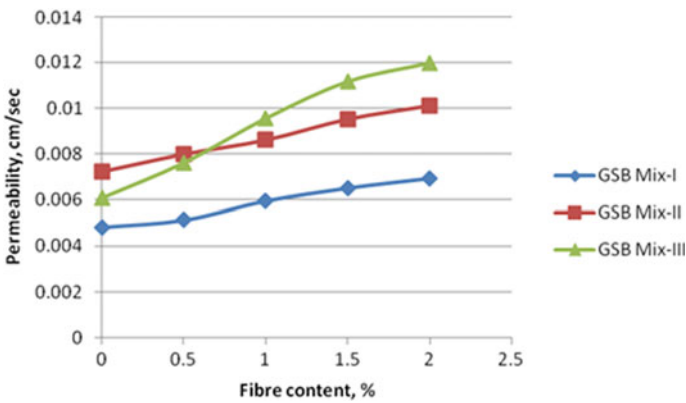


Fig. 7 Permeability value of GSB mixtures with varying percentage of fibre content

the most suitable GSB material which increases the value of permeability from 4.83×10^{-3} cm/s to 6.94×10^{-3} cm/s, 7.23×10^{-3} cm/s to 10.11×10^{-3} cm/s and 6.095×10^{-3} cm/s to 11.972×10^{-3} cm/s for GSB mixture-I, GSB mixture-II and GSB mixture-III, respectively.

References

1. H.R. Cedergren, *Drainage of Highway and Airfield Pavements* (Krieger Publishing Company, Florida, Robert E, 1994), p. 1987
2. E.J. Hoppe, The influence of fines on strength and drainage characteristics of aggregate bases, Report VTRC 96-R35RB, Virginia Transportation Research Council, Charlottesville, VA, p. 39 (1996)
3. V.E. Strohm, C.H. Nettles, C.C. Calhoun, Study of drainage characteristics of base course materials. Highway Research Record No.203, pp. 8–2 (1968)
4. A.S. Elsayed, J.K. Lindly, Estimating the Permeability of Untreated Roadway Bases. J. Transp. Res. Board **1519**, 15–19 (1996)
5. MORT&H, Specifications for road and bridge works. Indian Road Congress, New Delhi (2001)
6. IS:2720 (Part 8), Determination of water content-dry density relation using heavy compaction (1983)
7. IS:2720 (Part 17), Laboratory determination of permeability (1986)

Comparative Analysis of CFST Columns and RC Columns Under Uniaxial Compressive Loads



Shashank Kothari, Deepak K. Singh, and Pankaj Chamoli

1 Introduction

The steel–concrete composite sections provide a highly advantageous system which is capable of carrying very high amount of axial load resulting from the interaction between steel section and the concrete. The steel section provides reinforcement to the concrete to resist any tensile forces, shear forces and bending moments. If concrete is compacted in a very composite column, then apart from resisting the compressive loading it also effectively reduces the buckling effect of the steel section. In comparison with reinforced concrete columns, such composite columns either sheathed or in-filled leads to much reduction in size of columns needed for holding the equivalent load. Hence, appreciable economic savings may be achieved. Such columns of smaller cross-sections can be used in places where they are the main reason of hindrance like automotive parking and commercial workplaces. In high-rise buildings which are susceptible to experiencing large amount of lateral loads, composite columns with close spacing in connection with surface beams may be used to provide lateral resistance by the tabular idea. In several unstable resistant structures concrete sheathed steel composite sections are recommended for once the concrete enclosing cracks below severe overloading of flexural nature, the stiffness of the section reduces however the steel core provides ductile resistance and shear capability to succeeding cycles of overload.

S. Kothari · D. K. Singh (✉) · P. Chamoli
Graphic Era (Deemed to be University), Dehradun 248001, India

© The Author(s), under exclusive license to Springer Nature Singapore Pte Ltd. 2022
M. L. Kolhe et al. (eds.), *Smart Technologies for Energy, Environment and Sustainable Development*, Vol 2, Springer Proceedings in Energy,
https://doi.org/10.1007/978-981-16-6879-1_15

135

2 Literature review

Concrete filled steel tube (CFST) columns are also recommended for several columns in high-rise buildings, earthquake-resistant structures and bridge piers subjected to high strain rate from railways decks and traffic. Since the shoring system and formwork used in construction can be avoided by using the steel tubes, hence CFST structures may be having higher constructability. When used next with concrete sheathed steel composite sections, CFSTs give high compressive and torsional resistance concerning all axes. The very first research attempt in this field to study the structural behavior of CFST elements was made by Abdalla [1]. In his research, he conducted a test program on concrete, steel tube and CFST. According to the test results of his study, it has been observed that the CFST columns are having larger load-bearing capacity in comparison to the sum of steel and concrete capacities when tested individually. Several studies on CFST columns done by many of the researchers such as Neogi et al. [2], Klöppel and Goder [3], Salani and Sims [4], it was concluded that due to the confinement of steel tube on concrete infill, development of ultimate axial resistance of CFST columns occurs. The study conducted by Prichard and Perry [5] suggests that on providing additional lateral confinement to the minimum fundamental, maximum contact force can be gained inhibiting the dilation of concrete. However, increasing the thickness will not decrease dilation by any significant degree. Also, increasing the stiffness of the confining materials will increase contact forces among the confined specimens. But the stiffness of confining materials and contact force are non-linearly proportioned. O'Shea and Bridge [6] observed that local buckling is significantly affecting load-carrying capacity in case of hollow circular steel tubes. However, by providing internal lateral restraint in square-shaped tubes, buckling strength of columns can be improved but this is not valid for circular steel tubes. Instead, the internal concrete did not affect the outward buckle of tube. Also, the degree of confinement provided by a thin-walled circular steel tube to the concrete infill depends upon the loading condition. Maximum degree of confinement can only be achieved by such loading where the axial load is transferred purely upon the concrete while the steel tube in CFST column is acting as circumferential restraint. Also, such composite sections result in high resistance to local buckling if the bond between concrete and steel tube is sufficiently strong. Thus, the effect for local buckling needs not to be considered in provisions of Euro code 4 [7] when strength of concrete infill is up to 80 MPa without reducing the steel's strength from local buckling and biaxial effects and without increasing confinement of infill concrete. Hou et al. [8] modeled and analyzed the CFST sections using finite element analysis software ABAQUS and by verifying it against the experimental data extracted from previous work done by Huang et al. [9]. Numerical analyses on circular CFST columns have proved that smaller width to thickness ratio (b/T) can provide larger confinement effect to the in-filled concrete. Square-shaped CFST columns are not capable of providing a large confining effect to the in-filled concrete particularly when the width to thickness ratio (b/T) ratio is large. Confinement of in-filled concrete in square CFST columns can be improved by providing reinforcing

ties which are closely spaced and larger in diameter. Na et al. [10] discussed the impact behavior of CFST and CFT stub columns and concluded that it is noticeable that for the same magnitude of impact loading, the CFST strain is lesser than the CFT indicating the improvement in resistance. The model also clarifies that the impact wave was getting transferred in form of unidirectional plane wave through specimen. However, due to avoiding the concrete damage in modeling of material, the calculated maximum strain for test results is comparatively greater than that of calculated using the model.

3 Description of the Model

The results reported in this paper are for service axial load on RC columns when compared with the similar dimensioned CFST columns for von-misses stress, vertical displacement and critical buckling load capacity.

Columns: The RC column is having length of 3.5 m and diameter of 450 mm. The concrete used is of M25 grade and grade of steel is Fe250 whereas for CFST columns the thickness of steel tube is 8 mm contributing the overall diameter of 450 mm and length of 3.5 m.

Loading: The columns are subjected to axial compressive load of 30 kN/mm² over the top cross-sectional area and the bottom end is fixed at base with the foundation for stress analysis whereas for critical buckling analysis, the axial load has been taken as 100 kN (Fig. 1).

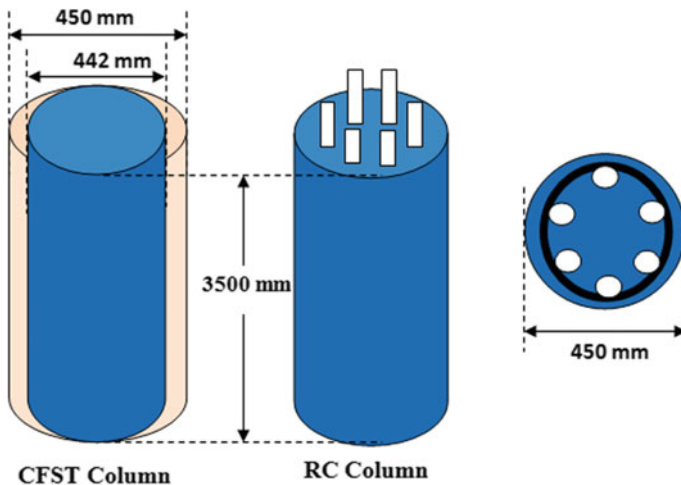


Fig. 1 Description of column dimensions for RC and CFST columns

4 Numerical (Finite) Modelling of the Columns

The columns are modeled in ABAQUS 6.13 software, as 3-D element where the concrete and steel reinforcement are modeled using eight node brick element (C3D8) as rigid elements and instanced in their positions for binding those using rigid embedded connection so that it may behave as a composite section. In CFST columns the steel tube is modeled as general purpose linear 4-sided shell component (S4R). The load applied on top of column is taken as distributed load over the whole cross-section.

5 Results and Analysis

For stress along Y-direction on equating the radial strain in concrete and radial strain in steel at the interface we get (Fig. 2),

$$\frac{\sigma_y}{E_c} - \frac{\mu * \sigma_z}{E_c} = \frac{\sigma_y * D}{2 * t * E_s} \left(1 - \frac{\mu}{z}\right) + \frac{\sigma_y}{E_s}$$

$$\frac{\sigma_y}{25000} - \frac{0.3 * 30}{25000} = \frac{\sigma_y * 450}{2 * 0.004 * 2 * 10^5} \left(1 - \frac{0.3}{30}\right) + \frac{\sigma_y}{2 * 10^5}$$

$$\sigma_y = -1.4788\text{N/mm}^2$$

The stresses, strains and displacements are evaluated and compared for all the three axes. The results are graphically presented as in figures (Figs. 3, 4, 5, 6, 7, 8, 9, 10, 11 and 12).

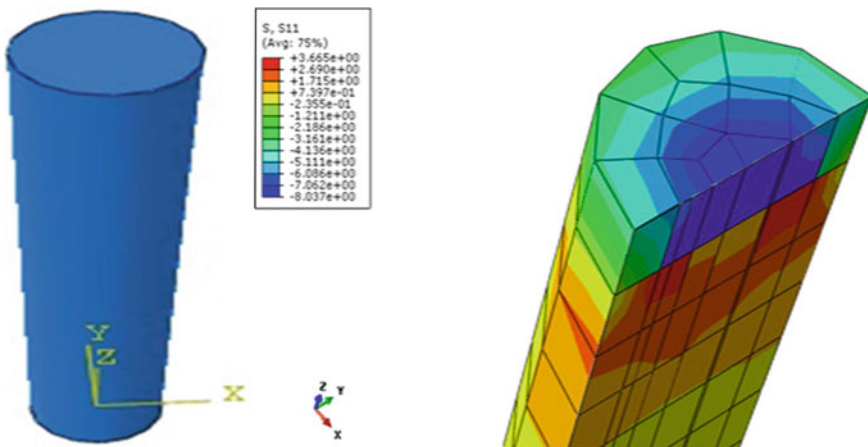


Fig. 2 FE model of CFST column and cross-sectional view of stresses along Y-direction

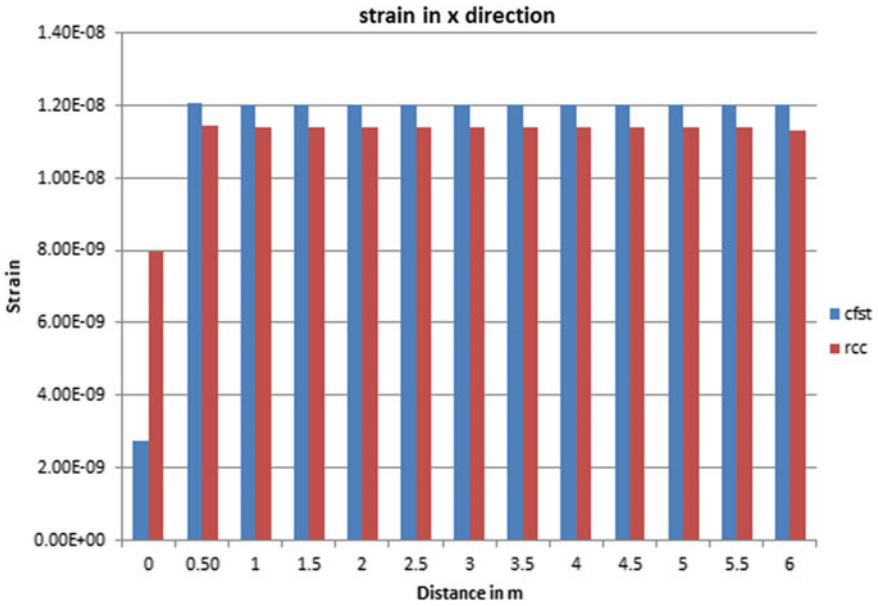


Fig. 3 Strain in x-direction (for CFST and long RC columns)

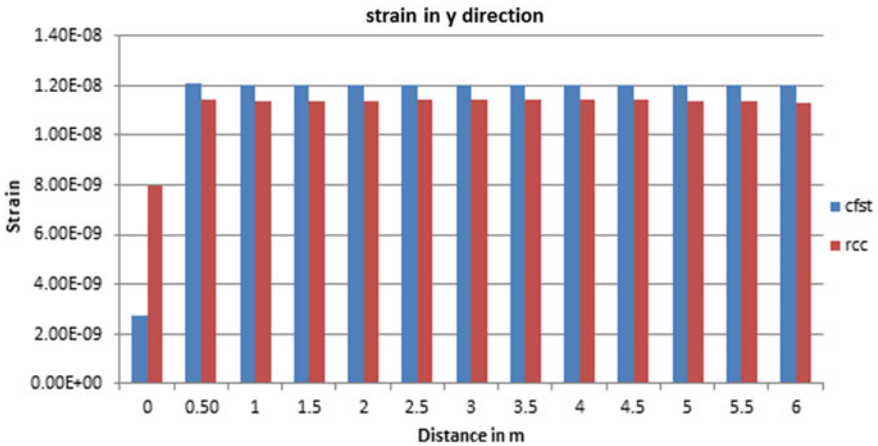


Fig. 4 Strain in y-direction (for CFST and long RC columns)

Now for buckling analysis of columns we need to assume it as a wired steel column using 2-D FE analysis. Using the given dimensions and finding the eigen value. Based on the calculated eigen value the different buckling modes are graphically analyzed for different shapes of columns.

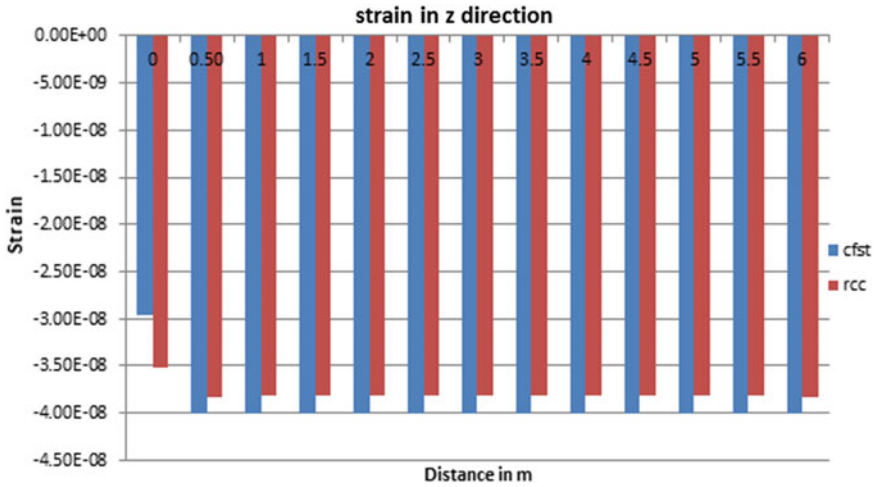


Fig. 5 Strain in z-direction (for CFST and long RC columns)



Fig. 6 Stress in x-direction (for CFST and long RC columns)

On comparing the stress in steel at interface, it has been observed that analytically it is -1.4788 N/mm^2 whereas using FE analysis it is -1.211 N/mm^2 . Also on comparing the results of buckling analysis the critical buckling load is 1.774% more in case of FE analysis as compared to analytical result.

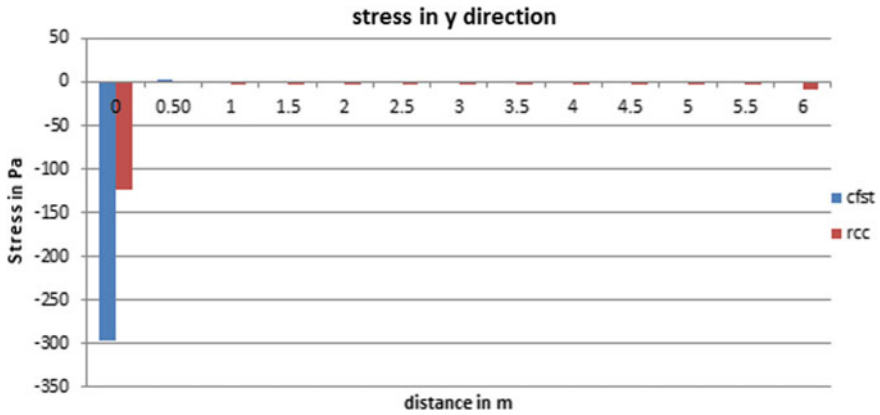


Fig. 7 Stress in y-direction (for CFST and long RC columns)

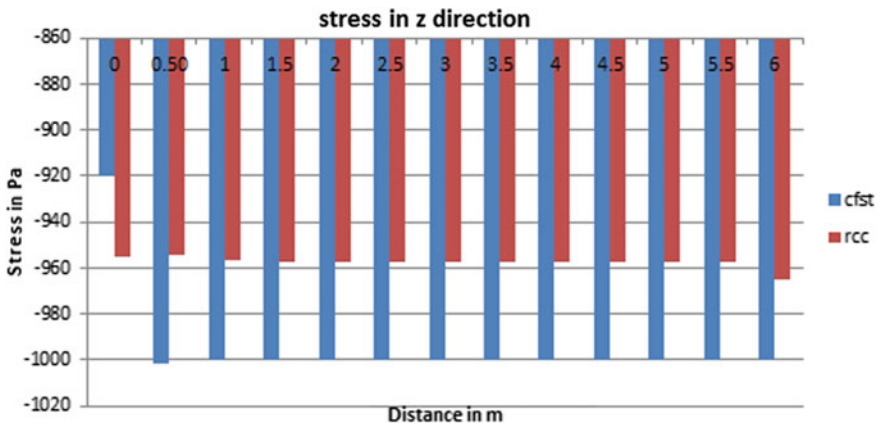


Fig. 8 Stress in z-direction (for CFST and long RC columns)

6 Conclusion

1. The critical buckling load of CFST column is more than RCC column. A negative buckling factor simply means that the structure will buckle when the directions of the applied loads are all reversed. It implies that shell would buckle if subject to excessive external pressure.
2. The critical buckling load in square column is more than circular shape of column. Moment of inertia is the important factor in the buckling analysis of the column. Moment of inertia of the square column is more than the circular column so the value of critical buckling of a square column is more as compared to circular column.

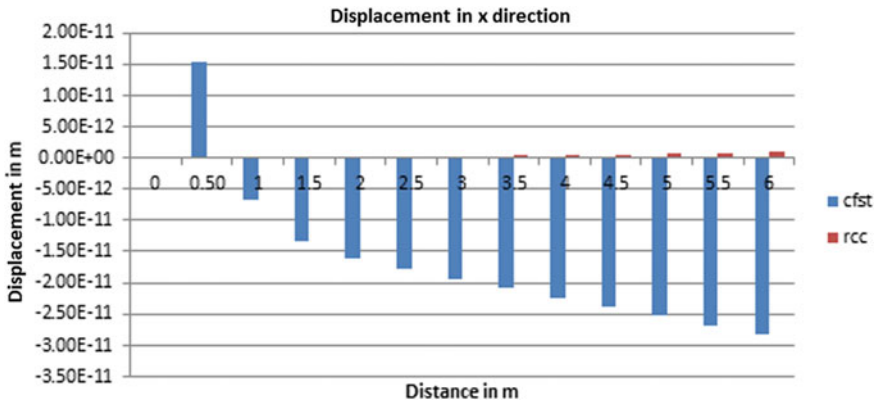


Fig. 9 Displacement in x-direction (for CFST and long RC columns)

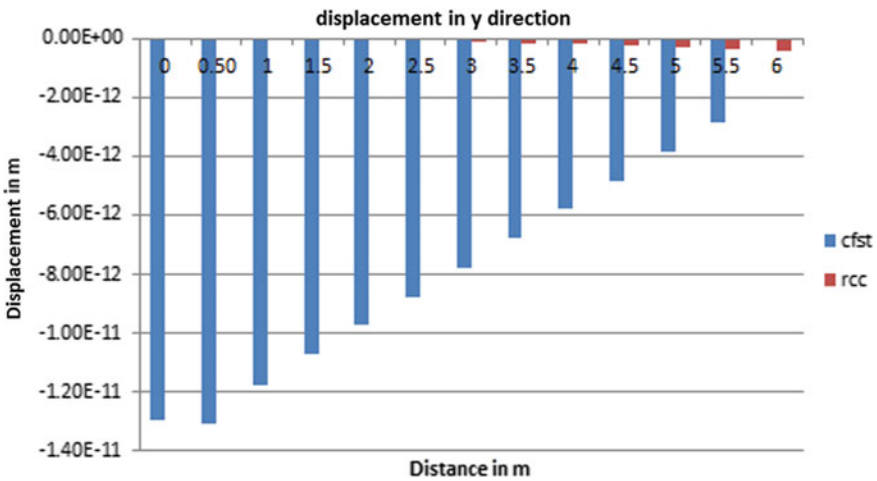


Fig. 10 Displacement in y-direction (for CFST and long RC columns)

3. The stress in CFST column is less as compared to RCC column in all directions. The strain in the CFST column is less than RCC columns in all directions.
4. Strain in a CFST short column is less as compared to strain in RCC short column. Displacements in both RCC and CFST columns are varying in different direction.

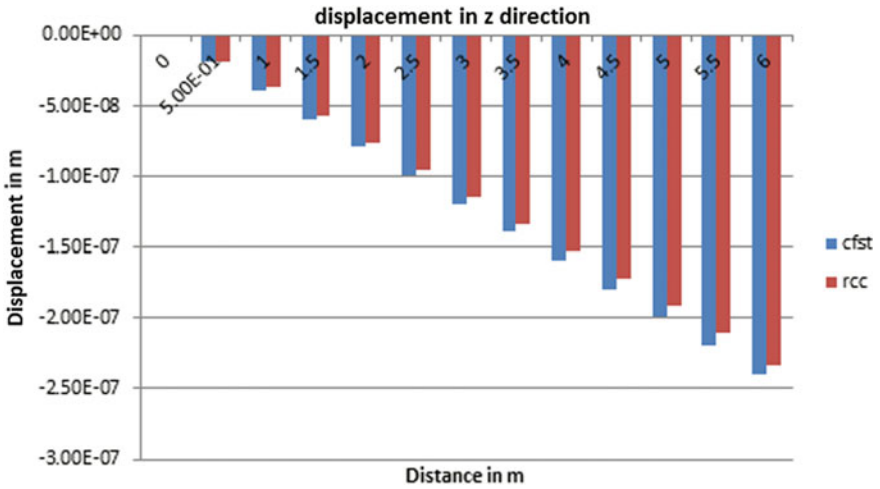


Fig. 11 Displacement in z-direction (for CFST and long RC columns)

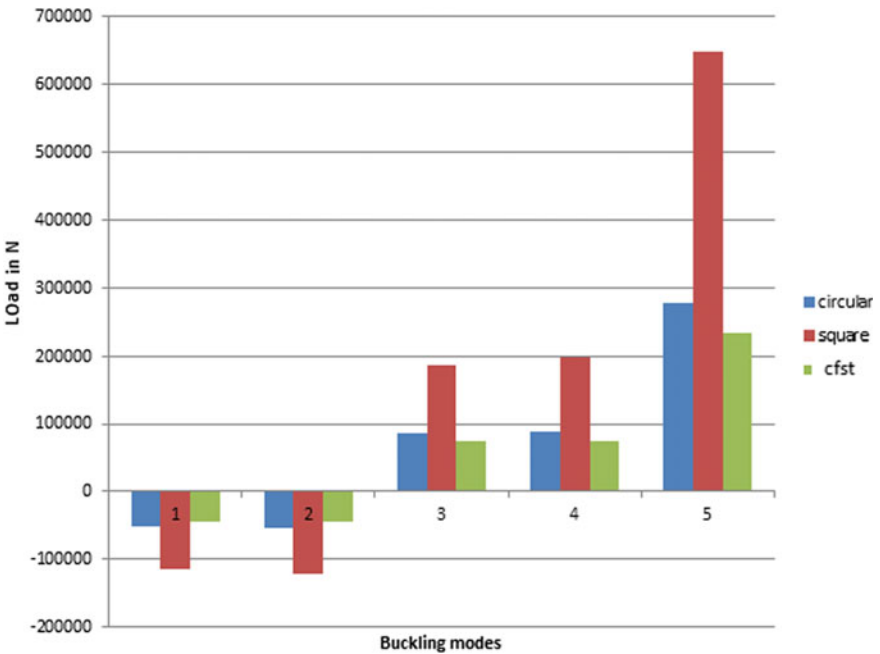


Fig. 12 Critical buckling loads for CFST and RCC columns

References

1. S.H. Abdalla, Behavior of Concrete Filled Steel Tube (CFST) under different loading conditions (Doctoral dissertation) (2012)
2. P.K. Neogi, Concrete-filled tubular steel columns under eccentric loading. *Struct. Eng.* **47**(5), 187–195 (1969)
3. V.K. Kloppel, W. Goder, An investigation of the load carrying capacity of concrete-filled steel tubes and development of design formula. *Der Stahlbau* **26**(1), 1–10 (1957)
4. H.J. Salani, J.R. Sims, Behavior of mortar filled steel tubes in compression. *J. Proc.* **61**(10), 1271–1284 (1964)
5. S.J. Prichard, S.H. Perry, The impact behaviour of sleeved concrete cylinders. *Struct. Eng.* **78**(17), 23–27 (2000)
6. M.D. O'Shea, R.Q. Bridge, Design of circular thin-walled concrete filled steel tubes. *J. Struct. Eng.* **126**(11), 1295–1303 (2000)
7. S. Park, EN 1994-Eurocode 4: Design of composite steel and concrete structures (1994)
8. C.C. Hou, L.H. Han, F.C. Wang, C.M. Hu, Study on the impact behaviour of concrete-encased CFST box members. *Eng. Struct.* **198**, 109536 (2019)
9. F. Huang, X. Yu, B. Chen, The structural performance of axially loaded CFST columns under various loading conditions. *Steel Compos. Struct.* **13**(5), 451–471 (2012)
10. L. Na, L. Yiyang, L. Shan, L. Lan, Slenderness effects on concrete-filled steel tube columns confined with CFRP. *J. Constr. Steel Res.* **143**, 110–118 (2018)

Use of Bagasse Ash as a Filler Material in Soils



Rahul Vaishnava, Ajit Kumar, and Sanjeev Kumar

1 Introduction

India is an agricultural country. Sugarcane is one of the important commercial crops grown in India and supports the livelihood of 50 million farmers and 5 lakh workers employed in sugar mills. Mainly, sugarcane is used for sugar production by crushing it in sugar mills. India on average produces 310 million tons of sugarcane annually. Bagasse produced after extracting juice from sugarcane is used as a fuel in boilers of sugar mill to produce steam and electricity, generating about 9 million tonnes of bagasse ash annually. Accretion and piling up of bagasse ash, demands for its safe and economical disposal. Therefore, the present study is an effort to explore the constructive use of bagasse ash in the stabilization of soils.

Hernández [1] observed that the reaction between lime and Sugarcane bagasse reaction has brought up changes in the microstructure of material as the formation of new products makes material denser and tougher to fracture. Cordeiro et al. [2] studied the filler and pozzolanic effects of Bagasse ash in lime and cement mortars and found that virtual packing density of BA increased with increase in grinding time period. Also, when compared to a material (Crushed Quartz) of same fineness he confirmed that due to the pozzolanic activity of bagasse ash the compressive strength of BA mortar was 31% greater than the strength of Crushed Quartz mixture. Anupam et al. [3] and Kharade et al. [4] found that the CBR values of soil increased with the addition of bagasse ash when compared to the virgin soil. Jain et al. [5] and Yadav [6] confirmed of reduction in the liquid limit of soil admixed with optimum BA dosage and on further addition of BA, the plastic limit of the soil mix decreased almost linearly as a result the plasticity index was reduced. Hasan et al. [7] and

R. Vaishnava · S. Kumar (✉)

Department of Civil Engineering, Graphic Era University, Dehradun, Uttarakhand, India

A. Kumar

Department of Civil Engineering, G.B.P.U.A&T, Pantnagar, Uttarakhand, India



Fig. 1 Bagasse ash collected from ash pond

Dang et al. [8] studied the use of bagasse ash with hydrated lime and the compaction results indicate that there was a decrease in dry density with increase in the admixture content.

2 Materials

The study is conducted on soil and sugarcane bagasse ash (BA). The soil used in the study was collected from Shaktifarm, Sitarganj region of district U.S. Nagar, state Uttarakhand, country India. Soil was classified as CL (Clay with low plasticity). Waste bagasse ash was collected from Ash pond of the Kichha Sugar Company Ltd. (Fig. 1) Kichha, District Udham-Singh Nagar (Uttarakhand) which was commissioned in the year 1972. Collected bagasse ash was thoroughly mixed and was sundried. Bagasse ash used in this study was sieved through various sieves so as to study the effect of fineness on the geotechnical properties of soil (Fig. 2; Tables 1 and 2).

3 Methodology

In order to examine the effect of fineness on various geotechnical properties of the soil different experimental programmes were carried out as per IS standard procedures.

- (a) Grain size analysis.
- (b) Specific gravity.
- (c) Atterberg's limit analysis.
- (d) Standard proctor test.

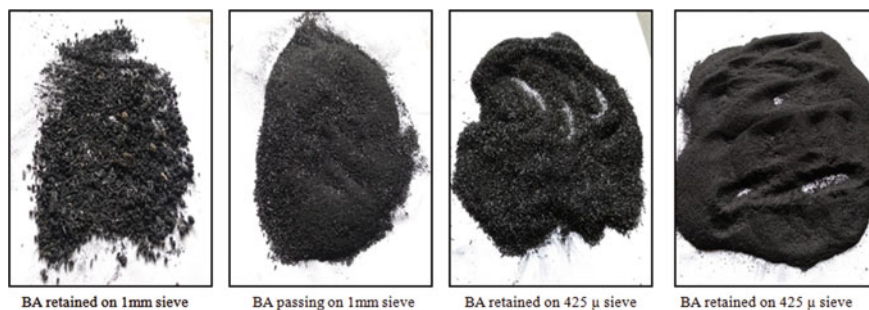


Fig. 2 Bagasse ash passed through various sieves

Table 1 Geotechnical properties of soil

S. no	Property	Value
1.	Specific gravity	2.58
2.	Particle size distribution	
	Gravel (%)	0.00
	Sand (%)	7.35
	Silt (%)	77.00
	Clay (%)	15.65
3.	Consistency limits	
	Liquid limit (%)	25.14
	Plastic limit (%)	14.00
	Plasticity index (%)	11.14
4.	Maximum dry density, kN/m ³	18.56
5.	OMC (%)	16.19

Table 2 Chemical composition of bagasse ash

S. no	Composition	Description	Percentage content	
			Nigeria*	India**
1.	CaO	Calcium oxide	3.23	2.75
2.	SiO ₂	Silica	41.17	65.03
3.	Al ₂ O ₃	Alumina	6.98	0.49
4.	Fe ₂ O ₃	Iron oxide	2.75	0.49
5.	MgO	Magnesia	0.11	3.26
6.	K ₂ O	Potassium oxide	0.872	1.73
7.	TiO ₂	Titanium dioxide	1.10	0.08
8.	LOI	Loss on ignition	17.57	24.84

Source *Osinubi et al. [9], **Umamaheswaran [10]

The overall testing programme was conducted in two phases:

First Phase: Geotechnical characteristics of the soil were determined by conducting grain size analysis, specific gravity test, consistency limits test, standard proctor test.

Second Phase: The soil was mixed with a constant dosage of 10% of bagasse ash obtained after passing the ash from different sieves. The ratio of Bagasse Ash to virgin soil (1:9) was considered as the optimal ratio obtained from the result of studies done by various researchers previously. Thereafter geotechnical properties of soil-bagasse ash mixes were determined by performing a series of consistency limits tests and standard proctor tests.

4 Results and Discussion

The Particle size distribution curve of the bagasse ash shows a broad range of particle sizes ranging from 2 mm to 2 microns as shown in Fig. 3. Depending upon the percentage finer content obtained from the sieve analysis bagasse ash used for the study was of varying fineness. The collected bagasse ash was dark black in color and non-plastic in nature with the presence of some impurities and unburnt particulate matter.

Table 3 shows the grain size distribution and the increment in specific gravity of bagasse ash as its fineness increases by passing it through various sieves.

Consistency limits are essential in soil identification and its classification. These parameters are an indication for some of the common geotechnical problems such as workability, shrinkage and swell potential (Fig. 4).

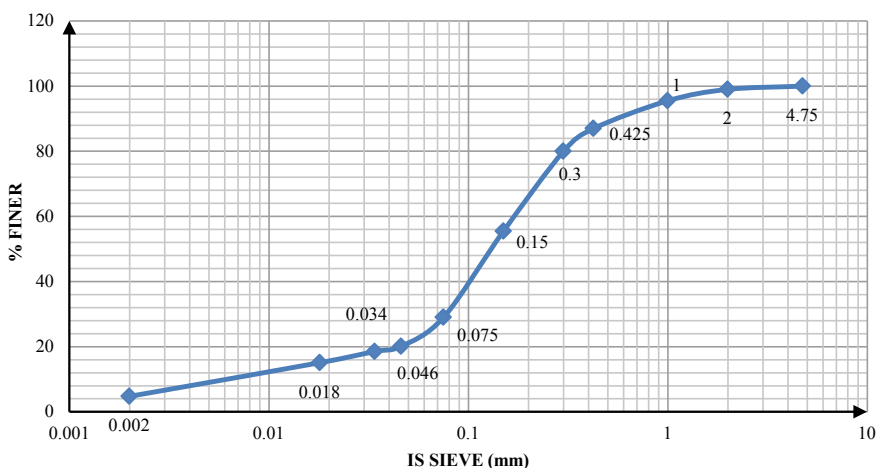


Fig. 3 Particle size distribution curve of bagasse ash

Table 3 Specific gravity and grain size distribution of the bagasse ash

S. no	Properties	Value
1	Specific gravity	
	B.Ash obtained from sugar factory	1.60
	B.Ash passing 1 mm sieve	1.70
	B.Ash passing 425 μ sieve	2.18
	B.Ash passing 75 μ sieve	2.29
2	Grain size distribution	
	% Finer than 1 mm	98%
	% Finer than 425 μ	87%
	% Finer than 75 μ	29%

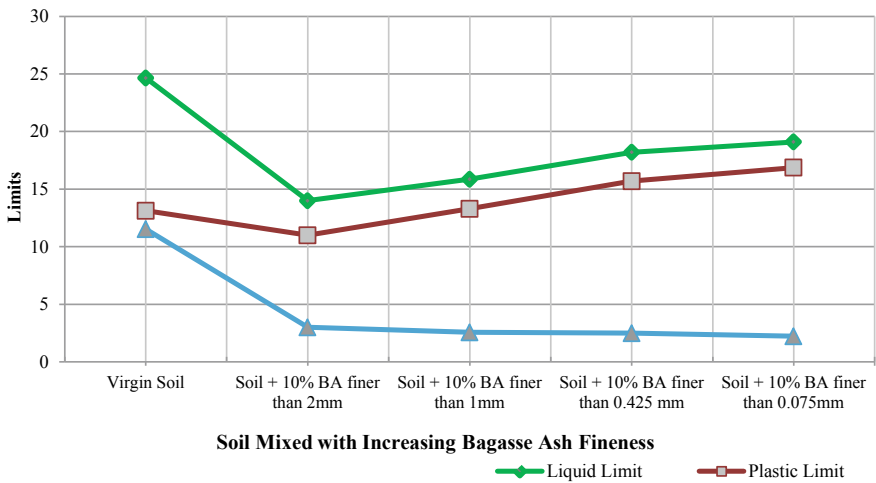


Fig. 4 Variation of consistency limits and plasticity index with increasing fineness of bagasse ash

As observed from the results of consistency limits, soil initially can be classified as medium plastic but as soon as the bagasse ash was introduced in the virgin soil its plasticity index reduced by 75%. Also, as the particle size of the bagasse ash was reduced plasticity index of the mix showed a linear decrement (Fig. 5).

The engineering properties of soil depend upon the moisture and density at which the soil is compacted. Generally, a higher degree of compaction improves the engineering properties of a soil. As seen from the compaction curve it was observed that as the bagasse ash was introduced into the soil moisture demand initially got reduced but as the fineness of the bagasse ash was increased moisture demand of the soil mix got amplified from its initial value.

The increase in the moisture demand might be due to the increase in the reactivity between free silica and free lime present in the soil and bagasse ash as confirmed by the Cordeiro et al. [2] Hasan et al. [7] and Dang et al. [8] (Fig. 6).

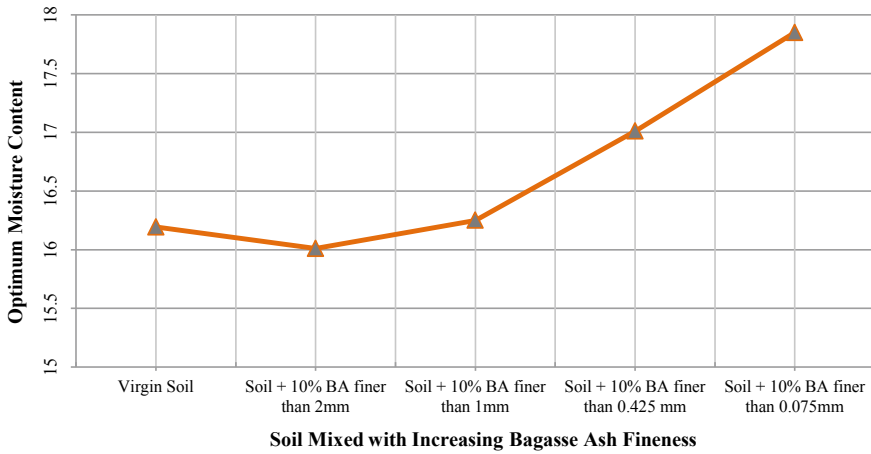


Fig. 5 Variation of optimum moisture content with increasing fineness of bagasse ash

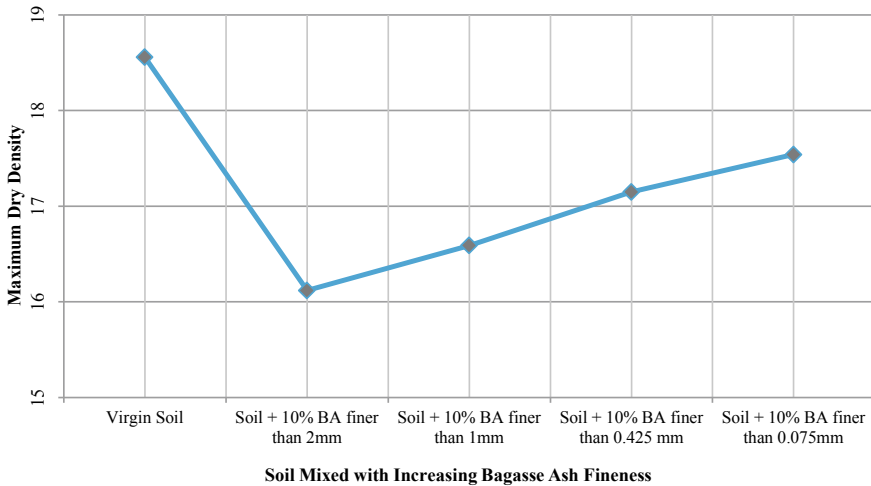


Fig. 6 Variation of maximum dry density with increasing fineness of bagasse ash

Maximum dry density of soil got reduced with the introduction of the additives but as the fineness of bagasse ash was increased dry density of the soil mix started to increase. The decrease in the dry density might be due to the replacement of higher specific gravity of soil particles by lighter bagasse ash particles. Also, as the fineness of bagasse ash was increased the dry density started to grow. It might be due to increase in the specific gravity with the increase in fineness of bagasse ash. Cordeiro et al. [2] also found that virtual packing density of BA increased with increase in grinding time period.

5 Conclusions

It was observed that the bagasse ash is very much efficient in curtailing down the plasticity Index of the medium plastic soils. Also, greater the degree of fineness of bagasse ash higher is the specific gravity values. Also, fineness will increase the surface area of the bagasse ash particles which will increase the rate of reaction between free silica and lime present in the soil and bagasse ash. From the compaction test it was confirmed that with the addition of bagasse ash, moisture demand of soil got increased while maximum dry density (MDD) got reduced. But as the fineness of bagasse ash was increased moisture demand and maximum dry density values of the mix got increased. From the complete study, it can be concluded that the fineness of bagasse ash has a great impact on the geotechnical properties of soil. Further, the study can be used in determining the effect of bagasse ash and cementitious material such as lime or cement admixed together with the plastic soils.

References

1. J.M. Hernández, B. Middendorf, M. Gehrke, H. Budelmann, Use of wastes of the sugar industry as pozzolana in lime-pozzolana binders: study of the reaction. *Cem. Concr. Res.* **28**(11), 1525–1536 (1998)
2. G.C. Cordeiro, R.D. Toledo Filho, L.M. Tavares, E.M.R. Fairbairn, Pozzolanic activity and filler effect of sugar cane bagasse ash in Portland cement and lime mortars. *Cem. Concr. Compos.* **30**(5) (2008)
3. A.K. Anupam, P. Kumar, Use of various agricultural and industrial waste materials in road construction. *Procedia Soc. Behav. Sci.* **104**, 264–273 (2013)
4. A.S. Kharade, V.V. Suryavanshi, B.S. Gujar, R.R. Deshmukh, Waste product bagasse ash from sugar industry can be used as stabilizing material for expansive soils. *Int. J. Res. Eng. Technol.* **3**(3), 506–512 (2014)
5. J. Tanmay, Y. Gulshan, B. Chandra, C.H. Solanki, Comparative study of effect of waste material on black cotton soils in surat region. *Proceedings of the 5th Indian Young Geotechnical Engineers Conference-2015 Indian Geotechnical Society Baroda chapter* (2015)
6. A.K. Yadav, K. Gaurav, R. Kishor, S.K. Suman, Stabilization of alluvial soil for subgrade using rice husk ash, sugarcane bagasse ash and cow dung ash for rural roads. *Int. J. Pavement Res. Technol.* **10**(3), 254–261 (2017)
7. H. Hasan, L. Dang, H. Khabbaz, B. Fatahi, S. Terzaghi, Remediation of expansive soils using agricultural waste bagasse ash. *Proc. Eng.* **143**, 1368–1375 (2016)
8. L.C. Dang, H. Hasan, B. Fatahi, R. Jones, H. Khabbaz, Enhancing the engineering properties of expansive soil using bagasse ash and hydrated lime (2016)
9. K.J. Osinubi, V. Bafyau, A.O. Eberemu, Bagasse ash stabilization of lateritic soil. In *Appropriate Technologies for Environmental Protection in the Developing World* (pp. 271–280). Springer Netherlands (2009)
10. K. Umamaheswaran, V.S. Batra, Physico-chemical characterization of Indian biomass ashes. *Fuel* **87**(6), 628–638 (2008)
11. The Commission for Agricultural Costs and Prices (CACP) (2016–17). Annual report on sugarcane cultivation, New Delhi, India, 2012

Assessing the Accuracy of Open Source Altitude Data for the Hilly Area in Tehri Garhwal District of Uttarakhand, India



Kishan Singh Rawat, Sanjeev Kumar, Anil Kumar Mishra,
and Sudhir Kumar Singh

1 Introduction

Digital surface model (DSM) envisage the earth's surface and includes all objects present on it and digital terrain model (DTM) represents a bare surface without any objects like plants and buildings whereas DEM represent raster or a vector-based triangular irregular network (TIN) and it is a subset of a DTM. DEM has many applications such as extracting terrain parameters for geomorphology, hydrological modeling [1], groundwater potential zone mapping [2–5], soil wetness, creation of relief, terrain analysis in geomorphology and physical geography, morphometry [6–10]; surface analysis [11], hypsometry [12]; land use planning [13, 14], infrastructure development, precision farming, intelligent transportation systems and many more. The DEM acquisition techniques such as photogrammetry, lidar, InSAR, land surveying, etc. [15].

Digital elevation model systematic stores the elevation information and remote sensing-based DEM model have wide applicability such as mitigation, management and planning works. Previous studies have focused on comparative evaluation of different remote sensing-based DEM model with the observed or mapped topographic points. The DEM data have horizontal and vertical accuracy. Rawat et al. [16] have compared the horizontal accuracy ASTER and SRTM DEM with respect

K. S. Rawat (✉) · S. Kumar
Geo-Informatics, Civil Engineering Department, Graphic Era (Deemed to be University),
Dehradun, Uttarakhand, India

A. K. Mishra
Water Technology Centre (WTC), Indian Agricultural Research Institute (IARI), New Delhi
110012, India

S. K. Singh
K. Banerjee Centre of Atmospheric Ocean Studies, IIDS, Nehru Science Centre,
University of Allahabad, Prayagraj, Uttar Pradesh, India

to CARTOSAT-1 DEM in a flat terrain. Szabo et al. [17] performed accuracy assessment of SRTM and GDEM and found that slope angle and aspect affects the vertical accuracy of SRTM. Xing et al. [18] estimated the glacier thickness change by SRTM DEM and ASTER GDEM and found that SRTM DEM results are consistent with the GPS measurements. Li et al. [19] compared the SRTM DEM (SRTM1), ALOS DEM (AW3D-30 m) and global DEM version 2 (GDEM2). They reported that terrain slopes and land cover types jointly affect the vertical accuracies of AW3D30, and the former is likely to have a greater impact than the latter. Suwandana et al. [20] have compared the ASTER GDEM2, SRTM DEM, Topo-DEM with Real-Time Kinematic differential Global Positioning Systems (RTK-dGPS) data and observed that ASTER GDEM2 have large number of undulations effects which may cause error in hydrological studies. Rawat et al. [21] evaluated vertical accuracy of SRTMDEM and ASTERDEM with respect to CARTOSAT-1DEM (IRS-P5) and statistical measures show that CARTOSAT-1DEM have good vertical accuracy.

In this paper, we have evaluated the suitability of SRTM DEM, ASTER DEM and Google Earth DEM with the Survey of India digital elevation model.

2 Methodology

2.1 Study Area

Tehri Garhwal district is located in mid Himalayas which comprises of low line peaks rising contiguously with the planes of the northern India. It is surrounded by Dehradun district in the west, Rudraprayag district in the east, Pauri Garhwal District in the south, and Uttarkashi District in the north. Total geographical area is 3796 km² [22]. Tehri district covered by four SOI toposheet, in which two SOI toposheet (Toposheet No: 53 $\frac{J}{11}$ and 53 $\frac{J}{12}$ are not for publication or frozen), therefore we constraint our study area within two toposheet No: 53 $\frac{J}{7}$ and 53 $\frac{J}{8}$. Agriculture is the main occupation of the people (see Fig. 1).

2.2 Statistics Test for Accuracy Assessment of Altitude Information

Total twelve statistical tests were applied for statistical analysis of altitude accuracy from different DEMs or source. These tests namely are Standard Error of Estimation (SEE, [22, 23], Root Mean Square Error (RMSE, [23, 24]); Relative RMSE (R-RMSE, [23–33]; Percentage RMSE (% RMSE); Volume Error (VE); Correlation Coefficient (CORR, [14, 23–26, 28–31, 33, 34]); Normalized RMSE (NRMSE); Mean Absolute Error (MAE, [22–34]); Mean Bias Error (MBE, [21, 23–26, 29, 30, 34, 35]); Mean Absolute Percentage Error (MAPE); Index of Agreement (d); Average

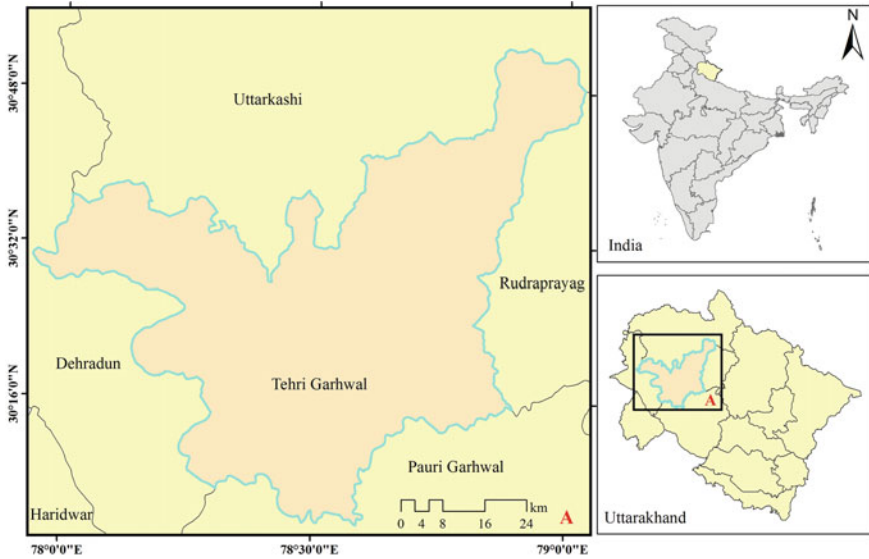


Fig. 1 Map of study area

Index Ratio (IR, [23–25]); Percentage of Error (PE). For ranking of altitude models, we used K factor analysis to provide proper weight to selected statistical index tests as Rawat et al. [28].

2.3 Data Arrangement for Analysis

For analysis data are arranged in such a way that, result must be appear for complete data set and classe wise (Forest, Settlement, Tower, Boundary pillars (BP), and Temple).

3 Result and Discussion

3.1 Statistical Performance Evaluation Under Full Data Set

Figure 2, show a co-relationship between elevation obtained from (i) Toposheet DEM and SRTM30m (T—SRTM30m), (ii) Toposheet DEM and SRTM90m (T—SRTM90m), (iii) Toposheet DEM and ASTER30m (T—ASTER30m), and (iv) Toposheet DEM and GE (T—GE). In each case correlation between toposheet and different models (SRTM30m, SRTM90, ASTER30m and GE) are very good. In each

case, correlation is higher because data sets estimated from toposheet and different models are so close. Due to this fact it was not a correct logic to assign rating and rank only based on correlation, therefore we used 12 statistical tests (SEE_M , $RMSE$, $R-RMSE$, $\%RMSE$, VE , $NRMSE$, MAE_M , MBE_M , $MAPE_M$, d , IR and PE) to accept correlation ($CORR$) test for fixing an appropriate rating to model. According Fig. 2 $SRTM_{30m}$, $SRTM_{90m}$, $ASTER_{30m}$ and GE models having R^2 value of 1.0, 1.0, 1.0, and 0.998, respectively. Now on the basis of r^2 value, it is very difficult to assign any rank among $SRTM_{30m}$, $SRTM_{90m}$, and $ASTER_{30m}$. Therefore we need other ways (except R^2 test) to distinguish in micro level. Therefore we adopt K factor/weightage analysis for ranking of models.

Table 1 is tabulated format of all statistics tests report. Table 1 reveal that SEE (1T) and $RMSE$ (2T) value (2.61 and 2.63) are least for $SRTM_{30m}$ model while 1T and 2T have highest value of 22.53 and 22.47 for GE model. Table 1 indicates all tests (1T–13T) values for $SRTM_{90m}$ and $ASTER_{30m}$ are existed between $SRTM_{30m}$ and GE model. Based on statistics tests and K factor analysis, a least value of K (0.0006) was assigned for $SRTM_{30m}$ while GE model score highest K (0.0044). $SRTM_{90m}$ and $ASTER_{30m}$ models have same K value of 0.0007.

Based on statistic test report and K factor analysis it is very difficult to decide which model is has high altitude accuracy. This problem can be easily solved by adopting weightage analysis [21]. Table 2 is show weightage value along nT (where n, is any number 1–13). Table 2 indicates rating column which is sum of all nW (where n, is any number 1–13) along corresponding row. Lowest rating converted into first rank (1st), similarly highest rating converted into last rank (4th). Based on Table 2, $SRTM_{30m}$, $SRTM_{90m}$, $ASTER_{30m}$ and GM models are ranked as first,

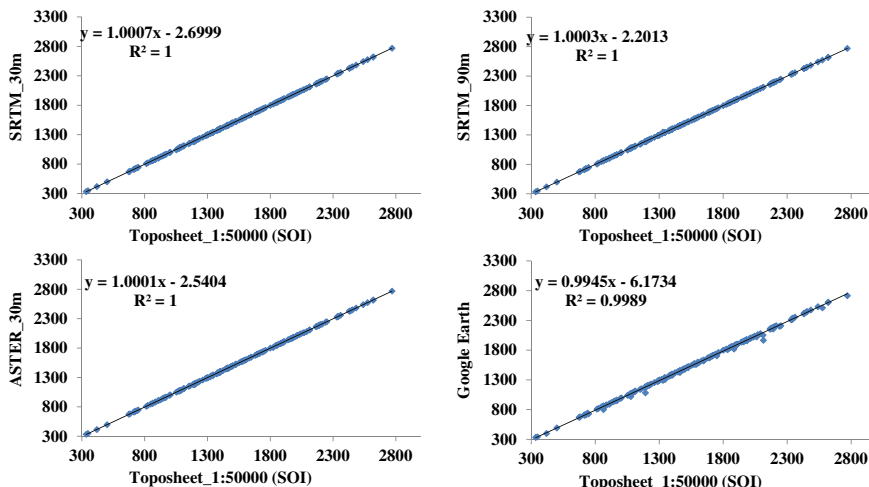


Fig. 2 The data sets plot of classes (Forest + Settlement + Tower + Boundary pillars (BP) + Temple) versus toposheet

Table 1 Statistical tests result for full data set

Model	Statistical tests													K
	1T	2T	3T	4T	5T	6T	7T	8T	9T	10T	11T	12T	13T	
SRTM_30	2.61	2.63	0.00	0.21	0.00	1.00	0.00	1.62	-1.62	0.13	1.00	1.00	-23.48	0.0006
SRTM_90	3.20	3.19	0.00	0.25	0.00	1.00	0.00	1.79	-1.79	0.16	1.00	1.00	-25.06	0.0007
ASTER_30	3.82	3.81	0.00	0.30	0.00	1.00	0.00	2.34	-2.34	0.17	1.00	1.00	-31.47	0.0007
Google Ele	22.53	22.47	0.02	1.78	0.01	1.00	0.01	14.72	-14.7	1.05	1.00	0.99	-191.8	0.0044

Note 1. SEE; 2. RMSE; 3. R-RMSE; 4. %RMSE; 5. VE; 6. CORR; 7. NRSME; 8. MAE_M; 9. MBE_M; 10. MAPE_M; 11. *d*; 12. IR; 13. PE; T. Test

Table 2 Ranking and performance evaluation of each model for full data set

Assigning of weightage to each statistical tests													Rank	DEMs model	
1W	2W	3W	4W	5W	6W	7W	8W	9W	10W	11W	12W	13W			
0.000	0.000	0.249	0.003	0.416	0.001	0.326	0.00	0.000	0.004	0.001	0.001	0.000	0.007	1	SRTM_30
0.000	0.000	0.251	0.003	0.422	0.001	0.318	0.00	0.000	0.004	0.001	0.001	0.000	0.009	2	SRTM_90
0.000	0.000	0.259	0.002	0.431	0.001	0.301	0.00	0.000	0.004	0.001	0.001	0.000	0.010	3	ASTER_30
0.000	0.000	0.266	0.002	0.416	0.004	0.299	0.00	0.000	0.004	0.004	0.004	0.000	0.057	4	GE

Note W represents to weightage of corresponding statistical test

second, third and fourth respectively. Rank of model is showing accuracy level of altitude with respect to SOI toposheet.

3.2 Statistical Performance Evaluation

Analysis with full data set will not give us altitude accuracy at class wise, it will provide an overall average accuracy level of altitude. Therefore, class wise altitude accuracy analysis is required, because Optical, Thermal and SAR remote sensing techniques output will be different with different classes.

Figure 3, represent 2D scatterplot of elevation value of forest area between (i) T—SRTM30m, (ii) T—SRTM90m, (iii) T—ASTER30m, and (iv) T—GE. All models are working well with Toposheet based altitude values, because R^2 value for all model is very high 1 or near to 1 (or ~ 0.9968). We have applied another statistical test also (Table 3). Total 13 statistical tests were applied for identified model accuracy (Table 3) but final identification result obtained as rank/rating in Table 4.

From Tables 3 and 4, SRTM30m matches with toposheet for forest group of data sets. This is due to high resolution and SAR technique (in SRTM30m and SRTM90m) based mapping of hill forest. Because, SAR technology is capable to easily identify altitude differences between ground and dense group of trees (or forest). This ability will be increasing with increasing of resolution of sensing like 90–30 m. In case of thermal remote sensing, identification of temperature differences between ground and forest for plane area are somehow easy. But in hilly region (cold area) both (ground + forest) temperature will be almost same sometime. Therefore ASTER30m ranked

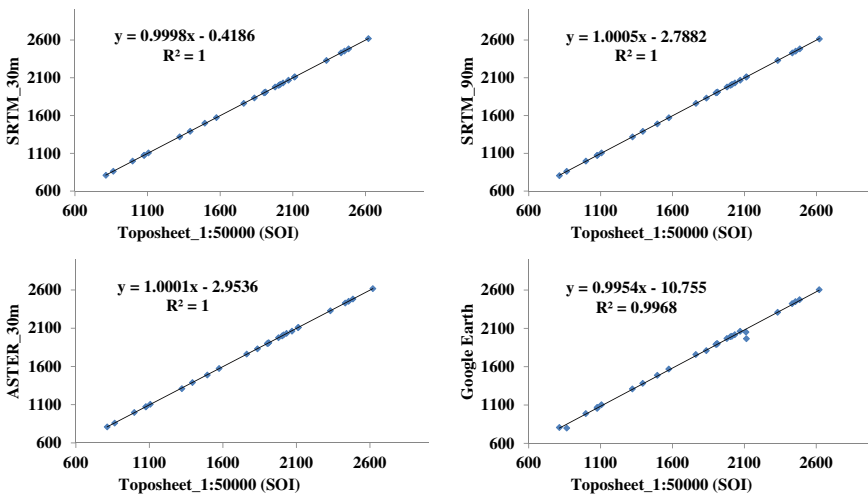


Fig. 3 Forest class wise data sets

Table 3 Statistical tests result for forest class

Model	Statistical tests											K		
	1T	2T	3T	4T	5T	6T	7T	8T	9T	10T	11T		12T	13T
SRTM_30	1.67	1.64	0.00	0.09	0.00	1.00	0.00	0.82	-0.82	0.08	1.00	1.00	-1.46	0.0003
SRTM_90	2.61	2.56	0.00	0.14	0.00	1.00	0.00	1.86	-1.86	0.14	1.00	1.00	-3.59	0.0005
ASTER_30	3.78	3.71	0.00	0.20	0.00	1.00	0.00	2.71	-2.71	0.19	1.00	1.00	-4.78	0.0007
Google Ele	34.91	34.29	0.02	1.87	0.01	1.00	0.02	18.86	-18.8	1.20	1.00	0.99	-32.31	0.0054

Table 4 Ranking and performance evaluation of each model for forest class data set

Assigning of weightage to each statistical tests													Ranking	Rank	DEMs model	
1W	2W	3W	4W	5W	6W	7W	8W	9W	10W	11W	12W	13W				
0.00	0.00	0.26	0.00	0.38	0.00	0.35	0.00	0.00	0.00	0.00	0.00	0.00	0.00	0.004	1	SRTM_30
0.00	0.00	0.23	0.00	0.39	0.00	0.37	0.00	0.00	0.00	0.00	0.00	0.00	0.00	0.007	2	SRTM_90
0.00	0.00	0.27	0.00	0.38	0.00	0.34	0.00	0.00	0.00	0.00	0.00	0.00	0.00	0.009	3	ASTER_30
0.00	0.00	0.24	0.00	0.45	0.01	0.28	0.00	0.00	0.00	0.01	0.01	0.00	0.00	0.071	4	GE

as third (3th) while SRTM30m and SRTM90m are ranked as first (1st) and second (2nd), respectively.

From Fig. 3, 2D scatter plot of Tower’s altitude data set from toposheet against SRTM30m, SRTM90m, ASTER30m, and GE. According to Fig. 3, toposheet based and altitude from SRTM30m DEM have high and best value R^2 as compared to other models and topographic sheet-based altitude. High value of R^2 ($=1$) is due to good resolution and use of microwave technology in ground mapping. In case of other models and topographic sheet based altitude data also show high value of R^2 , because data sets value is very high (in range of 1000 m) but variation or differences between two (models and topographic sheet) data sets is very low in unit degree of order.

From Tables 5 and 6, all statistical tests for SRTM30m suggest that SRTM30m has high rank (Table 6).

Figure 4 are graphical representation of settlement elevation group data from different models (SRTM30m, SRTM90m, ASTER30m, and GE drive elevation) with respect to altitude information from topographic sheet. According to Fig. 4, toposheet based and altitude from SRTM30m and SRTM90m DEM have high value of R^2 in compare to other model with respect to topographic sheet-based altitude. Again, high value of R^2 ($=1$) is due to SAR technology used in ground mapping of AOI. In case of another two models (ASTER30m and GE) also show good value of R^2 because data for settlement from thermal mapping and aerial photograph based extracted altitude information are almost near to real value or a low variation between models and topographic based altitude (see Fig. 5).

Based on Tables 7 and 8, SRTM model of 30 and 90 m both are good for predicting altitude value for settlement. In SRTM90m has low or less corner effect therefore

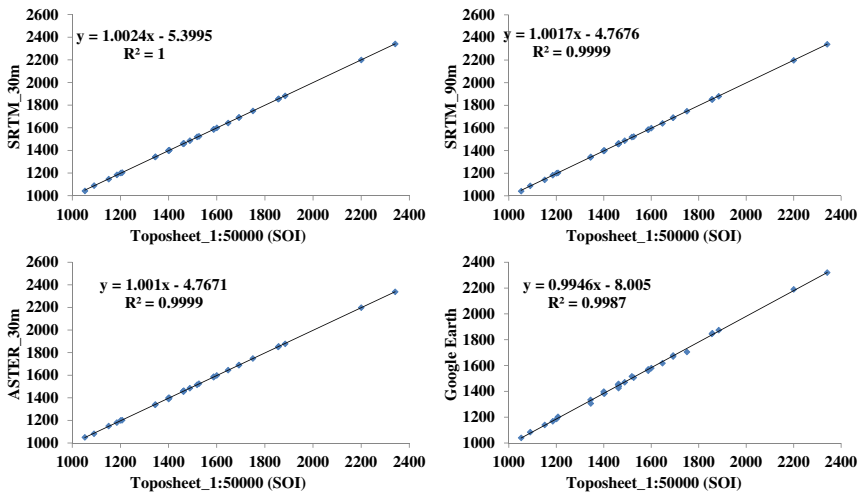


Fig. 4 Tower class wise data sets

Table 5 Statistical tests result for Tower class data set

Model	Statistical tests											K		
	1T	2T	3T	4T	5T	6T	7T	8T	9T	10T	11T		12T	13T
SRTM_30	2.70	2.65	0.00	0.25	0.00	1.00	0.00	1.68	-1.68	0.13	1.00	1.00	-3.86	0.0006
SRTM_90	3.41	3.36	0.00	0.32	0.00	1.00	0.00	2.23	-2.23	0.17	1.00	1.00	-4.96	0.0007
ASTER_30	4.10	4.04	0.00	0.38	0.00	1.00	0.00	3.19	-3.19	0.22	1.00	1.00	-6.85	0.0008
Google Ele	19.65	19.33	0.01	1.84	0.01	1.00	0.01	16.16	-16.1	1.09	1.00	0.99	-33.22	0.0040

Table 6 Ranking and performance evaluation of each model for Tower class data set

		Assigning of weightage to each statistical tests													Ranking	Rank	DEMs model
		1W	2W	3W	4W	5W	6W	7W	8W	9W	10W	11W	12W	13W			
0.000	0.000	0.252	0.002	0.419	0.001	0.321	0.000	0.000	0.000	0.004	0.001	0.001	0.000	0.007	1	SRTM_30	
0.000	0.000	0.260	0.002	0.413	0.001	0.318	0.000	0.000	0.000	0.004	0.001	0.001	0.000	0.009	2	SRTM_90	
0.000	0.000	0.289	0.002	0.382	0.001	0.320	0.000	0.000	0.000	0.004	0.001	0.001	0.000	0.011	3	ASTER_30	
0.000	0.000	0.305	0.002	0.364	0.004	0.313	0.000	0.000	0.000	0.004	0.004	0.004	0.000	0.052	4	GE	

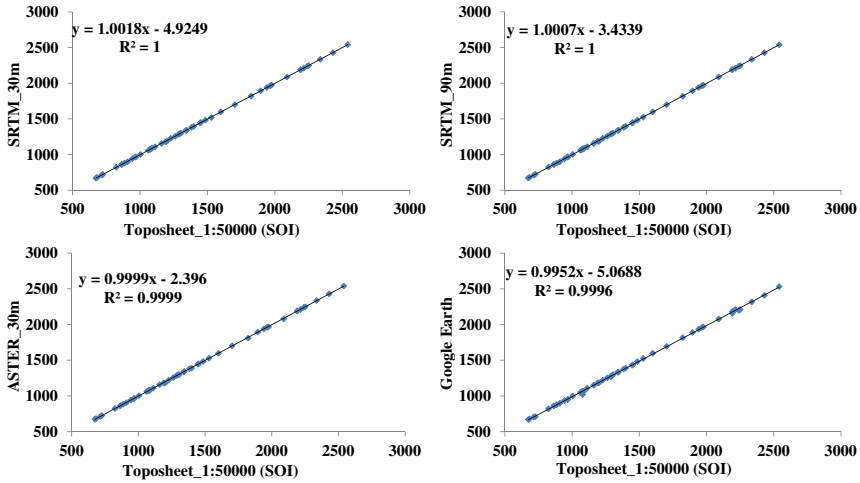


Fig. 5 Settlement class wise data sets

SRTM90m ranked as first (1st). Another models (ASTER and GE) are comparable and not fit for predicting altitude for settlement area.

Boundary pillars (BPs) are cement constructed small size pillars build by survey of India (SOI), it has fixed latitude, longitude and altitude values which also mentioned in SOI toposheet of particular place. Therefore, these fixed BPs are selected for accuracy assessment of models. This is a good way to assess accuracy of models because BP's lat., long., and altitude are fixed and known. From Fig. 6 SRTM30m

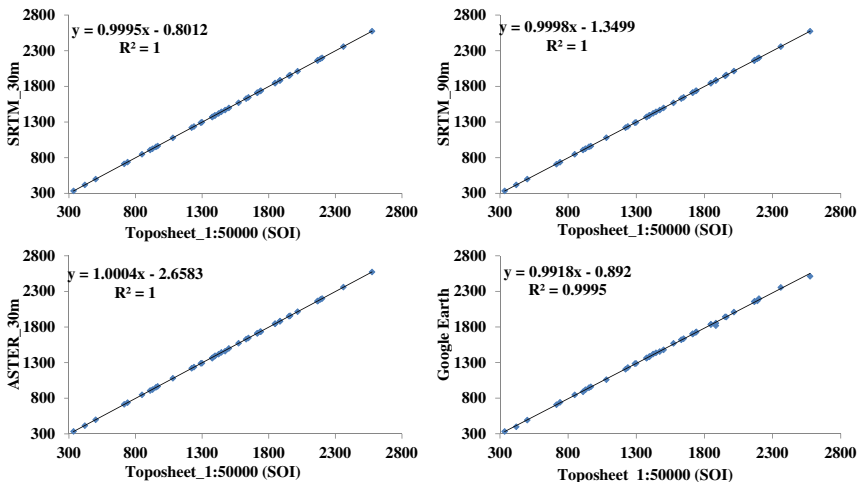


Fig. 6 BPs class wise data sets

Table 7 Statistical tests result for Settlement class data set

Model	Statistical tests													K
	1T	2T	3T	4T	5T	6T	7T	8T	9T	10T	11T	12T	13T	
SRTM_30	3.79	3.75	0.00	0.41	0.00	1.00	0.00	2.37	-2.37	0.22	1.00	1.00	-10.85	0.0009
SRTM_90	3.50	3.46	0.00	0.38	0.00	1.00	0.00	2.45	-2.45	0.20	1.00	1.00	-10.39	0.0008
ASTER_30	4.58	4.54	0.00	0.50	0.00	1.00	0.00	2.61	-2.61	0.20	1.00	1.00	-10.04	0.0009
Google Ele	16.24	16.08	0.01	1.77	0.01	1.00	0.01	11.88	-11.8	0.91	1.00	0.99	-45.60	0.0035

Table 8 Ranking and performance evaluation of each model for Settlement class data set

		Assigning of weightage to each statistical tests													Rank	DEMs model
		1W	2W	3W	4W	5W	6W	7W	8W	9W	10W	11W	12W	13W		
0.000	0.000	0.255	0.002	0.404	0.001	0.331	0.000	0.000	0.000	0.004	0.001	0.001	0.000	0.0114	2	SRTM_30
0.000	0.000	0.265	0.002	0.395	0.001	0.331	0.000	0.000	0.000	0.004	0.001	0.001	0.000	0.0105	1	SRTM_90
0.000	0.000	0.260	0.002	0.452	0.001	0.279	0.000	0.000	0.000	0.005	0.001	0.001	0.000	0.0116	3	ASTER_30
0.000	0.000	0.281	0.002	0.390	0.004	0.312	0.000	0.000	0.000	0.004	0.004	0.004	0.000	0.0461	4	GE

and SRTM90m are showing a perfect alignment with toposheet based altitude information of fixed BPs. ASTER30m also showing a good match with known altitude information because these BPs are not close to each other therefore easily altitude information can be read by space-based sensor like SRTM and ASTER.

From Table 9, all statistical test is showing a good value for SRTM30m, like least RMSE ss 2.13, respectively. Therefore, in Table 10 SRTM30m has first rank.

Figure 7, showing a co-relationship between known altitude information of fixed small size constructed structure named as Temples and models (SRTM30m, SRTM90m, ASTER30m and GE-based altitude information) based altitude of these permanent structure. Figure 7 show SRTM30m model giving perfect alignment with known altitude information from SOI toposheet (No: $53\frac{J}{7}$ and $53\frac{J}{8}$). From Tables 11 and 12, ASTER30m model is best out of other three (SRTM30m, SRTM90m, and GE) because rating/ranking processes are based on combination of 13 statistical test results and Fig. 7 is based on only single statistical test of correlation. Therefore, ASTER30m has rank one (or 1st) while SRTM30m has greatest value of $R^2 (=1.0)$. Both Tables 11 and 12 are inter-connected where Table 11 showing 13 statistical tests result cross-ponding to each model. Where Table 12 represent weightage with each model rank/rating.

From Fig. 8, 2D scatterplot of altitude of different tree species of the temperate forests including Himalayan cedar (Deodar cedar), Himalayan (blue) pine, oak, silver fir, spruce, chestnut, elm, poplar, birch, yew, cypress, and rhododendron tree (not part of forest) over the AOI. Tree height of different tree species can be measured using SAR technology because in SAR technology microwave signal penetrate the tree crown and give the correct information of tree altitude with high resolution of sensing like SRTM30m. In few cases thermal sensor it also give correct altitude information because thermal sensor mapping temperature differences. In case of ground/land,

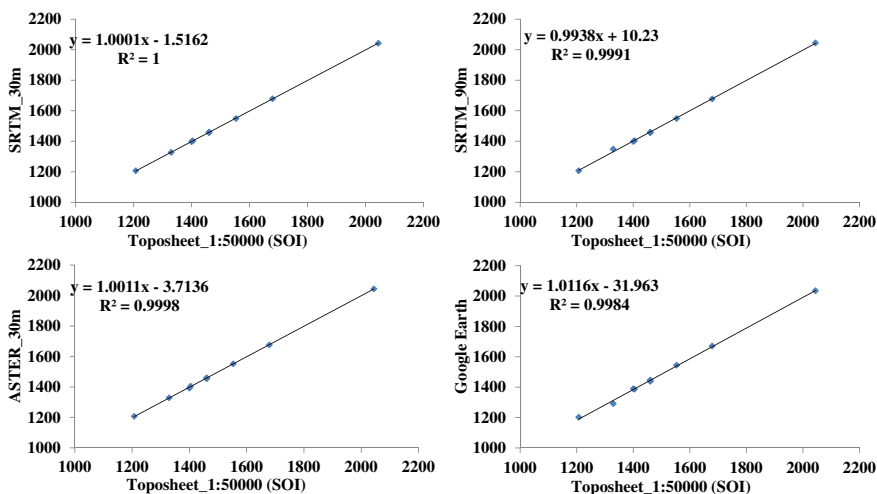


Fig. 7 Temples class wise data sets

Table 9 Statistical tests result for BPs class data set

Model	Statistical tests													K
	1T	2T	3T	4T	5T	6T	7T	8T	9T	10T	11T	12T	13T	
SRTM_30	2.13	2.10	0.00	0.28	0.00	1.00	0.00	1.58	-1.58	0.11	1.00	1.00	-4.63	0.0004
SRTM_90	2.46	2.44	0.00	0.33	0.00	1.00	0.00	1.70	-1.70	0.13	1.00	1.00	-5.40	0.0005
ASTER_30	3.71	3.66	0.00	0.50	0.00	1.00	0.00	2.07	-2.07	0.17	1.00	1.00	-7.20	0.0007
Google Ele	18.57	18.36	0.01	2.48	0.01	1.00	0.01	13.05	-13.0	0.97	1.00	0.99	-40.65	0.0038

Table 10 Ranking and performance evaluation of each model for BP class data set

		Assigning of weightage to each statistical test													Ranking	Rank	DEMs model
		1W	2W	3W	4W	5W	6W	7W	8W	9W	10W	11W	12W	13W			
0.000	0.000	0.293	0.002	0.398	0.000	0.302	0.000	0.000	0.000	0.004	0.000	0.000	0.000	0.000	0.006	1	SRTM_30
0.000	0.000	0.256	0.002	0.417	0.001	0.319	0.000	0.000	0.000	0.004	0.001	0.001	0.001	0.000	0.007	2	SRTM_90
0.000	0.000	0.245	0.002	0.445	0.001	0.302	0.000	0.000	0.000	0.004	0.001	0.001	0.001	0.000	0.010	3	ASTER_30
0.000	0.000	0.282	0.002	0.394	0.004	0.308	0.000	0.000	0.000	0.004	0.004	0.004	0.004	0.000	0.050	4	GE

Table 11 Statistical tests result for Temples class data set

Model	Statistical tests											K		
	1T	2T	3T	4T	5T	6T	7T	8T	9T	10T	11T		12T	13T
SRTM_30	1.61	1.57	0.00	0.14	0.00	1.00	0.00	1.00	-1.00	0.08	1.00	1.00	-1.58	0.0003
SRTM_90	1.92	1.88	0.00	0.17	0.00	1.00	0.00	1.09	-1.09	0.09	1.00	1.00	-1.37	0.0003
ASTER_30	1.88	1.84	0.00	0.17	0.00	1.00	0.00	0.96	-0.96	0.06	1.00	1.00	-1.17	0.0003
Google Ele	30.01	29.35	0.02	2.64	0.01	1.00	0.02	18.30	-18.3	1.35	1.00	0.99	-29.80	0.0057

Table 12 Ranking and performance evaluation of each model for Temples class data set

Assigning of weightage to each statistical tests													Rank	DEMs model	
1W	2W	3W	4W	5W	6W	7W	8W	9W	10W	11W	12W	13W			
0.000	0.000	0.271	0.002	0.397	0.000	0.325	0.000	0.000	0.004	0.000	0.000	0.000	0.004	2	SRTM_30
0.000	0.000	0.288	0.002	0.398	0.000	0.307	0.000	0.000	0.004	0.000	0.000	0.000	0.005	3	SRTM_90
0.000	0.000	0.266	0.002	0.464	0.000	0.262	0.000	0.000	0.005	0.000	0.000	0.000	0.003	1	ASTER_30
0.000	0.000	0.234	0.002	0.421	0.006	0.321	0.000	0.000	0.004	0.006	0.006	0.000	0.074	4	GE

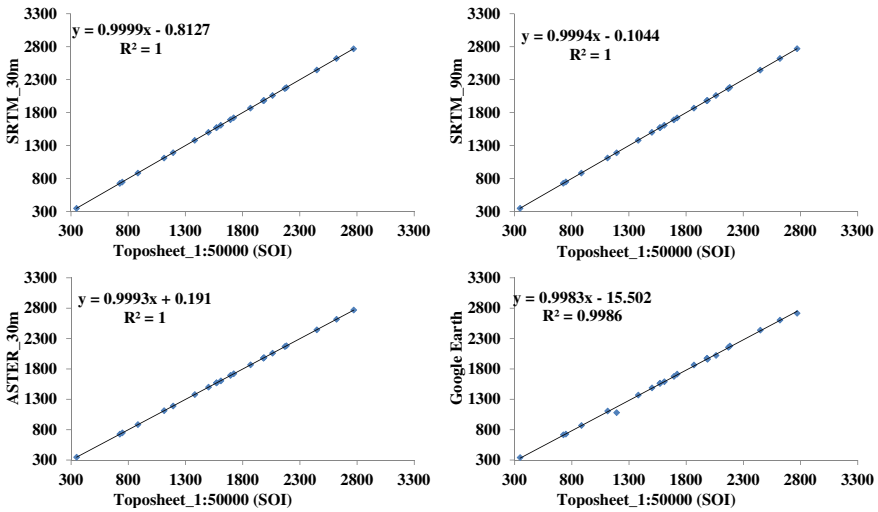


Fig. 8 Trees class wise data sets

tree and atmosphere temperature never same, based on this concept or idea thermal sensor (like ASTERT30m) may give the correct information about tree height or altitude.

From Tables 13 and 14, it is clear that SRTM30m and ASTER30m having good statistical tests values hence SRTM30m and ASTER30m score 1 and 2 rank, respectively.

4 Conclusion

Results show GE model have constant rank (in term of accuracy) of fourth (4th) for all classes with respect to SOI toposheet (No: $53\frac{1}{7}$ and $53\frac{1}{8}$). Other models are showing fluctuating ranking for all classes except Forest and Tower. Based on statistical accuracy analysis SRTM30m, SRTM90m, ASTER30m and GE models having ranking of first, second, third and fourth respectively with respect to toposheet altitude information for Forest and Tower. For Settlement classes SRTM30m showing a fourth ranking due to high corner effect. Ranking process revealed that ASTER30m model has first rating among all four models for Temples class. It show that altitude of tree or forest can be estimated using SRTM30m model while same model show high corner effect for settlement class. In case of Temples class thermal based DEM models give good altitude information.

Table 13 Statistical tests result for palms and other trees class data set

Model	Statistical tests													K
	1T	2T	3T	4T	5T	6T	7T	8T	9T	10T	11T	12T	13T	
SRTM_30	1.94	1.84	0.00	0.12	0.00	1.00	0.00	1.4	-1.4	0.09	1.00	1.00	-0.95	0.0004
SRTM_90	6.92	6.57	0.00	0.42	0.00	1.00	0.00	0.9	0.9	0.23	1.00	1.00	0.75	0.0011
ASTER_30	3.73	3.54	0.00	0.23	0.00	1.00	0.00	2.1	-2.1	0.16	1.00	1.00	-1.43	0.0007
Google Ele	18.11	17.18	0.01	1.11	0.01	1.00	0.01	14.6	-14.6	1.03	1.00	0.99	-10.10	0.0037

Table 14 Ranking and performance evaluation of each model for palms and other Trees class data set

		Assigning of weightage to each statistical test													Rank	DEMs model	
		1W	2W	3W	4W	5W	6W	7W	8W	9W	10W	11W	12W	13W			
0.000	0.000	0.298	0.003	0.392	0.000	0.302	0.000	0.000	0.000	0.004	0.000	0.000	0.000	0.000	0.005	1	SRTM_30
0.000	0.000	0.236	0.003	0.488	0.001	0.260	0.001	0.001	0.001	0.005	0.001	0.001	0.001	0.002	0.015	3	SRTM_90
0.000	0.000	0.275	0.003	0.429	0.001	0.287	0.000	0.000	0.000	0.004	0.001	0.001	0.001	0.000	0.009	2	ASTER_30
0.000	0.000	0.296	0.003	0.362	0.004	0.324	0.000	0.000	0.000	0.004	0.004	0.004	0.004	0.000	0.048	4	GE

Acknowledgements We express our sincere thanks to reviewers in this work.

References

1. N. Kumar, S.K. Singh, P.K. Srivastava, B. Narsimlu, SWAT Model calibration and uncertainty analysis for streamflow prediction of the Tons River Basin, India, using Sequential Uncertainty Fitting (SUFI-2) algorithm. *Model. Earth Syst. Environ.* **3**(1), 30–34 (2017)
2. S. Singh, C. Singh, S. Mukherjee, Impact of land-use and land-cover change on groundwater quality in the Lower Shiwalik hills: a remote sensing and GIS based approach. *Open Geosci.* **2**(2), 124–131 (2010)
3. S.K. Yadav, A. Dubey, S. Szilard, S.K. Singh, Prioritisation of sub-watersheds based on earth observation data of agricultural dominated northern river basin of India. *Geocarto Int.* **33**(4), 339–356 (2018)
4. C.B. Pande, K.N. Moharir, S.K. Singh, B. Dzwairo, Groundwater evaluation for drinking purposes using statistical index: study of Akola and Buldhana districts of Maharashtra, India. *Environ. Dev. Sustain.*, 1–19 (2019)
5. P. Murmu, M. Kumar, D. Lal, I. Sonker, S.K. Singh, Delineation of groundwater potential zones using geospatial techniques and analytical hierarchy process in Dumka district, Jharkhand, India. *Groundw. Sustain. Dev.* **9**, 100239 (2019)
6. S.K. Yadav, S.K. Singh, M. Gupta, P.K. Srivastava, Morphometric analysis of Upper Tons basin from Northern Foreland of Peninsular India using CARTOSAT satellite and GIS. *Geocarto Int.* **29**(8), 895–914 (2014)
7. K.S. Rawat, A.K. Mishra, Evaluation of Relief aspects Morphometric Parameters derived from different sources of DEMs and its effects over time of concentration of runoff (T_C). *Earth Sci. Inf.* **9**, 409–424 (2016)
8. N. Kumar, S.K. Singh, H.K. Pandey, Drainage morphometric analysis using open access earth observation datasets in a drought-affected part of Bundelkhand, India. *Appl. Geomat.* **10**(3), 173–189 (2018)
9. P.P. Choudhari, G.K. Nigam, S.K. Singh, S. Thakur, Morphometric based prioritization of watershed for groundwater potential of Mula river basin, Maharashtra, India. *Geol. Ecol. Landsc.* **2**(4), 256–267 (2018)
10. S.K. Yadav, A. Dubey, S.K. Singh, D. Yadav, Spatial regionalisation of morphometric characteristics of mini watershed of Northern Foreland of Peninsular India. *Arab. J. Geosci.* **13**, 435 (2020)
11. E. Maliqi, S.K. Singh, Quantitative estimation of soil erosion using open-access earth observation data sets and erosion potential model. *Water Conserv. Sci. Eng.* **4**(4), 187–200 (2019)
12. V. Singh, S.K. Singh, Hypsometric analysis using microwave satellite data and GIS of Naini-Gorma river basin (Rewa district, Madhya Pradesh, India). *Water Conserv. Sci. Eng.* **3**(4), 221–234 (2018)
13. S.K. Singh, S. Mustak, P.K. Srivastava, S. Szabó, T. Islam, Predicting spatial and decadal LULC changes through cellular automata Markov chain models using earth observation datasets and geo-information. *Environ. Process.* **2**(1), 61–78 (2015)
14. S.K. Singh, P.B. Laari, S.K. Mustak, P.K. Srivastava, S. Szabó, Modelling of land use land cover change using earth observation data-sets of Tons River Basin, Madhya Pradesh, India. *Geocarto Int.* **33**(11), 1202–1222 (2018)
15. Z. Li, C. Zhu, C. Gold, *Digital terrain modeling: principles and methodology* (CRC press, Boca Raton, FL, 2004)
16. K.S. Rawat, A.K. Mishra, V.K. Sehgal, N. Ahmed, V.K. Tripathi, Comparative evaluation of horizontal accuracy of elevations of selected ground control points from ASTER and SRTM

- DEM with respect to CARTOSAT-1 DEM: a case study of Shahjahanpur district, Uttar Pradesh, India. *Geocarto Int.* **28**(5), 439–452 (2013)
17. G. Szabó, S.K. Singh, S. Szabó, Slope angle and aspect as influencing factors on the accuracy of the SRTM and the ASTER GDEM databases. *Phys. Chem. Earth, Parts A/B/C* **83**, 137–145 (2015)
 18. Q. Xing, Z. Li, J. Zhou, P. Zhang, Comparison of ASTER GDEM and SRTM DEM in deriving the thickness change of Small Dongkemadi Glacier on Qinghai-Tibetan Plateau, in *2011 IEEE International Geoscience and Remote Sensing Symposium* (IEEE, 2011 July), pp. 3171–3174
 19. H. Li, J. Zhao, Evaluation of the newly released worldwide AW3D30 DEM over typical land-forms of China using two global DEMs and ICESat/GLAS data. *IEEE J. Sel. Topics Appl. Earth Observ. Remote Sen.* **11**(11), 4430–4440 (2018)
 20. E. Suwandana, K. Kawamura, Y. Sakuno, E. Kustiyanto, B. Raharjo, Evaluation of ASTER GDEM2 in comparison with GDEM1, SRTM DEM and topographic-map-derived DEM using inundation area analysis and RTK-dGPS data. *Remote Sens.* **4**(8), 2419–2431 (2012)
 21. K.S. Rawat, S.K. Singh, M.I. Singh, B.L. Garg, Comparative evaluation of vertical accuracy of elevated points with ground control points from ASTERDEM and SRTMDEM with respect to CARTOSAT-1DEM. *Remote Sens. Appl. Soc. Environ.* **13**, 289–297 (2019)
 22. Central Ground Water Board, Ground Water Brochure, District Tehri Garhwal, Uttarakhand (2011). http://cgwb.gov.in/District_Profile/Uttarakhand/Tehri%20Garhwal.pdf
 23. K.S. Rawat, A. Bala, S.K. Singh, R.K. Pal, Quantification of wheat crop evapotranspiration and mapping: a case study from Bhiwani District of Haryana, India. *Agric. Water Manag.* **187**, 200–209 (2017)
 24. K.S. Rawat, A.K. Mishra, N. Ahmad, Surface runoff estimation over heterogeneous foot hill of aravalli mountain using medium resolution remote sensing rainfall data with SCS-CN method: A case of semi-arid ungauged manesar nala watershed. *Water Environ. J.* **31**(2), 262–276 (2017)
 25. K.S. Rawat, A.K. Mishra, S.K. Singh, Mapping of groundwater quality using normalized difference dispersal index of dwarka sub-city at Delhi National Capital of India. *ISH J. Hydraul. Eng.* **23**(3), 229–240 (2017)
 26. K.S. Rawat, V.K. Sehgal, S.S. Ray, Retrieval and validation of soil moisture from FRS-1 data set of Radar Imaging Satellite (RISAT-1). *Arab. J. Geosci.* **10**, 445–454 (2017)
 27. K.S., Sehgal, V.K.: Ray S.S: Semi-empirical model for retrieval of Soil Moisture using RISAT-1 C-band data over a Sub-Tropical Semi Arid Area of Rewari District State of Haryana (India). *Journal of Earth System Science.* 127:18 (2018).
 28. K.S. Rawat, S. Pradhan, V.K. Tripathi, J. Lordwin, S.K. Singh, Statistical approach to evaluate groundwater contamination for drinking and irrigation suitability. *Groundw. Sustain. Dev.* **9**, 1–12 (2019)
 29. K.S. Rawat, S.K. Singh, R.L. Ray, An integrated approach to estimate surface soil moisture in agricultural lands. *Geocarto Int.* (2019). <https://doi.org/10.1080/10106049.2019.1678674>
 30. K.S. Rawat, V.K. Sehgal, S.S. Ray, Downscaling of MODIS thermal imagery. *Egypt. J. Remote Sens. Space Sci.* **22**, 49–58 (2019)
 31. K.S. Rawat, S.K. Singh, A. Bala, Estimation of crop evapotranspiration through spatial distributed crop coefficient in a semi-arid environment. *Agric. Water Manag.* **213**(1), 922–933 (2019)
 32. K.S. Rawat, S.K. Singh, R.L. Ray, S. Szabó, K. Sanjeev, Parameterizing the modified water cloud model to improve soil moisture data retrieval using vegetation models. *Hungarian Geograph. Bull.* **69**(1), 17–26 (2020)
 33. K.S. Rawat, K.S. Sudhir, R.L. Ray, S. Szilard, Parameterization of modified water cloud model (MWCMM) using normalized difference vegetation index (NDVI) for winter wheat crop: a case study. *Geocarto Int.* (2020). <https://doi.org/10.1080/10106049.2020.1783579>
 34. K.S. Rawat, L. Jeyakumar, S.K. Singh, V.K. Tripathi, Appraisal of groundwater with special reference to nitrate using statistical index approach. *Groundw. Sustain. Dev.* **8**, 49–58 (2019)
 35. K.S. Rawat, S.K. Singh, R.K. Pal, Synergetic methodology for estimation of soil moisture over agricultural area Using Landsat-8 and Sentinel-1 satellite data. *Remote Sens. Appl. Soc. Environ.* **15**(2019) 100250 (2019). <https://doi.org/10.1016/j.rsase.2019.100250>

Crop-Type Classification Using Sentinel-2A and in Situ Data: Case Study of Shri Dungargarh Taluk of Rajasthan, India



Pritam K. Meshram, Kishan Singh Rawat, Sanjeev Kumar,
and Sudhir Kumar Singh

1 Introduction

In the present scenario of climate change and rapid population growth increasing food demand requires regular food supply which can be obtained by proper management of agricultural activities and improved crop productivity. Improved and optimized management practices can also increase food production of existing croplands [1]. Since remote sensing data cover large areas in various spatial and temporal scales, it is used to identify crop types generally. From early 1980s, use of temporal and spectral characteristics to distinguish various crop types [2].

Previously, various crop types were identified with the highest difference between time periods and crop types [3]. For crop type mapping, hierarchical classification approaches have been used effectively [4–6] to integrate with the expert knowledge for establishing classification rules. Waldhoff et al. [7] has classified crop types in Germany with supervised classification and support vector machines, they applied a knowledge-based approach. The classification has been examined in studies of crop types in the early season [8, 9].

Food and Agriculture Organization (FAO) in a few provinces of Afghanistan in the year 2016, carried out mapping of rice from Sentinel data [10]. Similarly, annual assessment of opium poppy sown areas was conducted by the United Nations Office of Drugs and Crime (UNODC) using high-resolution satellite images [11]. Earlier, United States Department of Agriculture (USDA) also conducted the mapping of wheat sown area with NDVI for some qualitative assessments in the past [12].

P. K. Meshram · K. S. Rawat (✉) · S. Kumar
Geo-Informatics, Civil Engineering Department, Graphic Era (Deemed to be University),
Dehradun, Uttarakhand, India

S. K. Singh
K. Banerjee Centre of Atmospheric Ocean Studies, IIDS, Nehru Science Centre, University of
Allahabad, Prayagraj, Uttar Pradesh, India

Remote sensing helps in crop monitoring and is extensively used in past several decades. It provides data at a regular interval which helps to timely assess the development and growth of agricultural crops [13]. The main objective was crop-type classification in Rabi season using Sentinel-2A and in situ data of Shri Dungargarh taluk of Rajasthan (see Fig. 1).

2 Material and Method

2.1 Study Area

The Sri Dungargarh is a taluk, located in Bikaner district of Rajasthan state, India. The taluk is under Trans Gangetic Plain Region (VI) and surrounded by naturally occurring sandy soil on all sides. The total geographical area of Sri Dungargarh is 299035.28 ha out of which agriculture area is 31.71%, non-agriculture area (68.28%) and waterbodies (0.01%). The area receives maximum rainfall during south-west monsoon season (June–September). The normal rainfall is 228.70–240.0 mm. The annual temperature ranges from 31 to 41 °C and soil is deep yellowish-brown sandy soils.

2.2 Sentinel-2A Data

Sentinel-2A satellite data was used for this study and it was downloaded freely from Copernicus Open Access Hub (<https://scihub.copernicus.eu/dhus/#/home>). Sentinel-2A imagery of 17 February 2020 was selected for classification of crop type. It has spatial and temporal resolution of 10 m and 10 days respectively at no cost. For crop area classification, B3 (Green), B4 (Red) and B8 (NIR) band were selected and used for the present work. Due to quick change in crop appearance with the course of the phenological cycle, a highly dense observation in key phenological stages may be helpful in the separation of crop types. The brief information about the data used is given in Table 1.

2.3 Field Data Information and Reference Data

Field data was collected with the aid of Global Positioning System (GPS) for all the crops which are grown in rabi season (as [14–16]). The information of crop such as date of sowing, crop variety, growth stage, crop covered, crop condition and expected date of harvesting which help in specific crop type classification. Agriculture crop mask was prepared to classify the crop type which help to reduce the misclassification

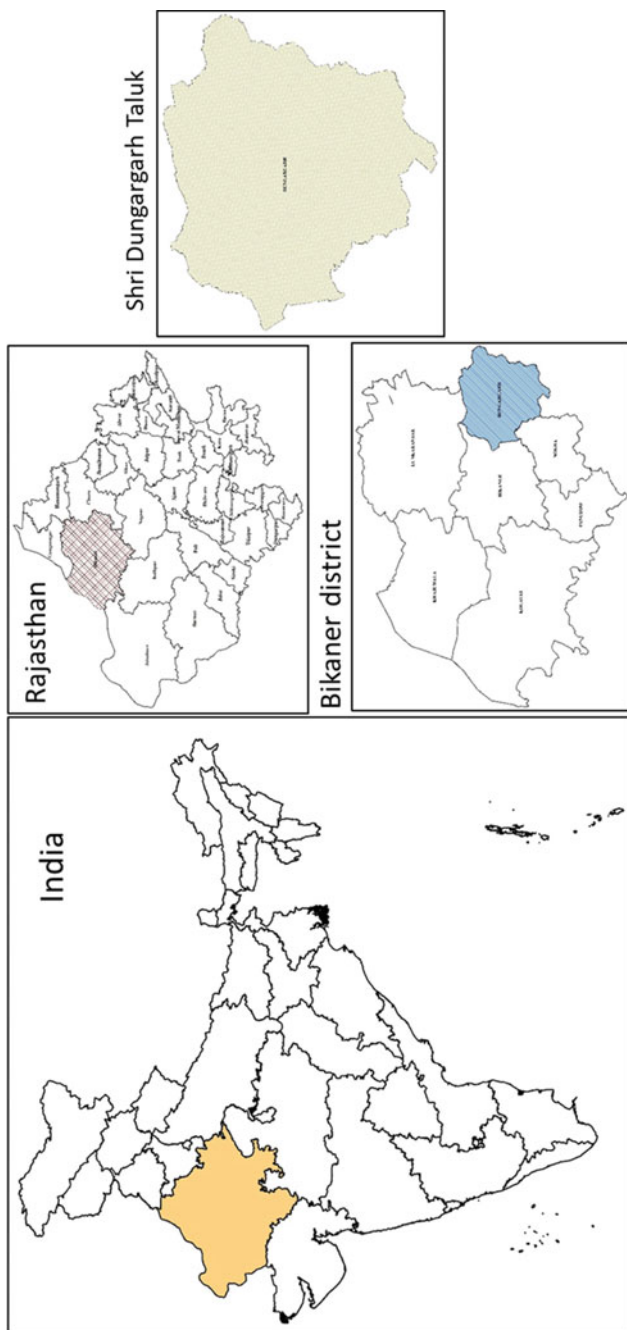


Fig. 1 Study area location map of Sri Dungargarh is a taluk, located in Bikaner district of Rajasthan

Table 1 Description of satellite image used for the study

Sr. no.	Scene	Satellite	Spatial resolution	Swath	Date of acquisition and time	Radiometric/geometric quality
1	T43RCL	Sentinel-2A (MSI)	10 m	290 km	2020-02-17 and T05:39:11	Passed
	T43RCM				2020-02-17 and T05:39:11	Passed
	T43RDL				2020-02-17 and T05:39:11	Passed
	T43RDM				2020-02-17 and T05:39:11	Passed

in non-agriculture area. The SRTM-30 m DEM was downloaded from the following portal (<https://earthexplorer.usgs.gov/>) and slope map was prepared for generating the information about elevation and steepness.

2.4 Method

In remote sensing the supervised and unsupervised classification method was used to classify the satellite data [15–18]. In hilly and remote areas, visual classification is popular [15, 16, 19]. The maximum likelihood classification (ML) approach is most popular and widely used quantitative analysis method in the field of remote sensing [20, 21]. The ML is defined as the classification of pixels to a specific class based on probability, with an assumption that all classes have equal probability while the input band has normal distribution. The representation of ground cover is done by labelling the pixel in an image through appropriate algorithm. By applying a classification algorithm, the training sample set was identified, and classification of the image was carried out. It is done by calculating covariance matrix of the cluster and statistical distance which is based on the mean value. The class cluster gets the pixel with respect to highest probability (see Figs. 2 and 3).

3 Results and Discussions

The maximum likelihood classification method was used to classify the crop and accuracy assessment [22–28] was performed to evaluate the classified map with the ground truth data.

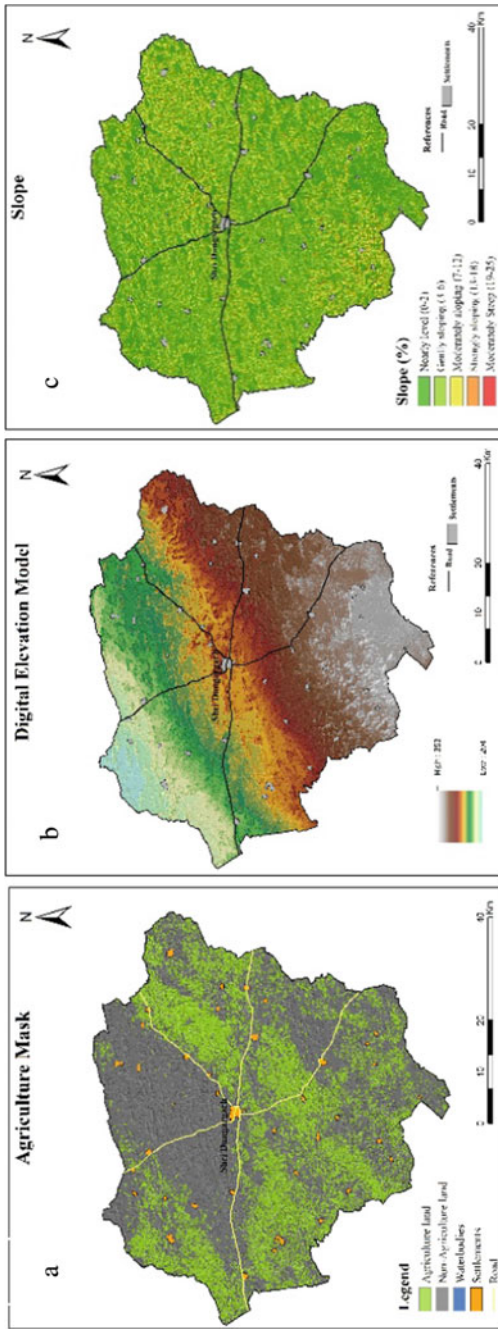


Fig. 2 Map of (a) Agriculture mask, (b) Digital elevation model generated from 30 m SRTM DEM, and (c) Slope (%) of the study area

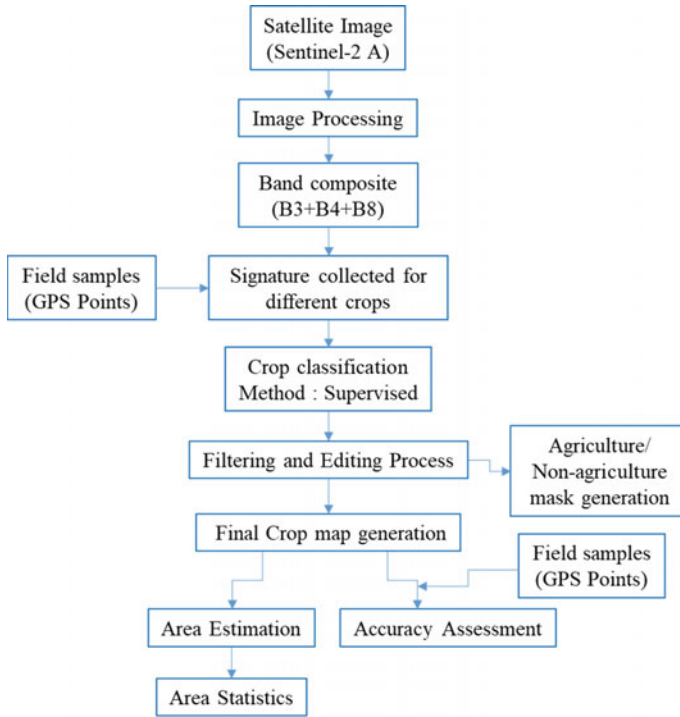


Fig. 3 Flow chart of methodology

3.1 Accuracy Assessment

Accuracy assessment decides the accurateness of classification. A selected sample of test pixels on a classified image with their class identity was compared with the ground truth data. According to Rawat and Singh [29], by determining appropriate size of sample with a sampling scheme is beneficial in the assessment of classification accuracy. The error matrix is presented in Table 2. There were total 40 points were selected which shows the higher user’s accuracy of wheat crop (92.31%), gram (86.67%), mustard (83.33%) and other crop (83.33%). The assessment of its accuracy

Table 2 Error matrix of crop classification

Classified data	Gram	Mustard	Wheat	Other crop	Row total
Gram	13	0	1	1	15
Mustard	0	5	0	1	6
Wheat	1	0	12	0	13
Other crop	0	1	0	5	6
Column total	14	6	13	7	40

level is 87.50% while its calculated KAPPA statistics is 0.825, shows good results and good agreement between classified image and reference respectively. In the Shri Dungargarh taluk, the crop status has been evaluated with the help of digital analysis from satellite data indicating that most of area belongs to wheat and gram crop (nearly 11.63%, 9.00%, respectively, of total agriculture area).

3.2 Crop Classification

Different types of crops namely gram, mustard, wheat and other crops were classified and results are presented in Fig. 4. Wheat crop has the maximum area (36.67%), gram crop (28.39%), other crops (19.69%) and mustard (15.25%). In Sri Dungargarh wheat and gram is dominant crop during Rabi season and covers 34,774.46 ha, 26,926.96 ha, respectively followed by other crops (18,675.99 ha) and mustard (14,460.41 ha) in the study area (see Table 3).

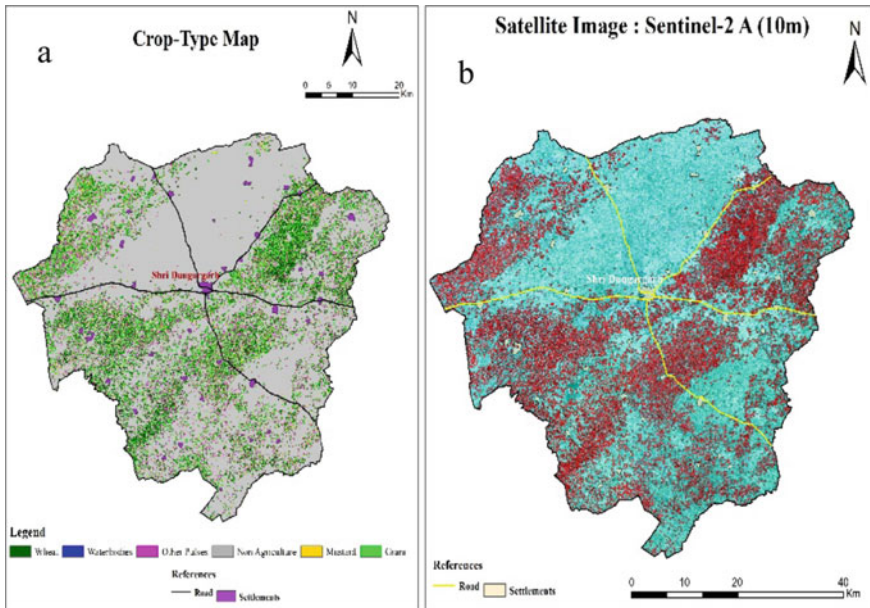


Fig. 4 Map of (a) Crop type map, and (b) Sentinel-2A (17 February 2020) of study area

Table 3 Cropped feature and their respective area over the study area

Sr. no.	Crop	Area in 'ha
1	Gram	26,926.96
2	Wheat	34,774.46
3	Mustard	14,460.41
4	Other crop	18,675.99

4 Conclusion

The present study shows the applicability of Sentinel-2A in crop level classification. Separation of different types of crop is done using maximum likelihood classifier. The overall classification accuracy was achieved more than 87%. The classified data of crop can be used in different domains like yield estimation, water resource management, field resource management, efficient policy planning, economic development, change detection in cropping pattern, etc. The continued up-to-date mapping of crops and its data generation is necessary to assess the various aspects related to agriculture.

References

1. J.A. Foley, R. DeFries, G.P. Asner, C. Barford, G. Bonan, S.R. Carpenter, J.H. Helkowski, Global consequences of land use. *Science* **309**(5734), 570–574 (2005)
2. J.B. Odenweller, K.I. Johnson, Crop identification using Landsat temporal-spectral profiles. *Remote Sens. Environ.* **14**(1–3), 39–54 (1984)
3. D. Bargiel, A new method for crop classification combining time series of radar images and crop phenology information. *Remote Sens. Environ.* **198**, 369–383 (2017)
4. P. Villa, D. Stroppiana, G. Fontanelli, R. Azar, P.A. Brivio, In-season mapping of crop type with optical and X-band SAR data: a classification tree approach using synoptic seasonal features. *Remote Sens.* **7**(10), 12859–12886 (2015)
5. G. Fontanelli, A. Crema, R. Azar, D. Stroppiana, P. Villa, M. Boschetti, Agricultural crop mapping using optical and SAR multi-temporal seasonal data: a case study in Lombardy region, Italy, in *2014 IEEE Geoscience and Remote Sensing Symposium* (IEEE, July 2014), pp. 1489–1492
6. A. Bala, K.S. Rawat, A.K. Mishra, Assessment and Validation of Evapotranspiration using SEBAL algorithm and Lysimeter data of IARI Agricultural Farm, India. *Geocarto Int.* **28**(5), 439–452 (2016)
7. G. Waldhoff, U. Lussem, G. Bareth, Multi-data approach for remote sensing-based regional crop rotation mapping: a case study for the Rur catchment, Germany. *Int. J. Appl. Earth Obs. Geoinf.* **61**, 55–69 (2017)
8. J. Inglada, A. Vincent, M. Arias, C. Marais-Sicre, Improved early crop type identification by joint use of high temporal resolution SAR and optical image time series. *Remote Sens.* **8**(5), 362 (2016)
9. C. Conrad, M. Rahmann, M. Machwitz, G. Stulina, H. Paeth, S. Dech, Satellite based calculation of spatially distributed crop water requirements for cotton and wheat cultivation in Fergana Valley, Uzbekistan. *Global Planet. Change* **110**, 88–98 (2013). <https://doi.org/10.1007/s411018-0042-x>

10. B.T. Haworth, E. Biggs, J. Duncan, N. Wales, B. Boruff, E. Bruce, Geographic information and communication technologies for supporting smallholder agriculture and climate resilience. *Climate* **6**(4), 97 (2018)
11. A. Avetisyan, Afghanistan Opium Survey 2017 Cultivation and Production. United Nation Office of Drugs and Crime. https://www.unodc.org/documents/crop-monitoring/Afghanistan/Afghan_opium_survey_2017_cult_prod_web.pdf (2017)
12. M.S. Pervez, M. Budde, J. Rowland, Mapping irrigated areas in Afghanistan over the past decade using MODIS NDVI. *Remote Sens. Environ.* **149**, 155–165 (2014)
13. P.C. Doraiswamy, P.W. Cook, Spring wheat yield assessment using NOAA AVHRR data. *Can. J. Remote Sens.* **21**(1), 43–51 (1995)
14. K.S. Rawat, V.K. Sehgal, S.S. Ray, Retrieval and validation of soil moisture from FRS-1 data set of Radar Imaging Satellite (RISAT-1). *Arab. J. Geosci.* **10**, 445–454 (2017)
15. K.S. Rawat, A.K. Mishra, R. Bhattacharyya, Soil erosion risk assessment and spatial mapping using LANDSAT7 ETM+, RUSLE and GIS-A case study. *Arab. J. Geosci.* **9**, 288 (2016)
16. K.S. Rawat, A.K. Mishra, V.K. Sehgal, V.K. Tripathi, Comparative evaluation of horizontal accuracy of elevations of selected ground control points from ASTER and SRTM DEM with respect to CARTOSAT-1 DEM: a case study of district Shahjahanpur (Uttar Pradesh), India. *Geocarto Int.* **28**(5), 439–452 (2013)
17. S. Singh, C. Singh, S. Mukherjee, Impact of land-use and land-cover change on groundwater quality in the Lower Shiwalik hills: a remote sensing and GIS based approach. *Open Geosci.* **2**(2), 124–131 (2010)
18. S.K. Singh, P.B. Laari, S.K. Mustak, P.K. Srivastava, S. Szabó, Modelling of land use land cover change using earth observation data-sets of Tons River Basin, Madhya Pradesh, India. *Geocarto Int* **33**(11), 1202–1222 (2018)
19. M. Kumar, D.M. Denis, S.K. Singh, S. Szabó, S. Suryavanshi, Landscape metrics for assessment of land cover change and fragmentation of a heterogeneous watershed. *Remote Sens. Appl. Soc. Environ.* **10**, 224–233 (2018)
20. T. Shimrah, K. Sarma, O.G. Varga, S. Szilard, S.K. Singh, Quantitative assessment of landscape transformation using earth observation datasets in Shirui Hill of Manipur, India. *Remote Sens. Appl. Soc. Environ.* **15**, 100237 (2019)
21. S.K. Singh, P.K. Srivastava, S. Szabó, G.P. Petropoulos, M. Gupta, T. Islam, Landscape transform and spatial metrics for mapping spatiotemporal land cover dynamics using Earth Observation data-sets. *Geocarto Int.* **32**(2), 113–127 (2017)
22. K.S. Rawat, A.K. Mishra, V.K. Tripathi, Sediment yield index mapping and prioritization of media sub-watershed, sagar district of M.P. (India). *Arab. J. Geosci.* **7**(8), 3131–3145 (2013)
23. K.S. Rawat, S. Pradhan, V.K. Tripathi, J. Lordwin, S.K. Singh, Statistical approach to evaluate groundwater contamination for drinking and irrigation suitability. *Groundw. Sustain. Dev.* **9**, 1–12 (2019)
24. K.S. Rawat, V.K. Sehgal, S.S. Ray, Downscaling of MODIS thermal imagery. *The Egypt. J. Remote Sens. Space Sci.* **22**, 49–58 (2019). <https://doi.org/10.1016/j.ejrs.2018.01.001>
25. K.S. Rawat, S.K. Singh, A. Bala, Estimation of crop evapotranspiration through spatial distributed crop coefficient in a semi-arid environment. *Agric. Water Manag.* **213**(1), 922–933 (2019)
26. K.S. Rawat, S.K. Singh, R.K. Pal, Synergetic methodology for estimation of soil moisture over agricultural area Using Landsat-8 and Sentinel-1 satellite data. *Remote Sens. Appl. Soc. Environ.* **15**(2019), 100250 (2019)
27. K.S. Rawat, S.K. Singh, R.L. Ray, An integrated approach to estimate surface soil moisture in agricultural lands. *Geocarto Int.* (2019). <https://doi.org/10.1080/10106049.2019.1678674>
28. K.S. Rawat, S.V. Mishra, S.K. Singh, Integration of earth observation data and spatial approach to delineate and manage aeolian sand-affected wasteland in highly productive lands of Haryana, India. *Int. J. Geophys.* (2018)

29. K.S. Rawat, S.K. Singh, Appraisal of soil conservation capacity using NDVI model based C-factor of RUSLE model for a semiarid ungauged watershed: a case study. *Water Conserv. Sci. Eng.* **3**, 47–58 (2018)
30. M.K. Arora, K. Agarwal, A program for sampling design for image classification accuracy assessment. *Photogramm. J. Finl.* **18**(1), 33–43 (2002)

Evaluation of Total Dissolved Solids and Quality Zones of Groundwater Using Vertical Electrical Soundings and GIS Method



Kishan Singh Rawat, Sanjeev Kumar, and Sudhir Kumar Singh

1 Introduction

Groundwater is a major source of fresh water which is generally used for domestic, agricultural and industrial purpose in many countries of the world. Total dissolved solids (TDS) are important to measure because it is combined content of all organic and inorganic substances present in groundwater as molecular/ionized/micro granular (10–6 m, size particles solution) forms. Generally, major sources of TDS in groundwater are geochemical (groundwater and underground rock chemical process) and leaching process from agricultural contamination, and anthropogenic sources (discharge from sewage and industrial plants). Generally, TDS can be considered a primary water quality measurement because it is showing combined effect of different pollutants and it may be used as a basic characteristic of drinking water. Collection of groundwater from boreholes for groundwater quality analysis generally or may not be readily available mainly because water of those boreholes is without geochemical analyses. In such case, geoelectric sounding may provide a useful way to estimate TDS concentration [1]. Vertical electrical sounding (VES) method is subtle and can be utilized precisely to determine groundwater quality [2–4].

For present states of groundwater quality on the basis of TDS during VES survey without hydrogeochemical analysis of groundwater, resolving this problem to calculate the TDS (without hydrogeochemical analysis) of groundwater, We developed a mathematical empirical model in this work that can capture the in-situ aquifer

K. S. Rawat (✉) · S. Kumar
Geo-Informatics, Civil Engineering Department, Graphic Era (Deemed to be University),
Dehradun, Uttarakhand, India

S. K. Singh
K. Banerjee Centre of Atmospheric Ocean Studies, IIDS, Nehru Science Centre, University of
Allahabad, Prayagraj 21102, Uttar Pradesh, India

groundwater TDS. We are unaware with the fact that the VES technique has the capability to determinate the TDS with the help of ρ of groundwater at the aquifer. With this idea, we attempted to develop an empirical relationship between TDS and ρ of groundwater, in order to use ρ of groundwater to predict the TDS of groundwater.

There is limited literature work exists which revealed a relationship to predict the TDS based on ρ of groundwater. However, Mehrdadi et al. [5] and Maedeh et al. [6] try to predict TDS on the basis of ρ , using Artificial Neural Network (ANN, a black box model) to predict TDS in groundwater. But they used less number of samples (one hundred only) date for training of network process in ANN while ANN requires voluminous data for good prediction. While work is available for prediction of TDS on the basis of other hydrogeochemical component (like EC, Ca, pH, SO₄, [7]) of groundwater. Therefore, we outlined an objective to estimate TDS on the basis of ρ of groundwater during VES survey.

2 Material and Method

2.1 Study Area

The study area has a geographical area of 87.25 km² (Fig. 1). The two rivers Koovam (or Cooum) river in North, Adyar river in South, Bay of Bengal coast in East bound the study area and in the city boundary in West. The elevation ranges from 5 to 15 m above mean sea level. The Survey of India (SOI) Topographic sheet 66C/1 and

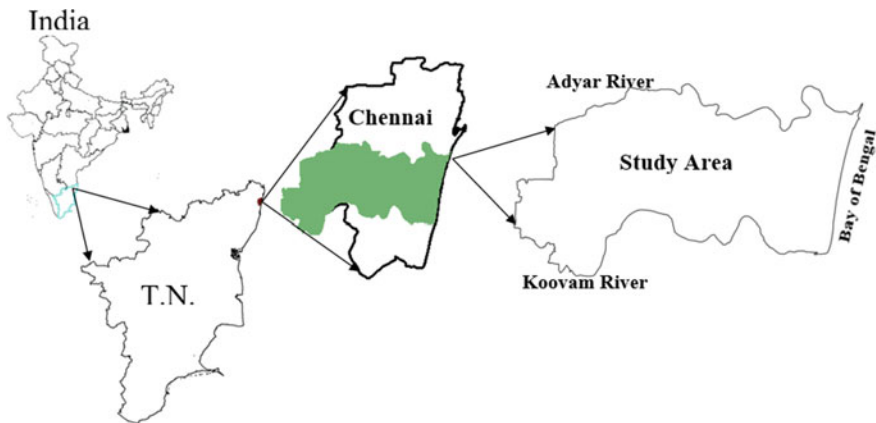


Fig. 1 Location map of the study area

66C/4 covers the whole study area. The rivers have deposited substantial amount of alluvium—mixture of sand sit and clay—that forms an important aquifer in Chennai city.

Geologically, the alluvial deposits rest on hard rock in the eastern and southern parts. The hard rock is mainly charnockites of Archaean age. In the northern and western part, the alluvium rests over tertiary and gondwana group of rocks. The average thickness of alluvium varies from 10 m along the southern boundary to a maximum of 30 m in the central and eastern part of the study area. Shallow open dug wells of depth varying from 8 to 10 m and borewells in the depth range of 30 m to 75 m are the common groundwater extraction structures in the area [8]. The study area has a tropical climate with mean annual temperature is 24.3 (min) to 32.9 °C (max) and humidity ranges from 58 to 84%. Chennai receives the major part of the rainfall during the north-east monsoon period and south-west monsoon is generally erratic [9]. The normal annual rainfall recorded in the Meenambakkam observatory is 1323.7 mm and in the Nungambakkam observatory is 1285.6 mm.

2.2 Method

Total twenty-three wells water samples have been collected ((Table 1) 7 for model generation and 16 for model validation) for laboratory-based (or gravimetric method) TDS measurement while 70 points were used for VES examination within study area. For VES survey we have used resistivity meter (SSR MP ATS). Statistical tests have been used to establish the relationship between the TDS and ρ of groundwater. The quadratic least square regression/non-linear/second order regression (QLSR/NLR/SOR) method was used to calculate regression coefficient (a, b and c) and the fitted value to establish relationship as Eq. (1) as

$$y = ax^2 + bx + c \tag{1}$$

Table 1 TDS and Resistivity of groundwater data sets at fixed location borewells

Sl. no.	Well ID	TDS (mg/l)	Resistivity (ρ)
1	4	500	59.219
2	47	1100	29.963
3	56	780	243.427
4	64	400	70.48
5	76	600	5.676
6	99	2040	356.85
7	108	1120	61.551

The residual sum of the square of differences for all n is given by:

$$S = \sum_{i=1}^n (ax^2 + bx + c)^2 \quad (2)$$

Values of a , b and c have to be determined so that S must be a minimum value:

$$\frac{\partial S}{\partial a} = 0, \quad \frac{\partial S}{\partial b} = 0 \quad \text{and} \quad \frac{\partial S}{\partial c} = 0 \quad (3)$$

Coefficients (a , b , c) values are given as:

$$a = \frac{((S(x^2y) \times S(xx)) - (S(xy) \times S(xx^2)))}{((S(xx) \times S(x^2x^2)) - (S(xx^2))^2)} \quad (4)$$

$$b = \frac{((S(xy) \times S(x^2x^2)) - (S(x^2y) \times S(xx^2)))}{((S(xx) \times S(x^2x^2)) - (S(xx^2))^2)} \quad (5)$$

$$c = ((S(y_i)/n) - (b \times ((S(x_i)/n))) - (a \times (S(x_i^2)/n))) \quad (6)$$

where,

$$S(xx) = (Sx_i^2) - ((Sx_i)^2/n) \quad (7)$$

$$S(xy) = (Sx_i y_i) - ((Sx_i) \times (Sy_i)/n) \quad (8)$$

$$S(xx^2) = (Sx_i^3) - ((Sx_i) \times (Sx_i^2)/n) \quad (9)$$

$$S(x^2y) = (Sx_i^2 y_i) - ((Sx_i^2) \times (Sy_i)/n) \quad (10)$$

$$S(x^2x^2) = (Sx_i^4) - ((Sx_i^2)^2/n) \quad (11)$$

2.3 Validation of Model

Statistical testing is a good tool to estimate the efficiency of any developed empirical model. Before testing the efficiency of a model based on observed and predicted data sets some statistical tools exist which can show that X (ρ of groundwater) and Y (TDS) are highly correlated (based on R^2 statistical tool) and a good model may be generated which have good power to express X in term of Y. Therefore we have used few statistical tests (Table 2) for estimating the efficiency of generated model based on observed data sets of TDS and ρ of groundwater.

Table 2 Mathematical expression of statistical tests

Coefficient of determination (R^2)	$R^2 = \left(\frac{\sum_{i=1}^n (V_M - \bar{V}_M) \times (V_O - \bar{V}_O)}{\sqrt{\sum_{i=1}^n (V_M - \bar{V}_M)^2 \sum_{i=1}^n (V_O - \bar{V}_O)^2}} \right)^2$
Standard error of estimate (SEE)	$SEE_M = \left(\frac{\sum_{i=1}^n (V_O - V_M)^2}{n-1} \right)^{0.5}$
Root mean square error (RMSE)	$RMSE = \sqrt{(n-1 \sum_{i=1}^n (V_M - V_O)^2)}$
Relative-RMSE (R-RMSE)	$R - RMSE = \sqrt{\left(n-1 \sum_{i=1}^n \left(\frac{V_M - V_O}{V_M} \right)^2 \right)}$
Percent RMSE (%RMSE)	$\%RMSE = \left(\frac{RMSE}{\sum_{i=1}^n (V_O)} \times 100 \right)$
t-statistic test	$t = \sqrt{\left(\frac{(n-1)MBE^2}{RMSE^2 - MBE^2} \right)}$
Volume error (VE)	$VE = n^{-1} \sum_{i=1}^n \left \frac{V_O - V_M}{V_M} \right $
Normalized RMSE (NRMSE)	$NRSME = \frac{\sqrt{(n-1 \sum_{i=1}^n (V_M - V_O)^2)}}{V_O}$
Mean absolute error (MAE)	$MAE_M = \frac{\sum_{i=1}^n V_O - V_M }{n}$
Mean bias error (MBE)	$MBE_M = \frac{\sum_{i=1}^n (V_M - V_O)}{n}$
Mean absolute percent error (MAPE)	$MAPE_M = \frac{\sum_{i=1}^n \left \frac{V_O - V_M}{V_O} \times 100 \right }{n}$
Average index ratio (IR)	$IR = \frac{V_M}{V_O}$
Percent of error (PE)	$PE = \sum \left(\frac{V_M - V_O}{V_O} \right) \times 100$

V_O , observed value and V_M model value

2.4 TDS Zoning Map

After generation and validation of model, we have used model to predict TDS value of 47 points using ρ from VES survey. These predicted TDS values were interpolated within study area using ArcGIS-10.1 [10–14] for creating TDS zoning map of study area.

3 Result and Discussion

Twenty-three (7 + 16) bore wells water samples were collected for TDS measurements while seventy ρ from VES across study area were carried out and used to establish and validate the existing relationship between ρ and TDS. TDS hydro-geochemical parameter tested by using QLSR coefficients (a, b and c) driving by Eqs. 4–11. Results of the QLSR coefficients revealed that TDS has good correlation. Thus, Eqs. (2)–(9) were used to establish relationship that relates TDS of groundwater to ρ of groundwater as Eq. 12:

$$\text{TDS} = 0.027 \times \rho^2 - 6.7857 \times \rho + 965.84 \quad (12)$$

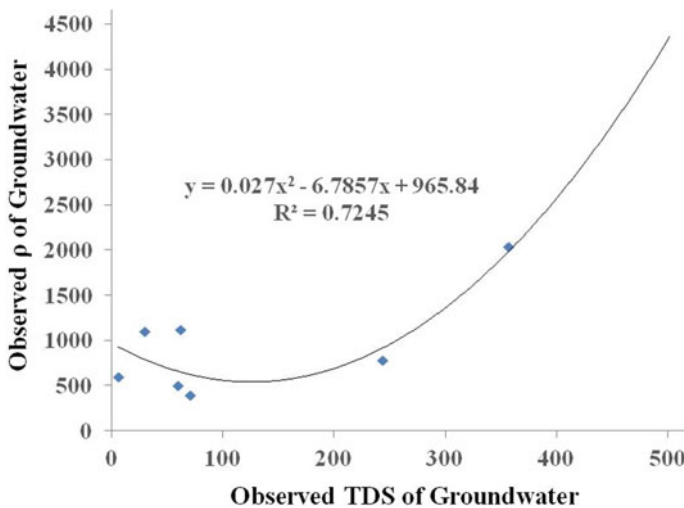


Fig. 2 Correlation between observed TDS and ρ of groundwater

where, TDS is Total dissolved solid of groundwater and ρ is apparent resistivity of groundwater while $a = 0.027$, $b = -6.7857$; and $c = 965$.

Equation 12 and Fig. 2, is showing a good R^2 value of 0.72 which revealed that ρ and TDS of groundwater are strongly correlated and both can be used to translate ρ into TDS or TDS into ρ of groundwater.

3.1 Empirical Models Validation

Equation 12 has been used to predicate TDS for study area. It has been decided by statistical tests only therefore we have applied statistical test over 16 model-predicted and observed TDS value of 16 fixed points (Table 3). Table 3 shows TDS value comparison between TDS_{Observed} and TDS_{Model} using statistical test. The statistical analysis gives level of accuracy of developed empirical models TDS_{Model} with respect to TDS_{Observed} . Based on statistical parameters RMSE, R-RMSE, MAE and MBE statistics test, TDS_{Model} is more closer to SM_{Observed} due to low value of error indexes (RMSE = 89.37, R-RMSE = 0.10, MAE = 55.17, MBE = 35.20 and SEE = 0.16, Table 3). Higher value of R^2 , Adj R and Multi R test (Table 3) revealing that TDS_{Model} values how much closer to TDS_{Observed} and also TDS_{Model} value can be translated into TDS_{Observed} value due to high value of R^2 0.899 (≈ 0.9 , Fig. 3) (TDS_{Model} with

Table 3 Statistical test result or validation of developed model

Sl.No	TDS_{Observed}	TDS_{Model}	Statistical test	Statistical values
1	624.27	604.95	RMSE	89.37
2	947.01	826.69	R-RMSE	0.10
3	757.60	577.48	MAE	55.17
4	927.33	882.09	NRMSE	0.10
5	793.75	781.30	MBE	35.20
6	804.08	779.40	MAPE	0.40
7	935.12	812.80	RMSE%	0.64
8	653.68	614.91	IR (average index ratio)	0.94
9	886.82	897.01	PE (% Error)	-6.94
10	693.09	667.26	R^2	0.90
11	1031.48	911.02	p (at 95%)	0.01
12	1001.93	997.93	Multi R	0.95
13	696.05	549.82	Adj. R	0.89
14	1333.06	1372.97	Standard error	66.77
15	800.00	814.99	t-test	1.66
16	1039.12	951.02	SEE	0.16
17	-	-	VE	0.09

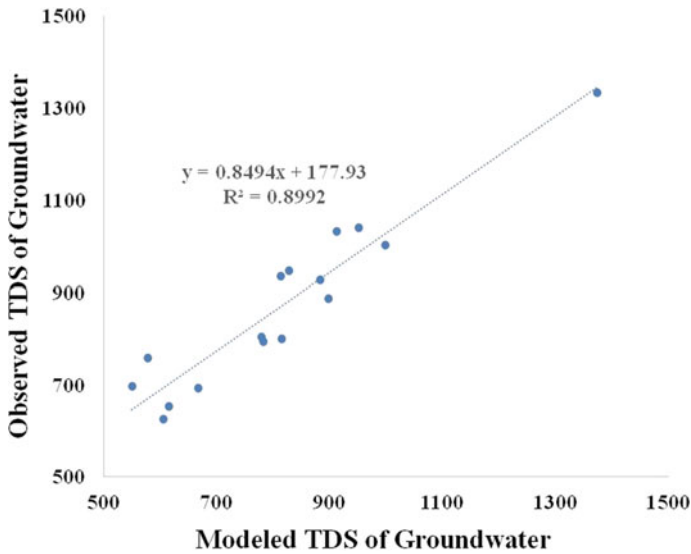


Fig. 3 Correlation between Observed and modelled TDS of groundwater

TDS_{Observed} , Table 3). Very good (or less) value of p-value test for TDS_{Model} with TDS_{Observed} has revealed that more probability of obtaining value from TDS_{Model} similar to TDS_{Observed} . Lower value of RMSE% ($=0.64$) and VE ($=0.09$, Table 3) showed a good agreement of model based on TDS with respect to TDS_{Observed} . IR approach to (≈ 1) one, which is revealed model-based predicted TDS (TDS_{Model}) can be shows 1:1 line properties (less noise in model-based TDS with respect TDS_{Observed} . Overall on the statistical tests (Table 3), developed model (Eq. 12) on the basis of ρ parameter for study area is well working. By using this model easily TDS value may be forecasted. Based on above statistics result (Table 3), it is inferred that present model (Eq. 12) performs good (with respect to observed TDS) for retrieval of TDS from ρ of groundwater.

3.2 TDS Zoning

TDS values to be less than 465 mg/l, an indication of very good quality of water and in TDS map such area (or red colour patches) are very less. TDS values that range from 465 to 965 mg/l, an indication of good quality water. In TDS maps such value covers nearly about 20% of the study area and have yellow colour patches. TDS values that range from 965 to 1620 mg/l, an indication of saline region (light blue to dark blue colour patches) and such type of area is almost 70% of the study area. WHO has recommended 600 and 1000 mg/l as the lower and upper limits of TDS acceptability for drinking use. In our case, the TDS maps have majority of area fall in upper limit of TDS (1000 mg/l<). Hence our study area groundwater is suitable for industrial and agricultural purposes, and this is logical also because one side of our study area is sea and another two side are two polluted rivers Adyar [15] and Koovam (or Cooum). Contour maps of the ρ at 100 mg/l interval has revealed that most part of the study area is affected by two directions as middle of upper (Adyar river a major source to contaminate to groundwater, [15] with 700 mg/l< contour values (Fig. 4) and middle-lower side (Koovam/Cooum river a major source to contaminate to groundwater, [1, 16, 17]) of study area with higher value of contour (Fig. 4). From sea direction slight salt/saline water intrusion (in aquifer) is also identified which is normal and natural process in coastal region.

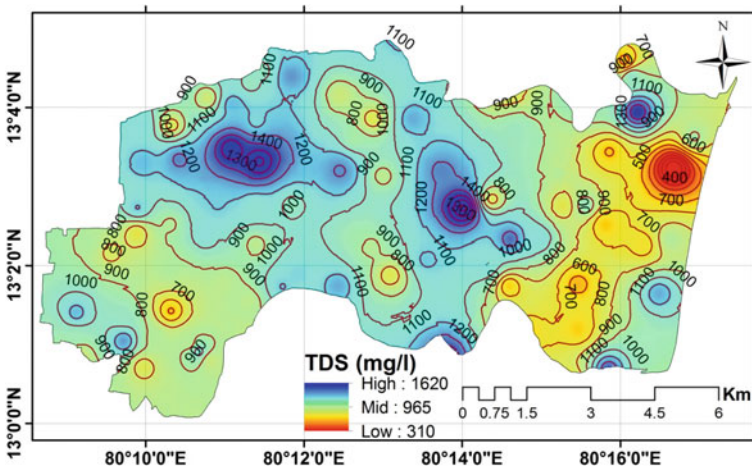


Fig. 4 TDS zoning of groundwater with TDS concentration contour at 100 mg/l interval

4 Conclusion

Results show a significance of present work and its ability to estimate the TDS from ρ data and to predict and map salinity of groundwater. Good prospects exist for freshwater development in the study area where the TDS values range from 465 to 604 mg/l (or >965 mg/l). The predicted TDS from TDS and ρ measurements is in good agreement with the TDS observed/measured values. The TDS value from ρ data gives reliable and logical estimate therefore ρ can be used to understand the salinity of groundwater. Based on the TDS and ρ (as a primary objective), three groundwater quality zones (>310 mg/l, 310–965 mg/l and 965–1620 mg/l) were mapped. Present research work has offered a better understanding of the groundwater system at study area and such type of relationship will be guided in development of future groundwater exploration strategies in the study area and also eradicate the problem of saltwater and abortive wells in the area.

References

1. Anonymous, Three large industrial units in North Chennai major polluters of Cooum (The Hindu, July 28, 2015)
2. W.E. Kelly, Geoelectric sounding for delineating groundwater contamination. *Ground Water* **14**, 6–10 (1976)
3. D.W. Urish, The practical application of surface electrical resistivity to detection of groundwater pollution. *Ground Water* **21**, 144–152 (1983)
4. O. Mazac, W.E. Kelly, I. Landa, Surface geoelectrics for groundwater pollution and protection studies. *J. Hydrol.* **93**, 277–294 (1987)
5. N. Mehrdadi, J. Hasanlou, M. Hasanlou, H. Abodolabadi, Simulation of low TDS and biological units of fajar industrial water treatment plant using artificial neural network and principal component analysis hybrid method. *J. Water Resour. Prot.* **4**, 370–376 (2012)
6. P.A. Maedeh, N. Mehrdadi, N.G.R. Bidhendi, H.A. Zare, Application of artificial neural network to predict total dissolved solids variation in groundwater of tehran plain, Iran. *Int. J. Environ. Sustain.* **2**, 1–20 (2013)
7. W.L. Daniels, M. Beck, M.J. Eick, Z.W. Orndorff, Predicting contaminant leaching potentials for central appalachian overburden and coal refuse materials. Final Report to OSM Applied Science Research (2009)
8. J. Saravanan, K.S. Rawat, S.K. Singh, Groundwater quality of coastal aquifer evaluation using spatial analysis approach. *Oriental J. Chem.* **34**(6), 5–9 (2018)
9. J. Saravanan, K.S. Rawat, S.K. Singh, Study of sub surface hydrogeology of chennai metropolitan area. *Curr. World Environ.* **13**(3) (2018)
10. <https://www.thehindu.com/news/cities/chennai/one-lakh-tonnes-of-waste-polluting-cooum-river/article19744423.ece>
11. <https://www.thehindubusinessline.com/news/national/three-large-industrial-units-in-north-chennai-major-polluters-of-cooum/article7474501.ece>
12. K.S. Rawat, V.K. Tripathi, S.K. Singh, Groundwater quality evaluation using numerical indices: a case study (Delhi, India). *Sustain. Water Resour. Manag.* (2017). <https://doi.org/10.1007/s40899-017-0181-9>
13. K.S. Rawat, S.K. Singh, Water quality indices and GIS-based evaluation of a decadal groundwater quality. *Geol. Ecol. Landsc.*, 1–12 (2018). <https://doi.org/10.1080/24749508.2018.1452462>

14. K.S. Rawat, A.K. Mishra, V.K. Sehgal, V.K. Tripathi, Spatial variability of ground water quality in Mathura district (Uttar Pradesh, India) with geostatistical method. *Int. J. Remote Sens. Appl.* **2**(1), 1–9 (2012)
15. K.S. Rawat, A.K. Mishra, S.K. Singh, Mapping of groundwater quality using normalized difference dispersal index of dwarka sub-city at Delhi National Capital of India. *ISH J. Hydraul. Eng.* **5010**, 1–12 (2017)
16. K.S. Rawat, A.K. Mishra, V.K. Sehgal, V.K. Tripathi, Identification of geospatial variability of fluoride contamination in ground water of Mathura district, Uttar Pradesh, India. *J. Appl. Nat. Sci.* **4**(1), 117–122 (2013)
17. S. Haridoss, Study on air quality management in adyar river basin: a review. *J. Ind. Pollut. Control* **1**(2), 730–740 (2017)
18. K.M.M. Sheriff, A.Z. Hussain, Monitoring the quality of groundwater on the bank of Cooum River at Chennai City, Tamil Nadu, India. *Adv. Appl. Sci. Res.* **3**(6), 3587–3592 (2012)
19. Anonymous, One lakh tonnes of waste polluting Cooum River (The Hindu, September 23, 2017)

Monitoring Drought of Maharashtra, India by Using Standardized Precipitation Index



Smruti Ranjan Sahu, Kishan Singh Rawat, Sanjeev Kumar, Anil Kumar Mishra, and Sudhir Kumar Singh

1 Introduction

Drought is the outcome of reduction in rainfall over a long span of time period; and it is the worst natural disaster. The shortfall of precipitation results into shortage of water which forms drought: and it damages crops, livestock and other. Wheaton et al. [1], insufficient surface water supply, lack of precipitation, low soil moisture and above-normal air temperature in the region of prairies are closely related to the droughts. A drought is a universal problem as it affects any region directly by reducing farmers' crops while indirectly by job and business losses especially in the farmers communities. The rain and underground water drought may occur for less than one month and sometimes for a long time. Droughts can be characterized on the basis of their location, severity, timing and duration. Major types such as Agricultural drought, Meteorological drought, Socio-economic drought, Hydrological drought, Socio-economic drought and edaphic drought. Meteorological drought is defined as dry pattern in the area caused by low precipitation, high temperature and humidity. Agricultural drought usually occurs during insufficient soil moisture; result in the lack

S. R. Sahu

Centre for Remote Sensing and Geoinformatics, Sathyabama Institute of Science and Technology, Chennai 600119, Tamil Nadu, India

K. S. Rawat (✉) · S. Kumar

Geo-Informatics, Civil Engineering Department, Graphic Era (Deemed to be University), Dehradun, Uttarakhand, India

A. K. Mishra

Water Technology Centre (WTC), Indian Agricultural Research Institute (IARI), New Delhi 110012, India

S. K. Singh

K. Banerjee Centre of Atmospheric and Ocean Studies, IIDS, University of Allahabad, Prayagraj, Uttar Pradesh, India

of agricultural production and crop growth. Hydrological drought means shortage of water and it affects water supply.

Drought can be monitored by many drought indices namely; Normalized Difference Vegetation Index (NDVI, [2, 3]), Vegetation Condition Index (VCI, [2]), Vegetation Temperature Condition Index (VTCI), Standardized Precipitation Index (SPI, [4, 5]), Global Vegetation Index (GVI), Evaporative Stress Index (ESI), Soil Moisture Condition Index (SMCI) and Precipitation Condition Index (PCI).

According to Steinemann et al. [6], drought indices are the resultant of integration of different hydrological and climatic variables (groundwater levels, precipitation, streamflow, soil moisture, temperature, etc.) on a quantitative scale. Earlier, a lot of researchers have focused region-specific drought indices analysis and evaluation [7, 8] as well as region-specific drought prediction and characterization of a single well-developed drought index [7–11]. Every drought indices are used to analyse drought but SPI is used to evaluate meteorological drought because it was capable for calculating drought in different timescale [4, 5]. The objective was to study the drought using satellite data.

2 Study Area

Maharashtra is situated in the western part of Indian peninsular area, which occupies the substantial portion of the Deccan plateau lies between latitude $19^{\circ}44'$ to $20^{\circ}68'$ and longitude of $72^{\circ}73'$ to $80^{\circ}56'$. It spread over an area of $307,713 \text{ km}^2$ ($118,809 \text{ sq mi}$). Maharashtra having 35 districts which are divided into 5 division according to geological classification. Those divisions are; (1) Amaravati division, (2) Aurangabad division, (3) Konkandivision, (4) Nagpur division, (5) Nashik division and (6) Pune division (see Fig. 1).

3 Methodology

3.1 Standardized Precipitation Index (SPI)

McKee et al. [12] was pioneer in the field of SPI as he introduced the SPI method. This effort was accomplished by quantifying the rainfall deficit at multiple time scales. More specifically, McKee et al. [12] estimated and monitored the Standardized Precipitation Index for a range of time scale of four years as 3rd, 6th, 12th, 24th and 48th months. SPI is a widely used index and an effective and reliable tool in characterizing meteorological drought at different timescale [4, 5]. The important aspect of SPI is that it is based on precipitation only. It is a versatile parameter as it could be calculated on any timescale. SPI is capable in the monitoring of precipitation-related conditions which are important for both hydrological and agricultural applications of

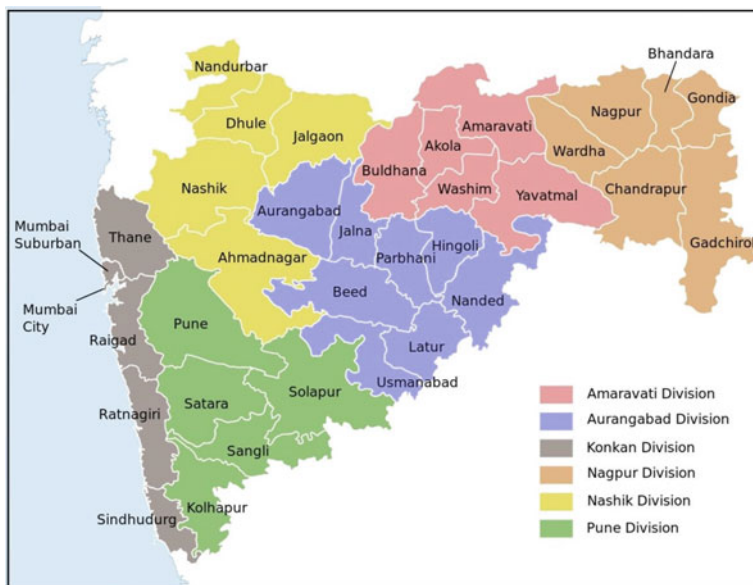


Fig. 1 Map of Maharashtra, India

any region [4, 5, 8, 9]. It was the most common drought monitoring index. Generally, drought occurs when SPI is $-ve$ with an intensity of -1.0 or less while when the SPI becomes $+ve$, then the drought event ends. The $+ve$ value of SPI for all the months within a drought event is known as drought’s magnitude [4, 5] (see Table 1).

Formula for calculating SPI;

$$SPI = (X - \bar{X}) / \sigma \tag{1}$$

where, X = precipitation series, \bar{X} = longterm data (avg. rain), σ = stdev (rain).

Table 1 Ranges of SPI values and its classification [12]

Sl. no.	Ranges	Classes
1	2 and above	Extremely wet
2	1.5–1.99	Very wet
3	1.0–1.49	Moderately wet
4	–0.99 to 0.99	Near normal
5	–1 to –1.49	Moderately normal
6	–1.5 to –1.99	Severely dry
7	–2 and less	Extreme dry

3.2 Data Used

12 years precipitation data (from 2003 to 2014) of all districts of Maharashtra collected from <http://creams.iari.res.in> (Division of Agricultural physics, IARI, New Delhi, India). Data are collected on weekly basis. There are several indices which can calculate drought from precipitation. But we take SPI by following McKee et al., [12] for our study because it is capable of calculating drought in different timescale (1, 3, 6, 9, 12-month). SPI calculation required long-term precipitation data. From the long-term precipitation value, we calculate SPI. After calculating SPI values we have taken only the kharif season (June-Oct) SPI values for the further process. We put all the SPI values of kharif season into the ArcGIS. ArcGIS gives the full map of Maharashtra showing drought according to the values of SPI. Values more than +2 showing extreme wet and less than -2 showing extreme dry condition.

4 Result and Discussion

From the above analysis, we found that some area of Maharashtra facing severe drought in kharif season of year 2013. The main reason behind this disaster was less rainfall during the monsoon time in Maharashtra. In Fig. 2a, it showing drought between 20th May and 4th June. In this time period, some districts like Nagpur, Wardha, Gondia, Chandrapur, Bhandara, Gadchiroli and Amravati faced severe drought. Other parts of Maharashtra have less drought or no drought in these 16 days. Figure 2b, showing drought between 5th June and 20th June. In this time period some districts like Sindhudurg, Kolhapur, Ratnagiri, Sangli facing severe drought. In these 16 days time period some parts of Latur, Nagpur, Wardha, Yavatmal, Nandurbar also facing drought. Figure 2c showing drought between 21st June and 6th July. Between these 16 days' time period Gadchiroli, Chandrapur, Nagpur, Wardha, Pune districts of Maharashtra facing severe drought. Other areas of Maharashtra have high rainfall, so other areas have no drought. Figure 2d, showing drought between 7th July and 22nd July. In between these 16 days some districts of Maharashtra like Nandurbar, Dhule, Jalgaon, Raigad, Ratnagiri, Pune, Satara, Kolhapur, Sangli and some parts of Thane facing severe drought. Figure 2e shows drought between 23rd July and 7th Aug. During these 16 days the districts of Maharashtra which are affected by drought are Sindhudurg, Kolhapur, Nandurbar, Usmanabad, Latur, Nanded, Beed, Parbhani, Ahmadnagar and some parts of Satara and Nandurbar. Figure 2f shows drought between 8th Aug and 23rd Aug. During this time period, some districts of Maharashtra affected by drought are Gadchiroli, Raigad, Ratnagiri, Satara, Solapur, Latur, and some parts of Chandrapur, Nanded, Usmanabad and Pune. Figure 2g, showing drought between 24th Aug and 8th Sept. Between these 16 days' time period those districts of Maharashtra which are affected by drought are Gondia, Bhandara, Nagpur, Amravati, Akola, Jalgaon, Dhule, Nandurbar, Nashik, Thane, Mumbai and also some parts of Ratnagiri, Sindhudurg, Raigad and Aurangabad.

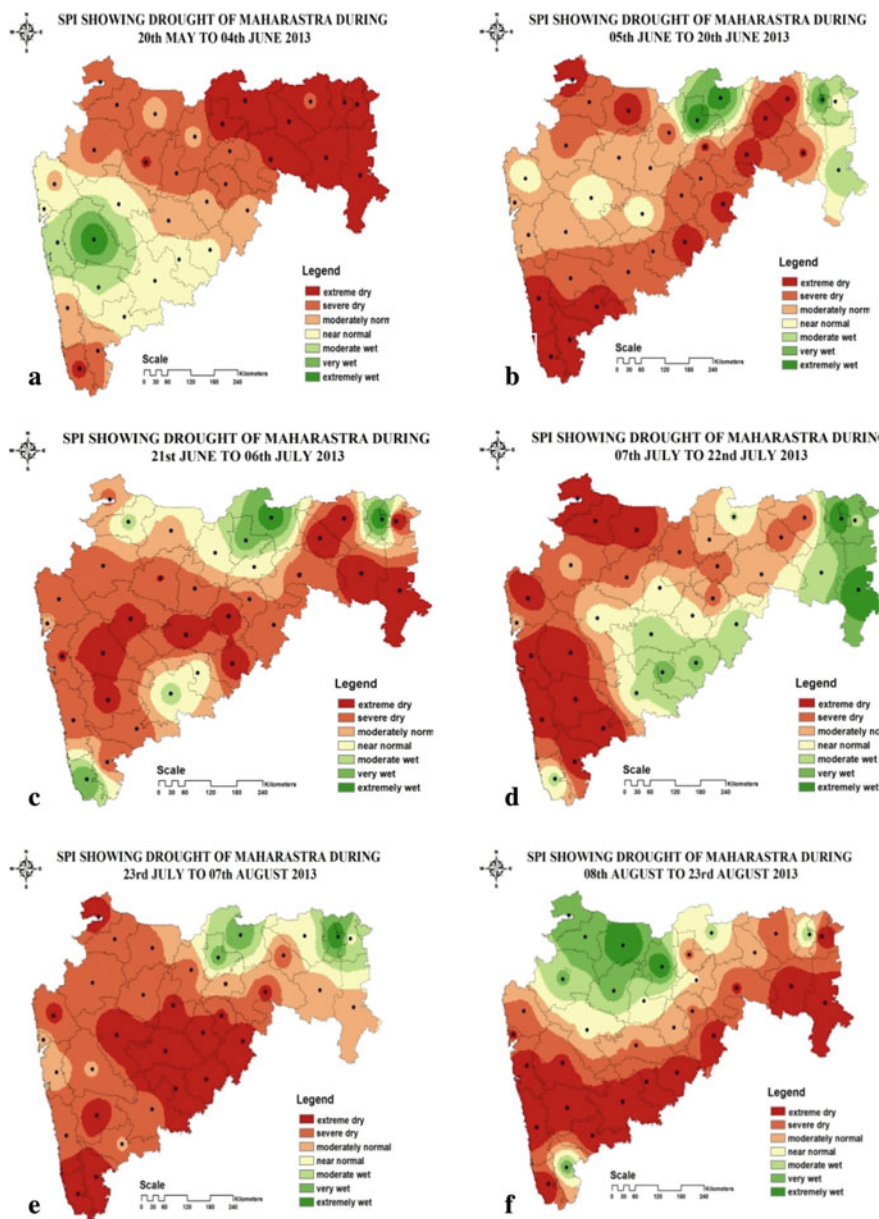


Fig. 2 a-j Spatial distribution of SPI drought indicator during different date over Maharashtra state of India

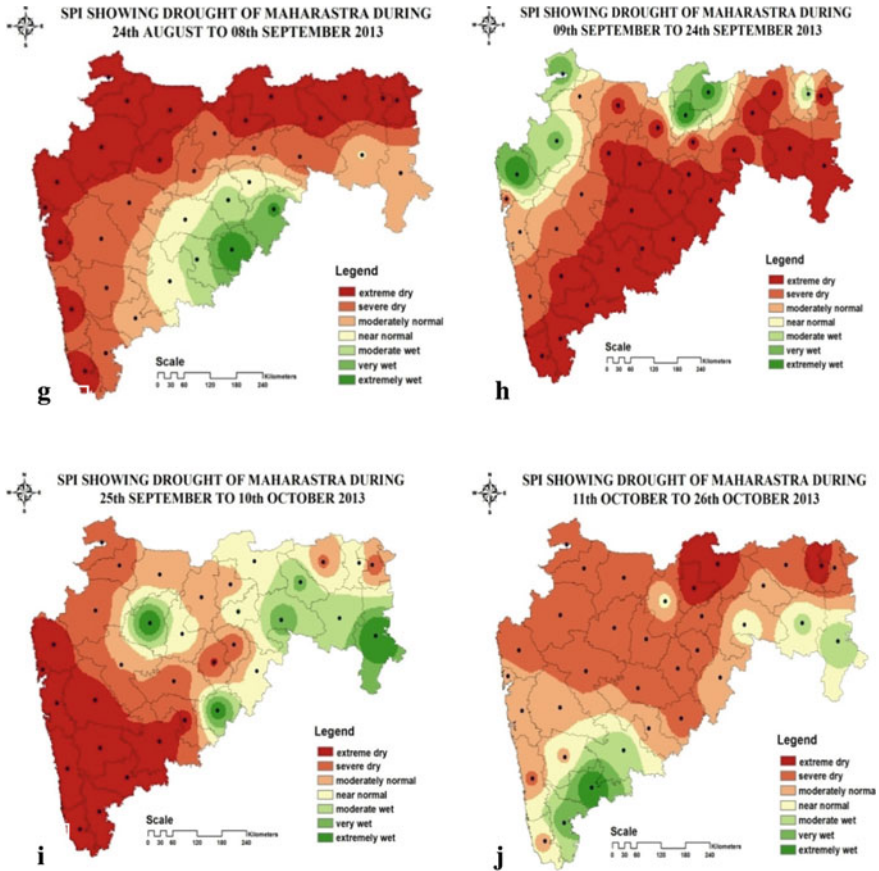


Fig. 2 (continued)

Figure 2h, showing drought between 9 and 24th Sept. In these 16 days almost half part of Maharashtra faced drought. Those districts are Sindhudurg, Kolhapur, Sangli, Solapur, Usmanabad, Latur, Nanded, Parbhani, Beed and some parts of Gadchiroli, Nagpur, Chandrapur, Wardha, Yavatmal, Hingoli and Aurangabad. Figure 2i shows drought between 25th Sept and 10th Oct. In these 16 days, districts of south Maharashtra like Thane, Mumbai, Raigad, Ratnagiri, Sindhudurg, Kolhapur, Sangli, Satara and some parts of Pune facing severe drought. Figure 2j shows drought between 11th Oct and 26th Oct. In these 16 days only some parts of Amravati, Akola, Bhandara have extreme drought, and other districts have less or no drought.

In Fig. 2a–j, we analyse that during the kharif season the drought-prone areas have less rainfall with the average of 3.41 mm or no rainfall and high temperature upto 48 °C. Due to less or no rainfall during monsoon time the land didn't get sufficient amount of water and these areas became dry.

5 Conclusion

With the development of SPI in 1993, it has the capability of monitoring the onset and duration of droughts. SPI is very flexible in the observation of drought at different timescales. During 2013, the SPI has proved to be a reliable tool as it detected and monitored the drought in the Maharashtra state of India. SPI monitoring that in 2013 kharif season many area of Maharashtra facing drought. For monitoring drought of Maharashtra we have taken every 16 days SPI values of kharif seasons. The map was classified drought into 7 classes. Few areas falls under extreme dry condition and few under extreme wet condition. According to this analysis during 2013 (June, July, Aug, Sept, Oct) the temperature in some districts are too high and these districts also reported less or light rainfall. These are the main reason for facing a severe drought in these areas.

Acknowledgements We express sincere thanks to Dr. Anil Kumar Mishra (Water Technology Center, IARI, New Delhi) for his technical support in this research work.

References

1. E.E. Wheaton, L.M. Arthur, B. Chorney, S. Shewchuk, J. Thorpe, J. Whit-ing, V. Wittrock: The prairies drought of 1988. *Climatol. Bull.* **26**, 188–205 (1992)
2. K.S. Rawat, R. Kumar, Vegetation condition index pattern (2002–2007) over Indian agro-climate regions, using of GIS and SPOT sensor NDVI data. *J. Appl. Nat. Sci.* **4**(2), 214–219 (2012)
3. K.S. Rawat, S.K. Singh, Appraisal of soil conservation capacity using NDVI model based C-factor of RUSLE model for a semiarid ungauged watershed: a case study. *Water Conserv. Sci. Eng.* **3**, 47–58 (2018). <https://doi.org/10.1007/s411018-0042-x>
4. K.S. Rawat, V.K. Tripathi, The standard precipitation index analysis for drought assessment in indian agro-climate regions, using of GIS and remote sensing data, in NCWES–2014, Centre for Water Resources Institute of Science and Technology JNTU Hyderabad Kukatpally, Hyderabad-85, pp. 223–232, ISBN 978-93-83635-13-9 (2014)
5. K.S. Rawat, V.K. Tripathi, Standardized precipitation index based approach for development of regional drought monitoring system. *J. Remote Sens. Technol.* **4**(1), 48–57 (2016)
6. A.C. Steinemann, M.J. Hayes, L.F.N. Cavalcanti, Drought indicators and triggers, in *Drought and Water Crises: Science, Technology, and Management Issues*, ed. by D.A. Wilhite (CRC Press, Boca Raton, 2005), pp. 71–92
7. G.M. Guenang, F.M. Kamga, Computation of the standardized precipitation index (SPI) and its use to assess drought occurrences in Cameroon over recent decades. *J. Appl. Meteorol. Climatol.* **53**(10):2310–2324 (2014)
8. P. Angelidis, F. Maris, N. Kotsovinos, V. Hrissanthou, Computation of drought index SPI with alternative distribution functions. *Water Resour. Manag.* **26**(9), 2453–2473 (2012)
9. M. Palchaudhuri, S. Biswas, Analysis of meteorological drought using standardized precipitation index: a case study of Puruliya District, West Bengal, India. *Int. J. Environ. Earth Sci. Eng.* **7**(3), 6–13 (2013)
10. O. Adedeji, A. Olusola, G. James, H.A. Shaba, I.R. Orimoloye, S.K. Singh, S. Adelabu, Early warning systems development for agricultural drought assessment in Nigeria. *Environ. Monit. Assess.* **192**(12), 1–21 (2020). <https://doi.org/10.1007/s10661-020-08730-3>

11. V. Pandey, P.K. Srivastava, S.K. Singh, G.P. Petropoulos, R.K. Mall, Drought identification and trend analysis using long-term CHIRPS satellite precipitation product in Bundelkhand, India. *Sustain.* **13**(3), 1042 (2021). <https://doi.org/10.3390/su13031042>
12. T.B. McKee, N.J. Doesken, J. Kleist, The relationship of drought frequency and duration to time scales, in *Proceedings of the 8th Conference on Applied Climatology*, vol. 17, no. 22 (American Meteorological Society, Boston, MA, 1993), pp. 179–183
13. A. Bala, K.S. Rawat, A. Misra, A. Srivastava, Vegetation indices mapping for Bhiwani district of Haryana (India) through LANDSAT-7ETM+ and remote sensing techniques. *J. Appl. Nat. Sci.* **7**(2), 874–879 (2015)

Precipitation Trends Along the Himalayan and Pir Panjal Mountains of Jammu and Kashmir



Mohammd Rafiq, Kishan Singh Rawat, Sarish Mukhtar,
Anil Kumar Mishra, Sanjeev Kumar, and K. K. Gupta

1 Introduction

There is tremendous importance of water especially fresh water in this world as 70% of the earth contains water of which 2.5% is fresh water. Only 1% of this fresh water is easily accessible, most of which, is confined to snow and glaciers. Basically, 0.007% of the water available on earth is available for drinking. Although this concentration of water has remained constant over time but due to increase in population and effect of thermodynamical parameter are of a significant concern. The competition for clean and ample supply of water for sustainability of life is going to intensify day by day. While climate change has altered the ecosystems globally there are changes in the processes responsible for exchange of this precious water.

Precipitation patterns are changing worldwide and this change is responsible for water crises and disasters. Heavy rains often cause flash floods, landslides, GLOFS, etc., and due to rise in temperature and atmospheric pollution the events of heavy precipitation are increasing and low precipitation event are diminishing resulting in frequent floods and droughts. Many researchers reported rises in the heavy precipitation and declines in the low precipitation events which may result in the rise of floods

M. Rafiq

Department of Space, National Atmospheric Research Laboratory, Gadanki, Andhra Pradesh, India

K. S. Rawat (✉) · S. Kumar · K. K. Gupta

Geo-Informatics, Civil Engineering Department, Graphic Era (Deemed to be University), Dehradun, Utrakhand 248002, India

S. Mukhtar

Department of Earth Sciences, University of Kashmir, Srinagar, India

A. K. Mishra

Water Technology Centre (WTC), Indian Agricultural Research Institute (IARI), New Delhi 110012, India

and droughts. There is going to be an increase of 54% in heavy precipitation over India due to unit degree increase in temperature [1]. However, numerous researches state the significant increases in the winter temperatures, i.e. the minimum temperatures are increasing. This increase has far more effects on the ecosystem of the mountainous regions where snow and glaciers are the dominant sources of waters. Due to increase in the minimum temperature there are chances of more liquid precipitation events which in turn can enhance the snow and glacier melt resulting in glacier-related disasters and unavailability of water during summers. These changes are going to affect the Himalayan regions mostly.

Jammu and Kashmir being most vulnerable to these changes is explored in this study. Previous studies explored the rainfall data from 6 IMD stations located across the Valley, however these cannot represent the overall scenario of Kashmir due to their sparse location and complex topography of the region. They are almost 100 km from each other and located at different environmental settings. In this study, the IMD gridded data is used to analyse the precipitation patterns along different elevations and environmental settings.

2 Materials and Methods

Precipitation data at 0.25° available from IMD was procured from 1900 to 2013. The data includes 6329 station of rain-gauge interpolated to generate an overall rainfall of Indian region on daily basis. The air temperature from IMD observatories and NCEAP (esrl.noaa.gov/psd/data) is used to explore the impacts of changing precipitation patterns. The Statistical analysis was done on each data set for analysis of annual, monthly, seasonal and daily trends. Furthermore, the precipitation extremes were analysed for the different zones including their corresponding temperature trends.

2.1 Study Area

The study area is Kashmir valley, Pir Panjal mountain Range and the Greater Himalayan mountain range. The Kashmir valley comprising an area of around 15,534 km², and is surrounded by the Pir-Panjal (lesser Himalayas) and Great Himalayan mountain ranges (Fig. 1). The elevation of Pir Panjal varies from 1,400 to 4,100 m and connects the valley with Rajouri and Poonch Via Mughal road/Pir Panjal pass. Kashmir valley appears to be an oval-shaped place surrounded by the Himalayan range of mountains on one side and the lesser Himalayan range on the other side. The valley has complex terrain, and possess features resembling to the Himalayas which exhibits an all-pervading impact on its tectonic, geological, and geographic setting. The oval shape given to the valley is due to the geomorphic settings of the Great Himalayan and Pir Panjal mountain range. The length of the valley floor is

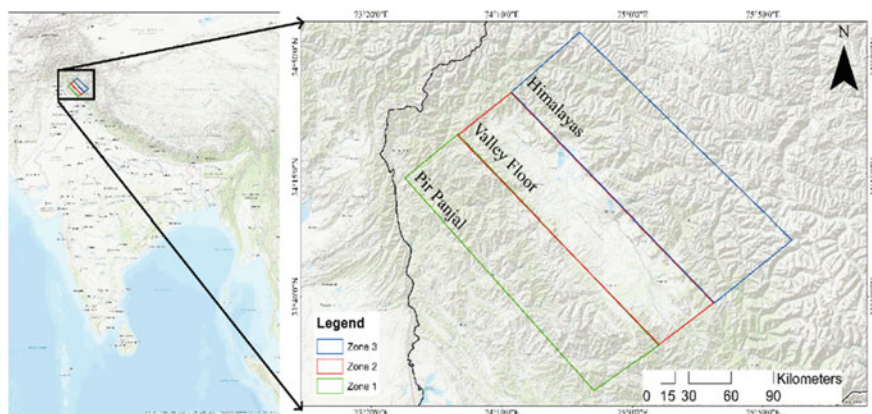


Fig.1 Displaying the zones of study along Jammu and Kashmir region

about 190 km and the width is about 120 km. The Study area is categorized into 3 different zones (a) Pir Panjal mountain Range (lesser Himalaya) (zone 1) (b) Valley floor/plains (zone 2) (c) Himalayan mountain range (Great Himalayan) (zone 3).

3 Results and Discussion

The study area is categorized into 3 different zones representing a unique environmental setting. Zone 1, i.e. Pir Panjal acts as a barrier between the Jammu Hills and valley of Kashmir. Zone 2 comprises of the Kashmir valley floor and is densely populated area of Kashmir almost 75% of the valley's population come inside this zone and this is very critical for any changes in the precipitation patterns. Zone 3 encompasses the Himalayan range and hosts many important glaciers of the region including the valley's largest glacier (Kolahoi).

All the zones show different response to the climate change which is reflected from 1980 onwards. As the lapse rate change can go beyond $10\text{ }^{\circ}\text{C}/[2]\text{ km}$ in this region its difficult to estimate precipitation in this area using only 6 stations as the phase and structure of hydrometeors can change here within a km [3]. IMD data hence can give better scenario to the actual phenomenon in the area. The Pir Panjal range of mountains (Zone 1) are somewhat affected by the monsoon also. The water in this area is mostly snow dependent and there are very few glaciers in this area. Many researchers have studied the changes in the glaciers of this area which show a significant decline [4, 5]. Also, there is a significant decline in the snowfall and increase in the winter temperature in this area [6]. There is not any significant trend but the extreme events of rainfall have increased from 1986 also the data shows a decrease in the rainfall during 1965–1972 (Fig. 2).

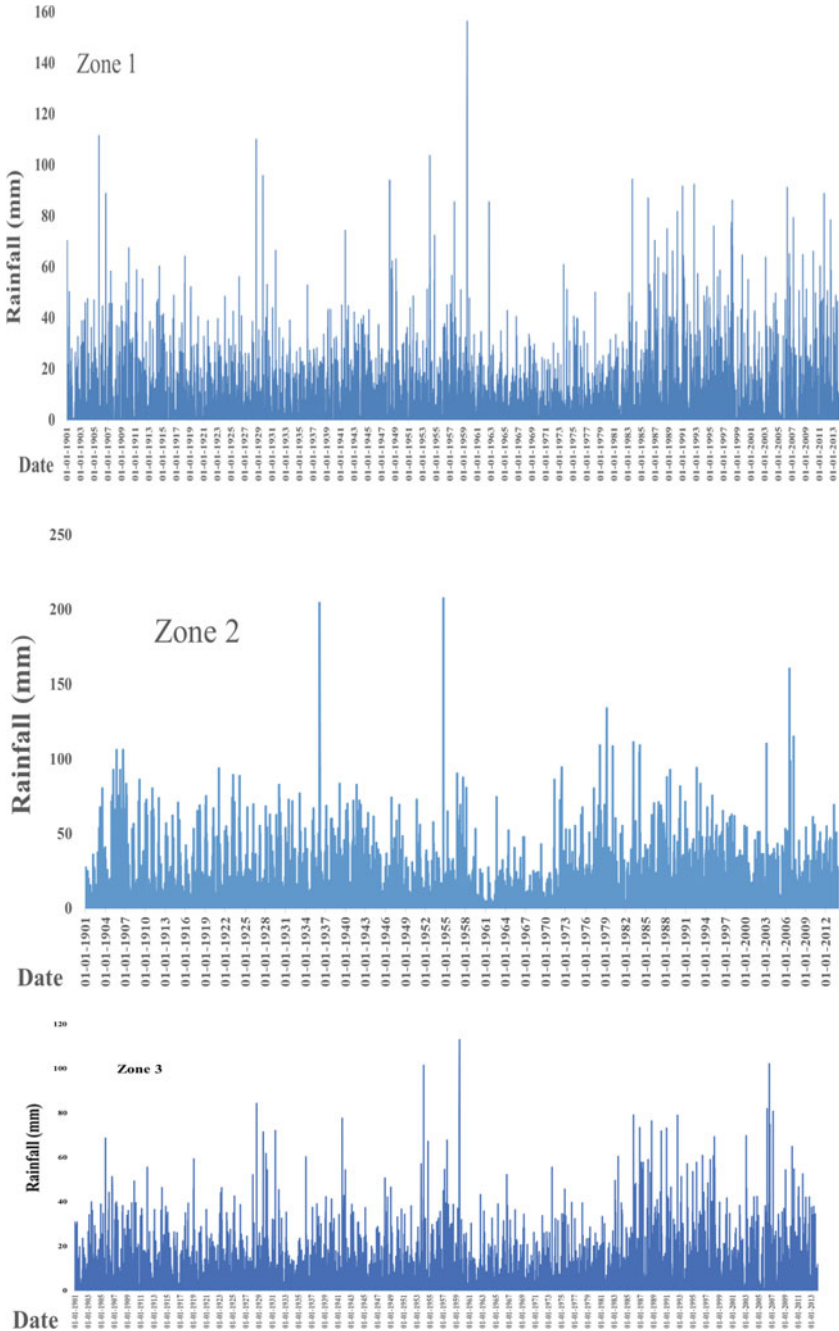


Fig. 2 Showing the rainfall patterns of 3 zones

Many researchers have reported the droughts in these years across many states in India including Jammu and Kashmir [7, 8]. The temperature in this zone is showing a significant increasing trend of 1.2 °C from 1980 before that no such significant trend was observed in the temperature.

The valley floor is explored separately and is marked under zone 2 of the study area. The overall precipitation from last 112 shows no significant trend, but a decreasing trend is also observed here from 1960 to 1970 (Fig. 2). The peaks are found beyond 1984 and more frequent as compared to previous decadal data. In this region, moderate rainfall events have increased however there is decline in the low rainfall events which are usually used to recharge the ground water. This has significantly affected the groundwater recharge and also poses a threat to the decline of this precious source of fresh water in the valley. As people in many parts of valley use this ground water for drinking and agricultural purposes. Recently a study by Rafiq et al. [9] stated the conversion of agriculture into the horticulture due to limitation in the irrigation to rice fields. This also acts as an indicator for the future changes in the water resource of this region.

Zone 3 comprises of Himalayan mountain range large scale changes in the precipitation patterns in this area can be seen. The high rainfall events >24 mm per day have doubled in last 3 decades. The number of rainfall events recorded above 24 mm/day from 1952 to 1982 are 108 and it has increased to 275 from 1983 to 2013 (Fig. 3). Increases in the extreme events and the temperature (1.8 °C per decade) over this region are showing a significant trend. This will lead to the increase in the frequency of disaster as the place is mountainous there are possibilities of flash floods, snow avalanches, glacier lake outburst floods, landslide lake outburst floods, etc. Also, these disasters were recently reported in many parts of the Himalayan region [10–12]. Many studies suggest that there is an increasing trend is observed in long term meteorological variables [13–16] which has many adverse impact like floods and droughts and lead to human migration [17].

Figure 4 shows the temperature trend in the study area from more than 6 decades. There is a significant increase in the temperature over all the three zones. This rise in the temperature is responsible for changing the precipitation patterns over the area of study. Especially, the winter snowfall precipitation has been affected as there are prominent changes in the winter temperatures the IMD station data from (1980 to 2010) shows a significant increase of 1.2 °C and 0.8 °C in the winter temperature along the zone 3 and 1, respectively. A unit degree in the increase of minimum temperature has reduced the Snowfall by $24 \pm 9.8\%$ over zone 3. Similarly, Zone 1 displays a decrease of about $9.25 \pm 8.7\%$ for a degree of surge in the minimum temperature [6].

4 Conclusion and Future Scope

Given the current status of climate over the study area, its likely projected to increase the disaster like floods, Glacier Lake Outburst Floods, snow avalanches, Landslides,

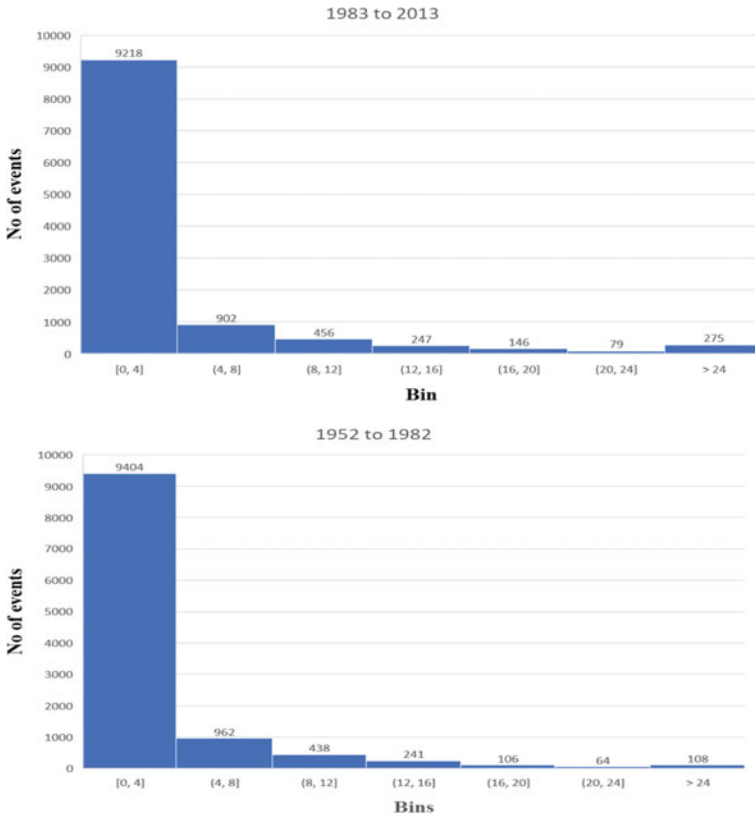


Fig. 3 Trends in the precipitation from 1983 to 2013 and 1952 to 1982

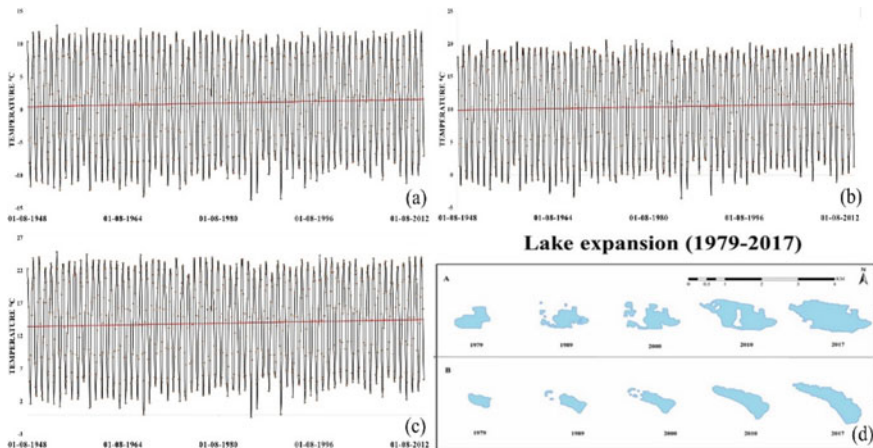


Fig. 4 Temperature trends of zone 1 (a) zone 2 (b) and zone 3 (c), expansion in the glacier lake (d)

etc. [11, 12, 18]. Also, the non-availability of water for irrigation is going to affect the large section of population which is reported to have changed the agricultural practices [9]. These changes on the Land use Land cover are further alarming as they are capable of changing the state of the study area. Keeping in view the current scenario there is a need for strategic development and installation of Early warning systems. Government managers need to decide the grades of severity and earnestness of these disasters and then put forward risk control and prevention programs. Particularly, during planning of mountainous townships. There is a need for realistic engineering measures and development of an efficient early warning system also. This can be achieved when people from all sectors like administration at all levels, enterprises, NGOs, local residents and experts actively participated in various fields of development and management. Furthermore, we need to do more research in the climate science so that we can predict these kinds of events well in advance and develop an effective Early Warning System.

Acknowledgements We express sincere thanks to Dr. Kishan Singh Rawat (Geo-Informatics, Civil Engineering Department, Graphic Era (Deemed to be University) Dehradun-248002 (Uttarakhand), India) for his technical support in this research work.

References

1. A.K. Mishra, Quantifying the impact of global warming on precipitation patterns in India. *Meteorol. Appl.* **26**(1), 153–160 (2019)
2. S.A. Romshoo, S. Altaf, I. Rashid, R.A. Dar, Climatic, geomorphic and anthropogenic drivers of the 2014 extreme flooding in the Jhelum basin of Kashmir, India. *Geomat. Nat. Hazards Risk*, **9**(1), 224–248 (2018)
3. M. Rafiq, I. Rashid, S.A. Romshoo, Estimating land surface temperature and its lapse rate over Kashmir Valley Using MODIS Data, in *Geostatistical and Geospatial Approaches for the Characterization of Natural Resources in the Environment* (Springer, Cham, 2016), pp. 723–728
4. A.V. Kulkarni, B.P. Rathore, S.K. Singh, I.M. Bahuguna, Understanding changes in the Himalayan cryosphere using remote sensing techniques. *Int. J. Remote Sens.* **32**(3), 601–615 (2011)
5. H.S. Gusain, M. Kala, A. Ganju, V.D. Mishra, Snehmani, Observations of snow–meteorological parameters in Gangotri glacier region. *Curr. Sci.*, 2116–2120 (2015)
6. A.K. Mishra, M. Rafiq, Analyzing snowfall variability over two locations in Kashmir, India in the context of warming climate. *Dyn. Atmos. Ocean.* **79**, 1–9 (2017)
7. H.N. Bhalme, D.A. Mooley, Large-scale droughts/floods and monsoon circulation. *Mon. Weather Rev.* **108**(8), 1197–1211 (1980)
8. L. Ahmad, S. Parvaze, M. Majid, R.H. Kanth, Analysis of historical rainfall data for drought investigation using standard precipitation index (SPI) under temperate conditions of Srinagar Kashmir. *Pak. J. Meteorol.* **13**(25), 1–5 (2016)
9. M. Rafiq, A.K. Mishra, M.S. Meer, On land-use and land-cover changes over Lidder Valley in changing environment. *Ann. GIS* **24**(4), 275–285 (2018)
10. S. Kaushik, M. Rafiq, P.K. Joshi, T. Singh, Examining the glacial lake dynamics in a warming climate and GLOF modelling in parts of Chandra basin, Himachal Pradesh, India. *Sci. Total Environ.* **714**, 136455 (2020)

11. M. Rafiq, S.A. Romshoo, A.K. Mishra, F. Jalal, Modelling chorabari lake outburst flood, Kedarnath, India. *J. Mt. Sci.* **16**(1), 64–76 (2019)
12. M. Rafiq, A.K. Mishra, A study of heavy snowfall in Kashmir, India in January 2017. *Weather* **73**(1), 15–17 (2018)
13. S. Gajbhiye, C. Meshram, S.K. Singh, P.K. Srivastava, T. Islam, Precipitation trend analysis of sindh river basin, India, from 102-year record (1901–2002). *Atmos. Sci. Lett.* **17**(1), 71–77 (2016)
14. S.G. Meshram, S.K. Singh, C. Meshram, R.C. Deo, B. Ambade, Statistical evaluation of rainfall time series in concurrence with agriculture and water resources of Ken River basin, Central India (1901–2010). *Theor. Appl. Climatol.* **134**(3), 1231–1243 (2018)
15. L.L. Mahato, M. Kumar, S. Suryavanshi, S.K. Singh, D. Lal, Statistical investigation of long-term meteorological data to understand the variability in climate: a case study of Jharkhand, India. *Environ., Dev. Sustain.* **23**, 16981–17002 (2021). <https://doi.org/10.1007/s10668-021-01374-4>
16. V.D. Banda, R.B. Dzwauro, S.K. Singh, T. Kanyerere, Trend analysis of selected hydro-meteorological variables for the Rietspruit sub-basin, South Africa. *J. Water Clim. Change* **12**(7): 3099–3123 (2021). <https://doi.org/10.2166/wcc.2021.260>
17. Z. Islam, S.K. Singh, Geospatial analysis of the impact of flood and drought hazards on crop land and its relationship with human migration at the district level in Uttar Pradesh, India. *Geomatics Environ. Eng.* **15**(4):117–127 (2021). <https://doi.org/10.7494/geom.2021.15.4.117>
18. A.K. Mishra, A study on the occurrence of flood events over Jammu and Kashmir during September 2014 using satellite remote sensing. *Nat. Hazards* **78**(2), 1463–1467 (2015)

Evaluation of Critical Performance Parameter for Tube Settlers



M. P. Bhorkar and P. B. Nagarnaik

1 Introduction

Turbidity in raw water becomes a great challenge for a water treatment plants. For the plants where raw turbidity of raw water goes beyond 500 NTU requires special attention and provision of alternatives to decrease the turbidity. The alternatives like pre-settling tank, increase in dose of coagulant, addition of coagulant aids, etc., but all these leads towards the uneconomic. To overcome these situations at water treatment plants, high rate sedimentation concept comes in to picture. It is an important component of water treatment process. The term high rate settling refers to the shallow depth gravity settling simple equipment's which reduces the detention time in tune of 10–20 min. The turbidity removal efficiency of high rate settlers is more than the conventional settling systems like clarifiers.

This concept of high rate settling was originally developed by Hazen in 1904 [1] which was explored by Camp T R in 1946. Camp initially suggested the application of shallow depth trays in sedimentation tank in 1946 [2]. Many researchers have carried out lot of experiments and conclusions with different size and shape of tube settlers. In 1967, Hansen demonstrated the application of circular tubes of 1.3–10.2 cm diameter & 2.44 m length in sedimentation process with 96% turbidity removal efficiency [3] wherein Culp G. studied the depiction of tube settlers giving less settling depth to particles in 1968 [4]. In addition to this many researcher-developed models based on the high rate settling. The critical performance parameter is designated for circular, square & for parallel plates are $4/3$, $11/8$ & 1 , respectively [14]. In this research paper, an attempt is made to compare the performance of (conventional &

M. P. Bhorkar (✉)

Civil Engineering Department, G. H. Raisoni College of Engineering, Nagpur, India

P. B. Nagarnaik

Department of Civil Engineering, G. H. Raisoni Institute of Engineering & Technology, Nagpur, India

modified) square & hexagonal shape tube settler as well as the critical performance parameter study for the hexagonal cross-section.

2 Literature Review

Culp and his associates introduced the basic two configurations of tubes initially viz. essentially horizontal & steeply inclined. Essentially horizontal tubes were kept at 5° inclination for desludging operation during backwashing. As it requires multiple backwashing for desludging the tubes results in consumption of manpower and water for backwashing. To overcome this issue tubes were then kept at an angle of 45° which were helping in continuous desludging automatically [4].

Thomas in 1958 developed the theoretical work on settling of particles in horizontal tubes under gravity. His main concern was to determine the quantity of particles loss in smoke & dust of incinerators and boilers through horizontal tubes under gravity [5]. Later McMichael developed an equation as follows [6].

$$F = 1 - \frac{2}{\pi}[\alpha.\beta + \sin^{-1}\beta - 2.\alpha^3.\beta] \quad (1)$$

where,

$$\alpha = \left[\frac{3XV_s}{8.\mu.R} \right]^{\frac{1}{3}}$$

$$\beta = (1 - \alpha^2)^{1/2} \quad (2)$$

And $0 < \alpha < 1$.

where,

F = Fractional removal

X = Horizontal length of tube

Vs = Particle settling velocity

μ = Average fluid velocity

R = Tube radius

The above equations assumed for particle path in laminar flow and assumed to be particles are discrete and doesn't get mixed. The removal is 100% when $\alpha = 1$. X is the maximum distance along the length of tube that particle travels before intersecting the wall of tubes.

McMichael derived value of removal parameter α for inclined tubes with the suspended solids removal on the same principle represented by Eq. 1.

$$\alpha = \left[\frac{3 \cdot X \cdot V_s \cdot \cos\theta}{8 \cdot \mu \cdot R} X \frac{1}{\left(1 - \frac{V_s \cdot \sin\theta}{2 \cdot \mu}\right)^{3/2}} \right]^{1/3}$$

$$\alpha = \frac{R}{r_o} \cdot \left[\frac{3 \cdot X \cdot V_s \cdot \cos\theta}{8 \cdot \mu \cdot R} \right]^{1/3} \tag{3}$$

where θ = angle of inclination with horizontal

$$r_o^2 = R^2 \cdot \left(1 - \frac{V_s \cdot \sin\theta}{2 \cdot \mu}\right) \tag{4}$$

The particle can be removed when its path crosses the boundary, i.e. $r = r_o$ for inclination and for horizontal tube, particle can be removed when it crosses the boundary $r = R$. Equation 3 reduced to Eq. 2 in case of $\theta = 0$.

Yao (1970, 1973), prepared a theoretical study on various shapes of tube settlers and gave the Eq. 5 based on the parameter overflow rate. Equation 5 is mostly used in design of water treatment process and is appropriate for universal application [7, 8].

$$V_s = S_c \cdot \frac{V}{(\sin\theta + L' \cos\theta)} \tag{5}$$

where

- V_s = overflow rate
- V = velocity of water through tubes
- S_c = the critical performance S value (4/3 for circular tubes)
- θ = angle of inclination of tubes to the horizontal, and
- L' = relative length (l/d);
- l = length of tube and
- d = diameter of tubes.

During the experimentation work, Yao found out that, a transition state develops at the entry of inlet of setup prior to laminar zone developed fully. In such case, the relative length of this transition zone at inlet is given by Eq. 6

$$L' = 0.058 \cdot \frac{Vd}{\nu} \tag{6}$$

where,

- ν = Kinematic viscosity of the suspension medium.

3 Objective

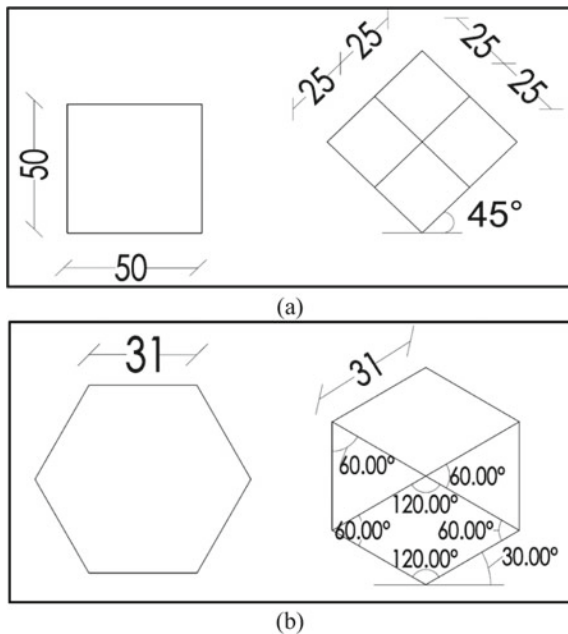
The objective of this paper is to compare the performance of modified tube settlers, and thereby to suggest critical performance parameter of hexagonal cross-section of tube settler.

4 Fabrication and Installation of Model

The two basic configurations of tube settlers are selected in this study viz. Square & Hexagonal shape as shown in Fig. 1 a and b.

The above two shapes 6 in numbers each are fabricated and installed inside the fabricated tank and analysed for the turbidity removal efficiency. The basic shapes were converted into modified shapes as shown in Fig. 1 and termed as modified tube settlers. The setup was installed at locally located water treatment plant. The raw water turbidity coming to the plant was in tune of 1000–3000 NTU in rainy season. The removal of such a higher turbidity is a great challenge for the setup. The flocculated raw water was taken into inlet of the setup with the help of siphon with special attention so that flocs should not break during flowing through pipe. The poly aluminium chloride chemical was used as a coagulant in addition to the anionic polymer as a coagulant aid. The coagulant dose was decided on the basis of

Fig. 1 Basic cross-section of **a** Square Shape & **b** Hexagonal Shape



optimum dose of coagulant process with Jar Test Apparatus. When raw water passes through the inlet and then through the tubes, the flow must be laminar to prevention from short-circuiting inside the tank. The designed flow was kept as 4 L/ minute. The sludge removal valves are provided at the bottom of tank to desludging at regular interval.

As a result of passing of flocculated raw water to setup, it provided tremendous results and the turbidity removal efficiency was obtained in the range of 95–97%. The results are discussed in the next section of paper.

4.1 Inclination of Tubes and Flow Rate

By considering the opinion of many researchers like Culp G (1968), Yao, K. M (1970), Viraraghavan T. (1973), Eshwar K. (1981), Bhole A G (1996), Gurjar A. (2017), Bhorkar M. P. (2018) in view of inclination of tubes, 60° angle of inclination is considered for the evaluation of performance in this study [4, 7, 9–13].

The rate of flow of flocculated raw water for all 6 tubes with total cross-section area of 0.015 m² was kept as 4 L/minute. This flow was regulated by the ball valve fixed between the pipe and inlet of fabricated tank. The flow rate design considerations are considered as per the guidelines given in textbook of Bhole A. G. [14].

5 Conceptual Analysis

The analysis was carried out for the said conventional & modified tube settler units in rainy season. The results are shown with the graphical figures below in Figs. 2, 3 and 4.

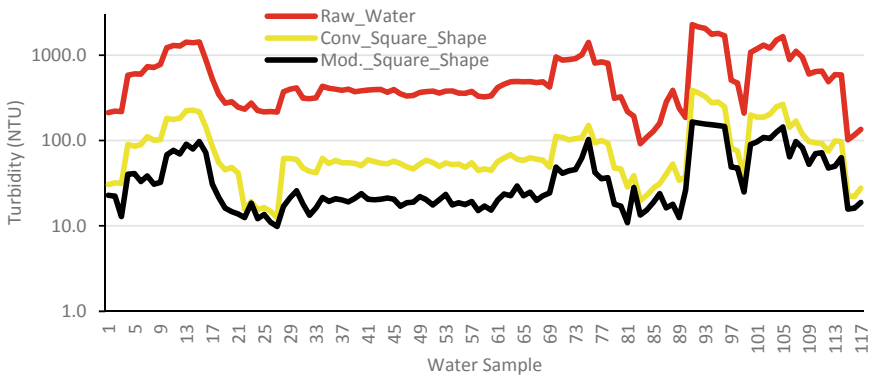


Fig. 2 Comparison between turbidity remained by conventional & modified square shape tube

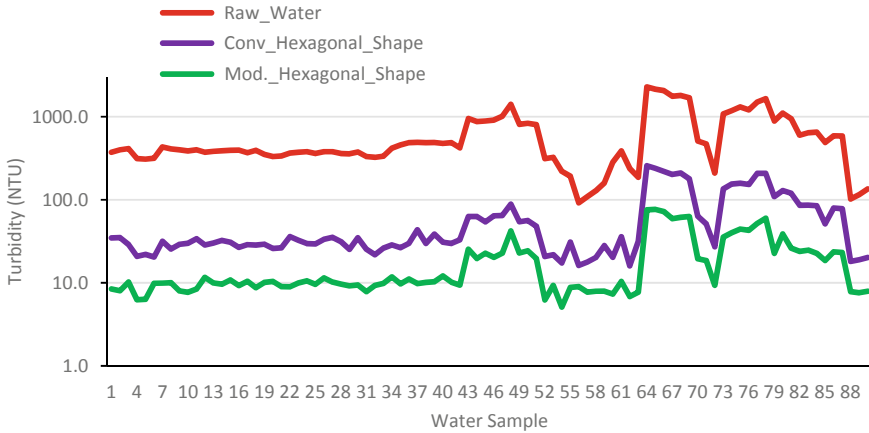


Fig. 3 Comparison between turbidity remained by conventional & modified hexagonal shape tube

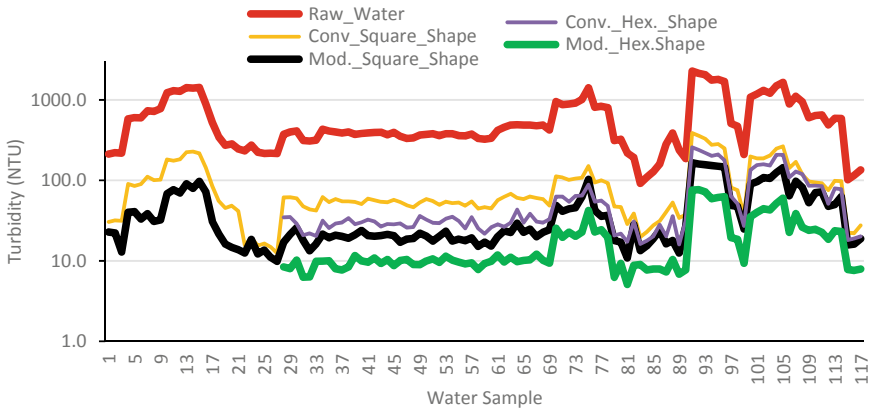


Fig. 4 Comparison between turbidity remained by conventional & modified square & hexagonal shape tube

Figure 2 shows the comparative analysis of conventional & modified square shape tubes settlers. For the above graph, it comes in picture that, the modified square tube settlers are more effective than the conventional square shape. The raw water turbidity is in tune of 1200 NTU (Red Color) which can bring down to range of 50–60 NTU by conventional tubes (Yellow Color) and in range of 20–25 NTU by modified square shape tubes (Black Color).

Figure 3 shows the analysis of hexagonal shape tubes (conventional & modified). In this graph the turbidity remained in water by use of conventional tube shown with purple color line is in tune of 30–40 NTU wherein by use of modified tube turbidity remained in range of 10–20 NTU (Green Color).

The overall comparison between all four cross-sections viz. conventional, modified square and hexagonal shape tubes. The overall performance is depicted from the above graph in which both modified tubes i.e. square & hexagonal shapes performed well in comparison with conventional shapes. In view of modified cross-sections modified hexagonal proven to be very much effective (Shown with green color line). The remaining turbidity will be removed in the next process of water treatment, i.e. filtration process.

6 Critical Performance Parameter

The critical performance parameter for tube settler is given by

$$S_c = \frac{V_{Sc}(\sin\theta + L_R \cos\theta)}{V_0} \tag{7}$$

where

- V_{Sc} = Critical settling Velocity of particle (m/d)
- V_0 = Velocity of flow of water through tube (m/d)
- θ = Angle of inclination of tube.
- L_R = Relative Length of tube settler = L/D (Ratio up to 20).
- L = Actual length of tube (m).
- D = Diameter of tube (m).
- The values of critical performance parameter for.
- Circular tube = 4/3 (1.33).
- Square tube = 11/8 (1.375).
- Parallel plate = 1 (1).

The relative length may be increased by an amount L' on account of transition zone at inlet. It can be determined as

$$L' = 0.058 \frac{V_0 \cdot D}{\nu} \tag{8}$$

where

- ν = Kinematic Viscosity of fluid.
- So,

$$S_c = \frac{V_{Sc}}{V_0} \left[\sin\theta + \left\{ \frac{L}{D} - 0.058 \frac{V_0}{\nu} \right\} \cos\theta \right] \tag{9}$$

The above Eqs. 8 and 10 are used for determination of critical performance parameter for given shapes [15].

Table 1 Details of critical performance parameter for hexagonal shape for 1200 kg/m³ Density

Details	Symbol	Unit	Value
Acceleration gravity	g	m/s ²	9.81
Particle density (Assumed Value)	ρ_s	kg/m ³	1200
Water density	ρ	kg/m ³	1000
Particle diameter	d	m	0.0001
Fluid dynamic viscosity	μ	Ns/m ²	8.9E-04
Particle settling velocity	V _{sc}	m/d	105.81573
Velocity of flow	V _o	m/d	2304
Angle with horizontal	θ	degree	60
Act. Length of tube	L	m	1
Dia./ Width of tube	D	m	0.062
Relative length (up to 20)	LR	L/D	16.1290323
Critical Parameter for Hexagonal shape	Sc	–	0.41

In this study the critical performance parameter for hexagonal shape is given on the basis of observation taken during study.

Following Table 1 shows the details of particle settling velocity.

The critical performance parameter evaluated by considering the particle density and width of tube. In case of given hexagonal tube shape (0.031 m side), the width of tube is 0.062 m and hence for 1200 kg/m³ particle density, Sc value is calculate as 0.41 likewise by changing the values.

7 Discussion and Conclusion

The modified tubes are proven better than the conventional shapes. The turbidity remained is in tube of 10–20 NTU by modified hexagonal shape and hence can be considered for application in treatment plant. The filtration unit is required after this unit, because turbidity should be less than 5 NTU and can bring below that by using filtration process. The places like small communities, fair, camps, etc., where raw water turbidly is no bar then these tubes can be used directly for settling purpose. The critical performance parameter is determined for hexagonal shape and can be used for further research work.

References

1. A. Hazen, On sedimentation. Trans. ASCE **53**, 63 (1904)
2. T.R. Camp, Sedimentation & the design of settling tank. ASCE **111**, 895 (1946)
3. S.P. Hansen, G.L. Culp, Applying shallow depth sedimentation theory. J. AWWA **59**, 1134 (1967)
4. G. Culp, S. Hansen, G. Richardson, High Rate Sedimentation in water treatment works. J. Am. Water Works Assoc. **60**, 218 (1968)
5. J.W. Thomas, Gravity settling of particles in a horizontal tube. J. Air Pollut. Control Associat. **8**(1), 32 (1958)
6. F.C. McMichael, Sedimentation in inclined tubes and its application for the design of high rate sedimentation devices. J. Hydraul. Res. **10**(1) (1972)
7. K.M. Yao, Theoretical study of high rate sedimentation. Jour. Water Pollut. Cont. Fed. **42**, 213 (1970)
8. K.M. Yao, Design of high-rate settlers. J. Env. Eng. Div. ASCE. **99**, 621, (1973)
9. A.G. Bhole, Field performance of modified tube settler unit. J. IWWA, 17–20 (1996)
10. K. Eshwar, Role of flow through velocity in tube settler. J. IWWA, 87–91 (1981)
11. T. Viraraghavan, Tube settler theoretical & design consideration. J. IWWA, 194–198 (1973)
12. A. Gurjar, Performance study of tube settlers module. Int. J. Eng. Res. Appl. 52–55 (2017)
13. M.P. Bhorkar, Application of modified tube settler to improve sedimentation process. ASCE, 28–37 (2018)
14. A.G. Bhole, A text book on “Design of Water Treatment Plant” Published by IWWA (2006)
15. G.M. Fair, J.C. Geyer, D.A. Okun, *Elements of Water Supply and Waste water Disposal*. 2nd edn. (John Wiley and Sons, Inc. New York) (1971)

Climate Change: Understanding the Frail Associations Between Scientific Evidence and Public Perception



A. Arun Kumar, Sanjeev Kumar, Ramesh Krishnamurthy,
and Vandana Rani

1 Introduction

The general public's awareness and understanding of climate change and global warming have been debated and appraised since the 1980s [4, 7]. Over the years, studies show considerable progress regarding what people know about climate change. Nevertheless, there are misperceptions around the topic, and several kinds of research have been conducted to improve the effective communication of science-backed climate information to the general public [17]. Although, much of the scientific focus has been given to understanding climate change science, very few efforts have been spent in educating people and to comprehend how they see and perceive the causes and impacts of climate change at the local scale [5]. Since India has a centralized federal system that has a significant role in policymaking and implementations, most of the Indian climate policies show a strong emphasis on national-level strategies and adaptations [1, 2, 8, 15]. However, emerging literature highlights the importance of developing subnational and local policies on climate actions and their implementation along with the national policies [9, 13]. Though, climate change is largely seen as an important issue that needs society's addressing but, is often considered as a distant problem from common person's everyday lives [21]. Most public engagement on climate action fails owing to this emotional disconnect of people from the issues pertaining to climate change at the local scale [25]. Finding methods to reduce psychological and emotional disconnect and to improve public awareness of climate change impacts are the key research and policy objectives in recent times

A. Arun Kumar (✉) · S. Kumar
Graphic Era (Deemed to be University), Dehradun, Uttarakhand, India

R. Krishnamurthy
Wildlife Institute of India, Dehradun, Uttarakhand, India

V. Rani
Army Pre-Primary School, Chandigarh, India

[10, 22]. Although most people are conscious of “Climate Change”, it is only the majority of those in the meteorological sciences understand the concept of climate change [20]. Similarly, [12] argued that effective and informed scientific policies on climate action can be formulated by the understanding of public perceptions and level of understanding about climate change issues.

Understanding how people apprehend information on climate change and what inspires them to take individual action to respond to climate change has key relevance in designing and implementing effective climatic policies [6]. A substantial volume of studies has been carried out on largescale public opinion surveys from developed nations in the Americas and Europe. And these studies help in differentiating views, attitudes, depth of understanding, and apprehension among a diverse set of populaces [3, 14, 16]. It is apparent that numerous researches have been conducted to understand the science behind climate change and to recognize the cause, impact, and mitigation tactics [23], but still the public perception about this development is still at its infancy, at least in the developing countries. People’s awareness of climate change could be the most important influence on their readiness to accept the scientific inferences on climate change effects [18]. And this could encourage to adapt to climate-positive behavior, which would aid in the designing and implementation of approaches to tackle the climate change effects. This study will provide new information on public perception of climate change and other environmental issues. Besides, the survey will identify the significant incentives for and challenges to climate-conscious behavior. The results should also shed light on the gaps in the mass media on disseminating climate change related information.

2 Method of the Study

For this survey, we have used a combination of qualitative and quantitative methods to assess people’s perception of climate change. A random quantitative survey was conducted, and a set of qualitative methods were conjointly applied to get a full understanding of people’s insights. A structured survey form was designed based on the survey followed by Whitmarsh, 2005 to gauge public consciousness and awareness of climate change in the Indian Himalayan State of Uttarakhand. The survey was conducted online, and one hundred and sixty respondents took the survey until August 2020 from all over the state. The respondents were requested to fill out the online form and to provide a response to each of the queries. The survey form comprised of 22, largely close-ended queries, categorized into 2 sections. The first section focused on socio-demographic details of the participants, such as their age, sex and education level. The second section explored the perception of changes in the environment and participants’ familiarity with the climate change actions. Further, this section analyzed whether participants thought about the environment and climate change before making everyday choices, as well as their incentives and barriers to environmental- and climate-friendly behavior.

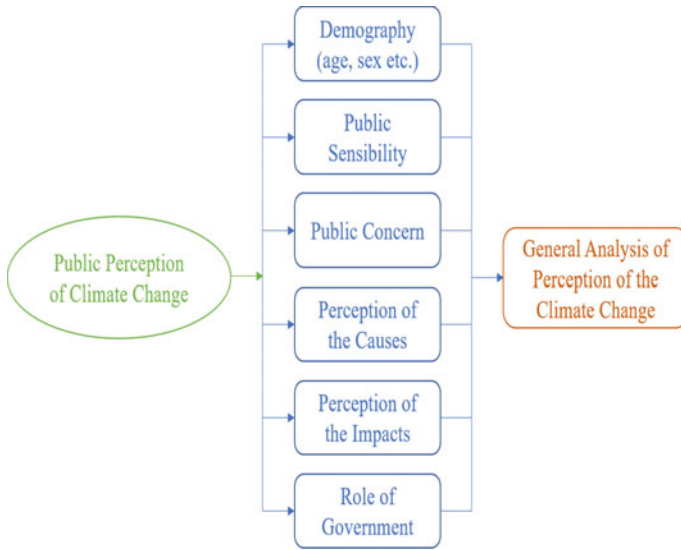


Fig. 1 Research framework

We conjointly collected answers about the participants’ comprehension of climate change, their favored sources of the climate information, their personal observations on changing climate. Aside from the first section, most of the queries were of a multi-response type and had fields accessible for added comments. The form was hosted on the Google Forms platform, as this provides automatic analysis and insights into the answers provided by the participants [11]. the general public was invited to participate through social networking sites including Facebook and Twitter.

The research framework of this study is to analyses the public awareness, concerns, their understanding of the causes and impacts of changing climate and their response to climate change (Fig. 1).

3 Results and Discussion

3.1 First Part of the Survey Form: Demographic Information

A total of one hundred and sixty respondents participated in the online survey. Figure 2 shows the basic demography of the respondents. Of the respondents, 47.5% were male, while 51.9% were female. 58.9% of the respondents were falling in the age group of 25–50 years old, 35.43% between 18 and 25 years old, 1.9% were between 10 and 17 years old and 3.8% were above 50 years old. Concerning educational qualification, 57.6% of the respondents reported they have master’s degree

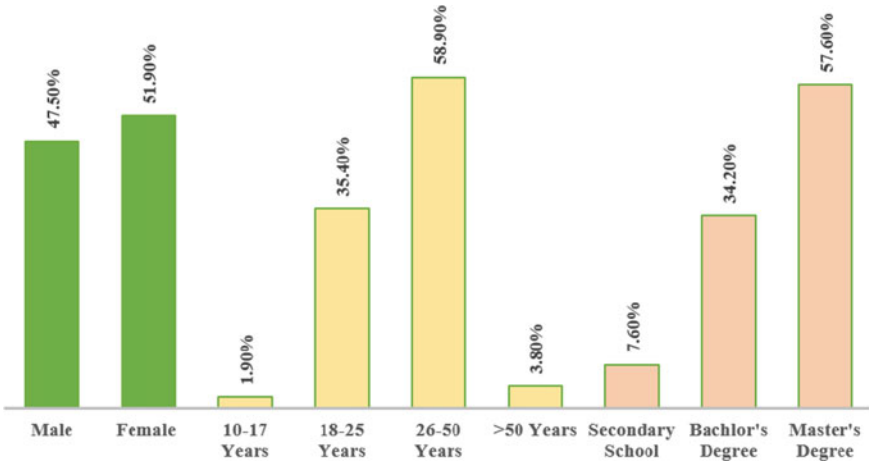


Fig. 2 Basic demographic information of the respondent

and 34.2% with bachelor’s degree, and 7.6% accomplished secondary level education. 0.6% of the respondents had no formal education. This indicates that the major percent of the respondents were educated and between the young and middle age groups. This might be justified by the fact that Uttarakhand has an average literacy rate of 76.31% [24].

3.2 Second Part of the Survey Form: General Questions About the Environment

The first part in the form deals with basic general knowledge about environmental and issues around climate change. Although there are numerous environmental issues when asked to rate the issues that concern the respondents the most, the results (Table 1) show the respondents are most concerned about air pollution (67.90%), poor waste management (62.90%), and water pollution (53.50%). Interestingly not many people

Table 1 Most concerning environmental issues

Q. 8. What are the environmental issues that concerns the most?	
Air pollution	67.90%
Poor waste management	62.90%
Pollution of rivers and seas	53.50%
Climate change	48.40%
Overpopulation	45.90%
Extinction of species	21.40%

are very concerned about climate change (48.40%), overpopulation (45.90%), and extinction of species (21.40%).

The results also revealed that 95% of the participants agreed that they are aware of the term “Climate Change” and some basic scientific knowledge on the subject while the remaining 1.9% indicated that they have not heard the term, whereas the rest 3.1% was not sure. Most of the respondents (94.3%) agreed that that the pattern of weather has changed. While only 5% believe that the weather pattern has not changed remaining 0.6% were not sure of it.

3.3 Third Part of the Survey Form: Perception on Climate Change

When the respondents were asked about possible causes of climate change, most of them (74.8%) agreed it is the combination of human activities and natural processes, wherein 54.1% relates climate change directly to human activities including agriculture activities and industries (Fig. 3).

Most of the respondents (87.4%) agreed that climate change might have serious consequences on their lives and 85.5% of them believe in curtailing the effects of climate change through climate actions. Of these respondents, most of them are convinced that climate change will lead to catastrophic implications including flood, desertification, and drought (Fig. 4).

In the form, the respondents were asked about who they sense to be responsible for responding to climate change, and the results are shown in Fig. 5. The results show 78% of respondents agree that individual actions play an important role in response to climate change, followed by the national government (59.7%) and local government (54.7%). Interestingly, only 40.9% of respondents felt businesses and industries play a major role in responding to climate change.

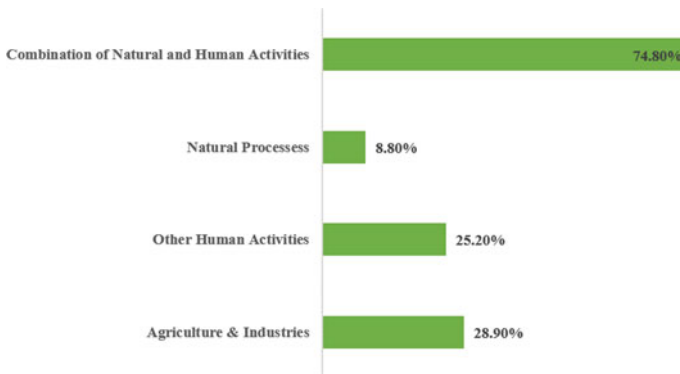


Fig. 3 Possible causes of climate change

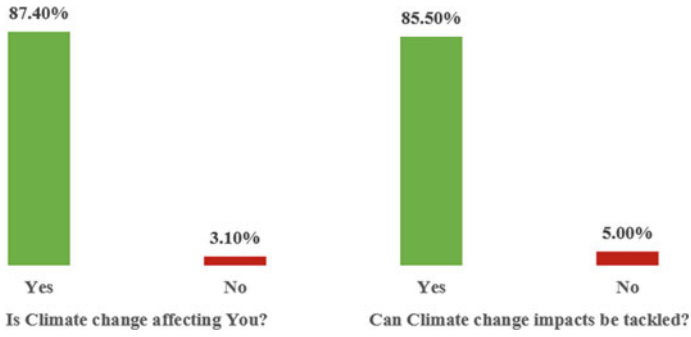


Fig. 4 Climate change impacts

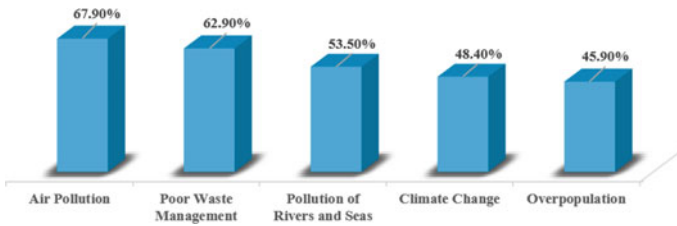


Fig. 5 Responsible for climate action

3.4 Fourth Part of the Survey Form: Climate Change Information

The different climate information sources the respondents preferred are shown in Fig. 6. The figure shows that the most widespread information source on climate

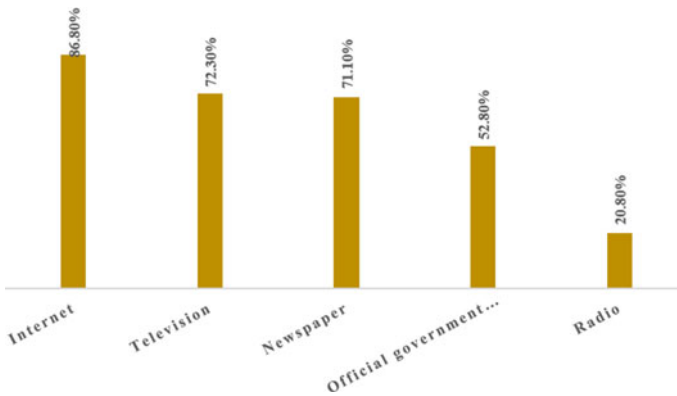


Fig. 6 Sources of climate information

Table 2 Trusted source for climate information

Q. 12. How much do you trust information about climate change if you heard it from?					
	A lot	A little	Not very much	Not at all	Cannot decide
A. A family member / friend	18.87	59.75	17.61	1.89	1.89
B. A Scientist	87.42	8.18	2.52	1.89	0.00
C. Government Agencies	43.40	38.99	15.72	1.26	0.63
D. Newspaper	38.99	42.14	18.24	0.63	0.00
E. Internet	46.54	38.36	13.21	1.89	0.00

change is the Internet (86.8%). Then comes Television where 72.3% of the samples have pointed out and the Newspaper with 71.1%. At the bottommost of the information source is Radio (20.8%) followed by official government sources and environmental agencies (52.8%). When the respondents were asked who they would consider as a trusted source for climate information (Table 2), 59.75% said they would trust a little if the climate information is shared by a family member or a friend. Whereas if the information is from a scientist 87.42% of the respondents said they trust the information a lot. Remarkably, the responses show that the public view is to not strongly trust when the information is shared by the government agency or by newspaper and over the Internet.

3.5 Fifth Part of the Survey Form: Climate Change Action

In this part, various climate-conscious actions that may be undertaken to reduce the impacts of climate change were asked to be rated by the respondents. Most of the individuals surveyed (65.6%) are in agreement that they take regular action out of concern for climate change, whereas 19.1% aforesaid they never took any action and 15.3% weren't sure about any actions. The overwhelming majority of the respondents stated they recycle to protect the environment (60.49%); buy organic food for health reasons (45.83%); buy energy-efficient light bulbs to protect the environment (43.29%); turn off the unused lightbulbs to protect the environment (37.13%); use public transport as a result of its convenience (36.82%), and walk or cycle to work attributable to the health reasons (Fig. 7).

The following Table 3 shows the general trends of responses on the questionnaire and the questions are adopted from Whitmarsh and Özdem et al. [19, 26].

From the responses we received for the above questions, it is very evident that most of the participants believe that individual actions matter against climate change (78.48%); reducing their energy consumption will limit the climate change effects (50.63%). 42.41% of the respondents settled that climate change is going to be catastrophic and 48.73% of them agreed that climate change is something that frightens them. Of the participants 66.46% strongly believed climate change to be a real problem and agreed that humans are abusing the planet (60.13%), they also

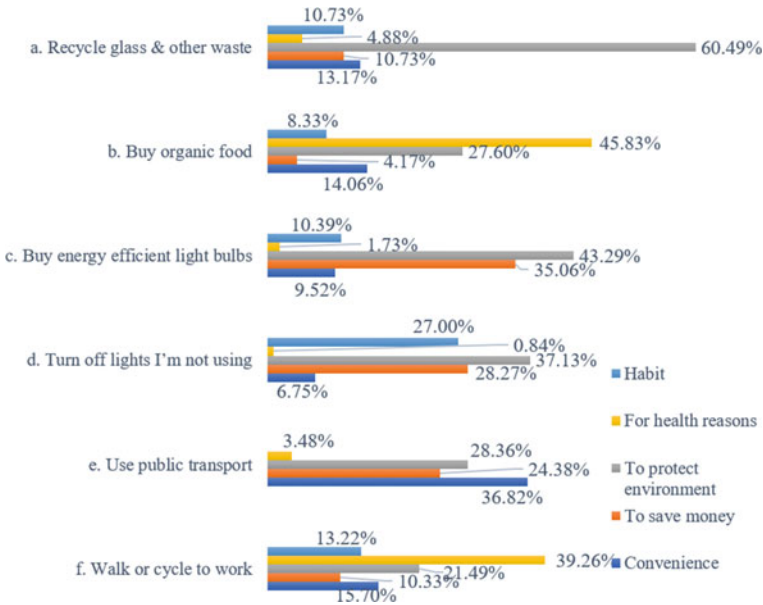


Fig. 7 Climate change actions

strongly believe that all lifeforms have the same rights as humans to exist on the Earth (74.05%).

4 Conclusion

Regardless of being a country with an ambitious Intended Nationally Determined Contribution (INDC) commitments to influence global climate actions, reinforced by plans and programs, the common people of India are not aware of these strategies and in most cases are not been included in these plans. Despite being well aware of the term ‘climate change’, the common people and the stakeholder’s understanding of what causes the climate to change and what will be effects of changing climate, varied widely. Regardless of the common populace’s varied understanding of climate change science, the study found people are highly aware of the consequences of changing climate. The survey outcomes are relatively important not just for evaluating the current state of society’s awareness concerning climate change in the Indian Himalayan state of Uttarakhand but also to enhance the awareness campaigns on other environmental issues in general. Furthermore, this study provides baseline data to the policymakers with regard to the climate change awareness and perception among the general public in Uttarakhand. Consequently, relevant stakeholders will use these results to direct the future climate action strategies and climate information policies for efficient and constructive adaption and mitigation processes.

Table 3 General trends of responses on the questionnaire (%)

Questions	Agree strongly	Agree	Neither agree nor disagree	Disagree	Can't choose
1. Can individual action reduce the effects of climate change?	78.48	18.99	1.27	1.27	0.00
2. Climate change is inevitable because of the modern development	25.95	43.67	15.82	14.56	0.00
3. Climate change is just a natural fluctuation in earth's history	8.86	17.09	29.11	40.51	4.43
4. Energy consumption reduces climate change	50.63	34.18	12.66	1.90	0.63
5. Incentives should be given to people who take up climate actions	43.67	36.08	13.92	5.06	1.27
6. I would do take up climate actions only if everyone else did the same	18.35	20.89	12.66	43.04	5.06
7. Humans have no significant impact on the globe	8.23	7.59	22.15	53.80	8.23
8. Climate change is something that alarms me	32.91	48.73	13.92	3.80	0.63
9. Developing countries are to be blamed for climate change	17.09	31.65	29.11	18.99	3.16
10. Leaving the lights on when not in use adds to climate change	33.54	43.67	16.46	1.27	5.06
11. The climate change effects are likely to be catastrophic	37.34	42.41	12.03	1.90	6.33
12. I cannot change the outcome of climate change one way or another	2.53	16.46	27.22	46.20	7.59
13. Industrial pollution is the main cause of climate change	27.22	52.53	15.19	5.06	0.00
14. Do you believe that climate change is a real problem	66.46	24.68	6.96	1.90	0.00
15. The government is not doing enough to intercept climate change impacts	33.54	37.97	21.52	6.33	0.63
16. Humans are severely abusing the natural resources	60.13	28.48	7.59	3.80	0.00
17. All life forms have the same rights as humans to exist on the Earth	74.05	18.35	5.06	1.90	0.63
18. The balance of nature is highly dynamic and easily gets disturbed	43.67	38.61	11.39	5.06	1.27
19. Nature is strong enough to cope with the unchecked human activities	15.82	24.05	24.05	32.28	3.80

Although media has immense potential to bring change in the society, the current study reveals a lost opportunity in triggering actions and decisions from the public and decision-makers. While the media depends on the government as the main source of information, the government's climate actions don't involve individuals' actions on the ground, thus failing to stimulate adaptation and mitigation from the bottom up. This gap is even more evident in the academia, where although there is a growing number of publications on climate science, only small efforts have been made to translate scientific publications to communications that are accessible to the public and that attract the attention of media. This calls for more research in the areas of translating the climate communication strategies and improving the efficiency of the communications that emerge from the government and academia.

The study also recommends collaboration and partnerships between various relevant stakeholders as an essential constituent of the climate change mitigation and adaptation process. The partnership will help build powerful movements and innovative solutions needed to overcome the climate challenges and ensure the involvement of common people in the climate change mitigation and adaptation plans right from the development phase. In addition, climate change science and sustainable environmental practices should be incorporated into the school and universities' course curriculum. If the individuals are well informed on climate change effects that would reassure the people to accept and act on the government's mitigation and adaptation strategies. Also, this knowledge will motivate the general public to adhere to climate positive and sustainable behavior that would help achieve sustainable socioeconomic and environmental management.

Acknowledgements The authors are thankful to all the researchers and authors whose papers are taken as references, to the Wildlife Institute of India and to the Graphic Era Deemed to be University. They are also very much thankful to all the individuals who have taken part in this survey.

References

1. A. Atteridge, M.K. Shrivastava, N. Pahuja, H. Upadhyay, Climate policy in India: what shapes international, national and state policy? *Ambio* **41**(1), 68–77 (2012)
2. K.M. Bahauddin, N. Rahman, M.T. Hasnine, Environmental reviews and case studies: public perception, knowledge, and participation in climate change adaptation governance in the Coastal Region of Bangladesh using the Social Ecological Inventory (SEI) Tool. *Environ. Pract.* **18**(1), 32–43 (2016)
3. R.J. Bord, A. Fisher, E.O. Robert, Public perceptions of global warming: United States and international perspectives. *Climate Res.* **11**(1), 75–84 (1998)
4. R.J. Bord, R.E. O'connor, A. Fisher, In what sense does the public need to understand global climate change? *Public Underst. Sci.* **9**(3), 205–218 (2000)
5. A.S. Buloshi, E. Ramadan, Climate change awareness and perception amongst the inhabitants of Muscat governorate, Oman. *Am. J. Clim. Change* **4**(04), 330 (2015)
6. M. Burke, D. Ockwell, L. Whitmarsh, Participatory arts and affective engagement with climate change: the missing link in achieving climate compatible behaviour change? *Glob. Environ. Chang.* **49**, 95–105 (2018)

7. S. Capstick, L. Whitmarsh, W. Poortinga, N. Pidgeon, P. Upham, International trends in public perceptions of climate change over the past quarter century. *Wiley Interdiscip. Rev. Clim. Change* **6**(1), 35–61 (2015)
8. N.K. Dubash, The politics of climate change in India: narratives of equity and co-benefits. *Wiley Interdiscip. Rev. Clim. Change* **4**(3), 191–201 (2013)
9. N.K. Dubash, A. Jogesh, From margins to mainstream? State climate change planning in India. *Econ Polit. Weekly* 86–95 (2014)
10. P.J. Egan, M. Mullin, Psychology: local weather and climate concern. *Nat. Clim. Chang.* **4**(2), 89–90 (2014)
11. R.J. Haddad, Y. Kalaani, Google forms: a real-time formative feedback process for adaptive learning. In *Proceedings of the 2014 ASEE Annual Conference & Exposition, Indianapolis, IN*, age (Vol. 26, No. 11) (2014)
12. J. Hansen, M. Sato, R. Ruedy, Perceptions of climate change: the new climate dice. National academy of sciences. PNAS Early Edition. <http://www.pnas.org/content/early/2012/07/30/1205276109> (2012)
13. K. Jörgensen, *The Role of the State Laboratories in Multi-Level Climate Policy Research—Considering India* (University of Berlin, Germany, 2012)
14. A. Leiserowitz, E. Maibach, C. Roser-Renouf, N. Smith, *Climate Change in the American Mind: Americans' Global Warming Beliefs and Attitudes* (Yale University and George Mason University, Connecticut, USA, 2010)
15. K. Michaelowa, A. Michaelowa, India as an emerging power in international climate negotiations. *Clim. Policy* **12**(5), 575–590 (2012)
16. S.C. Moser, Toward a deeper engagement of the US public on climate change: an open letter to the 44th president of the United States of America. *Int. J. Sustain. Commun.* **3**, 119–132 (2008)
17. E. Moxnes, A.K. Saisel, Misperceptions of global climate change: information policies. *Clim. Change* **93**(1–2), 15 (2009)
18. O. Ohwo, Public perception of climate change in Yenagoa, Bayelsa State, Nigeria. *Geogr. J.* **4**, 139–142 (2015)
19. Y. Özdem, B. Dal, N. Öztürk, D. Sönmez, U. Alper, What is that thing called climate change? An investigation into the understanding of climate change by seventh-grade students. *Int. Res. Geograph. Environ. Edu.* **23**(4), 294–313 (2014)
20. P.A. Pam, Climate change and the information technology. *J. Sci. Technol.* **5**(1), 64–80 (2007)
21. N. Pidgeon, Public understanding of, and attitudes to, climate change: UK and international perspectives and policy. *Clim. Policy* **12**(sup01), S85–S106 (2012)
22. J.P. Reser, G.L. Bradley, M.C. Ellul, Encountering climate change: 'seeing' is more than 'believing.' *Wiley Interdiscip. Rev. Clim. Change* **5**(4), 521–537 (2014)
23. O.V. Rukevve, The science of climate change: Implication for Africa. *J. Arid Environ.* **7**(1), 72–85 (2008)
24. School Education–Govt of Uttarakhand, <https://schooleducation.uk.gov.in>, last accessed 2020/07/12
25. A. Spence, W. Poortinga, N. Pidgeon, The psychological distance of climate change. *Risk Anal.* *An Int. J.* **32**(6), 957–972 (2012)
26. L.E. Whitmarsh, A study of public understanding of and response to climate changing the South of England [Unpublished Ph.D thesis]. University of Bath (2005)

Comparative Analysis of MIVAN Formwork and Conventional Formwork



Prakash Patil and Palash Mundhada

1 Introduction

MIVAN construction is firstly introduced in 1990 by a European construction company, MIVAN Ltd., with a view to providing a decisive system for mass construction in developing countries like India.

MIVAN is designed (design and engineered) in aluminum formwork for constructing monolithic structures. In this system, walls, beams, columns, and slabs are cast together in a well-ordered manner. The finish work obtained from MIVAN is good and hence requires no plasterwork, which is best suited for mass constructions and conditions like India. This construction technology can substantially increase the productivity of construction, quality, and durability of creation by using dynamic construction tools and materials, thus saving the cost compared to the conventional method.

This imperative study provides important information on total building cost and per sq.m cost of construction comparison between the conventional method and MIVAN technology, where economy, manpower, and material play a vital role.

2 Literature Review

- Kapoor [1] concluded that MIVAN construction requires less time and cost to complete construction as compared to conventional brickwork construction. In

P. Patil (✉)

G. H. Raisoni College of Engineering, Nagpur 440016, India

e-mail: prakash.patil@raisoni.net

P. Mundhada

Palash Mundhada, Mathilakath Creations Pvt. Ltd., D-Hosahally, Karnataka, India

this construction, there is no requirement of plastering as aluminum formwork will provide a better finish surface than conventional brickwork construction.

- Khan [2] describes, in brief, the need for MIVAN formwork in the Indian construction industry. They describe the comparative analysis of conventional formwork and MIVAN formwork on the basis of cost, quality, and strength parameters.
- Prathul [3] compared the construction productivity of conventional formwork and MIVAN technique. They concluded that conventional formwork is best suited for small-scale construction where it can be molded into different shapes without many repetitions. MIVAN formwork is best suited for large-scale construction with typical floors where the number of repetitions is high.
- Gulghane [4] concluded that construction by using MIVAN technology is quite cheaper than the conventional method and saves about 12.5% of the total cost. Many finishing works are saved like plastering, brickwork, etc. The advantage of MIVAN includes higher durability of material, uniform quality of construction, low maintenance of formwork, and speedy work.

3 Objectives

- a. Literature study—Current Condition Assessment in the construction industry
- b. Comparison of MIVAN and Conventional Shuttering on the basis of the cost of material and labor requirement.
- c. Material, Man-Power, Time and cost analysis
- d. To obtain the Break-Even Point

4 Theoretical Aspect

1. Setting up the wall reinforcement steel – The wall reinforcing with steel is used to give a structure to the building and support the concrete until they gain half of the required strength. The aluminum formworks are cast around the steel mesh, which is factory made and directly erected on the construction site (Fig. 1).
2. Placement of aluminum formwork—Along the wall reinforcing steel, prefabricated room-sized walls and floor slabs are erected. Spaces for windows, ducts, doors and other features such as staircases, façade panels, loft slabs (kitchen counter slab with supporting walls) and chajjas are also integrated into these structures (Fig. 2).
3. Pouring of concrete—After casting the forms, high-quality concrete is poured such as SCC type concrete with good and acceptable flow rates specially designed with a rich mix (Fig. 3).



Fig. 1 Wall reinforcement

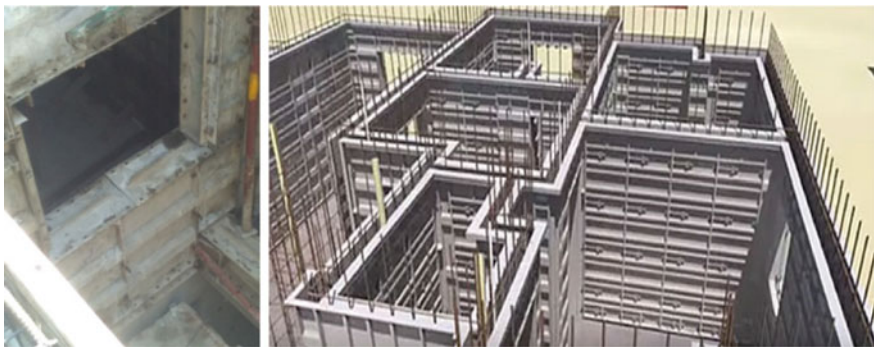


Fig. 2 Aluminum Formwork



Fig. 3 Pouring of concrete

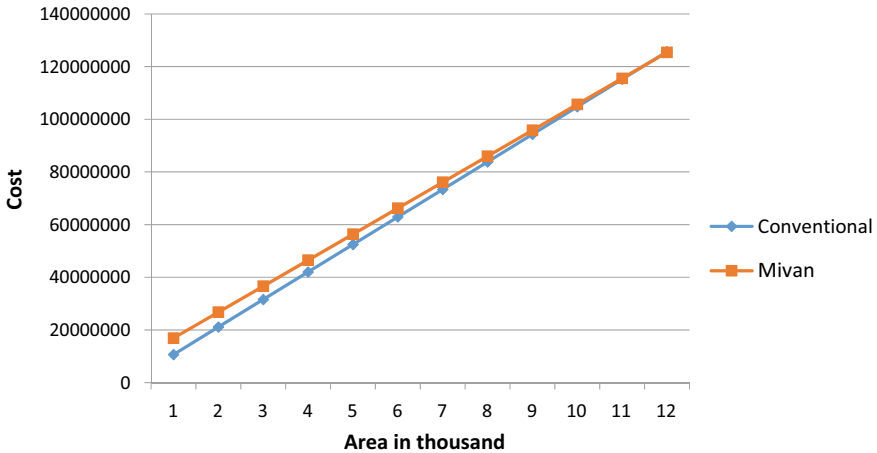


Fig. 4 Comparison between Conventional and MIVAN

5 Methodology Adopted

1. Collecting the data; material cost (Shuttering material, Cement, Sand, Concrete, Reinforcement, etc.), Labor cost (Carpenters, Mistri, bar-benders, etc.).
2. Calculating the cost of construction for conventional shuttering including labor and material cost for every 50 sq.m.
3. Calculating the cost of construction for MIVAN shuttering including labor and material cost for every 50 sq.m.
4. Comparing the cost of construction for conventional and MIVAN shuttering.
5. Determining the area of construction at which the cost of construction is same in the conventional type of construction and through MIVAN, called as Break-Even Point.

6 Result

See Figs. 4, 5, 6, 7 and 8, Tables 1 and 2.

7 Conclusion

Economy is the key aspect of any construction. From the above data, it is concluded that with the increase in the area of construction the cost of MIVAN formwork is gradually decreasing. It can be seen that the cost of construction with MIVAN and

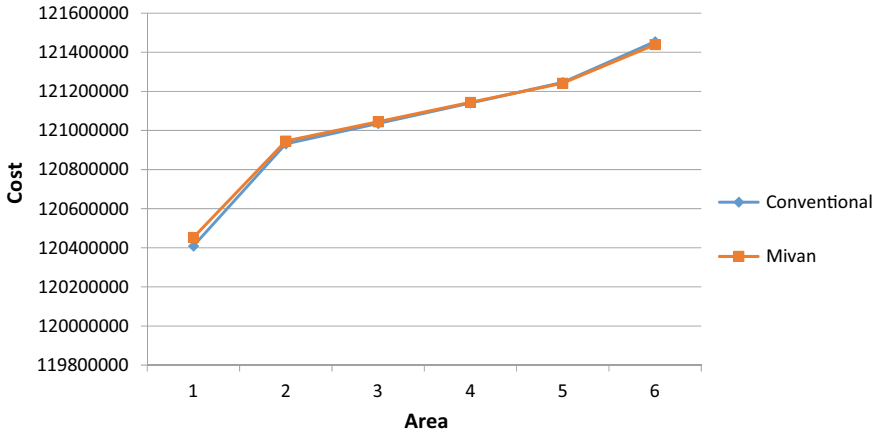


Fig. 5 Comparison between Conventional and MIVAN for Break-Even Point

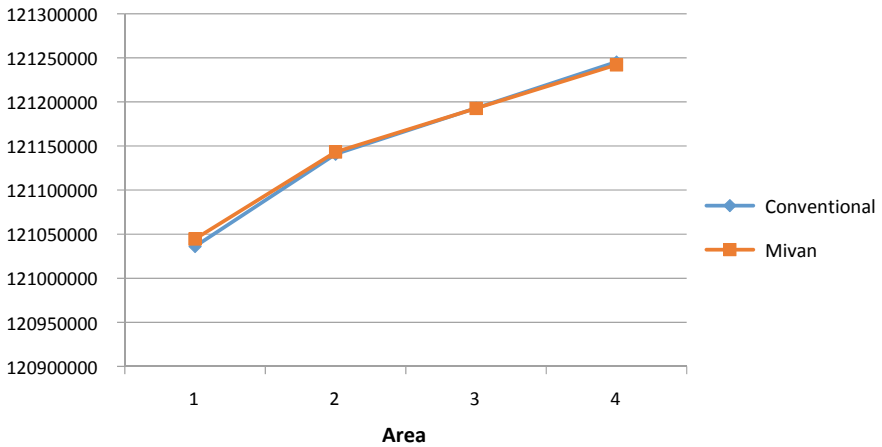


Fig. 6 Comparison between Conventional and MIVAN for Break-Even Point

conventional formwork is almost the same at 11,575 sq. m, it is also observed that conventional formwork is suited for small construction whereas MIVAN is best suited for mass and repetitive construction.

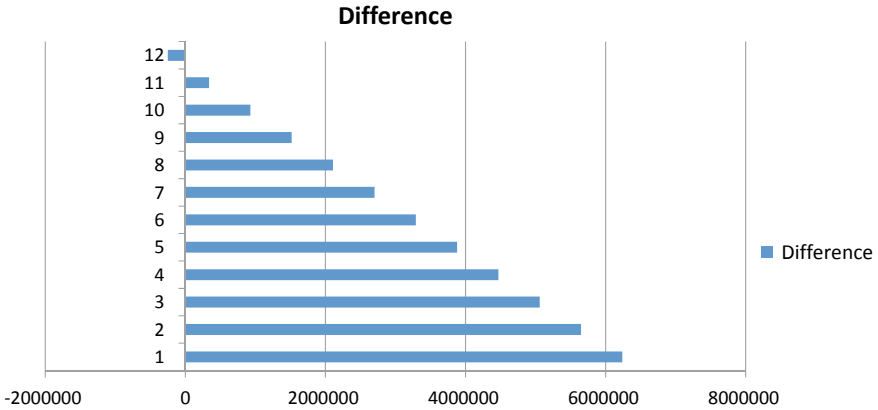


Fig. 7 Difference between Conventional and MIVAN

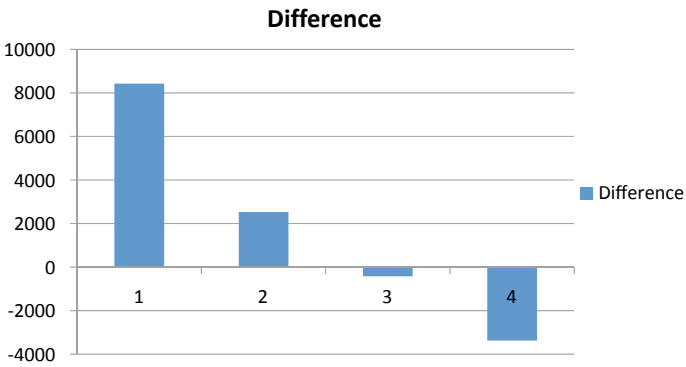


Fig. 8 Difference between Conventional and MIVAN for Break-Even Point

Table 1 Required area of scaffoldings

AREA m ²	Grand total (Conventional)	Grand total (MIVAN)	Difference
1000	10,625,555.33	16,865,454.1	6,239,898.77
2000	21,081,110.67	26,730,908.21	5,649,797.54
3000	31,536,666	36,596,362.31	5,059,696.31
4000	41,992,221.33	46,461,816.41	4,469,595.08
5000	52,447,776.66	56,327,270.51	3,879,493.85
6000	62,903,331.99	66,192,724.62	3,289,392.63
7000	73,358,887.32	76,058,178.72	2,699,291.4

(continued)

Table 1 (continued)

AREA m ²	Grand total (Conventional)	Grand total (MIVAN)	Difference
8000	83,814,442.65	85,923,632.82	2,109,190.17
9000	94,269,997.98	95,789,086.92	1,519,088.94
10,000	104,725,553.3	105,654,541	928,987.7
11,000	115,181,108.6	115,519,995.1	338,886.5
12,000	125,636,664	125,385,449.2	-251,214.8

Table 2 Required area of scaffoldings

AREA m ²	Grand total (Conventional)	Grand total (MIVAN)	Difference
11,500	120,408,886.3	120,452,722.2	43,835.87082
11,550	120,931,664.1	120,945,994.9	14,330.80928
11,560	121,036,219.6	121,044,649.4	8429.79697
11,570	121,140,775.2	121,143,304	2528.784662
11,580	121,245,330.7	121,241,954.7	-3376.035338
11,600	121,454,441.8	121,439,267.6	-15,174.25226

References

1. A. Kapoor, S. Upadhyay, D.P. Chauhan, A. Dohare, Comparison between conventional brickwork construction vs MIVAN construction
2. A.M. Khan, C. Kumar, Impact of MIVAN formwork over conventional formwork (2017)
3. A. Gulghane, N. Pitale, S. Sanghai, Time and cost optimization of construction project using MIVAN technology (2018)
4. H. Chauhan, Dr. K.B. Parikh, Comparison and effectiveness of MIVAN formwork over the conventional formwork (2017)

Study of Indirect Traffic Parameters Along Metro Construction Route



Smita Pataskar and Sunil Pimplikar

1 Introduction

Metro rail is a widely used mass rapid transit system that is gaining popularity in many metro cities in India and abroad. It operates on an exclusive right-of-way (mostly underground or elevated), which is separated from all modes of transport in an urban area. These systems generally operate at an average speed of 20–35 km/h, and carry 50,000–75,000 passengers per hour, per direction with a high frequency of operation. The capital cost of construction is between 20 and 30 times that of the Bus Rapid Transit system, depending on whether the metro systems are underground or elevated [1]. With the consumption of 1/5th of energy per passenger, it carries the same amount of traffic as 5 lanes of bus traffic or 12 lanes of private motor cars (either way). It is more reliable, comfortable, and safer than the road-based system which reduces journey time by 50 and 75% depending on road conditions.

A significant amount of study is done related to the impact of short-term and long-term construction work zones on queue lengths, congestion cost, traffic delay cost, and road user cost. A number of parameters that make an impact on these costs were studied and analyzed using genetic algorithm, simulation tool, neural network, simulated annealing, etc. These studies were based on the parameters that govern the road conditions for short-term or long-term work zones. These parameters are studied through various research works and are represented in the literature survey.

S. Pataskar (✉)
Department of Technology, Savitribai Phule Pune University, Pune, India

S. Pimplikar
Department of Civil Engineering, MIT WPU, Pune, India
e-mail: Sunil.pimplikar@mitwpu.edu.in

2 Literature Survey

Earlier researchers have considered relevant work zone decision variables as work zone segment length, construction start time, use of shoulder, lateral clearance between work zone, and traffic control barriers. The results of the performance evaluation phase were used to generate optimal tradeoffs between minimizing traffic delays and construction cost [1, 2].

A study of three performance measures representative of the level of service (LOS), travel delays, and environmental impacts was done that simulated work zones under various configurations. The results of the analysis provided clear evidence that work zone length is insignificant with respect to facility performance [3].

Impact of metro rail construction work zones on traffic environment and consequently quantify these impacts for the present situation was simulated and total economic losses are calculated for different types of vehicles for elevated metro construction [4].

Traffic Congestability Value (TCV) which is affected by travel time, average speed, and proportion of time stopped for vehicles at different locations are studied in the respective spatial zones and the results were validated in the field [5].

The variables such as number of lanes, percent of heavy vehicles, length of work zone, speed of vehicles, fuel cost, accident rate, and accident cost are evaluated for the work zone model, through correlation analysis, comparison of calculation assumptions, and data input analysis [6].

In a study conducted in the Texas region, capacity and road user cost on freeway work zones were calculated depending upon work intensity, provision of entrance ramp, percent of heavy vehicles, number of open lanes, lateral distance, grade of roads, work duration, weather conditions, average speed, access control, road curvature, and annual average daily traffic [7].

Travel time of each vehicle for traffic delay and queue length are estimated at work zone which depends on original flow rate, space mean speed, traffic density, length of work zone, number of closed lanes, and duration of work zones [8].

Another researcher studies a new freeway work zone traffic delay and cost optimization model which considers the length of the work zone segment, starting time of the work zone using average hourly traffic data, number of lane closures, darkness factor, and seasonal variations in travel demand to calculate the total work zone cost [9].

The delays for different flow levels and different lengths of the reconstruction area were evaluated with the use of a tailored newly developed microscopic traffic simulation model [10].

Effect of work zone configuration, traffic flow, and heavy vehicle percentage are evaluated on traffic delay by using heterogeneous cellular automata (HCA) model, which concludes that transition area length has much greater effect than activity area length on traffic delays [11]. In this paper, apart from these parameters, considering the road conditions in Pune city, more elaborative parameters are studied which affect the speed of vehicles ultimately affecting the delay and road user cost.

Traffic congestion cost is estimated in Karachi which comprises of value of time (based on socio-economic survey from commuters), opportunity cost (based on the value of time, travel delay, number of vehicles, and average occupancy), and vehicle operating cost (based on fuel consumption and fuel price) [12].

A road user cost RUC model is developed based on traffic analysis methods published in the Highway Capacity Manual, which comprises of the value of time VOT, vehicle operating cost VOC, and accident cost AC. The variables studied included the number of lanes, percent of heavy vehicles, length of work zone, speed of vehicles, fuel cost, accident rate, and accident cost. Case studies were compared with two other existing models, the Arizona model and the queue and user cost evaluation of the work zone model, through correlation analysis, comparison of calculation assumptions, and data input analysis [6].

A simple mathematical model was developed [13] to optimize the work zone lengths on four-lane highways where one lane in one direction at a time is closed. The objective was to minimize the total cost, including the agency cost, the accident cost, and the user delay cost by optimizing work zone length. Sensitivity results generated from a numerical example were also presented in this study.

3 Research Study

Pune metro corridor II spans between Vanaz to Ramwadi and the section from Vanaz to Deccan is considered for the study of delay and congestion cost due to its unique characteristics. Reduction in the road width, heavy traffic, route diversions are the major challenges faced along the route of Vanaz to Deccan leading to increased time of travel. Various traffic control measures are implemented to mitigate its effect and at present, it is showing success in its implementation. From Deccan, the metro route is diverted along the river side and hence, there is no disruption to traffic in that zone. From Vanaz to Deccan, there are major intersections identified which affect the time of travel due to lateral entries and the travel time is observed.

Due to the traffic restrictions imposed by the construction of the metro, the following additional parameters are observed which affect the speed of vehicles.

- (a) As metro construction occupies the space at the median of the road for equipment and labor, openings are blocked which otherwise permit the turning of vehicles. This leads to a tendency of riders to travel in the opposite/wrong direction.
- (b) There are vehicles that enter laterally in the cordon lines which decreases the speed. This effect is more in the vicinity of the metro construction sites.
- (c) On-street parking is allowed on major length of the road. Increase in the parking space demand leads to double parking along road side affecting the speed of the vehicles along cordon lines.

- (d) Road traffic is a combination of cycles, two-wheelers, three-wheelers, four-wheelers, light motor vehicles, and heavy motor vehicles. Slow-moving vehicles which travel ahead of the fast-moving vehicles, reduce the speed of succeeding vehicles until the road width is substantial. Hence, in the vicinity of the construction site, where the road width is reduced, slow-moving vehicles affect the traffic at large and speed in particular.

4 Preliminary Survey

In order to study the effect of metro construction on the delay and congestion time at various sections between Vanaz to Deccan (and Deccan to Vanaz), a test vehicle is run for 16 hours from 6 am to 10 pm. The salient features of these surveys are as follows:

- Speed of the test vehicle is maintained between 30 to 35 kmph until the congestion, speed breakers, or crossings are faced. This speed limit is chosen as the metro authorities have suggested to keep the speed in this limit to avoid clashes or accidents on roads.
- All the traffic rules and signals are followed.
- The test vehicle is kept in the middle lane unless the road width is less.
- The metro route under study, is divided into nodes depending upon major intersections. There are 18 nodes identified from the direction of travel between Vanaz and Deccan while there are 16 nodes identified for the route between Deccan and Vanaz. This is due to diversions at two places along the Vanaz-Deccan route. The total length of the travel is found to be 5.566 km from Vanaz to Deccan whereas from Deccan to Vanaz, it is 5.12 km.
- The distances between the nodes are measured from the center point of the intersections. Travel times between the nodes are measured along with the signal stop time. These readings are used to calculate average speeds between the nodes.

5 Data Collection

While the test vehicle is traveling between Vanaz to Deccan and back, video recordings are taken and the data is collected for each run and categorized as per the parameters considered for the study. The methodology and the traffic compositions are given for each parameter as under.

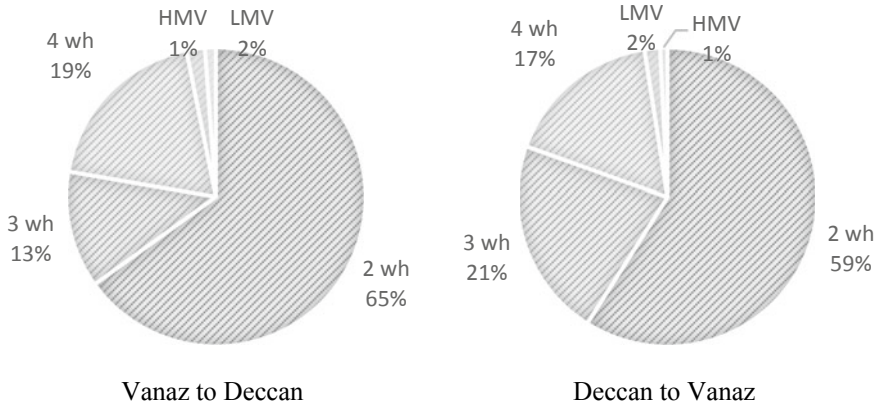


Fig. 1 Composition of types of vehicles in lateral entries

5.1 Lateral Entries at Work Zone

While taking the observations of vehicles in lateral entries, the following points are considered:

- i. Vehicle count is taken when the test vehicle achieves the designed speed.
- ii. Vehicles that are ahead of signals are not counted.
- iii. Vehicles that are immediately ahead of the test vehicle affecting the speed are counted.
- iv. Count is taken for different types of vehicles (Fig. 1).

5.2 Presence of Slow-Moving Vehicles (Speed < Average Speed of Queue)

While taking the observations for this parameter, the following points are considered:

- i. Number of vehicles are counted which travels slowly and could not be overtaken.
- ii. Number of slow-moving vehicles at signals is not considered as all the vehicles are slowing their speeds.
- iii. The vehicles are counted which are slowly moving ahead of the test vehicle and which reduced the speed of the test vehicle in between the consecutive intersections (Fig. 2).

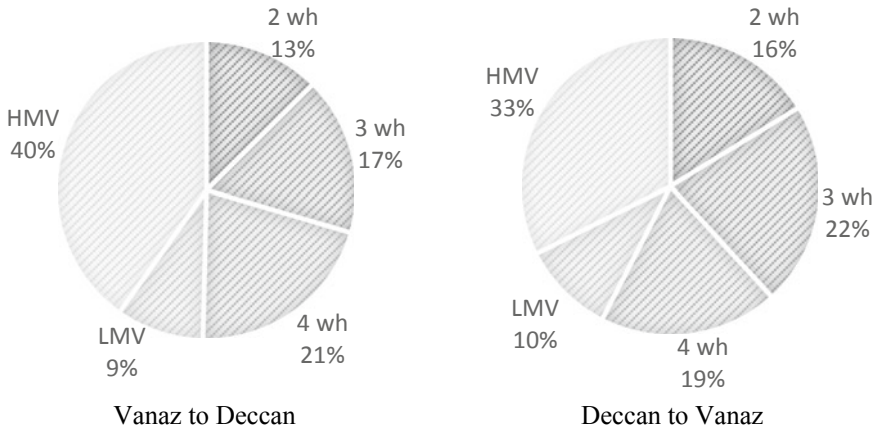


Fig. 2 Composition of slow-moving vehicles

5.3 Vehicles in Wrong Entry

These counts are taken for the vehicles coming in the wrong direction. It is observed that the number of two-wheelers violating the traffic rules is maximum. In general, more vehicles are traveling in the wrong direction from Deccan to Vanaz in the stretch between Gujrat colony and Kothrud Police station (Fig. 3).

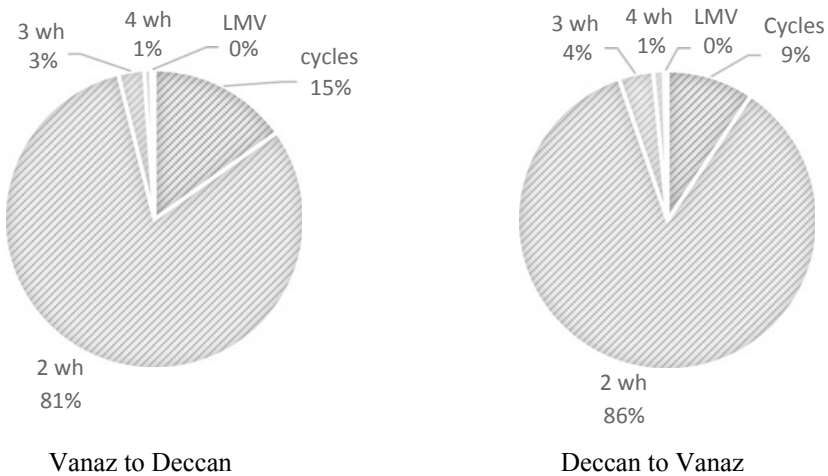


Fig. 3 Composition vehicles in wrong entry

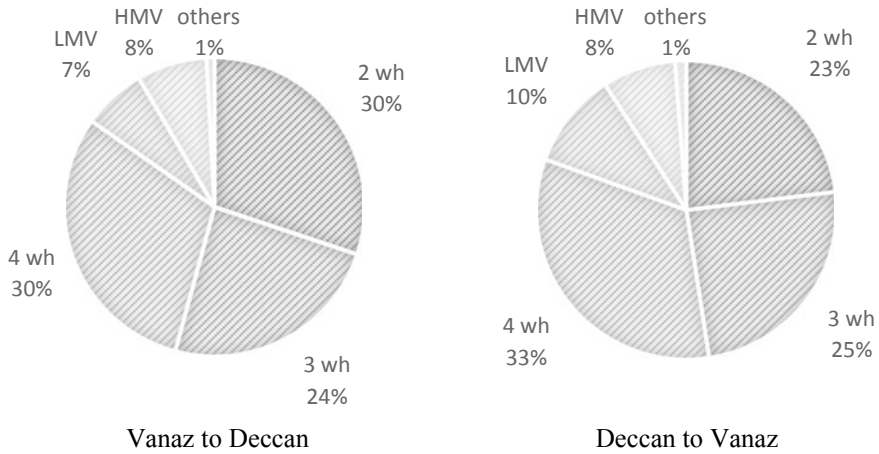


Fig. 4 Composition of parked vehicles near the work zone

5.4 Reduction in Road Width Due to Parking Near Work Zone Areas

While taking the observations, the following points are to be considered:

- i. The stretch from Vanaz to Deccan and Deccan to Vanaz are marked as no parking zone partially. Parked vehicles occupy a width equal to the width of the vehicle in these zones. It varies as per the type of vehicle.
- ii. The count is taken for the vehicles which are standing after these parked lane widths and which occupy the road space reducing the effective road width.

It is observed that.

- i. Two-wheelers, three-wheelers, and four-wheelers occupy maximum parking double spaces in both directions.
- ii. In peak hours, these numbers are maximum (Fig. 4).

6 Data Analysis

Speeds of test vehicle between various time duration of the day are calculated and represented as follows (Fig. 5).

2. The observations are taken for the days before the pandemic and after pandemic situations that arose due to COVID-19 situation. The observations are as follows (Fig. 6).

Average speed calculations of the test vehicle for the periods before lockdown and after lockdown have a significant difference. Also, as the restrictions on societal

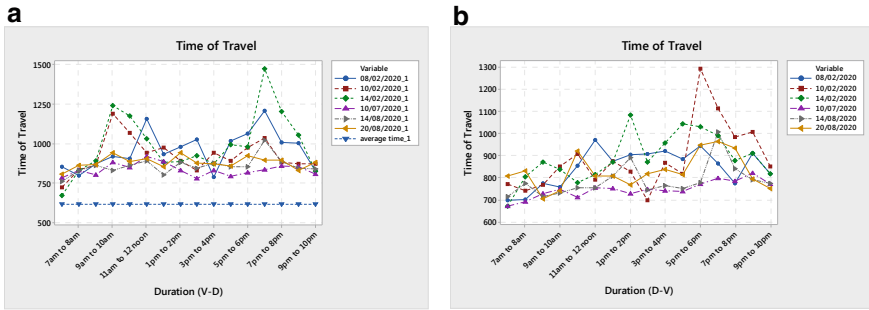


Fig. 5 Speed of test vehicle between **a** Vanaz to Deccan and **b** Deccan to Vanaz

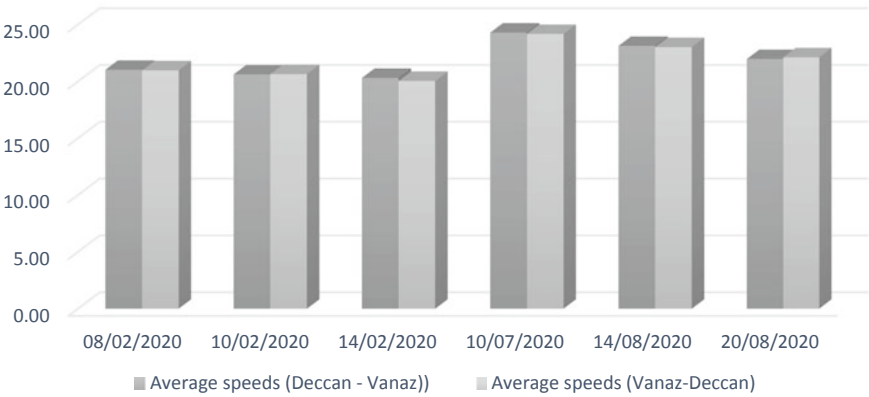


Fig. 6 Average speeds of the test vehicle on various days before and after the pandemic situation

activities are gradually lifted, traffic increased, and hence, the speed of test vehicles decreased.

3. After collecting all the data, PCU factors are applied to the vehicles and the total PCU for sixteen hours is calculated. These are the additional PCUs that are added when a test vehicle is traveling along the metro route. For the conversion of different vehicles in the PCUs, factors recommended by IRC are considered.

The data is tabulated and the correlation between PCU calculations and the speed of vehicles is calculated by the Minitab 17 software and the values are represented as follows.

Table 1 Correlation between PCU and speed of vehicles

	February 8, 2020	February 10, 2020	February 14, 2020
Vanaz–Deccan	−0.25	−0.32	−0.486
Deccan–Vanaz	−0.411	−0.678	−0.797

Table 2 Summary of the composition of types of vehicles for various parameters

	Vanaz–Deccan					Deccan to Vanaz				
	2 wh	3 wh	4 wh	LMV	HMV	2 wh	3 wh	4 wh	LMV	HMV
Vehicles in lateral entry	45	21	26	4	4	38	30	26	3	3
Vehicles in wrong entry	85	12	2	1	0	88	9	2	1	0
Slow moving vehicles	4	14	14	9	59	6	19	14	10	51
Parked vehicles	15	29	30	9	17	11	28	31	14	16

7 Results and Discussions

- (a) From Table 1, it may be concluded that a negative correlation exists between PCU and speed of vehicles on February 10 and 14 (weekdays) between Deccan to Vanaz. On the weekend (February 8), the results show a weak correlation.
- (b) The composition of vehicles for the parameters considered are tabulated as follows (Table 2):

It is concluded from the table that






- i. Due to the higher share on the road, it is obvious that two-wheelers have more percentage which enters into the main traffic followed by three-wheelers and four-wheelers.
 - ii. Due to the size of the vehicles, the tendency of two-wheelers coming in the wrong direction is more as compared to other types of vehicles.
 - iii. Heavy moving vehicles are occupying the maximum width of roads and due to the decreased width of the road, overtaking is not possible. Hence, its percentage is more.
- (c) The double-parked vehicles in addition to the on-street parking space provided are found more for three-wheelers and four-wheelers. Two-wheelers occupy less width and can be parked very closely. Hence, its percentage is less as compared to three-wheelers and four-wheelers.

References

1. D. Mohan, Mythologies, metro rail systems and future urban, transport. *Econ. Pol. Wkly* **43**, 41–53 (2008)
2. A.Z. Abdelmohsen, K. El-Rayes, Optimal trade-offs between construction cost and traffic delay for highway work zones. *J. Construct. Eng. Manag.* ASCE, 05016004–1 to 10 (2016)
3. O.E. Ramadan, V.P. Sisiopiku, Modeling highway performance under various short-term work zone configurations. *J. Transp. Eng. Part A*, 04018050–1–7 (2018)
4. R. Bhutani, Dr S. Ram, Dr K. Ravinder, Impact of metro rail construction work zone on traffic environment. *Transp. Res. Proced.* 586–595 (2016)
5. N. Patel, A.B. Mukherjee, Assessment of network traffic congestion through traffic Congestibility Value (TCV): a new Index. *Bullet. Geogr. Socio-Econ. Series*, 123–134 (2015)
6. Y. Zhu, I. Ahmad, L. Wang, Estimating work zone road user cost for alternative contracting methods in highway construction projects. *J. Construct. Eng. Manag.* 601–608 (2009)
7. D.W. Borchardt, GezaPesti, D. Sun, L. Ding, Capacity and road user cost analysis of selected freeway work zones in texas”, project report, Texas Transportation Institute (2009)
8. S. Ghosh-Dastidar, H. Adeli, Neural network-wavelet micro simulation model for delay and queue length estimation at freeway work zones. *J. Transp. Eng.* 331–341 (2006)
9. X. Jiang, H. Adeli, Freeway work zone traffic delay and cost optimization model. *J. Transp. Eng.* 230–241 (2003)
10. V. Astarita, V.P. Giofre, G. Guido, D.C. Festa, Traffic delays estimation in two lane highway reconstruction. *Proced. Comput. Sci.* 331–338 (2014)
11. Q. Meng, J. Weng, Impact analysis of work zone configuration, traffic flow and heavy vehicle percentage on traffic delay at work zones. *Asian Transp. Stud.* 239–252 (2013)
12. M.S. Ali, M. Adnan, S.M. Noman, S.F. Abbas, Estimation of traffic congestion cost – a case study of a major arterial in Karachi. *Proced. Eng.* 37–44 (2014)
13. S. Chien, P. Schonfeld, Optimal work zone lengths for four lane highways. *J. Transp. Eng.* 124–131 (2001)

Performance Investigation of Desiccant Wheels for Air Dehumidification



Kishor Rambhad , Manoj Kumbhalkar , Vednath Kalbande ,
Rahul Jibhakate , Nikhil Jumde, and Pramod Walke 

1 Introduction

Nowadays, because of the decrease in customary assets of petroleum derivatives like coal, petroleum, flammable gas, and so on, energy emergency is a worldwide issue [1]. Raised energy use, energy worth, and pinnacle electrical interest coordinated at the introduction of substitute advancements. Endeavors for utilizing poor quality heat energy have been put to lessen the impact of oil esteem ascending in present years [2]. In numerous regions like air drying, water creation from environmental air [3], cooling and cooling applications desiccant is broadly perceived as a significant option in contrast to customary fume pressure refrigeration framework [4]. Desiccant materials have the capability to reduce humidity due to vapor pressure difference. Desiccants have been applied merely to materials with a high affinity to absorb moisture [5, 6]. For dehumidification, cooling and comfort conditioning solid and liquid desiccant is employed [7, 8]. Sunlight-based desiccant can be utilized to give achievable substitution to customary cooling frameworks [9, 10]. As of late, CD materials are celebrated for the same application with a lot higher productivity [2]. Chih-Hao Chen et al. consolidated polymer and SG CD turning bed for air dehumidification [11]. Tretiak et al. created and tried mud and calcium chloride [9]. Ramzy et al. utilized SG and a new desiccant composite molecule [12]. Chua et al. tested CD material with changing extent of SG, bentonite, calcium chloride, and LiCl and proposed [13, 14]. Zhang et al. created desiccant beds involving honeycomb-type adsorbent beds like SG 3A, SG RD, and so forth [15], Majumdar investigated a

K. Rambhad (✉) · M. Kumbhalkar
JSPM Narhe Technical Campus, Pune 411041, India

V. Kalbande · R. Jibhakate · P. Walke
G. H. Raison College of Engineering, Nagpur 440016, India

N. Jumde
CFD Engineer, HCL Technologies Limited, Pune 411028, India

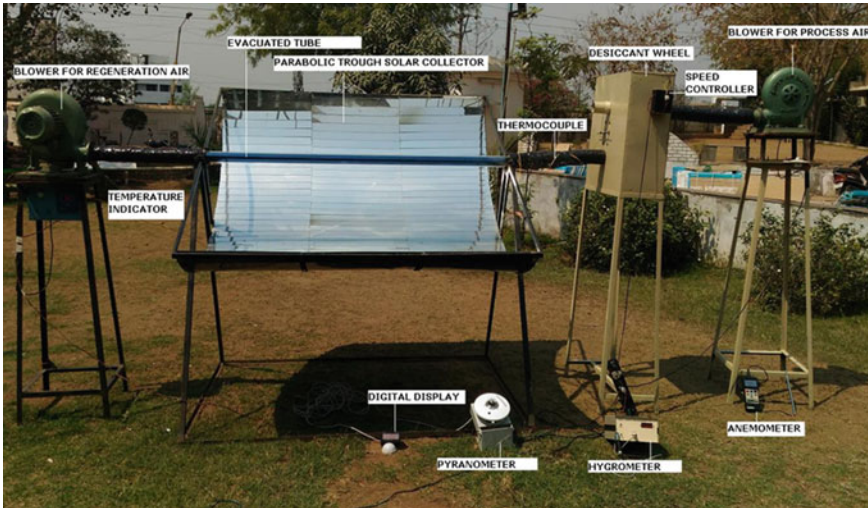


Fig. 1 Experimental setup of the desiccant wheel

CD for dehumidification made of missed inert and desiccant material [16], Jia et al. studied novel CD [17], Zhang et al. used SG, calcium chloride (CaCl_2), and CD(SG– CaCl_2) utilized to a corrugated paper based desiccant wheel [18]. G. Goodarzia et al. studied waste heat based solid desiccant wheel [19]. Researchers found a remarkable rise in moisture evacuating affinity of composite material compared with SG [2].

2 Experimental Execution of Desiccant Wheels

In this exploratory investigation, four desiccant wheels were created among them one was produced using SG, and the other three were produced using composite materials. Desiccant wheels were driven by a DC engine. In this work, two distinctive airflow areas were viewed as like in the first case 1/2 at process side and 1/2 at regeneration side and in second case 3/4 at process side 1/4 at regeneration side. Figure 1 shows the trial arrangement and Table 1 shows particular of desiccant wheel.

3 Result and Discussion

In this examination, the presentation of SG and three CD wheels have been experimentally explored. For recovery, PTSC was utilized in the temperature scope of 52.3–71.3 °C. CD wheel showed better performance than SG desiccant wheel. Adsorption and regeneration performance of each desiccant wheel was analyzed simultaneously

Table 1 Desiccant wheel specifications

Particulars	Values
Desiccant material	(a) SG (b) SG + LiCl (c) SG + MS (d) SG + LiCl + MS
Desiccant wheel diameter (m)	0.5
Desiccant wheel length (m)	0.1
Channel wall thickness (m)	0.0004
Flow passage height (m)	0.025
Flow passage pitch (m)	0.025
Matrix material density (kg/m^3)	7850
Matrix material thermal conductivity (W/mK)	54
Matrix material specific heat (J/kgK)	465

during daytime. The maximum AR and RR of the SG were found to be 0.276 kg/h and 1.500 kg/h at an airflow rate of 122.1 kg/h for process and regeneration. The maximum AR and RR of the CD wheel (SG-LiCl-MS) were found to be 0.497 kg/h and 1.707 kg/h, respectively.

3.1 Performance Boundaries of Desiccant Wheels

Table 2 shows the exhibition boundaries of various desiccant wheels. Table 3 shows the presentation boundaries of the desiccant wheel for the best outcome. It is seen that adsorption and recovery execution expanded by adding MS and LiCl.

Table 2 Operating parameters of the rotary desiccant wheel taken for experimentation

Parameters	Parametric variations
Rotational speed, N (rph)	10, 20, 30
Process air flow rate, m_p (kg/h)	48.83, 122.1
Regeneration air flow rate, m_r (kg/h)	48.83, 122.1
Process air sector angle, θ_p ($^\circ$)	180–270
Regeneration air sector angle, θ_r ($^\circ$)	90–180
Flow type	Parallel and counter
Material	SG, SG-LiCl, SG-MS 5A, SG-LiCl-MS 5A

Table 3 execution boundaries of desiccant wheel demonstrating best outcomes in adsorption and regeneration area

Parameters	Base value
Material	SG and composite desiccant
Rotational speed, N (rph)	20
Process air flow rate, m_p (kg/h)	122.1 kg/h
Regeneration air flow rate, m_r (kg/h)	122.1 kg/h
Process air sector angle, θ_p ($^\circ$)	270 $^\circ$
Regeneration air sector angle, θ_r ($^\circ$)	90 $^\circ$
Flow type	Counter flow

3.2 Percentage Improvement in AR and RR of CD Wheels

Table 3 shows the exhibition of unadulterated SG and CD wheels when presented to air with recovery temperature and relative stickiness shifting between 52.30–71.30 $^\circ\text{C}$ and 55.0–73.0% individually. From Figs. 2 and 3 plainly, the CD wheel produced using SG-LiCl-MS is the most ideal decision (Table 4).

The fundamental perceptions driven out from this work are as follows:

- CD wheel produced using SG-LiCl-MS shows the best execution in all working conditions which gives remarkable adsorption and recovery at 20 rph.
- In the same area plot for measure air and recovery air ($\theta_p = \theta_r = 180^\circ$), AR is exceptional when $m_p = 48.83$ kg/h and $m_r = 122.1$ kg/h and RR is remarkable when $m_p = m_r = 122.1$ kg/h and $m_p = 48.83$ kg/h and $m_r = 122.1$ kg/h.
- In diverse area plot for measure air and recovery air ($\theta_p = 270^\circ$ and $\theta_r = 90^\circ$), AR is extraordinary when $m_p = m_r = 122.1$ kg/h and $m_p = 48.83$ kg/h and $m_r = 122.1$ kg/h while RR is exceptional when $m_p = m_r = 122.1$ kg/h.
- In the counter stream game plan, AR is exceptional when $m_p = 48.83$ kg/h and $m_r = 122.1$ kg/h while RR is remarkable when $m_p = m_r = 122.1$ kg/h.
- In equal stream game plan, AR is remarkable when $m_p = m_r = 122.1$ kg/h and $m_p = 48.83$ kg/h and $m_r = 122.1$ kg/h while RR is extraordinary when $m_p = m_r = 122.1$ kg/h.

4 Conclusion

The fundamental target of the current examination work was to feature the possibility of sun-based strong desiccant dehumidifier for ordinary blistering and damp atmospheres, as a substitute to the customary fume pressure frameworks. More accentuation in this work was given to the CD dehumidifier. AR and RR of these SG alongside CD wheels were assessed, the most extreme AR and RR of the SG were discovered to be 0.276 kg/h and 1.500 kg/h when $m_p = m_r = 122.1$ kg/h. It was discovered that the expansion of MS and LiCl assists with expanding the dampness

Table 4 Adsorption and recovery abilities of the unadulterated SG and CD wheels with different rates of desiccant material in counter stream, with various area points at 20 rph for mass stream pace of air as 122.1 kg/h in cycle and recovery area

Sr. No	% Composition by Mass		AR (kg/h)	Wheel effectiveness in adsorption sector	RR (kg/h)	Wheel effectiveness in regeneration sector	PIAR of CD wheel (%)	PIRR of CD wheel (%)
	SG (%)	MS (%)						
1	100	0	0.276	0.141	1.500	2.099	—	—
2	90	10	0.359	0.179	1.581	2.203	34.998	5.650
3	90	0	0.380	0.188	1.601	2.230	43.580	7.088
4	80	10	0.479	0.234	1.707	2.366	85.508	14.431

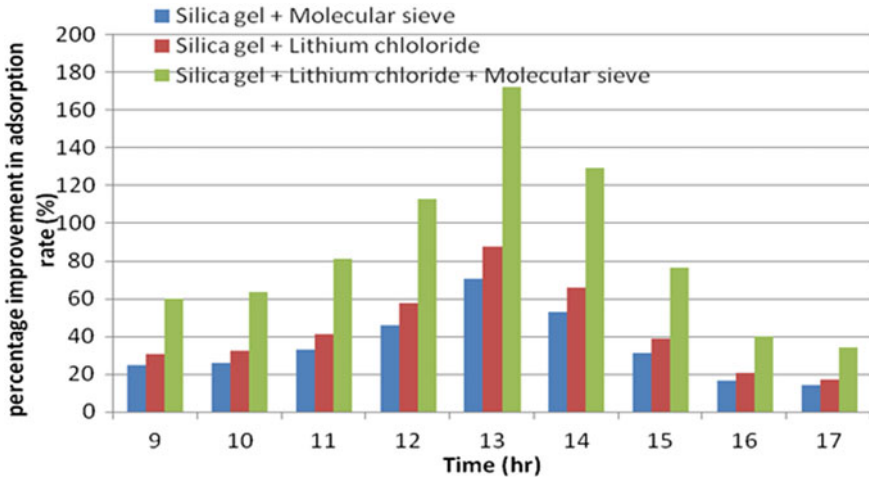


Fig. 2 Percentage improvement in AR for CD wheels

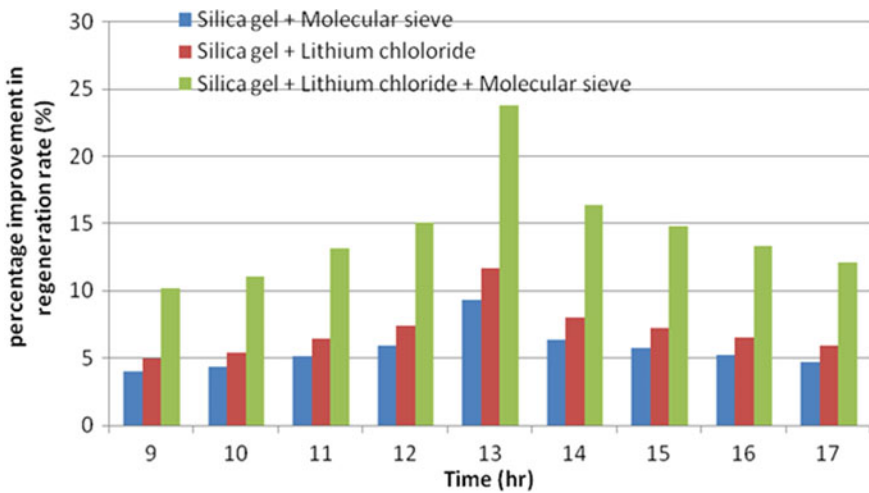


Fig. 3 Percentage improvement in RR for CD wheels

AR and RR when the delta air temperature differed. By adding 10% MS the AR and RR were expanded by 35% and 5.7%. By adding 10% LiCl the AR and RR were expanded by 43.6% and 7.1%. By adding 10% MS and 10% LiCl, the adsorption RR was expanded by 85.5% and 14.4%. The most extreme AR and RR of the CD wheel produced using SG-LiCl-MS was 0.479 kg/h and 1.707 kg/h individually.


References

1. T.S. Ge, Y.J. Dai, R.Z. Wang, Y. Li, Performance of two-stage rotary desiccant cooling system with different regeneration temperatures. *Energy* **80**, 556–566 (2015). <https://doi.org/10.1016/j.energy.2014.12.010>
2. C.X. Jia, Y.J. Dai, J.Y. Wu, R.Z. Wang, Experimental comparison of two honeycombed desiccant wheels fabricated with silica gel and composite desiccant material. *Energy Convers Manag* **47**, 2523–2534 (2006). <https://doi.org/10.1016/j.enconman.2005.10.034>
3. A. Ramzy, H. Abdelmeguid, W.M. Elawady, A novel approach for enhancing the utilization of solid desiccants in packed bed via intercooling. *Appl Therm Eng* **78**, 82–89 (2015). <https://doi.org/10.1016/j.applthermaleng.2014.12.035>
4. A.M. Hamed, W.R. Abd El Rahman, S.H. El-, Experimental study of the transient adsorption/desorption characteristics of silica gel particles in fluidized bed. *Energy* **35**, 2468–2483 (2010). <https://doi.org/10.1016/j.energy.2010.02.042>
5. D. La, Y.J. Dai, Y. Li et al., Technical development of rotary desiccant dehumidification and air conditioning: A review. *Renew Sustain Energy Rev* **14**, 130–147 (2010). <https://doi.org/10.1016/j.rser.2009.07.016>
6. X.N. Wu, T.S. Ge, Y.J. Dai, R.Z. Wang, Review on substrate of solid desiccant dehumidification system. *Renew. Sustain. Energy Rev.* **82**, 3236–3249 (2018)
7. J. Wrobel, P. Morgenstern, G. Schmitz, Modeling and experimental validation of the desiccant wheel in a hybrid desiccant air conditioning system. *Appl Therm Eng* **51**, 1082–1091 (2013). <https://doi.org/10.1016/j.applthermaleng.2012.09.033>
8. K.F. Fong, C.K. Lee, Impact of adsorbent characteristics on performance of solid desiccant wheel. *Energy* **144**, 1003–1012 (2018). <https://doi.org/10.1016/j.energy.2017.12.113>
9. C.S. Tretiak, A.N. Ben, Sorption and desorption characteristics of a packed bed of clay-CaCl₂ desiccant particles. *Sol Energy* **83**, 1861–1870 (2009). <https://doi.org/10.1016/j.solener.2009.06.017>
10. A. Alahmer, S. Alsaqoor, G. Borowski, Effect of parameters on moisture removal capacity in the desiccant cooling systems. *Case Stud. Therm. Eng.* **13**:100364. <https://doi.org/10.1016/j.csite.2018.11.015> (2019)
11. C.H. Chen, C.Y. Hsu, C.C. Chen et al., Silica gel/polymer composite desiccant wheel combined with heat pump for air-conditioning systems. *Energy* **94**, 87–99 (2016). <https://doi.org/10.1016/j.energy.2015.10.139>
12. K.A. Ramzy, R. Kadoli, T.P. Ashok Babu, Improved utilization of desiccant material in packed bed dehumidifier using composite particles. *Renew Energy* **36**, 732–742 (2011). <https://doi.org/10.1016/j.renene.2010.06.038>
13. K.J. Chua, M.R. Islam, on the experimental study of composite dessicants for energy efficient air dehumidification. *IJUM Eng J* **16**, 1–11. <https://doi.org/10.31436/iiumej.v16i2.600>(2015)
14. K.S. Rambhad, An experimental investigation of solar assisted air heating for solid desiccant regeneration using parabolic trough solar concentrator. *Int. J. Anal. Exp. Finite Elem. Anal.* **4**, 45–47. <https://doi.org/10.26706/IJAEEFA.3.4.20170803>(2017)
15. L.Z. Zhang, H.X. Fu, Q.R. Yang, J.C. Xu, Performance comparisons of honeycomb-type adsorbent beds (wheels) for air dehumidification with various desiccant wall materials. *Energy* **65**, 430–440 (2014). <https://doi.org/10.1016/j.energy.2013.11.042>
16. P. Majumdar, Heat and mass transfer in composite desiccant pore structures for dehumidification. *Sol Energy* **62**, 1–10 (1998). [https://doi.org/10.1016/S0038-092X\(97\)00080-7](https://doi.org/10.1016/S0038-092X(97)00080-7)

17. C.X. Jia, Y.J. Dai, J.Y. Wu, R.Z. Wang, Use of compound desiccant to develop high performance desiccant cooling system. *Int J Refrig* **30**, 345–353 (2007). <https://doi.org/10.1016/j.ijrefrig.2006.04.001>
18. X.J. Zhang, K. Sumathy, Y.J. Dai, R.Z. Wang, Dynamic hygroscopic effect of the composite material used in desiccant rotary wheel. *Sol Energy* **80**, 1058–1061 (2006). <https://doi.org/10.1016/j.solener.2005.07.008>
19. S. De Antonellis, D.S. Kim, Effectiveness of a symmetric desiccant wheel operating in balanced flow condition: modeling and application. *Int J Refrig* **88**, 347–359 (2018). <https://doi.org/10.1016/j.ijrefrig.2018.02.026>

Corruption and Its Mitigation Strategy Using Lean Philosophy



Brajesh Kumar Kanchan , Guddakesh Kumar Chandan, Roma Kumari, and Ojaswi Gautom

1 Introduction

Globalization prompted international businesses to invest in different parts of the world. Thereby, opening a new opportunity for business and contributing to the corresponding country's gross domestic product (GDP). In this background, it is well established that global investors avoid highly corrupted countries for their investment. Therefore, it is highly important to reduce corruption in an organization that varies from a small committee to large countries for administrators. Furthermore, corruption is inevitably present in each organization, however, the magnitude varies. In the assessment of corruption prevention, detection, and diagnostics, several researchers used different approaches. E-governance helps in higher performance of participatory individual satisfaction [1]. Right to information (RTI) laws are useful in maintaining good governance; however, the stakeholders who are accountable under RTI could not ensure RTI implementation as social-friendly [2, 3]. Audits play an important role in presenting the corruption status to decision-makers; however, biasedness in audit is still a prevailing matter [4, 5]. Judicial Independence directly affects corruption behavior as it can only ensure a proper judiciary system for tackling corruption cases [6, 7]. Accounting quality is a significant tool in mitigating corruption culture and better internal control, and forecast management decisions [8]. Education can be vital especially in developing countries to mitigate corruption [9]. Lean philosophy is especially resourceful in problem-solving for management. In the supply chain

B. K. Kanchan (✉) · G. K. Chandan
Department of Mechanical Engineering, National Institute of Technology, Silchar 788010, India

R. Kumari
Department of Management, Maulana Mazharul Haque Arabic and Persian University, Patna 800001, India

O. Gautom
Department of Management, Indian Institute of Management, Ranchi 834008, India

problem, lean philosophy was successfully implemented with just in time framework. [10]. Lean implementation in data management regarding decision-making is also successfully implemented with lesser losses [11]. Despite having a severe impact of corruption on almost every organization, very few investigations have been done on corruption issues using Lean Philosophy. The present investigation addresses that gap through the current study.

2 Research Methodology: Lean Philosophy

The research methodology that followed in the present study is the prevention, detection, and diagnostics (PDD) mechanism as illustrated in Fig. 1.

2.1 Prevention of Corruption

In mitigating corruption, the first milestone is to form a transparent advisory committee (TAC). This committee, comprised of representatives from different management levels of an organization, is selected to guide the transparent executive committee (TEC). The election of TEC needs to be having democratic and knowledge-based power division as illustrated in Fig. 2. It is well reported in the literature that elected representatives are critical in corruption-free horizontal coordination [12].

The number of representatives in TEC can vary from organization to organization. For this investigation, we have considered 4 representatives and 1 manager. The

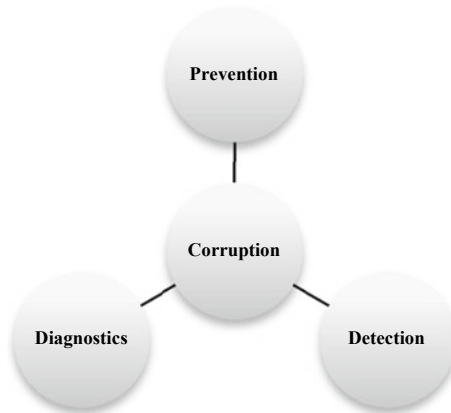


Fig. 1 Corruption checkpoints

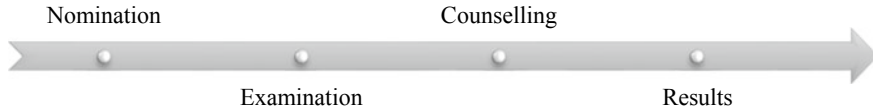


Fig. 2 Knowledge and democratic based representative election

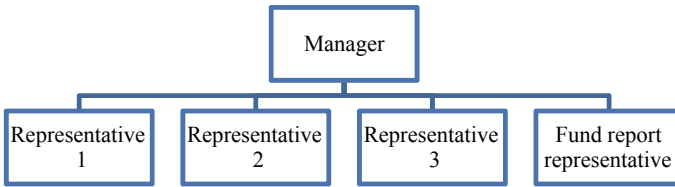


Fig. 3 The hierarchy of TEC

nomination for all posts was invited to all interested members of an organization. The hierarchy for the event was present in nomination call-up mail as shown in Fig. 3.

The duties of representatives will also be described in call-up mail. Representatives from 1 to 3 will ensure the general working of TEC whereas the fund report representative will ensure that fund status needs to be shared with all stakeholders at TAC agreed frequency. The manager will coordinate the representatives on different aspects of transparency. Different motivational techniques, viz. certificate, performance-based electric coins are used during the nomination process. The next task for the TAG is to formulate/detect the rules and regulations for the organization. As in most cases, organizations do have a dedicated rulebook/ethical guideline for this process. Hence, questions were asked from this rule book. The question comprised of direct rules, behavioral and conditional questions. Based on the scores of representatives. Further counseling based on their score was carried to elect the representatives based on the score and their previous expertise in administration and then TAG will declare the results of the election.

2.2 Detection of Corruption

The transparency execution committee (TEC) will detect the corruption cause and effect through the Ishikawa diagram. The elements for the Ishikawa diagram are man, method, management, measurement, and environment are categorized for corruption causes and effect in Figs. 4 and 5, respectively. The sub-elements of corruption in an organization vary from organization to organization and that is where TEC work is critical. A general corruption related cause and effect diagram is presented in Figs. 4 and 5.

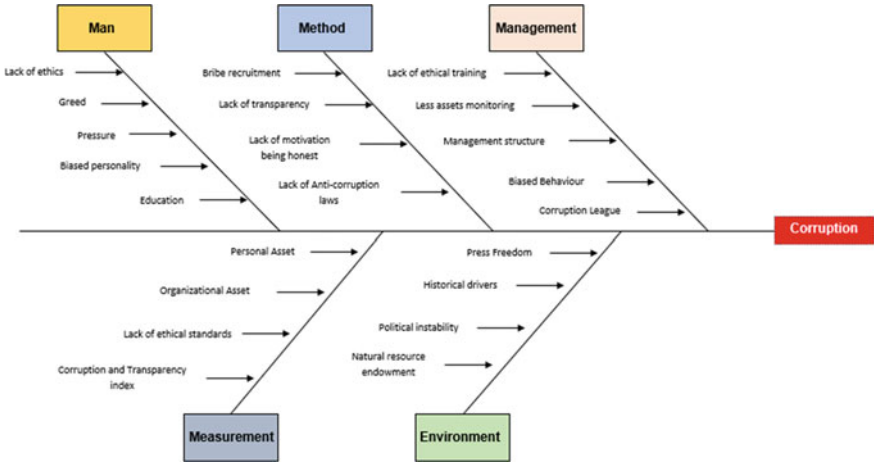


Fig. 4 Ishikawa diagram: causes of corruption

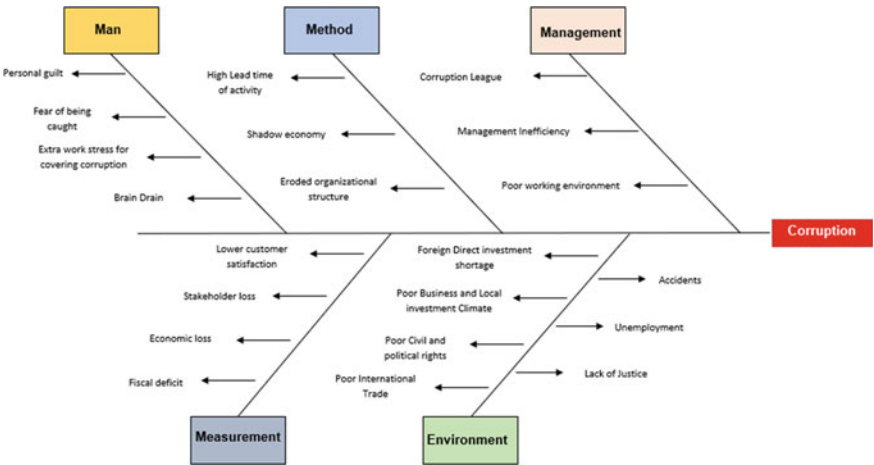


Fig. 5 Ishikawa diagram: effects of corruption

Causes of corruption

1. Man

- Lack of ethics: Ethics lacking is a key contributor to corruption. An unethical individual not only promotes corruption by himself but motivates others also to do corruption.
- Greed: Greed motivates corruption as an individual is not satisfied with his earning, status, etc., and does corruption to grow financially or non-financially.

- **Pressure:** Pressure is also a significant factor from a man's perspective as it can arise from family or colleagues or the boss which puts an individual in dilemma and sometimes the result becomes unethical.
- **Biased personality:** Corruption is not only defined in terms of monetary values, but it is also present in biasedness and favoring behavior based on social background, gender, and others.
- **Education:** Education is also contributing to corruption as an uneducated person will not be aware of the power and duties allocated to them and thus corruption probability is higher.

2. *Method*

- **Bribe recruitment:** The recruitment process used for joining the organization also impacts the behavior of the candidate. If the individual joins the organization through a bribe, there is a high possibility that he/she will involve in corruption.
- **Lack of transparency:** Transparency maintained by the organization is highly contributing to corruption. Transparency is the inverse function of corruption.
- **Lack of motivation being honest:** Honest and accountable individual has to sacrifice various aspects of life. If the organization does not ensure the motivation of that individual, it is a loss for the organization.
- **Anti-corruption laws:** The absence or weakened anti-corruption laws motivates the individual to do corruption.

3. *Management*

- **Lack of ethical training:** The absence of ethical training can lead individuals, groups, and then organizations to the path of corruption. So, management needs to ensure these training facilities are aligned with organizational ethics.
- **Less asset monitoring:** Asset monitoring is also a key parameter to look at by the management as the absence of it can lead to building a corruption hub in the organization.
- **Management structure:** Management size and structure contributes a lot to corruption as a decentralized management team has lesser chances to do corruption while centralized power leads to a higher corruption rate.
- **Biased behavior:** The biased behavior of management to an individual also leads to corruption or favoritism in one way or another.
- **Corruption leagues:** The formation of corruption leagues is the extreme level of corruption where each organizational member has a fixed share of corruption.

4. *Measurement*

- **Personal asset:** The measurement of a personal asset can lead to understanding how the individual is involved in corruption and up to what extent.
- **Organizational asset:** The organizational asset presents the growth of the organization and screening through it can present whether the organization is involved in any sort of corruption or not.

- Quantitative ethical standards: The lack of ethical standards makes it almost impossible to judge personal or group behavior.
- Corruption and Transparency index: The lack of corruption and transparency index deteriorates the morale of an honest and accountable individual.

5. *Environment*

- Press freedom: The lack of corruption reporting is a significant factor in environmental criteria. Corruption league always tries to check press power and affect public awareness.
- Historical drivers: The historical drivers show the previous record of that individual, organization in terms of corruption and related activities as these activities are not conducted one time rather it is a regular process of some individual and organization.
- Political instability: Political instability also contributes to corruption as corruption league can use their resources and power to do more corruption.
- Natural resource endowment: The higher the resources that are dealt with in a project or event, the higher the chance of corruption it will have.

Effect of corruption

Corruption has a strong influence on the demoralization of members, building mistrust against the organization. Corruption deeply affects national institutes, stakeholder services, and e-governance maturity.

1. *Man*

- Personal guilt: On the human ground, corrupt personnel always have a sense of guilt in their mind.
- Fear of being caught: Corruption also brings the fear of being caught by the public or end-users.
- Extra work stress for covering corruption: Corruption also increases the work stress of involved personnel as they have to work hard to cover up corruption.
- Brian drain: Corruption also leads to brain drain as an honest individual can leave or resign from their post and go somewhere else.

2. *Method*

- The high lead time of activity: Due to corruption, the end-users constantly wait in line such that they can offer some bribe or other favors. The process ultimately increases the lead time of activity.
- Shadow economy: Corruption starts a shadow economy in the form of black money and others which are dangerous for social development.
- Eroded organizational structure: Corruption regularly dents the organizational structure and slowly kills the organization.

3. *Management*

- **Corruption League:** The development of corruption leagues is the most intense effect of corruption as it is an organized way of doing corruption with stakeholders' share that is previously fixed.
- **Management inefficiency:** Corruption also make management inefficient in making a decision and other regular activities as incompetent individuals are placed everywhere.
- **Poor working environment:** The working environment becomes very poor in the high corruption index organizations or countries.

4. *Measurement*

- **Lower customer satisfaction:** Corruption mostly affects the end-user or customer and satisfaction would be low due to high corruption.
- **Stakeholder loss:** Corruption also leads to a loss in stakeholder members and consequently impacts every aspect of management.
- **Economic loss:** Corruption also significantly affects the organization economically due to lower customer satisfaction.
- **Fiscal deficit:** The organization will be under fiscal deficit if the corruption level is high in any organization.

5. *Environment*

- **Foreign direct investment shortage:** The outside funding in the form of FDI would be low if the corruption level is high in the organization.
- **Accidents:** Corruption impacts the development projects and thus affects the quality of services offered which ultimately converted into accidents.
- **Poor business and local investment climate:** The business and local investment climate would be poor for a corrupt organization as they will be in the fiscal deficit.
- **Unemployment:** Corruption certainly impacts the quality of education and training offered to individuals and thus leading to unskilled professionals who most of the time will be unemployed.
- **Poor civil and political rights:** The condition of civil and political rights would be a poor organization with a higher corruption index.
- **Lack of justice:** The probability of getting justice would be also less due to corruption involved leagues
- **Poor international trade:** The organizational international market and trade would also be impacted due to corruption loss in terms of stakeholders and economy.

2.3 *Diagnostics of Corruption*

Once a corruption case is reported, the transparency advisory committee activates the protocol as per the rule book of its organization. The schematic of a corruption

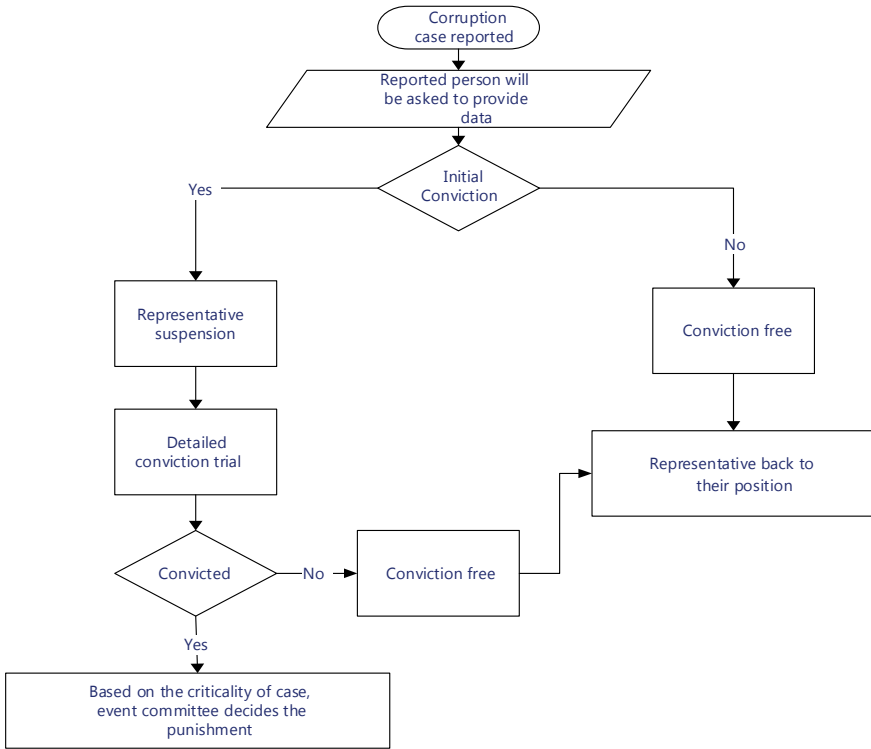


Fig. 6 Corruption diagnostic flow diagram

diagnostics is shown in Fig. 6. Figure 6 illustrates that the corruption reported person has to include the data or proof which can be utilized in initial conviction. The timeliness of the initial conviction can be based on the recommendation from TAC. Based on the initial conviction, the event guidance committee can either remove the charges from the representative based on the data and facts or summon him/her for a detailed conviction trial. The timeliness of a detailed conviction is based on the recommendation from TAC. During that period, the representative will be suspended from event responsibilities. After a detailed conviction trial, the representative can be either set free or punished by the laws based on the criticality of corruption.

3 Conclusion

The present investigation highlights the importance of prevention, detection, and diagnostic (PDD) mechanisms of corruption using lean philosophy. In the prevention phase, the transparency advisory and executive committee are formed. The committee ensures that democratic and knowledge-based power division philosophy is used for

the representative election. In the detection phase, the cause and effect of corruption are illustrated for a typical organization. It can be easily modified for any other organization. The integration of fund transparency and transparent leadership is utilized as a working tool. Furthermore, in the diagnostics phase, the event committee ensured the access, quality, and timeliness of justice, if any corruption case is reported. Some of the notable findings from the present investigation are as follows:

- PDD mechanism helps track the corruption at different checkpoints.
- Ishikawa diagram for cause and effect of corruption is presented.
- Corruption diagnostics is also illustrated for the PDD mechanism.
- The lean approach plays a significant role in framing an overall mechanism for a reduction in corruption.

References

1. C.H. Park, K. Kim, E-government as an anti-corruption tool: panel data analysis across countries. *Int. Rev. Administr. Sci.* 0020852318822055 (2019)
2. S. Yadav, *Journalism through RTI: Information Investigation Impact*. SAGE Publishing India, New Delhi (2017)
3. A. Chaudhary, Issues and challenges facing RTI act. *Indian J. Public Administr.* **62**(2), 270–281 (2016)
4. M.A. Khan, Role of audit in fighting corruption, in *Comunicação apresentada na Conferência: Ethics, Integrity, and Accountability. In the Public Sector: Re-building Public Trust in Government through the Implementation of the UN Convention against Corruption: Russia, St. Petersburg* (2006)
5. C. Ferraz, F. Finan, Electoral accountability and corruption: evidence from the audits of local governments. *Amer. Econ. Rev.* **101**(4), 1274–1311 (2011)
6. S. Rose-Ackerman, Judicial independence and corruption. *Transparency International Global Corruption Report: 15–24* At https://www.researchgate.net/profile/Susan_RoseAckerman/publication/265045845_Judicial_independence_and_corruption/links/55e0bf8008ae6abe6e89e9f3.pdf (2007)
7. A. Shah, J. Huther, Anti-corruption policies and programs: a framework for evaluation. *The World Bank E-government as an anti-corruption tool: Panel data analysis across countries* (1999)
8. Y. Chen, L. Che, D. Zheng, H. You, Corruption culture and accounting quality. *J. Account. Public Policy* **39**(2), 106698 (2019)
9. R. Truex, Corruption, attitudes, and education: survey evidence from Nepal. *World Dev.* **39**(7), 1133–1142 (2011)
10. B.K. Kanchan, G.K. Chandan, D. Rajenthirakumar, A framework for implementing Just in Time in a Valve manufacturing industry. *Int. J. Eng. Res.* **5**(4), 303–307 (2016)
11. K.S. Arun, B.K. Kanchan, G. Prabha, D. Rajenthirakumar, Increasing an overall equipment effectiveness visibility and analyzing in a manufacturing industry. *Int. J. Manuf. Mater. Process.* **2**(2), 89–103 (2016)
12. R. Samaratunge, D. O’Neill, K. Coghill, Building horizontal coordination in Sri Lanka, *Public Administration and Development* **37**(5), 319–330 (2017)

A New Approach for the Prediction of the Stability of Lotka-Volterra Model as a Biological Reaction



Pragati Dethé and Arvind Bodhe

1 Introduction

Alfred Lotka was one of the most interesting characters in the history of science. He wrote a handful of theoretical papers on chemical oscillation during the early decades of this century and authored a monograph (1925) [1] on theoretical biology that is filled with insights that still seem fresh today. In 1910, Lotka showed that a set of consecutive reactions can give rise to damped oscillations on the way to equilibrium [2]. He continued his search for oscillatory behavior arising from the mass action kinetics in a second paper published a decade later [3]. This latter model, though it does not apply to any real chemical system, has provided considerable inspiration to ecologists. Volterra [4, 5] used ideas similar to Lotka's to investigate a wide range of ecological problems, including the effects of migration and of several species simultaneously interacting. The best-known model of this type is today called the Lotka-Volterra model and is often used to characterize predator-prey interaction [3, 4, 6]. In this chapter, we investigate the thermodynamic stability of the Lotka-Volterra model [6, 7] proceeding at finite rates by Jacobian matrix analysis [1, 8–12] and Lyapunov function analysis [13].

1.1 Representative of the Model

The Lotka-Volterra prey-predator model [6, 7, 14, 15] consists of three reactions steps:

P. Dethé
Science College, Pauni, Bhandara, India

A. Bodhe (✉)
G H Rasoni University, Saikheda, MP, India



where the first two reaction steps follow second-order kinetics in which two reactants produce a product, while the third reaction is the first-order kinetics in which a single reactant in a single step produces a product. X is the population of rabbits, which reproduce autocatalytically, A is the amount of grass, which assumed to be constant, or at least in great excess compared with its consumption by the rabbits, Y is the population of lynxes (bobcats), and P represents the dead lynxes which again assumed to be constant. Assuming the reverse rate constants are insignificant, the expression for rate equations for the Lotka-Volterra reaction scheme is given by chemical kinetics [16, 17], which read as

$$\frac{d\xi_1}{dt} = v_1 = k_1[A][X] \tag{2}$$

$$\frac{d\xi_2}{dt} = v_2 = k_2[X][Y] \tag{3}$$

$$\frac{d\xi_3}{dt} = v_3 = k_3[Y] \tag{4}$$

$$\frac{d[X]}{dt} = k_1[A][X] - k_2[X][Y] = v_1 - v_2 \tag{5}$$

$$\left(\left(\frac{d[Y]}{dt} = k_2[X][Y] - k_3[Y] = v_2 - v_3 \right) \right) \tag{6}$$

where ξ_i ($i = 1, 2, 3$) is the extent of reaction, v_i ($i = 1, 2, 3$) is the rate of reaction. There is an initial transient behavior during which the intermediates show normal behavior of progression. After this, however, the system begins to move away from the steady state. The concentration of X and Y begins to oscillate and their rate becomes nonzero.

(1) Steady-State Analysis

In steady state, the concentrations of intermediate species X and Y remain time independent, that is,

$$\frac{d[X]^s}{dt} = k_1[A][X]^s - k_2[X]^s[Y]^s = v_1^s - v_2^s = 0 \tag{7}$$

$$\frac{d[Y]^s}{dt} = k_2[X]^s[Y]^s - k_3[Y]^s = v_2^s - v_3^s = 0. \tag{8}$$

where $[X]^s$ and $[Y]^s$ are the concentrations of X and Y in steady state, respectively. Notice that Eqs. (7) and (8) give a new identity that is

$$v_1^s = v_2^s = v_3^s = v \quad (9)$$

After solving Eqs. (10) and (11), the steady-state concentrations of X and Y are obtained as

$$[X]^s = \left(\frac{k_3}{k_1[A]} \right) [Y]^s, \quad [X]^s = \frac{k_3}{k_2}, \quad [Y]^s = \frac{k_1}{k_2} [A]. \quad (10)$$

The stability of steady state has been investigated by the Lyapunov direct method of stability of motion [13, 18] at constant T and p in subsequent sections.

(2) Stability analysis by Lyapunov method

Let us consider the case when mole numbers X and Y are perturbed by a sufficiently small amount from their steady-state concentration, namely;

$$[X] = [X]^s + \delta X \quad \text{and} \quad [Y] = [Y]^s + \delta Y \quad (11)$$

where δX and δY are the small change in concentrations of X and Y from their respective steady-state concentrations, $[X]$ and $[Y]$ are concentrations of X and Y in a perturbed state. The rate expressions given by Eqs. (2)–(6) are treated as the quantities in perturbed states and Eqs. (10)–(11) that in the unperturbed state. Adopting the identical procedure used in the preceding chapter to obtain the quantities in perturbation space, we have

$$\frac{d(\delta\xi_1)}{dt} = \delta v_1 = k_1[A]\delta X = v_1^s \frac{\delta X}{[X]^s} \quad (12)$$

$$\frac{d(\delta\xi_2)}{dt} = \delta v_2 = k_2[Y]^s\delta X + k_2[X]^s\delta Y = v_2^s \frac{\delta X}{[X]^s} + v_2^s \frac{\delta Y}{[Y]^s} \quad (13)$$

$$\frac{d(\delta\xi_3)}{dt} = \delta v_3 = k_3\delta Y = v_3^s \frac{\delta Y}{[Y]^s} \quad (14)$$

$$\frac{d(\delta X)}{dt} = k_1[A]\delta X - k_2[X]^s\delta Y - k_2[Y]^s\delta X \quad (15)$$

$$\frac{d(\delta Y)}{dt} = k_2[X]^s\delta Y + k_2[Y]^s\delta X - k_3\delta Y. \quad (16)$$

where

$$\frac{d(\delta\xi_i)}{dt} = \frac{d(\xi_i)}{dt} - \frac{d(\xi_i)^s}{dt}, \quad (i = 1, 2, 3) \quad (17)$$

$$\delta v_i = (v_i) - (v_i)^s, \quad (i = 1, 2, 3) \quad (18)$$

After rearranging Eqs. (17) and (18) and using Eqs. (12)–(13), we have

$$\frac{d(\delta X)}{dt} = (v_1^s - v_2^s) \frac{\delta X}{[X]^s} - v_2^s \frac{\delta Y}{[Y]^s} = -\frac{v_2^s}{[Y]^s} \delta Y \quad (19)$$

$$\frac{d(\delta Y)}{dt} = (v_2^s - v_3^s) \frac{\delta Y}{[Y]^s} + v_2^s \frac{\delta X}{[X]^s} = \frac{v_2^s}{[X]^s} \delta X \quad (20)$$

since $v_1^s - v_2^s = 0$ and $v_2^s - v_3^s = 0$. In steady-state condition, the reaction rate v_2^s numerically equals to

$$v_2^s = k_2[X]^s[Y]^s = \frac{k_1 k_3}{k_2}[A] \quad (21)$$

and

$$\frac{v_2^s}{[X]^s} = k_1[A], \quad \frac{v_2^s}{[Y]^s} = k_3. \quad (22)$$

On substituting these values in Eqs. (19) and (20), we obtain

$$\frac{d(\delta X)}{dt} = (v_1^s - v_2^s) \frac{\delta X}{[X]^s} - v_2^s \frac{\delta Y}{[Y]^s} = -k_3 \delta Y \quad (23)$$

$$\frac{d(\delta Y)}{dt} = (v_2^s - v_3^s) \frac{\delta Y}{[Y]^s} + v_2^s \frac{\delta X}{[X]^s} = k_1[A] \delta X. \quad (24)$$

These equations give the advancement of perturbation coordinates with time.

Similarly, the expressions for the affinities in perturbation space after sufficiently small perturbation in mole concentrations of X and Y from their steady-state position are obtained as

$$\frac{\delta \mathcal{A}_1}{T} = -R \frac{\delta X}{[X]^s} \quad (25)$$

$$\frac{\delta \mathcal{A}_2}{T} = R \frac{\delta X}{[X]^s} - R \frac{\delta Y}{[Y]^s} \quad (26)$$

$$\frac{\delta \mathcal{A}_3}{T} = R \frac{\delta Y}{[Y]^s} \quad (27)$$

where

$$\frac{\delta \mathcal{A}_i}{T} = \frac{\mathcal{A}_i}{T} - \frac{\mathcal{A}_i^s}{T}, \quad (i = 1, 2, 3) \quad (28)$$

The rate of entropy production for a chemically reacting system in steady-state condition (unperturbed state) is given by Gibbs equation [10, 19], which is

$$\sum_s = \frac{\mathcal{A}_1^s}{T} v_1^s + \frac{\mathcal{A}_2^s}{T} v_2^s + \frac{\mathcal{A}_3^s}{T} v_3^s > 0 \quad (29)$$

Similarly, on the perturbed trajectory the expression for the rate of entropy production reads as

$$\sum = \frac{\mathcal{A}_1}{T} v_1 + \frac{\mathcal{A}_2}{T} v_2 + \frac{\mathcal{A}_3}{T} v_3 > 0 \quad (30)$$

that is, the rate of entropy production is never negative as per the dictates of the second law of thermodynamics.

The Lyapunov function is the difference in the rate of entropy production between perturbed and unperturbed states. Thus, from Eqs. (19) and (20), the expression for Lyapunov function, L_s is obtained as

$$\begin{aligned} L_s = \sum - \sum^s &= \frac{\mathcal{A}_1^s}{T} (v_1 - v_1^s) + \frac{\mathcal{A}_2^s}{T} (v_2 - v_2^s) + \frac{\mathcal{A}_3^s}{T} (v_3 - v_3^s) \\ &+ \frac{(\mathcal{A}_1 - \mathcal{A}_1^s)}{T} v_1^s + \frac{(\mathcal{A}_2 - \mathcal{A}_2^s)}{T} v_2^s + \frac{(\mathcal{A}_3 - \mathcal{A}_3^s)}{T} v_3^s \end{aligned} \quad (31)$$

Using notations given in Eqs. (18) and (28), the expression for L_s reduces to

$$\begin{aligned} L_s &= \frac{\mathcal{A}_1^s}{T} \delta v_1 + \frac{\mathcal{A}_2^s}{T} \delta v_2 + \frac{\mathcal{A}_3^s}{T} \delta v_3 \\ &+ \frac{\delta \mathcal{A}_1}{T} v_1^s + \frac{\delta \mathcal{A}_2}{T} v_2^s + \frac{\delta \mathcal{A}_3}{T} v_3^s \end{aligned} \quad (32)$$

Substituting appropriate values of affinities and rate equations in Eq. (33), the expression for Lyapunov function reads as

$$\begin{aligned} L_s &= \left(\frac{\mathcal{A}_1^s}{T} v_1^s + \frac{\mathcal{A}_2^s}{T} v_2^s \right) \frac{\delta X}{[X]^s} + \left(\frac{\mathcal{A}_2^s}{T} v_2^s + \frac{\mathcal{A}_3^s}{T} v_3^s \right) \frac{\delta Y}{[Y]^s} \\ &+ R(v_2^s - v_1^s) \frac{\delta X}{[X]^s} + R(v_3^s - v_2^s) \frac{\delta Y}{[Y]^s} \end{aligned} \quad (33)$$

However, in steady-state situation, $v_2^s - v_1^s = 0$ and $v_3^s - v_2^s = 0$. These conditions give

$$L_s = \left(\frac{\mathcal{A}_1^s}{T} v_1^s + \frac{\mathcal{A}_2^s}{T} v_2^s \right) \frac{\delta X}{[X]^s} + \left(\frac{\mathcal{A}_2^s}{T} v_2^s + \frac{\mathcal{A}_3^s}{T} v_3^s \right) \frac{\delta Y}{[Y]^s} \quad (34)$$

This indicates that while calculating Lyapunov function in steady-state condition, the term

$$\frac{\delta \mathcal{A}_1}{T} + \frac{\delta \mathcal{A}_2}{T} v_2^s + \frac{\delta \mathcal{A}_3}{T} v_3^s = 0, \quad \left(\text{in general } \frac{\delta \mathcal{A}_i}{T} v_i^s = 0 \quad (i = 1, 2, 3 \dots) \right) \quad (35)$$

Further, using the identity from steady-state condition,

$$\begin{aligned} v_1^s &= v_2^s = v_3^s = v = \left(\frac{k_1 k_3}{k_2} \right) [A] \\ [X]^s &= \frac{k_3}{k_2}, \quad [Y]^s = \left(\frac{k_1 k_3}{k_2} \right) [A] \end{aligned} \quad (36)$$

the final expression for Lyapunov function L_s is obtained as

$$L_s = k_1 [A] \left(\frac{\mathcal{A}_1^s}{T} + \frac{\mathcal{A}_2^s}{T} \right) \delta X + k_3 \left(\frac{\mathcal{A}_2^s}{T} + \frac{\mathcal{A}_3^s}{T} \right) \delta Y. \quad (37)$$

Moreover, in Eq. (37) the coefficients of δX and δY are positive definite, and hence the sign of Lyapunov function, L_s , is solely determined by the sign of perturbation coordinates.

Notice that Eq. (37) indicates that the L_s is the function of perturbation coordinates, δX and δY are expressed as

$$L_s = L_s(\delta X, \delta Y). \quad (38)$$

Hence, the total time derivative of L_s is obtained as

$$\frac{dL_s}{dt} = \frac{\partial L_s}{\partial(\delta X)} \frac{d(\delta X)}{dt} + \frac{\partial L_s}{\partial(\delta Y)} \frac{d(\delta Y)}{dt}. \quad (39)$$

However, in steady-state situation, the local time derivative $\partial L_s / \partial t$ vanishes. The gradient of Lyapunov function is obtained from Eq. (37) as

$$\frac{\partial L_s}{\partial(\delta X)} = k_1 [A] \left(\frac{\mathcal{A}_1^s}{T} + \frac{\mathcal{A}_2^s}{T} \right) > 0, \quad (40)$$

$$\frac{\partial L_s}{\partial(\delta Y)} = k_3 \left(\frac{\mathcal{A}_2^s}{T} + \frac{\mathcal{A}_3^s}{T} \right) > 0. \quad (41)$$

Thus, from Eqs. (32), (33) and (40)-(41), and using steady-state concentrations of X and Y, we have

$$\frac{dL_s}{dt} = -k_1k_3[A] \left\{ \left(\frac{A_1^s}{T} + \frac{A_2^s}{T} \right) \delta Y - \left(\frac{A_2^s}{T} + \frac{A_3^s}{T} \right) \delta X \right\}. \tag{42}$$

The conclusions about the stability of a process are then drawn using fabrics of Lyapunov [20, 21] and Malkin [20, 21] theorem by establishing the sign of dL_s/dt and whether the magnitude of each $\partial L_s/\partial \alpha_i$ is finite or not. The unperturbed trajectory is said to be a stable one when,

$$L_s > 0, \quad \frac{dL_s}{dt} < 0 \quad \text{or} \quad L_s < 0, \quad \frac{dL_s}{dt} > 0 \tag{43}$$

In this analysis, it shows that the gradient of the Lyapunov function is finite and positive definite and hence, the behavior of perturbation coordinates, δX and δY with time is important for the identification sign of L_s and dL_s/dt , and then the stability of the state. Using Mathematica software, the graphical presentations of perturbation coordinates, L_s and dL_s/dt with time are shown in the following figures.

Figures 1 and 2 indicates that the steady state is unstable on perturbation. It is clearly observed that small disturbances to intermediates species lead to the onset of sustained oscillation. On perturbation, system parameters are varied so that the system passes through the bifurcation limit cycle or periodic orbit develops surrounding the steady state.

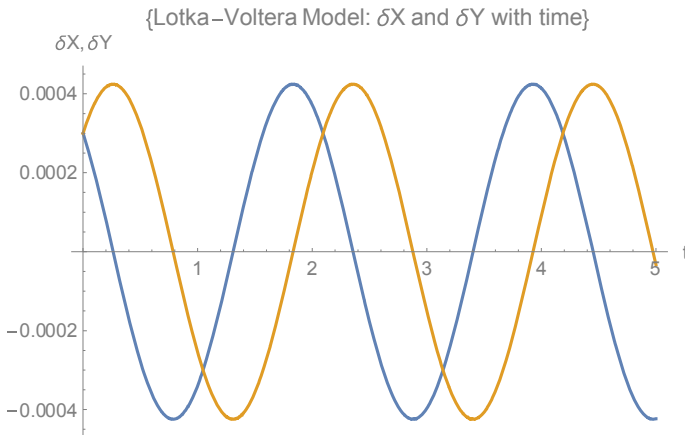


Fig. 1 Oscillating behavior of δX and δY with time

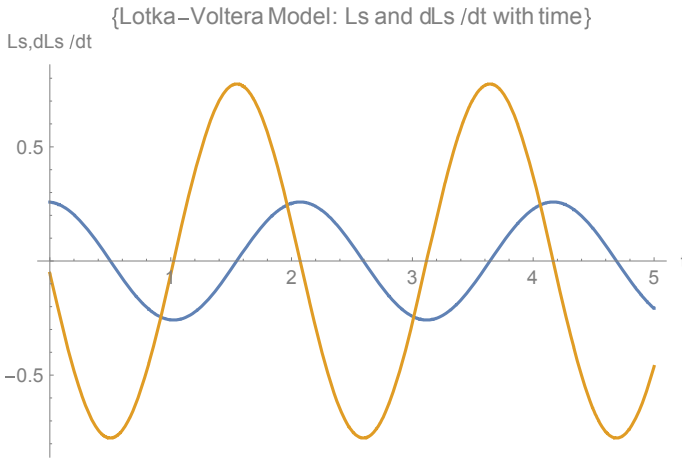


Fig. 2 Sustain oscillations of L_s and dL_s/dt with time

2 Conclusion

In this paper, we have explored the tools of the Lypunov Method of stability to investigate the stability of Lotka-Volterra model as a biological reaction. The domain of stability and instability is clearly revealed in our exercise. Thus it would be beneficial if it could be known by thermodynamic considerations what are the constraints under which the given process remains stable or becomes unstable. It indeed would save our time, efforts, and inputs that would otherwise may go waste. If a given real process turns out to be slightly unstable, then it would be worth trying to make it stable by some minor adjustments. Yet another possibility is that a given real process is stable but maybe dynamically unstable. In this event by thermodynamic controls, one may perhaps achieve dynamic stability too by a suitable manipulation of the system variables.

References

1. A.J. Lotka, Contribution to the theory of periodic reactions. *J. Phys. Chem.* **14**, 271–274 (1910)
2. A.J. Lotka, *Element of physical biology*. Williams and Wilkins, Baltimore (1925)
3. A.J. Lotka, Undamped oscillations derived from the law of mass action. *J. Am. Chem. Soc.* **42**, 1595–1599 (1920)
4. V. Volterra, Fluctuations in the abundance of a species considered mathematically. *Nature* **118**, 558–560 (1926)
5. V. Volterra, *Variazione fluttuazioni del numero d'individui in specie animali conviventi*. *Mem. Acad. Lincei* **2**, 31–113 (1926), Translation in R.N. Chapman: *Animal Ecology*, New York, McGraw Hill (1931)
6. I.R. Epstein, J.A. Pojman, *An Introduction to Nonlinear Chemical Dynamics*. Oxford University Press, Oxford (1998)

7. P. Gray, S.K. Scott, Chemical oscillations and instabilities, Nonlinear Chemical Kinetics. Clarendon Press, Oxford (1990)
8. Dethe Bionano frontier second World Congress for Man and Nature, Vol. 5(2-III), pp. 105–107 (ISSN 0974-067)
9. P.D. Dethe, Research J. Resent Sci. **3**(ISC-2013), 1–8, 1–5 (2014). ISSN No. 2277–2502
10. P.D. Dethe, Int. Res. Biosc. Agric. Technol. **1**(2), ISSN No. (Online) 2347–517X
11. P.D. Dethe, Int. J. Adv. Eng. Manage. Sci. (IJAEMS) Special Issue -3, 166–171 (2017). ISSN : 2454-1311
12. P.D. Dethe, Int. J. Manag. Technol. Eng. **IX**(I), 347–353 ISSN NO. 2249-7455 (UGC Journal)
13. K.J. Laidler, Chemical Kinetics. McGraw-Hill, New York (1961)
14. N.G. Chetayev, The Stability of Motion, Transl. M. Nadler, Pergamon, Oxford (1961)
15. J. LaSalle, S. Lefschetz, Stability by Lyapunov's Direct Method with Applications. Academic Press, New York (1961)
16. W. Muschik, J. Non-Equilib. Thermodyn. **4**, 277 (1979)
17. W. Muschik, Aspects of Non-Equilibrium Thermodynamics. World Scientific, Singapore (1990)
18. D. Kondepudy, I. Prigogine, Modern Thermodynamics. Wiley, New York (1998)
19. A.A. Frost, R.G. Pearson, Kinetics and Mechanism, A Study of Homogeneous Chemical Reactions. Second edition, Wiley Eastern Private Limited, New Delhi (1961)
20. R. Schmid, V.N. Sapunov, "Non-Formal Kinetics", Monographs in Modern Chemistry, Verlag Chemie, Weinheim (1982)
21. R. Hasse, Thermodynamic of Irreversible Processes. Addison-Wisley, Reading, MA (1969)

Review of Investigation in Performance of Magnetic Refrigeration System



Aniket R. Ingale, Pranay D. Kumbhare, Ram G. Sanodiya,
Ravindra A. Ravane, and Ashish S. Raut

1 Magnetic Refrigeration System

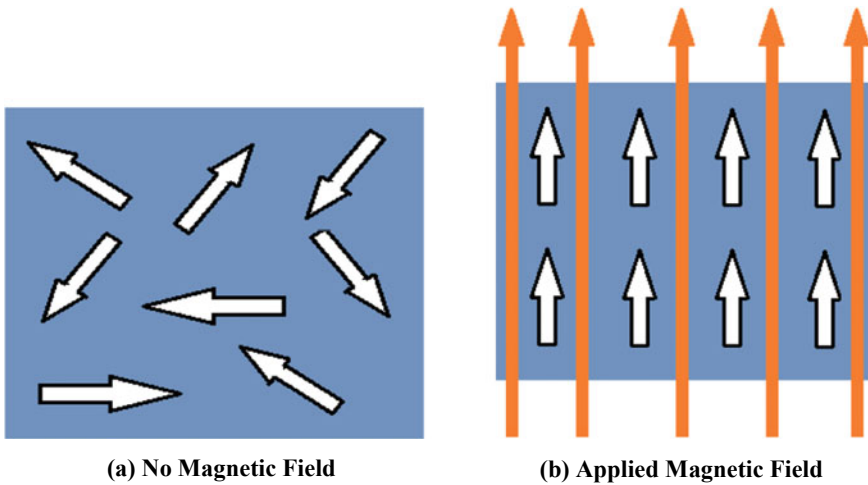
Magnetic refrigeration works on the principle of the magnetocaloric effect (MCE), which is a magneto thermodynamic phenomenon in which a reversible change in temperature of a suitable material is caused by exposing the material to a changing magnetic field. MCE is the behavior of a magnetic solid when it is exposed to a changing magnetic field: its temperature may be appreciably increased or decreased, with both the sign and the extent of the temperature difference between the final and the initial states of the material being dependent on numerous intrinsic and extrinsic factors [2].

The chemical composition, the crystal structure, and the magnetic state of compound are among the most important material parameters that determine its MCE. Magnetic refrigeration is based on a fundamental thermodynamic property of magnetic materials: the so-called magnetic effect which causes a temperature change if the material is subject to an applied magnetic field under adiabatic conditions [3].

A. R. Ingale · P. D. Kumbhare · R. G. Sanodiya (✉) · R. A. Ravane · A. S. Raut
Mechanical Engineering Department, G. H. Raisoni College of Engineering, Nagpur, India
e-mail: sanodiya_ram.me@ghrce.raisoni.net

© The Author(s), under exclusive license to Springer Nature Singapore Pte Ltd. 2022
M. L. Kolhe et al. (eds.), *Smart Technologies for Energy, Environment and Sustainable Development, Vol 2*, Springer Proceedings in Energy,
https://doi.org/10.1007/978-981-16-6879-1_29

285



2 Magnetic Materials for Magnetic Refrigeration

Pure gadolinium is mostly used, it is added in the various compounds to achieve the greater COP. It considers an ideal substance for magnetic refrigeration, just as the ideal gas is for conventional refrigeration [4]. But magnetic refrigeration shows a better performance, not like conventional refrigeration, some following list of magnetocaloric materials for application in magnetic refrigerators which gives the different properties and also varies in performance:

- Binary and ternary intermetallic compounds
- Gadolinium-silicon-germanium compounds
- Manganites
- Lanthanum-iron based compounds
- Manganese-antimony arsenide
- Iron-manganese-arsenic phosphides
- Amorphous fine met-type alloys (very recent).

At present, a number of toxic substances in such compounds are being replaced by more acceptable elements. A discussion on the different types of materials with their distinct properties is found in extended topical reviews [5]. Currently, the total entropies and the related refrigeration capacity, the adiabatic temperature change, and the costs of the materials are under investigation. Bruck states that in the near future, other properties such as corrosion resistance, mechanical properties, heat conductivity, electrical resistivity, and environmental impact will also become important [6]. Some other materials with temperature or entropy with the help of some research paper are as follows:

Nanosheets (OH) ₂ and, La _{0.8} Ce _{0.2} Fe _{11.4} Si _{1.6} , Bx, La _{0.8} Ce _{0.2} Fe _{11.4} Si _{1.6} Bx compounds & alloy of Mn _{0.94} Ti _{0.06} CoGe	$T_{cuire} = 174,184 \text{ K}$
(Fe _{0.72} Cr _{0.28}) ₃ Al	$TC = 285 \text{ K}$
(Ni ₂ , 1-xCox)Mn _{0.9} Ga	Max. $-\Delta SM_{peak} = 2.8 \text{ J/kg.k}$
4 similar geometry regenerators with 3 different materials Pr _{0.65} Sr _{0.35} MnO ₃ , La(FeCo) _{13-x} Si ₆ and Gd	$\Delta T_{spain} = 16 \text{ k}$, $\Delta T_{spain} = 14$
La _{0.67} Ba _{0.33} Mn _{0.9} Cr _{0.103}	$-\Delta SM = 4.20 \text{ J/Kg k}$
LaFe _{13-x-y} CoxSiy	$T_{peak} = 276\text{--}286 \text{ \& } 288 \text{ k}$ $-\Delta SM = 6.2\text{--}5.1$

3 Design for Magnetic Refrigerator

There are two designs that we have selected

1. Linear: In this setup, magneto-caloric material remains stationary and the magnet moves linearly or vice versa. This way when MCM comes under magnetic field, it shows magneto-caloric effect or large magnetic effect and heats up, and when removed, it cools down more than its initial temperature.

Constant supply of refrigerant liquid (say water) is provided through MCM and gradually after several cycles overall temperature drops. This method is not cost-effective and efficient as it requires more magnets for more MCM beds. Open circuits and inefficient use of magnetic fields are also major drawbacks of this design [7].

2. Rotary: The most common design used by developers all over the world is a rotary magnetic field source, as it is compact, optimized magnetic field, leakage proof continuous liquid supply through multiple MCM beds, and efficient use of magnets [8].

Basically, MCM is setup in a Halbach array manner in the circular stator and Neodymium magnets inside rotating at a constant frequency of 12–15 rpm. This way multiple MCM beds can be magnetized and demagnetized simultaneously by fewer number of magnets. This optimizes the use of magnets as well as more bed for cooling within a cycle. As permanent magnets are very expensive, this setup is cost-effective [9].

Note that while MCM is magnetizing and demagnetizing, a constant supply of cooling liquid is passing through all the MCM beds and overall temperature drops by the completion of the cycle from initial temperature.

The magnets are rotating with the help of a rotating shaft connected to a low rpm motor, and this is the main component that will require electricity.

Magnetocaloric material	Gd
Weight of magnetocaloric material	0.6–0.75 kg
Fluid of heat transfer	Distilled water
Magnet	NdFeB
Magnetic flux	0.4–0.98 T
Operating frequency	0–4 Hz
Number of AMR	34

4 Demand for Magnetic Refrigeration

Driver: Increasing government initiatives on green technology

The impact of global warming is one of the major challenges faced by the refrigeration and air conditioning (RAC) industry as the existing technology is not environmentally friendly. Increasing global concerns to reduce polluting emissions, especially gases that are harmful to the Earth's environment, has created the need for some alternative source for cooling purposes [10]. Magnetic refrigeration offers a green cooling technology that would enable manufacturers to reduce their carbon footprint. Magnetic refrigeration-based products do not use refrigerants such as chlorofluorocarbons (CFCs), hydrochlorofluorocarbons (HCFCs), and other gases such as ammonia and chlorine, thereby reducing their direct gas emissions. Currently, the majority of refrigerants available in the market have a high global warming potential (GWP), and especially those releasing chlorine largely lead to the depletion of the ozone layer [11]. Refrigerants with low GWP, such as ammonia and CO₂, have been introduced but have safety-related issues such as flammability, toxicity, pressure, and temperature limitations. Refrigeration systems are expected to hold the largest market size of the magnetic refrigeration market during the forecast period.

Magnetic refrigeration has a huge potential for the refrigeration market as it does not use refrigerants and consumes less energy. Moreover, magnetic refrigeration systems do not require a lot of maintenance and are also quieter than traditional units and create fewer vibrations [12]. The different types of refrigeration systems include beverage coolers, cabinet displays, ice cream cabinets, freezers, and refrigerators. Of them, beverage coolers are expected to lead in the segment. These products can be used in domestic, commercial, transportation, and industrial applications. The demand is also likely to be driven by players focusing on entering the market with refrigeration systems.

Some of the key driving factors of the magnetic refrigeration market are

- (1) Increasing government initiatives on green technology, low maintenance costs, compact design, and high energy efficiency offered by magnetic refrigeration technology.

- (2) The adoption of magnetic refrigeration in the commercial sector and high potential across the industrial sector are expected to create growth opportunities for the market.
- (3) The expansion of cold chain infrastructure, the growing retail sector, and the government's focus to reduce the use of harmful refrigerators across the various industries are expected to drive the growth of the market.

Recent Developments

In January 2020, France Brevets, a French company serving the valuation and protection of high-potential technological innovations and the promotion of patents in Europe, launched its license program Kione for a series of patents specialized in magnetic refrigeration technology. The first company licensed as part of this new program was Ubiblue [12].

GE Appliances, a Haier company, and the Office of Energy & Renewable Energy (US) collaborated on a project to successfully harness the Magneto Caloric Effect (MCE) at the Oak Ridge National Laboratory (US). The project was initiated in June 2017 and was planned to finish by June 2020, with the outcome of achieving cooling through MCE. MCE has the potential to reduce energy consumption by 20–30% beyond vapor compression while also eliminating any risk of direct refrigerant emissions to the atmosphere [13].

In October 2019, Cambridge Ltd. participated in a roadshow at the Zhejiang Province (China) to demonstrate its magnetic cooling technology. The event was attended by a highly qualified public composed of Chinese officials, investors, companies, entrepreneurs, etc.

In June 2016, Haier Smart Home completed the acquisition of General Electric's (US) GE Appliances unit. This would help the company to further strengthen its technical capabilities and increase its customer base.

Benefits

- *Reduced operating cost*: As it eliminates the most inefficient part of today's refrigerator, i.e., compressor. The cost reduces as a result.
- *Compactness*: It is possible to achieve a high energy density compact device. It is due to the reason that in the case of magnetic refrigeration the working substance is a solid material (gadolinium) and not gas as in the case of vapor compression cycles.
- *Reliability*: Due to the absence of gas, it reduces concerns related to the emission into the atmosphere and hence it is a reliable one.
- *Noiseless technology* (no compressor) [14].

Applications

Some of the other future applications of magnetic refrigeration are the following:

- Refrigeration in medicine.
- Cooling in food industries and storage.

- Cooling in electronics.
- Cooling in transportations.
- Magnetic cooling and air conditioning in buildings and houses.

Future Aspects

If we think about the future perspective of Magnetic Refrigeration, it can be seen from the earlier description that the main signs of progress have been made in America. However, with the continual phasic progress of magnetic refrigeration, the whole world has accelerated in the research [15]. It is notable that the main work is concentrated on the investigation of magnetic materials, lack of experimental explorations of magnetic refrigerators. From the former results achieved by researchers, it can be seen that there is still a great performance difference between Magnetic Refrigerator and Vapor Compression refrigerator in terms of cooling capacity and temperature span.

The magnetic refrigeration market is expected to be commercialized by 2022 at USD 4 million, and it is expected to grow at a CAGR of 105.4% from 2022 to 2027 to reach USD 165 million by 2027 [16].

References

1. Review of magnetic refrigeration system as alternative to conventional refrigeration system
2. Physical behaviour and properties at the first order phase transition of magnetocaloric materials
3. I.A. Abdel-Latif, M.R. Ahmed, Use of magnetocaloric material for magnetic refrigeration system: a review
4. A Review Paper on Development of Magnetic Refrigerator at Room Temperature Prakash Chawla, Ankit Mathur Jodhpur, India
5. Magnetocaloric effect in the intermetallic compound Gd₇Pd₃
6. Advanced materials for magnetic cooling: fundamentals and practical aspects
7. Large magnetocaloric effect and adiabatic demagnetization refrigeration with YbPt₂Sn
8. I. Jaime, A. Lozano, M.S. Capovilla, P.V. Trevisolia, K. Engelbrecht, C.R.H. Bahlb, J.R. Barbosa, Development of a novel rotary magnetic refrigerator
9. Superconducting Magnet Technology for Future High Energy Proton Colliders
10. Global Warming: a key issue for refrigeration and air conditioning
11. Refrigerants for vapour compression refrigeration systems
12. Magnetic Refrigeration Market by Product ((Refrigeration Systems (Beverage Cooler, Cabinet Display, Refrigerator), Air Conditioning Systems)), Application (Domestic, Commercial, Transportation, and Industrial), and Geography—Global Forecast to 2027
13. Magnetocaloric refrigerator
14. V.S. Patel, J.D. Patel, B.K. Khalasi, A review on: magnetic refrigeration—emerging technology in the field of refrigeration
15. B.F. Yu, Q. Gao, B. Zhang, X.Z. Meng, Z. Chen, Review on research of room temperature magnetic refrigeration
16. Magnetic Refrigeration Market to Reach \$163 Million by 2023: Analysis By Product & Application

A Comparative Study on the Effect of Nanoparticles in Vapour Compression Refrigeration System



Saroj Chavhan Borkar  and Sanjeo Choudhary

1 Introduction

In the new era of rapid industrialization and technology, the world faces an enormous energy crisis. Nearly, 20%–50% of the total production of energy is utilized in thermal systems like refrigeration and air conditioning systems [1]. To overcome this problem, there is a need to develop the energy-efficient thermal system. By introducing nanoparticles in the conventional refrigerant, the thermal performance of the system is improved because nanoparticles have high thermal conductivity than conventional refrigerants. When nanoparticles are added to the refrigerant a new class of fluid is formed called refrigerant-based nanofluid. This type of nanofluid is called nanorefrigerants. For the very first time, Wang et al. [2] introduced the new term of refrigerant called “nanorefrigerants”. Subsequently, innumerable experimental studies have been performed on nanorefrigerants. Many researchers have been trying to work on the refrigeration and air conditioning system utilizing nanorefrigerants as nanofluids to improve the thermal performance of the system [3–5]. Nanorefrigerants can enhance the heat transfer coefficient in evaporator and condenser whereas nanolubricants reduce the energy consumption, thus making the system more compact, lighter and energy efficient [1]. Preparation of nanorefrigerant can be done by dispersing the nanoparticles into the refrigerant whereas by dispersing the nanoparticles into the lubricant in VCRS as shown in Fig. 1.

The purpose of this paper is to explore the effect of various parameters of nanoparticles on the thermal performance of VCRS. In this study, our main aim is to observe the coefficient of performance (COP) and performance improvement of the system by adding different nanoparticles, i.e. Al_2O_3 , TiO_2 , ZnO and CuO in refrigerants like R-12, R-134a, R-600a, R-290/R-600a (Hydrocarbon blend), R-152a, etc.

S. C. Borkar (✉) · S. Choudhary
K. D. K. College of Engineering, Nagpur, India

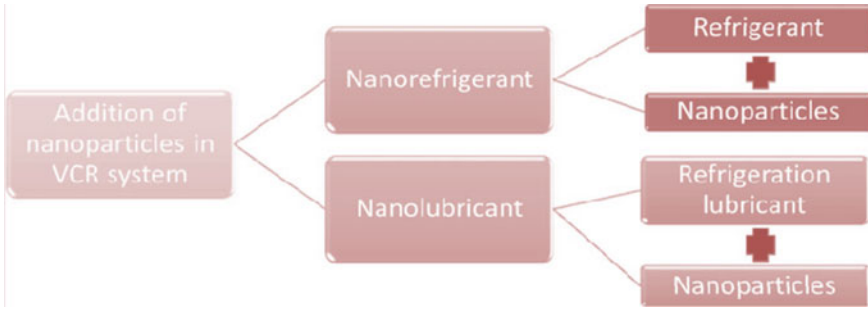


Fig. 1 Addition of nanoparticles in VCRS [6]

2 Study on Various Nanoparticles in Vapour Compression Refrigeration System (VCRS)

Nanorefrigerant enhances the heat transfer rate in evaporator and condenser whereas nanlubricant improves compressor work due to tribological performance. Volume concentration and mass fraction of nanoparticles are calculated using Eqs. (1) and (2) [7] (Fig. 2).

Volume concentration

$$\varphi_n = \omega_n \rho_o / [\omega_n \rho_o + (1 - \omega_n) \rho_n] \tag{1}$$

Mass fraction

$$\omega_n = m_n / (m_n + m_o) \tag{2}$$

where φ_n is the volume fraction.

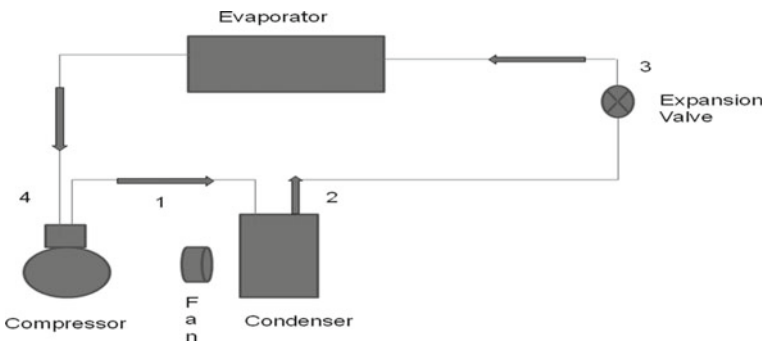


Fig. 2 Conventional VCRS cycle

ρ_n and ρ_o are densities of nanoparticles and lubricant, respectively.

w_n is the mass fraction.

m_n and m_o are masses of nanoparticles and lubricant, respectively.

2.1 Effect of Al₂O₃ Nanoparticles

Subramani and Prakash [7] observed that cooling capacity was improved and there was 25% less energy consumption. The COP of vapour compression refrigeration system was also increased by 33% when refrigerant R-134a was mixed with alumina nanoparticles (Al₂O₃). Yusof et al. [8] performed experimentation on a domestic refrigerator by adding 0.2% Al₂O₃ with polyester (POE) oil in R-134a refrigerant and observed a 7% COP improvement. Also, 2.1% less energy consumption was reported. Kumar and Elansezhian [9] investigated VCRS using Al₂O₃ + PAG oil in R-134a refrigerant and found 10.32% less energy consumption. It was suggested there was reduced capillary tube length and cost-effective refrigeration system using nanorefrigerant. Jwo et al. [10] observed the effect of 0.1% Al₂O₃ nanoparticles suspended in R-600a/R-290/blend (HC) with mineral oil (MO) and found 2.4% less power consumption. Also reported a 4.4% increase in COP. Soliman et al. [11] added 0.1 mass fraction% Al₂O₃ in mineral oil and POE with R-134a and stated VCRS is more useful than a conventional refrigeration system. Also, the author reported nanoparticles Al₂O₃ with polyester oil have given better results than nanoparticles Al₂O₃ with mineral oil.

2.2 Effect of TiO₂ Nanoparticles

Babu et al. [12] observed the effect of Al₂O₃ and TiO₂ nanoparticles with refrigerant R-134a and recorded increased COP and reduction in energy consumption by a compressor on both nanolubricants. Also stated that TiO₂/MO nanolubricants showed higher performance improvement than Al₂O₃/MO nanolubricants. Saba-reesh et al. [13] added 0.05–0.015 vol.% TiO₂ nanoparticles in lubricant used in compressor and showed 0.01% volume fraction gives better tribological properties. They also found a 3.6% increased average heat transfer rate and an 11% reduction in the average compressor work whereas a 17% increase in the COP. Adelekan et al. [14] observed maximum cooling capacity and higher COP using an LPG-TiO₂ nanolubricant mixture in a domestic refrigerator without any modification in length of a capillary tube. Also, stated that this nanolubricant mixture is safe and efficient in the system. Bi et al. [5] experimentally investigated the performance of TiO₂-R600a nanorefrigerant in a domestic refrigerator with no changes in the construction of the system and found 9.6% less energy consumption by adding 0.1 g/L and 0.5 g/L

nanorefrigerant. Mahabubul et al. [15] added TiO_2 nanoparticles gradually in R-123 refrigerant and observed an increased pressure drop.

2.3 Effect of CuO Nanoparticles

Henderson et al. [16] dispersed CuO and SiO_2 nanoparticles of concentration 0.5 vol.% and 0.05 vol.% in refrigerant R-134a and R-134a/POE oil blend and observed reduction in thermal performance of horizontal tube during flow conditions of boiling. Akhavan-Behabadi et al. [17] added 0–1.5 wt% CuO nanoparticles in R-600a and significantly reported up to 63% enhancement in heat transfer coefficient. Sanukrishna et al. [18] added CuO/PAG oil blend with R134a refrigerant in VCRES and found improvement in COP as well as in thermal conductivity of the nanolubricant by adding 0.1 vol.% CuO nanoparticles. Kumar et al. [19] added 0.2–1 wt% CuO nanoparticles in compressor lubricant and found 7% less energy consumption. It was recorded that 46% improvement in COP and decrease in friction and wear. Abdel-Hadi et al. [20] added 0.05–1% CuO nanoparticles sized 15–70 nm and found increased evaporation heat transfer coefficient with optimum concentration of 0.55% with optimum particle size 25 nm.

2.4 Effect of ZnO Nanoparticles

Sendhil Kumar and Elansezhian [21] added 0.1–0.5 vol.% ZnO nanoparticles with 50 nm particle size with R-152a refrigerant in vapour compression refrigeration system. It was recorded that the maximum COP and reduced energy consumption with 0.5 vol.% ZnO/R-152a nanorefrigerant. It was reported that with the increased nanoparticle concentration, the temperature of the evaporator and pressure ratio was reduced. Maheshwary et al. [22] analyzed the effect of cubical and spherical shapes of ZnO nanoparticles added in refrigerant R-134a and observed the shape of nanoparticles significantly affect the thermophysical properties and heat transfer properties. It was found that ZnO nanoparticles are suited for refrigeration and air-conditioning system. Kumar and Singh [23] experimentally investigated the effect of ZnO nanoparticles added with R-290/R-600a hydrocarbon blend in a vapour compression refrigeration system. It was found a 7.48% reduction in energy consumption and about 46% improvement in COP adding 0.2–1.0 wt% nanoparticle concentration. Kumar et al. [24] observed a reduction in energy consumption by 0.44–10% by adding 0.1 g/L–0.7 g/L of ZnO nanoparticles in LPG-based refrigeration system.

Table 1 Al₂O₃ Nanoparticles in VCRS [7–11]

Concentration (%)	0.06 mass%	0.2 vol.%	0.2 vol.%	0.1 wt%	0.1 mass%
COP (%)	33	2.67	–	4.4	–
Energy saving (%)	25	2.1	10.32	2.4	10
Performance improvement (%)	–	–	–	–	22.5

Table 2 TiO₂ Nanoparticles in VCRS [4, 5, 12–15]

Concentration (%)	0.1 mass%	0.5 g/L	0.2 g/L	0.01 vol.%
COP (%)	–	–	20.2	17
Energy saving (%)	26.1	9.60	9.65	11
Performance improvement (%)	–	–	–	–

Table 3 CuO Nanoparticles in VCRS [17–19]

Concentration (%)	0.1 vol.%	0.2–1.0 wt%	0.06 vol.%
COP (%)	7.5	47	19.6
Energy saving (%)	5.2	7	11.5
Performance improvement (%)	11.1	–	–

Table 4 ZnO Nanoparticles in VCRS [21–23]

Concentration (%)	0.5 vol.%	0.2–1wt%	0.1 g/L–0.7 g/L
COP (%)	–	46	–
Energy saving (%)	21	7.48	0.44–10
Performance improvement (%)	–	–	–

3 Summary on the Effect of Various Parameters of Nanoparticles in VCRS

See the Tables 1, 2, 3 and 4.

4 Conclusion

In the present study, four different nanoparticles were added in various refrigerants to observe their effect in VCRS. The following conclusions are extracted from the present study.

- Nanoparticles added with a refrigerant called nanorefrigerant play a great role in VCRS.

- The COP of VCERS enhances by adding nanoparticles to the base refrigerant.
- The energy consumption of a VCERS reduces with the use of nanorefrigerants.
- VCERS performance improvement depends on the concentration of nanoparticles.
- The present study shows the maximum enhancement in COP and energy saving by adding 0.2–1.0 wt% concentration of CuO nanoparticles.
- Therefore, the present study gives CuO nanoparticles as a better option for VCERS.

References

1. I.M. Mahbulul, S.A. Fadhilah, R. Saidur, K.Y. Leong, M.A. Amalina, Thermophysical properties and heat transfer performance of Al₂O₃/R-134a nanorefrigerants. *Int. J. Heat Mass Trans.* **57**, 100–108 (2013)
2. K. Wang, G. Ding, W. Jiang, Development of nanorefrigerant and its rudiment property. International Symposium on Fluid Control, Measurement and Visualization pp. 13–13, Chengdu, China (2005)
3. S. Bi, L. Shi, Experimental investigation of a refrigerator with a nano-refrigerant. *Quinghua Daxue xuebao/Journal of Tsinghua University* **47**, 2002–2005 (2007)
4. S. Bi, L. Shi, L. Zang, Application of nanoparticles in domestic refrigerators. *Appl. Thermal Eng.* **28**, 1834–1843 (2008)
5. S. Bi, K. Guo, Z. Liu, J. Wu, Performance of a domestic refrigerator using TiO₂-R600a nano-refrigerant as working fluid. *Energy Conver. Manag.* **52**, 733–737 (2011)
6. M.Z. Sharif, W.H. Azmi, R. Mamat, A.I.M. Shaiful, Mechanism for improvement in refrigeration system performance by using nanorefrigerants and nanolubricants-a review, 56–63 (2018)
7. N. Subramani, M.J. Prakash, Experimental studies on a vapour compression system using. *Int. J. Eng. Sci. Technol.* **3**(9), 95–102 (2011)
8. T.M. Yusof, A.M. Arshad, M.D. Suziyana, L.G. Chui, M.F. Basrawi, Experimental study of a domestic refrigerator with POE-Al₂O₃ nanolubricant. *Int. J. Mech. Eng. Technol.* **11**, 2243–2252 (2015)
9. D.S. Kumar, R.D. Elansezhian, Experimental study on Al₂O₃-R134a nanorefrigerant in refrigeration system. *Int. J. Modern Eng. Res.* **2**(5), 3927–3929 (2012)
10. C.S. Jwo, L.Y. Jeng, T.P. Teng, H. Chang, Effects of nanolubricant on performance of hydrocarbon refrigerant system. *J. Vacuum Sci. Technol. B: Microelectron. Nanometer Struct. Proces.* **27**(3), 1473–1477 (2009)
11. M.A. Aly, Soliman, A.K. Abdel Rahman, S. Ookawara, Enhancement of vapor compression cycle performance using Nanofluids Experimental results. *J. Thermal Anal. Calorimetry* (2018)
12. M. Babu, S. Nallusamy, K. Rajan, Experimental analysis on vapour compression refrigeration system using nanolubricant with HFC-134a refrigerant. *Nano Hybrids* **9**, 33–43 (2016)
13. R.K. Sabareesh, N. Gobinath, V. Sajith, S. Das, C.B. Sobhan, Application of TiO₂ nanoparticles as a lubricant additive for vapor compression refrigeration systems—an experimental investigation. *Int. J. Refrigeration* **35**, 1989–1996 (2012)
14. D.S. Adelekan, O.S. Ohunakin, T.O. Babarinde, M.K. Odunfa, R.O. Leramo, S.O. Oyedepo, Experimental performance of LPG refrigerant charges with varied concentration of TiO₂ nanolubricants in a domestic refrigerator. *Case Studies Thermal Eng.* **9**, 55–61 (2017)
15. I.M. Mahbulul, R. Saidur, M.A. Amalina, Pressure drop characteristics of TiO₂-R123 nanorefrigerant in a circular tube. *Eng. Trans.* **6**, 124–130 (2011)
16. K. Henderson, Y. Park, L. Liu, A.M. Jacobi, Flow-boiling heat transfer of R-134abased nanofluids in a horizontal tube. *Int. J. Heat Mass Transf.* **53**, 944–951 (2010)

17. M.A. Akhavan-Behabadi, M. Nasr, S. Baqeri, Experimental investigation of flow boiling heat transfer of R-600a/oil/CuO in a plain horizontal tube. *Exp. Thermal Fluid Sci.* **58**, 105–11 (2014)
18. S.S. Sanukrishna, A.S. Vishnu, M. Jose Prakash, Nanorefrigerants for energy efficient refrigeration systems. *J. Mech. Sci. Technol.* **5**, 3993–4001 (2017)
19. R. Kumar, J. Singh, P. Kundal, Effect of CuO nanolubricant on compressor characteristics and performance of LPG based refrigeration cycle: experimental investigation. *Heat Mass Transf.* **54**, 1405–1413 (2018)
20. E.A. Abdel-Hadi, S.H. Taher, A.H.M. Torki, S.S. Hamad, Heat transfer analysis of vapor compression system using nano CuO-R134a, in *International Conference on Advanced Materials Engineering IPCSIT*, Vol. 15, pp. 80–84 (2011)
21. D. Sendil Kumar, R. Elansezhian, ZnO nanorefrigerant in R152a refrigeration system for energy conservation and green environment. *Front. Mech. Eng.* **9**(1), 75–80 (2014)
22. P.B. Maheshwary, C.C. Handa, K.R. Nemade, Effect of Shape on Thermophysical and Heat Transfer Properties of ZnO/R-134a Nanorefrigerant *Materials Proceedings* **5**, 1635–1639 (2016)
23. R. Kumar, J. Singh, Effect of ZnO nanoparticles in R290/R600a (50/50) based vapour compression refrigeration system added via lubricant oil on compressor suction and discharge characteristics. *Heat Mass Transf.* **53**, 1579–1587 (2017)
24. R. Kumar, D.K. Singh, S. Chander, An experimental approach to study thermal and tribology behavior of LPG refrigerant and MO lubricant appended with ZnO nanoparticles in domestic refrigeration cycle. *Heat Mass Transf.* **56**, 2303–2311 (2020)

An Experimental Evaluation of FEA-Based Helical Compression Spring to Design a Shock Absorber



Amol Vikas Joshi, Devanand Tayade, and Wasim Patel

1 Introduction

A shock absorber is a mechanical device designed to smooth out or damp shock impulse & dissipate kinetic energy. Shock absorber or suspension system contains helical spring, hydraulic or pneumatic piston-cylinder combination called as a damper. In this static structural analysis, work is on helical spring, so design procedure is carried out on helical spring [1, 2].

Helical spring: The helical spring is made up of a wire coiled in the form of a helix and is primarily intended for a compressive or tensile load. The cross-section of wire from which the spring is made may be circular, square, or rectangular. Two types of helical spring: (A) compression and (B) tension in nature. Compression spring is used for the suspension system of the bike.

Selection of material: The material of the spring should have high fatigue strength, high ductility, high resilience and it should be creep resistant. It largely depends upon the service for which they are used, i.e., severe service, average service, or light service [1–4]. Average service material is used for the automobile suspension system. Carbon steel material is used for the suspension system of a helical spring [4, 5].

1.1 Problem Definition

The important problem that is faced by the automotive industry is that vehicle handling becomes difficult and leads to uncomfortable rides when spring bouncing

A. V. Joshi (✉) · D. Tayade · W. Patel
Department of Mechanical Engineering, G H Raisoni Institute of Business Management, Jalgaon, India

is uncontrolled. This is based on a number of parameters such as load applied and the duration of it. Therefore, the existing design is modified in order to minimize the stress and discomfort experienced by the passengers. In this study, calculations are done analytically and trials are conducted by simulation, in order to find out the results.

Objective

- To study the various parameters influencing the stress and deformation induced.
- To conduct experiments on helical compression springs to obtain desired results.
- To compare the results of existing and modified design through ANSYS and analytical methods for different load conditions.

1.2 Loading Conditions

While taking analysis on helical spring forces is assume in the form of bike weight 125 kg, single man 65 kg double man weight 130 kg, similarly single man 70 kg and double man 140 kg. By using these loading conditions, compare the modified spring results with standard spring. Consider 65% of weight is transferred to rear suspension system [6].

2 Methodology

2.1 Technical Specification

In this work, modify the dimension of standard helical spring such as wire diameter, coil diameter, named as modified helical spring. With the help of loading conditions check the modified and standard helical spring and find a suitable helical spring to design a bike suspension system.

2.2 Maximum Shear Stress and Deformation of Spring Calculations for Both Springs

See the Table 1.

Table 1 Technical specification of compression spring

Specification	Standard spring	Modified spring
Modulus of rigidity	$80 \times 10^3 \text{ N/mm}^2$	$80 \times 10^3 \text{ N/mm}^2$
Modulus of elasticity	$210 \times 10^3 \text{ N/mm}^2$	$210 \times 10^3 \text{ N/mm}^2$
Wire diameter	7.00 mm	7.60 mm
Outside diameter	50.00 mm	57.00 mm
Mean diameter	43.00 mm	49.40 mm
Total no. of coils	18	18
Active coils	16	16
Free length	240 mm	240 mm
Spring index = D_m/d	6.143	6.5
Wahl's stress factor = $\frac{4C-1}{4c-4} + \frac{0.615}{C}$	1.25	1.2309

3 Analytical and Experimental Methods

3.1 Analytical Method

This method uses the calculation of stresses and deformation by applying various loading conditions.

$$\text{Maximum shear stress } \tau = \frac{8K_cWC}{\pi d^2}$$

$$\text{Deformation } \delta = \frac{8Wc^3N_A}{Gd}$$

3.2 FEA Method

Geometric modelling

See Figs. 1, 2, 3, 4, 5 and 6.

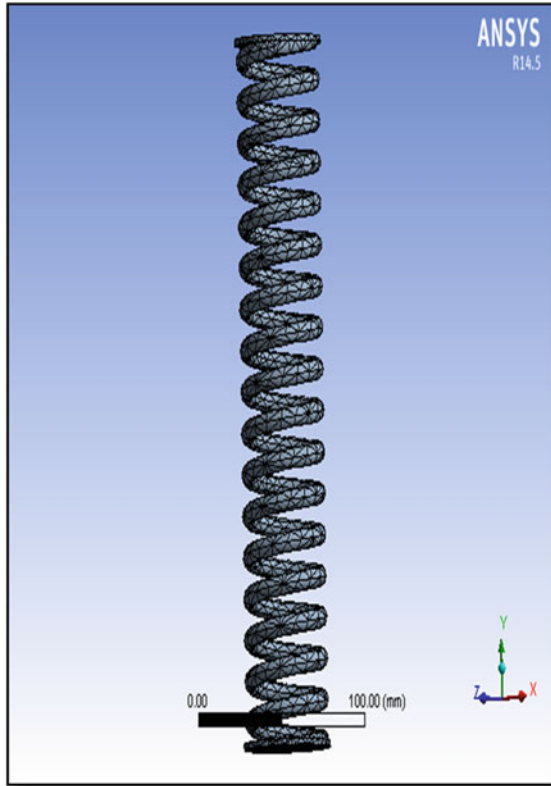


Fig. 1 Meshing on the existing spring model

3.3 *Experimental Method*

To compare the analytical and F.E. analysis results in this work, U.T.M. machine is used. U.T.M machine has the capability to calculate deformation by the compressive or tensile load. In this work, a compressive load on the helical spring is applied and the results are checked (Fig. 7).

4 **Results**

Stresses and deformation values for the existing and modified design of the helical compression spring are found out through the analytical FEA tool and experimental calculations for different loading conditions are compared (Tables 2, 3 and Figs. 8, 9, 10, 11 and 12).

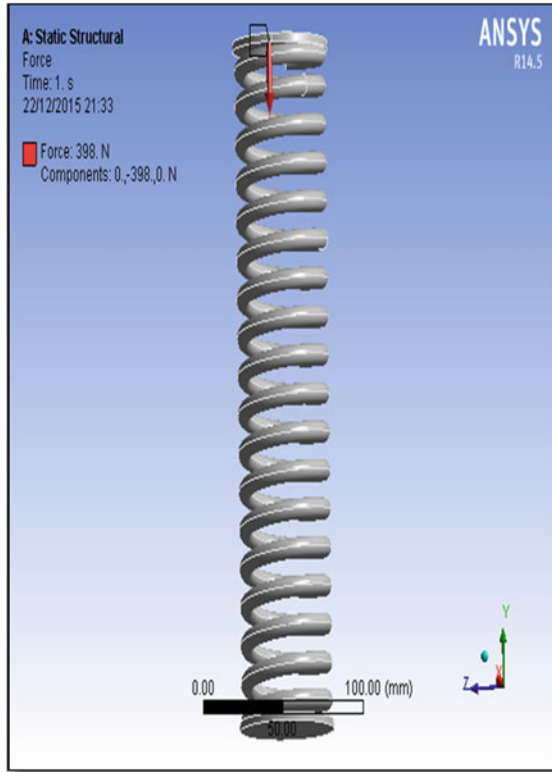


Fig. 2 Load on the existing spring model

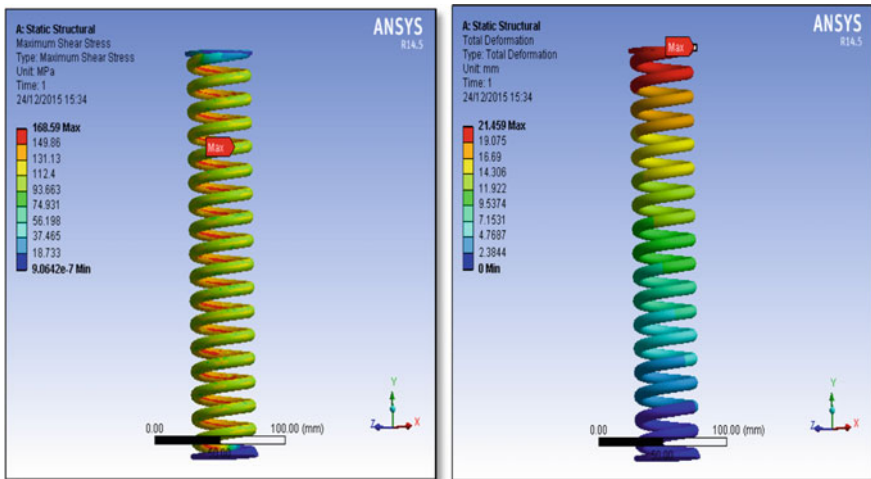
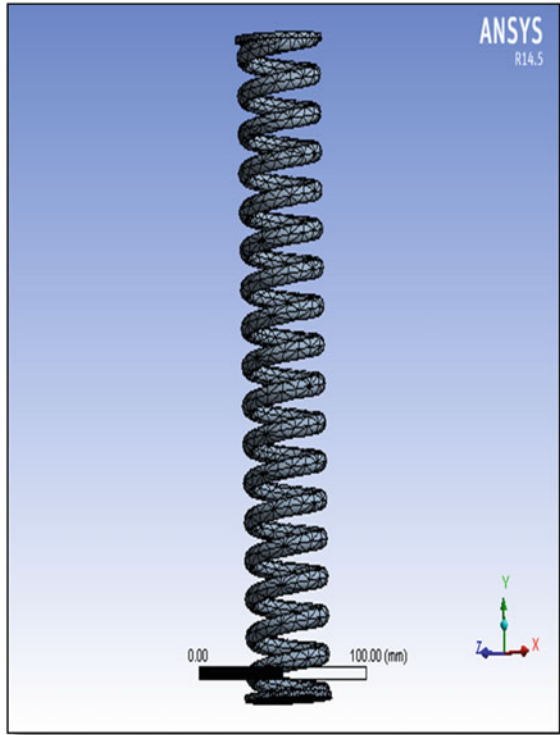


Fig. 3 Shear Stress 168 N/mm^2 and deformation 21 mm on existing spring

Fig. 4 Meshing on modified spring model



5 Conclusions

In this study, the helical compression spring is modified for the shock absorber so that stresses acting on it are reduced, but the deformation of spring is slightly increased by application of suggested loading conditions. By comparing the results obtained from analytical, F.E.A., and experiment based, it has been concluded that the modified design of a helical spring for a shock absorber is safe for loading conditions.

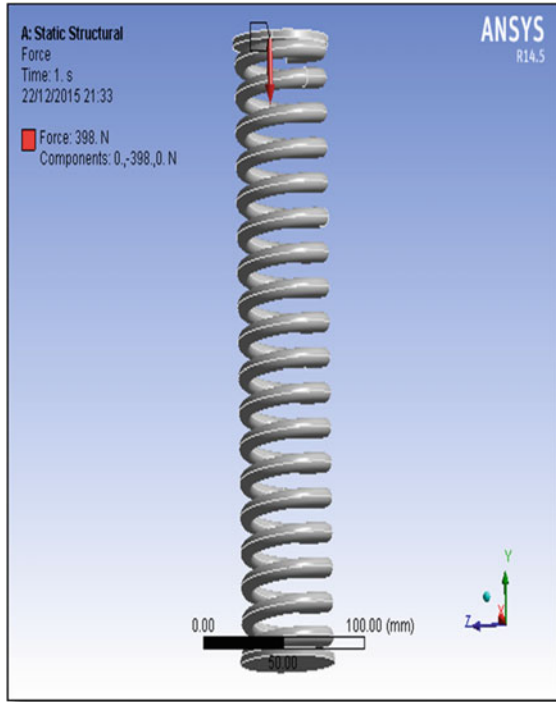


Fig. 5 Load on modified spring model

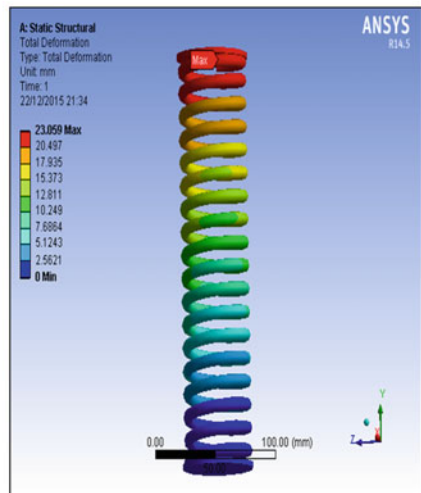
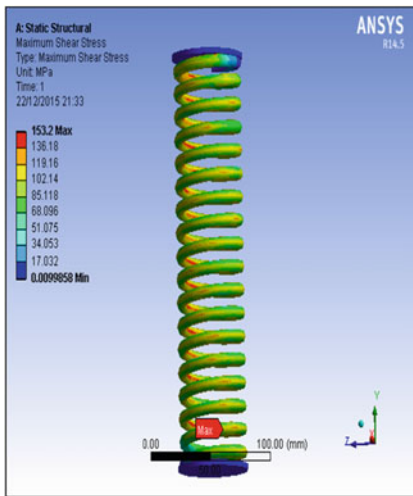


Fig. 6 Shear Stress 153.2 N/mm² & deformation 23 mm on existing spring

Fig. 7 Spring model on U.T.M



Table 2 Stresses on helical compression spring

Load (N)	Analytical stress		F.E.A. stress	
	Standard	Modified	Standard	Modified
398.53	159.03	140.58	168.59	153.2
605.76	241.73	213.67	256.28	232.89
813	324.43	286.77	344.39	312.95
621.7	248.09	219.29	263.06	239.04
844.88	337.15	298.01	357.52	324.89

Table 3 Deformation of helical compression spring

Load (N)	Analytical deformation (mm)		F.E.A. deformation		Experimental deformation	
	Standard	Modified	Standard	Modified	Standard	Modified
398.53	21.12	23.04	21.45	23.04	22.24	23.80
605.76	32.09	35.02	32.62	35.05	33.50	34.92
813	43.07	47	43.83	47.1	43.80	46.20
621.7	32.94	35.94	33.48	35.97	34.55	35.15
844.88	44.77	48.84	45.5	48.9	46.10	48.72

Fig. 8 Stresses on helical compression spring analytically

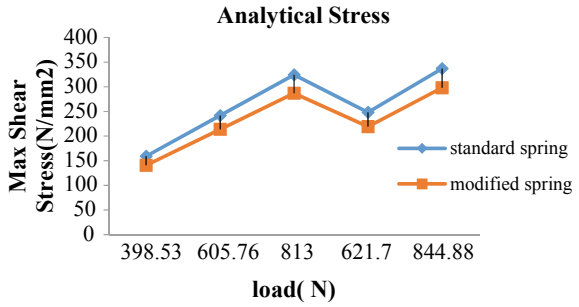


Fig. 9 Stresses on helical compression spring by FEA

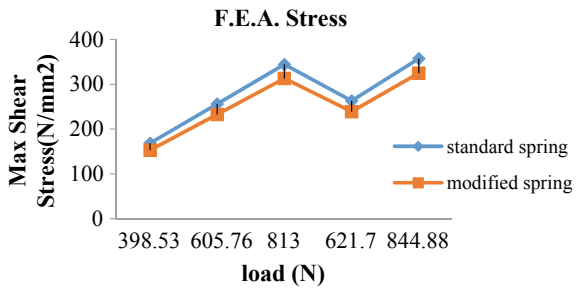


Fig. 10 Deformation on helical compression spring analytically

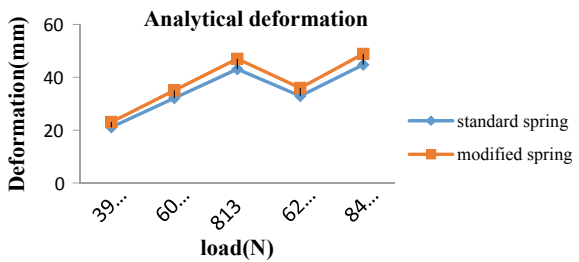


Fig. 11 Deformation on helical compression spring FEA

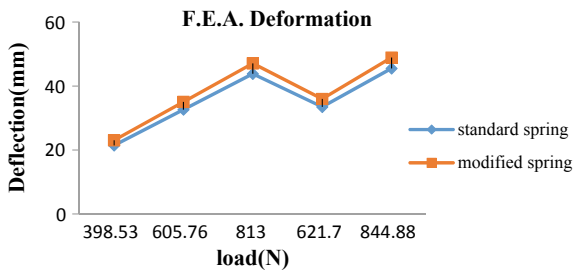
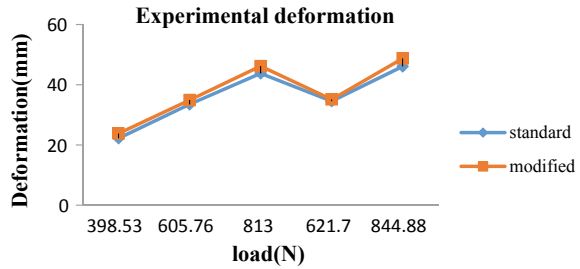


Fig. 12 Deformation on helical compression spring experimentally



References

1. J.M. Gallardo, L. Soria, E.J. Herrera, Investigation of service failures in automobile shock absorbers. *Eng. Failure Anal.* **14**, 355–363 (2007)
2. P. Yang, Yonghong, T. Jianmin, Measurement, simulation on dynamic characteristics of a wire gauze–fluid damping shock absorber. *Mech. Syst. Signal Proc.* **20**, 745–756 (2006)
3. A.K. Samantaray, Modeling and analysis of preloaded liquid spring/damper shock absorbers. *Simul. Model. Pract. Theory* **17**, 309–325 (2009)
4. P. Achyut, D. Nitin, Bhusale, V. Kautuk, Totawar design and analysis of shock absorber using FEA tool. *Int. J. Eng. Res. Dev.* **10**(2), 22–28 (2014)
5. ANSYS workbench Tutorial Release 14 by Kent L. Lawrence SDC publication edition (2014)
6. Q. Xian, S. Zhan, Optimization design and calculation of the variable stiffness coil spring applied to vehicles. *Int. J. Sci. Res. (IJSR) ISSN (Online): 2319–7064* (2012)
7. V. Bhandari, *Machine Design* Tata Mcgraw Hill Education Private Limited Publication Third Edition (2007)
8. R. Khurmi, *Machine Design* by S. Chand publication (Pvt.) Ltd. Publication Fourteenth Edition (2005)

Laboratory Investigation of Composite Made of Alumina Dispersed Aluminium Prepared by UTM Pressed Powder Metallurgy Method



M. K. Manik, Mani Bhushan Singh, and Vishal Vhagat

1 Introduction

Al–Al₂O₃ composites are an important member of the metal matrix composites (MMCs) and are widely being used in the aerospace and automobile industries [1–7]. These materials have received large demand due to their improved mechanical, tribological and high-temperature properties [1–8]. Composite is a product made up of two or more different types of materials that are combined together to form something totally different than that of the original constituents [9]. They are combined in such a way that the resulting material or composite possesses superior properties than any of their individual constituents. Composites are widespread among natural and engineering materials, a composite made of ceramics is shown in Fig. 1. The essential components in the composite are matrix and fibre, fibre is generally load-carrying members in composites, whereas matrix protects fibres from damage and acts as envelop around the fibres. The method of production has a strong influence on the mechanical and tribological properties of these composites via its effects on the matrix grain size, porosity and distribution of reinforcing particles [10–12]. Among the different processing methods, powder metallurgy (PM) is an important one for the production of MMCs. Two important advantages of PM over other casting techniques include the uniform distribution of reinforcing particles within the matrix and less degradation due to lower processing temperatures [4, 10–18]. The basic manufacturing steps in the PM technique for producing particulate MMCs include the mixing of a matrix alloy powder with reinforcing particles, followed by compacting and sintering [3, 4, 10, 12, 13, 17–19].

M. K. Manik (✉) · M. B. Singh

Department of Mechanical Engineering, LDC Institute of Technical Studies, Soraon Prayagraj 211025, India

V. Vhagat

CCET, Bhilai, Chhattisgarh 492026, India

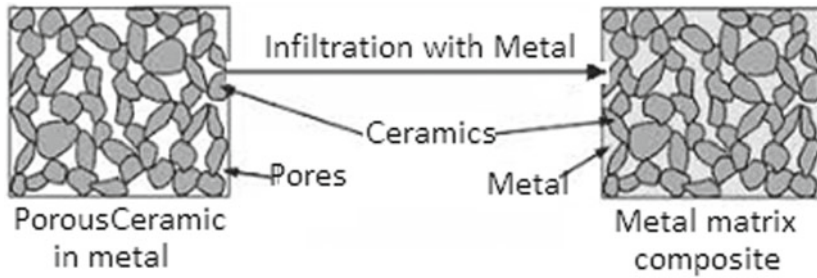


Fig. 1 Shows metal and Ceramic formed metal matrix composite

In general, there are three different types of composites:

1. Particles reinforced composites
2. Short fibre MMCs
3. Continuous fibre or sheet reinforced Composites

The widespread application of MMCs in different fields has boosted up in the last 20 years due to the availability of suitable reinforcements with low-cost processing techniques which gives rise to reproducible properties. Interfacial zone between the matrix and reinforcement phase acts as an essential part of MMC. When considering the design of an MMC, the root interfacial phenomenon which governs the transmission of mechanical, thermal and electrical properties is of absolute importance [7]. The current advancement of Al_2O_3 reinforcement's makes it possible to control the physical and mechanical properties of MMCs that has directed to extensive use of Al_2O_3 composites in power electronics, aerospace, packaging and heat transfer purposes.

Latest progress in this field advocated that step-up growth of procurement of MMC economically appreciated and suggested for bright future for these types of materials. Augmented demand of MMCs have noticeably been viewed from the last decade due to their improved mechanical properties such as modulus, strength; wear resistance, thermal resistance and fatigue resistance and other performance compared to the unreinforced matrix alloys. The reinforcements are added externally or formed internally by different reactions. The properties of MMCs mainly depend on the properties of matrix material, reinforcements and the matrix-reinforcement interface [8]. The shape and size of Matrix, as well as reinforced particles, their orientation within composite play a very crucial part in the physical properties of the composite.

The metal used as matrix is the primary constituent for the fabrication of metal matrix composites (MMCs). The choice of metal mainly depends on the cost and other parameters for the expected applications. One of the most essential factors is the compatibility of the matrix material with the reinforcement. Compatibility means, there is no undesirable chemical reaction between the matrix and reinforced materials that may occur during the process of preparation or after the formation of the composite. The creation of dissimilar inters metallic compounds may lead to the redundant and dangerous effect of transferring load to the reinforcements.

Also, the reaction products may act as sites for the nucleation of cracks [10]. The improved mechanical property of MMCs often provided due to the presence of reinforcement are increased modulus, strength and fatigue strength. On the other hand, the ductility and fracture toughness of MMCs are known to be inferior to those of the unreinforced matrix alloys, because the ductility and toughness of most ceramic reinforcements are very low. These features are very essential for any load-bearing structural applications. Therefore, it is apparent that the matrix alloys having higher ductility and fracture toughness are desirable for MMC applications [10].

The author took an immense interest to make a composite of alumina dispersed aluminium prepared by the application of Powder metallurgy technique, where plastic deformation is done in the green sample under UTM pressing. Several studies have been reported that fine grain (FG) materials can be used as super high strength materials, intelligent and superplastic materials for various applications. The significant findings in this paper are to show the effect of defined speed and time during mixing and milling of fine grain materials before sintering process and change in microstructural as well as mechanical behaviour on pressing and thermal diffusion after sintering. As we know the effect of impurities in the powder plays an important role in the sintering, hence very high purity aluminium powder was used in this experiment.

2 Experimental Set Up and Process of Preparation of Material

For the requirement of experimental investigation, initially pure aluminium in the form of small bar is collected from the chemical supplier of laboratory, and the properties of pure aluminium is found out in our material laboratory by melting the supplied metal in an open furnace and pouring it into the mould cavity that is prepared with the help of wooden Pattern and green sand in the casting laboratory of MNNIT, Allahabad. The composition of supplied material is specified by the laboratory as tabulated below in Table 1.

Melting of the material in a furnace, preparation of moulding sand, preparation of wooden pattern and detailed procedure of casting is shown in Fig. 2(a–h). As soon as casting of pure aluminium is prepared, then samples for different tests have been cut from the casting block as shown in Fig. 2(a–h).

All the samples are prepared as per standard procedure and the same are tested under different testing equipment after checking their accuracy. The error of the

Table 1 Sample of aluminium is supplied by Bonnafied Chemicals, Kanpur

Components	Fe	Si	Mn	Mg	Al wt.%
Pure Al %	0.062	0.041	0.002	0.002	99.893



Fig. 2 a) Wooden patterns used for open casting, b) Preparation of green sand for casting, c) Patterns are placed to produce mould cavity, d) Mould cavity is ready for pouring liquid metal, e) and f) Aluminium is melted in an open furnace, g) Liquid metal is poured into the cavity and h) Casting of aluminium is ready for different samples for test

testing equipment is adjusted for each and every case by adding (+) or subtracting (–) error if recorded with any machine.

To find out the various test results of aluminium that was purchased for laboratory is tabulated in the datasheet for the purpose of comparison with different proportionate mixed composite of aluminium to alumina. Here, a single test procedure of tensile test is shown in Fig. 3(a–f). Similarly, all the samples are tested and the result of pure aluminium of various tests is tabulated in an excel sheet for comparison. The same sample is then transformed into powder form by chipping and ball milling methods for further application in composites.

2.1 Method of Mixing of Samples

Alumina (Al_2O_3) powder of 2, 4, 6, 8 and 10wt.%, respectively, added separately every time with pure aluminium metal powder and mixed in a planetary ball mill with the agate jar and agate balls having a ball to powder weight ratio (BPR) as 5:1 and allows rotating ball milling apparatus with the speed of 100 rpm for 2 h to certify regular distribution of alumina particles throughout the aluminium matrix. Mixing speed and time was maintained constant for every mixture for making a proper comparison. Toluene was used as a solvent to minimize frictional heat generation for the process; the balls for milling and charging were totally submerged in toluene (Table 2).

Five dissimilar mixing proportions were chosen and tabulated in Table 3 given below. Finally, all the samples were coded as Metal Ceramic Composite (MCC)

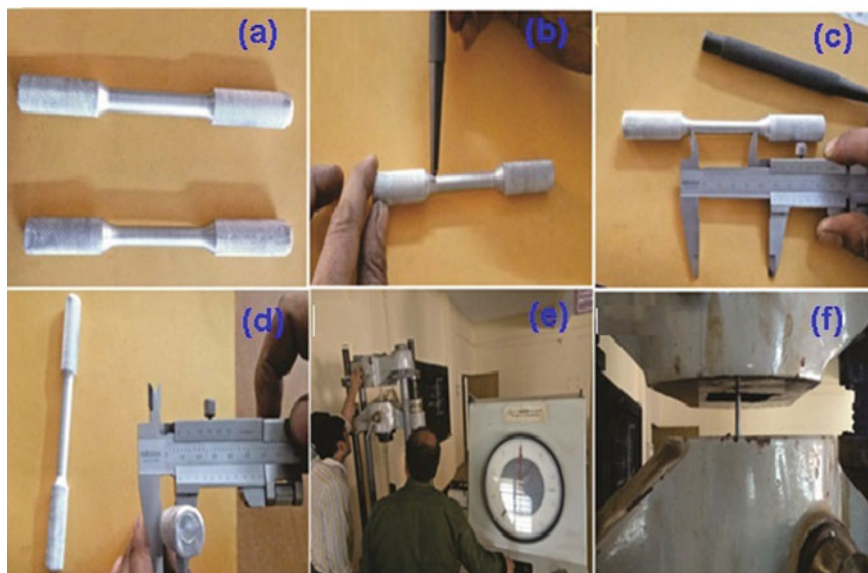


Fig. 3 a) Samples are prepared for UTM test, b) Punching is done to measure gauge length, c) and d) Measurement of gauge length and diameter with Vernier calliper, e) Setting of samples in UTM and process of testing is done and f) Final position sample at the end of the test

Table 2 Mixing Parameter

Mixing	Parameter
Planetary ball mill (Retsch PM 100)	Milling Media-Toluene
Milling jars-Agate jars	Ball to powder ratio-5:1
Milling Balls-Agate balls	Mixing Speed-100 rpm
	Mixing Time-2 h
	Powder mixture Weight-10gm

Table 3 Sample code and Composition for mixing

S.no	Sample code	Sample composition
1	MCC2	98wt% Al + 2wt% Al ₂ O ₃
2	MCC4	96wt% Al + 4wt% Al ₂ O ₃
3	MCC 6	94wt% Al + 6wt% Al ₂ O ₃
4	MCC 8	92wt% Al + 8wt% Al ₂ O ₃
5	MCC10	90wt% Al + 10wt% Al ₂ O ₃

Table 4 Milling parameter

Milling	Parameter
Planetary ball mill (Retsch PM 100)	Milling Media-Toluene Ball to powder ratio-10:1 Milling Speed-300 rpm
Milling jars-hard stainless-steel jar	Milling Time-10 h
Milling Balls-hard stainless steel	Powder mixture Weight-10gm

with their ceramic percentage as a suffix, as for example, two percent ceramics in the mixture (MCC2) and so on.

2.2 Method of Milling of Samples

Different proportionate of alumina is added into aluminium metal mixed and milled in a planetary ball mill. Retsch PM 100 ball mill which is a convenient benchtop model with 1 grinding station is used in this experiment. This is a very high-energy ball mill of maximum operating efficiency. The distinct combination of high friction with specified impact results in exceptionally fine elements within the shortest possible time. Toluene was used as the process control agent (solvent) for the milling, where the balls and charge were totally submerged in toluene. The detailed structural and working parameters of the planetary mill and its components are described in Table 4 (Fig. 4).

2.3 Compaction of Sample Materials

Thoroughly alumina mixed aluminium samples were then collected for cold compactions under Universal Testing Machine (UTM) is shown in Fig. 5, and the sample was placed for a specific time under pre-defined load in a material testing laboratory at MNNIT, Allahabad, for preparing green mould for the onward groundwork of Powder metallurgy method. Table 5 shows the detail of compaction parameters used in the experiment.

The starch solution is used as a binder for giving sufficient strength to green mould for handling before sintering. Stearic acid is used as a lubricant to minimize die wall-particle as well as inter particles friction in the processes of compaction.



Fig. 4 Initially all the materials required for the experiment were made ready in the Material testing laboratory **a)** Retsch PM100 Ball Mill used for mixing as well as milling, **b)** Hard stainless-steel jar used to hold hard steel ball that helps/milled the material under processes, **c)** Hard stainless-steel ball that is used with Jar **d)** ceramics powder, i.e. Al_2O_3 , **e)** Aluminium powder used here as a base material for composite **f)** Liquid toluene is used as a solvent and Stearic acid is used as lubricant in the material preparation method



Fig. 5 Die and plunger used for compaction

Table 5 UTM pressing parameter

Parameter	Detail
Die size	12 mm
Pressing force	Up to 50Kn
Pressing time	3 min
Binder	PVA(4 wt% of powder weight)
Lubricant	Stearic acid

2.4 Sintering of Samples

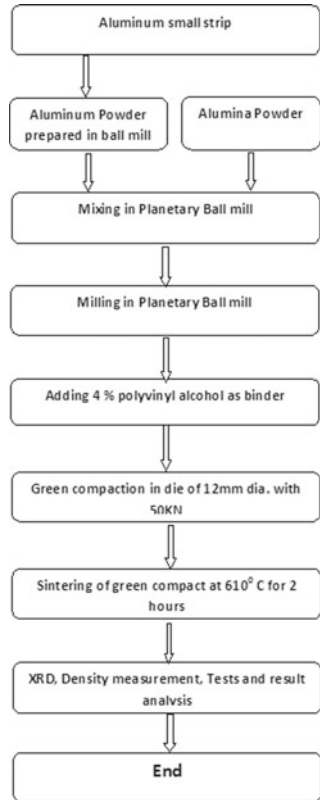
The compacted pellets of composites were further placed inside in a horizontal tubular argon atmosphere furnace where the temperature was constantly monitored at 610 °C for densification of the compacted powder samples. The heating rate of 10 °C/min. was maintained throughout the heating period and the holding time for the samples was predetermined for 2 h in all cases sustaining similarity for all samples.

Finally, cooling of the furnace was done at room temperature and the samples were taken away for the next process. The size of the pellets was determined as 12 mm in diameter and 4 mm–5 mm in thickness, so that it will be easy to prepare different test samples for carrying out necessary tests after sintering. An automatic constant heating high-temperature tubular furnace was used in IIT Roorkee for the sintering process that was shown in Fig. 6. The detailed procedure of formulation of composite is shown in the flow chart in Fig. 7.



Fig. 6 High-temperature tubular furnace and its different subassemblies Kept in Material testing laboratory in IIT, Roorkee

Fig. 7 Flow chart for complete procedure



3 Test Result and Discussion

3.1 Density Measurement

The calculation of theoretical density was determined by means of the standard formula of the mixture.

$$\frac{1}{\rho_c} = \frac{W_f}{\rho_f} + \frac{W_m}{\rho_m} \tag{1}$$

where ρ_f, ρ_m, ρ_c , are the density of reinforcement fibres, matrix and composite, respectively, and W_f, W_m are weight fraction of reinforced fibres and matrix, respectively. The experimental density of the sample was calculated from.

$$\rho = \frac{m}{v} \quad (2)$$

where v = Volume of samples and m = mass of sample after sintering.

Fabricated composites were reinforced with fine grains of Al_2O_3 particles in varying wt.% with pure aluminium. The mechanical properties of pure aluminium were examined in the material testing laboratory before reinforcing it and the details are specified in Table 1. The different weight portions of Al_2O_3 in the mix were chosen as 2, 4, 6, 8 and 10 wt.%, respectively. Composites of the diverse specification were produced one by one through UTM compressed powder metallurgy technique.

To find out the porosity content, measurement of density was calculated in both pure and composites reinforced with all different wt.% of fine grains of Al_2O_3 particles as per formula (1). The result of the mixed samples is tabulated in Table 6 taking into account as $\rho_{\text{Al}} = 2.77$ and $\rho_{\text{Al}_2\text{O}_3} = 3.67$, respectively.

The investigated outcome of the theoretical and experimental density of mixed and milled samples are tabulated in Table 6, where mixed, milled metal and ceramics powder for composites are abbreviated for 2, 4, 6, 8 and 10 as (MCC2 to MCC10), respectively. The plot of density versus wt.% of reinforced Al_2O_3 mixed and milled samples are revealed in Fig. 8a and b. The result demonstrated that the density of mixed samples increases proportionally with an increased weight percentage of reinforced Al_2O_3 because the mass of single Al_2O_3 ($m = 112$) molecules is almost 3.77 times heavier than the mass of one atom of pure aluminium ($\text{Al} = 37$). In the curve, it is clearly confirmed that the density of the mixed, as well as milled sample, sharply increases up to 4 Wt.% of Al_2O_3 , and thereafter the slope flattens up to 10% wt. Al_2O_3 . Sharp increase of density may be the cause of interstitial occupying of mixture molecule within the metal lattice and when excess (>4%) is added, then it occupies the place in interlayers spacing.

The plot clearly shows that the theoretical density is comparatively higher than that of the observed value because in the process of physical mixing, trapped and entrained air and gages remain in the mixture resulting in a lower density than the expected value. The maximum value of observed density of mixed sample increases

Table 6 Density of mixed and milled samples and their densifications

S.n	Sample code	Theoretical density (g/cm^3)	Experimental density of mixed samples (g/cm^3)	Experimental density of milled samples (g/cm^3)	% Densification of mixed sample	% Densification of milled sample
1	MCC2	2.79	2.51	2.53	92.60	89.96
2	MCC4	2.81	2.55	2.59	92.20	90.75
3	MCC6	2.83	2.57	2.57	91.93	89.75
4	MCC8	2.84	2.58	2.61	92.34	90.14
5	MCC10	2.85	2.59	2.63	93.26	90.75

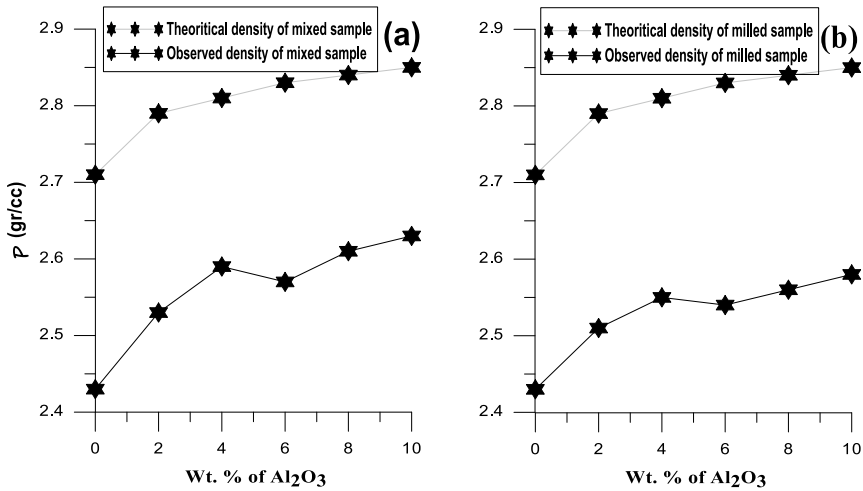


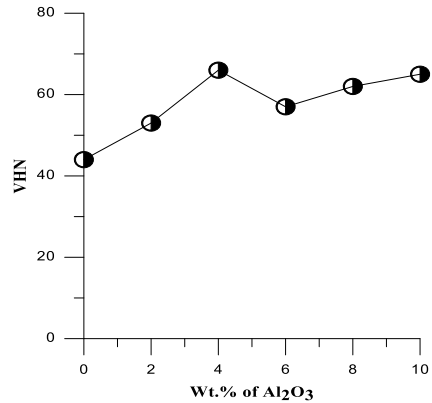
Fig. 8 a) Density variation of mixed and b) milled samples

about 8.23% and 6.17% in the milled sample for Wt.% of 10 Al₂O₃ /Al as compared to pure aluminium density. The cause of interface bonding between the two phases may be due to physical and chemical interaction, interface hooking between the surfaces, interfacial friction stresses, thermal stresses between the face boundaries and finally due to adhesion that plays a very vital role to strengthen the interfacial attachment that causes higher densification, low expansion coefficient and better mechanical properties. It is also viewed that the mixing sample possesses maximum densification closely as 93.26 for a mixture having 10 wt.% of Al₂O₃, whereas the milled sample possesses 90.75 densification for the same composition. A similar result has been notified in the literature [21, 22].

3.2 Hardness Measurement

Microhardness testing was performed on the surface of polished samples using a UHL Vickers microhardness tester kept in the Material testing Laboratory of MNNIT, Allahabad. The indents were taken at room temperature using 100 gf load and 15 s of dwell time. A minimum of 20 indents were taken to find the average and standard deviation for each value. The diagonal lengths of the square indentations were measured by the attached microscope. The Vickers hardness (H_v) was determined from the following equation: $H_v = 1.854 \frac{P}{d^2}$ and $d = \frac{d_1 - d_2}{2}$; where d, d₁ and d₂ are projected and two diagonals diameters of indenter, respectively, and P is the load acted on the indenter. Figure 9 shows the variation of the average VHN number of aluminium reinforced with 2, 4, 6, 8, 10 wt.% of Al₂O₃/Al, respectively. The diagram visibly expresses

Fig. 9 Variation of microhardness at different wt.% Al₂O₃ mixed Aluminium



the average hardness value for samples MCC2, MCC4, MCC6, MCC8 and MCC10 with the pure sample having Zero (0%) of ceramic powder.

The sharp increase in hardness up to 4 wt.% may be the cause of occupying of fine grain-particles of Al₂O₃ within the interstitial gap of aluminium matrix and partially due to grain refinement with particle strengthening effects. The value of hardness of composite increases more than 50% as compared to the hardness of pure aluminium with the same temperature. A similar observation has been reported in the literature [21, 22]. Generally, for a metal, the density is proportional to its hardness, so this result possesses good agreement with the metallic properties.

3.3 Result and Analysis Based on UTM Test

The accuracy of the equipment was tested by taking number of readings (12–15 readings) of similar samples as per standard operating conditions. The detail shape, specification of samples of pure aluminium and its result are given in Table 7 and the same for composites are recorded in Table 8.

Details of prepared samples are marked on the base of their Al₂O₃ percentage and testing in UTM also is shown in Fig. 10a–c. It was observed that the stress–strain relationship for all the samples follows a linear relationship from the beginning to the point of fracture. The deviation of linearity was observed in the testing graph just at the point of crack on the specimen. The average of the three results was taken for comparison in all cases. The result demonstrates that the Poisson ratio, Breaking load and UTS for pure samples are 0.23, 5.77 and 91.91, respectively.

Result illustrated that the elongation in the composite is temporarily restricted when the alumina percentage is close to 4%. It is also observed that breaking strength and ultimate tensile strength (UTS) are continuously increasing with the increase of ceramic percentage. Figure 11a confirmed that the lowest value of the Poisson ratio is recorded as 0.33 for the composite containing 4% wt. of ceramics and the highest

Table 7 details of the sample prepared from pure aluminium and its results

Sl.no	Job name	Testing /process	Total length(mm)	Grip Dia. (mm)	Initial Dia. (mm)	After Exp Dia. (mm)	Initial gauge length(mm)	After Exp gauge length (mm)	% Decrease Dia	% Increase length
1	1	UTM	145	15.2	10.18	10	51	55	1.76	7.84
2	2		145	15.2	10.14	9.91	48	51.4	1.75	7.083
3	3		146	15.2	10.15	9.97	49	51.8	1.75	7.09

Table 8 UTM test result of composites

Job name	Total length (mm)	Grip Dia. (mm)	Initial Dia. (mm)	After Exp Dia. (mm)	Initial gauge length (mm)	After Exp gauge length (mm)	% Decrease Dia.	% Increase length
MCC2	145	15.20	10.20	9.94	51.00	53.70	2.55	5.29
MCC4	145	15.20	10.10	9.91	49.00	50.90	1.88	3.88
MCC6	146	15.20	10.20	9.97	50.00	52.30	2.22	4.60
MCC8	146	15.20	10.10	9.88	51.00	53.30	2.18	4.51
MCC10	145	15.20	10.20	9.99	49.00	51.10	2.08	4.29



Fig. 10 a Five different test samples used for tensile test, b Initial setting of sample in UTM has been done and c shows the final elongation of the sample

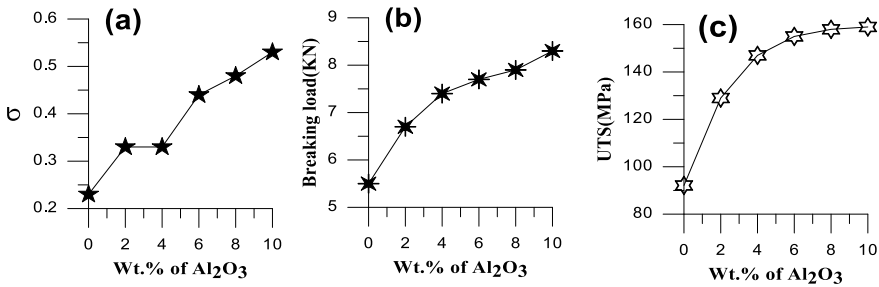


Fig. 11 a Plot of Poisson ratio (σ) with varying wt.% of Al₂O₃/Al, b Breaking loads versus wt.% of Al₂O₃/Al c shows the graph of UTS versus wt.% of Al₂O₃/Al

value is observed 0.53 for 10% Wt. of ceramic in the composite. The percentage increase of Poisson ratio for composites MCC2, MCC4to MCC10 is calculated as 43, 43, 91, 109 and 131 in comparison to pure metal, respectively. The value of the Poisson ratio remains constant within the range of 2–4% Al₂O₃/Al composite indicating the higher value of hardness for a specific composition.

Figure 11b illustrates that the breaking load continuously increases with the higher value of Al₂O₃ present in the composite. Breaking load sharply increases from 5.2 to 7.4 KN with the increase of Al₂O₃ percentage in the composite up to 4 wt.% and

the highest value is recorded as 8.3 KN for 10 wt.% of Al₂O₃ in composites. The peak value of breaking load for composite is calculated as 50.9% higher than the base metal.

The plot of the ultimate tensile strength (UTS) versus wt.% of Al₂O₃ in composite in Fig. 11c shows a very smooth curve from 92.1 to 155 MPa up to 4wt.% of Al₂O₃/Al composite and thereafter it looks like an equilibrium state with a higher percentage of Al₂O₃ in the composite. The enhancement in the result may be the cause of combining effect of grain boundary refinement in mixing, strong adhesion due to impact pressure and finally thermal stress generated at the grain boundary by the cause of the huge difference of thermal expansion coefficient between aluminium and alumina in the composite. A similar effect is also viewed in the literature [23, 24]. The best result comes out when the percentage of Al₂O₃ is 6 wt.% in the composite. Composite is recorded as 68.3% higher breaking loads than the pure Aluminium.

3.4 X-ray Diffraction (XRD) Analysis and Characterization of Samples

XRD is based on constructive interference of the monochromatic axis of crystalline samples. As we know, the pattern of XRD diffraction is the exact fingerprint of atomic arrangement pattern in the crystal lattice. In the XRD diffraction method, X-ray is produced by cathode ray tube, filter tube to construct monochromatic emission. This radiation is collimated as shown in Fig. 12. Electromagnetic radiation is only diffracted by the atomic planes when half of its wavelength is less than or equal to the atomic distance d. When the ray interacts with the sample, it produces constructive interference when condition satisfied as per Bragg’s law: $n \lambda = 2d \sin \theta$, where λ = wavelength of X-ray, d = distance of lattice plane and 2θ = diffraction angle of ray emitted from the X-ray tube,

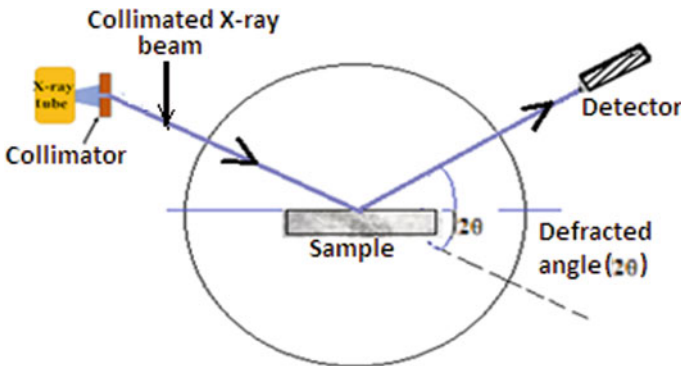


Fig. 12 shows that how collimated X-ray beam from X-ray tube is deflected by the planes of the sample

This law relates with the diffraction angle θ and wavelength of the diffracted ray with the lattice plane that is marked as d here.

The deflection of X-ray occurred due to the presence of electrons in the site. A huge number of deflections are the cause of the availability of large number of electrons in a particular spot that indicates large many atoms accessibility in that area. Peak intensities are determined by the position of atoms within a unit cell and the overall intensity of peak is because of the superposition of all the constructive and destructive contribution which is obviously guided by the position of atoms. The continuous deflection of X-ray in the particular site informed a closed array of atoms in that plane and produce a high intensity/peak of X-ray deflection. Therefore, higher intensity of deflection signifies strong orientation of crystalline structure and crystal size and lattice strain support the width of the peak of XRD. To read the grain size or Crystallite size from the XRD, another equation, i.e. $d = 0.9 \lambda / \beta \cos \theta$ **Scherer's formula**. where λ = wavelength of X-ray, β = Fullwidthathalfmaximatobemeasured (FWHM), d = Crystallite size and θ = Diffracted Bragg's angle ($2\theta/2$).

Phase analysis was done by XRD technique using Rigaku Smart lab diffract metre with Cu-K α radiation of wavelength ($\lambda = 1.5406 \text{ \AA}$), operating at an accelerating potential of 44 kV and 40 mA current. Crystallite size and lattice parameters were also calculated along with phase identification.

The intensity of all the diffracted beams against 2θ was recorded for all the samples for angle 2θ ranging from 10 to 900 at a Goniometric speed of 5 deg./min with 0.010 step size and holding time 0.2 s/step. Analytical X' Pert high score software using PAN-ICSD was used for identifying peaks of different phases present in the synthesized samples. The dimensions of regular crystallite of the powders were calculated by X-ray line broadening procedure employing **Scherer's formulae**. The photograph of XRD equipment used in the experiment is shown in Fig. 13a and b (Fig. 14).

The data in Table 9 clearly explained that for defined FWHM and for the diffracted angle of 38.4° , the estimated crystallite size for all five different samples.

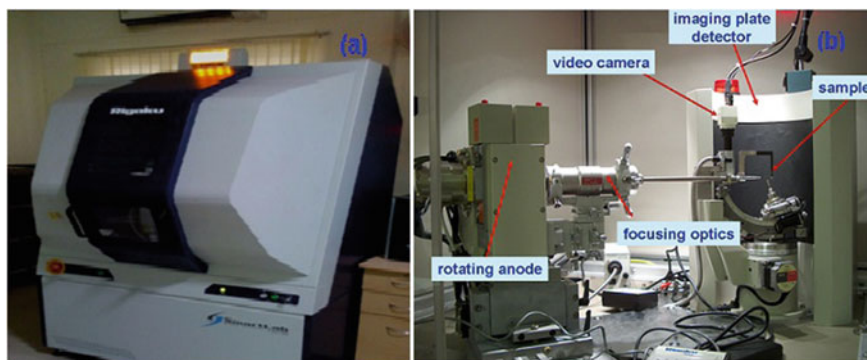


Fig. 13 a The photograph of X-Ray Diffractometer (XRD) and b all internal components of X-ray diffractometer are shown

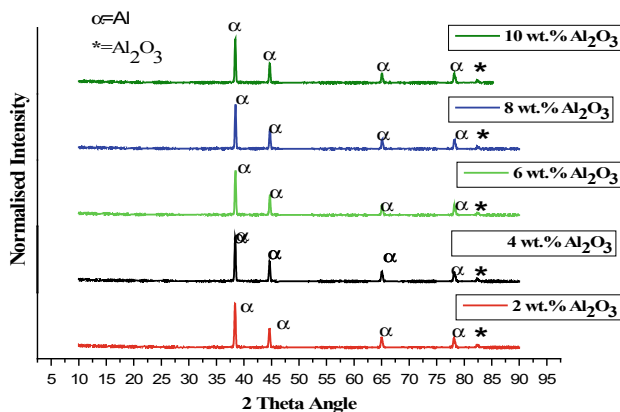


Fig. 14 Comparison of XRD image of mixed powder at different wt.% of Al_2O_3

Table 9 Crystallite Size of mixed powder

S. no	Sample	Position (2θ)	FWHM	Crystallite size (\AA)
1	MCC2	38.387	0.268	339.4201
2	MCC4	38.424	0.264	347.7815
3	MCC6	38.48	0.256	364.5862
4	MCC8	38.496	0.241	391.8318
5	MCC10	38.385	0.2545	360.4869

As FWHM positions were lightly changing for different compositions, the crystallite size also changed. It was also evidently clear that the gradual lower value of FWHM creates larger crystallite sizes of composites. The maximum size of crystallite size was viewed as 391.83 \AA for a mixture containing 8 Wt.% of Al_2O_3 in aluminium and the size crystallite changes within the range of 15.44% in the mixture (Table 10).

It was also clearly visible that crystallite size changes for different compositions of $\text{Al}_2\text{O}_3/\text{Al}$ in the milling sample. The lower value of FWHM indicates larger crystallite

Table 10 Crystallite size of milled powder

S. no	Sample	Position (2θ)	FWHM	Crystallite size (\AA)
1	MCC2	38.419	0.268	316.7628
2	MCC4	38.388	0.332	254.2476
3	MCC6	38.415	0.318	331.1415
4	MCC8	38.559	0.286	305.6197
5	MCC10	38.668	0.261	343.997

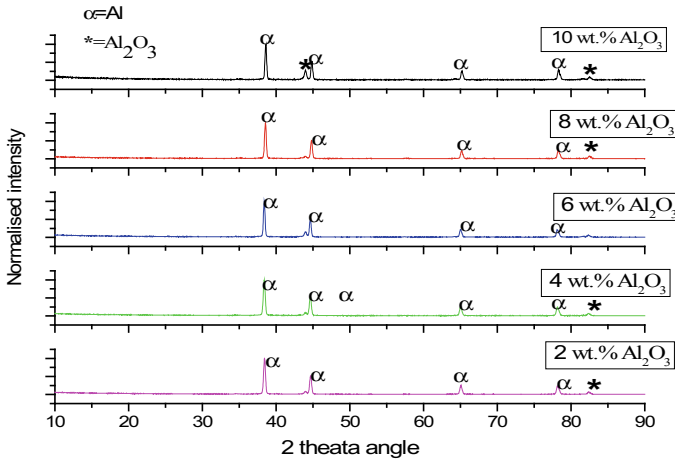


Fig. 15 Comparison of XRD image of milled powder at different wt.% of Al_2O_3

sizes of composites. Size of crystallite varies from minimum to maximum is recorded as 35.3% in milling mixture containing 2–10 wt.% of $\text{Al}_2\text{O}_3/\text{Al}$ (Fig. 15).

4 Conclusion and Future Scope of Work

The present laboratory experimental research brought out the following conclusions based on micro fine and nano $\text{Al}_2\text{O}_3/\text{Al}$ composites fabricated by the method UTM pressed powder metallurgy techniques:

- (1) The maximum value of observed density of mixed sample increases about 8.23% and 6.17% in the milled sample for 10 wt.% of $\text{Al}_2\text{O}_3/\text{Al}$ as compared to pure Aluminium. It is also viewed that the highest densification occurs when Al_2O_3 wt.% is 10 in the $\text{Al}_2\text{O}_3/\text{Al}$ composite.
- (2) The sharp increase in hardness up to 4 wt.% may be the cause of occupying of nano and micro-particles within the interstitial gap of aluminium matrix and partially due to grain refinement and particle strengthening effects. The value of hardness of composite increases more than 50% as compared to the hardness of pure aluminium with the same temperature.
- (3) The lowest value of Poisson ratio is recorded as 0.33 for the composite containing 4% wt. of ceramics and the highest value is observed at 0.53 for 10% wt. of ceramic in the composite.
- (4) Result illustrated that the elongation in the composite is temporarily restricted when alumina percentage is close to 4%. It is also observed that breaking strength and ultimate tensile strength (UTS) are continuously increasing with the increase of ceramic percentage.

- (5) Breaking load sharply increases from 5.2 to 7.4 KN with the enhancement of Al_2O_3 percentage in the composite up to 4 wt.% and the highest value is recorded as 8.3KN for 10 wt.% of Al_2O_3 in composites. The peak value of breaking load for composite is calculated as 50.9% more than the base metal.
- (6) Ultimate tensile strength (UTS) shows a very smooth curve from 92.1 to 155 MPa up to 4wt.% of Al_2O_3 /Al composite and thereafter it pursues an equilibrium status with higher percentage of Al_2O_3 in the mixture. The best result appeared at 6 Wt.% of ceramics composite which is approximately 68.3% higher than the breaking strength of pure Aluminium.
- (7) The micro graphical analysis vividly shows good distribution of constituents and very less agglomerations of Al_2O_3 within the composites made by the powder metallurgy method.
- (8) In the XRD comparison of mixed and milled powder, as FWHM positions were slightly dropping for different compositions, the crystallite sizes were increased. It was also vivid that the crystallite size of milled powder increased to 15.4% as Al_2O_3 powder in the mixture of Al_2O_3 /Al % increased from 2 to 8%, respectively.
- (9) Size of crystallite varies in milling is recorded as 35.3% and 15.44% in mixing sample containing 2–10 wt.% of Al_2O_3 /Al.
 - I. Study has been conducted within the specified range of Al_2O_3 in the composite but that can be extended some more higher/lower percentage also.
 - II. Mixing Al_2O_3 particles could be used within the smaller range like 20 to 40 nm to see the effect of nanoparticles in the lower dimension in the composite.
 - III. Thermal and electrical properties could be compared with pure aluminium, etc.
 - IV. Other metal and metallic oxides could also be added to detect mechanical and thermal properties of poly reinforced composites of aluminium.

References

1. M. Hoseini, M. Meratian, Fabrication of in situ aluminium–alumina composite with glass powder. *J. Alloy. Compd.* **471**, 378–382 (2009)
2. O. Yilmaz, S. Buytoz, Abrasive wear of Al/Al₂O₃-reinforced aluminium-based MMCs. *Compos. Sci. Technol.* **61**, 2381–2392 (2001)
3. A.M. Al-Qutub, I.M. Allam, T.W. Qureshi, Effect of sub-micron Al₂O₃ concentration on dry wear properties of 6061 aluminium based composite. *J. Mater. Process. Technol.* **172**, 327–331 (2006)
4. J. Ye, J. He, J.M. Schoenung, Cryomilling for the fabrication of a particulate B4C reinforced Al nano composite: Part I. Effects of process conditions on structure. *Metall. Mater. Trans. A Phys. Metall. Mater. Sci.* **37A**, 3099–3109 (2006)
5. K. Kawabata, E. Sato, K. Kuribayashi, Creep deformation behaviour of spherical Al₂O₃ particle reinforced Al–Mg matrix composites at high temperatures. *Acta Mater.* **50**, 3465–3474 (2002)
6. L. Yao-hui, D. Jun, Y. Si-rong, W. Wei, High temperature friction and wear behaviour of Al₂O₃ and/or carbon short fibre reinforced Al–12Si alloy composites. *Wear* **256**, 275–285 (2004)
7. E. Del-rio, J.M. Nash, J.C. Williams, M.C. Breslin, G.S. Daehn, Co-continuous composites for high-temperature applications. *Mater. Sci. Eng., A* **463**, 115–121 (2007)
8. S. Mahdavi, F. Akhlaghi, Effect of SiC content on the processing, compaction behavior, and properties of Al6061/SiC/Gr hybrid composites. *J. Mater. Sci.* **46**, 1502–1511 (2011)
9. M.K. Manik et al., Mechanical Properties of Epoxy Resin Matrix Composites Reinforced with Jute Fiber, Coconut Coir and Human Hair. *Int. Jo. Eng. Adv. Technol. (IJEAT)* **9**(1) (2019). ISSN: 2249–8958
10. F. Akhlaghi, S.A. Pelaseyyed, Characterization of aluminum/graphite particulate composites synthesized using a novel method termed in-situ powder metallurgy. *Mater. Sci. Eng. A* **385**, 258–266 (2004)
11. F. Akhlaghi, P. Delshad-Khatibi, Effect of silicon content on size distribution and morphology of Al–Si powder particles produced by solid assisted melt disintegration (SAMD) method. *Powder Metall.* **54**(2), 153–159 (2011)
12. B.S.B. Reddy, K. Das, S. Das, A review on the synthesis of in situ aluminum-based composites by thermal, mechanical and mechanical–thermal activation of chemical reactions. *J. Mater. Sci.* **42**, 9366–9378 (2007)
13. J.B. Fogagnolo, F. Velasco, M.H. Robert, J.M. Torralba, Effect of mechanical alloying on the morphology, microstructure and properties of aluminum matrix composite powders. *Mater. Sci. Eng. A* **342**, 131–143 (2003)
14. U.T.S. Pillai, B.C. Pai, K.G. Satyanarayana, A.D. Damodaran, Fracture behaviour of pressure die-cast aluminum–graphite composites. *J. Mater. Sci.* **30**, 1455–1461 (1995)
15. R. Asthana, S. Das, T.K. Dan, P.K. Rohatgi, Solidification of aluminum–silicon alloy in the presence of graphite particles. *J. Mater. Sci. Lett.* **5**, 1083–1086 (1986)
16. K.S. Dunnett, R.M. Mueller, D.P. Bishop, Development of Al–Ni–Mg–(Cu) aluminum P/M alloys. *J. Mater. Process. Technol.* **198**, 31–40 (2008)
17. C.P. Chen, C.Y.A. Tsao, Response of aluminum/graphite composite to deformation in the semi-solid state. *J. Mater. Sci.* **31**, 5027–5031 (1996)
18. J.F. Lin, M.G. Shih, Y.W. Chen, The tribological performance of 6061 aluminum alloy/graphite composite materials in oil lubrications with EP additives. *Wear* **198**, 58–70 (1996)
19. I.A. MacAskill, R.L. Hexemer Jr., I.W. Donaldson, D.P. Bishop, Effects of magnesium, tin and nitrogen on the sintering response of aluminum powder. *J. Mater. Process. Technol.* **210**, 2252–2260 (2010)
20. F. Akhlaghi, H. Esfandiari, Solid-assisted melt disintegration (SAMD), a novel technique for metal powder production. *Mater. Sci. Eng. A* **452–453**, 70–77 (2007)
21. G. Bajpai et al., Development of Al-nano composites through powder metallurgy process using a newly designed cold isostatic compaction chamber. *J. Mater. Today Proc.* **2**, 2737–2746 (2015)

22. S.A. Sajjadi et al., Fabrication of A356 composite reinforced with micro and nano Al_2O_3 particles by a developed compositing method and study of its properties. *J. Alloy. Compd.* **511**, 226–231 (2012)
23. X.S. Zeng, G.H. Zhou, Q. Xu, Y.J. Xiong, C. Luo, J. Wu, A new technique for dispersion of carbon nanotube in a metal melt. *Mater Sci Eng A* **527**, 5335–5340 (2010)
24. X.L. Zhong, W.L.E. Wong, M. Gupta, Enhancing strength and ductility of magnesium by integrating it with aluminum nanoparticles. *Acta Mater* **55**, 6338–6344 (2007)

A Computational Study of a Dump Combustor with and Without Swirler



Rohan R. Pande and Mohd Zeeshan

1 Introduction

This study focuses on the mathematical modeling of cold flow inside a dump combustor to understand the flow behavior inside the combustor. The cold flow of fluid inside the combustor is studied by observing the changes in properties of fluid and different parameter (e.g. combustor length, inlet diameter to length ratio, use of swirler etc.) and correlate these with the change in swirl vane angle [1–4]. The effect of Reynolds number on velocity profile and turbulent intensity, turbulent kinetic energy, and turbulent energy dissipation rate can be studied. The behavior of flow field inside the combustor in cold flow with and without swirler and the effect of various inlet parameters are studied.

The governing equations along with the other modeling equations have been solved using a computational fluid flow and heat transfer model package called ANSYS FLUENT. The required geometry and the mesh generation are done using the inbuilt ANSYS FLUENT processors. Once the grid is ready, all the remaining operations are performed, which includes setting boundary conditions, setting physical models, defining the fluid properties, executing the solution, and viewing and post-processing the results.

A pressure-based solver has been used in the study to solve the governing equations. In this method, a control-volume-based technique is used. The grid independence test has been carried out by choosing various element sizes until the two-grid size gives almost similar solution. 2D axis-symmetric geometry of combustor has been used for numerical simulation of combustion.

R. R. Pande · M. Zeeshan (✉)

Sardar Vallabhbhai National Institute of Technology, Surat, India

R. R. Pande

e-mail: rohanpande@med.svnit.ac.in

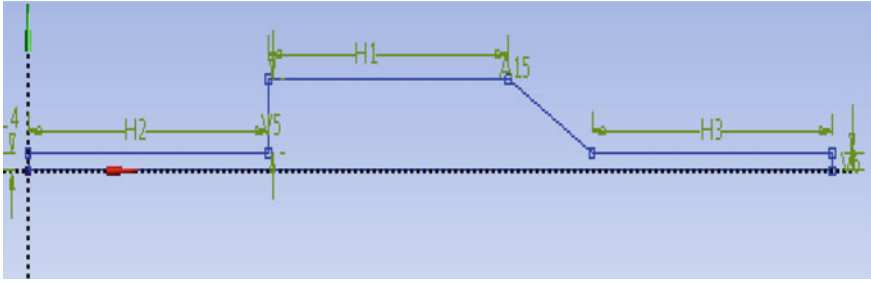


Fig. 1 Geometry of combustor

2 Methodology

The geometry used in the present study is created in ANSYS workbench integrated with Fluent, and mesh is generated in ANSYS meshing application that is also integrated with ANSYS fluent. A finer grid having an element size of 0.003 m has been selected in the region. The total numbers of cells in the domain are 4137.

A grid independent test is carried out to obtain better grid resolution and to bring the total number of grids within acceptable limits. A case study as discussed by Forrester and Evans [5] has been used for grid-independent test. Figure 1 shows the geometry of the reactor. Inlet and outlet diameter of reactor is 10 mm and inlet and exit length is 100 mm, taper exit angle is 30° , and $H1 = 100$ mm and $V5 = 20$ mm.

Flow behavior inside the dump combustor is related to cold flow with and without swirl. The cold flow of air is done at an inlet pressure of 60 psi. and average axial velocity of air at the inlet of the combustor is varied from 0.39 to 0.58 m/s at respective Reynolds number (2285 to 3428) and flow rate from 60 to 90 LPM (liter per minute) as the experimental study reported by various researchers [6, 7]. Inlet velocity for 60 LPM is 0.39 m/s. In the same way, velocity for 70 LPM is 0.45 m/s, for 80 LPM is 0.52 m/s, and for 90 LPM is 0.58 m/s. The variation of axial velocity, stream function is studied and the contour of each parameter is plotted at four different Reynolds numbers and the range of magnitude is found to be the same for all Reynolds numbers.

3 Results

Figures 2 and 3 show the contours of axial velocity of cold flow of air in dump combustor without swirler at Reynolds numbers, i.e., 2285, 2667, 3047, and 3428.

From Fig. 2, it may be inferred that there is a higher positive velocity zone at the center that represents the potential core. The negative velocity at the corner of the combustor shows the existence of recirculation [8]. While between the potential core and recirculation zone, there is a positive velocity field which represents the presence

Fig. 2 Contour of axial velocity of cold flow of air in dump combustor without swirler at varying Reynolds numbers: **a** 2285, **b** 2667, **c** 3047, and **d** 3428

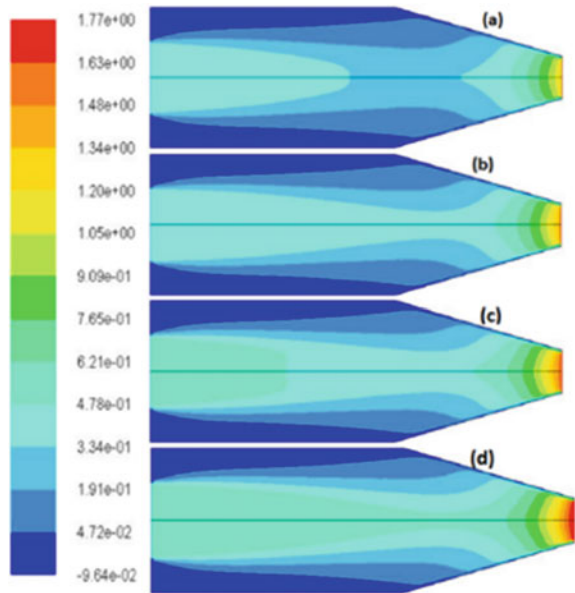
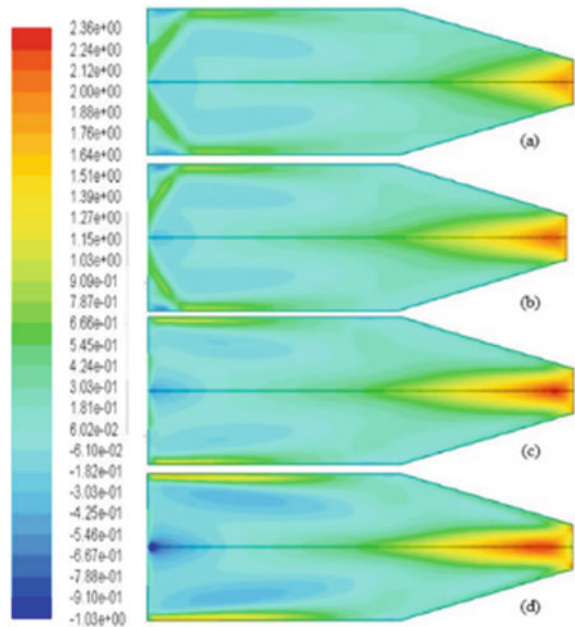


Fig. 3 Contour of axial velocity of cold flow of air in dump combustor with swirler at varying swirl angles: **a** 30°, **b** 45°, **c** 60°, and **d** 75°



of the shear layer. This axial velocity increases with an increase in Reynolds number. At the exit of the combustor, axial velocity becomes very high due to the tapered exit that creates contraction.

Whereas, Fig. 3 shows the variation in axial velocity along the axis of the combustor. Here due to the effect of swirler, axial velocity is negative at almost every point and this value of negative velocity increases with an increase in swirl vane angle. Air moves in a backward direction toward the swirler due to the pressure gradient created by the swirler. This is called as central recirculation zone in which hot gases recirculate and change the flame front according to swirl value [9]. From Fig. 3c and d, it shows that moving beyond the axis of combustor axial velocity become positive and its maximum value increases with increase in vane angle. The peak of axial velocity shift upstream with increase in vane angle.

Figure 4 shows the contour of stream function at four different Reynolds number values. Stream function shows the flow pattern of investigated flow and there are various regions that are also visible as discussed in Fig. 2. In this flow pattern, there is one recirculation zone that appears at the corner of the combustor, and the magnitude of stream function increases as the Reynolds number increases from 2285 to 3428. There is another layer as an intermediate layer between the recirculation zone and bulk fluid at the center.

Whereas Fig. 5 shows the stream function behavior at different swirl/vane angles. Figure 5a and b shows the presence of corner and central recirculation zone inside the

Fig. 4 Contour of stream function of cold flow of air in dump combustor without swirler at varying Reynolds numbers: **a** 2285, **b** 2667, **c** 3047, and **d** 3428

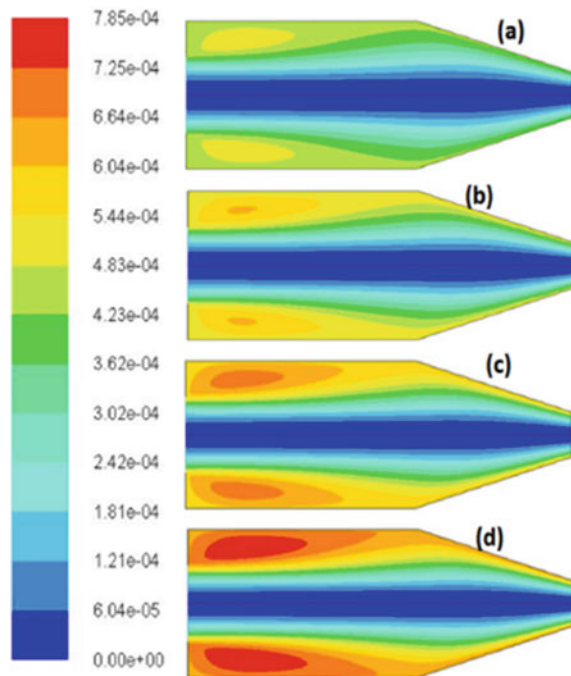
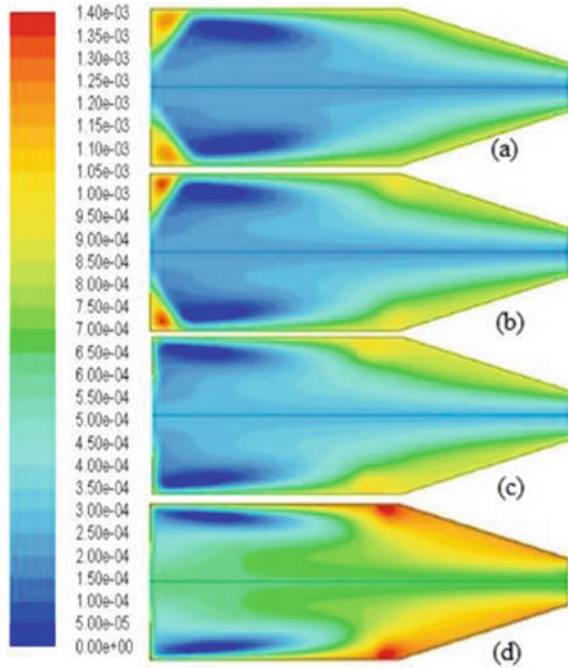


Fig. 5 Contour of stream function in dump combustor with swirler at varying swirl angles: **a** 30°, **b** 45°, **c** 60°, and **d** 75°



combustor. The flow pattern inside the combustor is changed due to the presence of swirl in comparison with non-swirl flow as discussed earlier. With an increase in the swirl vane angle, the strength of circulation increases, while the corner recirculation zone decreases due to increase axial flow due to the swirler [10] as shown in Fig. 5c and d.

Variation of non-dimensional axial velocity and non-dimensional distance

Figures 6 and 7 show the variation of non-dimensional axial velocity and non-dimensional distance. To make the axial velocity non-dimensional, it is divided by U_{avg} , and to make distance non-dimensionalized it is divided by L . Hence, u/U varies with distance (x/L). From Fig. 5, it is clear that there is recirculation at and above $r/R = 0.5$ as the strength of recirculation increases with an increase in ‘ x ’. It is evident that at the axis, the axial velocity decreases with ‘ x ’ and shows a similar result at some distance away from the axis, but it becomes negative when we move further which may be termed as the recirculation.

Effect of Reynolds Number on Flow Field

Figures 8, 9, 10 and 11 show the variation of axial and radial velocity at different radial locations with varying Reynolds numbers (Re). The axial velocity inside the combustor suddenly decreases due to the presence of potential, shear, and recirculation regions, but a very small variation is observed due to an increase in Re because of sudden expansion in flow as shown in Figs. 8 and 9. The small variation in radial

Fig. 6 Axial velocity variation of cold flow of air inside dump combustor at Reynolds number 3428 on different radial positions

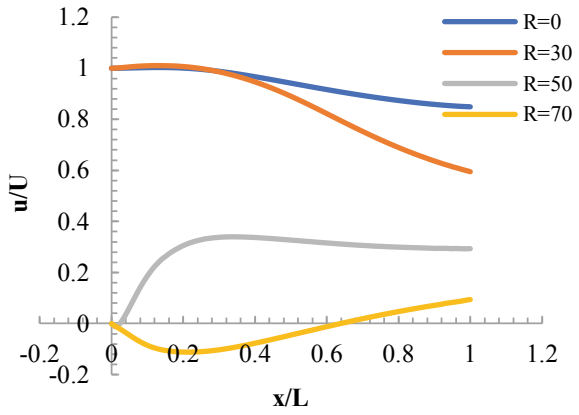


Fig. 7 Axial velocity variation of cold flow of air inside dump combustor at Reynolds number 3428 on different axial positions

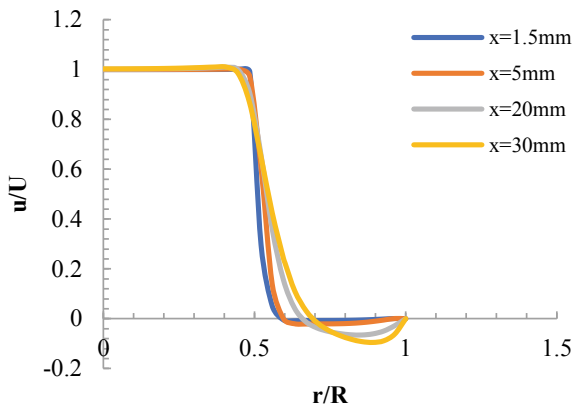


Fig. 8 Axial velocity at $x = 5\text{ mm}$ at varying Reynolds numbers along radius

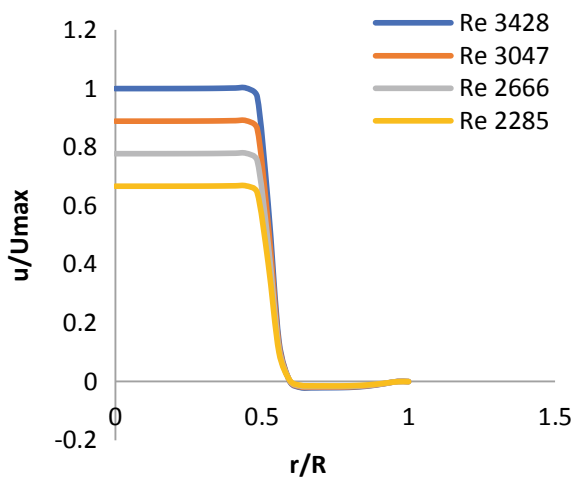


Fig. 9 Axial velocity at $x = 20$ mm at varying Reynolds numbers along radius

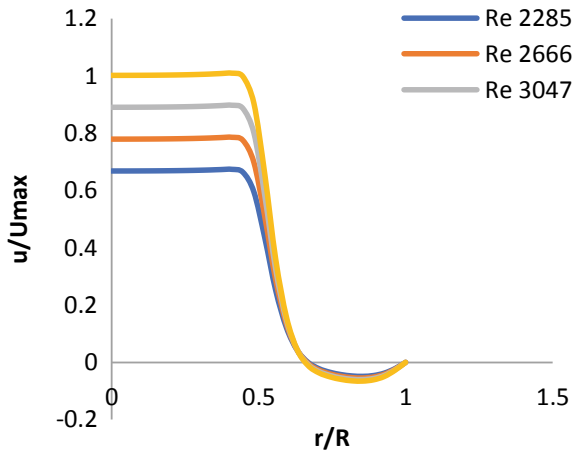
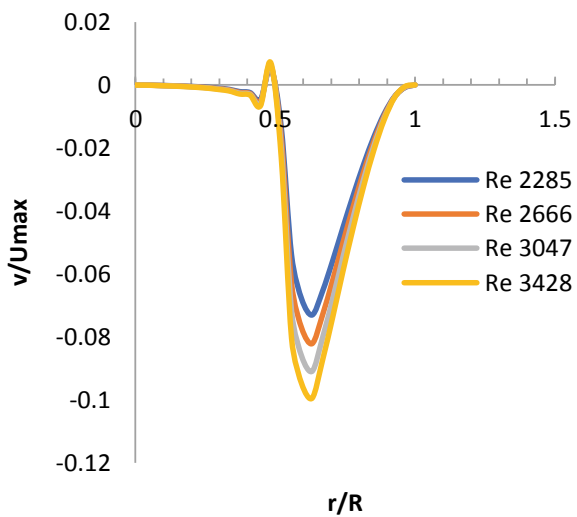


Fig. 10 Radial velocities at $x = 5$ mm at varying Reynolds numbers along radius



velocity in the potential core and shear region is seen, while in recirculation region magnitude increases, which represents that the strength of recirculation increases with increase in Re.

Figures 12, 13, 14 and 15 show the variation of axial and radial velocity at different axial locations with Reynolds number (Re) for the same radial location. The axial velocity inside suddenly decreases due to the presence of potential, shear, and recirculation regions, but appreciable change variation is observed due to an increase in Re because of sudden expansion in flow as shown in Figs. 12 and 13. The small variation in radial velocity in the taper exit section is observed due to increases in

Fig. 11 Radial velocities at $x = 20$ mm at varying Reynolds numbers along radius

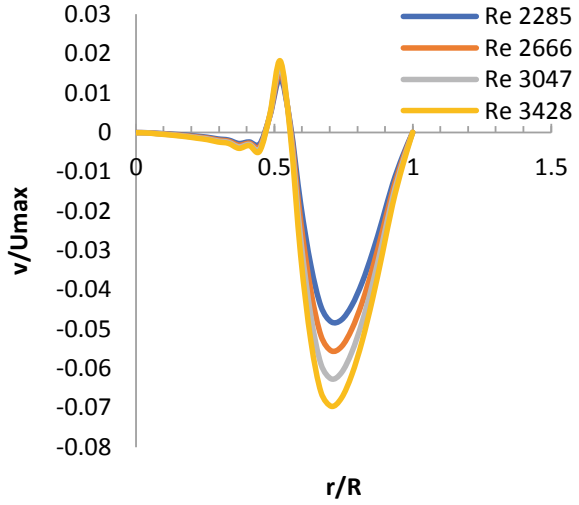
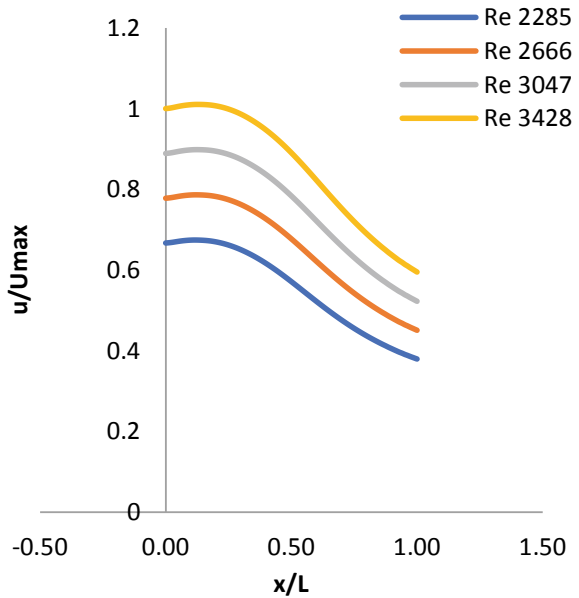


Fig. 12 Axial velocities at $r/R = 0.36$ at varying Reynolds numbers along the length of combustor



Re along axial direction at a same radial location which represents that the effect of flow reversal is due to the tapered exit of the combustor.

Fig. 13 Axial velocities at $r/R = 0.61$ varying Reynolds numbers along the length of combustor

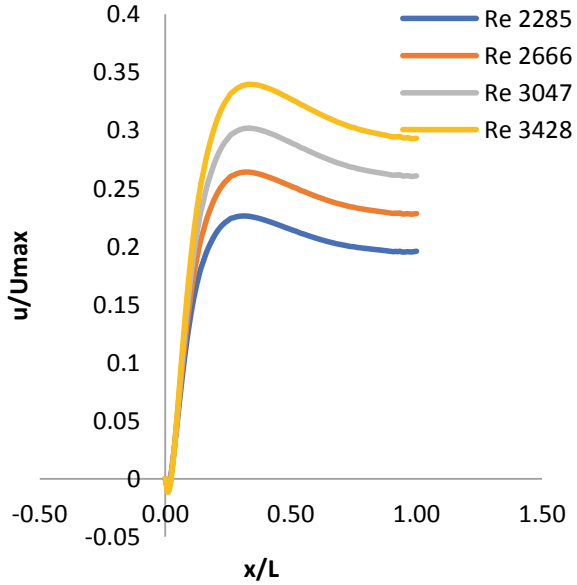
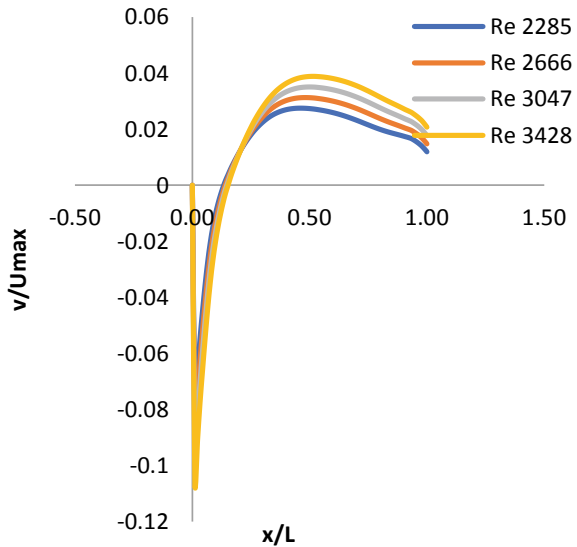


Fig. 14 Radial velocities at $r/R = 0.36$ at varying Reynolds numbers along the length of combustor



Effect of Swirler Vane Angle on Flow Field

Figures 16, 17, 18 and 19 show the variation of axial velocity along a radial direction at the same axial location. The axial velocity first increases in the radial direction and then decreases. The negative value of axial velocity near the tapered exit shows that the flow reversal is due to the tapered exit. The axial velocity near the inlet increases

Fig. 15 Radial velocities at $r/R = 0.61$ at varying Reynolds numbers along the length of combustor

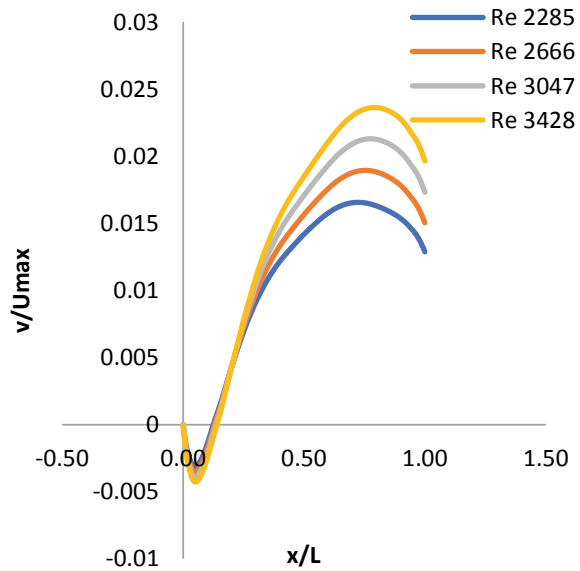
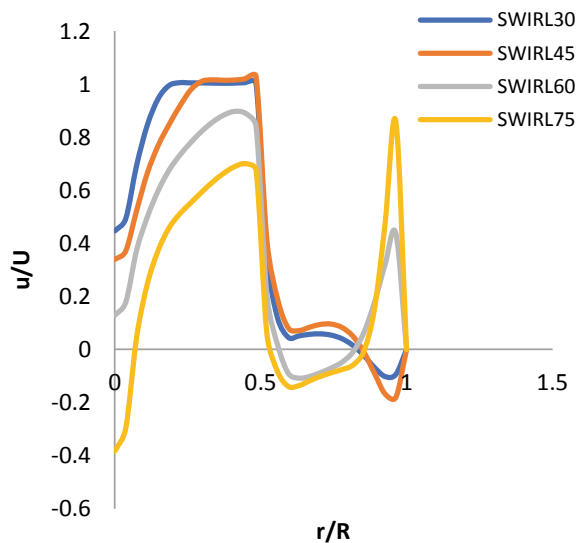


Fig. 16 Axial velocities at axial position $x = 1.5$ mm



with an increase in swirl angle from 30° to 45° , however, at a higher swirl angle (60° and 75°), a negative value of axial velocity is observed due to a higher value of axial flux of angular momentum. The variation of velocity is also affected due to an increase in the axial direction.

Figures 20, 21, 22 and 23 show the variation of radial velocity along a radial direction at the same axial location. The radial velocity first increases in the axial direction and then decreases at axial location $x = 1.5$ mm and $x = 5.0$ mm, however,

Fig. 17 Axial velocities at axial position $x = 5 \text{ mm}$

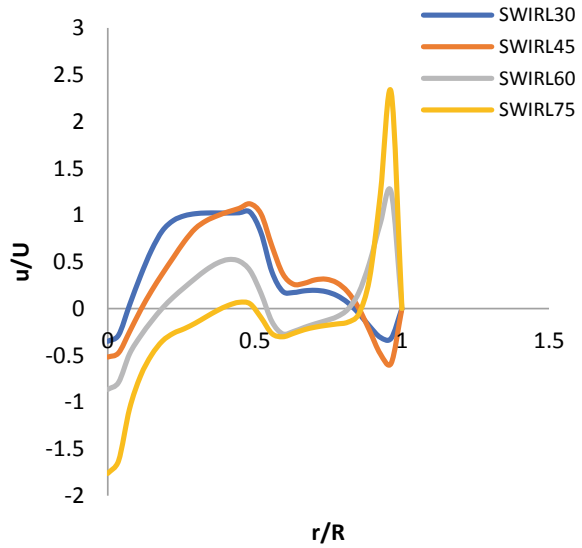
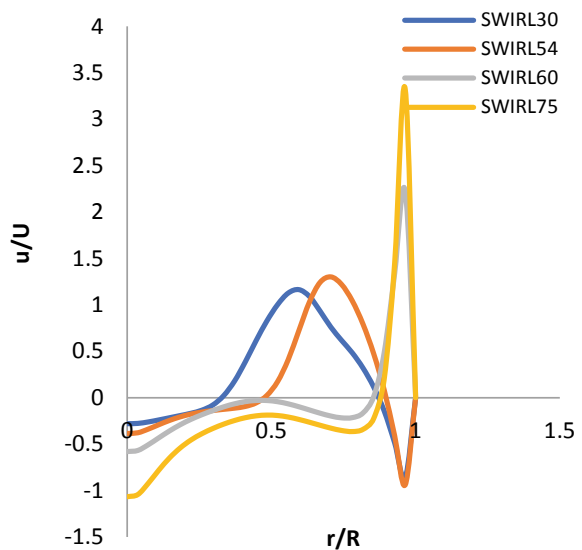


Fig. 18 Axial velocities at axial position $x = 20 \text{ mm}$



when moving in axial direction from 20 to 30 mm near the axis of combustor, very low velocity is observed which suggests that the presence of swirl causes a central recirculation zone and precision vortex [11, 12]. The radial velocity near the inlet increases with an increase in swirl angle from 30° to 75° , however, at a lower swirl angle (30° and 45°), negative value of radial velocity is observed beyond $r/R = 0.5$ at $x = 1.5 \text{ mm}$ and $x = 5 \text{ mm}$ due to lower value of axial flux of angular momentum.

Fig. 19 Axial velocities at axial position $x = 30$ mm

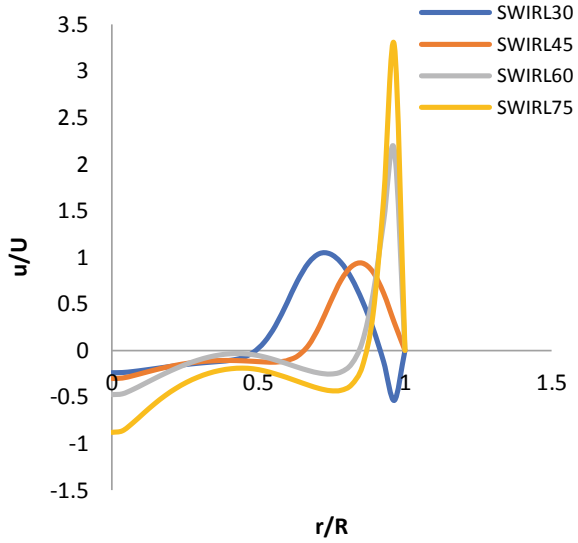
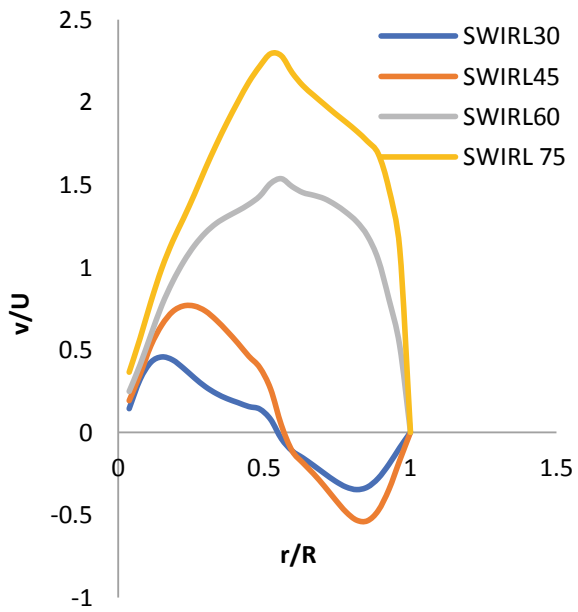


Fig. 20 Radial velocities at axial position $x = 1.5$ mm



Figures 24, 25, 26 and 27 shows the variation of axial velocity along axial direction at the given radial location. The axial velocity first increases in the axial direction and then decreases. The negative value of axial velocity near the tapered exit shows that the flow reversal is due to the tapered exit [13]. The axial velocity near the inlet increases with an increase in swirl angle from 30° to 45°, however, at a higher swirl

Fig. 21 Radial velocities at axial position $x = 5 \text{ mm}$

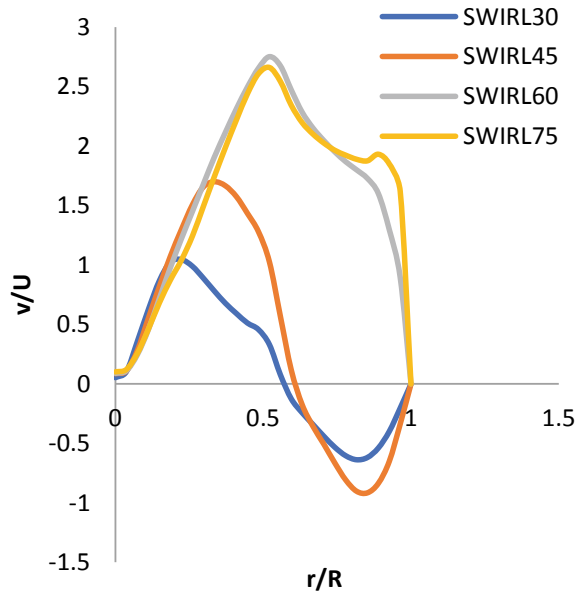


Fig. 22 Radial velocities at axial position $x = 20 \text{ mm}$

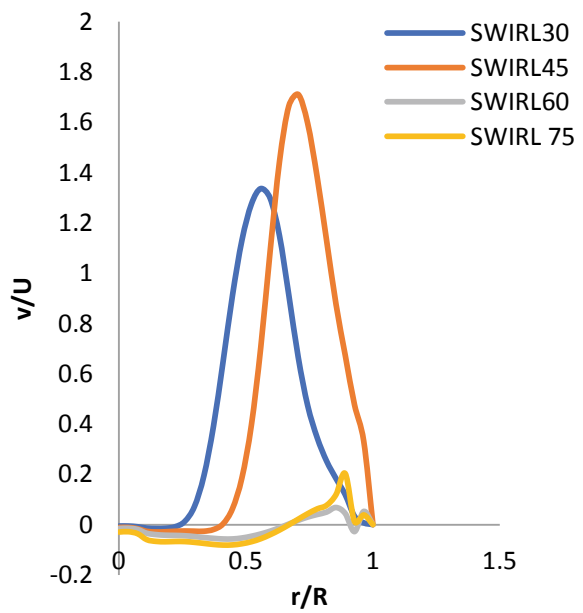


Fig. 23 Radial velocities at axial position $x = 30$ mm

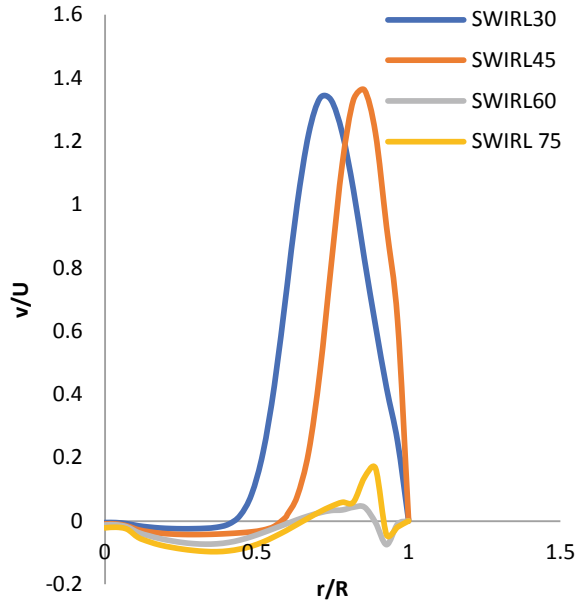


Fig. 24 Axial velocities at radial position $r/R = 0$

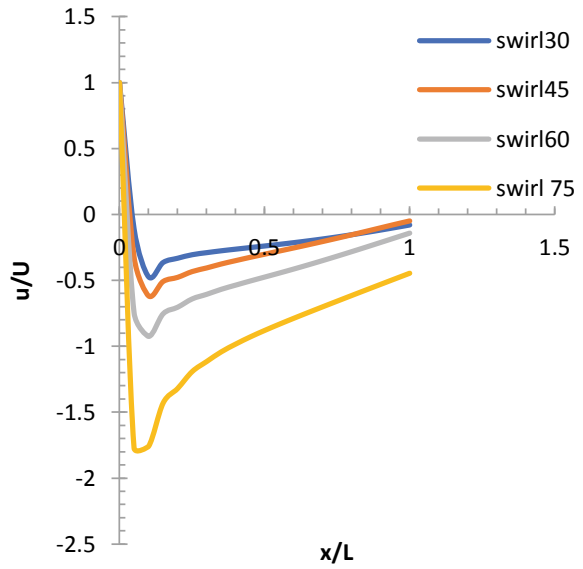


Fig. 25 Axial velocities at radial position $r/R = 0.36$

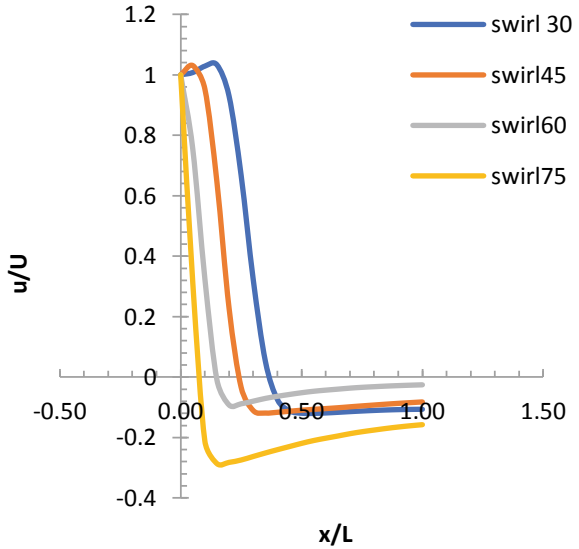
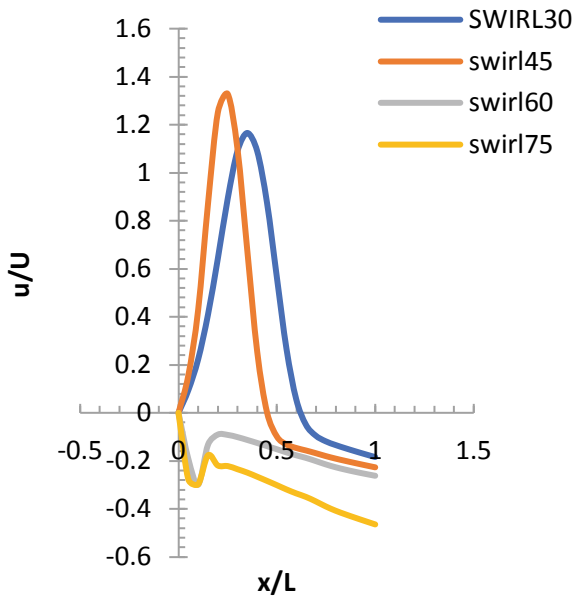


Fig. 26 Axial velocities at radial position $r/R = 0.61$



angle (60° and 75°), negative value of axial velocity is observed due to higher value of axial flux of angular momentum.

Figures 28, 29, 30 and 31 shows the variation of radial velocity along axial direction at the same radial location. The radial velocity first increases in the axial direction and then decreases. The negative value of radial velocity shows the presence of a

Fig. 27 Axial velocities at radial position $r/R = 0.85$

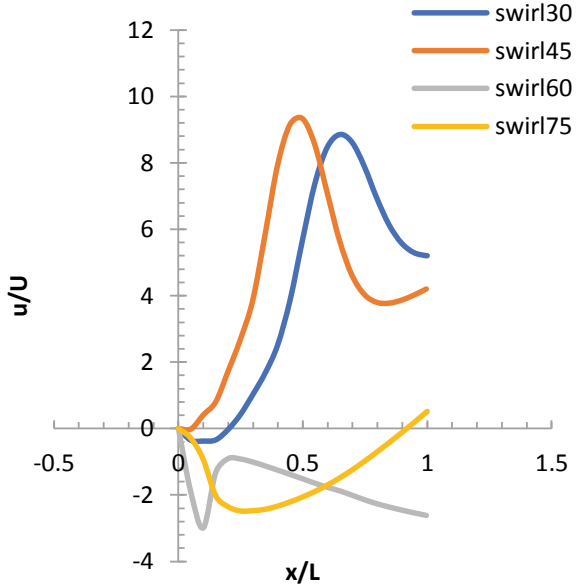
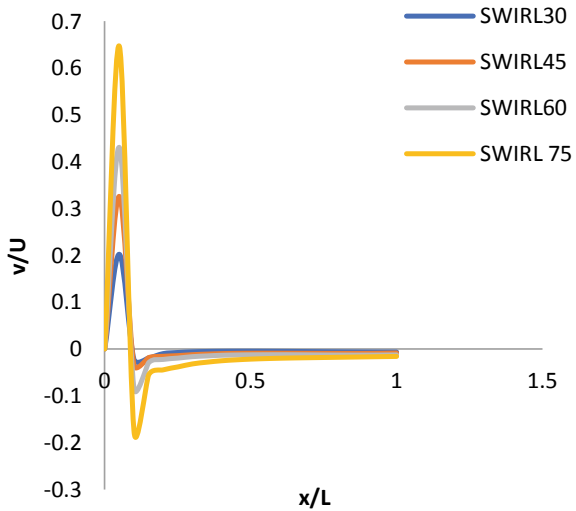


Fig. 28 Radial velocities at radial position $r/R = 0$



shear layer between the central recirculation zone and corner recirculation zone [14]. The radial velocity near the inlet increases with an increase in swirl angle from 30° to 45°, however, at a higher swirl angle (60° and 75°), a negative value of radial velocity is observed due to a higher value of axial flux of angular momentum.

Fig. 29 Radial velocities at radial position $r/R = 0.36$

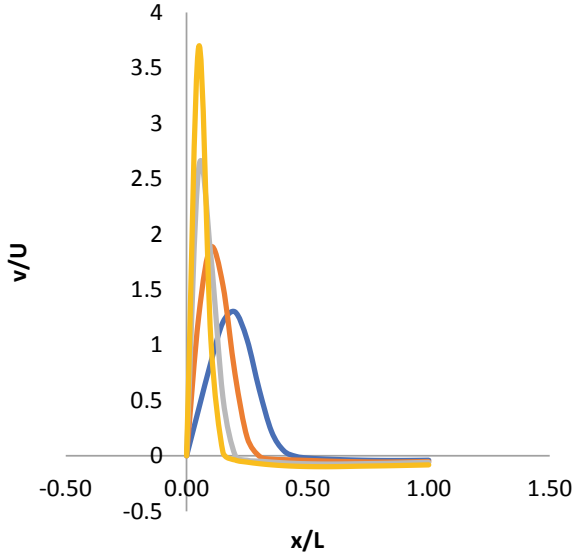
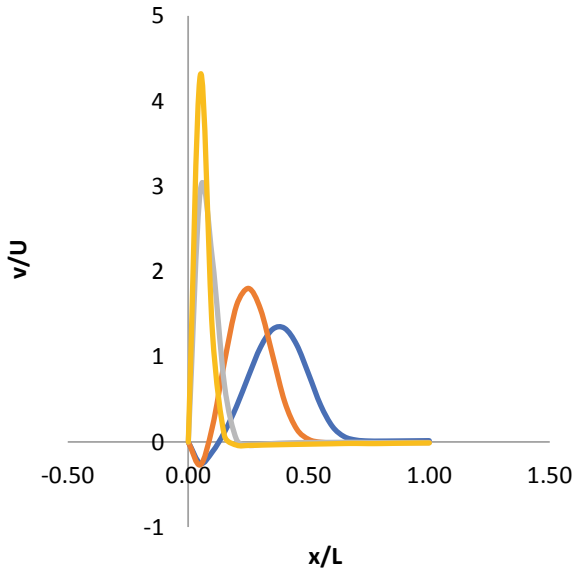


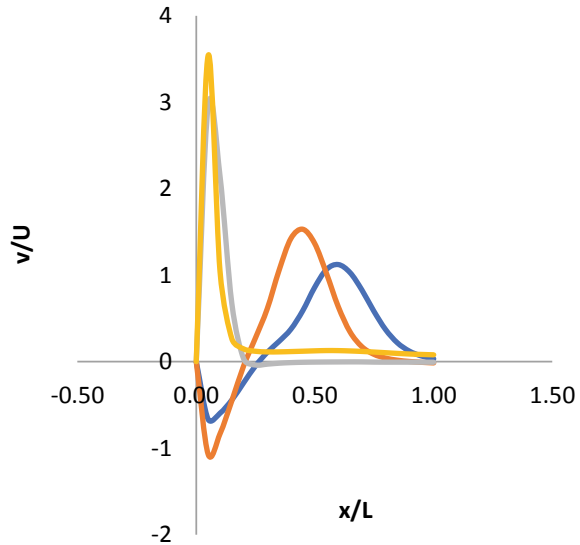
Fig. 30 Radial velocities at radial position $r/R = 0.61$



4 Conclusions

A numerical simulation of cold flow inside a dump combustor is done to understand the flow behavior in the combustor. The mathematical modeling for cold flow has been done for the same. The cold, swirling, and non-swirling flows in a

Fig. 31 Radial velocities at radial position $r/R = 0.85$



dump combustor are simulated using the $k-\epsilon$ turbulence model at varying Reynolds numbers and swirl vane angles. The parametric investigation of flow behavior inside the combustor is performed by using the computational package ANSYSFLUENT. The velocity field and turbulent behavior inside the combustor have been analyzed in presence of swirling and non-swirling flow. The flow behavior inside the combustor is investigated by including the effect of Reynolds number, swirl vane angles at different locations inside the combustor. The conclusions from the present study can be summarized as follows:

- The uniform velocity flow is observed due to axis-symmetric geometry of the combustor.
- The various regions are visualized in none swirling (potential core, recirculation, and shear zone) and swirling flow (central and corner recirculation as well as shears zone) inside the combustor.
- The effect of swirl can be seen clearly inside the combustor which increases the turbulence level inside the combustor. The higher turbulent level, as well as presence of central and corner recirculation zones, increases the mixing of fuel and flame stabilization in the combustor.
- The study of swirling flow is effectively done to investigate complex flows and to correlate combustion dynamics with fluids dynamics.
- The velocity flow field and large vertical flow structures were obtained from the isothermal flow which is helpful in understanding phenomena in combustion cases.

References

1. M. Yoon, Combustion instability analysis from the perspective of acoustic impedance. *J. Sound Vib.* 115500 (2020)
2. S. Sreedeeep, V. Ramanan, S.R. Chakravarthy, The role of closely spaced helical and axial disturbances in exciting beats in a partially premixed swirl combustor, in *AIAA Propulsion and Energy 2020 Forum* (2020), p. 3892
3. M.M. Ahmed, M. Birouk, Mixing tube length effect on the stability of confined swirling partially premixed methane flames off a concentric flow conical nozzle burner. *Combust. Sci. Technol.* 1–23 (2020)
4. K. Wang, F. Li, P. Zou, X. Lin, R. Mao, X. Yu, Effect of the fuel-air flow velocity on heat release rate of swirling non-premixed methane flames. *Aerosp. Sci. Technol.* 95, 105465 (2019)
5. S.E. Forrester, G.M. Evans, Computational modeling study of the hydrodynamic in sudden expansion-taper contraction reactor geometry. *Chem. Eng. Sci.* **52**, 3373–3385 (1997)
6. A.L. Pillai, J. Nagao, R. Awane, R. Kurose, Influences of liquid fuel atomization and flow rate fluctuations on spray combustion instabilities in a backward-facing step combustor. *Combust. Flame* **220**, 337–356 (2020)
7. S. Menon, A numerical investigation of aerodynamically trapped vortex combustor for premixed hydrogen combustion in gas turbines using detailed chemistry (2019).
8. Z. Li, Y. Yuan, B. Guo, V.L. Varsegov, J. Yao, The recirculation zone characteristics of the circular transverse jet in crossflow. *Energies* **13**(12), 3224 (2020)
9. G. Li, X. Jiang, Z. Lei, C. Liu, J. Yang, Y. Xu, G. Xu, Central recirculation zone induced by the DBD plasma actuation. *Sci. Rep.* **10**(1), 1–9 (2020)
10. D. Stefan, P. Rudolf, M. Hudec, V. Uruba, P. Prochazka, O. Urban, Experimental investigation of vortex ring formation as a consequence of spiral vortex re-connection, in *IOP Conference Series: Earth and Environmental Science*, vol. 405, no. 1. (IOP Publishing, 2019), p. 012033
11. D.K. Sharaborin, R.V. Tolstoguzov, V.M. Dulin, D.M. Markovich, On the Structure of an Impact Jet with Flow Swirling and Combustion. *Combust. Explos. Shock Waves* **56**(2), 131–136 (2020)
12. Z. Mansouri, M. Aouissi, T. Boushaki, A numerical study of swirl effects on the flow and flame dynamics in a lean premixed combustor a numerical study of swirl effects on the flow and flame dynamics in a lean premixed combustor
13. A. Kalani, S.G. Kandlikar, Flow patterns and heat transfer mechanisms during flow boiling over open microchannels in tapered manifold (OMM). *Int. J. Heat Mass Transf.* **89**, 494–504 (2015)
14. S.K. Dhanuka, J.E. Temme, J.F. Driscoll, H.C. Mongia, Vortex-shedding and mixing layer effects on periodic flashback in a lean premixed prevaporized gas turbine combustor. *Proc. Combust. Inst.* **32**(2), 2901–2908 (2009)

Effect of Aspect Ratio on Fatigue Behaviour of Steel Shear Wall



R. K. Chethan Gowda , K. Ashwini, and H. M. Rajashekaraswamy

1 Introduction

The Asia continent alone has 403 tall buildings which is 63% of overall buildings around the globe. In 2016, 342 natural hazards were registered in the Asian continent. Alone in India, there are several such scenarios, in the year 1988 Kathmandu experienced an earthquake of Richter magnitude 6.7, that triggered the landslide and took the lives of more than thousands. A similar catastrophic earthquake has occurred in Uttarkashi of 7.2 magnitude on the Richter scale. Many buildings are built in recent days keeping earthquakes in mind. Even though buildings are designed safe against earthquakes, buildings always fall short against safety due to carelessness and the use of cheap materials during construction without the consultation of engineers and bribing inspectors has been practiced which are some of the reasons for building failure. According to a survey, 8 out of 10 buildings are unlikely to be earthquake resistant. There are many earthquake resisting structures, some are base isolators, dampers, shear walls, etc. The element we choose should be strong and ductile to act on shaking with preventable damage [5]. The secondary system that prevents structures from getting affected by lateral loads is shear walls. Shear wall is provided in tall structures to resist earthquake and wind loads and provide structural stiffness as a secondary element in the building. Generally, shear walls are provided around the periphery of tall structures or as shear core as in elevator shaft or stair wall providing adequate stiffness to the structure. Shear walls can be built using masonry, steel, wood and concrete. Behaviour shear walls depend on the material used, wall thickness, wall length, wall positioning in the building frame. Shear walls are integrated with roofs or floors, these walls have to resist the uplift forces caused by the pull of the wind and resist the shear forces that try to push the walls [6]. In the late '50 s and early '60 s, plywood walls were used as an alternate to diagonally

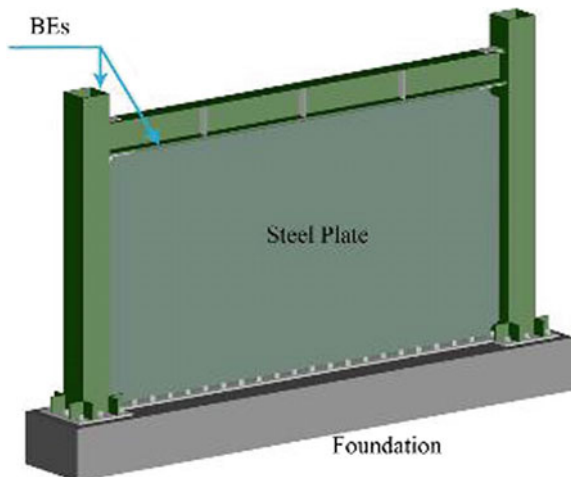
R. K. Chethan Gowda (✉) · K. Ashwini · H. M. Rajashekaraswamy
M. S. Ramaiah University of Applied Sciences, Bengaluru, India

braced wall sections. Their acceptance for this purpose was based on their ability to meet certain load or deflection criteria. Based on experiment and testing data and by incorporating knowledge gained from plywood diaphragm testing, in 1967, Uniform Building Code for the first time provided allowable load tables for plywood shear walls. Then various studies were made on shear walls with various other materials such as masonry, steel, RCC. Now, RCC and steel frames are used worldwide. Steel shear walls are very popular in foreign countries due to various advantages such as durability, strength, cost-effectiveness, and easy installations.

2 Background Theory

In the past two decades, the steel shear wall are widely used in many countries as part of lateral force resisting structure. In earlier days, it was a conservative method that steel shear walls were vertically oriented plate structures. Although recent studies have erased these kinds of conservative methods of designing, a very criterion is that steel shear wall showcases high bending strength and stiffness. These members are expected to have a significant effect on the overall behaviour of a building [7]. High buildings are mostly soft storied and have irregularities that significantly cause a difference in stiffness and resistance in structures. In the first half of the twentieth century, it was believed that assumptions on architectural design having open storey would have advantages, but these were the main reasons for seismic vulnerabilities SPSW studies were carried out in 1980s and satisfactory usage of SPSW in Northern rige and Japan has emphasized researchers and practicing engineers to use SPSW in greater extent [8] (Fig. 1).

Fig. 1 Steel plate shear wall [2]



The Canadian steel design standard has outlined design requirements of steel plate shear wall based on studies carried out by [7] and standard bolted type shear wall by [8]. Steel plate shears were a major contribution to the civil field by researchers. In spite of their robustness and ductility, they provide better resistance to seismic degradation. The low mass steel shear walls have lesser self-weight compared to reinforced concrete shear walls and transfer the seismic load to the foundation. From various studies, it was found that stiffened shear plate produces more energy dissipation characters, but the cost of construction also increased.

3 Validation

The numerical evaluation of experimental work derived from the paper “Economical Steel Plate Shear Walls for Low-seismic Regions [1] is used for validation work which is taken as input for parametric study. The geometry of the steel plate shear wall is modelled using the available CATIA V5 modelling software. Figure 2 indicated a 3D model created using CATIA software.

Material properties of the steel plate shear wall.

Elastic modulus = 20000 MPa, Density of steel = 7850 kN/m³, Poisson’s ratio = 0.3. Table 1 shows details geometry used for designing.

Then imported into the ANSYS Workbench, Version 15.0 for Analysis meshing is created for finite element analysis. Figure 3 shows tetrahedral meshing of the structure whose sizing can be varied for refined results.

Fig. 2 Steel plate shear wall (SPSW)

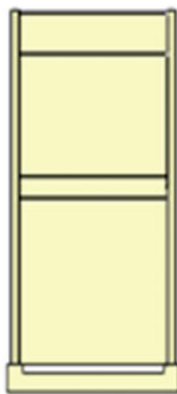


Table 1 Section Details of Experimental Model

Section	Dimension details (mm)
Horizontal member	W 460 X 67
Vertical member	W 250 X 58
Plate	4.8 mm Thick

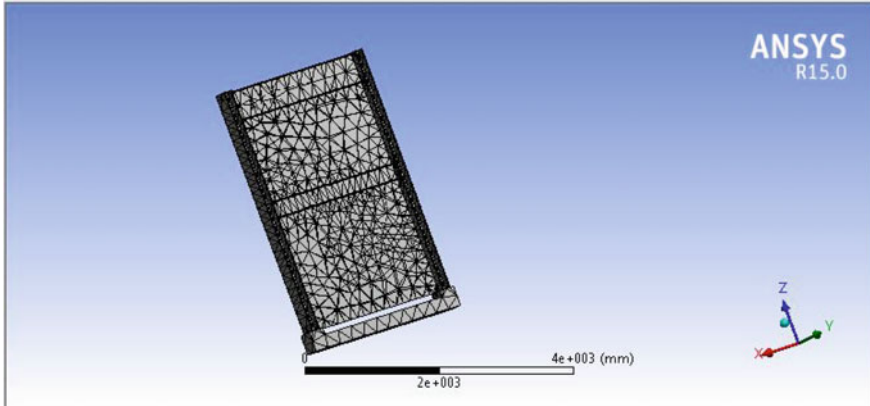


Fig. 3 Discretized model

In boundary conditions, the structure is fixed at the bottom, axial loads of $6 + e05$ N are applied on the column to resist an overturning moment. Loading case details are derived from AISC (341–10) FEMA 1997. Figure 4 shows the stress contour obtained for the structure after analysis. Experimental and numerical study results are given in Table 2, and it can be observed that the percentage of difference

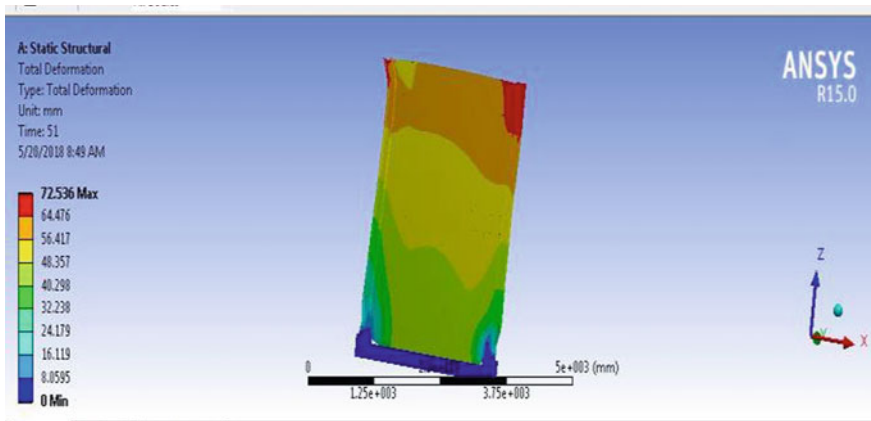


Fig. 4 Stress contour plot

Table 2 Comparison of experimental and numerical results

Displacement (mm)	Experimental results (Load in kN)	Numerical results (Load in kN)	Percentage of difference
1.5	200	185	7.5
3.2	400	378	5.5
5.2	600	570	5
6.7	800	764.5	4.43
9.2	1000	940	6
22	1920	1756.8	8.5

Table 3 Parametric study details

Aspect ratio (L/H)	Dimension details (mm)		Member details
	L	H	
0.5	L = 950	H = 1900	Vertical member ISMB 350
1.0	L = 1900	H = 1900	
1.5	L = 2850	H = 1900	Horizontal member ISMB 200
2.0	L = 3800	H = 1900	
2.5	L = 4750	H = 1900	Steel plate 4.8 mm thick
3.0	L = 5700	H = 1900	

is within the acceptable range, hence a similar methodology has been adapted for further numerical study.

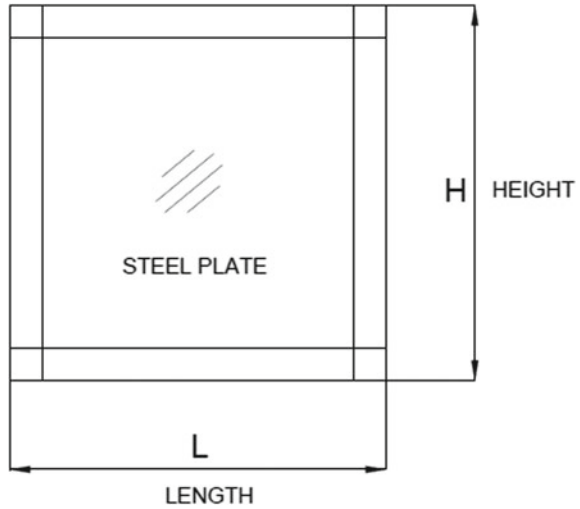
4 Parametric Study

The parametric study is carried on aspect ratio to know its influence on energy dissipation. Parameters considered for the study are given in Table 3. Aspect ratio is a very important parameter for the design of steel shear wall. Shear distribution, ductility and stiffness of steel shear wall is based on aspect ratio. The parametric model is shown in Fig. 5, where L is the length of the wall and H is the height of the wall. In this study, various models for varying aspect ratio are studied.

5 Results and Discussions

The performance of all the models is compared based on the energy dissipation capacity, i.e. total area of the hysteresis loop. The hysteresis graph is plotted load v/s

Fig. 5 Parametric model



displacement. Figure 6 shows a typical hysteresis graph plotted from the analysis. From the numerical study, it was found that the energy-dissipating capacity was increased with an increasing aspect ratio. Stable energy dissipation was seen from an aspect ratio 1.5.

From Table 4, it can be observed that energy dissipation is increased with an increase in the aspect ratio of all parameters and there is less increment in energy dissipation after an aspect ratio of 1.5. It can also be observed that the load-carrying capacity has gradually increased and suddenly decreased for the aspect ratio 3. Permanent deformation was found to increase with the increase in aspect ratio.

A comparison graph is plotted for energy dissipation and ultimate load-carrying capacity (Fig. 7) by steel plate shear wall for varied aspect ratios. From Fig. 8 it

Fig. 6 Typical hysteresis graph

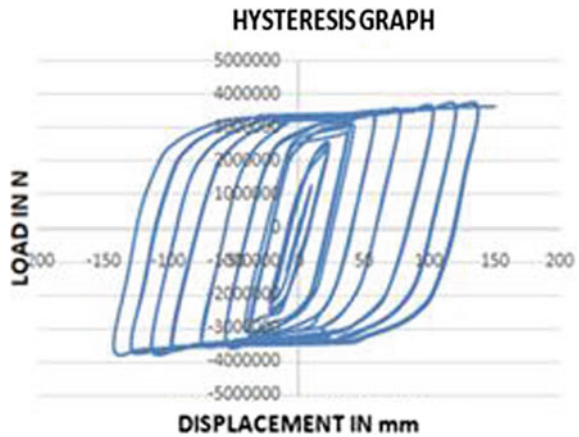


Table 4 Results of parametric study

Aspect ratio	Energy dissipation (kN-mm)	Ultimate load (kN)	Permanent deformation
0.5	24,050	978	82
1.0	482,151	1400	89
1.5	541,838	1568	93
2.0	558,146	1685	94
2.5	561,215	2276	98
3.0	575,254	1265	105

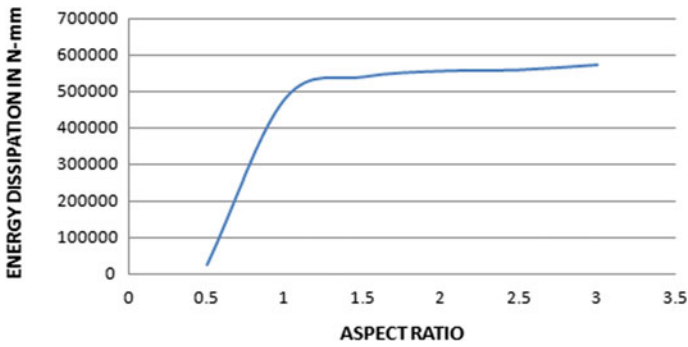


Fig. 7 Energy dissipation versus aspect ratio

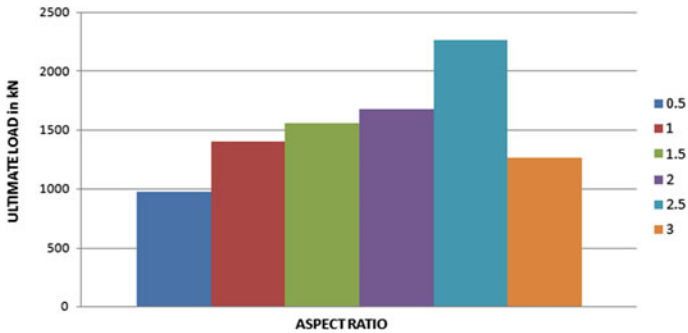


Fig. 8 Ultimate load versus aspect ratio

is evident that energy dissipation is increased with an increase in the aspect ratio and stable hysteresis graph obtained after aspect ratio of 1.5. From Fig. 8, it can be observed that the load-carrying capacity of the shear wall was found to be increased up to an aspect ratio of 2.5. further increase in the aspect ratio leads to the buckling of the plate thus reducing load-carrying capacity.

6 Conclusions

- Energy dissipation for aspect ratio initially has 9–11% variation in results and stable energy dissipation is seen after an aspect ratio 1.5
- Energy dissipation of aspect ratio 1.5, 2, 2.5 and 3 has increased by 37%, 43%, 54% and 48%, respectively.
- Length of steel shear wall having an aspect ratio 2.5 is 20% higher than the aspect ratio 2, which indirectly consumes more material than aspect ratio 2. Likewise, energy dissipation capacity of the shear wall having an aspect ratio 2 is only 5% lesser than the aspect ratio 2.5. Since the aspect ratio 2.5 is not economical, therefore, aspect ratio 2 can be opted for economical designing of steel shear wall.

Acknowledgement I would like to express my sincere gratitude to my advisor Dr. H. M. Rajashekaraswamy, Head, Department of Civil Engineering, M. S. Ramaiah University of Applied Sciences for guiding the research work.

References

1. H. Moghimi, R.G. Driver, Economical steel plate shear walls for low-seismic regions. *J. Struct. Eng.* © ASCE, 379–388 (2013)
2. P.P. Chandurkar, Dr. P.S. Pajgade, Seismic analysis of RCC building with and without shear wall. *Int. J. Modern Eng. Res. (IJMER)*, 1805–1810 (2013)
3. R.G. Driver, G.L. Kulak, D.J. Laurie Kennedy, A.E. Elwi, Cyclic test of four-story steel plate shear wal. *J. Struct. Eng.* 112–120 (1988)
4. S. Azimi, M. Rozbahani, M. Alirezaee, Study of effect of steel plate thickness of non-linear behaviour of steel walls. *J. Fundam. Appl. Life Sci. ISSN* (2015)
5. S. Sabouri-Ghomi, C.E. Ventura. M.H. Kharrazi, Shear analysis and design of ductile steel plate walls. *J. Struct. Eng.* © ASCE, 12 (2000)
6. T.M. Roberts, S. Sabouri-Ghomi, Hysteretic characteristics of unstiffened perforated steel plate shear panels. *Thin-Walled Struct.*, 139–151 (1992, 11 October)
7. L.J. Thorburn, G.L. Kulak, C.J. Montgomery, *Analysis of Steel Plate Shear* (Department of Civil Engineering, University of Alberta, Edmonton, AB, 1983)
8. T. Hitaki, C. Matsui, Experimental study on steel shear wall with slits. *J. Struct. Eng. @ASCE*, 586–595 (2013)

Life Cycle Analysis for Biodiesel Fuels—A Holistic Approach



Anurag Mishra, R. Arjun Thangaraj, and Pramod S. Mehta

1 Introduction

The most crucial challenge of the twenty-first century is to meet the unceasing demand for energy while preserving the integrity of the biosphere. The dependence on fossil fuels must reduce, to not only cope with imminent resource shortages but also to avoid damage to biosphere and ensure global economic and energy security concerns caused by the reliance on the more expensive supplies of Middle Eastern crude oil [1]. In India, it is expected that with an average per annum growth rate of 4.2%, the overall energy consumption will rise to 1,921 million tonne of oil equivalent (Mtoe) in 2040 from 724 Mtoe in 2019, and in the same period the oil demand, including petroleum products, will grow by 129% from 4 million barrels per day (Mbbpd) to 10 Mbbpd [2]. Thus, developing alternative energy systems is one of the most crucial needs of the hour, not just from the environmental point of view but also economic security standpoint. Biodiesel is seen as a potential renewable source of energy, but a thorough understanding of the effects of its production is required to make an informed decision. Therefore, a holistic analysis of biodiesel fuels considering energy, environment, and techno-economic aspects, provides an idea whether the generation of energy using biodiesels is a sustainable approach.

Spirinckx and Ceuterick [3], Prueksakorn [4], Sheehan [5], Kumar [6], Pradhan [7], and Yadav [8] investigations form the basis of the present analysis. In their work, Spirinckx and Ceuterick analyzed the sustainability of the two fuels based on specific impact categories: energy, greenhouse gas emissions, acidification, eutrophication, and photochemical oxidation. Apart from these impact categories that mainly

A. Mishra (✉)

Indian Institute of Technology Delhi, South Delhi 110016, India

e-mail: mez168540@iitd.ac.in

R. A. Thangaraj · P. S. Mehta

Indian Institute of Technology Palakkad, Palakkad, Kerala 678557, India

consider the environment, there is a need for social and techno-economic factors to be considered to bring out a holistic analysis of the sustainability of the fuel.

Life Cycle Analysis (LCA) evaluates the complete environmental cradle to grave consequences of a product/process by quantifying energy and materials consumed as well as wastes and emissions discharged to the environment [9]. It is useful to know the renewability of biofuel for two reasons, viz. to indicate the use of petroleum-derived energy for production of biofuels and to use it as criteria for policymakers to compare biofuels. The renewability of the biodiesel is mostly assessed by a factor of the amount of fossil energy used for its production. Renewability along with other considerations, such as environmental, economic, and social criteria, can be used to assess the benefits of biofuels [10]. However, energy and equivalent CO₂ emissions alone do not give the full picture of the environmental impacts associated with the production of biodiesel. The critical effects that are required to be considered include phenomena called eutrophication and acidification. Land use impacts are also part of the LCA study, which are generally remains challenging to assess due to the unavailability of data. Besides this, there is another entity called the human appropriation of net primary productivity (HANPP) arising while considering the land use impacts due to the cultivation of the feedstock for biodiesel.

2 Methodology

Figure 1 provides a holistic view of the LCA of biodiesel starting from the cultivation of the crops to the burning of the biodiesel in an engine. This “farm-to-fire” analysis is broken down into various stages (farm to fuel and fuel to fire), and the input at each stage required for that process contributes to the effects caused due to the process. These effects accumulate to give the overall impact that the production and usage of biodiesel have on the environment as well as the living things (humans, animals, and aquatic life) inhabiting the earth. The different impact categories mentioned in Fig. 1 have their methodology of estimation as under [11].

2.1 Energy

Energy is measured in terms of the amount of fossil energy used to produce a given unit of energy from the desired fuel. 1 Gigajoule (GJ) is used as a functional unit throughout the life cycle analysis calculation. Fossil energy Ratio (FER) quantifies the fossil energy needed to produce energy from the fuel [7].

$$\text{FER} = \text{Renewable Fuel Energy output} / \text{Fossil energy input}$$

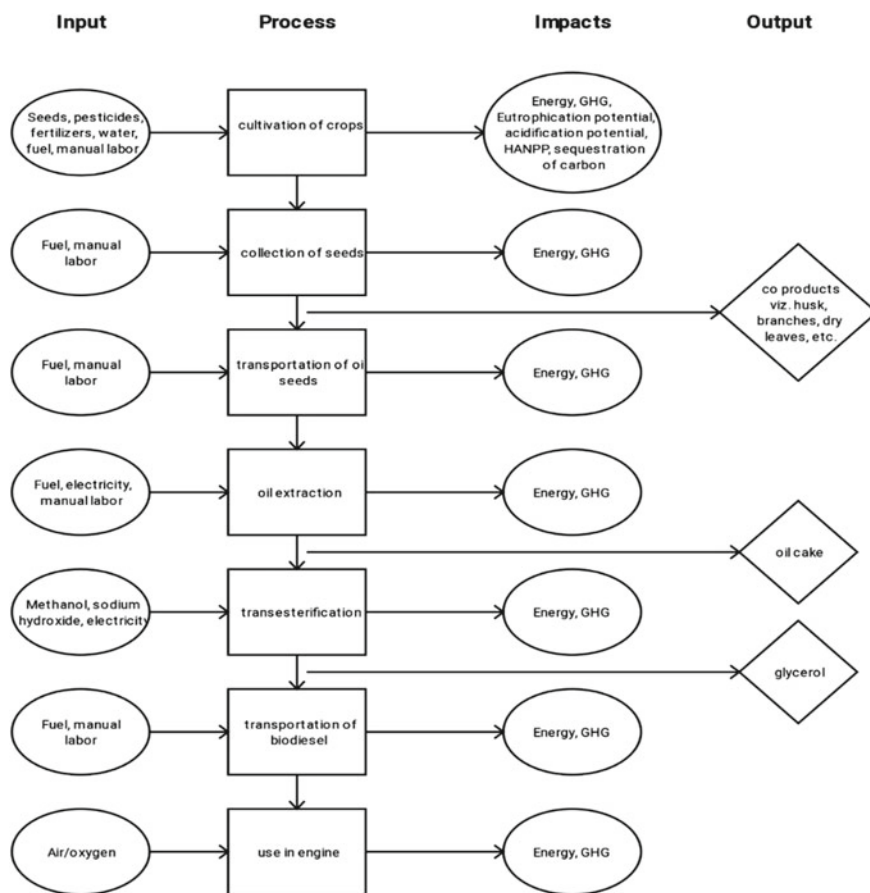


Fig. 1 Elements of life cycle—Schematic representation

2.2 Greenhouse Gas Emissions

This impacts the environment and the impact is quantified using “gram equivalent of CO₂” in Table 1. The emissions at various stages of the fuel production are estimated

Table 1 Carbon dioxide equivalence of gases [12]

Greenhouse gas	Formula	100-year GWP
Carbon dioxide	CO ₂	1
Methane	CH ₄	25
Nitrous oxide	N ₂ O	298
Sulphur hexafluoride	SF ₆	22,800

Table 2 PO₄ Equivalence Values of Various Nutrients [13]

Nutrients	PO ₄ equivalence factor (kg eq. PO ₄)
Nitrogen	0.42
Phosphorous	3.07
NH ₃	0.35
NH ₄ ⁺	0.33

by converting the different gases into the equivalent effect that CO₂ will produce using the global warming potential (GWP) values for the other gases.

2.3 Eutrophication

This is a phenomenon in which an excessive growth of algae is induced in water overly enriched with minerals and nutrients. Due to the generation of biomass and consequent sedimentation of dead organic material, the oxygen dissolved in deep water is consumed faster through aerobic decomposition. Eutrophication is generally caused by the discharge of nitrate or phosphate-containing detergents, fertilizers, or sewage into a water body. Also, the direct toxic effects on higher organisms, including humans, are to be considered if certain species of algae appear in a large amount. Eutrophication potential (kg PO₄-eq or kg N-eq) is calculated as

$$EP = \sum_i (m_i \times EP_i), \quad (1)$$

where m_i and EP_i are the mass in kg of inventory flow 'i' and the phosphorus with the same eutrophication potential as one kg of inventory flow, respectively.

Table 2 provides all equivalent values for 1 kg of nutrient i of inventory flow.

2.4 Acidification

There are many forms of acidification which include acidifying gas emissions and acidification of soil and water. Atmospheric emissions of acidifying substances like SO₂ and NO_x can persist in the atmosphere for a few days and can be transported over long distances where they undergo chemical conversions to sulphuric and nitric acid. Table 3 indicates the SO₂ equivalent factors for different acidifying gases of interest in the environment context.

Soil acidification is a natural phenomenon in medium to high rainfall regions. Agricultural production systems can increase the rate of soil acidification primarily due to the perturbation of the natural cycles of nitrogen (N), phosphorus (P), and sulfur (S) in soil, the removal of agricultural produce from the land, and the addition

Table 3 Acidification Potential of Various Gases in the Atmosphere [13]

Acid producer (in air) per kg	SO ₂ equivalence factor (kg eq. of SO ₂)
HCl	0.88
NO ₂	0.70
H ₂ S	1.88
SO ₂	1.00

Table 4 Acidification potential of fertilizers on soil [14]

Fertilizer	Acidification potential (kg lime eq. to neutralize acidity per kg N)	
Nitrogen fertilizers	If all nitrate leached	If all nitrate is taken up
NO ₃	0	−3.6
NH ₄ NO ₃	3.6	0
Urea	3.6	0

of fertilizers that can either acidify soil or make it more alkaline. Table 4 provides the acidification factors expressed in terms of kg lime equivalent to neutralize the acidity generated by one kg of nutrients added in different forms for various fertilizer types.

2.5 Human Appropriation of Net Primary Productivity (HANPP)

This is a sociological aspect that impacts sustainability. While human appropriation implies consumption for one's own use, the net primary productivity (NPP) is a measure of the formation of chemical energy in the form of organic compounds by living biological organisms [15]. HANPP tracks the percentage of the global net primary productivity that humans use, such as the cultivation of food crops, rearing of livestock, fuel extraction, and its use. In a nutshell, the HANPP gives an estimation of the impact that human activities have on the environment and how it disturbs the existing ecological balance.

2.6 Techno-Economic Analysis

Life cycle cost assessment (LCCA) is the assessment of the economic performance of a product over its entire life cycle, including costs of installing, operating, maintaining

the resources, and distributing products and disposing of the by-products. Economic performance can be calculated for two scenarios.

Scenario 1: Production of biodiesel starting from the cultivation of seeds and the time taken for trees to mature and bear seeds.

Scenario 2: Production of biodiesel excluding the cost of cultivation, i.e., assuming the feedstock is bought directly from the market.

The costs of production are majorly divided into two categories:

Fixed Cost (FC) includes cost of construction of a shed or building for a biodiesel plant, cost of procurement of machinery, utility cost, viz. boiler, cooling towers, reaction, and storage tanks and miscellaneous costs.

Production costs include the cost of land, labor, electricity, feedstock procured from the market, catalysts and reactants, other materials, maintenance [16] @ 10% of FC, insurance, and taxes [16] @ 4% of FC.

To calculate the daily requirement of fuel in the case of the rural setting, the average number of pumps used in villages in India and the fuel consumption of the pump was used to get the estimate, which was around 400 L per day. The commercial plant capacity to meet these requirements is assumed to be of different sizes ranging from 1000 L per day to 10,000 L per day of biodiesel production. Also, the biodiesel price is determined based on two periods of Return on Investment (ROI), viz. 1 year and 5 years, respectively. The costs incurred during the setting up of the biodiesel plants have several cost elements, which include structural costs, machinery cost, utility cost, cost of labor, electricity cost, cost of the reactants and catalysts, cost of feedstock, and other miscellaneous costs. The structural costs include the costs required for the construction of a building based on the production capacity of the biodiesel plant. The machinery costs include the cost of storage and reaction tanks, pumps, vapor condenser, and effluent treatment plant. The utilities include cooling towers, boilers, and dry wash systems. The labor costs are based on the MGNREGA scheme by the government for laborers in rural settings. The miscellaneous costs include costs of laboratory equipment, pipes and fittings, and firefighting units for the plant.

3 Results and Discussion

The results concerning energy estimation, equivalent CO₂ emission reduction for four different biodiesel fuels are presented and compared in this study.

3.1 Fossil Energy Ratio Estimation

The values of fossil energy ratio (FER) per GJ obtained in the farm-to-pump and farm-to-fire analyses of four biodiesel test fuels are shown in Fig. 2. These data are compared with the well-to-pump and well-to-wheel analyses of the fossil diesel system. In the farm-to-pump analysis of four biodiesels systems, Neem has the highest net energy ratio value of 2.96, followed by Coconut (2.9), Karanja (2.82), and Jatropha (2.11). This parameter for fossil diesel has a value of 0.79, as obtained in its well-to-pump analysis. In the farm-to-fire study of biodiesel systems, significant reductions are observed in the values of FER compared to the farm-to-pump analysis of biodiesel systems due to their utilization in the stationary diesel engine, which has around 30% energy output. In the farm-to-fire analysis of four biodiesel, Neem has the highest FER value (0.97) followed by Karanja (0.96), Coconut (0.96), and Jatropha (0.87).

The higher FER value of neem compared to the other three biodiesels investigated in this study is due to the fact that neem requires no fertilizers during its cultivation, has higher seed yield per hectare (5250 kg/ha/year), yields large amount of seed cake as a by-product which offsets the energy input and the neem biodiesel fueled engine gives higher efficiency (~30%). All these factors decrease the net energy input and hence increases the FER. Higher the FER, lesser is the amount of non-renewable resources that are being used during the production of the biodiesel. Hence, the FER can be a basis to decide between various kinds of biodiesel that can be used to replace fossil diesel. The differences in FER values of various biodiesels are statistically significant as observed P-value is found to be 0.025. Also, it is evident from the fact that a higher FER corresponds to the biodiesel that has a higher energy output for the same energy input. It may also be noted that a higher FER generally corresponds to lower emissions, but carbon sequestration capacity of the crops must also be accounted for to make an informed decision.

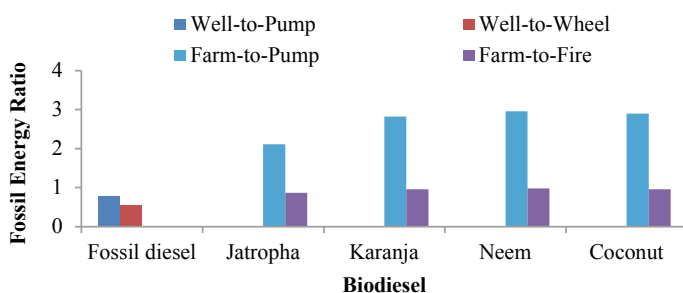


Fig. 2 Comparison of net energy ratio (NER) of four biodiesels with fossil diesel

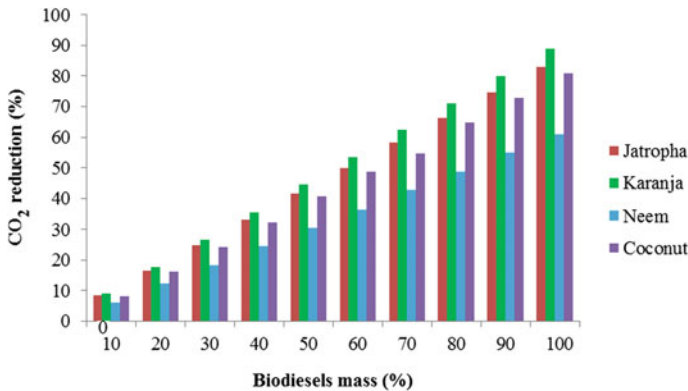


Fig. 3 Equivalent CO₂ emission reduction in the farm-to-fire analyses of four biodiesels

3.2 Equivalent CO₂ Emission Reduction

The CO₂ equivalent emission reductions of biodiesel systems in the farm-to-fire analysis concerning the fossil diesel system in its well-to-wheel analysis are estimated. It may be noted that the CO₂ equivalent reduction (%) is calculated based on fossil diesel mass percent replacement with biodiesel mass percent. The results of the equivalent CO₂ reductions for four biodiesel test fuels are shown in Fig. 3. It is found that the Karanja biodiesel system provides 89% reductions in equivalent CO₂ during its complete life cycle. The equivalent CO₂ emission reduction from Coconut (83%), Jatropha (81%), and Neem (61%) would follow in that order. Karanja biodiesel system has the highest CO₂ reduction ability due to the highest average carbon sequestration capacity (kg CO₂/ha/year) of its plant. For a given sequestration capacity of a plant, an average CO₂ absorption capacity can be estimated. It is known that 1 kg CO₂ absorption is equivalent to 0.27 kg carbon fixation [8].

3.3 Techno-Economic Analysis

Figure 4 compares the prices of coconut biodiesel based on 1- and 5-year return on investments. The prices are lesser in 5 years as expected because of the longer period to get back the costs of the establishment of the infrastructure. The prices will drop further as the number of years increases.

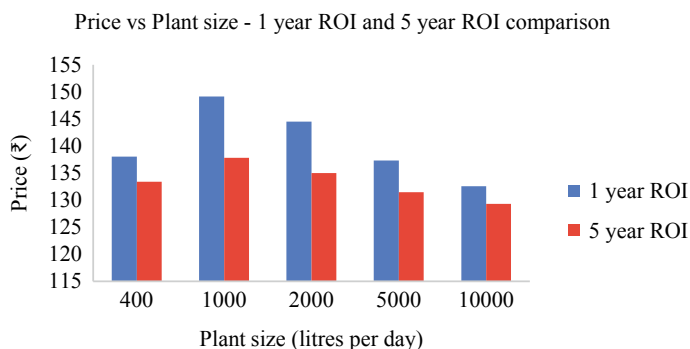


Fig. 4 Price comparison between 1- and 5-year return on investment

4 Sensitivity Analysis

4.1 Sensitivity Analysis for Fossil Energy Ratio

The fossil energy ratio for Karanja biodiesel is 2.82 in its production process. The sensitivity analysis is performed to identify the critical quantities in the estimation of the fossil energy ratio by varying the case study data of $\pm 10\%$ and shown in Table 5. One quantity is changed at a time, and the corresponding percentage change in FER value is observed. If the percentage variation in FER is $> 2\%$, then it is assumed to be

Table 5 Sensitivity analysis for the estimation of FER

Quantity changed by $\pm 10\%$	Percentage change in FER (%)	
	+10%	-10%
Diesel in seed cultivation process	-1.72	+1.78
Fertilizers in seed cultivation process	-3.26	+3.41
Seed yield	-2.23	+2.34
Oil content in seed	-2.03	+2.12
Mechanical expeller efficiency	-2.15	+2.25
Raw oil yield	-2.51	+2.64
Electricity consumption in oil extraction	-2.23	+2.34
Electricity consumption in trans-esterification	-0.21	+0.22
Trans-esterification efficiency	-0.95	+1.00
Methanol consumption	-1.57	+1.63
NaOH consumption	-0.09	+0.09
Co-products yield	+3.40	-3.40
Biodiesel yield	+6.60	-6.60

Table 6 Sensitivity analysis for equivalent CO₂ emission reduction

Parameters	Change in CO ₂ reduction (%) with \pm 10% variation	
	+10%	-10%
Energy equivalent CO ₂ emission during biodiesel production ($e_{p, bd}$, kg/GJ)	-1.01	+1.45
Energy equivalent CO ₂ emission during diesel production ($e_{p, d}$, kg/GJ)	+1.10	-0.71
Brake thermal efficiency of biodiesel fueled engine (η_{bd} , %)	+9.33	-10.92
Brake thermal efficiency of diesel engine (η_d , %)	-2.30	+2.87
Energy equivalent CO ₂ emission from biodiesel combustion ($e_{c, bd}$, kg/GJ)	-9.81	+10.25
Energy equivalent CO ₂ emission from diesel combustion ($e_{c, d}$, kg/GJ)	+2.62	-2.57
CO ₂ absorption capacity (X_{abs} , tonne/ha/yr)	+7.98	-7.54
Karanja seed yield (S_y , tonne/ha/yr)	-8.46	+11.41
Gross energy value of seeds/fruits (E_{seed} , MJ/kg)	-7.75	+10.26
Energy input in the seed cultivation (E_f , MJ/ha/yr)	+2.29	-1.74

a significant variation in FER. This criterion is used for finding the critical quantities in FER estimation.

4.2 Sensitivity Analysis for Equivalent CO₂ Reduction

The equivalent CO₂ reduction value from the farm-to-fire analysis of Karanja biodiesel is obtained at 89%. To perform the sensitivity analysis for equivalent CO₂ reduction, the parameters involved are varied once at a time by $\pm 10\%$, and the corresponding percentage variations in equivalent CO₂ reduction is observed. If the percentage variation in equivalent CO₂ reduction is $>2\%$, then it is assumed to be of significance in equivalent CO₂ reduction. The sensitivity analysis for different parameters of equivalent CO₂ reduction is shown in Table 6.

5 Conclusions

The useful inferences from this study concerning four biodiesels are:

- The Coconut biodiesel system requires 67% lesser overall energy consumption compared to fossil diesel system in its production process, followed by Neem (53%), Karanja (51%), and Jatropha (48%).

- Sensitivity analysis performed by changing the one parameter at a time suggests that biodiesel yield is the most sensitive parameter for estimating the FER value in the farm-to-pump analyses of all the four biodiesel fuels investigated here.
- The FER values of farm-to-fire analyses and farm-to-pump analyses of all four biodiesel can be correlated with the efficiency of the utilization system e.g., engine or heating appliance. For conforming to the renewability, there is a minimum brake thermal efficiency value required for particular biodiesel fueled engine depending upon its FER estimate.
- From an energy standpoint, to be a sustainable fuel, either biodiesel source yield should be higher, or it should be utilized in the end-use system more efficiently.
- From the global warming standpoint, Karanja biodiesel is a potential candidate for reducing the equivalent CO₂ emission (89%) in the atmosphere due to the high CO₂ absorption capacity of its plant. The equivalent CO₂ emission reduction from Coconut (83%), Jatropha (81%), and Neem (61%) would follow in that order.
- Wherever there is an issue with food versus fuel with edible resources like Coconut biodiesel system, one can judiciously apportion their use as food and fuel particularly in regions where there is plenty of such resource to ensure local energy security.

References

1. V. Smil, *Energy at the Crossroads* (First MIT Press Paperback Edition, Global Perspectives and Uncertainties, 2005)
2. <https://energy.economictimes.indiatimes.com/news/oil-and-gas/india-will-overtake-china-as-largest-market-for-energy-by-late-2020s-bp-energy-outlook/63024657>
3. C. Spirinckx, D. Ceuterick, Biodiesel and fossil diesel fuel: comparative life cycle assessment. *Int. J. Life Cycle Assess.* **1**, 127–132 (1996)
4. K. Prueksakorn, H.S. Gheewala, Full chain energy analysis of biodiesel from Jatropha Curcas L in Thailand. *Environ. Sci. Technol.* **42**(9), 3388–3393 (2008)
5. J. Sheehan, V. Camobreco, J.A. Duffield, M. Graboski, H. Shapouri, Life-cycle Inventory of Biodiesel and Petroleum Diesel for Use in an Urban Bus. A Joint Study Sponsored by U.S. Department of Agriculture and U.S. Department of Energy. NREL/SR-580–24089 Golden, CO: National Renewable Energy Laboratory. U.S. Department of Energy (1998)
6. S. Kumar, J. Singh, S.M. Nanoti, M.O. Garg, A Comprehensive life cycle assessment (LCA) of Jatropha biodiesel production in India. *Biores. Technol.* **110**, 723–729 (2012)
7. A. Pradhan, D.S. Shrestha, A.J. McAloon, W. Yee, M.J. Haas, J. Duffield, Energy life-cycle assessment of soybean biodiesel revisited. *Am. Soc. Agric. Biol. Eng.* **54**(3), 1031–1039 (2011)
8. Yadav A and Singh O (2010) Energy Estimations for Life-Cycle Analysis of Jatropha, Neem and Karanja Biodiesel - A Parametric Study, Proceeding of the Institution of Mechanical Engineers. Part A: *Journal of Power and Energy* 224:1049.
9. F. Cherubini, N.D. Bird, A. Cowie, G. Jungmeier, B. Schlamadinger, S. Woess-Gallasch, Energy- and greenhouse gas-based LCA of biofuel and bioenergy systems: key issues, ranges and recommendations. *Resour. Conserv. Recycl.* **53**, 434–447 (2009)
10. A. Pradhan, D.S. Shrestha, J.V. Gerpen, J. Duffield, The energy balance of soybean oil biodiesel production: a review of past studies. *Trans. Am. Soc. Agric. Biol. Eng.* **51**(1), 185–194 (2008)
11. K. Lee, A. Inaba, Life cycle assessment best practice of ISO 14040 series (Asia- Pacific Economic Co-operation, Singapore, 2004)

12. Intergovernmental Panel on Climate Change (IPCC), Fourth Assessment Report (AR4)
13. GHK Consulting and BIO Intelligence Service (submitted to European Commission), A Study to Examine the Costs and Benefits of the ELV Directive, Final Report, Annex 5 Environmental Impacts Analysed and Characterisation Factors (2006)
14. Fertiliser Technology Research Centre Technical Bulletin: Fertilizers and Soil Acidity, University of Adelaide, www.adelaide.edu.au/fertiliser.
15. H. Haberl, K.H. Erb, F. Krausmann, Human appropriation of net primary production: patterns, trends, and planetary boundaries. *Ann. Rev. Environ. Res.* **39**, 363–391 (2014)
16. S.N. Gebremariam, J.M. Marchetti, Economics of biodiesel production. *Rev. Energy Convers. Manage.* **168**, 74–84 (2018)

The Role of 3D Printing in the Biomedical Application: A Review



Ujwal Sontakke and Santosh Jaju

1 Introduction

From the time, when industries started using fuel and steam as an energy source to the use of digital computers, the world has witnessed many revolutionary changes. The fourth industrial revolution is now gaining the attention of manufacturers due to its disruptive technologies. From many such technologies, additive manufacturing is one of the most researched areas. In the 1980s, Charles Hull patented the first 3D printing apparatus and also developed the STL file format. For his contribution to the field, he is considered the pioneer of 3D printing [15]. 3D printing is an additive technology that includes the addition of material in layers to create an object and differs from conventional manufacturing which generally includes the removal or subtraction of material from the base material. It allows manufacturing objects in a single run, which is not possible by subtractive manufacturing. Both terms 3D printing and additive manufacturing are interchangeable. Sometimes, this technique is also referred to as desktop manufacturing or rapid manufacturing [5]. Additive manufacturing is now a well-known technology but still improving day by day on which many researchers are focusing. From the 1980s to 2020, much advancement has brought 3D printers to another level by making them more reliable and user-friendly. Also nowadays, 3D printing technology is not limited to any single technology, it is now a combination of many. Stereolithography (SLA), Fused deposition modeling (FDM), PolyJet and Inkjet printing, Selective laser sintering (SLS), Electron beam melting (EBM), Digital light processing (DLP), and Selective laser melting (SLM) are some of the most common 3D printing technologies. This technology includes the intake of a digital model or blueprint of the object

U. Sontakke (✉) · S. Jaju

Department of Mechanical Engineering, G. H. Raisoni College of Engineering, Nagpur, Maharashtra, India

e-mail: sontakke_ujwal.mtechcc@ghrce.raisoni.net

and layered deposition of the suitable printing material to get the desired 3D model. 3D printing is a tool-less manufacturing technique and can give flexibility in design and shorten time to market. Additive manufacturing provides many advantages like customized products with small batch sizes, concept modeling and rapid prototyping, micro-machining, and intricate shapes preparation, benefits may also include cost-effectiveness, increased productivity, enhanced collaboration, etc. One of the most important fields is medicine, which is extensively using 3D printing technology as a wide variety of materials that are now available for 3D printing. These materials have different mechanical and physical properties and can be used in the printing of objects for any situation. 3D printing technology shows a promising future for medical and pharmaceutical companies. The application of the technology includes the creation of 3D printing of organs and tissue engineering, the creation of surgical guides and prostheses, and customized drug delivery, etc. [1].

Considering all these points, this context includes the systematic review of 3D printing in various fields of medicine. The review is divided into three sections. Section two of the review discusses the role of 3D printing in biomedical applications. The third section of the paper discusses the applications of 3D printing and its development in medical science. The fourth section of the context discusses the transition of 3D printing into 4D printing and its necessity.

2 The Role of 3D Printing in Bio-Medical Application

As the years are passing, numbers of new technologies are continuously coming into the market. The same scenario is also showing rapid improvement in 3D printing technology. The computer-aided design (CAD) systems and its integration with well-developed 3D scanners, highly improved imaging techniques, and fast printing capability has brought this technology to a new height. Many companies, startups are now taking an interest and working for more reliable 3D printers. A very small build layer up to 16-micron thickness is now achievable by using industrial 3D printers [3]. With an improvement in 3D printers, many companies are also now developing new materials for 3D printing materials. Many companies, like Stratasys Ltd., The Hewlett Packard Company (HP), EOS GmbH, 3D Systems Inc., Proto labs Inc., are now continuously focusing on the development of affordable and reliable 3D printers and also contributing to developing materials for 3D printing applications (Table 1).

3D models required for printing can be prepared by a CAD system or with well-developed scanners. But for medical science applications, X-rays or computed tomography can also be used for model generation. Advancements in 3D printing technology not only depend upon the improvement of printers but also on scanners and 3D software [5]. Materials like polymers (both synthetic and natural), ceramics, and metals are more common in medical applications. Each of these materials can be used for specific applications because of their specific characteristics. 3D printing technology can effectively start the customization of goods on large scale. The economy of scale is another important feature of 3D printing. When

Table 1 3D printing methods (Features, Limitations, and Applications)

Method	Features	Limitations	Applications	References
Stereolithography	High level of details, Smooth surface finish and tight tolerances, cheap method	High initial cost and liquid resins are expensive, Objects are brittle and prone to cracking, support structure limits the degree of freedom	Patient-specific surgical guides and prostheses, Tissue engineering, Molds and casting patterns, Rapid tooling, etc.	[14]
Selective laser sintering	High strength and stiffness, Good chemical resistance, Availability of a range of materials with different properties, Does not require a support structure	The properties of the fabricated parts depend upon the material properties and process factors, Prone to shrinkage and warping, Expensive	Foundry patterns, Aerospace parts, Medical and healthcare, Jigs and fixtures, etc.	[6]
Fused deposition modeling	A cost-effective and fast method, Clean process	Rough surface finish and low strength, Thermo-sensitive medicines are not suitable, physical instability and degradation issues with printed medicine because of high temperature	Functional testing, Concept models, Tooling jigs and fixtures, Drug delivery and 3D printed medical devices	[10, 13]
PolyJet printing	Multiple materials can be printed hence flexible and multi-colored objects are possible, controlled accuracy, and good surface finish	Poor mechanical properties and very expensive method	Organ printing, Prosthetic limbs and joint replacement, Dentistry, Automobile, Architecture, and Industrial applications	[7]
Digital light processing	Fast speed, High resolution, Mild condition, Medical models have a fine shape, No support structure, Complex Personalized production	Structures are more sensitive, The material choice is limited, materials are required to be combined with photosensitive materials	Medical models, Medical implants, Tissue engineering, Organ printing like heart, lungs, liver, etc.	[22]

(continued)

Table 1 (continued)

Method	Features	Limitations	Applications	References
Electron beam melting	Processing of brittle material is possible, Low risk of deformation and Good mechanical properties, Significant weight reduction	Slow process and Expensive, High bed temperature and overnight cooling time required, Optimizing process parameters are difficult	The aerospace industry for lightweight components and Medical prosthesis	[8]

compared to 3D printing in the case of traditional manufactured large-scale production is still cheaper but when considering smaller quantities production, 3D printing is becoming cost-effective [18]. These developments are now attracting many industries to use additive manufacturing in their processes. As the numbers of developed and qualitative 3D printing materials are coming into the market, this technology is now successful in attracting the attention of medical and dental experts. Also, the very high accuracy of these 3D printers makes them suitable to use in complicated medical situations. Every year new researches are coming up with extensive use of 3D printing in the bio-medical field. From the last ten years, additive manufacturing technology has offered many applications which are now greatly contributing to medical and dental implants. These applications may include the preparation of patient-specific surgical tools, providing the surgeon a physical 3D model, modeling of customized prosthetics, validating the results achieved by a more accurate estimation of the patient's bone condition, etc. With the improvement in 3D printing materials, the 3D printers now also allow modeling of implantable tissues, synthetic skin for patients suffering burn injuries, replicating for heart valves, and replicating of human ears, etc. Nowadays it has become quicker to produce prototypes of new concepts (rapid prototyping) and making changes in them as per application through the use of 3D printing. 3D printed anatomic model can help doctors to know the actual condition and to understand the patient. Similarly, 3D printed models can give a better understanding while investigating the crime scenes and to demonstrate them in the courtrooms [1]. This significant change gives more accurate and precise results for treatments. The next section of the paper discusses the various medical science fields which are now extensively using additive manufacturing in their treatments.

3 Application of 3D Printing in Medical Science

The application of 3D printing in this field is not new but it is constantly growing with great speed. Improvements in 3D printers, a well-developed range of materials are the reasons behind the increased demand for 3D printing in medicine. This section of the context discusses the various fields in medicine that are extensively using additive manufacturing.

3.1 3D Printing in Surgical Guides

The technology of additive manufacturing is now improving at a good pace and the quality of the print and material is also improving which is the reason for the increased use of technology in medicine. The technology allows the use of 3D printers to visualize 3D drawings to realistic physical objects. The use of additive manufacturing in the field is not new. 3D printing technology is now extensively used in neurosurgery, orthopedics, dentistry, spinal surgery, and many other disciplines. Advantages of technology such as improved visualization and better surgical outcomes are now giving a push to the use of 3D printed surgical guides, patient-specific implants, and prosthetics [20]. 3D printing technologies such as Stereolithography (SLA), and Fused deposition modeling (FDM) are generally used for manufacturing models and surgical guides whereas, Selective laser sintering (SLS), Selective laser melting (SLM), and Electron beam melting (EBM) are used for medical implants. Generally, available CAD programs are best suited for industrial use and are not easy to understand for everyone. As there are many CAD program developers are now focusing on improvising their interface, in the future CAD programs become more friendly and boost their use in medicine [19].

The use of 3D printed surgical guides is more common in the medical application. These surgical guides are widely used in neurosurgery, spinal surgery, and dentistry in many other fields. The use of surgical guides is very favorable for new surgeons and complex procedural surgeries. Implementation of these 3D printed surgical guides reduces time, and also improves surgical outcomes with model simulation and accurate translation of surgery [20]. In spinal surgery, a surgical guide improves the outcome and this outcome will be less dependent on the experience of surgeons. Similarly, in maxillofacial surgery, the creation of surgical guides is common for the reconstruction of jaws and skulls, etc. The final surgical outcome depends upon the accuracy of surgical guides and their accurate placement. And the accuracy of these surgical guides depends on the 3D printer used, printing material, and the time between the scan [20]. In the future, there is a need for 3D printing to increase resolution, speed, and compatibility with relevant materials. 3D printing in medicine is not very cost-effective, but in complex cases, it justifies the additional cost. The overall cost of printing depends upon the printing facilities. The use of the cheap printer and cheap material will result in the creation of low-quality models and surgical guides, but for medicine application, the use of qualitative material and printer must be the priority [20].

3.2 3D Printing in Orthopedics

The healthcare field is now very rapidly adopting 3D printing technology. Additive manufacturing is quite a mature technology and is now well known in the

field of medicine. The potential of orthopedics in personalized treatment is continuously rising. Hence, personalized or patient-specific modeling is now gaining huge attention. In medical applications, from planning to training, education, and implant design, the scope of 3D printing is continuously growing [21]. Every junior surgeon should take the advantage of this technology for a better understanding of the patient's situation. Governments need to make more efforts on the policies and regulations for manufacturing the 3D printing-based customized implants. Many developed nations like the United States and European nations have already started to provide licenses for orthopedic and dental implants. For surgical operations, developed imaging technologies can reconstruct the bones, and then prototypes creation becomes easy using this layered manufacturing technique. With proper visualization, analyzing the information, planning, and diagnosis becomes more efficient. These medical imaging technologies are the reason for the success of 3D printing technology in medical science applications [21].

The physical models and created CAD files could be stored to form a database so that whenever necessary it can be again be reprinted. Recent advances in 3D printing technology, the drop in forming equipment prices, shorter operative time, and improved accuracy have got the attention of medical practitioners. The customized implants and developed metallic implants are some of the most valuable contributions in the field of orthopedics. Many times standard size implants cannot be fitted for the specific patient, in such a situation custom implants can be a perfect solution for the unique anatomy of the patient. Titanium, cobalt alloys, and stainless steel are some common metals available for printing in medicine. Many ongoing pieces of research are quite successful in overcoming the weakness of 3D printing materials and hence broaden the application of 3D printing in orthopedics [2]. Biodegradable material is another important topic of research because 3D printed bones should have properties similar to bone. Polyether ether ketone is such a material that can be effectively used as a biomaterial for implantable medical devices (Wong 2016).

3.3 3D Printing in Dentistry

Dentistry is another important medical field which is extensively working with additive manufacturing. In dentistry, technology can be widely used to produce drill guides, personalized dental implants, copings, dental restorations, and frameworks for implants. 3D printing makes comparatively easy to replicate required geometries without the use of molds and tooling, which are expensive and not feasible with conventional manufacturing [9]. Scanning or imaging technologies such as CT, MRI, and intraoral scanning in combination with the use of CAD programs are gaining more importance in dentistry. To create a physical model of the human jaw, the use of an intraoral scanner is moreover common. Nowadays, CAD software is not only common in industries and manufacturing environment but also common in dental laboratories. The subtractive operations and milling were more common in dentistry, but now 3D printing provides the facilities of reconstruction or restoration with a high

Table 2 3D printing application in medicine

Application	3D printing method	Material used	References
Surgical guides and dentistry	Stereolithography (SLA) and Fused deposition modeling (FDM), etc.	Acrylonitrile butadiene styrene (ABS), Titanium, Stainless Steel, etc.	[19, 20]
Customized implants and prostheses	Electron beam melting (EBM), Stereolithography, etc.	Carbon fiber reinforced (CFR) filament, Flexible filaments like thermoplastic polyurethane (TPU), conductive filaments, Cobalt chrome, etc.	[2, 21]
Tissue engineering and organ printing	Digital light processing (DLP), Polyjet and Inkjet printing, etc.	Stem cells or cells cultivated from tissue samples, etc.	[9, 17]
Drug delivery	Fused deposition modeling (FDM), Selective laser sintering, etc.	Silicone, Acrylonitrile butadiene styrene (ABS), Polylactic acid (PLA), etc.	[12, 15]

level of complexity and precision. The range of materials available for 3D printing is long. Still, many new kinds of 3D printing materials are under the development stage which can make good improvements in properties [4].

The faulty or less accurate 3D printer and improper material can cause serious health issues to the patient, hence choosing a précised 3D printer is necessary, and the most appropriate printing materials must be considered. 3D printing has great potential to make possible new and complicated treatments successful [4]. CAD software still requires well-trained operators but they are now becoming more user-friendly and smarter. These improvements are now giving a boost to the use of digital technologies in dentistry. Hence, 3D imaging and printing are making a positive impact on all aspects of dentistry. As 3D printers are becoming cheaper day by day, their use is also growing. But while using these printers, other aspects such as running cost, material cost, maintenance, and need for skilled operators should also be considered with keeping in mind, the strict health and safety protocols [4] (Table 2).

3.4 3D Printing in Neurology

Recent development has shown many applications for AM in the field of neurology, which include cerebrovascular, spinal, and endoscopic neurosurgery, brain tumors, neuro-oncology treatments, etc. For surgical planning, tissue-engineered implants, simulation, and training, 3D printing technology is evolving as a more accurate and practical solution. Expanding such implementation can contribute to advancing neurosurgical operations. Almost every surgical procedure in neurosurgeries involves

intricate and minute operations that cannot be observed easily. 3D printing can help in such a situation and can help to visualize the 3D structures for treatments. Rapid prototyping could provide a solution to the issue related to the two-dimensional images from X-ray, computed tomography, and MRI [17]. 3D representations of 2D images can give a better understanding of the problems associated with surgeries.

The translation of MRI, CT data into models can show the association between the tissue, tumors, vasculature, skull, and neuropathology tissue with 3D printing technology. Application of 3D printing in neurology also includes the creation of anatomical models, the design of neurosurgical devices, and the creation of biological tissue implants. 3D printed head models are very helpful for novel treatments of brain tumors. In cerebrovascular surgeries, 3D printing can be effectively used for surgical and simulation-based training methods [17]. Similarly, 3D printing can also address a procedural skill for spinal surgery in the form of simulation. The field is now exploring the technology for intervertebral disk degeneration treatment with tissue-engineered solutions. Another important area of application is pituitary tumor removal by transnasal sphenoid endoscopy with the integration of 3D printing in simulation developments [17].

3.5 3D Printing in Drug Delivery

The major advantage of 3D printing is its ability to fabricate the models and prototypes quickly and with the best level of accuracy. These abilities can now be applied to clinical medicines to produce individualized models, implants, and personalized medicine. Also, 3D printing can precisely control the droplet size, with complex drug release profiles, and can give high reproducibility. With the precisely controlled distribution of dosage waste reduction can also be controlled [15]. One of the important goals which are achievable with the application of 3D printing is getting intended results and reduction in the risk and adverse effects through personalized medicines. Fused deposition modeling (FDM), 3D inkjet printing, and powder-based inkjet printing are more common in pharmaceutical applications. The advantage of powder-based inkjet printing is that it can use different materials, powder, or substrates for 3D printing. Different cellulose, coated or uncoated paper, microporous bioceramics, and potato starch films, etc., are some of the more commonly used substrates [12]. Many pharmaceutical companies are currently using 3D printing to produce microcapsules, antibiotic printed micropatterns, and layered drug delivery devices, etc. Also, the creation of many novel drug-release profiles for drug delivery devices is possible with 3D printing technology [12].

The oral medications which come as solid tablets, capsules, etc., are generally prepared by a combination of the processes such as mixing, milling, granulation of powder ingredients, and then forming into an oral tablet through compression or molds. Every step included in this process can cause degradation of drug or form change and sometimes it may also lead to complete batch failure. These all issues

associated with traditional manufacturing can be easily overcome with the implementation of 3D printing [12]. In the future, it may be possible that the pharmacist will look after the patient's characteristics like age, gender, and patient's health condition to create personalized medicine doses with the help of available databases and 3D printing technology.

4 The Transition of 3D Printing into 4D Printing

Many researchers are currently working on the development of new materials. These new materials have excellent physical and mechanical properties. Biomaterial in medical applications still requires new developments. The need for new material properties in 3D printing is the reason for the development of the concept of 4D printing. The concept of 4D printing just added one extra dimension of time in 3D printing. This fourth dimension is only possible because of the entry of smart materials in additive manufacturing. The smart materials are the cornerstone for 4D printing. The printed objects with smart materials can change their shape and properties over time [11]. Smart materials provide more flexible, deformable, and expandable characteristics in printing materials [16]. These smart materials are capable to sense the changes in the environment and can give a corresponding response. 3D printing methods such as SLA, SLS, inkjet printing, and FDM are more common in the use of smart materials for printing. The performance of 4D printing depends upon the smart material's combination such as shape memory alloys, smart Nanocomposites, and polymers [16]. Shape memory materials can deform with external stimuli by directly converting and mechanical work known as the shape memory effect. Piezoelectric polymers with unique characteristics are very suitable for biocompatible and mechanical flexibility applications [11]. The abilities of these smart materials can be very advantageous for various industrial applications. 4D printing is now evolving with the introduction of many smart materials. The important reason behind the evolution of 4D printing is the creation of objects with self-shape change characteristics. Then these printed models can be very helpful in many industrial and medical applications. In the future, many researchers will come with more advanced smart materials having brilliant physical and mechanical properties. 4D printing in the future will be one of the important technologies which will help additive manufacturing to grow its market shares in every domain of engineering and the field of medicine.

5 Conclusion

The paper represents a systematic review of additive manufacturing and its medical application. 3D printing technology is rapidly growing and continuously improving. The field of medicine is now widely exploring the advantages and applications of 3D

printing. The main application of 3D printing in medicine includes the creation of complex geometries, customized implants, surgical devices, précised drug delivery, tissue engineering, organ printing, training of new surgeons, proper visualization and surgical planning, etc. These applications give advantages of better surgical outcomes, low equipment prices, and short operative time. Many new materials are now coming which are compatible with medical applications and hence technology is quite successful in grabbing the attention of medical practitioners. Still, there is a need for an improvement like increased resolution, increased speed, machine cost, compatibility with relevant materials, quality of prints and post-processing, etc. Increased use of 3D printing allows new surgeons to grab the opportunity for self-training, the best surgical outcomes, and to explore the new areas of medicine for 3D printing applications. Also, for researchers, it provides an opportunity to develop and improve the process to make it simple and more reliable for medical practitioners. 4D printing is such an opportunity that can make many desirable changes in this development. Additive Manufacturing has a good scope in medicine and its great potential will gain a huge market share in the future. Therefore, this article reviews the developments of 3D printing and explores its promising applications in medicine, its improvement areas, and opportunities for medical practitioners and researchers.

References

1. A. Aimar, et al.: The role of 3d printing in medical applications: a state of the art. *J. Healthc. Eng.* 2019, (2019). <https://doi.org/10.1155/2019/5340616>
2. H. Cai, Application of 3D printing in orthopedics: status quo and opportunities in China. *Ann. Transl. Med.* **3**, 3–5 (2015). <https://doi.org/10.3978/j.issn.2305-5839.2015.01.38>
3. H.N. Chia, B.M. Wu, Recent advances in 3D printing of biomaterials. *J. Biol. Eng.* **9**(1), 1–14 (2015). <https://doi.org/10.1186/s13036-015-0001-4>
4. A. Dawood et al., 3D printing in dentistry. *Br. Dent. J.* **219**(11), 521–529 (2015). <https://doi.org/10.1038/sj.bdj.2015.914>
5. H. Dodziuk, Applications of 3D printing in healthcare. **13**(3), 283–293 (2016). <https://doi.org/10.5114/kitp.2016.62625>
6. S. Farid et al., A review on powder-based additive manufacturing for tissue engineering: selective laser sintering and inkjet 3D printing a review on powder-based additive manufacturing for tissue engineering: selective laser sintering and inkjet 3D printing. *Sci. Technol. Adv. Mater.* **16**(3), 1–20 (2015). <https://doi.org/10.1088/1468-6996/16/3/033502>
7. A.T. Gaynor, et al, Multiple-material topology optimization of compliant mechanisms created via polyjet 3D printing. August (2013)
8. P.K. Gokuldoss, et al., Additive manufacturing processes : selective laser melting, electron beam melting, and binder (2017). <https://doi.org/10.3390/ma10060672>
9. R. Jain, et al., Recent trends of 3-D printing in dentistry-a review. *Ann. Prosthodont. Restore. Dent.* **2**(4), 101–104 (2016). <https://doi.org/10.18231/2455-8486.2016.0001>
10. B. Khatri, et al., Fused deposition modeling of ABS-barium titanate composites: a simple route towards tailored dielectric devices (2018). <https://doi.org/10.3390/polym10060666>
11. Z.X. Khoo et al., 3D printing of smart materials: a review on recent progress in 4D printing. *Virtual Phys. Prototyp.* **10**(3), 103–122 (2015). <https://doi.org/10.1080/17452759.2015.1097054>
12. C. Lee Ventola, Medical applications for 3D printing: current and projected uses. *Pharm. Ther.* **39**(10), 704–711 (2014)

13. J. Long, et al., Application of fused deposition modelling (FDM) method of 3D printing in drug delivery. March 2017 (2016). <https://doi.org/10.2174/13816128226661610261>
14. F.P.W. Melchels et al., A review on stereolithography and its applications in biomedical engineering. *Biomaterials* **31**(24), 6121–6130 (2010). <https://doi.org/10.1016/j.biomaterials.2010.04.050>
15. L.K. Prasad, et al., 3D printing technologies for drug delivery : a review 3D printing technologies for drug delivery : a review. 9045 (2016). <https://doi.org/10.3109/03639045.2015.1120743>
16. M. Quanjin et al., Recent 3D and 4D intelligent printing technologies: a comparative review and future perspective. *Procedia Comput. Sci.* **167**, 1210–1219 (2020). <https://doi.org/10.1016/j.procs.2020.03.434>
17. M. Randazzo et al., 3D printing in neurosurgery: a systematic review. *Surg. Neurol. Int.* **7**(34), S801–S809 (2016). <https://doi.org/10.4103/2152-7806.194059>
18. C. Schubert, et al., Innovations in 3D printing: a 3D overview from optics to organs, 159–161 (2014). <https://doi.org/10.1136/bjophthalmol-2013-304446>
19. D. Shilo, et al., Printing the future—updates in 3D printing for surgical applications. *Rambam Maimonides Med. J.* **9**(3), e0020 (2018). <https://doi.org/10.5041/rmmj.10343>
20. P. Tack et al., 3D-printing techniques in a medical setting: a systematic literature review. *Biomed. Eng. Online.* **15**(1), 1–21 (2016). <https://doi.org/10.1186/s12938-016-0236-4>
21. K.C. Wong, 3D-printed patient-specific applications in orthopedics, 57–66 (2016)
22. J. Zhang, et al., Digital light processing based three-dimensional printing for medical applications. (2020). <https://doi.org/10.18063/ijb.v6i1.242>

Microsurfacing Machines: A Review



Kratika Ravekar and Santosh B. Jaju

1 Introduction

Microsurfacing is usually blended, and applied utilizing, a deliberately assembled truck, by and large alluded to as a “slurry truck.” This machine is fit for steady or constant blending and use of microsurfacing because of its enormous stockpiling compartments and ability to append to total conveyance trucks and big haulers containing microsurfacing emulsion. This constant activity gives the advantage of having scarcely any creases in the street which happen when activity stops [1].

Microsurfacing is applied so as to help save and ensure the hidden asphalt structure and give another driving surface. Streets picked for microsurfacing application have low to direct misery and limited split width. Microsurfacing is normally applied on an irregular, venture explicit premise. Area, climate, traffic stacking, and asphalt conditions are factors used to decide whether a microsurfacing application is suitable. Streets chose for microsurfacing treatment are regularly those which have slight to direct misery, no rutting, and for the most part restricted split widths, and in which a microsurfacing treatment would help broaden the asphalt life until reemerging gets essential. Streets picked for repeating microsurfacing applications would ordinarily be dealt with each 5–7 years.

Slurry trucks and nonstop machines contain different compartments which hold the total (fine-squashed stone), water, polymer adjusted emulsion, and different added substances, which are blended in the on-board blender. The microsurfacing blend streams out of the back and onto the asphalt inside the limits of a back mounted box

K. Ravekar (✉) · S. B. Jaju

Department of Mechanical Engineering, G. H. Raisoni College of Engineering Nagpur 440016, Maharashtra, India

e-mail: ravekar_kratika.ghrcemtechcad@raisoni.net

S. B. Jaju

e-mail: Santosh.jaju@raisoni.net

alluded to as a “miniature box.” This container contains a drill which goes to consistently appropriate the blend over the width. Laborers with squeegees follow behind and help with spreading the blend, revising territories not appropriately secured, and keeping the blend off of solid upgrades, for example, drains [2].

2 Manufacturers of Microsurfacing Machine

2.1 Bergkamp Incorporated

Bergkamp Incorporated has been a specialist in asphalt upkeep gear for over 40 years, and works with clients all through the globe. The organization’s prosperity keeps on developing through hands-on information on the business and its items, and the organization’s commitment to client care.

The company is the main maker in the business to deliver a full-size constant slurry seal and miniature surfacing paver. Bergkamp Bituminous Solutions is hotspot for a full scope of black-top emulsion factories and plants. Situated in the USA and has experience of more than 40 years [3].

2.2 Metong

The compost seal/microcoating machine from the METONG brand was recently developed in 2006 by the METONG Company. Unlike the comparative model in domestic advertising, the METONG LMT5310TXF becomes increasingly practical, reliable and robust performance, maintenance and common sense through the use of imported high-caliber and domestic sectors with high cost. Smaller surfaces are good answer for roads that are in the early stage of decay. A mixture of aggregate asphalt, water and fibre is applied to the existing asphalt in a top coat. Small-scale coating offers several advantages: incremental slip resistance, shade contrast, surface restoration and management life for fast, heavy roads. METONG’s richness is based on quality, imaginative design and first-class customer care [4].

3 Microsurfacing Machine of Various Company

3.1 Bergkamp M Series

M Series of slurry seal and miniature surfacing hardware has gained notoriety for conveying top notch black-top asphalt remerging of thruways, streets, parking

garages and other asphalt surfaces. Bergkamp has produced intense, solid and excellent asphalt upkeep gear that joins the most recent in innovation with the effectiveness that contractual workers need to convey incredible outcomes at a sensible expense.

Working intimately with clients, Bergkamp has put resources into innovative work to constantly improve the quality and dependability of its items while minimizing expenses to give prevalent worth.

The organization 100% of endeavours into assembling quality gear and working with their clients. Each bit of gear is sponsored by experienced specialized help, broad parts supplies and start-up administrations—including alignment and upkeep preparing, exhaustive parts and administrator manuals, and continuous security and administrator preparing. The company adopt an alternate strategy to help kick off the business. They ordinarily go to the places of work and train the entire group [3].

3.1.1 Continuous Pavers—Series M1

The M1 and M1E are the main full-size ceaseless pavers made on the planet. These self-impelled slurry seal and miniature surfacing pavers advance productivity and diminish the quantity of development links, making a plane driving surface. They get a consistent gracefully of material from committed portable help units while moving—making it ideal for all positions, incorporating those with severe quality necessities (Fig. 1).

Upgrade quality by diminishing development joints and expanding tons-per-hour cleared with oneself impelled, the company’s Series M1 (incorporates the M1 and



Fig. 1 M1 series continuous paver [5]

M1E) constant slurry seal and miniature surfacing pavers. With the assistance of Mobile Support Units—which bring water and black-top emulsion to the paver—the Series M1 pavers ceaselessly manufacture and spot the black-top blend to expand clearing rates and asphalt quality.

The Series M1 is explicitly intended for simplicity of support; all key segments are effectively open, water, the black-top emulsion and added substance tanks can undoubtedly be taken out. The front powerfully flexible pivot raises and brings down each unit for simplicity of stacking, better mobility and more noteworthy admittance to upkeep focuses.

The M1E has taken the demonstrated abilities of the M1 and outfitted it with its inventive Electronic Mix Control and Diagnostic System. All significant segment grips, chains and sprockets on the standard M1 have been supplanted with direct-drive hydrodynamics to work with Electronic Mix Control and Diagnostic System, decreasing the quantity of wear parts furthermore, support focuses on the machine [5].

3.1.2 Truck and Trailer-Mounted Pavers—Series M2

The Series M2 offers exceptional highlights not found on other slurry seal and miniature surfacing pavers. Accessible in truck- and trailer-mounted variants, these demonstrated units are most appropriate for state streets and private and gatherer roads. The most mainstream model, the M210 is the most effortless pavers in the business to utilize and keep up—furnishing fulfilled clients with overall effective street upkeep for quite a long time (Fig. 2).

The Series M2 comprises of various models to fit the necessities of all slurry seal and miniature surfacing clearing clients. The company has a machine like: the M206 that has a shorter wheelbase and gives greater mobility, to the biggest model, the M216 that has an enormous material limit and is ideal for expressway and huge preventive upkeep occupations. It is simple to acknowledge how simple the hardware is to run and keep up, and anticipate its long stretches of dependability (Figs. 3 and 4).

The M2 Series have everything of the highlight's clients require to effectively finish preventive support occupations. These incorporate a distant side shift control that lets the spreader box administrator control the case from the beginning, a pure steel added substance tank. All tanks are dashed in instead of welded, including additional toughness and simple support. The black-top emulsion and water tanks are independent parts, wiping out rust-through and cross-tainting of items.

The bigger M2 Series permit clients to include additional label axles as well as pusher axles to all the more likely oversee lawful burden prerequisites and the Federal Bridge law. The 55-degree edge container dividers limit connecting, and the container's polyethylene lining diminishes grinding. This takes out the requirement for a vibrator, which diminishes issues with free jolts and harm to welds and parts [6] (Table 1).



Fig. 2 M212 truck mounted paver [6]



Fig. 3 M206 truck mounted paver



Fig. 4 M216 truck mounted paver [6]

Table 1 Capacities of series M2

	Aggregate	Asphalt emulsion	Water
M206	4.5 m ³	1,011 L	1,011 L
M210	8.0 m ³	2,271 L	2,271 L
M212	9.2 m ³	2,616 L	2,616 L
M216	12.2 m ³	5,678 L	3,785 L

3.1.3 Truck Mounted Paver M310

The M310, the most exceptional paver, incorporates an electronic control framework that disentangles alignment and permits you to screen and alter creation without any problem. Built-in diagnostics reduce troubleshooting time, while an end-of-day material usage printout helps to manage the business better. Likewise, accessible in M310E, no-side-motor choice [7] (Fig. 5).

3.2 METONG

Metong’s achievement of this creation has originated from high qualified and experienced human asset, imaginative present-day building innovations and which cutting-edge PC helped fabricating offices. Microsurfacing has the advantages of expanding



Fig. 5 M310 truck mounted paver [7]

elusive obstruction, high shading contrast and off kilter the smooth surface rebuilding wraps up. Microsurfacing can be utilized structure minor feeder streets to rapid substantial traffic interstates [8].

3.2.1 LMT5310TXF Microsurfacing Paver

Microsurfacing paver LMT5310TXF is a Metong brand item recently created by METONG partnership in 2009. In contrast to existing comparative items locally, METONG LMT5310TXF is more productive, dependable and has a long life expectancy. The item has high calibre in its tendency as it was made with trend setting innovation and made with high sturdy materials which are imported just as nearby materials.

Microsurfacing is an imaginative answer for fixed streets that are in their beginning phases of crumbling. The blend of aggregate, water, asphalt and added substance are applied in a smooth layer over decayed streets. Slurry seal/Microsurfacing paver effectively fuses building configuration blend, particular necessities and better answer for different field issues [9] (Fig. 6).



Fig. 6 Microsurfacing machine LMT5310TXF [9]

3.2.2 LMT5256TXF Slurry Seal/Microsurfacing Paver Equipment

1. The back significant distance speed control gadget introduced in the slurry seal gear causes the development to go smooth and simple.
2. The emulsified black-top tank and water tank are made of the consumption safe composite materials to draw out their administration life.
3. It is controlled by the water-driven drive framework. The different system controlled autonomously so that there is no fiery aggravation to ensure the steady operation of this system.
4. The twofold shaft ground-breaking instigator tank doesn't permit any dead corners and would clean the dead corners to ensure the blend evenly spread [10] (Fig. 7).

3.2.3 LMT5255TXF Slurry Seal/Microsurfacing Paver Equipment

LMT5255TXF Microsurfacing gear, as the unique hardware for asphalt pavement development, is created by the organization and can be generally utilized in the quick simultaneous splashing work of thruways. The black-top and total can be splashed together or individually. It has some certain highlights including coat sparing, surface wear obstruction, hostile to sliding, water evidence and brisk resumption of ordinary traffic after development. It is appropriate enemy the development of the roadways in various levels (Fig. 8).



Fig. 7 Microsurfacing machine LMT5256TXF [10]



Fig. 8 Microsurfacing machine LMT5255TXF

Table 2 Features of various models

Models	Features
Series M1	<ul style="list-style-type: none"> • Dual-driver stations and itemized tool boards give the potential to drive from either side to make sue straight clearing lines • The slide out element encourages simple cleaning on the grounds that the base bowl remains in the paver and the abundance material drops out of the base. Power through pressure effectively disengages for well-being • Hopper–Steep dividers limit crossing over issues, and sensor behind the container consequently closes down the unit in the event when it runs out of aggregate
Series M2	<ul style="list-style-type: none"> • The gigantic 3-inch gear siphon controls and passes on the dark top emulsion into the pugmill—it mixes with aggregates. The jacketed gear-type emulsion siphon turns on and off with the mix start change to ensure the emulsion isn’t over siphoned and darts to the complete belt to ensure reliable proportioning • Conveniently amassed for basic access and methodology on the full-width stage, the circumstance of the controls allows the executive to adequately watch the spreader box and material being set
M310	<ul style="list-style-type: none"> • EMCAD System gives precise data on the M310’s presentation and incorporates: Current and Average Material Ratios, Absolute Materials Used, Material Rates • Slide-out pugmill improves access and makes clean-up and upkeep simpler, Inline black-top emulsion sifter framework eliminates debasements and helps produce a greater item
LMT5310TXF	<ul style="list-style-type: none"> • It is applied to upgrade the street anti-slipper execution, waterproofness, surface perfection and driving solace. Slurry seal/microsurfacing paver hardware is generally utilized in development workmanship in like manner slurry seal, changed slurry seal and miniature surfaces
LMT5255TXF	<ul style="list-style-type: none"> • The asphalt and total can be showered together or individually. It has some certain highlights including cost sparing, surface wear opposition, against slipping, water evidence and fast resumption of ordinary traffic after development. It is reasonable for the development of the parkways in various levels
LMT5256TXF	<ul style="list-style-type: none"> • It is powered by the hydraulic drive system. The different framework is controlled freely so that there is no vivacious unsettling influence to ensure the steady activity of this framework

4 Key Features Available in Various Models

See (Table 2).

5 Conclusions

In this paper, different types of Microsurfacing Machines has been reviewed like M1 Series Continuous Paver, M212 Truck-Mounted Paver, M206 Truck-Mounted Paver, M216 Truck-Mounted Paver, M310 Truck-Mounted Paver, Microsurfacing

Machine LMT5310TXF, Microsurfacing Machine LMT5256TXF and Microsurfacing Machine LMT5255TXF. The manufacturers of these machines are METONG and Bergkamp Inc. and also there are number of manufacturers which manufacture different microsurfacing machines depending on the various requirement. But in this paper, we took only two manufacturers and their manufactured machines under consideration for review purpose.

Acknowledgements Authors are thankful to G. H. Raisoni College of Engineering Nagpur for giving necessary permission and useful technical support to carry out this work.

References

1. R. Kratika, B.J. Santosh, Comparative analysis of material for material discharge plate of microsurfacing machine, in *2nd International Conference Manufacturing, Material Science & Engineering* (2020). <https://doi.org/10.1016/j.matpr.2020.07.633>. (Materials Today: Proceedings (Elsevier) Journal)
2. M. Zalnezhad, E. Hesami, Effect of steel slag aggregate and bituchem emulsion types on performance of microsurfacing mixture (2019)
3. Bergkamp Inc. Asphalt and pavement maintenance equipment. <https://www.bergkamp.com/>
4. R. Kratika, B.J. Santosh, Performance improvement of microsurfacing machine: a case study, in *1st International Conference on Energy, Materials Science and Mechanical Engineering*. Lecture Notes in Mechanical Engineering (2020)
5. Bergkamp Incorporated. <https://www.bergkampinc.com/products/m1-continous-paver/>
6. Bergkamp Incorporated. <https://www.bergkampinc.com/products/m206/>
7. Bergkamp Incorporated. <https://www.bergkampinc.com/products/m310-new/>
8. Microsurfacing and sealcoating machine, Hangzhou Sansan Metong Machinery Co.Ltd.
9. R. Kratika, B.J. Santosh, Design and analysis of material discharge plate of microsurfacing machine, in *International Conference & Exposition on Mechanical, Material and Manufacturing Technology* (2020). <https://doi.org/10.1016/j.matpr.2020.07.167>. (Materials Today: Proceedings (Elsevier) Journal)
10. <https://m.made-in-china.com/product/Lmt5256txf-Asphalt-Slurry-Seal-Machine-725852385.html>

Shape Memory Alloy as a Smart Material: A Review



Shrutika Dahake, Nilesh Awate, Rupesh Shelke, and Abhay Khalatkar

1 Introduction

Smart material are also called as intelligent materials or advanced materials. For only one specific purpose, it cannot be defined but having a special property to regain their original shape after deformation, and such type of material called as shape memory alloys material [1]. There are two types of smart materials passive and active [2]. passive material having capacity to transfer a energy from one medium to another medium such as optical fibre are capable to carry electromagnetic waves. There are also two types of active materials. First active metal type cannot modify their shape and size when external energy act on it such as photo chromatic glass; when it take in sunlight, colour only modifies. Second active metal type passes energy (mechanical, chemical, thermal, optical and electrical) from one medium to another such as piezoelectric material. Shape memory alloy (SMA) has some native properties, especially regains its original form by increasing or decreasing temperature. In 1938, Mooradian and Greninger observe the shape memory effect for (Cu–Sn). In 1961, Buehler and Wiley invented a Nickel–Titanium alloy called NiTi-NOL [3]. In Nitinol, Ni contains 55 wt% and the rest is Ti [4].

The demand for SMAs has been climb sharply in various fields, such as in biomedical [5], robotics and micro-electromechanical systems(MEMS) [6], aerospace [7], Automotive, structure and composite, industrial applications, consumer product and in fashion also. Based on copper and iron, SMAs like Cu–Al–Ni and Cu–Zn–Al are low cast and commercially available because of their poor thermo-mechanic performance [8], instability, impracticability(e.g. brittleness) [9], NiTi-based SMA shaving more applications.

S. Dahake (✉) · N. Awate · R. Shelke · A. Khalatkar
Department of Mechanical Engineering, G. H. Rasoni Collage
Of Engineering Nagpur, Nagpur, India

2 Properties and Principles

SMA works on the principle of shape memory effect (SME). In SME, previously deformed alloy can be made to recover its original shape simply by heating. When the alloy is stressed and it returns to the original shape without heating then it is called Super Elasticity (SE). Material is in the austenite phase at high temperature and in the martensite phase at low temperature. When a material is cooled, it changes phase from austenite to martensite, but this martensite is in the form of twinned martensite. When a material is loaded, the material gets deformed and its form changes from twinned martensite to de-twinned martensite. The maximum deformation is limited to 8%. When heat is applied, SMA recovers its original form. Martensite is converted back to austenite by heating. The phase transformation from parent phase may be actuate by a stress increase or temperature decrease. In four transition temperatures, SMAs are characterized, i.e. M_f , M_s , A_s and A_f . A refers to Austenitic and M refers to the Martensitic state phase. s and f are reference to the start and finish temperatures of the transformation process, respectively. When temperature is below the final Martensite, then Martensite is stable, when temperature more than final Austenite, then Austenite is stable, when temperature is between starting phase of martensite and austenite. When SMA is heated again and it reaches above (A_s), it begins to regain the original shape. The name austenite and martensite were originally used to refer to phase changes in steels; like an ordinary metallic material, the SMA is permanently deformed when it reaches martensite finish phase [10]. This shape change effect is called SME and pseudo-elasticity, and it can be divided into three SMEs (Fig. 1).

2.1 One-Way Shape Memory Effect (OWSME)

During heating the shape changes, this transformation is called the one-way shape memory effect. OWSME delivers more economical solution. Diverse training method [12], such as spontaneous and load-assisted induction, was proposed.

2.2 Two-Way Shape Memory Effect (TWSME)

SMA's the ability to recover a native shape when heated and then return to an alternative shape when cooled down, Its transformation temperature is called two-way shape memory. Mild heating in two-way systems destroys SME. Two-way SMAs are more dynamic than SMAs used in one-way systems.

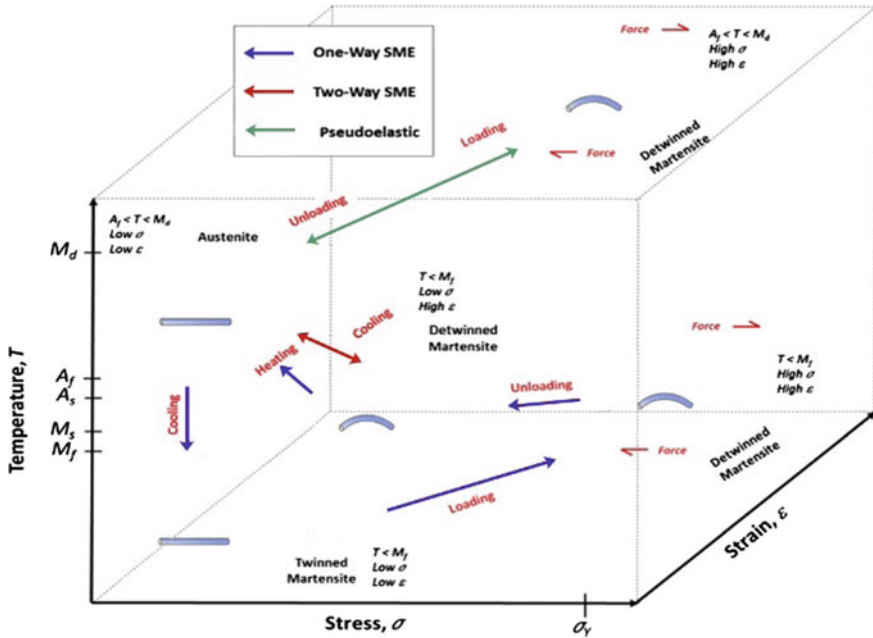


Fig. 1 SMA phases and crystal structures [11]

2.3 Super Thermo-Elastic Effect

The basic behaviour is same as in the case of TWSME: some of the mechanical and physical properties belong between thermal conductivity, Young’s modulus, thermal expansion and electrical resistivity [13]

3 Applications

The SMAs can be categorized into four types as per their basic function.

3.1 Automotive Applications

SMA actuators are an excellent replacement for the electromagnetic actuators in automotive applications [14]. SMA wires decrease the weight, cost and scale of automotive components. Most of the linear actuators (e.g. climate flaps movement, rear-view mirror folding, latch/loch control) and as active thermal actuators (e.g. Engine lubrication, engine temperature control)are occasionally functioning in vehicle[15].

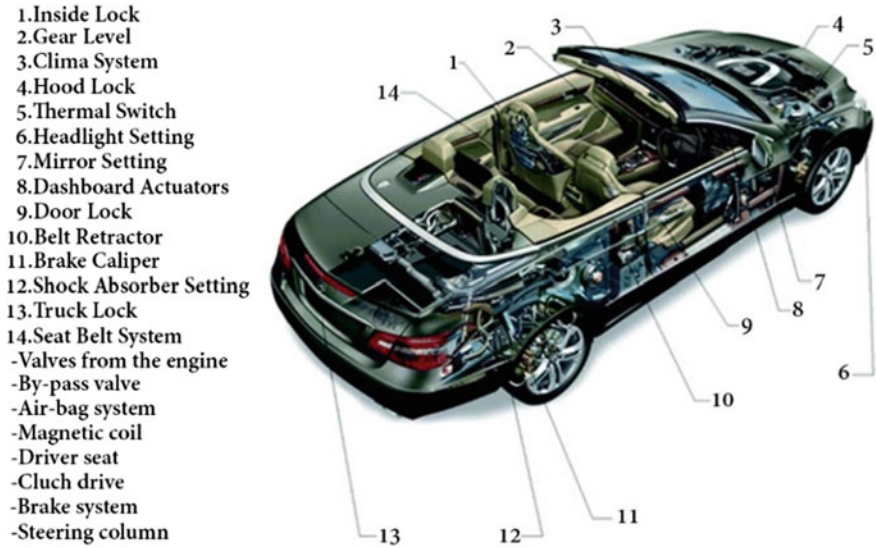


Fig. 2 Applications in car

SMA application in automotive tumble flaps is the replacement of pneumatic effectors and electromagnetic conventional effectors, a side mirror actuators [16] of an object angle and distance with an FSMA actuator [17] (Fig. 2).

3.2 Aerospace Applications

In 1960s, Raychem developed Cryofit connectors for F-14 airplane hydraulic circuit. It is the first industrial SMA applications in aeronautics [3], because of unique properties of SMA having huge application in aerospace such as actuators (15), sealer, release or deployment mechanism, vibration dumper, manipulators and the pathfinder applications and structural connectors [3].

In space craft, SMAs used as low shock release mechanism. Best example is Cryofit. CryoFit in which coupling is made from SMA material. The inner diameter of coupling is kept smaller than the outer diameter of the tubes to be joined at room temperature. At this temperature, it is in the austenite phase. When the coupling is placed in liquid nitrogen, it changes its phase from austenite to martensite. Then its inner diameter is expanded so that it becomes more than the outer diameter of the tubes using tapered steel mandrel. After that, two tubes are joined and when the heat is applied, it shrinks down with high radial force. The coupling has radial teeth formed circumferentially on the inner surface. The teeth enhance the tensile strength of the joint and the seal between the coupling and the tubes,

Fig. 3 Dragfly [21]

Applications of Cryofit are such as tubes used in aircraft, hydraulic lines and fuel lines. When these tubes are broken, they often have to be repaired by people working in confined conditions. In this situation, it is very difficult to use welding and brazing because these processes require bulky equipment. Hence, CryoFit coupling is used, because it releases slowly with minimum vibration. QWKNUT [3] and Frangibolt [18] are some examples of small device which shape memory alloys material.

3.3 *Robotic Applications*

From 1980, SMAs play important role in various applications commercial robotic system, especially in artificial muscles [19]. There are some important technical issues and need to be solved again, e.g. low electrical resistance, small strain output, very low efficiency and control issues. Hence, some issues were solved by control technique and feedback sensors. The Chee Siong et al. introduced a latest SMA actuator design for prosthetic hand [20]. SMA actuators used for movement of the robotic finger are an alternative to conventional pull push and biased spring types. The two actuators having main function are guide and heat sink.

Various flying robots developed with Shape memory alloys, like Bat Robot and BATMAV. Recently Festo Group developed a 44 cm dragonfly with 63 cm wingspan. These robot ‘dragonfly’ also called as ‘Bionic Opter’ [21] (Fig. 3).

3.4 *Biomedical Applications*

Hallux valgus, Orthodontic wire, Endoscopic Guidewire, Biliary Stents, Regional chemotherapy catheter, etc. are some applications in biomedical. In 1975, dental braces of SMAs were first installed in biomedical [22]. And then many more applications are introduced and utilized into the market. SMAs has exquisite unique properties which is used in biomedical applications such as bio-compatible, bones and human tissues, non-magnetic, high corrosion resistance [23]. SMAs medical devices used in various field such as neurology, interventional radiology. Kim et al. invented

Table 1 Applications of shape memory alloys

Name of smart material	Applications	Advantages	Disadvantages
Shape Memory Alloys	<ul style="list-style-type: none"> • Automobile • Robotics • Aerospace • Biomedical • Clothing and fashion industries • 4D 	<ul style="list-style-type: none"> • High strength • High damping capacities • Corrosion resistant • High fatigue failure life 	<ul style="list-style-type: none"> • Temperature sensitive • Complicated design and high weight • High cycle fatigue

a micro-muscle fibre from SMAs coiled springs, using many of SMAs properties (flexibility, scalability etc.) which provide body deformation and locomotion. Stirling et al. also did similar work [24] to create a soft orthotic for the knee.

In the last few decades, various experiments were conducted with SMAs and known SMAs will discover more applications in the future [25] (Table 1).

4 Conclusion

This review paper discusses the SMA applications, also known as Nitinol, as a smart material having wide applications in different domains like automobile, aerodynamic and biomedical engineering. SMAs designed in the form of wire work on the principle of the Shape Memory Effect (SME). When SMA material is loaded, it gets deformed and, when it is heated, it regains its original parent shape. Here, we studied SMAs need, advantages, future technology, some unique properties and applications. Due to its unique applications, it is also called intelligent material, Nitinol. There is a huge scope for researchers for self-growth by learning and developing new applications in SMAs.

References

1. R. Bogue, Smart materials: a review of capabilities and applications. *Assem. Autom.* **34**(1), 16–22 (2014). <https://doi.org/10.1108/AA-10-2013-094>
2. M. KÖK, İ.N. Qader, F. Dağdelen, Y. AYDOĞDU, Akıllı Malzemeler üzerine derleme: araştırmalar ve uygulamaları. *El-Cezeri Fen ve Mühendislik Derg.*, no. September, 2019. <https://doi.org/10.31202/ecjse.562177>
3. A.G. Shivasiddaramaiah, U.S. Mallik, R. Mahato, C. Shashishekar, L. Shivaramu, S. Prashantha, Evaluation of biocompatibility of Cu-Al-Be-Mn quaternary shape memory alloys using antibacterial test by agarwell diffusion method. *Mater. Today Proc.* **17**, 61–69 (2019). <https://doi.org/10.1016/j.matpr.2019.06.401>
4. E. Farber, J.-N. Zhu, A. Popovich, V. Popovich, A review of NiTi shape memory alloy as a smart material produced by additive manufacturing. *Mater. Today Proc.* **30**(xxxx), 761–767 (2020). <https://doi.org/10.1016/j.matpr.2020.01.563>

5. J. Van Humbeeck, Non-medical applications of shape memory alloys. *Mater. Sci. Eng. A* **273–275**, 134–148 (1999)
6. L. Sun et al., Stimulus-responsive shape memory materials: a review. *Mater. Des.* **33**(1), 577–640 (2012). <https://doi.org/10.1016/j.matdes.2011.04.065>
7. C. Bil, K. Massey, E.J. Abdullah, Wing morphing control with shape memory alloy actuators. *J. Intell. Mater. Syst. Struct.* **24**(7), 879–898 (2013). <https://doi.org/10.1177/1045389X12471866>
8. W. Huang, On the selection of shape memory alloys for actuators. *Mater. Des.* **23**(1), 11–19 (2002). [https://doi.org/10.1016/s0261-3069\(01\)00039-5](https://doi.org/10.1016/s0261-3069(01)00039-5)
9. J. Cederström, J. Van Humbeeck, J. Cederström, J.V.H. Relationship, B.Shape, M. Material, Properties and applications to cite this version: HAL Id: jpa-00253636 (1995)
10. T.W. Duerig, A.R. Pelton, Ti-Ni shape memory alloys. *Mater. Prop. Handb. Titan. Alloy.* **683**, 1035–1048 (1994)
11. I. Mihálcz, Fundamental characteristics and design method for nickel-titanium shape memory alloy. *Period. Polytech. Mech. Eng.* **45**(1), 75–86 (2001)
12. S. Miyazaki, My experience with Ti–Ni-based and Ti-based shape memory alloys. *Shape Mem. Superelasticity* **3**(4), 279–314 (2017). <https://doi.org/10.1007/s40830-017-0122-3>
13. J. Mohd Jani, M. Leary, A. Subic, M.A. Gibson, A review of shape memory alloy research, applications and opportunities. *Mater. Des.* **56**(April), 1078–1113 (2014). <https://doi.org/10.1016/j.matdes.2013.11.084>
14. S. Gopinath, S. Mathew, P.R. Nair, Shape memory actuators, *Actuators*, no. March (2020) pp 139–158. <https://doi.org/10.1002/9781119662693.ch6>
15. D. Stoeckel, S Im ## A I. *Mater. Des.* **11**(6), 302–307 (1991)
16. E.A. Williams, G. Shaw, M. Elahinia, Control of an automotive shape memory alloy mirror actuator. *Mechatronics* **20**(5), 527–534 (2010). <https://doi.org/10.1016/j.mechatronics.2010.04.002>
17. A. Sellitto, A. Riccio, Overview and future advanced engineering applications for morphing surfaces by shape memory alloy materials. *Materials (Basel)*, **12**(5) (2019). <https://doi.org/10.3390/ma12050708>.
18. A.D. Johnson, Non-explosive separation device, **100**(362), 625, 1992. <https://patentimages.storage.googleapis.com/08/4b/25/b2e425eeeca67/US5119555.pdf>
19. C. Naresh, P.S.C. Bose, C.S.P. Rao, Shape memory alloys: a state of art review, in *IOP Conference Series: Materials Science and Engineering*, vol. 149, no. 1 (2016). <https://doi.org/10.1088/1757-899X/149/1/012054>
20. C.S. Loh, H. Yukoi, T. Arai, New shape memory alloy actuator: Design and application in the prosthetic hand, in *Annual International Conference of the IEEE Engineering in Medicine and Biology–Proceedings*, vol. 7, no. 16360118, pp. 6900–6903 (2005). <https://doi.org/10.1109/iembs.2005.1616092>
21. J.F.B and K. Althoefer, Soft pneumatic prosthetic hand jan. *Toward. Auton. Robot. Syst.*, **8069**, 15–27 (2014). <https://doi.org/10.1007/978-3-662-43645-5>
22. D. Mantovani, Shape memory alloys: properties and biomedical applications. *Jom* **52**(10), 36–44 (2000). <https://doi.org/10.1007/s11837-000-0082-4>
23. *Ocean Engng*, vol. 1, pp. 105–120. Pergamon Press 1968. Printed in Great Britain, *Ocean Eng.*, vol. 1, pp. 105–120 (1968)
24. L. Stirling et al., Applicability of shape memory alloy wire for an active, soft orthotic. *J. Mater. Eng. Perform.* **20**(4–5), 658–662 (2011). <https://doi.org/10.1007/s11665-011-9858-7>
25. A.R. Pelton, V. Schroeder, M.R. Mitchell, X.Y. Gong, M. Barney, S.W. Robertson, Fatigue and durability of Nitinol stents. *J. Mech. Behav. Biomed. Mater.* **1**(2), 153–164 (2008). <https://doi.org/10.1016/j.jmbbm.2007.08.001>

Influence of Room Temperature Rolling Process on Mechanical and Corrosion Behaviors of Al 6061alloy



Alok Singh Verma and Anuj Jain

1 Introduction

With increasing the complex and demanding applications, modern world requires stronger and higher corrosion resistant materials. There is a need to improve the properties of an existing material by changing their grain size, dislocation density, etc., by suitable processing. It has been reported that multipass rolling process is the process by which ultrafine grain metals and alloys can be obtained with improved mechanical properties [1–5] as well as corrosion behavior [6, 7]. The processed materials with the severe deformation like multipass rolling process directly relate to weight saving in the structural frames and hardware component such as gearing, pedals, shifters, rims, etc. In SPD, misorientations and formation of high-angle boundaries occur due to large deformation. The processed material has average grain size of less than 1 μm [8]. After severe deformation, strength of material improved it can be seen by Hall–Petch equation [9].

$$\sigma_y = \sigma_0 + \frac{K}{\sqrt{d}} \quad (1)$$

where σ_y is the yield strength;

σ_0 is a materials constant for the starting stress for dislocation movement;

K is the strengthening coefficient; and.

d is the average grain diameter.

Aluminum and its alloys find its wider application because of its high strength to weight ratio as compared to the ferrous alloy in weight-sensitive products such as marine, aircraft, bicycles, boats, and automobiles, etc. It also offers good corrosion

A. S. Verma (✉) · A. Jain

Department of Ceramic Engg, IIT(BHU), Varanasi, Uttar Pradesh, India

e-mail: aloksv.rs.cer15@itbhu.ac.in

resistance because of formation of fine passivity film of Al_2O_3 (Aluminum Oxide) [10–12]. Al6061 being highly ductile, this may be processed through suitable severe deformation techniques to improve its properties further. In the present study, attempt is made to study the change in mechanical and corrosion behaviors of Aluminum alloy, Al6061, after multiple pass room temperature rolling (RTR).

Lee et al. [13] reported that after eight cycles of accumulated roll bonding tensile strength becomes 363 MPa which is three times to initial. In general, T6 treatment tensile strength becomes 310 MPa with elongation 17%, where in this study, without heat-treated strength becomes more but elongation reduces 5%. After ARB process, specimens show the inhomogeneous distribution in hardness through the thickness, having peak values near the surfaces, and the center. Kitahara et al. [14] reported that Ti sheet, which is rolled up to 50% of initial thickness and equivalent strain of 4.8, shows the enhancement in tensile strength with an increase in strain. Rika et al. [15] reported that ARB-processed sheet has tensile strength of 783 MPa, ARB processed and annealed at 500 °C for 0.5 h flow stress increased rapidly but strength lower than 600 °C for 0.5 h, 850 °C for 20 h tensile strength of 408 MPa which is half of the 600 °C for 0.5 h. Strength decreases and elongation increases with the increasing annealing temperature. Wei et al. [16] reported that, after deformation of Al–Mn alloy sheet (annealed at 573 K for 1 h) by ARB methods at room temperature up to 50% reduction, grains are bounded by clear but uneven-shaped boundaries, and the number of dislocations at the area of boundaries seems large, in dissimilarity, nearly free inside some smaller grains. Raducanu et al. [17] reported that, after deformation of Ti–Zr–Ta–Nb alloy by ARB up to 85% reduction, passivation is easier and passive current density is lower which indicates more stable passive state and polarization resistance R_p is also higher. It has been found that the severe deformation process converts coarse grain material into ultrafine grain material. All the materials which are severely deformed have improved tensile strength and hardness at expense of ductility. With the help of annealing, process ductility can be improved with a slight decrement of the strength of the material. In this paper, mechanical behavior like tensile strength, hardness, and percentage elongation of room temperature rolled 6061-Al alloy have been investigated. Also corrosion behavior of the 6061-Al alloy, after rolling with different reduction passes, has been investigated.

2 Experimental Detail

Aluminum 6061 Alloy is deformed through the rolling process at room temperature for 20%, 40%, 60%, and 80% thickness reduction. For all types of thickness, reduction sample hardness, tensile, and corrosion test are done. Hardness test is done to investigate the surface property and tensile test is done to evaluate the strength and percentage elongation of the material. Corrosion test is performed to investigate the corrosion behavior of the rolled material and compared with bulk material. For corrosion test, the immersion tests are performed by weight loss method.

2.1 Mechanical Testing

For the tensile test sample preparation is done according to ASTM code E8. According to ASTM code E8, prepare 5 sample of dimension $(200 \times 20 \times t)$ mm, where t is the thickness of the specimen which is different for different reduction passes in room temperature rolling. The samples were loaded on a UTM (make: Tinius Olsen) testing machine.

Elongation of the material measure by stress vs strain curve. If the strength of the material increases, elongation (ductility) decreases. It can be measured by the formula given below [18]:

$$\% \text{elongation} = \frac{\text{change in gauge length}}{\text{gauge length}} \times 100 \quad (2)$$

In the present study, the gauge length is 50 mm as per E8 ASTM format.

Basically, the area under the stress–strain curve gives toughness of the material. In this thesis, toughness is measured by area under the curve method [18].

$$\text{energy per vol} = \int_0^{\varepsilon_f} \sigma d\varepsilon \quad (3)$$

where ε_f is a strain upon failure, ε is the strain, and σ is stress.

For calculating the hardness, Brinell Hardness (BHN) Testing Machine is used. BHN is calculated for all the samples as received, 20% RTR, 40% RTR, 60% RTR, and 80% RTR having dimension $10 \times 10 \times t$ mm, where t is the thickness after different thickness reduction passes of rolling.

$$\text{BHN} = \frac{2P}{\pi D[D - \sqrt{D^2 - d^2}]} \quad (4)$$

where P is the applied load, D is the diameter of ball, and d is the diameter of indentation.

2.2 Corrosion Test

After room temperature rolling with different reduction passes, corrosion testing is done. For this testing, immersion test is done by weight loss method. In this test, samples having dimension $(10 \times 10 \times t)$ mm, where t is the thickness of the sample, which is different for different rolling passes listed above in Table no.2, are immersed in 3.5% NaCl solution of pH 7.5 for 96 h. The weight loss measurements are done in the interval of 12 h. The sample after stipulated hours (12 h) up to 96 h of the exposure to the corrosion medium are taken out, gently rubbed with papers to remove

the corrosion product, washed with distilled water and acetone, and then air-dried. The weight of the corroded sample is the determined weight loss which is calculated to find the corrosion penetration rate (CPR) [19] given by Eq. 5.

$$\text{CPR} = \frac{KW}{\rho At} \quad (5)$$

where W is the weight loss after exposure time t , ρ is the density, A is exposure area, and K is a constant depending on a system of the unit used. The CPR is conveniently expressed in terms of either mils per year (mpy) or millimeters per year (mm/yr.). In the first case, K is 534 for measuring the CPR in mpy (where 1 mil = 0.001 inch), and W , s , A , and t are specified in units of milligram, gram per cubic centimeter, square inches, and hours, respectively. For second case, K is 87.6 for calculating CPR in mm/yr, and units for other parameters are same as for mils/yr, except that A is given in square centimeter.

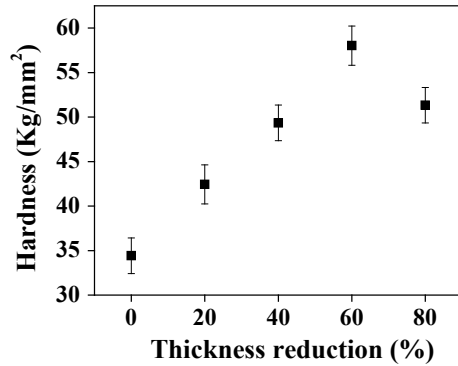
3 Result and Discussion

In this section, mechanical properties like tensile strength, percentage elongation, toughness, and hardness and corrosion properties are investigated for the specimens having different thickness reduction passes. Specimens with different thickness reductions show different and improved properties. Hardness test is done using Brinell Hardness Testing Machine. Hardness is measured in terms of hardness number which is given in unit kg/mm^2 . There are five types of samples having different thicknesses due to different rolling reduction passes at room temperature.

Al 6061 shows appreciable increment in the hardness of material due to the room temperature rolling. As rolling passes increase, the dislocation density of the material increases due to which more and more grain boundaries are formed and surface resistance for indentation and scratches increases. So, as the rolling passes increase, hardness increases. But if the thickness of the material decreases below threshold limit after rolling passes, then hardness of the material decreases. Hardness of Al 6061 alloy specimens having variable thicknesses as received, 20% reduction, 40% reduction, 60% reduction, and 80% reduction in thickness 34 kg/mm^2 , 42 kg/mm^2 , 49 kg/mm^2 , 58 kg/mm^2 and 51 kg/mm^2 are achieved, respectively, as shown in Fig. 1. This indicates that reduction in thickness during rolling increases the hardness of the material. This occurs due to the absorption of energy during cold-forming which increases the residual internal stress of the material. Moreover, there is an increase in dislocation density and refinement of grain, which generate more grain boundaries throughout the material that increases the hardness. Rolling is a forming process which increases the mechanical strength of the material.

As the rolling passes increases, accumulation of strain in the material also increases. Due to an accumulation of strain, dislocation density increases so the

Fig. 1 The variation of hardness values with the reduction of thickness



ultimate strength of the material Al 6061 alloy increases as rolling thickness reduction passes increase. Figure 2 shows the variation of the strength with respect to the rolling condition. The maximum tensile strength (432 MPa) is achieved after 80% RTR and 54 minimum (316 MPa) for as-received samples. And according to literature survey, strength is directly proportional to grain refinement. As strain hardening increases in the material, grain refinement occur.

After rolling passes, grains are divided into the fine grain and ultrafine grain. In the experiment, it has been seen that strength for the as-received material is 316 MPa, for 20% RTR is 355 MPa, for 40% RTR is 373 MPa for 60% RTR is 404 MPa, and for 80% RTR it is 432 MPa. That means there is an appreciable increment in the strength after multiple rolling passes. Due to brittleness, the ductility of the material and percentage elongation go down as shown in Fig. 3. The strength of the material increases after multiple RTR passes but ductility decreases, so toughness goes down. Toughness is reported as the area under the stress–strain curve.

Figure 4 shows that toughness of the material goes down as rolling thickness reduction passes increase. For as-received material, toughness is 2001 MPa, for 20% RTR, 1668 MPa, for 40% RTR, 1077 MPa, for 60%, 1157 MPa, and for 80% RTR, 1188 MPa obtained. Up to 40% RTR toughness decreases continuously because

Fig. 2 The variation of tensile strength values with the reduction of thickness

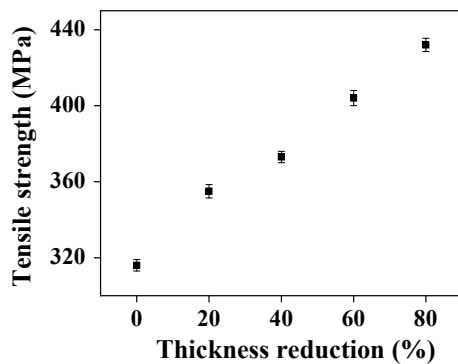


Fig. 3 The variation of elongation (ductility) with the reduction of thickness

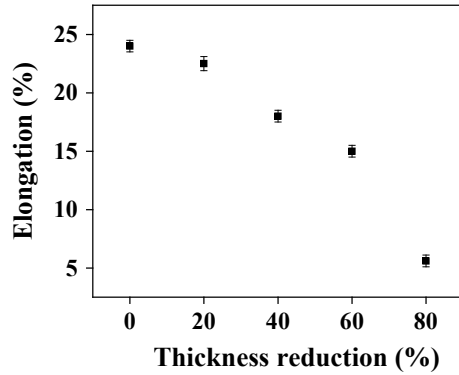
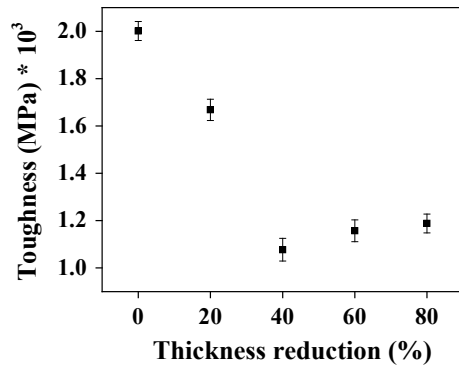


Fig. 4 The variation of toughness values with the reduction of thickness



ductility decreases. Beyond that (for 60% and 80% RTR), slightly increment in toughness is achieved due to strain hardening.

For corrosion testing, immersion test by weight loss method is done. In this test, specimens of size $10 \times 10 \times t$, where t is the thickness of the material after multiple passes, are immersed in 3.5% NaCl solution of pH 7.5 for 96 h and the weight loss in the interval of 12 h obtained. Figure 5 (a) shows the comparative study of different kinds of samples which are used for the immersion test for finding the corrosion property. The individual color shows the nature of the individual type of sample. Red bullet shows 60% RTR, black rectangle shows 80% RTR, the blue triangle shows 40% RTR, green rectangle shows as-received, and purple triangle shows 20% RTR conditioned sample. The figure shows that the CPR values are decreased for every sample. After 96 h of the experiment, the red graph (60% RTR) shows the maximum CPR 7.27mpy and blue graph (40% RTR) shows minimum CPR 0.472 mpy. It means the best corrosion property is achieved in 40% RTR material.

Initially, the CPR value for every kind of samples are decreased, but as the time of exposure increases, CPR value fluctuated as shown in Fig. 5b. After 96 h, it has been seen that when rolling reduction passes increases up to 40% RTR corrosion property improved. After that (for 60% and 80% RTR), corrosion property diminished. Grain

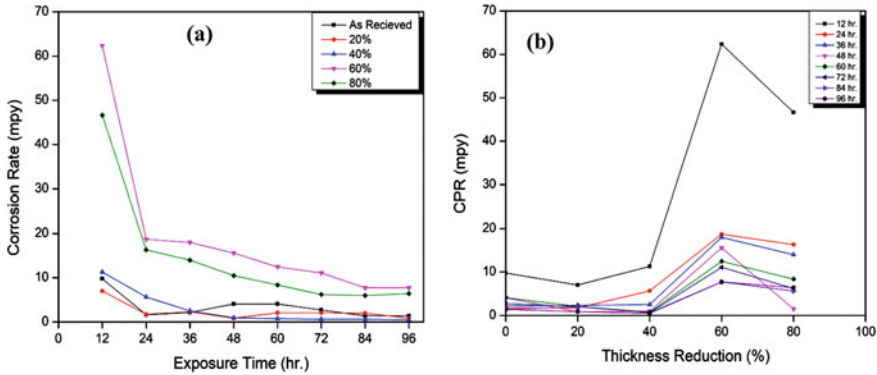


Fig. 5 **a** The variation of corrosion rate with exposure time, **b** CPR variation with multiple thickness reduction

refinement may provide more sites to initiate corrosion which enhanced corrosion rate and consequently decreased corrosion resistance. Because as the reduction passes increase, more surfaces are susceptible to corrosion.

4 Conclusion

Based on the experiments performed in this work, it can be concluded that the Al 6061 alloy exhibits a great cold-forming capacity. The hardness and strength of the samples increased with increasing the rolling reduction passes which are possibly due to the strain hardening and increased dislocation density after the mechanical forming process. The experiments for corrosion test are performed in 3.5% NaCl solution which showed that corrosion resistance increases up to 40% RTR, beyond that (for 60% and 80% RTR) corrosion resistance decreases. Previous works reported in the literature [20] point that grain refinement leads to a high density of grain boundaries which have higher energy than the bulk of the grain. This enhances electron diffusion and leads to a more stable passive film and therefore to an enhanced corrosion resistance. A contradiction grain refinement may provide more sites to initiate corrosion which enhanced corrosion rate and consequently decreased corrosion resistance. Whether grain refinement is detrimental or not, corrosion resistance could be related to the material nature and environment [21]. It is clear from present results that the grain refinement of the rolled Al alloy to some extent was accompanied by increased susceptibility to corrosion. It is well established that internal stresses, especially related to high dislocation accumulation generated by room temperature rolling, may or may not result in the improvement of the corrosion resistance depending on the material [13]. As per experiment following, results are concluded:

- As the rolling passes increase, the strength of the material also increases. Initially, for as-received material, strength is 316 MPa. After that, for 20% RTR, 40% RTR, 60% RTR, and 80% RTR, 12.34%, 18.04%, 27.85%, and 36.71% increment in the strength are achieved, respectively.
- As the rolling passes increase, brittleness of the material also increases because of the accumulation of dislocation density. So elongation goes down. For as-received material, the elongation is 24%. After that, for 20% RTR, 40% RTR, 60% RTR and 80% RTR, 6.25%, 25%, 37.5%, and 76.6% decrement in elongation are obtained, respectively.
- As rolling passes increase, strength increases at the expense of ductility. So toughness is decreased. For as-received material, toughness of 2001 MPa is obtained. For 20% RTR, 40% RTR, 60% RTR, and 80% RTR, 16%, 46.17%, 42.2%, and 40.6% decrement in toughness is obtained, respectively. This is due to strain hardening and accumulation of dislocation density.
- The hardness of the as-received material is 34.42 kg/mm². As rolling passes increase, the hardness of the material also increases. For 20% RTR, 40% RTR, 60% RTR, and 80% RTR, 23%, 43.37%, 68.58%, and 49.13% increment in hardness values are achieved, respectively.
- Corrosion rate in terms of CPR of as-received material after 96 h is 1.395 mpy. As rolling passes increase, (up to 40% RTR) corrosion rate decreases. After that, (for 60% and 80% RTR) corrosion rate increases. For 20% RTR, 40% RTR, 60% RTR, and 80% RTR, the CPR values 0.87 mpy, 0.47 mpy, 7.27 mpy, and 6.41 mpy are achieved.

Since rolling strength and hardness improved, this can be used where high strength equipment requires the missile. As rolling corrosion property also improved in the jet application, marine application, etc., these rolled material can be used.

Acknowledgements The authors gratefully acknowledge for the financial support of MNNIT Allahabad, IIT (BHU) and MHRD, New Delhi, India.



References

1. L. Zaharia, R. Comaneci, R. Chelariu, D. Luca, A new severe plastic deformation method by repetitive extrusion and upsetting. *Mater. Sci. Eng. A* **595**, 135–142 (2014)
2. M.W. richert, J. Richert, A. Hotloś, M. Mroczkowski, T. Tokarski, The effect of reciprocating extrusion (CEC) on the consolidated silver powders microstructure archives of metallurgy and materials, **58**, 73–75 (2013)
3. V.M. Segal, Equal channel angular extrusion: from macromechanics to structure formation. *Mater. Sci. Eng. A* **271**, 322–333 (1999)
4. A. Azushima, R. Kopp, A. Korhonen, D.Y. Yang, F. Micari, G.D. Lahoti, P. Groche, J. Yanagimoto, N. Tsuji, A. Rosochowski, A. Yanagida, Severe plastic deformation (SPD) processes for metals. *CIRP Ann. Manuf. Technol.* **57**, 716–735 (2008)
5. Y.T. Zhu, D.J. Alexander, X. Liao, T.C. Lowe, R.J. Asaro, Development of repetitive corrugation and straightening. *Mater. Sci. Eng. A* **371**, 35–39 (2004)

6. L.S. Toth, C. Gu, Ultrafine-grain metals by severe plastic deformation. *Mater. Charact.* **92**, 1–14 (2014)
7. J.R. Davis, *Corrosion Understanding the Basics*, ed. by Davis & Associate (2000) p. 517
8. L. Collini, Fatigue crack growth in ECAPed commercially pure UFG copper. *Procedia Eng.* **2**, 2065–2074 (2010)
9. M. Alizadeh, E. Salahinejad, A comparative study on metal–matrix composites fabricated by conventional and cross accumulative roll-bonding processes. *J. Alloy. Compd.* **620**, 180–184 (2015)
10. I. Sabirov, M.Y. Murashkin, R.Z. Valiev, Nanostructured aluminium alloys produced by severe plastic deformation: New horizons in development. *Mater. Sci. Eng. A* **560**, 1–24 (2013)
11. B. Horst (ed.), *Advanced Aerospace Materials* (Springer, Berlin, 2012)
12. F.A. Ovat, F.O. David, A.J. Anyandi, Corrosion behaviour of Al (6063) Alloy (As Cast and Age Hardened) in H₂SO₄ solution. *J. Mat. Sci. Res.* **1**, 35–40 (2012)
13. L. Li, T. Ungar, Y.D. Wang, Simultaneous reductions of dislocation and twin densities with grain growth during cold rolling in a Nano crystalline Ni–Fe alloy. *Scripta Mater.* **60**, 317–320 (2009)
14. H. Kitahara, K. Uchikado, J. Makino, N. Iida, M. Tsushida, N. Tsuji, S. Ando, H. Tonda, Fatigue crack propagation behavior in commercial purity Ti severely deformed by accumulative roll bonding process. *Mater. Trans.* **49**, 64–68 (2008)
15. R. Yoda, Formability of ultrafine-grained interstitial-free steel fabricated by accumulative roll bonding and subsequent annealing. *Scripta Materialia*, **65**, 175–178 (2011).
16. W. Wei, Corrosion and tensile behavior s of ultra- fine grained Al -Mn alloy produced by accumulative roll bonding. *Mater. Sci. Eng., A* **454–455**, 536–541 (2007)
17. D.Raducanu, E. Vasilescu, V.D. Cojocaru, I. Cinca, P. Drob, C. Vasilescu, S.I. Drob, Mechanical and corrosion resistance of a new nanostructured Ti–Zr–Ta–Nb alloy. *J. Mech. Behav. Biomed. Mat.* **4**(7), 1421–1430 (2011)
18. I. Faridmehr, M.H. Osman, A.B. Adnan, A.F. Nejad, R. Hodjati, M. Azimi, Correlation between engineering stress-strain and true stress-strain curve. *Am. J. Civil Eng. Archit.* **2**, 53–59 (2014)
19. K.O. Oparaodu, G.C. Okpokwasili, Comparison of percentage weight loss and corrosion rate trends in different metal coupons from two soil environments. *Int. J. Environ. Bioremediat. Biodegrad.* **2**, 243–249 (2014)
20. J.W. Schultze, B. Davepon, F. Karman, C. Rosenkranz, A. Schreiber, O. Voigt, Corrosion and passivation in nanoscopic and microscopic dimensions: the influence of grains and grain boundaries. *Corros. Eng. Sci. Technol.* **39**, 45–52 (2004)
21. A. Rebhi, T. Makhlof, N. Njah, Y. Champion, J. Couzinie, Characterization of aluminium processed by equal channel angular extrusion: effect of processing route. *Mater. Charact.* **60**, 1489–1495 (2009)

Enhancement of Activated Flux Tungsten Inert Gas Welding Using SiO₂ Flux for Joining 304L Stainless Steel Sheets



Dattatray Chopade , Prashant Lugade, Nitish Sinha , Avinash Panchal, and Shivji Kumar

1 Introduction

Gas Tungsten Arc Welding (GTAW), also known as TIG welding, uses an arc between a non-consumable tungsten electrode and workpiece to be welded under a shielding gas. High level of weld quality combined with considerable precision is the characteristic of this process. Hard-to-weld metals such as titanium, aluminum, stainless steel, and magnesium are commonly welded by this method. Less weld penetration limits the thickness of the sheets that are joined using TIG.

A lot of research has been conducted on A-TIG process on morphology of the weld, hardness, δ ferrite content, and angular distortion [1, 2]. MnO₂, TiO₂, MnO₃, SiO₂, and Al₂O₃ are some of the most commonly used oxide fluxes for A-TIG welding. It was observed that A-TIG increases joint penetration and weld depth to width ratio. The reason behind this increased penetration is the Marangoni effect of thermo-capillary convection [1]. Mixture of the fluxes in proper percentage is also found to be very effective in A-TIG [2]. An attempt to make oxide flux with different composition is also carried out. Good spreading ability is observed in flux powders comprising oxide, sulfide, and fluoride mixed with methanol or ethanol [3]. Instruments, like an optical microscope, are used to measure the weld bead shape parameters like depth of penetration bead width and reinforcement height [4]. Some researchers even carried out finite element simulation of the welding process using software like SYSWELD [5]. A 2D axial symmetric model can also be used to simulate the flow behavior in the melting pool [6]. Microparticle oxides of oxides like SiO₂ and Al₂O₃ are also used as fluxes [7]. Use of different fluxes are found

D. Chopade (✉) · N. Sinha · A. Panchal · S. Kumar
Department of Mechanical Engineering, G. H. Raisoni Institute of Business Management, Jalgaon
425002, India

P. Lugade
Senior Design Engineer, Tata Technologies Limited, Pune, India

to give different weld penetrations and weld hardnesses [1, 7–9]. SiO_2 flux is found to be more effective flux as compared to other oxide fluxes [1, 7]. Joining of two dissimilar metals using A-TIG process is also carried out and found to weld the two metals better than normal TIG welding process [10]. Newer methods like advanced active flux tungsten inert gas (AA-TIG) welding technique, also called cap active flux tungsten inert gas (CA-TIG) welding uses atmospheric oxygen and is found to increase the depth of penetration of the weld multiple times [11].

In this study, an attempt is being made to use SiO_2 as flux for TIG welding of 304 L steel plates using different combinations of process parameters, viz. electrode gap, welding speed, welding current, and gas flow rate. Taguchi statistical design of experiment is used to decide the combination of process parameters. Most influential factors are found out affecting the A-TIG process. Subsequently, tensile tests, microhardness tests, and metallographic tests are performed.

2 Experimental Details

2.1 Specimen Preparation for Welding

The base metal used in present investigation is AISI 304L stainless steel. The plates of this material are cut into 18 specimens of size $300 \times 60 \times 6$ mm (length \times width \times thickness). For rough polishing of the specimen surfaces, 400 grit silicon carbide abrasive paper is used. They are then cleaned by acetone to remove oil, dust, scale, rust, moisture, etc.

Silicon dioxide (SiO_2) flux powder gives better results for tensile strength and weld depth penetration over other fluxes like TiO_2 . SiO_2 flux powder (105–420 microns) along with acetone (pure acetone for laboratory purpose) as suspension medium is used to make uniform mixture of flux. A thin uniform layer of this flux mixture was applied on to the joint of plates before welding. The coating density of the flux was about 5–6 mg/cm² and approximately 0.2 mm thick and 10 mm wide.

2.2 Taguchi Method

Electrode gap, welding speed, welding current, and gas flow rate are the most influential parameters for TIG welding and hence these are selected as the process parameters for this study. Three levels of their values are considered and are tabulated in Table 1. L9 orthogonal array is selected for designing the experiment and the corresponding level value are stated in Table 2.

The process variables of the TIG welding process are stated in Table 3. An autogenous TIG welding was conducted to join two plates along their width to produce butt

Table 1 Levels of process parameters

Parameters	Electrode gap (mm)	Welding speed (mm/min)	Welding current (A)	Gas flow rate (lit/min)
Level 1	1	100	140	7
Level 2	2	130	170	10
Level 3	3	160	200	13

Table 2 Combination of process parameters according to *L9* orthogonal array

Exp. no.	Electrode gap (mm)	Welding speed (mm/min)	Welding current (A)	Gas flow rate (lit/min)	Heat input (kJ/mm)	Tensile strength (N/mm ²)	S/N ratios
1	1	100	140	7	1.51	486	53.7327
2	1	130	170	10	1.41	478	53.5886
3	1	160	200	13	1.35	458	53.2173
4	2	100	170	13	1.83	486	53.7327
5	2	130	200	7	1.66	498	53.9446
6	2	160	140	10	0.9	415	52.3610
7	3	100	200	10	2.16	478	53.5886
8	3	130	140	13	1.16	400	52.0412
9	3	160	170	7	1.14	422	52.5062

Table 3 Welding process variables

Welding voltage	18 V
Electrode tip angle	60°
Shielding gas	Pure argon (99.99%)
Oxide flux powder	Silicon dioxide
Root gap	0 mm
Joint design	Close square butt joint
Filler material	No filler material was used
Diameter of electrode	2.4 mm tungsten electrode with 2% thorium

joint between them. Nine welded samples are thus made, by carrying out welding at different levels of current, speed, gas flow rate, and arc gap, as stated in Table 2.

2.3 Specimen Preparation for Testing

The specimens for tensile testing, microhardness testing, and microstructural studies were cut from these welded plates as shown in Fig. 1. From both sides, 5 mm length

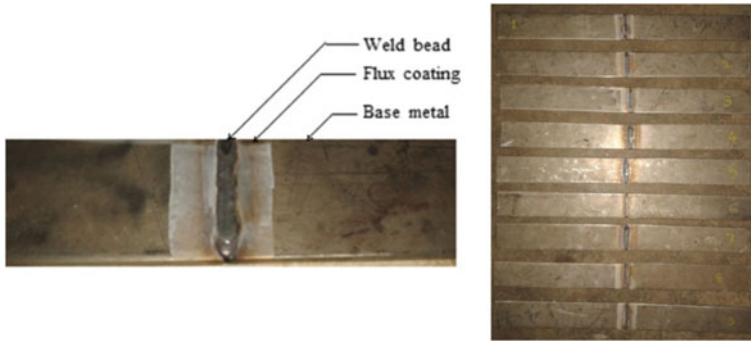


Fig. 1 Welded specimen plates

plate is cut to avoid defects in weld pool at start and end of welding. As shown in Fig. 1, sample 1 ($300 \times 30 \times 6$ mm), sample 2 ($300 \times 10 \times 6$ mm), and sample 3 ($300 \times 10 \times 6$ mm) are used for tensile test, metallographic test, and microhardness test, respectively.

Ultimate tensile strength (UTS) test is performed on the nine samples. The values of ultimate tensile strength obtained are stated in Table 2. The specimens (sample 2) are polished by using of silicon carbide paper of successive grit sizes 150, 400, 600, 1000, and 1200. Further, it is polished by velvet cloth using alumina powder and water as a suspension medium. Specimens are etched with solution of 10 g $\text{CuSO}_4 + 50$ ml $\text{HCL} + 50$ ml H_2O and dried in air. The etched sample were cleaned by cotton. These samples are observed under computer integrated Carl Zeiss PL-A662 microscope (Fig. 2).

The Vickers microhardness value of weld sample is taken in transverse direction of weld at 11 different points spaced by 1 mm distance. There are five points in weld pool and six points in heat affected zones. Test samples are cut into the size 50 mm length, 10 mm width, and 6 mm thickness and polished by using silicon carbide paper followed by buffing. Microhardness test is carried out in the longitudinal direction, i.e., parallel to base plate surface. The measurement were taken across the weld section at 100 gm load and 15 s dwell time.

Heat input to the process depends on process parameters such as welding current, voltage, and arc travel speed. Out of these three parameters, welding voltage is kept constant. Heat input plays an important role while achieving desired mechanical properties and calculated by Eq. (1). The values of heat input (kJ/mm) obtained are stated in Table 2.

$$\text{Heat Input} = \frac{\text{Current (A)} \times \text{Voltage (V)}}{\text{Travel speed (mm/s)} \times 1000} \text{kJ/mm} \quad (1)$$

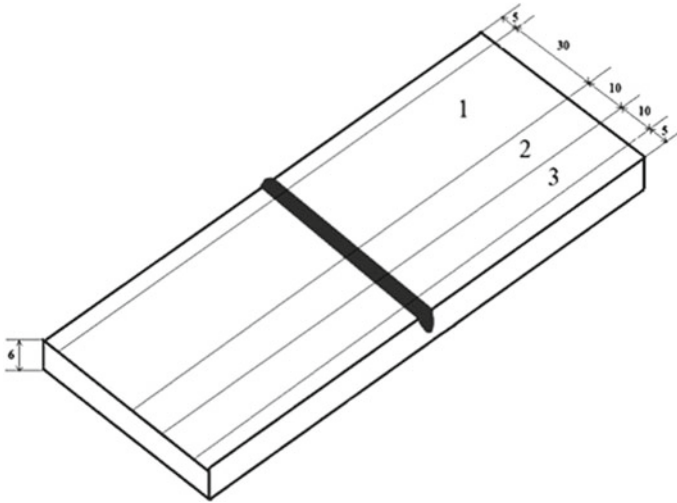


Fig. 2 Specimen preparation for testing

Table 4 Response table for S/N ratios

Parameter	Level 1	Level 2	Level 3	Delta = Max–Min	Rank
Electrode gap	53.51	53.35	52.71	0.80	3
Welding speed	53.68	53.19	52.69	0.99	1
Welding current	52.71	53.28	53.58	0.87	2
Gas flow rate	53.39	53.18	53.00	0.40	4

3 Results and Discussion

3.1 Effect of Process Variables

The response table for S/N ratios based on values of tensile strength is shown in Table 4. Different values show the most influential process parameters and their rank based on decreasing influence. The main effects plot for S/N ratios is shown in Fig. 3. The trends for each process parameters on tensile strength based on their levels can be seen in Figs. 3 and 4.

3.2 Metallographic Studies

From the optical micrographs, it was observed that, as heat input increases, the dendrite length and inter-dendrite spacing in the fusion zone increase. The dendrite

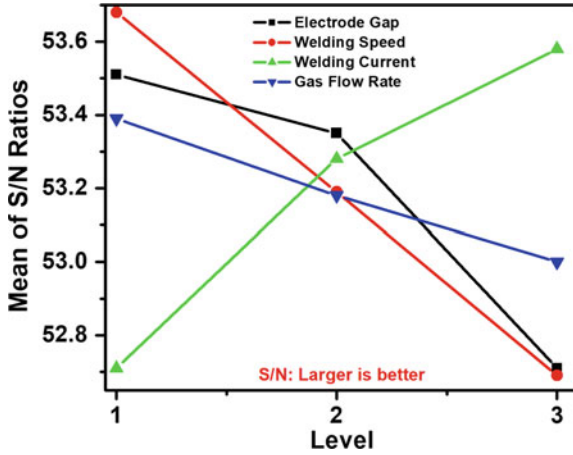


Fig. 3 Main effects plot for S/N ratios

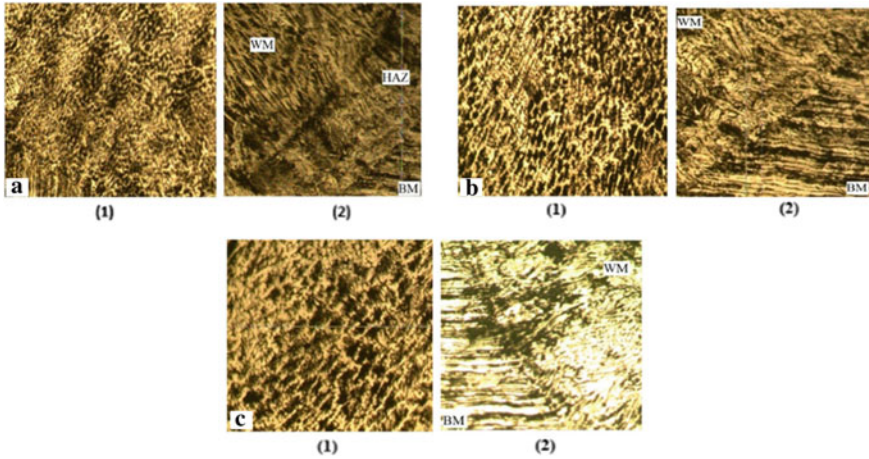


Fig. 4 Optical micrograph showing (1) grain structure, (2) base metal and weld metal at a) low heat input, b) medium heat input, c) high heat input

size variation is observed due to the fact that, at low heat input, cooling rate is relatively higher, due to which steep thermal gradients are established in the weld metal, which in turn allows less time to grow dendrites. At high heat inputs, cooling rate is slower, due to which low thermal gradients are established, which provide ample time for dendrites to grow further into the fusion zone. It is observed that, at low heat input, grain size is lesser than that of high heat input.

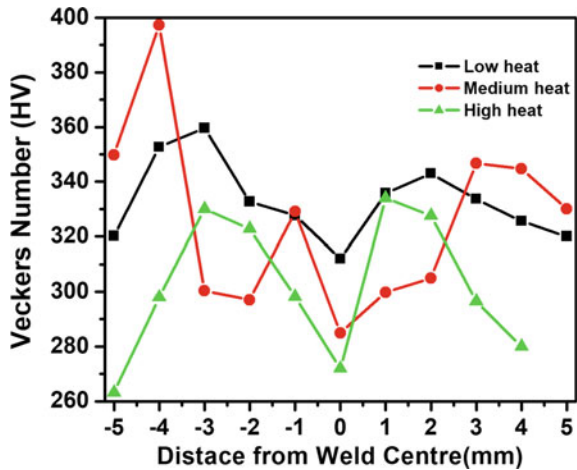
With the use of activated flux in TIG welding for hot rolled stainless steel 304 L plate, the weld zone contained austenite and δ -ferrite phases. However, during non-equilibrium cooling process, the primary δ -ferrite solidifies in the fusion zone

and then δ to γ transformation takes place. The fast cooling rate in TIG welding process does not offers sufficient time to complete δ to γ phase transformation. Use of activated flux in TIG welding results in the increase in δ ferrite content of weld. Due to this small amount of δ ferrite retained in weld zone, it is necessary to avoid hot cracking of weld during solidification. As heat input increases, peak temperature of weld also increases which results in more δ ferrite formation in A-TIG welding. Due to this, there is no hot cracking observed in test specimens.

3.3 Microhardness Test

From Fig. 5, it is observed that, as the indenter transverses from center of fusion/weld zone toward the fusion boundary, microhardness increases for all heat inputs. Fusion boundary or transition zone encountered while traveling in this direction is indicated by a steep rise in the microhardness with a value of 359.6 VHN for low heat input, 397.3 VHN for medium heat input, and 334 VHN for high heat input. At fusion boundary zone (FBZ) in all joints, high hardness value is observed because of the presence of partially melted grains at the fusion boundary which are partially adopted as nuclei by the new precipitating phase of the weld metal during the solidification stage. Further reaching this high value, microhardness shows decreasing trends in the heat-affected zone (HAZ). Hardness value for all weld metals was lower than that of base metal. This is due to the weldment structure that contains δ ferrite phase distribution in austenite matrix and as hardness of phase δ ferrite was lower than that the austenite phase of base metal.

Fig. 5 Microhardness profile of weld metal produced by different heat input



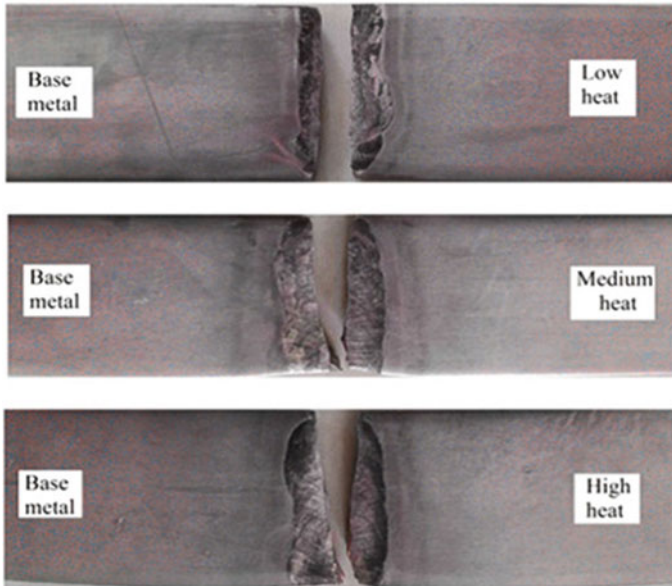


Fig. 6 Fracture behavior of specimen

3.4 Tensile Test

It is observed that dendrite size is smaller and inter-dendritic spacing is much lesser in the fusion zone of less heat input welded joints as compared to medium and high heat input welded joints. Hence, comparatively lower tensile strength and ductility are observed by the samples welded at high heat input because of longer dendrite sizes and larger inter-dendrite spacing. From tensile strength test, it was found that all specimens fail at weld metal rather than base metal. This is due to the lower strength of weld zone than base metal. Joint efficiency, defined as ratio of ultimate tensile strength (UTS), of weld joint to the UTS of base metal of specimens at low heat input is 92.49%, while at medium heat input is 90.44% and at low heat input is 88.56%. As heat input increases, joint efficiency decreases (Fig. 6).

4 Conclusions

In the present work, activated flux tungsten inert gas (A-TIG) welding is used for butt welding of AISI 304L austenitic stainless steel by using various combinations of arc gap, welding current, welding speed, and gas flow rate. Most influential process parameters, tensile strength of weld, micro-hardness tests, and metallographic tests are performed and following conclusions are drawn:

1. All the welded joints showed superior joint strength which indicates that the welding of 6-mm-thick AISI 304L stainless steel sheet with A-TIG welding can be carried out in single pass and without any joint preparation.
2. Activated flux SiO₂ along with acetone solvent is efficient technique to increase weld depth penetration and increasing joint strength.
3. Welding speed, welding current, and electrode gap are found to significantly affect the welding, while gas flow rate has very less effect.
4. Low heat input joints showed smaller dendrite size in the fusion zone compared to the dendrites observed in medium and high heat inputs. Low heat input weld joints showed maximum tensile strength and ductility.
5. Increase in the heat input increases the HAZ and fusion zone area. Significant grain coarsening is observed in the HAZs of all the joints with an increase in heat input.
6. Weld metal is found to have less hardness than the base metal for all joints. It is observed that increase in heat input decreases the hardness values of weld metal.

References

1. C. Hsu, K. Tsengm, Performance of activated TIG process in austenitic stainless steel welds. *J. Mater. Process. Technol.* **211**, 503–512 (2011)
2. H. Huang, S. Shyu, K. Tseng, C. Chou, Evaluation of TIG flux welding on the characteristics of stainless steel. *Sci. Technol. Welding Joining* **10**(5), 566–573 (2005)
3. K. Tseng, Development and application of oxide-based flux powder for tungsten inert gas welding of austenitic stainless steel. *J. Powder Technol.* **233**, 72–79 (2013)
4. M. Vasudevan, A. Bhaduri, B. Raj, Development and evaluation of activated flux for TIG welding of type 304 LN and type 316 LN stainless steel. *International Institute of Welding, International Congress*, Chennai, 25–32 (2008)
5. M. Zuber, V. Chaudhari, V. Suri, S. Patil, Effect of flux coated gas tungsten arc welding on 304L. *IACSIT Int. J. Eng. Technol.* **6**(3), 177–181 (2014)
6. E. Ahmadi, A. Ebrahimi, R. Khosroshahi, Welding of 304L stainless steel with activated tungsten inert gas process (A-TIG). *Int. J. ISSI* **10**(1), 27–33 (2013)
7. P. Lin, K. Tseng, UNS S31603 stainless steel tungsten inert gas welds made with microparticle and nanoparticle oxides. *J. Mater.* **7**, 4755–4772 (2014)
8. A. Sambherao, Use of activated flux for increasing penetration in austenitic stainless steel while performing GTAW. *Int. J. Emerg. Technol. Adv. Eng.* **3**(12), 520–524 (2013)
9. R. Duhan, S. Choudhary, Effect of different fluxes on hardness and microstructure of SS 304 in GTAW welding. *Int. J. Mech. Eng.* **3**(4), 1–8 (2014)
10. S. Nayee, V. Badheka, Effect of oxide-based fluxes on mechanical and metallurgical properties of dissimilar activated flux assisted- tungsten inert gas weld. *J. Manuf. Process.* **16**, 137–143 (2014)
11. Y. Morisada, E. Hormaza, Characterization of failure modes for different welding processes of AISI/SAE 304 stainless steels. *Eng. Failure Anal.* **18**, 1791–1799 (2011)

An Overview on the Microstructure and Mechanical Properties of Vibrated Magnesium Alloy During Solidification



Vatsala Chaturvedi and Trinath Talapaneni

1 Introduction

Magnesium alloys have a great potential for applications in the automotive, railway, and aerospace industries due to their comprehensive properties, such as the improved damping property, electromagnetic shielding capacity, excellent machinability, and good castability [1]. However, their application is still limited because of their poor mechanical property compared to that of the other conventional materials. Since the grain size is one of the most important factors determining the mechanical property of materials, fine-grained magnesium alloys are preferred [2, 3]. Recently, the mechanical properties of the wrought magnesium alloys were reported to be superior to those of cast magnesium alloys [4] due to their fine-grained structure. Although grain refinement of magnesium can be achieved by the wrought process (i.e., extrusion, rolling or forging), the procedure produces a fiber-like structure such as the bimodal structure consisting of both coarse grains and fine grains. In some coarse grains, deformation twins are easily formed and result in a limited ductility at the crack initiation sites. Therefore, an improvement of this structure is necessary to enhance the mechanical properties. The primary problem is that the developed dendrites are always yielded in normal castings because the alloy has a large freezing interval, in which a constitutionally undercooled region can be readily produced and thus to form dendrites. Therefore, how to suppress the formation of coarse dendrites is a key issue in improving the alloy properties. Several techniques have been developed to fabricate ingots with refined microstructures. One of the widely used methods is the particle incubation method used in which the TiB_2 is added externally to Al alloys resulting in the increase of heterogeneous nucleation sites. Though, the addition of external additives to α -Mg alloy could be detrimental to the recyclability of the alloy. Metallic

V. Chaturvedi (✉) · T. Talapaneni
Department of Metallurgical Engineering, OP Jindal University, Raigarh 496109, India
e-mail: vatsala.chaturvedi@opju.ac.in

© The Author(s), under exclusive license to Springer Nature Singapore Pte Ltd. 2022
M. L. Kolhe et al. (eds.), *Smart Technologies for Energy, Environment and Sustainable Development*, Vol 2, Springer Proceedings in Energy,
https://doi.org/10.1007/978-981-16-6879-1_41

materials with fine microstructures possess many advantages like good mechanical properties, thermal stability and low temperature, and/or high strain rate superplasticity [5]. This refinement of grains can either be done by applying external forces to encourage fluid flow during solidification which include rotation of the mold, mechanical/electromagnetic stirring of melt and rheocasting, or by imposing very large plastic strains through several techniques which include, multiaxial forging, accumulative roll-bonding, and equal-channel angular pressing (ECAP) [6]. Grain refinement is an impulsive change observed in various pure metals and alloys above a critical undercooling, ΔT^* . The coarse columnar grain structure evident below ΔT^* is replaced by an equiaxed structure [7]. Though, various commercial alloys do not have a conventional inoculating agent or chemical grain refiner. Although aluminum-free Mg alloys can be readily grain-refined with zirconium, it is difficult to grain-refine the more common Mg–Al-based alloys by inoculation. It is required to get an alternative route for refining these alloys. The other method is to use physical fields such as pulsed electric current, magnetic fields, and vibration during the solidification of Mg alloys to refine the microstructure.

2 Grain Refinement by External Force

Following are the techniques that are used during the solidification of metals and alloys to enhance the microstructure and mechanical properties.

2.1 *Mechanical Vibrations*

In this method, the entire mold is set into vibrations by means of a vibration source. Although the use of mechanical vibrations allows limited degrees of freedom to the operator, it is the most promising method of applying vibrations to solidifying melts due to its simplicity and the ruggedness of the equipment needed for introducing vibrations.

Use of mechanical vibrations in castings.

Sokoloff [8] was probably the first to report on the use of mechanical vibrations for grain refinement. Campbell [9] reported that mechanical vibrations cause improvement in the mechanical and corrosion properties of the alloys. Mechanical vibrations have also been linked to the reduction or complete removal of the tendency for pipe formation in ingots of pure metals [10].

Dommaschk et al. [11] studied the effect of vibrations on pure aluminum, Al–7wt%MgSi and Al–12wt%Si alloys along with other non-ferrous alloys. Their research focused on the effect of mechanical vibrations on grain refinement and mechanical properties. They observed that the cooling rate and the degree of grain refinement increase with the intensity of vibrations, and the grain size becomes more

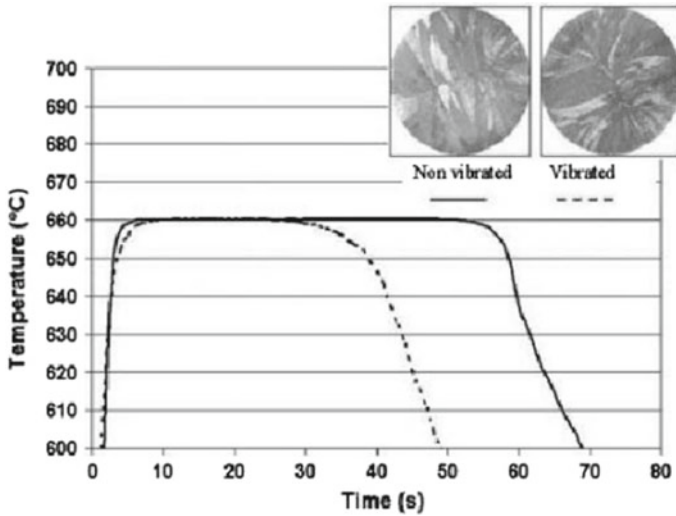


Fig. 1 Effect of mechanical vibrations on the cooling curve of pure Aluminum [13]

homogenous. The effect of mechanical vibrations on the solidification behavior of pure aluminum is shown in Fig. 1.

Dommaschk et al. [11] also reported that the dependence of the castings, wall thickness on casting characteristics could be minimized with the use of mechanical vibrations.

Pillai et al. [12] used very low-frequency vibrations (100 and 200 cycles per minute) to study its effect on A356 and Al–12Si alloy. They concluded that mechanical vibrations improve the density, hardness, UTS, and elongation of the cast components. They attributed these improvements to the enhanced coagulation of hydrogen bubbles and their escape from the melt brought about by vibrating the mold. Thus, porosity was reduced and wetting of the mold walls by the melt was enhanced, this, in turn, promoted faster heat transfer and fragmentation of the solids formed on the mold wall. However, the method that Pillai et al. [12] used for generating the low-frequency vibrations (hand tapping and mold tilting) is highly impractical in a production foundry environment.

Kocatepe et al. [14] applied vibrations of 15–41.7 Hz frequency and 0.125–0.5 mm amplitude to Al–12.3Si alloy ingots poured in a graphite mold. It was observed that at 41.7 Hz, the solidification time was reduced by 24%, volume of pipe formation was reduced by 55% and grain size was reduced by 52% as compared to the un-vibrated casting (Fig. 2).

Kocatepe et al. [14] also found that the vibrations caused an increase in diffusivity of silicon in the liquid resulting in coarsening of the eutectic silicon. They also observed that grain refinement is mainly due to the fragmentation of dendrites and the growing crystallites during the beginning of solidification.

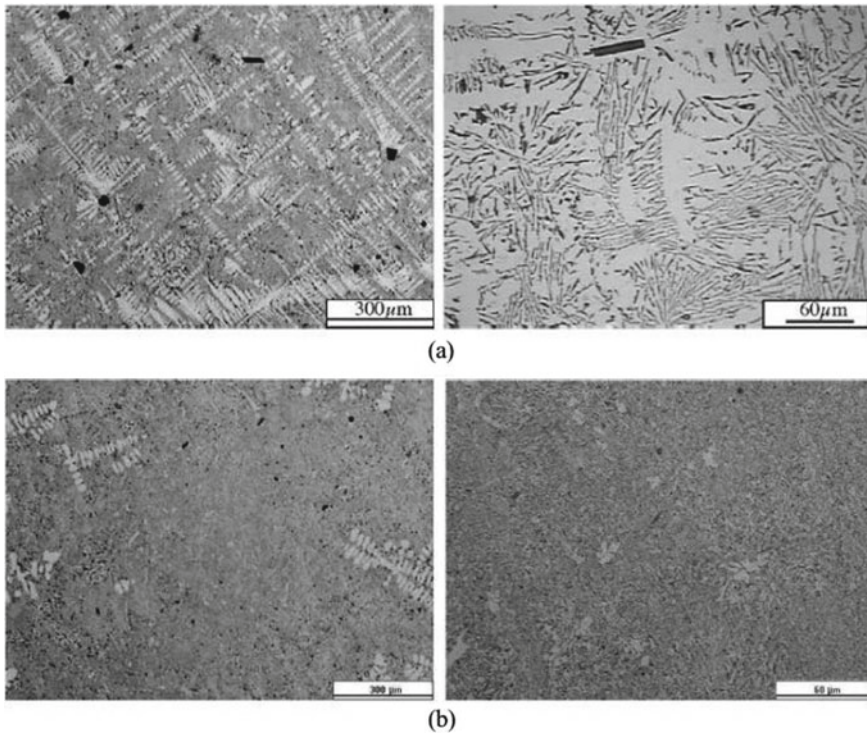


Fig. 3 Morphology of eutectic silicon **a** without vibrations **b** with vibrations at a frequency 100 Hz and amplitude 149 μm [15]

dendrites are primarily produced in the alloy during casting process, which are detrimental and results into poor mechanical and chemical properties. Therefore, in order to enhance mechanical and chemical properties, refined microstructures are required.

Vives [19] observed in AZ91D alloy that substantial consumption of energy is required to yield refinement of grains. It was found that optimum vibration timing is critical to facilitate minimize energy consumption. Imposing vibration from the liquidus temperature of the alloy results in the agitation of the melt. This produces a severe fluid flow of considerable importance in endorsing growing dendrites to fragment into small particles resulting in refined microstructures. Besides, the melt flow is capable of rotating and/or transferring crystals in the mushy zone consequently making the texture random. The primary solid is produced as the starting temperature for vibration is reduced in the mushy zone. A higher solid fraction can be produced at the lower starting temperature of the EMV. More viscosity of semisolid slurry weakens the fluid flow which may not be adequate to fragment the crystals into pieces resulting into coarse microstructure. Additionally, owing to the magnetic anisotropy of the alloy, the magnetization torque force crystals to orient along their preferential crystallographic orientations. For the AZ91D alloy, effective vibration for grains

refinement should be carried out above $T \frac{1}{4} 570 \text{ }^\circ\text{C}$ (843 K) [20]. Furthermore, the melt can be contaminated as the molten alloy is always aggressive to the transmitter. The electromagnetic vibration (EMV) method depends on the periodic motion of a conductor in a static magnetic field. The strong flow of electric current through the conductor results in no attenuation within the entire volume of the alloy. Also, the processing of the melt in an inert atmosphere makes the melt free from contamination. Vives [21] investigated a series of aluminum alloys and observed that the grain size could be reduced on imposing the vibration beyond a certain electromagnetic pressure. The solidification behavior using EMV had also been investigated to see the grain refinement in various metals and alloys. During EMV processing, basically there are three main processing parameters; i.e., the magnetic flux density of the static magnetic field, B_0 , the effective electric current, J_e , and the frequency of the alternating current, f . The effect of vibration frequency had been investigated in various alloys and found that, at low frequency, the alloys have coarse structure, becomes refined at a medium frequency, and, finally, coarsens at high frequency. It has been observed that the AZ91D alloy [22] exhibits an almost similar pattern in microstructure as a function of vibration frequency. On imposing the vibration at a frequency of 900 Hz, the average grain size of $57 \text{ }\mu\text{m}$ was achieved [23]. Dond et al. [24] and Asai [25] investigated the solidification behavior of AZ31 and AZ91 D alloys. Coarse microstructure with equiaxed rosette dendrites was observed at low and high frequencies in the microstructures of both the alloys. The refined microstructures with equiaxed grains were observed at medium vibration frequencies from $f = 500 \text{ Hz}$ to $f = 2000 \text{ Hz}$ and $f = 900$ for AZ31 and AZ91 D alloys, respectively (Fig. 4). During the microstructure formation, there is a considerable variation in electric resistivity between a solid and a liquid in the mushy zone of the alloy making the solid move faster than the liquid thus causing uncoupled motion between the mobile solid and the sluggish liquid during EMV processing resulting into melt flow. The melt flow intensity strongly depends on the vibration frequency.

2.3 Ultrasonic Vibrations

The imposition of ultrasonic vibrations (UV) during the solidification of the alloy melts results in refined microstructure and increased homogeneity. UV pretreatment along with extrusion of the AZ91 alloy resulted in the fine uniform grains with the fraction of a fiber-like, partially recrystallized, fragmented eutectic, and the precipitated β -phases. It also exhibited improved mechanical properties, such as a yield strength of 256 MPa, an ultimate tensile strength of 320 MPa and a fracture elongation of 9.7% [27]. The enhancement in the properties was mainly due to the grain refinement and composition homogeneity in the as-cast alloy with UV treatment (Fig. 5) [28].

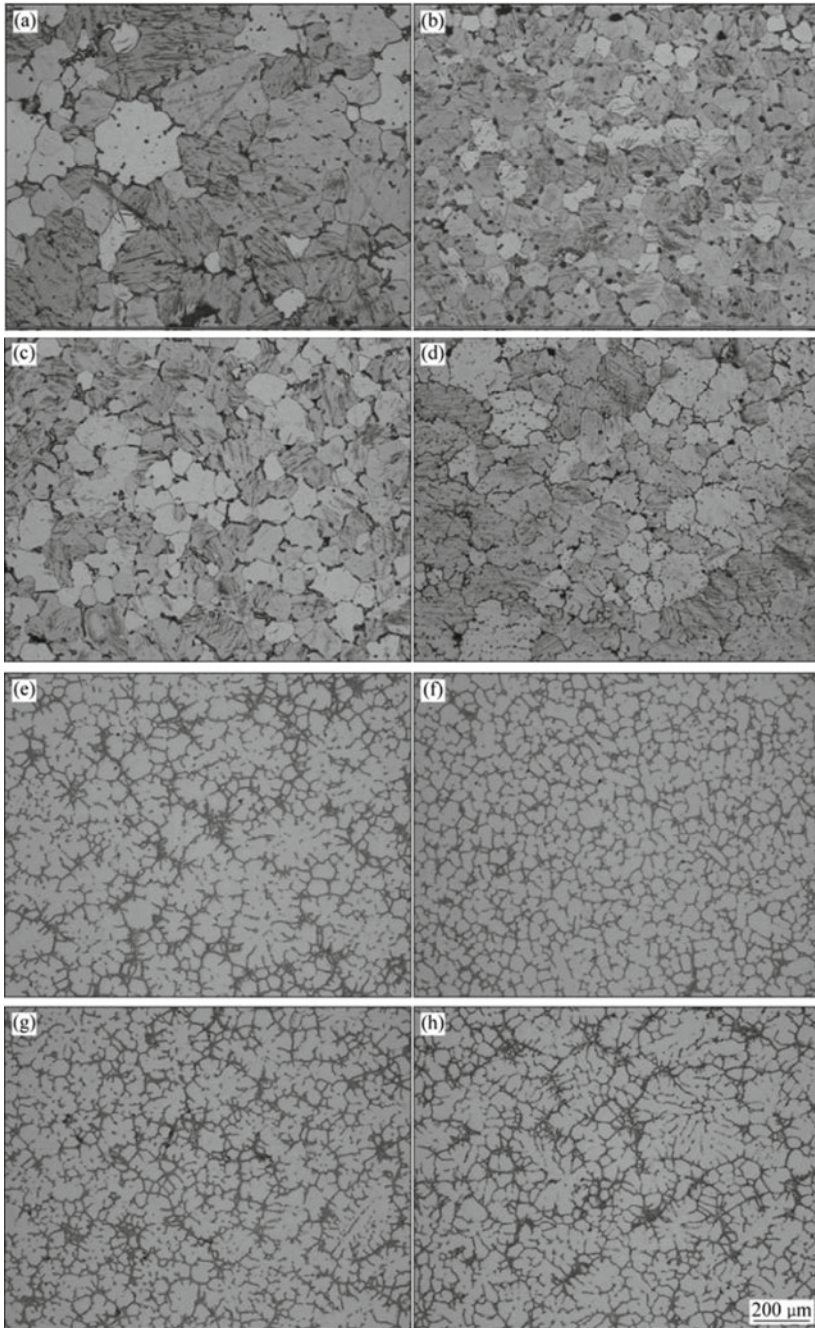


Fig. 4 Microstructures of AZ31 alloy **a–d** and Az91 alloy **e–h** ($B_0 = 10$ T, $I = 50$ A) solidified at different vibration frequencies: **a** $f = 50$ Hz; **b** $f = 500$ Hz; **c** $f = 1000$ Hz; **d** $f = 5000$ Hz; **e** $f = 50$ Hz; **f** $f = 900$ Hz; **g** $f = 2000$ Hz; **h** $f = 5000$ Hz [26]

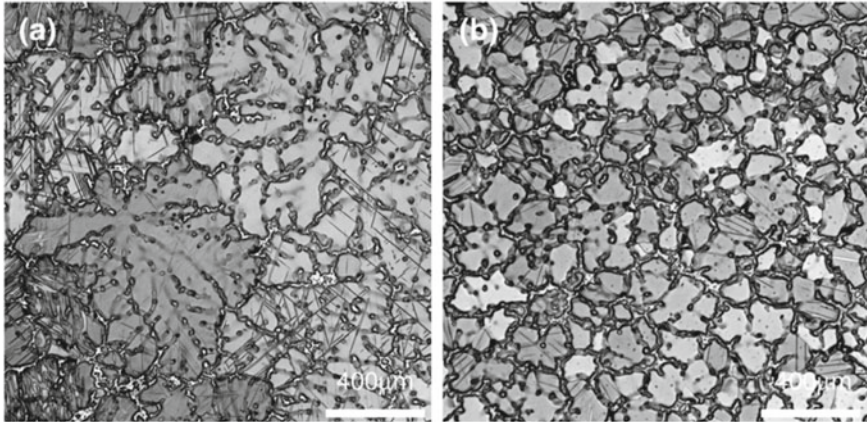


Fig. 5 Microstructures of the AZ91D alloy, **a** without ultrasonic vibration and **b** with ultrasonic vibration at temperatures from 615 °C to 580 °C [28]

2.4 Conclusion

Reviews of the literature have reported on the beneficial influence of vibrations during the solidification of metals and alloys. The application of vibrations during solidification usually leads to the refinement of grains and improved fluidity. The mechanical properties are improved with grain refinement, equiaxed texture, and better distribution of micro-alloyed constituents [29].

References

1. Y. Kojima, Project of platform science and technology for advanced magnesium alloys. *Mater. Trans.* **42**, 1154–1159 (2001)
2. R. Armstrong, I. Codd, R.M. Douthwate, N.J. Petch, The plastic deformation of polycrystalline aggregates. *Philos. Magaz. J. Theoret. Exp. Appl. Phys.* **7**, 45–58 (2006)
3. T. Mukai, M. Yamanoi, H. Watanabe, K. Higashi, Effect of grain refinement on tensile ductility in ZK60 magnesium alloy under dynamic loading. *Mater. Trans.* **42**, 1177–1181 (2001)
4. H. Somekawa, A. Singh, T. Mukai, High fracture toughness of extruded Mg–Zn–Y alloy by the synergistic effect of grain refinement and dispersion of quasicrystalline phase. *Scripta Mater.* **56**, 1091 (2007)
5. S. Komura, Z. Horita, M. Furukawa, M. Nemoto, T.G. Langdon, An evaluation of the flow behavior during high strain rate superplasticity in an Al–Mg–Sc Alloy. *Metall. and Mater. Trans. A.* **32A**, 707–716 (2001)
6. G. Alexandre, S. Olegi, S. Taku, K. Rustam, M. Hiromi, Grain refinement in as-cast 7475aluminium alloy under hot equal-channel angular pressing. *Mater. Trans.* **44**(4), 766–774 (2003)
7. Aramide Fatai Olufemi, Ibitoye Simeon Ademola: Effects of melt vibration during solidification on the mechanical property of Mg–Al–Zn Alloy. *Int. J. Mech. Eng.* **3**(1), 40–43 (2012)

8. D.N. Abu, M. Khraisheh, K. Saito, A. Male, Silicon morphology modification in the eutectic Al–Si alloy using mechanical mold vibration. *Master. Sci. Eng. A* **393**, 109–117 (2005)
9. J. Campbell, Effect of vibration during solidification. *Int. Metal Rev.* **26**(2), 71–108 (1981)
10. T.P. Fisher, Effects of vibrational energy on the solidification of aluminum alloys. *British Foundryman* **66**(3), 71–84 (1973)
11. C. Dommaschk, Influence of vibration on the microstructure of solidifying molten metals. Ph.D. Thesis, University of Freiberg, Germany (2003)
12. R.M. Pillai, K.S. Biju Kumar, A simple inexpensive technique for enhancing density and mechanical properties of Al7Si alloys. *J. Mater. Process. Technol.* **146**, 338–348 (2004)
13. Bast et al., *Adv. Eng. Mater.* **6**(7), 550–554 (2004)
14. K. Kotatepe, C.F. Burudett, Effect of low frequency vibration on macro and micro structures of LM6 alloys. *J. Mater. Sci.* **35**, 3327–3335 (2005)
15. N. Abu-Dheir, Solidification of aluminum alloys. *Miner. Metals Mater. Soc.*, 361–368 (2004)
16. Ch. Vives, Effects of forced electromagnetic vibrations during the solidification of aluminum alloys: Part I. solidification in the presence of crossed alternating electric fields and stationary magnetic fields. *Metallurg. Mater. Trans. B* **27**, 445–455 (1996)
17. A. Radjai, K. Miwa, T. Nishino, An investigation of the effects caused by electromagnetic vibrations in a hypereutectic Al–Si alloy melt. *Metall. Mater. Trans. A.* **29**, 1477–1484 (1998)
18. Y. Mizutani, T. Tamura, K. Miwa, Microstructural refinement process of pure magnesium by electromagnetic vibrations. *Mater. Sci. Eng.* **413–414**, 205–210 (2005)
19. Ch. Vives, Grain refinement in aluminum alloys by means of electromagnetic vibrations including cavitation phenomena. *J. Miner. Metals Mater. Soc. (TMS)* **50**(2) (1998).
20. M. Li, T. Tamura, N. Omura, K. Miwa, Effect of vibration timing on the microstructure and micro texture formation of AZ91 D magnesium alloys during electromagnetic vibration. *Mater. Trans.* **50**(8), 2015–2020 (2009)
21. Ch. Vives, Electromagnetic refining of aluminum alloys by the CREM process: Part I. Working principle and metallurgical results. *Metallurg. Trans. B.* **20**, 623–629 (1989)
22. M. Li, T. Tamura, K. Miwa, On the role of vibration frequency on the solidification of AZ91D magnesium alloys during electromagnetic vibration. *J. Mater. Res.* **24**, 145–155 (2009)
23. M. Li, T. Tamura, N. Omura, K. Miwa, Effects of magnetic field and electric current on the solidification of AZ91 D magnesium alloys using an electromagnetic vibration technique. *J. Alloys Compounds* **487**, 187–193 (2009)
24. J. Dong, J. Cui, F. Yu, C. Ban, Z. Zhao, Effect of low-frequency electromagnetic casting on the castability, microstructure, and tensile properties of direct-chill Cast Al–Zn–Mg–Cu alloy. *Metall. Mater. Trans. A.* **35**, 2487–2494 (2004)
25. S. Asai, Application of high magnetic fields in inorganic materials processing. *Modell. Simul. Mater. Sci. Eng.* **12** (2004)
26. M.J. Li, T. Tamura, N. Omura, K. Miwa, Microstructure formation and grain refinement of Mg-based alloys by electromagnetic vibration technique. *Trans. Nonferrous Met. Soc. China* **20**, 1192–1198 (2010)
27. Y. Osawa, X. Liu, S. Takamori, H. Somekawa, T. Mukai, Effect of ultrasonic vibration pretreatment on microstructural evolution and mechanical properties of extruded AZ91 alloy. *Mater. Trans.* **49**(5), 972–975 (2008)
28. X. Liu, Y. Osawa, S. Takamori, T. Mukai, Grain refinement of AZ91 alloy by introducing ultrasonic vibration during solidification. *Mater. Lett.* **62**, 2872–2875 (2008)
29. A. Maltais, M. Fiset, D. Dube, Grain Refinement of magnesium alloy AZ91 D cast in permanent mold using mechanical vibrations. *Mater. Sci. Forum* **426–432**, 527–532 (2003)

CFD Analysis of Waste Heat Recovery (WHR) System of Diesel Generator Set



Tejas Shankhpal, Vikrant Haribhakta, and Santosh Trimbake

1 Introduction

The present modern life largely depends on Internal Combustion Engines (ICEs). Although the fact that some new technologies have been presented recently, the majority of vehicles are still powered by either Gasoline or Diesel engines. Diesel engines possess a wider field of applications as prime movers due to their better efficiency. Governments and OEM (Original Equipment Manufacturers) are encouraged to improve the fuel efficiency of diesel engines and minimize its emissions due to uncontrolled growth of greenhouse gases fossil fuel exhaustion and escalating fuel costs. Accordingly, several measures have been taken in the recent past to improve diesel engine efficiency additionally.

During DG set run time, there are different places in the engine's structure where a significant amount of heat is dissipated to the atmosphere. The rejected heat includes heat from the water jacket, the exhaust, and in more recent engines, the heat energy from the turbocharger after-cooler. This heat energy can be harnessed for domestic or commercial purposes by using a recovery process, although this requires addition of significant hardware which adds to the expense of installation. In the past, fuel was cheap and it was challenging to justify the overall cost of the heat recovery system.

Furthermore, high sulfur fuel results in corrosive condensates, requiring either expensive alloys for heat recovery from exhaust systems or costly replacements. Cogeneration systems (which produce both electricity and heat for immediate use) recover exhaust heat from the generator exhaust to improve overall efficiency and

T. Shankhpal (✉) · V. Haribhakta

Department of Mechanical Engineering, Government College of Engineering, Pune 411005, Maharashtra, India

S. Trimbake

Department of Mechanical Engineering, College of Military Engineering, Pune 411031, Maharashtra, India

significantly reduce fuel demands. Cogeneration processes, such as combined heat and power (CHP) have been in practice in large-scale systems for several decades. However, recent advances in small-scale “micro-cogeneration” have opened a door for the application of these technologies in radiant heating of residential/commercial spaces.

To successfully implement cogeneration, the WHR system design must be simple to construct, it must use readily accessible components and it must not adversely affect generator operation. The idea of using exhaust heat from an engine to heat a space is not unique to this research, but there are very few applications of heat recovery from diesel generator exhaust.

The objective of this study was to design and develop WHR system for diesel generators (DG) employed for radiant heating of residential/commercial spaces and analyze its feasibility with potential payoffs. Direct Injection (DI) technology, Advance combustion technologies like HCCI [1, 2], a combination of advanced injection timing, high injection pressure, and high boost pressure [3] have been successfully developed to enhance the performance of engines.

Irrespective of the enhancements in efficiency, diesel engines endure liberating a significant share of chemical energy of fuel in terms of heat energy to the environment through lubricating oil, jacket coolant, and exhaust gases [4]. At rated capacity, generally, diesel engine can convert around 38% [5] of its fuel energy to brake power whereas 30% of energy goes to engine exhaust, 25% through the lubricating oil and jacket coolant, and 7% to the frictional losses [6–9].

A typical heavy-duty DG engine exhaust temperature ranges from 450–700 °C due to a higher percentage of heat in the exhaust [10]. The exhaust gas possesses higher recovery potential than the jacket coolant due to higher temperature and exergy [11]. This high exhaust temperature provides a significant opportunity to recover heat using WHR technology for various applications.

This can contribute to a substantial improvement to the CHP efficiency of a DG set engine [12]. Conventional technologies to utilize WHR are turbocharging, reducing engine warmup time and cabin air-heating [13–15], but with a low recovery rate. Recent innovative key technologies of WHR includes turbo-compounding, thermal WHR based on the Rankine cycle (RC) and Thermoelectric (TE) power generations.

In RC-based WHR, additional power is produced by employing a steam generator to generate steam with exhaust heat as input energy which generally expands in a steam turbine. In a turbo-compounding (TC) system, a supplementary gas turbine is employed downstream of the turbocharger. This gas turbine is coupled to the engine by a suitable gear train to enhance the diesel engine power output [16].

Nevertheless, this technology possesses inherent limitations of higher engine backpressure and pumping losses [17]. Under the limitations discussed above, this system is not widely utilized for WHR. Dolze et al. [18] carried out a thermodynamic analysis to examine WHR from DG set engines. They showed 8% enhancement in the efficiency of WHR based on RC system from the exhaust gas of the engine

The exceptional heat storage capacity of the steam which acted as an energy buffer was highlighted to favor the RC in comparison to the TC system. A comparative study between the RC system and the TC system of WHR was carried out by Weerasinghe

et al. [19] using numerical simulation for comparing power output and fuel savings. The result validated the relative advantage of RC over TC system.

Based on the above studies, it was concluded that 8% of the power was recovered by using the RC system, whereas only 4% of the power was recovered by using TC system. Thermoelectric (TE) generator is a sophisticated WHR system. This technique directly converts the heat energy of exhaust into electric energy using the thermoelectric concept [16].

Due to the low conversion efficiency of the TE technology and the exorbitant costs of the semiconductor materials, thermoelectric technology is not yet matured to apply for practical applications [20]. Way back in 1970, a research program was conducted by Thermo Electron Corporation and Mack Trucks based on the fundings of the department of energy, US to evaluate recovery from exhaust waste heat of the heavy-duty diesel engine based on RC system [21–23].

Based on this program, an RC system was retrofitted with a heavy-duty diesel engine and the highway test results showed an improvement of the brake specific fuel consumption (bsfc) of 12%. In the following years, parallel research programs were carried out by other research institutes and vehicle OEMs. Aly [24] was able to show 16% additional power using RC system with R-12 as the working fluid utilizing the exhaust gas heat energy of a Mercedes-Benz diesel engine.

2 Methodology

Exhaust gas temperatures, air, and fuel-flow rates were noted to calculate the potential heat from the exhaust at constant speed of 1500 rpm at different load conditions. For a given heat duty and fixed exhaust inlet and exit temperature, water outlet temperature was evaluated using energy conservation equation. Quasi dimensional modeling of WHR was done using Kern's algorithm. Further numerical 3D modeling of WHR was carried out using ANSYS FLUENT. Parametric analysis for varied helical angle of baffles was carried out to identify the optimal helical angle of baffle. Load variation analysis was done for segmental baffled and optimal helical baffle angle to estimate the outlet temperature of water.

3 Numerical Modeling

DG set calculations are performed to evaluate the heat duty from the exhaust gases. 25% baffle cut is normally used in the design of shell-and-tube heat exchanger; whereas, 37% baffle cut value is selected to place the cut slightly below the central row of tubes to ensure minimum pressure drop on the shell side. The shell side fluid is exhaust gas, whereas the tube side is water. Thermo-physical properties of water and exhaust gas are defined at bulk mean temperature. Initially, overall heat transfer coefficient was assumed as $190 \text{ W/m}^2\text{k}$ [25]. Due to space constraints tube length

Table 1 DG set parameters

Kirloskar DG set	62.5 KVA/50 kW
Exhaust gas temperature (Manifold)	500 °C
Exhaust gas flow rate (m)	300 kg/hr
A/F ratio	22.25:1

Table 2 Design parameters of WHR

Inner Diameter	97.18 mm
Number of tubes	14
Tube diameter	12.95 mm
Pitch	19.05 mm
Length of tube	1000 mm
Baffle spacing	68.0 mm
Number of baffles	7
Length of Baffle cut	85.02 mm
Area of tubes	1.526 m ²

has been maintained up to 1 m. Inlet and exit temperatures of exhaust gas are 500 °C and 180 °C whereas temperatures of waterside are 30 °C and 80 °C and above the desired output. Table 1 presents design parameters of DG set, due to condensation limit at 180 °C, exhaust gas temperature cannot be less than 180 °C. With that set of data available numerical modeling was carried out on MATLAB. Table 2 exhibits the design parameters of WHR. Figure 2 depicts the developed EHR system. It is a gas-to-liquid type of heat exchanger. A shell-and-tube type heat exchanger (STHX) were selected wherein; the exhaust gas passes through the shell and liquid passes through the core side, that is, through the inner pipes. This design enables better exhaust escape to the atmosphere in a single pass without building much backpressure. This design configuration also allows the exhaust temperature to be above the water vapor dew point to reduce exhaust condensation and acid formation (Fig. 1).

4 CFD Analysis

4.1 Geometry Modeling

Geometry is modeled based on the design parameter obtained with the 1D Numerical analysis. Geometry is modeled as shown in Fig. 1. Figure 3 shows a cross-sectional view of segmental baffled WHR for CFD analysis. Figure 4 shows a cross-sectional view of helical baffled WHR for CFD analysis. Governing equations are solved with the software package of ANSYS R19.3. WHR is modeled with Ansys Design Modeler software. Figure 5 and 6 show 3D geometry of both WHR.

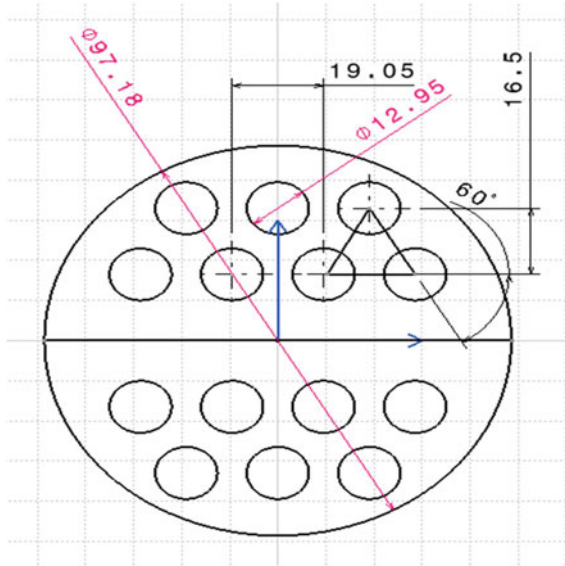


Fig. 1 Cross-sectional view of conventional WHR



Fig. 2 Developed WHR system

4.2 Grid Generation and Boundary Conditions

The heat exchanger model is discretized into solid and fluid domains to have improved control over the number of nodes. The fluid mesh is ensured to be more delicate than

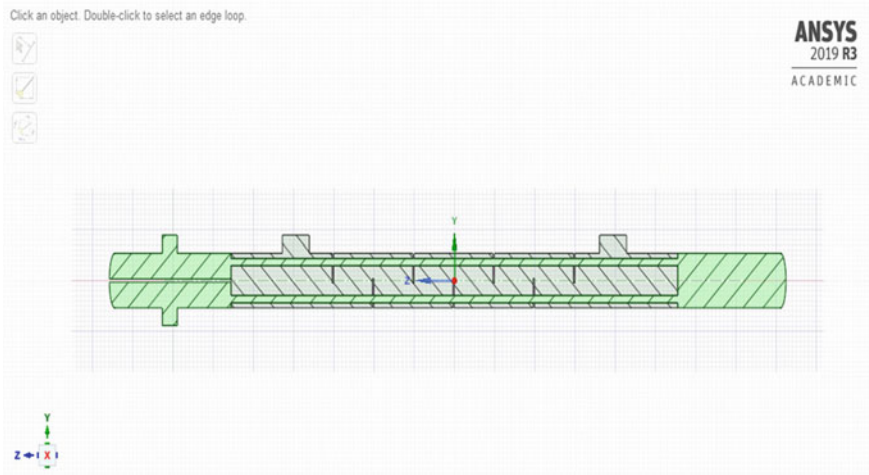


Fig. 3 Geometry of conventional WHR

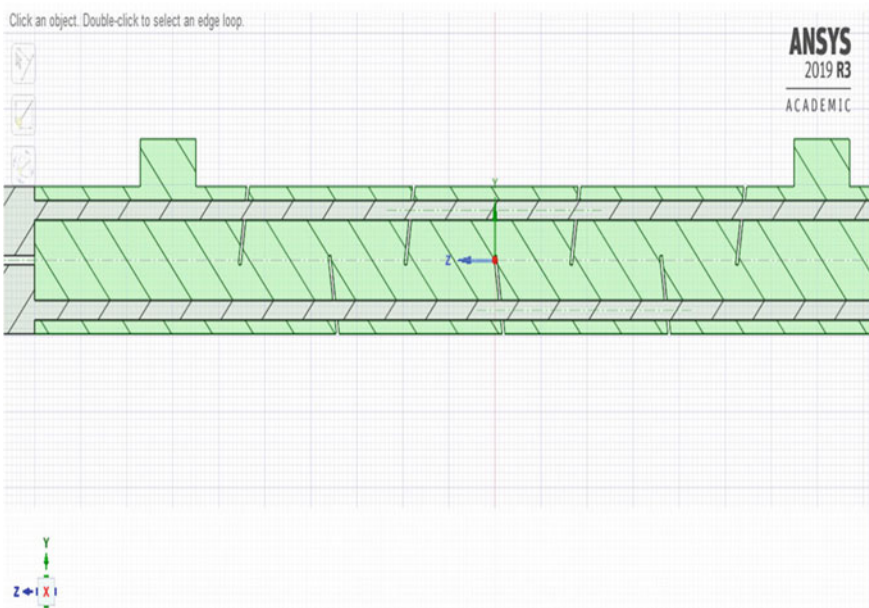
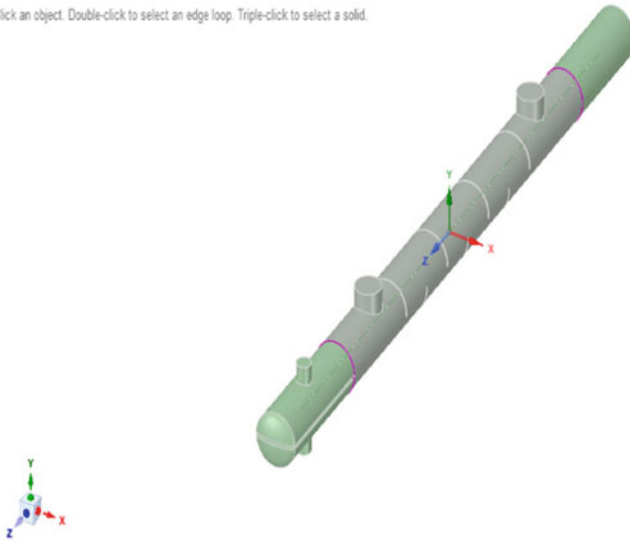


Fig. 4 Geometry of Helical Baffled WHR

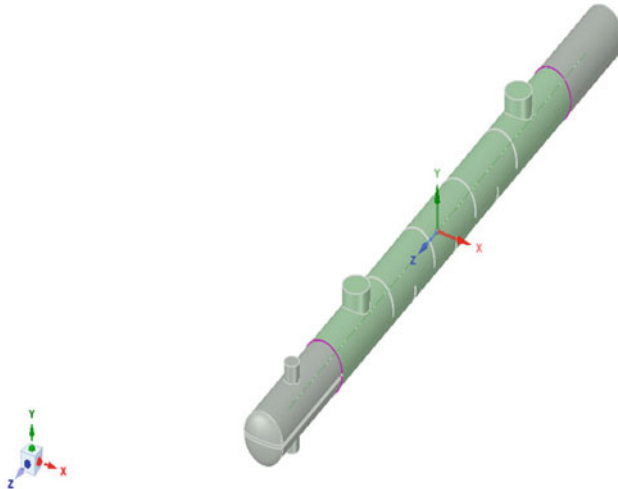
Click an object. Double-click to select an edge loop. Triple-click to select a solid.



ANSYS
2019 R3
ACADEMIC

Fig. 5 Geometry of conventional WHR

Click an object. Double-click to select an edge loop. Triple-click to select a solid.



ANSYS
2019 R3
ACADEMIC

Fig. 6 Geometry of helical baffled angle WHR

solid mesh for simulating the conjugate heat transfer phenomenon. Conjugate heat transfer refers to the CFD analysis, where solid and fluid are in direct contact with each other. In this case, solid domain refers to a tube of WHR whereas fluid refers to

Geometry



Fig. 7 Meshed view of the model

the water flowing from the tubes and exhaust gas flowing over the tube banks of shell side of WHR. Geometry was meshed in a manner to capture thermal and velocity boundary layer.

When fluid flows over and inside the tubes, there is a boundary layer formation. To capture this thermal and velocity boundary layer, Y^+ value was appropriately applied on both sides of the tubes. Meshed model is presented in Fig. 7. The model is meshed as per the standard meshing quality criteria for which importance is given to skewness of the meshing.

Skewness refers to a deviation from an ideal cell. As per the literature survey, it was seen that better results can be accomplished if the skewness is below 0.9. Automesher of Ansys controls meshing size and provides better results. Element size taken for the meshing is 76 mm and after the analysis grid, sensitive analysis was performed for checking variation in results for different mesh sizes.

The total number of elements generated in the meshing is 5499688. Skewness ideally should be zero, but in this case, it is around 0.2.

ANSYS Fluent v19.3 was used for simulation. In the Fluent, pressure-based steady-state solver for incompressible flow type is selected. For temperature distribution energy equation is selected and the turbulence model selected is standard k-epsilon, standard wall function.

In cell zone fluid water-liquid was selected. Water-liquid and steel were chosen as materials for simulation. The governing equations for the flow and conjugate heat transfer were modified according to the conditions of the simulation setup. As the problem was assumed to be steady, the time-dependent parameters were dropped from the equations.

The resulting equations were:

Continuity equation:

$$(\rho \vec{V}) = 0 \tag{1}$$

Momentum equations:

X—momentum equation:

$$(\rho u \vec{V}) = -\frac{\partial p}{\partial x} + \frac{\delta \tau_{xx}}{\delta x} + \frac{\delta \tau_{yx}}{\delta y} + \frac{\delta \tau_{zx}}{\delta z} \tag{2}$$

Y—momentum equation:

$$(\rho v \vec{V}) = -\frac{\partial p}{\partial y} + \frac{\delta \tau_{xy}}{\delta x} + \frac{\delta \tau_{yy}}{\delta y} + \frac{\delta \tau_{zy}}{\delta z} \tag{3}$$

Z—momentum equation:

$$(\rho w \vec{V}) = -\frac{\partial p}{\partial z} + \frac{\delta \tau_{xz}}{\delta x} + \frac{\delta \tau_{yz}}{\delta y} + \frac{\delta \tau_{zz}}{\delta z} \tag{4}$$

Energy equation:

$$\rho C_p \left(u \frac{\delta T}{\delta x} + v \frac{\delta T}{\delta y} + w \frac{\delta T}{\delta z} \right) = \lambda \left(\frac{\delta^2 T}{\delta x^2} + \frac{\delta^2 T}{\delta y^2} + \frac{\delta^2 T}{\delta z^2} \right) \tag{5}$$

Appropriate boundary conditions are required to solve any CFD problem. In this case, Dirichlet boundary condition was selected for inlet and Neumann boundary condition was selected for outlet. Whereas Dirichlet refers to the type of boundary condition where the fixed value of the dependent variable was applied at the boundary of the model, Neumann refers to the boundary condition where the fixed value of the gradient of the dependent variable was applied at the boundary. In this analysis, Dirichlet boundary refers to the mass flow inlet, whereas Neumann boundary refers to the pressure outlet. No slip for wall type boundary condition is applied at the tube side and the baffles of WHR. Table 3 shows boundary conditions and Fig. 8 shows boundary conditions at applied points. Tables 4 and 5 show solver details and solution control.

Table 3 Boundary conditions

Shell side mass flow inlet	0.077 kg/s @ 500 °C
Tube side mass flow inlet	0.138 kg/s @ 30 °C
Shell side pressure outlet	Atmospheric pressure
Tube side pressure outlet	Atmospheric pressure
Wall	No slip @ Tube side wall. And @ Baffles

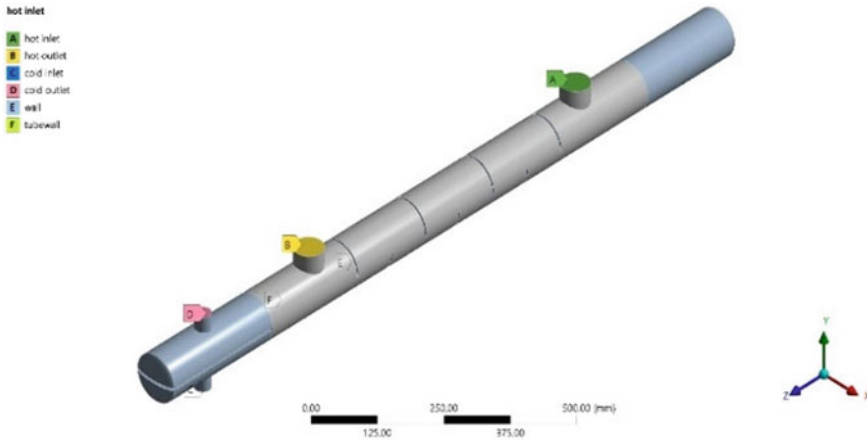


Fig. 8 Boundary conditions for WHR

Table 4 CFD solver details

Pressure velocity coupling	SIMPLEC
Skewness correction	0
Momentum	First order upwind
Turbulent kinetic energy	First order upwind
Energy	Second order upwind

Table 5 Solution control parameters

Pressure	0.7
Density	1
Body force	1
Momentum	0.2
Energy and turbulent viscosity	1

5 Results and Discussions

5.1 Variation of Temperature

From CFD analysis of WHR system, it is found that inclination of helical baffle angle has led to significant improvement in the outlet temperature of water. Figure 9 outlines temperature variation in WHR system. From Fig. 9, it is seen that shell side exhaust gas temperature drops from 500 °C to 180 °C and heat given by the exhaust is picked up by the water so water temperature rise is seen from 30 °C to 92 °C. Figure 10 shows the variation of outlet temperature of water versus helical baffle angle. From the above analysis, outlet temperature of water is found to be 92 °C with

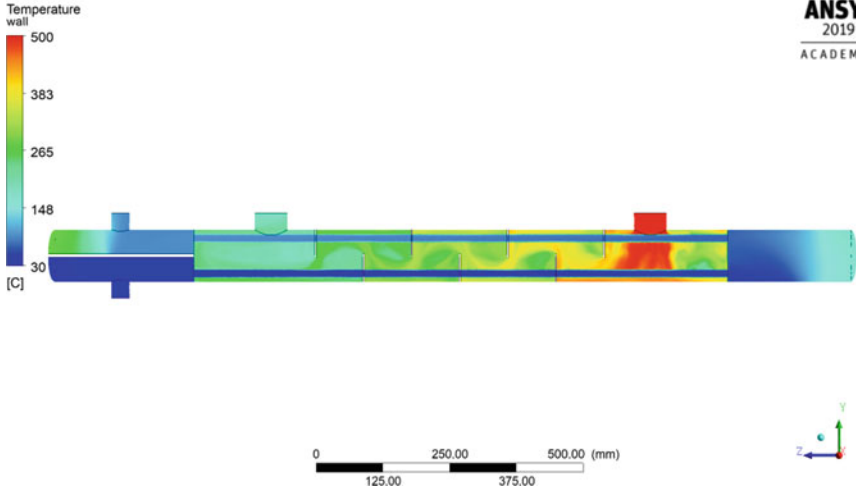


Fig. 9 Variation of temperature in the WHR

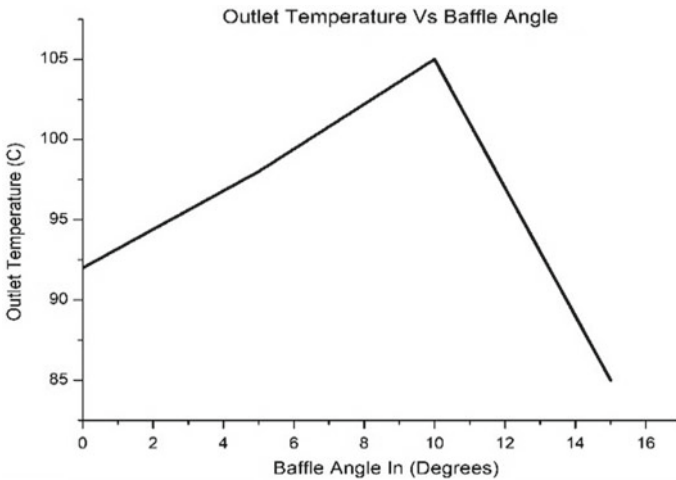


Fig. 10 Outlet Temperature of water versus Baffle inclination angle

conventional segmental baffle. If the helical baffle angle is increased to 10°, outlet temperature of water increases to 105 °C and with further increase in helical baffle angle the outlet water temperature drops. The reason behind the decrease in the outlet temperature beyond 10° inclinations is the higher pressure drop and less residential time available on the shell side. Therefore, the aim is to increase residential time and find an optimum angle. In the present case, it is found to be 10°.

5.2 Pressure Variation

It is prevalent to use baffles on the shell side of WHR. This ensures ‘crossflow’ conditions and promotes the shell side heat transfer coefficient. Pressure varies appreciably along with the baffles of WHR. Hence, it is crucial to analyze the variation in the pressure along with the baffles. Pressure variation in WHR is shown in Fig. 11. From Fig. 12, it is observed that pressure decreases as the exhaust gas moves across WHR. However, pressure drop variation in WHR along tube side is negligible. At the entry of WHR on the shell side, the pressure is around 0.2 bar and close to the exit, the pressure is around 0.11 bar. The total pressure drop across the WHR on shell side is 0.09 bar. The variation of pressure drop with a helical baffle angle is presented in Fig. 13.

The pressure gradually decreases with the increase in helical baffle angle. Numerical analysis was carried out in MATLAB to analyze the pressure drop for various inclinations which is compared to the segmental baffle. In the case of segmental baffle with 37% cut, the pressure drop is approximately around 0.1 bar whereas in the case of helical baffles, the pressure drop goes on decreasing with an increase in helical baffle angle and pressure drop values for 5° 10° and 15° helical baffle angle are 0.08, 0.06, and 0.003 bar respectively.

Pressure drop variation for shell-and-tube side is shown in Fig. 14. In contrast to the shell side, flow on the tube side is better streamlined, and resulting in a lower pressure drop. It has been observed that pressure drop variation for shell side is more than the tube. It is due to the higher rate of turbulence generated at the shell side that wall roughness creates a barrier for pressure drop.

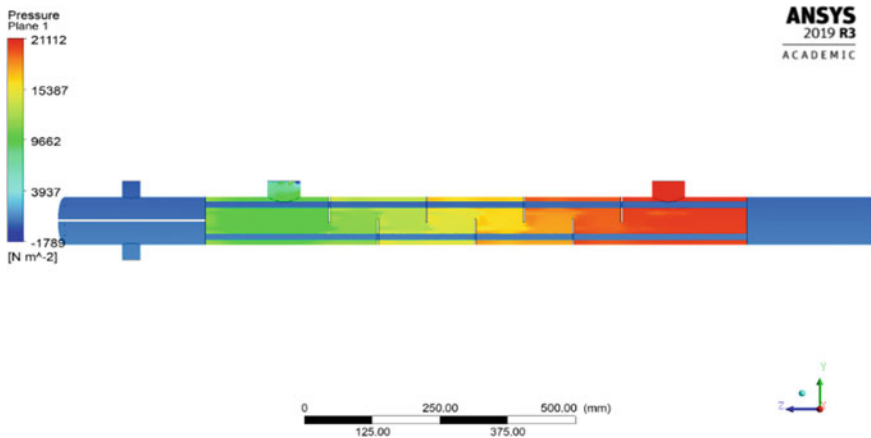


Fig. 11 Variation of pressure in the WHR

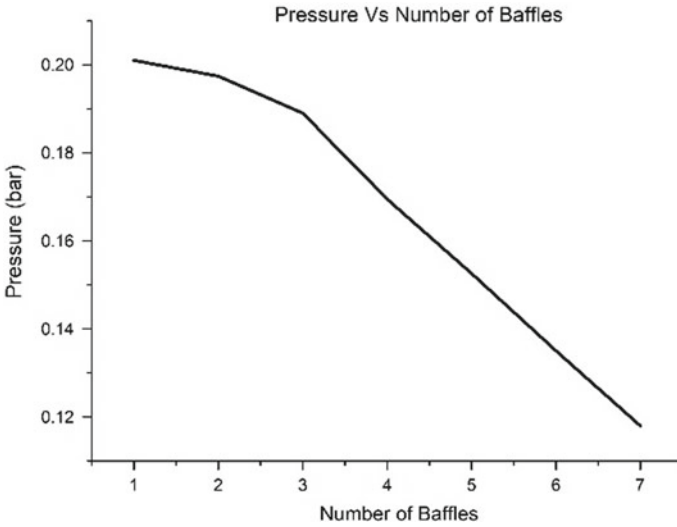


Fig. 12 Pressure variation versus No of baffles

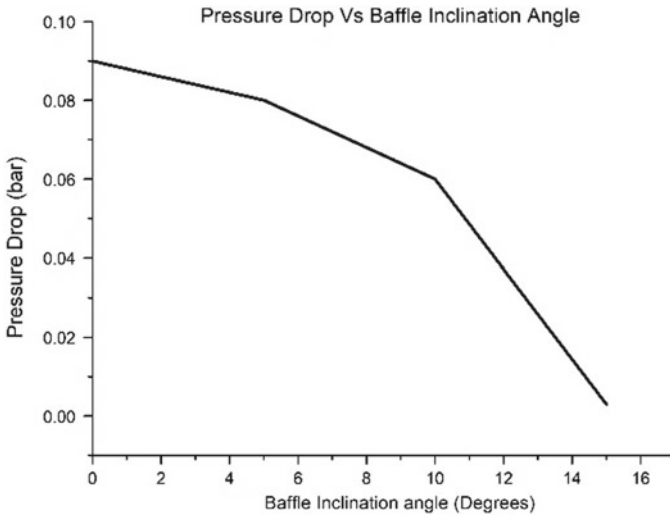


Fig. 13 Pressure drop versus Baffle inclination angle

5.3 Velocity Variation

The velocity profile is studied to understand the flow distribution across the cross-section of WHR. From Figs. 15 and 16, it is observed that there is not much variation in tube side velocity as compared to shell side velocity, as the magnitude of the shell

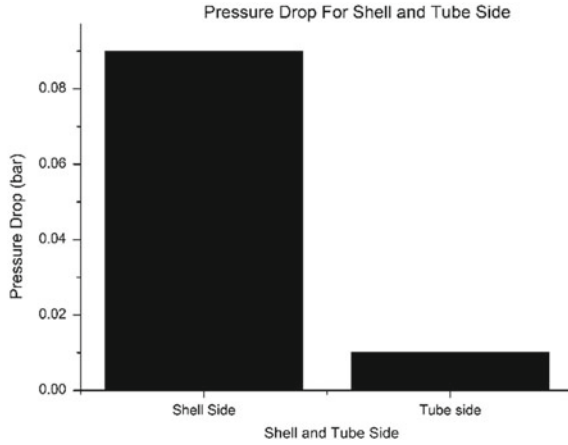


Fig. 14 Pressure drop shell-and-tube side

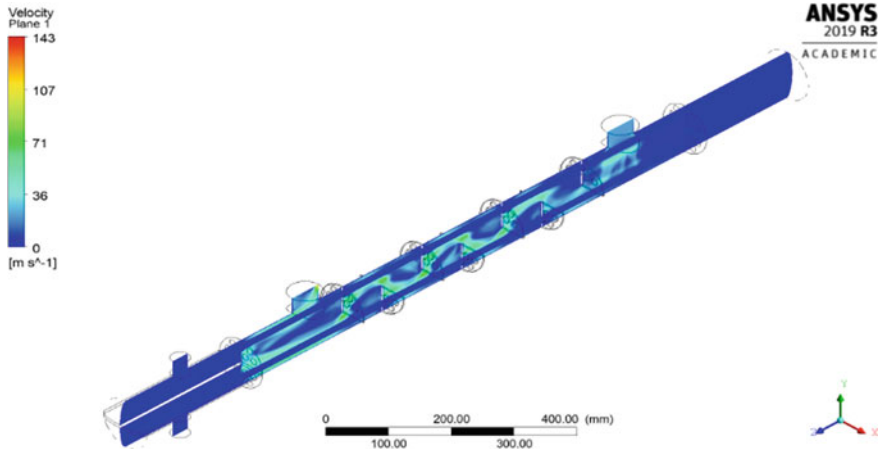


Fig. 15 Shell side velocity variation

side velocity is very high compared to the tube side velocity. Tube side velocity streamline contour plot shows the movement of tube side fluid from inlet to outlet.

5.4 Effectiveness of WHR

Heat exchanger effectiveness is defined as the ratio of the actual heat transferred to the maximum possible heat transfer. This WHR system will be operated in the cold regions where the temperature of water drops to $1\ ^\circ C$. From Fig. 17, it is observed

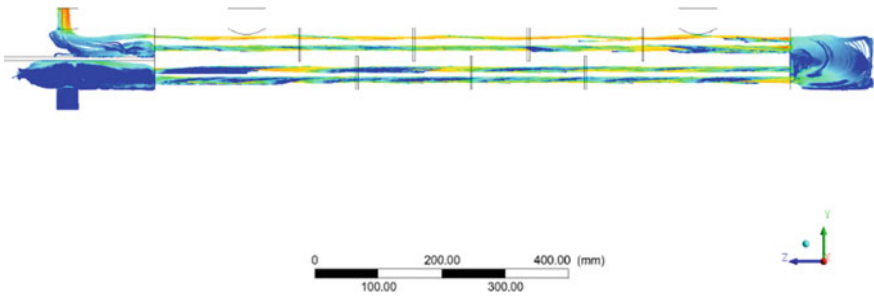


Fig. 16 Tube side velocity variation

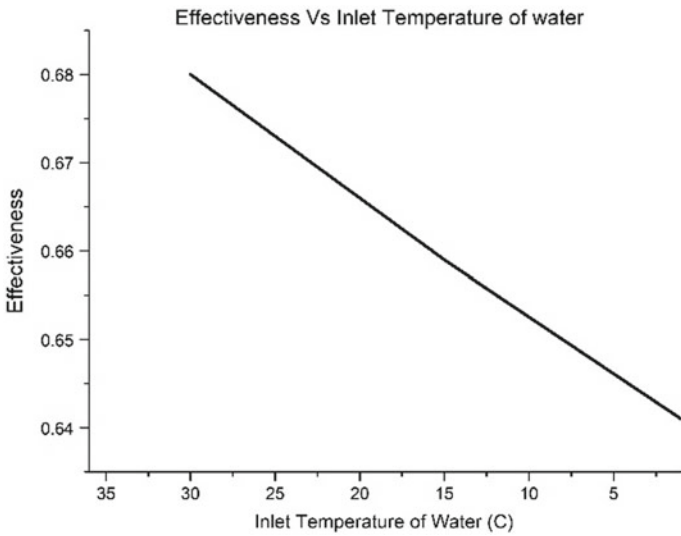


Fig. 17 Effectiveness versus Inlet temperature of water

that as inlet temperature of water decreases from 30 °C to 1 °C, the corresponding drop in effectiveness is just 6%. So, the proposed WHR integrated with DG set can be effectively implemented in high altitude area where water temperature is close to 1 °C in winter season.

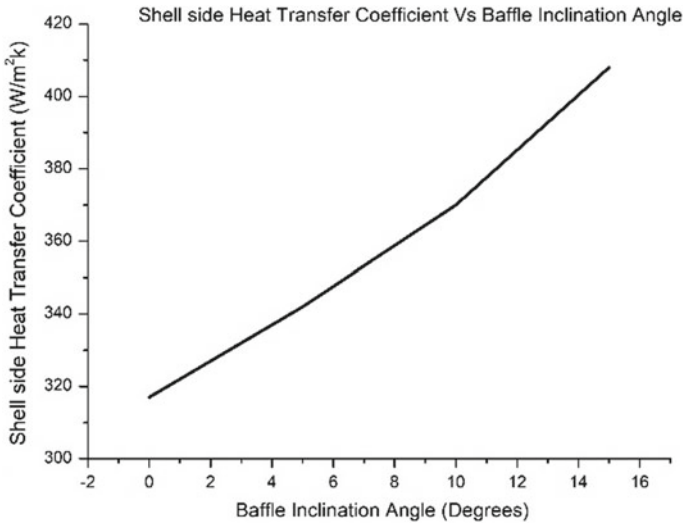


Fig. 18 Shell side heat transfer coefficient versus Helical baffle angle

5.5 Shell Side Heat Transfer Coefficient

Shell side heat transfer coefficient versus helical baffle angle is shown in Fig. 18. It is observed that the shell side heat transfer coefficient increases as the baffle inclination angle increases. It was stated earlier that with the rise of baffle inclination angle, the decrease in pressure drop is appreciable, and shell side heat transfer coefficient increases in the small inclination angle region. The overall effect of increasing heat transfer coefficient and a decrease in pressure drop is seen optimal at 10° baffle inclination angle in terms of outlet water temperature (105 °C).

6 Conclusion

- Heat energy harnessed from the exhaust of DG set of 50 kW was estimated to be 27 kW which was used for targeted water heating up to 80 °C and above.
- For the given heat duty of 27 kW, WHR design parameters based on Kern's algorithm are in good agreement with the Aspen Tech software design parameters.
- CFD analysis of WHR with segmental baffle and varied helical baffle (5°, 10° and 15°) was carried out and it was found that 10° as an optimum helical baffle angle which gives least pressure drop, optimum heat transfer coefficient, and maximum outlet temperature of the water.
- For conventional baffle segmental WHR effectiveness obtained is 0.79, whereas for 10° helical baffle inclination angle effectiveness is 0.96.

- The analysis shows that the effectiveness predicted by CFD simulation with 10° helical baffled WHR is 15% higher than segmental baffled WHR.
- Based on the CFD analysis, it has been observed that pressure drop on shell side at DG set rated capacity was 0.09 bar and it is much lower than the allowable limit of 0.1 bar hence, it will not create any impact of backpressure on DG set performance.
- Pressure drop obtained based on CFD analysis and Aspen Tech software is in good agreement with each other which indicates that CFD analysis was rightly implemented.

References

1. Z. Sahin, O. Durgun, C. Bayram, Experimental investigation of gasoline fumigation in a single-cylinder direct injection (DI) diesel engine. *Energy* **33**, 1298–1310 (2008)
2. K. Sudheesh, J.M. Mallikarjuna, Diethyl ether as an ignition improver for biogas homogeneous charge compression ignition (HCCI) operation e an experimental investigation. *Energy* **35**, 3614–3622 (2010)
3. D.T. Hountalas, G.C. Mavropoulos, T.C. Zannis, V. Schwarz, Possibilities to achieve future emission limits for HD DI diesel engines using internal measures, in *SAE Technical Paper*, vol. 2005-01-0377, SAE, Detroit, MI, USA (2005)
4. D.T. Hountalas, T.C. Zannis, G.C. Mavropoulos, Potential benefits in heavy duty diesel engine performance and emissions from the use of variable compression ratio, in *SAE Technical Paper*, Detroit, MI, USA (2006)
5. I. Taymaz, An experimental study of energy balance in low heat rejection diesel engine. *Energy* **31**, 364–371 (2006)
6. C. Yu, K.T. Chau, Thermoelectric automotive Exhaust heat energy recovery using maximum power point tracking, *Energy Convers. Manage.* **50**, 1506–1512 (2009)
7. F. Stabler, Automotive applications of high efficiency thermoelectric, in *DARPA/ONR/DOE High Efficiency Thermoelectric Workshop*, pp. 1–26 (2002)
8. E.H. Wang, H.G. Zhang, B.Y. Fan, M.G. Ouyang, Y. Zhao, Q.H. Mu, Study of working fluid selection of organic Rankine cycle (ORC) for engine Exhaust heat recovery. *Energy* **36**, 3406–3418 (2011)
9. F. Yüksel, M. Ceviz, Thermal balance of a four stroke SI engine operating on hydrogen as a supplementary fuel. *Energy* **28**, 1069–1080 (2003)
10. T. Wang, Y. Zhang, Z. Peng, G. Shu, A review of researches on thermal exhaust heat recovery with Rankine cycle. *Renew. Sustain. Energy Rev.* **15**, 2862–2871 (2011)
11. M. He, X. Zhang, K. Zeng, K. Gao, A combined thermodynamic cycle used for Exhaust heat recovery of internal combustion engine. *Energy* **36**, 6821–6829 (2011)
12. J. Fu, J. Liu, C. Ren, L. Wang, B. Deng, Z. Xu, An open steam power cycle used for IC engine exhaust gas energy recovery. *Energy* **44**, 544–554 (2012)
13. S. Jiangzhou, R.Z. Wang, Y.Z. Lu, Y.X. Xu, J.Y. Wu, Experimental study on locomotive driver cabin adsorption air conditioning prototype machine. *Energy Convers. Manage.* **46**, 1655–1665 (2005)
14. T.C. Hung, M.S. Shai, B.S. Pei, Cogeneration approach for near shore internal combustion power plants applied to seawater desalination. *Energy Convers. Manage.* **44**, 1259–1273 (2003)
15. P. Diehl, F. Haubner, S. Klopstein, F. Koch, Exhaust heat recovery system for modern cars. *SAE Trans.* **110**, 988–998 (2001)

16. D. Hountalas, C. Katsanos, D. Kouremenos, E. Rogdakis, Study of available exhaust gas heat recovery technologies for HD diesel engine applications. *Int. J. Altern. Propul.* **1**, 228–249 (2007)
17. D.T. Hountalas, C. Katsanos, V. Lamarinis, *Recovering Energy from the Diesel Engine Exhaust Using Mechanical and Electrical Turbocompounding*. SAE Technical Paper, pp. 1556–1563 (2007)
18. V. Dolz, R. Novella, A. García, J. Sánchez, HD Diesel engine equipped with a bottoming Rankine cycle as an Exhaust heat recovery system. Part 1: study and analysis of the Exhaust heat energy. *Appl. Therm. Eng.* **36**, 269–278 (2012)
19. W.M.S.R. Weerasinghe, R.K. Stobart, S.M. Hounsham, Thermal efficiency improvement in high output diesel engines a comparison of a Rankine cycle with turbo-compounding. *Appl. Therm. Eng.* **30**, 2253–2256 (2010)
20. J.C. Bass, N. Elsner, F. Leavitt, *Performance of the 1 KW Thermoelectric Generator for Diesel Engines*. IOP (Institute of Physics) Publishing Ltd, pp. 295–296 (1995)
21. F. DiBella, L. DiNanno, M. Koplow, *Laboratory and On-highway Testing of Diesel Organic Rankine Compound Long-haul Vehicle Engine*. SAE Technical Papers (1983)
22. E. Doyle, L. DiNanno, S. Kramer, *Installation of a Diesel-organic Rankine Compound Engine in a Class 8 Truck for a Single-vehicle Test*. SAE Technical Papers (1979)
23. P. Patel, E.F. Doyle, *Compounding the Truck Diesel Engine with an Organic Rankine-cycle System*. SAE Technical Papers (1976)
24. S.E. Aly, Diesel engine Exhaust-heat power cycle. *Appl. Energy* **29**, 179–189 (1988)
25. The capture of Heat Energy from Diesel Engine Exhaust, Final Report, Arctic Energy Technology Development Laboratory, Institute of Northern Engineering, University of Alaska Fairbanks. November (2008)

Optimization of Solar Hot Water Storage Tank Performance During Charging Process Using Buckingham's Theorem



Mahesh V. Kulkarni, Dheeraj S. Deshmukh, S. P. Shekhawat,
and M. S. Deshmukh

Nomenclature

L	Length of storage tank
D	Diameter of storage tank
V	Volume of storage tank
C_p	Specific heat of water in $\frac{J}{kgK}$
ρ	Density of water in Kg/m^3
U	Overall heat transfer coefficient in W/m^2K
β	Fluid Thermal expansion Coefficient per degree K
Q_s	Heat supplied in J
t_M	Mean layer temperature in tank in $^{\circ}C$
T_M	Mean layer temperature in tank in K
$g\beta\Delta t$	Buoyant force parameter m/sec^2
Δt	Thermal Stratification (temperature difference between top & bottom layer in tank)
T_1	Temperature of Layer 1 (Top)
T_2	Temperature of Layer 2
T_3	Temperature of Layer 3
T_4	Temperature of Layer 4
T_5	Temperature of Layer 5 (Bottom)

M. V. Kulkarni (✉) · S. P. Shekhawat
Department of Mechanical Engineering, SSBT's College of Engineering and Technology,
Bambhori, Jalgaon 425 001, India

D. S. Deshmukh
Department of Mechanical Engineering, G. H. Rasoni College of Engineering, Nagpur, India

M. S. Deshmukh
Department of Mechanical Engineering, AISSMS, College of Engineering, 1-Kennedy Road,
Pune 411001, India

T_6	Temperature at collector inlet
T_7	Temperature at collector outlet
T_L	Load Temperature
π_{a1}	Dependent π term
π_{a2}	Independent π term for five Variables $U, C_p, \rho, V,$ and $g\beta\Delta T$
π_{a3}	Independent π term for four Variables $Q_s, \rho, V,$ and $g\beta\Delta T$
Z	Maximization function
$X_1 \& X_2$	Independent variable in maximization function

1 Introduction

A major potential demand side management asset within energy systems is defined by domestic hot water tanks. It is necessary to maintain a stratified temperature distribution during operation to perform effectively as energy storage devices; this paper outlines experimental and numerical work carried out to understand the impact of wall material specification on de-stratification inside domestic hot water tanks. Armstrong et al. [1] discussed improving the energy storage capability of hot water tanks through wall material specification. Castell et al. [2] discussed various dimensionless numbers used to characterize stratification in water tanks for discharging at low flow rates. In order to examine the effect of the location of the submerged coil heat exchanger within a storage tank on the charging and discharge output of the hot water tank, tests have been carried out. To evaluate the performance of hot water tanks, discharge efficiency and charging efficiency were implemented to evaluate. Li [3] discussed a study on performance of storage tanks in solar water heater system in charge and discharge progress. Van Berkel [4] studied important aspects of short-term thermally stratified energy storage, thermocline mixing, and thermocline thickness, analytically, experimentally, and numerically. Ekici et al. [5] developed a new solar radiation estimation model based on Buckingham theorem. Kalogirou et al. [6] used an Artificial Neural Network (ANN) to predict the output of a solar water heater of the thermosyphon type with the minimum input data. This is calculated in terms of the usable energy and the increase in water temperature. Kalogirou et al. [7] trained to predict results from examples, are fault tolerant, are able to deal with non-linear problems, and once trained can perform prediction at high speed to predict o flat-plate collector performance parameter using artificial neural networks. Fan et al. [8] presented numerical investigations of thermal stratification in a vertical cylindrical hot water tank established by standby heat loss from the tank. Dimensionless analysis technique using Buckingham π theorem is useful in heat transfer and fluid mechanics [9, 10]. The stratification generally took place at very low circulating fluid rate. Hence, an analysis of storage tank with and without stratification was discussed [11, 12]. All the observations of dataset cannot be exactly the same as their arithmetic mean (AM). Variability of observations around AM is measured by standard deviation. Similarly in regression, all Y-values cannot be the same as

predicted Y-values. Variability of Y-values around prediction line is measured by standard error [13] which clarified the artificial neural network implementations in various solar thermal systems by Sharma et al. [14]. Kulkarni et al. [15] determined the water replenishment profile (i.e., the quantity of the cold makeup water to be supplied to the storage tank over a day) that optimizes the overall system. Kalogirou et al. [16] optimized solar systems using artificial neural networks and genetic algorithms. Kalogirou et al. [17] explained the solar water heater's performance prediction using artificial neural networks. In order to increase the thermal stratification efficiency of hot water storage tanks, Kulkarni et al. [18] created an advanced flat-plate collector and storage volume. Linear programming problem optimization technique and regression equations solver in MATLAB was given by [19, 20].

An exhaustive literature survey was carried out regarding performance, modeling, and optimization of solar hot water storage tank performance. Previous research mainly focused on performance parameters and different prediction techniques but optimization is yet to be found during the charging process based on scientific fact. In this work, a simple and realistic mathematical modeling was developed during the charging process to study the performance of a solar hot water storage tank. Further mathematical modeling was compared with ANN modeling and optimized by linear programming problem (LPP). A mathematical model based on experimental data makes the model realistic, easy to analyze, and set optimal conditions based on scientific knowledge during the charging process which is a unique advantage of this research.

2 Experimental Setup

The experimental setup consists of a hot water storage tank 125-L capacity and a flat plate collector of area 2.079 m². The hot water storage tank is made up of a Mild Steel sheet of 2 mm thickness and thermal conductivity 35 W/m K, 50 mm thickness of puff insulation, and an outer-cladding cover of Mild Steel sheet. The collector is made up of aluminum casing of 1.2 mm thickness; GI color coated back covers 1.1 × 1.94 × 0.0005 m, header tube 0.025 m diameter and 1.05 m length, copper riser tube 0.012 m diameter and 1.89 m length, top cover toughened glass of 0.0004 m thick and digital indicator with PT 100 temperature sensor installed for temperature measurement at the various location as shown in Fig. 1.

3 Development of Mathematical Modeling

The process of mathematical modeling carried out in this work is divided into two main stages—dimensional analysis and regression analysis. Buckingham's theorem uses dimensional analysis to provide fundamental mathematical simulation concepts by reducing the number of parameters in the equations, making qualitative research simpler. It can be reduced to a relationship between a full set of dimensionless

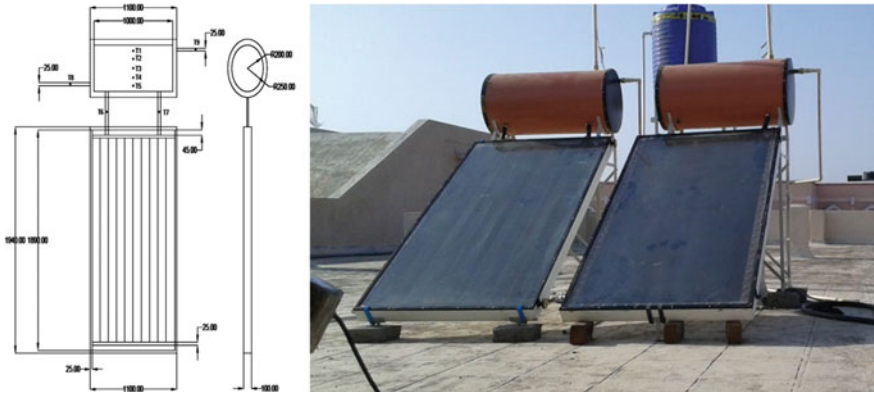


Fig. 1 Experimental set up details

products if an equation is dimensionally homogeneous. Buckingham has claimed that in a complete set, the number of dimensionless products is equal to the total number of variables minus the number of simple dimensions in the problem.

3.1 Selection of Variables

The numbers of repeating variables are equal to the number of fundamental dimensions of the problem. The choice of repeating variable is governed by the following considerations:

- 1 As far as possible, the dependant variable should not be selected as a repeating variable.
- 2 The repeating variable should be chosen in such way that one variable contains geometric property (Length, Diameter, Volume), other variables contain flow property (Velocity, Acceleration), and the third variable contains fluid properties (Dynamic viscosity μ , Density ρ and Kinematic viscosity ν) and thermodynamic property (Conductivity k and Connectivity h) in case of heat transfer problem.
- 3 The repeating variable selected should not form a dimensionless group.
- 4 The repeating variable together must have the same number of fundamental dimensions.
- 5 No two repeating variables should have the same dimension.

The load temperature (T_L) of solar hot water storage tank depends upon volume V , Buoyant force parameter, specific heat C_p density ρ , Overall Heat Transfer Coefficient U and heat supply Q_s . Express the functional relationship between these variables and Load temperature (T_L). Using Buckingham's π theorem following Table 1 gives the list and brief details of important operating variables of a solar hot water storage tank under consideration (Table 2).

Table 1 Tabular summary of variables (T_L , V , $g\beta\Delta T$, C_p , ρ , U , Q_s) for determination of π term

Sr. No	Parameters	Symbol	Units	LMT θ
1	Load temperature	T_L	$^{\circ}\text{C}$	θ
2	Volume	V	m^3	L^3
3	Heat supply	Q_s	J	ML^2T^{-2}
4	Flow property	$g\beta\Delta T$	m/sec^2	LT^{-2}
5	Specific heat	C_p	$\text{J}/\text{kg K}$	$\text{L}^2\text{T}^{-2}\theta$
6	Density	ρ	Kg/m^3	ML^3
7	Overall heat transfer coefficient	U	$\text{W}/\text{m}^2 \text{K}$	$\text{MT}^{-3}\theta^{-1}$

Table 2 List of independent and dependent π terms

Sr. No	Description of π terms	π terms and their equations
1	Π term for response variable T_L and three independent Variables C_p , V & $g\beta\Delta T$	$\pi_{a1} = \frac{C_p T_L}{\sqrt[3]{V g \beta \Delta T}}$
2	Π term for five independent variables U , C_p , ρ , V , and $g\beta\Delta T$	$\pi_{a2} = \frac{U}{C_p \rho V^{\frac{1}{6}} \sqrt{g \beta \Delta T}}$
3	Π term for four independent variables Q_s , ρ , V , and $g\beta\Delta T$	$\pi_{a3} = \frac{Q_s}{\rho V^{\frac{4}{3}} g \beta \Delta T}$

3.2 Formation of Mathematical Model

Using the theorem of Buckingham, the relationship between Π_1 , Π_2 , and Π_3 is specified as Eq. 3.1. Π_1 primary variables are written as the product of the powers of the other two products Π_2 and Π_3 . For this phenomenon, a possible exact mathematical type may be

$$\pi_{a1} = K \pi_{a2}^B \pi_{a3}^C \tag{3.1}$$

The dimensionless variables constructed from a functional analysis are now used to form a right dimensional relationship, one that is homogeneous, as the regression variables. To find and match the undisclosed relationship, all the power of conventional data analysis and regression is used.

$$\pi_{a1} = 2.693 \times 10^{10} \pi_{a2}^{0.7694} \pi_{a3}^{-0.0002} \tag{3.2}$$

Development of Eq. 3.2, its formation and different techniques are detailed in Appendix 1 (Fig. 2).

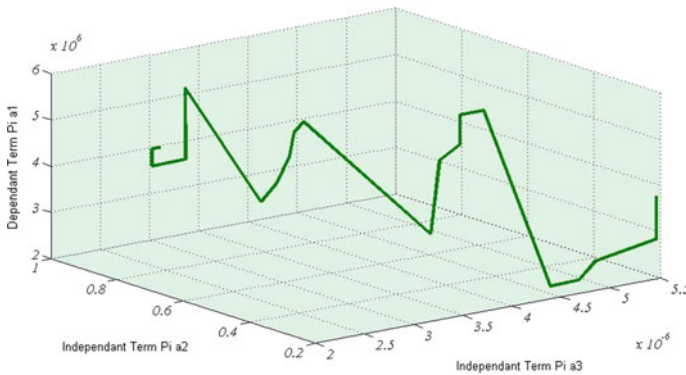


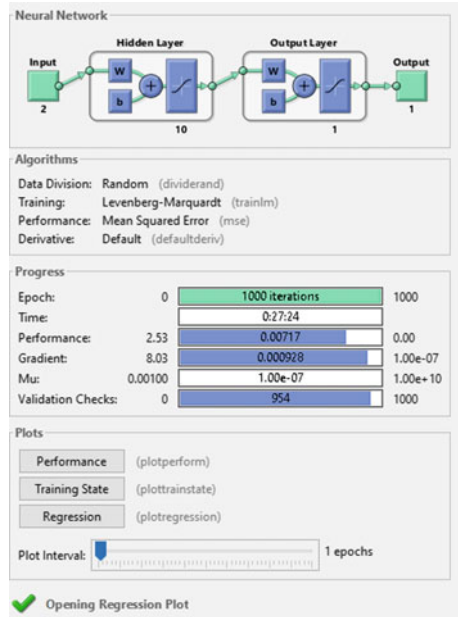
Fig. 2 3D Plot showing variation of π_{a1} with independent Pi terms π_{a2} and π_{a3}

4 Artificial Neural Network Modeling

One of the main issues in research is the prediction of future results. The experimental data-based modeling achieved this through mathematical models for the dependent π terms. Models using the artificial neural network are also planned to evolve in certain complex phenomena involving non-linear systems (ANN). It is possible to test the performance of this network by comparing it with observable data and data calculated from mathematical models. The designer needs to understand the fundamental trends to create ANN. When this is completed, preparation is mostly a fine-tuning method for the network.

Three layers of nodes, viz., consist of an ANN. The input layer, the invisible layer, and the output layer use nodes to represent the neurons in the brain and these layers are related to each other in processing layers. ANN's basic mapping relies on its architecture and synaptic weight values between the neurons. As such, ANN is a dynamically distributed representation and transformation that operates simultaneously and has distributed power over several highly interconnected nodes. Using these black box notions, ANN was made. Much like the human brain learns with the repetition of related stimuli, an ANN trains itself generally without a priory theory that directs or limits a relationship between inputs and outputs within historical pairs of input and output results. The purpose of the ANN model is to create a solution by allocating the weights in such a way that the true relationship between input and output actually exists. The process between the input and output neurons is efficiently interpolated by the ANN during training. An clear definition of this function is not constructed by ANNs. In structural pattern recognition, the prototypical application of ANN. In such a task, the ANN is faced with a set of characteristics and the input function pattern must be classified as belonging to one or more classes. In such instances, all the necessary information is presented to the network concurrently. In order to find the one that will result in the best overall results, various network architectures have been studied. Figure 3 displays the architecture that has produced

Fig. 3 Neural network architecture employed



the best performance. This is a forward feed architecture comprising 10 hidden slabs. Figure 3 indicates the activation functions used in both slabs.

The NNTOOL method was used. For the charging model of hot water storage tanks in solar water heating systems, as mentioned above, a total of 100 readings were obtained. 95 readings were used from this collection for the training of the network and 5 were used as network evaluation and validation. From the 100 readings available, both the testing and validation datasets were randomly chosen.

5 Optimization of Mathematical Model

The model (Eq. 3.2) has been developed for the investigation of the hot water storage tank performance during charging process. The ultimate objective of this work is not merely developing the model but to find out the best set of variable values, which will result in either maximization of the objective function. In this case load temperature is a basic dependent variable of hot water storage tank performance model. The objective function identified here is naturally maximization of the load temperature. The variable T_L is present in the dependent π term π_{d1} . Naturally the objective function will be to maximize π_{d1} . The model has non-linear form; hence it is necessary to convert it into a linear form for optimization purpose. This can be achieved by taking the log of both the sides of the model. To maximize this linear function uses the linear programming technique as shown below.

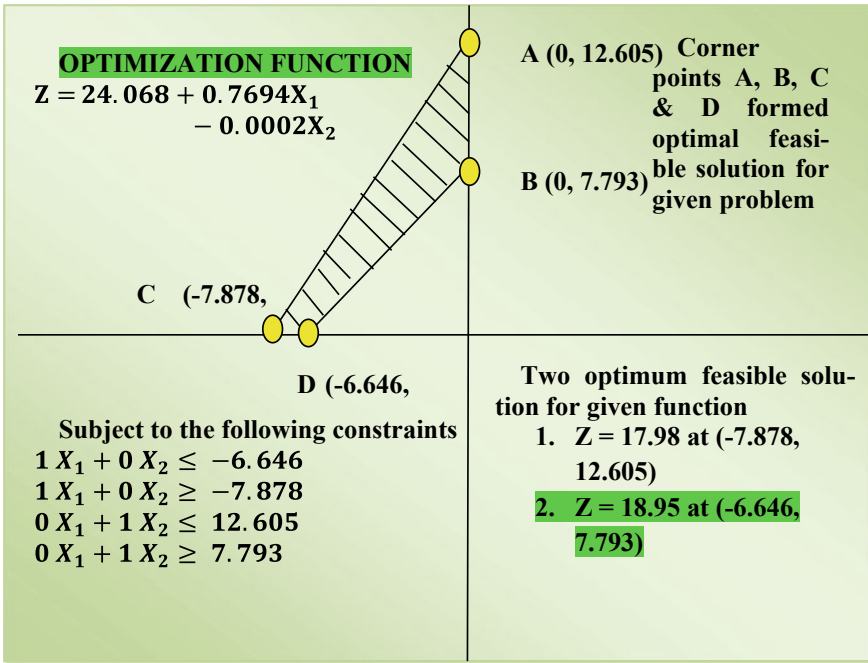


Fig. 4 LPP optimal solutions

$$\pi_{a1} = 2.693 \times 10^{10} * \pi_{a2}^{0.7694} * \pi_{a2}^{-0.0002} \tag{5.1}$$

$$Z = 24.068 + 0.7694X_1 - 0.0002X_2 \tag{5.2}$$

Thus, equation will be the objective function for the optimization or to be very specific for maximization of the load temperature, for the purpose of formulation of the linear programming problem. The next task is to define the constraints for the problem which is detailed in APPENDIX 2. The LPP solutions are shown below (Fig. 4 and Table 3).

6 Results/Validation

Mathematical model to study the performance of hot water storage tank during charging process developed successfully and expressed in Eq. 6.1

$$\frac{C_p T_L}{\sqrt[3]{V g \beta \Delta T}} = 2.693 X 10^{10} \left(\frac{U}{C_p \rho V^{\frac{1}{6}} \sqrt{g \beta \Delta T}} \right)^{0.7694} \left(\frac{Q_s}{\rho V^{\frac{4}{3}} g \beta \Delta T} \right)^{-0.0002} \tag{6.1}$$

Table 3 Sensitivity report

Cell	Name	Final value	Reduced value	Objective coefficient	Allowable increase	Allowable decrease
Adjustable cells						
B4	Independent variables X_1	-6.646	0	0.769	1.00E+30	0.769
C4	Independent variables X_2	7.793	0	-0.0002	0.0002	1.00E+30
Cell	Name	Final value	Shadow value	Constraint R.H. Side	Allowable increase	Allowable decrease
Constraints						
B13	$C_1 \times 1$	-6.646	0.769	-6.646	1.00E+30	1.232
B14	$C_2 \times 1$	-6.646	0	-7.878	1.232	1.00E+30
B15	$C_3 \times 1$	7.793	0	12.605	1.00E+30	4.812
B16	$C_4 \times 1$	7.793	-0.0002	7.793	4.812	1.00E+30

Equation 6.1 is verified with all the observed readings. The accuracy of the equation produced was found to be 97.45%. With each reading, the error was measured. For experimental and measured values, a coefficient of correlation was determined. It has been observed that the mean standard error is 2.086. It is obvious from Fig. 5 that the test’s p-value is less than 0.05, so the null hypothesis is dismissed and we infer that there is evidence of a linear association.

After a satisfactory degree of sample, target data mapping was accomplished in the artificial neural network; a collection of entirely unknown observed test data was added for verification. The training data was collected with exceptional accuracy. As seen in Fig. 6, the coefficient for multiple determinations (R–values) is 0.99768, 0.94491, 0.97869, and 0.98779 referring to preparation, validation, and testing and overall. The fact that all values are close to unity indicates that the mapping was

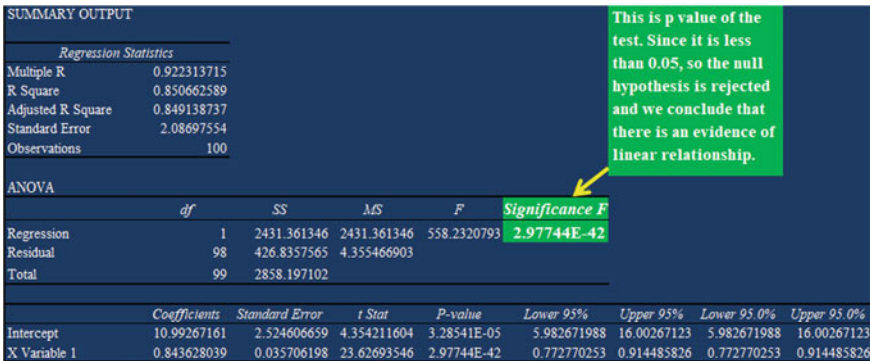


Fig. 5 Regression summary output for computed and Observed value

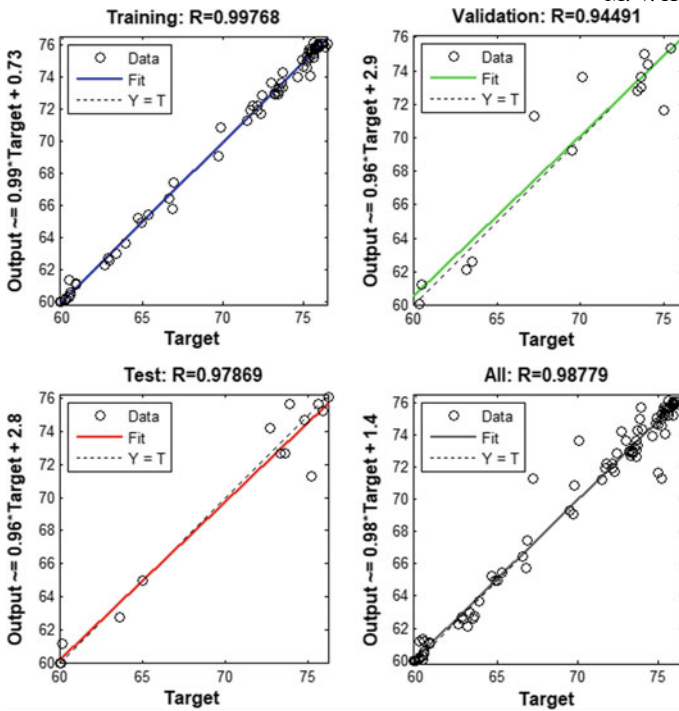


Fig. 6 Performance and testing status of ANN mapping

performed at a satisfactory level. Figure 7 displays the success graph and ANN training status. The findings obtained from ANN testing and validations are almost satisfactory, showing that the algorithm used for network and mathematical modeling

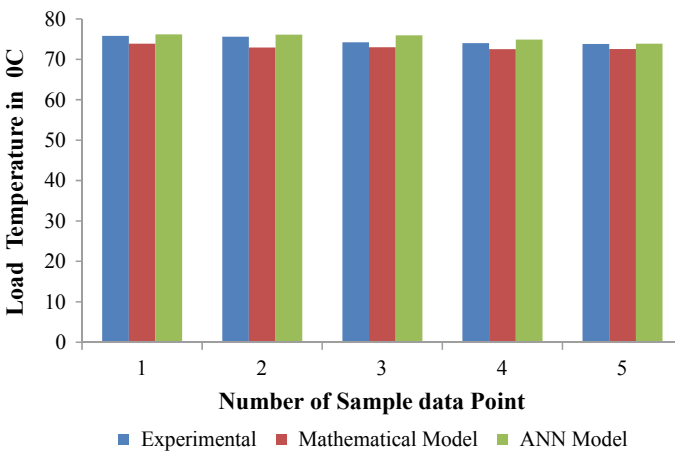


Fig. 7 Comparison of load temperature by experiment, mathematical, and ANN model

Table 4 Comparison of load temperature by experiment, mathematical modeling, and ANN

Input parameters			Output parameters and maximum difference load temperature			
Thermal stratification ΔT in $^{\circ}C$	Heat supply Q_s in J	Experimental load temperature	Correlation proposed load temperature	ANN model load temperature	Max difference correlation proposed	Max difference ANN
3.6	332,937.8549	75.8	73.9	76.16	1.9	0.361819
3.4	204,708.2534	75.6	72.9	76.10	2.7	0.499645
3.4	152,309.1737	74.2	73.0	75.96	1.2	1.763947
3.3	88,102.33895	74	72.5	74.88	1.5	0.880165
3.3	47,896.95156	73.8	72.5	73.88	1.3	0.078365

for hot water storage tank efficiency is accurate. Figure 7 indicates the similarities between the suggested correlation, ANN Model and experimental results for load temperature in Table 4 and Bar chart.

7 Conclusions

The following conclusion can be obtained from the present work and it is divided into four parts, i.e., formation of mathematical modeling, analysis with ANN simulation model, optimization of mathematical model, and appropriate new finding based on scientific fact.

- 1 Present work has shown the use of mathematical modeling based on the Buckingham π theorem. Regression analysis is performed to reveal the effectiveness of the model for 100 observations. The mean standard error is found to be 2.086 and the p-value of the test less than 0.05, so the null hypothesis is rejected which shows that there is evidence of a linear relationship, simplicity, and reliability of the mathematical modeling approach.
- 2 An Artificial Neural Network (ANN) trained to compare the mathematical model with a minimum of input data. Validation of mathematical modeling and ANN were performed with a sample of observed data. Maximum deviations of 2.7 and 1.76 $^{\circ}C$ were obtained, respectively.
- 3 Mathematical model performance was optimized by linear programming problem (LPP) and the optimization result shows that there are two optimal solutions of hot water storage tank during the charging process. The first optimum solution in LPP is $Z = 18.95$ @ $(-6.646, 7.793)$ and second optimal solution in LPP is $Z = 17.98$ at $(-7.878, 12.605)$. Dependant and independent pie terms in mathematical modeling help to find load temperature, thermal stratification, and heat supply at optimum condition.
- 4 In the early stage of charging after sunrise fresh cold water enters into a system that brings hot water temperature and thermal stratification in-tank set to a

minimum value is the first optimum solution. This is because of the chances to absorb solar heat at this stage is maximum. If a consumer tries to avoid the utilization of hot water at this early stage of charging the system will get maximum performance speedily. As the charging process goes ahead both hot water temperature and thermal stratification in the tank increase to reach maximum value, this is the second optimal solution. The top layer in-tank stagnates at a maximum temperature as a result bottom layer temperature starts to increase which decreases thermal stratification in the tank. Although the outside temperature at this stage is maximum and heat absorbs capacity after the second optimal condition reduces. So design engineer fraternity should focus to develop techniques and processes to retain the second optimal condition.

Experimentation Data

The device has been checked in Jalgaon Maharashtra, India. The experimental sample reading during the loading process is shown in Table 6. These were obtained from experiments carried out on a separate day and each observation at a daily interval of 30 min.

Appendix A: Development of Mathematical Model Using Bunckiggham Theorem

Using the theorem of Buckingham, the relationship between Π_1 , Π_2 , and Π_3 . Specified as Eq. 3.1. Π_1 Primary variables are written as the product of the powers of the other two products Π_2 and Π_3 . For this phenomenon, a possible exact mathematical type may be

$$\pi_{a1} = K \pi_{a2}^B \pi_{a2}^C \tag{A1}$$

Taking Natural logarithms

$$\log \pi_{a1} = \log k + b \log \pi_{a2} + c \log \pi_{a3} \tag{A2}$$

Let $Y = \log \pi_{a1}$, $X_1 = \log \pi_{a2}$ and $X_2 = \log \pi_{a3}$, $a = \log k$ and N be the number of observations. Using least square technique the Eq. A1 can be written as

$$\text{Let } Y = a + bX_1 + cX_2 \tag{A3}$$

Three equations for three unknown can be generated as under

$$\sum Y = Na + b \sum X_1 + c \sum X_2 \tag{A4}$$

$$\sum X_1Y = \sum X_1a + b \sum X_1^2 + c \sum X_1X_2 \tag{A5}$$

$$\sum X_2Y = \sum X_2a + b \sum X_1X_2 + c \sum X_2^2 \tag{A6}$$

The summations in the Eqs. A4, A5 and A6 are determined using the 100 experimental observations. Sample observation are shown in Table 5.

$$\begin{aligned} \Sigma Y &= 1825.787 \quad \Sigma X_1 = -748.159 \quad \Sigma X_2 = 1065.113 \quad \Sigma X_1Y = -13,650.509 \\ \Sigma X_1^2 &= 5609.47 \quad \Sigma X_1X_2 = -8006.795 \quad \Sigma X_2Y = 19,417.369 \quad \Sigma X_2^2 = 11,548.745 \end{aligned}$$

Coefficients are then determined using the Gauss Jordan process by solving simultaneous equations in three variables.

$$\begin{bmatrix} 1825.787 \\ -13650.509 \\ 19417.369 \end{bmatrix} = \begin{bmatrix} 100 & -748.159 & 1065.113 \\ -748.16 & 5609.47 & -8006.795 \\ 1065.113 & -8006.795 & 11548.745 \end{bmatrix} \begin{bmatrix} a \\ b \\ c \end{bmatrix}$$

$$x = 24.0168, 0.7694, -0.0002$$

$$Y = a + bX_1 + cX_2$$

$$Y = 24.068 + 0.7694X_1 - 0.0002X_2 \tag{A7}$$

Taking antilog of Eq. A7 the equation gets converted to the following.

$$\pi_{a1} = 2.693 \times 10^{10} \pi_{a2}^{0.7694} \pi_{a3}^{-0.0002} \tag{A8}$$

Table 5 Sample observations for modeling formulation

Sr No	Mean temperature of Layer T _m in K	Thermal expansion coefficient β per/K	Thermal stratification ΔT in °C	Heat Supply Q _s in J	π _{a1}	π _{a2}	π _{a3}
1	332.5	0.00301	1.8	9128.67	112,388,482	0.00087	2689.5
2	332.45	0.00301	1.3	9128.67	154,818,616	0.0012	3723.3
3	332.45	0.00301	1.1	16,218.9	182,663,017	0.00142	7818.0
4	332.7	0.00301	1.4	30,529.5	144,586,394	0.00111	11,571
5	334.9	0.00299	1.8	49,385.6	117,697,709	0.00087	14,655

Appendix B: Constraints for LPP

The restriction could be the limits established during the experiment for the multiple independent π terms involved in the function. The ranges for each independent π concept were established during the experimentation. Such ranges are the limits of the issue. Thus, for each individual π word as under, there would be two limitations.

Denote the independent maximum and minimal values π term π_{a2} by π_{a2max} and π_{a2min} . The first two limits to the problem can be obtained by taking log of these quantities and by substituting multiplier values for all other variables except the one under consideration equal to zero. Let the log of the limits be defined, as C_1 and C_2 . Then $C_1 = \log \pi_{a2max}$ and $C_2 = \pi_{a2min}$. Thus, each will have the two equations of the constraints as under

$$1X_1 + 0X_2 \leq C_1 \quad (A9)$$

$$1X_1 + 0X_2 \geq C_2 \quad (A10)$$

The other constraints are similarly found as given below

$$0X_1 + 1X_2 \leq C_3 \quad (A11)$$

$$0X_1 + 1X_2 \leq C_4 \quad (A12)$$

The maximum value of the Z and the set of values of the variables to reach this maximum value will be obtained after this linear programming problem has been overcome. The values of the independent term will then be derived by finding an antilog to the values of Z, X_1 , and X_2 . The exact values of the multipliers and the variables are found and replaced in the Eqs. A9 to A12, and the actual problem can be described below in this case. This can now be solved by using the MS solver available in MS excel as a linear programming problem.

Thus the actual problem is to maximize Z, where

$$Z = 24.068 + 0.7694X_1 - 0.0002X_2$$

Subject to the following constraints

$$1X_1 + 0X_2 \leq -6.646$$

$$1X_1 + 0X_2 \geq -7.878$$

$$0X_1 + 1X_2 \leq 12.605$$

$$0X_1 + 1X_2 \geq 7.793$$

LPP problem is formulated and MS solver found a solution. All constraints and optimality conditions are satisfied.

Appendix C: Modification/Conversion of The Experimental Data

The raw data obtained from Table 5 can be utilized only after modifying or converting this data in the desired form. The various values recorded in Table 5 are converted into desired form for performance analysis. The π terms connecting the performance parameter of solar water heating system involves the independent variables, i.e., C_p , ρ , V , U , and $g\beta\Delta T$ is π_{a2} . The equations for the independent π terms are given below

$$\pi_{a2} = \frac{U}{C_p \rho V^{\frac{1}{6}} \sqrt{g\beta\Delta T}}$$

The data related to this independent π term during the test is recorded and range for this π term is computed, as given below

$$\pi_{a2} = \frac{U}{C_p \rho V^{\frac{1}{6}} \sqrt{g\beta\Delta T}}$$

$$\pi_{a2Min} = 0.00037885$$

$$\pi_{a2Max} = 0.0015578$$

Similarly, using the dimensional equation for the π term π_{a3} , the data related to this independent Pi term during the test is recorded, and range for this π term is computed, as given below

$$\pi_{a3} = \frac{Q_s}{\rho V^{\frac{4}{3}} g\beta\Delta T}$$

$$\pi_{a3Min} = 2423.46$$

$$\pi_{a3Max} = 298220.333$$

Table 6 Experimental sample reading during day

Sr No	Day and time	Sensor	Location	Temperature in °C
1	Day 1 7.00 am	T ₁	Layer 1 (From Top)	60.4
		T ₂	Layer 2	60.2
		T ₃	Layer 3	59.3
		T ₄	Layer 4	58.9
		T ₅	Layer 5	58.6
		T ₆	Collector In	56
		T ₇	Collector out	56.6

Table 7 Training data set (SAMPLE) ANN

Input parameters		Output parameters
Thermal stratification ΔT in °C ΔT	Heat supply Qs in J	Load temperature
1.8	9128.67	60.4
1.3	9128.67	60.1
1.1	16,218.9	60
1.4	30,529.5	60.4
1.8	49,385.6	62.8

Appendix D: Data Selection for Experiment and ANN

Data from 100 experiments during the trial were used for the preparation of an artificial neural network. This variety of data was deemed necessary to allow the ANN to learn a wide range of cases. Out of a total of 100 datasets, 5 were randomly chosen and used for model validation and the remaining 95 for network training and research.

It is beneficial to reduce the amount of data needed for measurements in order to promote the work of designers. The data used for network training are those that often influence the efficiency of the system and can be easily accessed. These include load temperature in storage tank, thermal stratification, heat supply. Readings from actual tests have been used for network preparation and research. A sample of the system experimental observations and the system efficiency parameters considered as input and output to the neural network are shown in Tables 6 and 7, respectively. The network was educated using a wide variety of weather conditions.

References

1. P. Armstrong, D. Ager, I. Thompson, M. McCulloch, Improving the energy storage capability of hot water tanks through wall material specification. *Energy* **78**, 128–140 (2014). <https://doi.org/10.1016/j.energy.2014.09.061>
2. A. Castell, M. Medrano, C. Solé, L.F. Cabeza, Dimensionless numbers used to characterize stratification in water tanks for discharging at low flow rates. *Renew. Energy* **35**(10), 2192–2199 (2010). <https://doi.org/10.1016/j.renene.2010.03.020>
3. S. Li, Y. Zhang, K. Zhang, X. Li, Y. Li, X. Zhang, Study on performance of storage tanks in solar water heater system in charge and discharge progress. *Energy Procedia* **48**, 384–393 (2014). <https://doi.org/10.1016/j.egypro.2014.02.045>
4. J. Van Berkel, Mixing in thermally stratified energy stores. *Sol. Energy* **58**, 4, 203–211 (1996)
5. C. Ekici, I. Teke, Developing a new solar radiation estimation model based on Buckingham theorem. *Results Phys.* **9**, 263–269 (2018). <https://doi.org/10.1016/j.rinp.2018.02.064>
6. S.A. Kalogirou, S. Panteliou, A. Dentsoras, 99/03797 Modeling of solar domestic water heating systems using artificial neural networks. *Fuel Energy Abstr.* **40**(6), 399–400 (1999). [https://doi.org/10.1016/S0140-6701\(99\)99003-3](https://doi.org/10.1016/S0140-6701(99)99003-3)
7. S.A. Kalogirou, Prediction of flat-plate collector performance parameters using artificial neural networks. *Sol. Energy* **80**(3), 248–259 (2006). <https://doi.org/10.1016/j.solener.2005.03.003>
8. J. Fan, S. Furbo, Thermal stratification in a hot water tank established by heat loss from the tank. *Sol. Energy* **86**(11), 3460–3469 (2012). <https://doi.org/10.1016/j.solener.2012.07.026>
9. R.K. Bansal, *Fluid mechanics and hydraulic machine* Revised Ni. (Luxmi Publication (P) Ltd., New Delhi)
10. Dr. D S KUMAR, *HEAT AND MASS TRANSFER*, Seventh Ed. S.K.KATARIA & SONS.
11. S.P. Sukhatme, J.K. Nayak, *Solar energy principle of thermal collection and storage*, 3rd edn. (The McGraw-Hill Companies)
12. H.P. Garg, J. Prakash, *Solar energy fundamental and application*. 1st edn. (Tata McGraw-Hill)
13. C.R. Kothar, G. Garg, *Research methodology methods and techniques*. 3rd edn. (New Age International Publishers)
14. N. Sharma, M.K. Chauhan, R. Kumar, Applications of artificial neural network in solar thermal systems : a review, in *Proceedings of the National Conference on Trends and Advances in Mechanical Engineering*. (YMCA Univ. Sci. Technol. Faridabad, Haryana, 2012), pp. 188–194
15. G.N. Kulkarni, S.B. Kedare, S. Bandyopadhyay, Optimization of solar water heating systems through water replenishment. *Energy Convers. Manag.* **50**(3), 837–846 (2009). <https://doi.org/10.1016/j.enconman.2008.09.019>
16. S.A. Kalogirou, Optimization of solar systems using artificial neural-networks and genetic algorithms. *Appl. Energy* **77**(4), 383–405 (2004). [https://doi.org/10.1016/S0306-2619\(03\)00153-3](https://doi.org/10.1016/S0306-2619(03)00153-3)
17. S.A. Kalogirou, Performance prediction of a solar water heater using artificial neural networks, in *World Renewable Energy Congress*, (Elsevier Sci, 2000) pp. 749–754
18. M.V. Kulkarni, D.S. Deshmukh, S.P. Shekhawat, I.D. Patil, Solar water heating system using innovative flat plate collector and storage volume. *Int. J. Innov. Res. Sci. Eng. Technol.* **6**(1), 570–577 (2017)
19. P.K. Gupta, D.S. Hira, *Operations research*, 7th edn. (S.Chand Publication)
20. R. Pratap, *Getting started with MATLAB A quick introduction for scientists and engineers*. (Oxford, Oxford University Press, 2002)

Performance Analysis of Photovoltaic Module Using Microchannels and Nanofluids



S. M. Lawankar, Shoeb J. Inamdar , and Shubham K. Changole

1 Introduction

In present scenario solar energy is one of the promising sources of renewable energy that can be used in different ways like solar cooling, solar heating, and photovoltaic. The solar cell or PV module can generate electrical energy from sunlight with the aid of photovoltaic effect. PV module gets overheated due to associated thermal energy with solar radiation, due to which its performance is considerably limited. For 1 °C overheating over its evaluated value (normally 25 °C), the power output reduces by 0.5–0.6%. This dependence leads to an emerging concept of “cooling of PV module” [1, 2]. The cooling of PV module is achieved by heat dissipation [3, 4]. Different techniques/methods have been applied for the cooling of module to optimize its performance [5–7].

Krauter [8] studied thin film of liquid water nozzle flow over the panel surface. The result showed that the film reduced the surface temperature upto 22 °C with 10.3% increase in electrical yield. Royné and Dey [9] performed the experimental investigation on “effect of jet impingement cooling device technique for an array of dense packed PV module”. The investigation summarized that this method minimized the impact of overheating on electrical performance of PV module, hence found to be efficient for PV module cooling.

Abdolzadeh and Ameri [10] experimentally evaluated the effect of water spraying on the front surface of PV module on its performance. Moreover, Nizeticet al. [11] found that better performance of PV module can be achieved by spraying water on back and front surface of PV module. Similarly Bahaidarahet al. [12] investigated water cooling on the front and back surface to assess the performance of PV module using EES software. They found that module temperature has reduced from 37.8 to

S. M. Lawankar · S. J. Inamdar (✉) · S. K. Changole
Department of Mechanical Engineering, Government College of Engineering, Amravati,
Maharashtra, India

35 °C by front surface cooling. In addition, the back surface cooling magnified the temperature drop from 42.8 to 25.9 °C. Tina et al. [13] and Rosa et al. [14] carried out an analysis to observe the behavior of PV module submerged in water and they observed some enhancement in performance [15–17].

Again, there is another approach of cooling of PV module by air or water through forced or natural convection [18–20]. Swapnil Dubey et al. [27] developed an analytical explanation for the electrical performance of PVT hybrid air collector. The results explained that the overall electrical power of the module could be enhanced by reducing the temperature of solar module by dissipating thermal energy incorporated with the PV module. Ahmad Fudholi et al. [28] in 2014 experimentally analyzed PV thermal water receivers (Table. 1).

The electrical and thermal performances of photovoltaic thermal water receivers were analyzed under 500–800 W/m² solar irradiance levels. The PVT receivers were tested concerning thermal efficiency and electrical efficiency. They concluded that the spiral movement gain exhibited the excellent performance at a radiance distribution level of 800 W/m² and mass flow rate of 0.042 kg/s. This absorber gave thermal efficiency of 54.6% and PV efficiency of 13.8%.

The density of heat dissipation from the given area can be a major parameter of evaluation. Microchannels have the great wisdom in this approach and hence proved to be the vibrant area of research and a solution in the present scenario [22]. Microchannel in micro technology is a channel with a hydraulic diameter ranging from 200 μm to 1 mm [23]. Hence researchers have been showing great interest in the expansion of microcooling techniques for several applications [24–26].

In 2011, Agrawal et al. [29] conducted the energy study of a hybrid microchannel photovoltaic thermal (MCPVT) module having steady mass flow velocity of air in expressions of design and atmospheric parameters. By numerical estimates it was concluded that over the year thermal performance and exergy absorption improved by 71.62 and 61.19%, respectively, for the MCPVT module for Srinagar climatic condition. Karami and Rahimi [30] experimentally investigated the performance of hybrid PV module by cooling with water-based Boehmite (AlOOH × H₂O) nanofluid. A plate consisted of 40 rectangular parallel microchannels with a hydraulic diameter of 0.783 mm, attached to the back surface of PV module. Three different concentrations of nanofluid (0.01, 0.1, and 0.3 wt. %) were used and their performance was compared with base fluid. They found that the PV panel's average surface temperature decreased from 62.29 to 32.5 °C at a flow rate of 300 ml/min for 0.01 wt.% nanofluid. However, the maximum rise in electrical efficiency was about 27% for 0.01 wt. % concentration of the nanofluid at flow rate of 300 ml/min.

The literature explores the works that have been the solution for overheating of PV module. Cooling of PV module using nanofluids is one of the emerging trends. In current study, the experimentation is carried out on PV module with microchannels heat sink and nanofluids [31–33]. The study focuses on thermal and electrical performance of the PV and PVT system and comparison of the same.

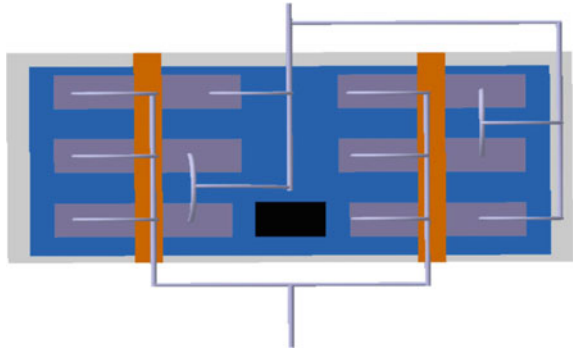
Table 1 Nomenclature, Symbols, and Suffix

Nomenclature	
D_h	Hydraulic Diameter (mm)
w	Width of channel (mm)
d	Depth of channel (mm)
h	Heat transfer coefficient (W/m ² K)
Q	Heat transfer (Watt)
C	Specific Heat (J/kg.K)
T	Temperature (°C)
m	Mass flow rate (kg/Sec)
V	Voltage (Volt)
I	Current (Ampere)
A	Surface Area
m	Mass (kg)
k	Thermal Conductivity (W/mK)
PV	Photovoltaic Module
E	Energy
<i>Latin/Greek Symbols</i>	
ρ	Density (kg/m ³)
Φ	Volume Fraction of nanoparticles
Δ	Difference
η	Efficiency
<i>Suffix</i>	
f	Fluid
in	Inlet condition
out	Outlet condition
sun	Solar irradiance
ele	Electrical
mass	Mass flow
sc	Short circuit
oc	Open circuit
thermal	Thermal energy

2 Experimental Setup

Figure 1 shows the schematics of PVT experimental setup; it consists of polycrystalline silicon photovoltaic module of 30 W capacity. Microchannel heat sink is connected to the rear surface of the module and divided into six equal parts. An arrangement is made to circulate the working fluid through microchannel with equal flow rate which is ensured by rotameter and a valve. A heat exchanger is used to cool

Fig. 1 PV module with Microchannel heat sink



down the working fluid using tap water and hence maintain the closed flow circuit. The setup is tilted at an angle of 21° with horizontal plane.

K-type thermocouples are used to measure the temperature of all points of interest. Short circuit current and open circuit voltage are obtained by rheostat and the same is measured by ammeter and voltmeter respectively. The microchannels are of rectangular cross section as shown in Fig. 2 of dimensions $(1 \times 1 \times 260 \text{ mm})$.

Experimentation is carried out on simple PV module and then on PVT system using base fluid (water) and different concentrations of nanofluids. Nanofluids are synthesized at different concentration (0.02, 0.06, 0.1 wt.%) using sonication apparatus as shown in Fig. 3.

The complete flow diagram is shown in Fig. 4 showing all the basic components.

Fig. 2 Design of microchannels

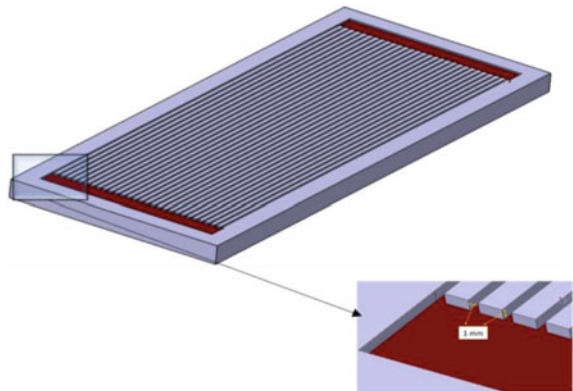




Fig. 3 Sonication device

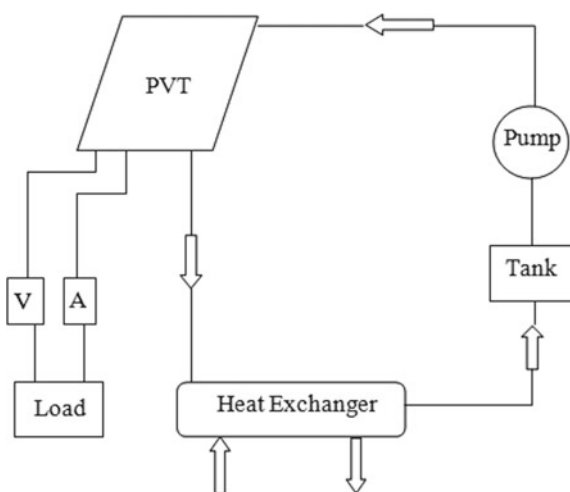


Fig. 4 Flow diagram of experimental setup

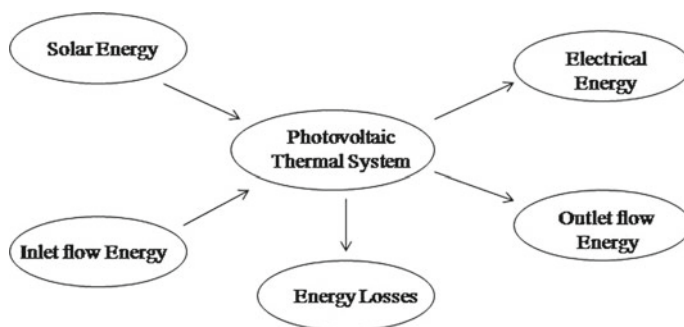


Fig. 5 Energy Balance diagram for PVT system

3 Data Reduction

As shown in Fig. 5 the heat sink and PV module combined forms a control volume system and exhibits the energy inflow and outflow.

The energy balance equation can be expressed as

$$E_{mass} + E_{sun} = E_{ele} + E_{mass} + E_{loss} \quad (1)$$

Thermal energy associated with the system, which is dissipated by working fluid can be written as

$$E_{mass,out} - E_{mass,in} = E_{thermal} \quad (2)$$

3.1 Heat Transfer Analysis

The rate of heat transfer can be evaluated as

$$(Q) = \rho_{nf} \times V \times C_p \times (T_{out} - T_{in})$$

where

The density of nanofluid (ρ) is given by

$$\rho_{nf} = \varnothing \cdot \rho_{np} + (1 - \varnothing) \cdot \rho_{bf}$$

The Volume fraction (Φ) of nanofluid is given by

$$\varnothing = \frac{m_{np} / \rho_{np}}{\frac{m_{np}}{\rho_{np}} + \frac{m_{bf}}{\rho_{bf}}}$$

Specific heat of nanofluid is given by

$$C_{p,f} = \frac{\varnothing(\rho_n \cdot C_{p,n}) + (1 - \varnothing) \cdot (\rho_{bf} \cdot C_{p,bf})}{\rho_{nf}}$$

mass flow rate is given by

$$(m) = \rho_{nf} \times V \text{ kg/Sec}$$

3.2 Electrical Analysis

The electrical power output of the PV module can be evaluated as follows

$$E_{ele} = V_{oc} \times I_{sc} \times FF \quad (3)$$

where the Fill factor (FF) is the maximum power conversion efficiency of the PV module which is the ratio of maximum power gained from the photovoltaic unit to the actual power based on I_{sc} and.

$$FF = \frac{E_{ele,max}}{V_{oc} \times I_{sc}} = \frac{V_{max} \times I_{max}}{V_{oc} \times I_{sc}} \quad (4)$$

Electrical efficiency of PV module is evaluated from Eq. (5),

$$\eta_{ele} = \frac{E_{ele}}{E_{sun}} \quad (5)$$

4 Results and Analysis

4.1 Distribution of Solar Irradiance

During experimentation the solar irradiance recorded for longitude: 77.78 °E and latitude: 20.94 °N.

The nature of global irradiance was found to be bell shape when plotted against time. It was further observed that the change in solar irradiance for consecutive days was comparatively small. Hence, for further analysis average solar irradiance is used as plotted in Fig. 6. The average solar radiation is observed 346 W/m² at morning, which reaches to its peak value 888 W/m² at noon then declines to 439 W/m² at 16.00. The mean value of total solar irradiance is found to be 684 W/m².

4.2 Working Fluid versus Surface Temperature

The variation of PV module average surface temperature is shown in Fig. 7a, b for different working fluids. The average surface temperature of PV module takes the similar trend of average daily distribution of solar irradiation for no cooling condition. Likewise for cooling with water and different concentrations of nanofluid the nature of temperature variation is similar as that of no cooling condition but there is a significant/major difference in peak temperature values as it drops drastically

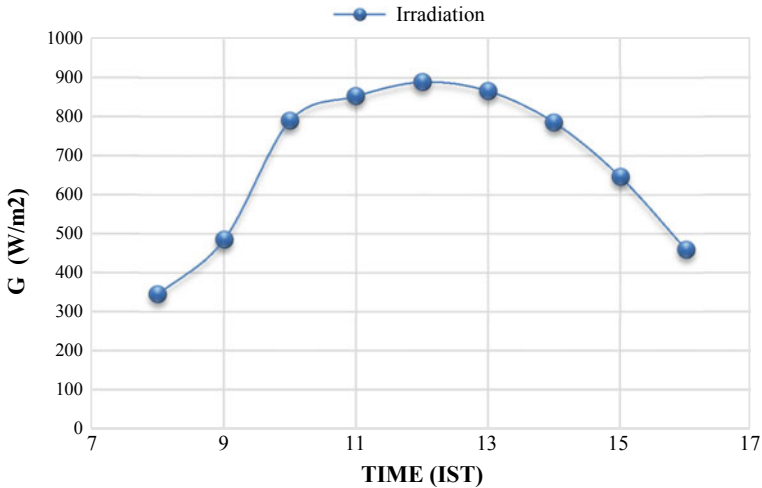


Fig. 6 Average daily distribution of global irradiance for all tests

with cooling. The average surface temperature reduction is found to be in the range of 18–20 °C by PVT system as compared to PV system.

The nanofluid shows better result than water. Figure 7a depicts PV module temperature for different concentrations of Al_2O_3 . It was further observed that with increase in concentration the temperature curve shifts downward. The lowest temperature values obtained at highest concentration of 0.1 wt.%. Similar observations are made for TiO_2 nanofluid as shown in Fig. 7b.

Among both the nanofluids TiO_2 show overall better cooling performance, also it shows highest enhancement in cooling effect at 0.1 wt.%, i.e., 33.31% with respect to no cooling condition, whereas Al_2O_3 the same concentration gives 32.18% enhancement.

The rise of cooling effect may be attributed to use of microchannels and nanofluids. Microchannels increase the surface area and nanofluids increase the surface and thermal conductivity; they all in turn increase the convective heat transfer. Further heat transfer is increased with concentration which may be attributed to rise in thermal conductivity with concentration.

4.3 Working Fluid versus Rate of Heat Transfer

The rate of heat transfer is calculated for all working fluids and plotted on the graphs for analysis as shown in Fig. 8a, b.

Figure 8a, b shows the heat transfer rate for Al_2O_3 System and TiO_2 System, respectively. As can be seen from figure, the nature of heat transfer curve is similar to global radiance distribution the reason of which is temperature difference which

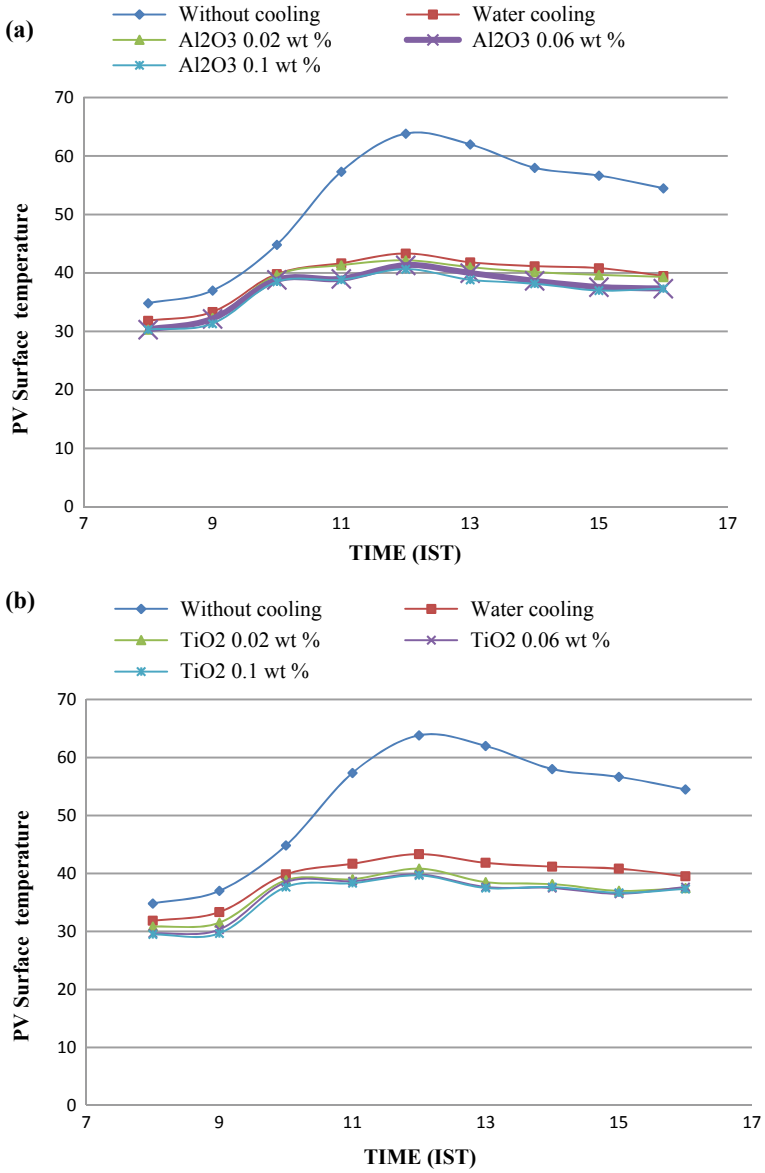


Fig. 7 a PV Surface Temp. Versus Time(Al₂O₃) b. PV Surface Temp. Versus Time (TiO₂)

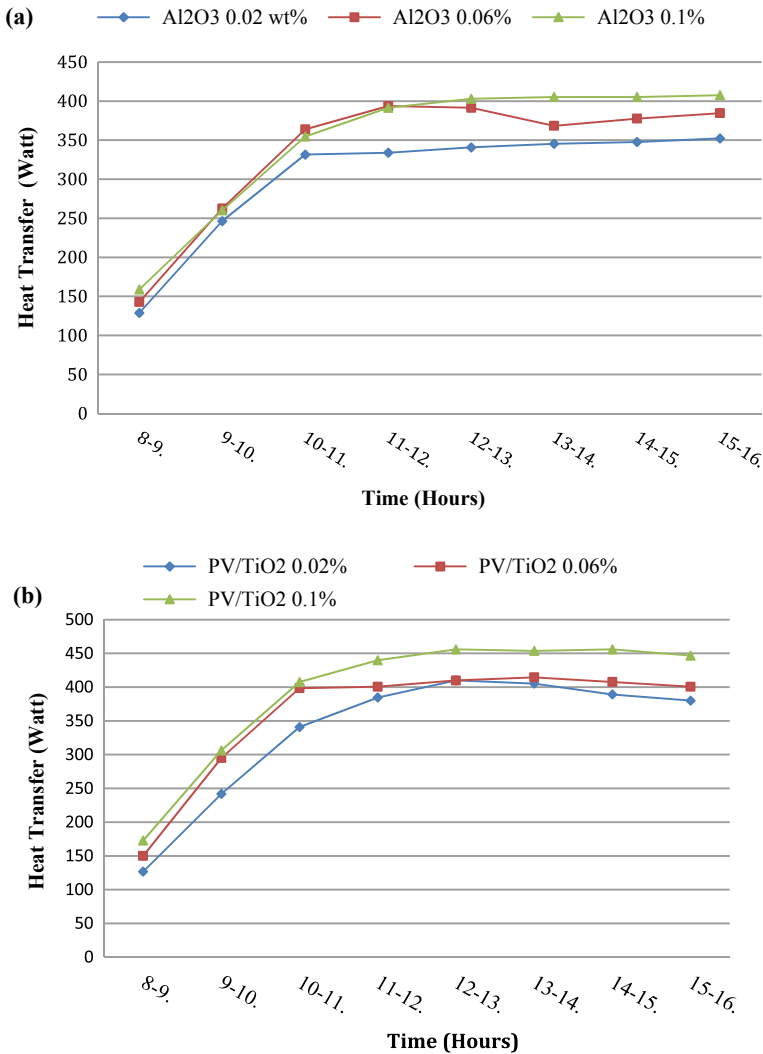


Fig. 8 a Avg. Heat Transfer Al₂O₃ System b Avg. Heat Transfer TiO₂ System

varies with radiation. As the temperature of module increases from morning, the temperature difference between fluid and PV module drives heat from module. The heat transfer rate increases as the concentration of nanofluid increases. Maximum heat transfer is obtained for highest concentration also its peak value reaches at maximum temperature difference between PV module and fluid, same is justified for both Al₂O₃ and TiO₂ from Fig. 8.

4.4 Current–Voltage (I–V) Characteristics

Figure 9a, b shows the current–voltage characteristics of PV module for no cooling (PV system) and PVT system (with cooling), respectively. Figure 9a depicts that short circuit current increases with respect to global irradiation, i.e., with temperature. It can be further observed that from morning to noon, the short circuit current increases

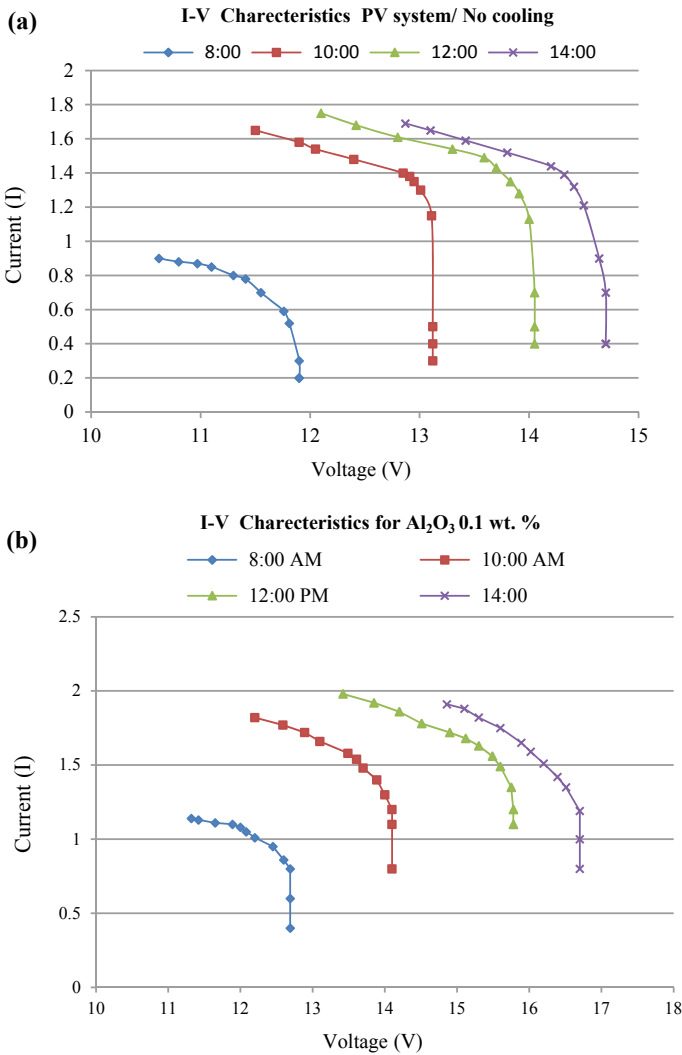


Fig. 9 a Current–Voltage (I–V) Characteristics for No cooling **b** Current–Voltage (I–V) Characteristics Al₂O₃ System

by 94.44% for no cooling and 75.44% for cooling. The rise in short circuit current for no cooling is more than that of cooling.

This is due to rise in temperature of PV module as global radiations increase from morning to noon. The temperature rise of PV module causes the band gap energy to decrease due to rise in intrinsic carriers, owing to this the short circuit current upsurges to some extent. But as the energy band gap reduces the potential difference, i.e., open circuit voltage gets limited and due to this the current falls linearly limiting the electric power generation, which can be noticed from area under I-V curve which get reduced by limited voltage range for no cooling. As the area under the I-V curve represents the electrical power, it can be noticed from the figure that the rise in open circuit voltage is limited to 16.66% for PV system (no cooling). Whereas for PVT system, voltage range is found to be increased significantly. For water cooling the open circuit voltage was increased by 20%. Whereas for Al_2O_3 it increases in the range of 10–25% as the concentration increases from 0.02 to 0.1 wt.%. Similar trends are noticed for TiO_2 for different concentrations and maximum voltage rise is found to be at 0.1 wt.% which is 30.86%. The rise in voltage may be attributed to cooling of PV module [34, 35].

The cooling of PV module keeps the energy band gap changed too little due to thermal energy dissipation. This unaltered band gap energy maintains the potential difference appreciable. Owing to this the PV module gives a desirable short circuit current with extended range of voltage and hence the area covered on I-V plot increases, which leads to an increase in electrical power generation [36].

4.5 Electrical Power Analysis

The electrical power of the PV module shows similar trend as that of global radiation when plotted against time. Figure 10a, b narrates the variation of electric power output. Initially from morning to noon (12.00 hrs) the electrical output increases due to rise in irradiation. The electrical power increases in the range of 1.2–1.6 times (or 120–160%) for PV system and then almost remains constant up to 15.00. After that the power output decreases because irradiation starts decreasing. Even though irradiation starts decreasing after 12.00 hrs, still power output almost remains constant due to a reduction in electrical losses of electron collision.

At 12.00 h for water cooling the electrical power is increased in the range of 12–18% as compared to PV system. Similarly for Al_2O_3 and TiO_2 at 0.1 wt.% electrical power rises in the range of 35–40% as compared to PV system. For PVT system working fluids lower the temperature of module. As mentioned in I-V characteristics section electrical power increases due to extended voltage range.

Among all the working fluids TiO_2 at 0.1 wt.% give maximum electrical power, i.e., 26.36 W/m^2 at 14.00. It is increased by almost 38% as compared to PV system.

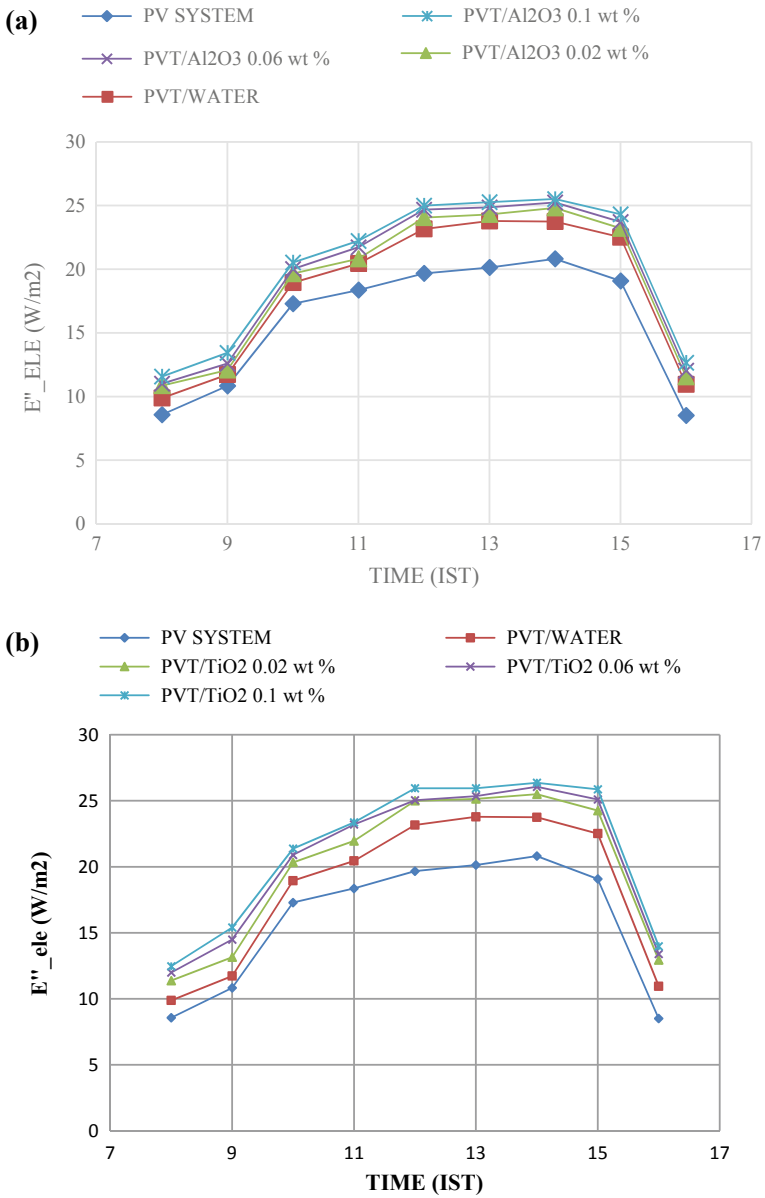


Fig. 10 a Electrical Power Versus Time Al_2O_3 system b Electrical Power Versus Time TiO_2 system

4.6 Electrical Efficiency Analysis

Figure 11a, b shows the efficiency of PV module. As efficiency is a relative fraction of input energy and output electrical energy. As noticed that efficiency initially goes reducing with irradiation upto noon. From morning to noon efficiency reduces in the range of 12–18% for PV system. Past noon the efficiency starts increasing and reaches the peak value at 15.00 h for all cases. For PV system past noon the efficiency increases by almost 37% till peak point.

In case of Al_2O_3 PVT System past noon efficiency is increased in the range of 40–50% till peak point. At peak point, i.e., at 15.00 h the efficiency of Al_2O_3 PVT system is enhanced by almost 25–30% as compared to PV system. The best value among all is obtained for TiO_2 at 0.1 wt.%, i.e., almost 30–35% enhancements as compared to PV system.

The temperature rise in PV module accelerates the collision of electrons that leads to the increased electrical losses. Hence, even though electrical power increases due to increased radiation till noon, but corresponding input radiation is comparatively large, hence efficiency steps down. As past noon the irradiation starts decreasing and also the electrical losses, the output power becomes more comparable to input radiation, hence efficiency starts increasing. It can be further observed that maximum value of efficiency is at 15.00 in all the cases. At 15.00 the input energy is relatively low while the output is considerably high in proportion that leads to high efficiency. Maximum electrical power is at 14.00 h. still efficiency is not maximum there due to relatively high input energy.

For PVT system the module temperature is reduced by nanofluid cooling and that leads to less electron collision and less electrical losses. Better the cooling of module, higher is the electrical power generation.

5 Conclusion

The experimental study outlines the performance of photovoltaic module using microchannel heat sink and nanofluid. The system without cooling is referred as PV system and with cooling arrangement is termed as PVT system. Microchannel heat sink is used to dissipate heat from PV module with different working fluids such as water (base fluid), Al_2O_3 , and TiO_2 nanofluids at different concentrations.

Both thermal and electrical performances of module are greatly enhanced after experimentation. The lower surface temperature after cooling leads to the enhancement of various performance parameters of PV module. The voltage range of module is found to be increased after cooling. The open circuit voltage is found to be increased by 25–30% at peak cooling conditions, thereby increasing the electrical power generation by almost 35–40%. Dissipation of thermal energy leads to the reduced electrical losses and hence, the electrical efficiency is found to be increased with cooling. At peak cooling conditions the electrical efficiency increases by almost 30–35%.

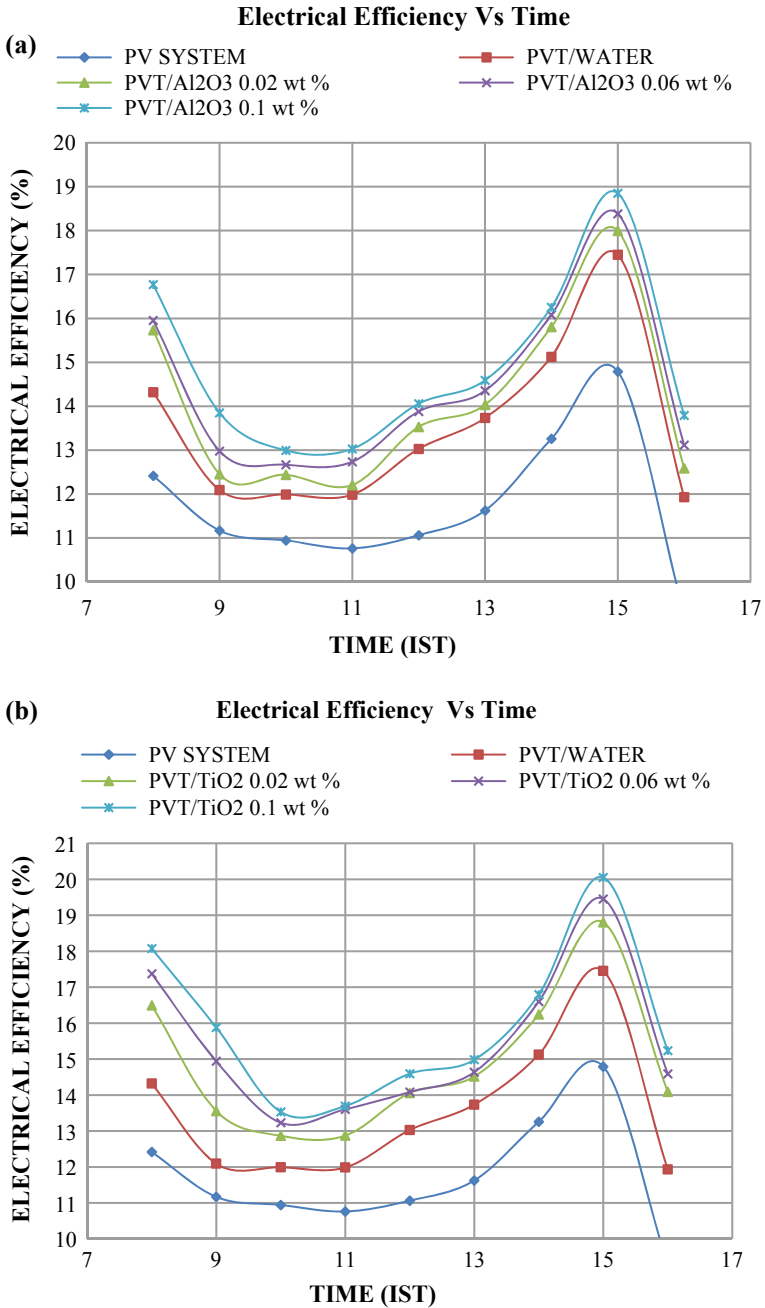


Fig. 11 a Electrical efficiency Versus Time (Al₂O₃) System b Electrical efficiency Versus Time (TiO₂)

As the concentration of nanofluids is increased, both thermal and electrical performance of PV module are found to be increased. Electrical power, electrical efficiency, and heat transfer, all these parameters enhance as the concentration is increased.

The microchannel PVT system leads to lower thermal energy incorporation. Lower thermal energy association gives less cell degradation and hence the life span of PV module is found to be increased. Microchannels in combination with the nanofluids observed to be a better solution for cooling of PV module in order to enhance its performance by lowering its operating temperature.

References

1. L. Alboteanu, Increase efficiency of stand-alone photovoltaic systems by reducing temperature of cells. *Annals of the "ConstantinBrancusi"University of TarguJiu* 3, 195–204 ISSN: 1842–4856 (2011)
2. L. Alboteanu, C.F. Ocoleanu, C.A. Bulucea, Cooling system for photovoltaic module: recent researches in environmental and geological sciences, in *Proceedings of the 7th WSEAS International Conference on Energy & Environment*. (Kos Island, Greece, 2012), pp. 133–138
3. E. Skoplaki, J.A. Palyvos, the temperature dependence of photovoltaic module electrical performance: a review of efficiency/power correlations. *Sol. Energy* **83**, 614–624 (2009)
4. E. Radziemska, E. Klugmann, thermally affected parameters of the current–voltage characteristics of silicon photocell. *Energy Convers. Manag.* **43**, 1889–1900 (2002)
5. J. Barrau, J. Rosell, D. Chemisana, L. Tadrst, M. Ibañez, Effect of a hybrid jet impingement/micro-channel cooling device on the performance of densely packed PV cells under high concentration. *Sol. Energy* **85**, 2655–2665 (2011)
6. H.G. Teo, P.S. Lee, M.N.A. Hawlader, An active cooling system for photovoltaic modules. *Appl. Energy* **90**, 309–315 (2012)
7. K.H. Do, T.H. Kim, Y.-S. Han, B.-I. Choi, M.-B. Kim, General correlation of a natural convective heat sink with plate-fins for high concentrating photovoltaic module cooling. *Sol. Energy* **86**, 2725–2734 (2012)
8. S. Krauter, Increased electrical yield via water flow over the front of photovoltaic panels. *Sol Energy Mater Sol Cells* **82**, 131–137 (2004)
9. A. Royne, C.J. Dey, (2007) Design of a jet impingement cooling device for densely packed PV cells under high concentration. *Sol. Energy* **81**
10. M. Abdolzadeh, M. Ameri, Improving the effectiveness of a PV water pumping system by spraying water over the front of photovoltaic cells. *Renew. Energy* **34**, 91–6 (2009)
11. S. Nizetic, F. Yadaf, G. Cabo, Water spray cooling technique applied on a photovoltaic panel: the performance response. *Energy Convers Manage* **108**, 287–296 (2016)
12. H. Bahaidarah, A. Subhan, P. Gandhidasan, S. Rehman, Performance evaluation of a PV (photovoltaic) module by back surface watercooling for hot climatic conditions. *Energy* **59**, 445–453 (2013)
13. G.M. Tina, M. Rosa-Clot, P. Rosa-Clot, P.F. Scandura, Optical and thermal behaviour of submerged photovoltaic solar panel: SP2. *Energy* **39**(1), 17–26 (2012)
14. C.M. Rosa, C.P. Rosa, G.M. Tina, P.F. Scandura, Submerged photovoltaic solar panel: SP2. *Renew. Energy* **35**(8), 1862–1865 (2010)
15. S.U.S. Choi, A. Estman, Enhancing thermal conductivity of fluids with nanoparticles, in *Proceedings of ASME International Mechanical Engineering Congress and Exposition*. (San Francisco, CA, USA, 1995), pp. 12–17
16. S. Lee, S.U.S. Choi, S. Li, J.A. Eastman, Measuring thermal conductivity of fluids containing oxide nanoparticles. *Transact ASME J Heat Transfer* **121**, 280–289 (1999)

17. Y.L.i. Zhou, J. Li, S. Tung, E. Schneider, S. Xi, A review on development of nanofluid preparation and characterization. *Powder Technol.* **196**, 89–101 (2009)
18. J.H. Lee, S.H. Lee, C.J. Choi, S.P. Jang, S.U.S. Choi, A review of thermal conductivity data, mechanics and models for nanofluids. *Int J Micro-Nano Scale Transport* **1**, 269–322 (2010)
19. A. Ghadimi, R. Saidur, H.S.C. Metselaar, A review of nanofluid stability properties and and characterization in stationary conditions (2011)
20. J. Fan, L. Wang, Review of heat conduction in nanofluids. *ASME J. Heat Transfer* **133**:040801 (2011)
21. R.S. Vajjha, D.K. Das, A review and analysis on influence of temperature and concentration of nanofluids on thermophysical properties, heat transfer and pumping power. *Int. J. Heat Mass Transfer* (2012)
22. A. Royne, C.J. Dey, D.R. Mills, Cooling of photovoltaic cells under concentrated illumination: a critical review. *Sol. Energy Mater. Sol. Cells* **86**, 451–483 (2005)
23. S.G. Kandlikar, S. Garimella, D. Li, S. Colin, M.R. King, Heat transfer and fluid flow in minichannels and microchannels 1–3 (2006)
24. P.-S. Lee, S.V. Garimella, D. Liu, Investigation of heat transfer in rectangular microchannels. *Int. J. Heat Mass Transf.* **48**, 1688–1704 (2005)
25. B. Schneider, A. Kosar, Y. Pe, Hydrodynamic cavitation and boiling in refrigerant (R-123) flow inside microchannels. *Int. J. Heat Mass Transf.* **50**, 2838–2854 (2007)
26. J.H. Ryu, D.H. Choi, S.J. Kim, Three-dimensional numerical optimization of a manifold microchannel heat sink. *Int. J. Heat Mass Transf.* **46**, 1553–1562 (2003)
27. S. Dubey, G.S. Sandhu, G.N. Tiwari, Analytical expression for electrical efficiency of PV/T hybrid air collector. *Appl. Energy* **86**, 697–705 (2009)
28. A. Fudholi, K. Sopian, M.H. Yazdi, M.H. Ruslan, A. Ibrahim, H.A. Kazem, Performance : analysis of photovoltaic thermal (PVT) water collectors. *Energy Convers. Manag.* **78**, 641–651 (2014)
29. S. Agrawal, G.N. Tiwari, Energy and exergy analysis of hybrid micro-channel photovoltaic-thermal module. *Sol. Energy* **85**, 356–370 (2011)
30. N. Karami, M. Rahimi, Heat transfer enhancement in a hybrid microchannel photovoltaic cell using Boehmite nanofluid. *Int Commun Heat Mass Transf* **55**, 45–52 (2014)
31. A. Behzadmehr, M. Saffar-Avval, N. Galanis, Prediction of turbulent forced convection of a nanofluid in a tube with uniform heat flux using a two phase approach. *Int J Heat Fluid Flow* **28**(2), 211–219 (2007)
32. S.K. Das, S.U.S. Choi, W. Yu, T. Pradeep, *Nanofluids Science and Technology* (John Wiley & Sons, Hoboken, NJ, USA, 2008)
33. R.B. Mansour, N. Galanis, C.T. Nguyen, Effect of uncertainties in physical properties on forced convection heat transfer with nanofluids. *Appl. Therm. Eng.* **27**(1), 240–249 (2007)
34. Y. Ding, H. Chen, L. Wang, C.Y. Yang, Y. He, W. Yang, L. Zhang, R. Huo, Heat transf intensificat using nanofluids. *KNOA* **25**, 23–36 (2007)
35. S.A. Nada, D.H. El-Nagar, H.M.S. Hussein, Improving the thermal regulation and efficiency enhancement of PCM-Integrated PV modules using nano particles. *Energy Convers. Manag.* **166**, 735–43 (2018)
36. M. Ali, H. Ali et al., performance enhancement of PV cells through micro channel cooling. *AIMS Energy* **3**(4), 699–710 (2015)

Thermal Analysis of Salinity Gradient Solar Pond in Nagpur City



Shyamal G. Chakrabarty, Uday S. Wankhede, and Rupesh S. Shelke

Nomenclature

A	Area (m ²)
C_p	Specific heat of fluid (J/kg °C)
T	Temperature (°C)
t	Time (hours)
X	Zone thickness (m)
UCZ	Upper convective zone
NCZ	Non-convective zone
LCZ	Lower convective zone
Q_{sr}	Solar radiation absorbed (W/m ²)
Q_{cond}	Conduction heat transfer (W/m ²)
Q_c	Convection heat loss (W/m ²)
Q_r	Radiation heat loss (W/m ²)
Q_e	Evaporation heat loss (W/m ²)
Q_g	Ground heat loss (W/m ²)
Q_{load}	Amount of heat extracted (W/m ²)

Greek Symbols

ρ Density of fluid (kg/m³)

S. G. Chakrabarty (✉)

Research Scholar, Department of Mechanical Engineering, G. H. Raisoni College of Engineering, Nagpur 440016, India

U. S. Wankhede

Associate professor, Department of Mechanical Engineering, Government College of Engineering, Chandrapur 442403, India

R. S. Shelke

Head & Associate Professor, Department of Mechanical Engineering, G. H. Raisoni College of Engineering, Nagpur 440016, India

1 Introduction

Energy security has become a major concern around the world. To meet the growing energy demand, excessive use of fossil fuel leads to global warming and other environmental problems. The salinity gradient solar pond can collect and store thermal energy simultaneously. It consists of three stratified layers. The UCZ consists of a low density solution. It prevents the gradient layer from rain and wind. The middle layer is known as NCZ. It consists of salinity gradient to suppress the convection heat loss [2]. The LCZ consists of a high density solution to store the thermal energy. The heat is extracted from the LCZ for various applications.

In recent years, most researchers have shown an increased interest in solar pond technology. Verma et al. [8] investigated the transient behavior of solar pond. Verma and Das [7] further conducted study for optimization of wall profile of solar pond. Goswami and Das [4] experimentally investigated the performance of thermoelectric power generation integrated with solar pond. Panchal et al. [5] reviewed the performance of solar still integrated with solar pond. The objective of the present work is to investigate the transient behavior solar pond for the period of 1 year.

2 Numerical Model

A transient heat transfer model is employed to study the performance of SGSP. The thickness of UCZ = 0.3 m, NCZ = 1.2 m, and LCZ = 1.5 m are assumed [2]. The area of solar pond is considered to 100 m². The heat balance equation of UCZ and LCZ is expressed in (1) and (3), respectively.

$$\rho_u C_{pu} A_u X_u \left(\frac{dT_u}{dt} \right) = Q_{ru} + Q_c - Q_{uc} - Q_{ur} - Q_{ue} \quad (1)$$

$$\rho_l C_{pl} A_l X_l \left(\frac{dT_l}{dt} \right) = Q_{rl} + Q_c - Q_g - Q_{load} \quad (2)$$

All the terms of (1) and (2) are determined according to the assumptions and procedure described by Chakrabarty et al. [1].

3 Result and Discussion

The governing equation is solved by using a numerical method in MATLAB. The variation of average solar radiation and ambient temperature of the Nagpur city for 1 year is shown in Fig. 1. It is observed that two peaks occur during a period of 1 year.

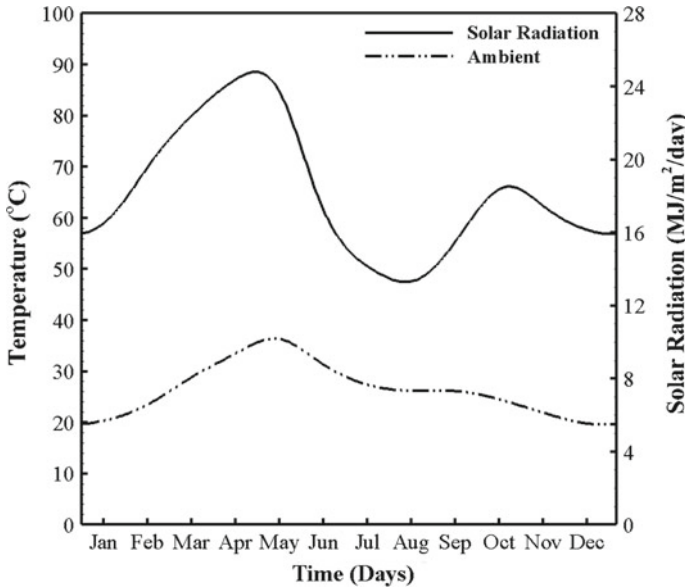


Fig. 1 Average solar radiation and average ambient temperature data of Nagpur city

The highest peak occurs in the summer season and the smaller peak is observed in the winter season.

Figure 2 shows the temperature variation of LCZ temperature and U CZ temperature during the period of 1 year. It can be seen that a phase lag of about 1 month exists between the maximum solar radiation and attainment of maximum temperature of LCZ in summer season. Whereas, the phase lag is found to be marginal during winter season. The variation in LCZ temperature is viewed to be negligible during winter season. The ambient temperature is found to be higher than U CZ temperature.

Figure 3 exhibits the development of LCZ temperature for various heat extraction rate. The process of heat extraction is considered to commence from the 60th day of maturation period. It is found that the temperature achieved by LCZ decreases with the rise in rate of heat extraction. During winter season, for heat extraction rate of 40 W/m² the difference between the LCZ temperature and ambient temperature is observed to be less than 20 °C. Such lower temperature may not be beneficial for some applications. Therefore the amount of heat extraction and desired temperature required by the application should be studied for a particular location.

Figure 4 presents the development of LCZ temperature for different starting days of heat extraction. The rate of heat extraction is considered as 30 W/m². It is seen that the increase in warm-up time results in the increase in maximum temperature of LCZ. The highest temperature of LCZ occurs during the month of May for the case of no heat extraction. Therefore, if heat is extracted during the month of May then higher temperature can be obtained. It is also attributed to higher heat loss as compared to other cases. The variation in minimum temperature is marginal. Figure 4 also

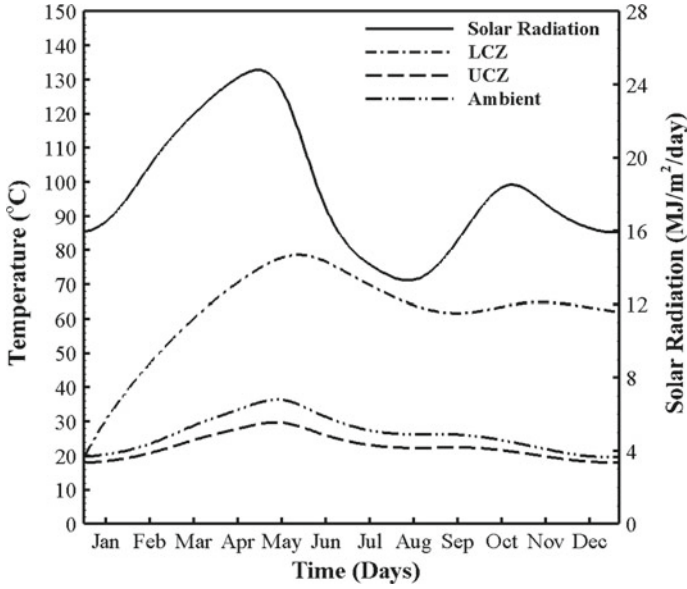


Fig. 2 Variation of LCZ temperature and UCZ temperature without heat extraction

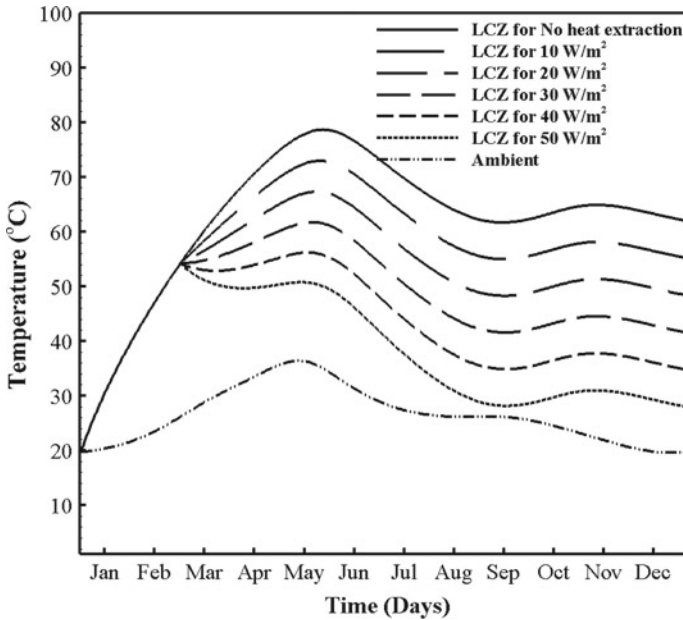


Fig. 3 Variation of LCZ temperature profile for a different rate of heat extraction

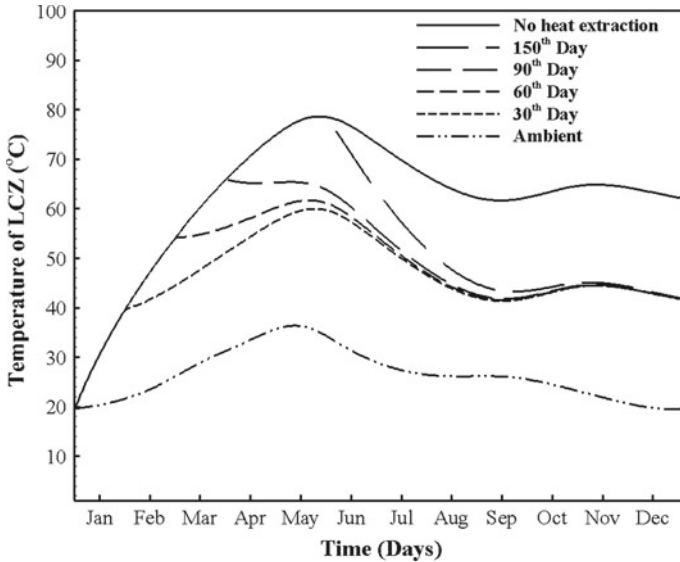


Fig. 4 LCZ temperature profile for different starting days of heat extraction at the rate of 30 W/m²

depicted that the change in warm-up time does not affect the temperature of LCZ during winter season for the given case. Therefore the warm-up period should be decided based on the temperature desired for the application.

The behavior of LCZ temperature and instantaneous efficiency for heat extraction rate of 30 W/m² is presented in Fig. 5. The heat extraction is commenced in the month of March. The behavior of instantaneous efficiency is similar to the result obtained by Date et al. [3]. Higher instantaneous efficiency is observed during the winter season.

4 Conclusion

The present study includes a transient analysis of salinity gradient solar pond in Nagpur city. The maximum temperature achieved by LCZ decreases with the rise in the rate of heat extraction. The commencing day of heat extraction also influenced the temperature of LCZ. The change in warm-up time does not affect the temperature of LCZ during winter season for the given case. The warm-up time and desired temperature of an application should be taken into account for economical assessment of the solar pond.

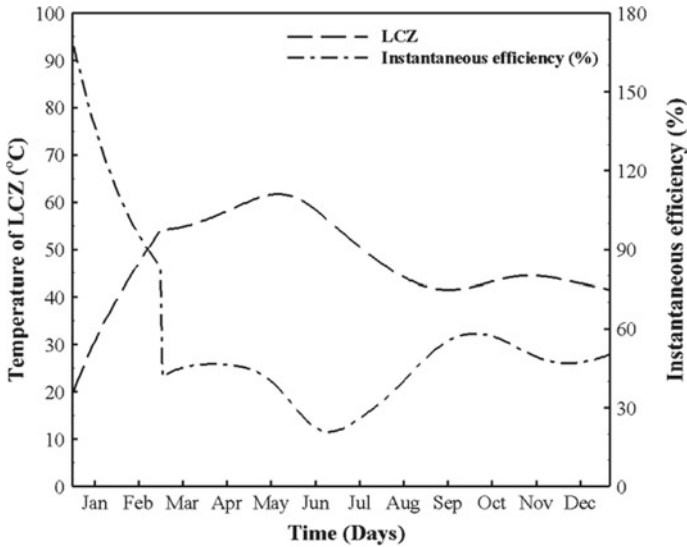


Fig. 5 Variation of LCZ and instantaneous efficiency

References

1. S.G. Chakrabarty, U.S. Wankhede, R.S. Shelke, T.B. Gohil, Investigation of temperature development in salinity gradient solar pond using a transient model of heat transfer. *Sol. Energy*, 202 (2020)
2. A. Date, A. Akbarzadeh, Salinity gradient solar ponds, in *Solar Energy Sciences and Engineering Applications* (2013), pp. 195–218.
3. A. Date, Y. Yaakob, A. Date, S. Krishnapillai, A. Akbarzadeh, Heat extraction from non-convective and lower convective zones of the solar pond: a transient study. *Sol. Energy* **97**, 517–528 (2013)
4. R. Goswami, R. Das, Investigation of thermal and electrical performance in a salt gradient solar pond. *J. Phys. Conf. Ser.* **1240**, 12111 (2019)
5. H. Panchal, K K. Sadasivuni, F.A. Essa, S. Shanmugan, R. Sathyamurthy, Enhancement of the yield of solar still with the use of solar pond: a review. *Heat Transfer* (2020)
6. "NASA," Prediction of Worldwide renewable Energy Resources (2019). <https://power.larc.nasa.gov/data-access-viewer/>. (Accessed 23 May 2019)
7. S. Verma, R. Das, Wall profile optimisation of a salt gradient solar pond using a generalized model. *Sol. Energy* **184**, 356–371 (2019)
8. S. Verma, R. Das, A. Kumar, Transient thermal modelling and optimization of a solar collector-type pond considering an improved decay of radiative intensity. *Int. J. Therm. Sci.* **139**, 440–449 (2019)

Mathematical and Thermal Modeling for Solar Drying of Tomato Slices



Rajendra C. Patil  and Yogesh S. Kulkarni

1 Introduction

Farmers in India have typically tiny land holdings and commit suicide in current years due to continual reduced rates of perishable foodstuff and market. Processing of perishable product to a processed foodstuff can be a worthy choice for such farmers, whereby shelf life of the foodstuff is enhanced [1, 2]. The spoilage and wastage of foodstuff can be reduced by cold storage and drying method. The cold storage method is quite expensive and thus farmers cannot afford it. The drying of perishable products by use of sun energy is the most appropriate method for extending shelf life and escalating the market value of the foodstuff. Basically, drying is the simultaneous heat and mass transfer process to reduce the moisture content up to the desirable extent by use of heat energy. The various technologies for drying are osmotic dehydration, hot-air drying, freeze drying, vacuum, and microwave drying. However, freeze, mechanized, and hot air oven solar drying methods are quicker, costly, and require high energy cost to function than that of open sun and solar drying method. Conventionally, preservation of foodstuff by open sun drying is commonly used and has abundant disadvantage like spoilage of foodstuff due to dust, animals, storms, wind, rain, and results in poor quality of dried product. Hence, to improve the quality and quantity of dried product, it is necessary to control the drying process and the attempt had been made to advance the open sun drying to solar drying [2, 3].

Tomato (*Lycopersicon esculentum* Mill) is one of the vital fruit or vegetable in human diet, as they are wealthy with vitamin C, vitamin E, lycopene, dietetic fiber, and can be consumed fresh or else processed due to its extraordinary flavor. Presently, India is the fourth main tomato producing nation having 10 tons per hectare yield out of 24 tons per hectare or world's average yield. Though India is a major exporter

R. C. Patil (✉) · Y. S. Kulkarni
Department of Mechanical Engineering, SNJB's Late Sau KBJ College of Engineering,
Chandwad, Nashik, Maharashtra, India

to Oman, Maldives, Turkey, Nepal, and Pakistan, an enormous quantity of tomato is being damaged due to the lack of appropriate processing technology and preservation facilities [1]. Studies on drying kinetics and characteristics of by-product of an ample range of agricultural produce have been reported such as onion flakes, cuminum cuminum, olive pomace, tomato pomace, pomegranate fruit peel, potatoes, Amla, carrot pomace, apple, Celeriac Slices, Casuarina Equisetifolia wood chips, and solid waste of olive oil. Studies on the drying kinetics and thermal modeling for tomato slices are limited.

In connection to this, the author has fabricated a simplified and affordable version of solar greenhouse dryer for drying of multiple foodstuffs under the forced convection mode and in the area of latitude of 15–30°N. Mostly, dried tomato is used in sauces, soups, pesto, and as a constituent in spicy dishes, pizzas, salads, and so forth [1]. From the literature survey, it is observed that the quality of dried foodstuffs in indirect dryers is better than direct dryers, while the faster drying is the key of direct type of dryer. In connection to this, the comprehensive survey of Hohenheim tunnel (direct type) and cabinet dryers (indirect type) has been made and both dryers are costly and have intricate mechanism and nor affordable to small landholders. Hence in this work, author tried to overcome the drawbacks of above dryers and proposed a simplified version of direct type of solar tunnel greenhouse dryer. The investigation of proposed dryer during drying of fresh tomato is the main goal of this research work. The specific objectives could be summarized as:

1. To fit the investigational data with several thin-layer mathematical models to illustrate drying kinetics of tomato slice.
2. To examine the thermal performance by calculating convective heat and mass transfer coefficient at each hour of drying time.

2 Materials and Method

2.1 *Experimental Setup and Features of Dryer*

Figure 1 demonstrates the schematic sight of proposed dryer of 4 m² aperture area. It consists of two tunnels of identical size with area of 2 m² each linked in succession with a small rectangular hole for circulation of hot drying air. On the basis of the foodstuff to be dried, 15–20 kg of agro-product can be laden in every tunnel. Each module of tunnel consists of two layers of trays with two trays in each layer. The surrounding air enters from bottom of first tunnel and moves through the product loaded in different trays. Later on the hot humid air then goes to second tunnel through a small rectangular opening, where its temperature is further increased due to greenhouse effect.

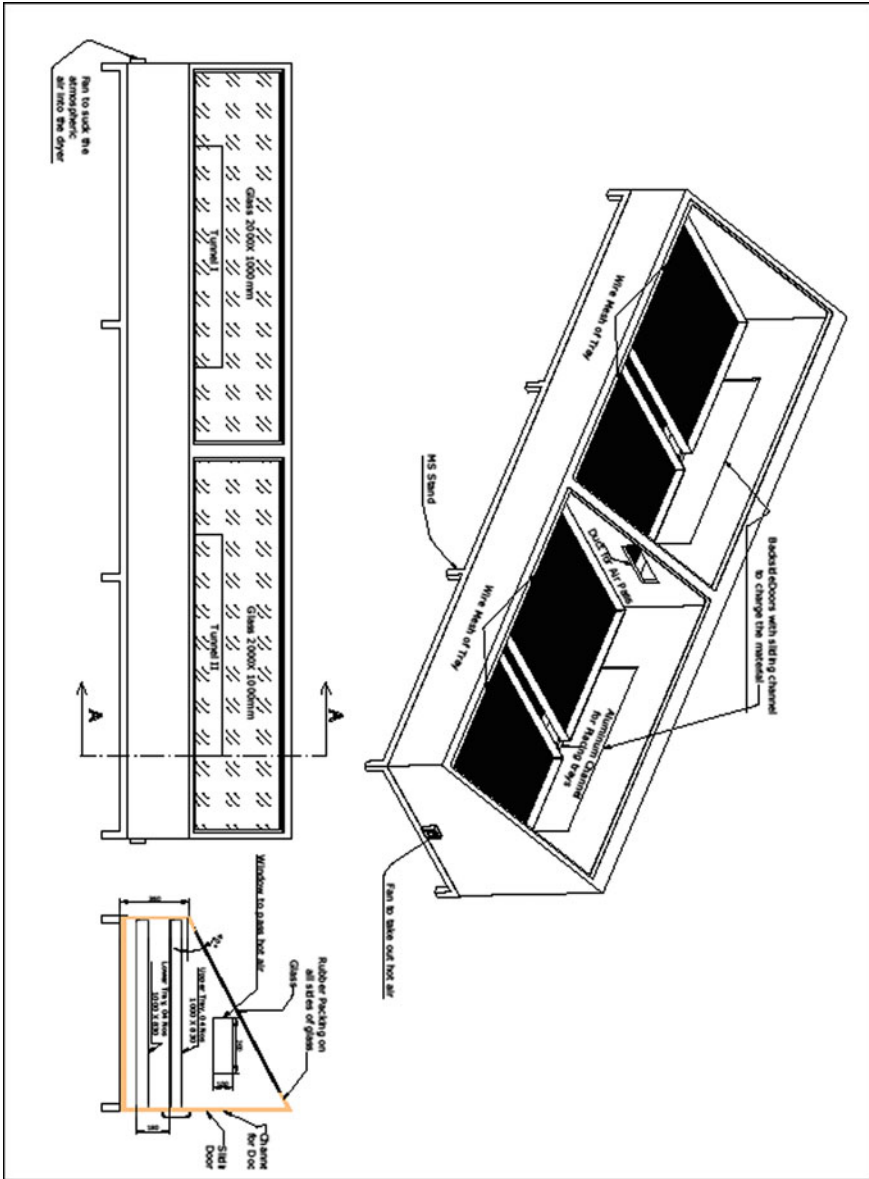


Fig. 1 Schematic of solar tunnel greenhouse dryer

2.2 Features of Proposed Dryer

The practical improvements in the proposed dryer with respect to the Hohenheim solar tunnel and solar cabinet dryer have been made and listed as below.

1. **Inclined glazing:** Dryer has a shape of home cabinet with tilted transparent toughened glass at one side and thus needs extremely fewer fragile material. Also the tilt of 40° permits utmost collection of solar insolation and improves loading capacity of dryer.
2. **Drying air temperature and flow rate:** A capability to change air quantity as per need is the principle method of avoiding extreme temperature within the dryer. Authors use the PV module to adjust the drying temperature by controlling the air flow rate. Improved exploitation of heated moist air in all trays of tunnel provides approximately consistent drying. The temperature in the range of 60–70 °C is attained in the dryer which is suitable for drying of nearly all agro-products. This increases the utilization of dryer.
3. **Modular design:** Depending on the necessity, the loading capacity of dryer can be effortlessly varied due to addition or removal of a number of tunnels in succession.
4. **Air filter:** A detachable and washable air filter has been installed on the positive side of the fans to eliminate dust from the incoming moist air and thus ensures high quality dried product.
5. **Material:** To overcome the troubles come across with dryers built from conventional materials like mild steel and wood, the proposed dryer has been fabricated from composite aluminum section and sheet. The light mass, strength, and durability are the major characteristics of aluminum material and allow subsequent advantages:
 - a. The exterior of dryer was fabricated from a single aluminum sheet devoid of any joints and thus diminish the leakage of hot drying air and improves drying rate.
 - b. A 30% weight of dryer is reduced which allows trouble-free handling, transportation, and effortless tracking of dryer with respect to the sun's position.
 - c. The life span of dryer is improved due to protection of dryer from untimely rain, yeast, mold, etc.
 - d. Easy to assemble and dismantle.
 - e. The idea of sliding door on back side has been used for effortless loading and unloading of the material to be dried.

The minor increase in the dryer's cost due to the composite aluminum sheet and section is compensated because of its more life span and better durability.

2.3 Instrumentation

Thermocouple (PT-100) with precision of ± 0.5 °C has been used for recording the temperature of air at different locations of dryer. For recording of relative humidity of drying and surrounding air, digital hygrometer of precision of $\pm 10\%$ was used. A solar meter with accurateness of $\pm 10\%$ was utilized for recording intensity of sun rays. The velocity sensor as well as an anemometer were employed to gauge wind speed all over the greenhouse. The photovoltaic module of 10 W has been used to run the 12 V DC fans to ensure mass flow rate of air throughout the dryer. A digital balance of ± 0.01 g precision having a maximum 8 kg capacity was used for weighing moisture content of tomato slices. A 16 channel (SUNPRO, India) data logger is also used for recording temperatures of drying air for every interval of 5 min.

2.4 Experimental Procedure

A good quality of tomatoes was purchased from the market place of Nashik and washed with fresh water and dirt-free cloth. The hygienic tomatoes were then cut into slices of 3-5 mm by stainless steel blade to shun the blackening of surface. All tomato slices were then pretreated with potassium metabisulfite for improving the drying rate and quality of dried product. The solar drying trials were carried out at the Department of Mechanical Engineering, Chandwad, Nashik (latitude of 20.32° N; longitude of 74.24° E). The initial moisture content of the tomato is determined by air oven method and found to be 90% (w.b.). Before testing, it is ensured that all equipments are in condition and whole setup was run without load for 30 min to attain the steady-state condition. Finally, the pretreated samples of tomato slice were weighed by digital weighing machine and loaded on the trays of every tunnel of dryer for drying. The drying of tomato slices was sustained until the desirable moisture content was achieved.

2.5 Thin-Layer Drying Models for Tomato Drying

In solar drying, the study of drying kinetics of products with drying time is estimated to be the most noteworthy area of drying. A thin-layer equation enlightens the drying performance in a unified way despite the controlling means and to simplify the drying curves. Hence, experimental studies are imperative and in consequence, thin-layer mathematical drying terms are imperative utensils in modeling of solar drying [3–7]. Several thin-layer drying models are presented and broadly employed for confirming the physics of solar drying method. These models are frequently labeled into three types as theoretical, semi-theoretical, and empirical. During this work, applicability of thin-layer mathematical drying models like Newton, Henderson &

Table 1 Thin-layer drying models

Sn.	Model name	Model equation
1	Newton’s model	$MR = \exp(-k \times t)$
2	Page model	$MR = \exp(-k \times t^n)$
3	Modified Page model	$MR = \exp[-(k \times t)]^n$
4	Henderson and Pabis model	$MR = a \times \exp(-k \times t)$
5	Wang and Singh model	$t = \{[a \times \ln(MR)] + [b \times [\ln(MR)]^2]\}$
6	Thompson model	$MR = 1 + a \times t + b \times t^2$

Pabis, Thompson, Page, Modified Page & Wang and Singh model has been tested and shown in Table 1. All thin-layer mathematical drying models are validated and judged against the measured data obtained by carrying out test with predicted values of moisture content [4, 5].

The regression analysis was used to guess honesty of fit and the model is said to be the most excellent model when it shows the slightest values for chi-square, RMSE, and utmost value for R^2 (coefficient of determination) and can be calculated by Eqs. (1) and (2) as [3–7]:

$$R^2 \text{ or } r^2 = 1 - \left\{ \frac{\left[\sum_{i=1}^N MR_{P,i} - MR_{E,i} \right]^2}{\left[\sum_{i=1}^N MR_P - MR_{E,i} \right]^2} \right\} \tag{1}$$

$$E_{RMS} \text{ or } RMSE = \left[\sqrt{\frac{\sum_{i=1}^N (MR_{P,i} - MR_{E,i})^2}{N}} \right] \tag{2}$$

where $MR_{P,i}$, $MR_{E,i}$, and MR_P is i th predicted, experimental, and mean value of MR; N is no. of observations.

2.6 Numerical Computation for Heat and Mass Transfer

The performance forecast of solar tunnel greenhouse dryer also depends upon the accurate assessment of convection heat and mass transfer coefficients. Following correlation, Eq. (3) is used for determination of convection heat transfer coefficient under forced convection [4, 8, 9]:

$$Nu = C \times (Re \times Pr)^n$$

$$\therefore h_c = \frac{K_{ha}}{L_c} \times c \times (Re \times Pr)^n \tag{3}$$

where Nu, Re, and Pr represents Nusselt, Reynolds, and Prandtl number; K_{ha} = thermal conductivity of humid air.

Equation (4) is used to evaluate the amount of heat required to evaporate the moisture [4]:

$$Q_{evap.} = 0.016 \times h_c \times [P(T_p) - RH \times P(T_{ap})] \tag{4}$$

Amount of moisture evaporated from the product can be written as:

$$m_v = Q_{evap.} \times \frac{A_{tray} \times \text{time interval}}{h_{fg}} \text{ in kg} \tag{5}$$

$$\therefore \frac{m_v}{Z} = C \times (\text{Re} \times \text{Pr})^n$$

where

$$Z = \frac{K_{ha}}{L_c} \times [P(T_p) - RH \times P(T_{ap})] \times A_{tray} \times t \tag{6}$$

Solving for getting a linear equation of line $Y = mX + c$

$$\therefore \ln\left(\frac{m_v}{Z}\right) = \ln C + n \times \ln(\text{Re} \times \text{Pr}) \tag{7}$$

Therefore, from equation of line, we can write

$$Y = \ln\left(\frac{m_v}{Z}\right); mX = n \times \ln(\text{Re} \times \text{Pr}) \tag{8}$$

i.e. $m = n$ and $X = n(\text{Re} \times \text{Pr})$

$$c = \ln C \text{ i.e. } C = \exp c$$

By use of regression tool, the values of X, Y, constants C, and n at prescribed interval of time can be determined. Later on values for convection heat and mass transfer coefficient along with amount of heat required to evaporate the moisture from the tomato slices can be found out at corresponding drying time. The mass transfer coefficient can be evaluated as [4, 8]:

$$h_m = 16.273 \times 10^{-3} \times h_c \times \left[\frac{(P(T_p) - RH \times P(T_{ap}))}{T_p - T_{ap}} \right] \tag{9}$$

The various physical properties related to moist air can be estimated from the mean temperature of product and drying air temperature by means of the following expressions [4, 8]:

$$\text{Density } : \rho_{ha} = \frac{353.44}{(T_m + 273.15)} \tag{10}$$

$$\text{Viscosity } : \mu_{ha} = [1.718 \times 10^{-5} + (4.620 \times 10^{-8} \times T_m)]$$

SpecificHeat :

$$C_{ha} = \left[\begin{matrix} 999.2 + 0.1434 \times T_m + 1.101 \times 10^{-4} \times (T_m)^2 \\ -6.578 \times 10^{-8} \times (T_m)^3 \end{matrix} \right] \tag{11}$$

Partial Vpour Pressure :

$$P(T) = \text{EXP} \left[25.317 - \left(\frac{5144}{T + 273.15} \right) \right] \tag{12}$$

$$\text{Viscosity } : \mu_{ha} = [1.718 \times 10^{-5} + (4.620 \times 10^{-8} \times T_m)]$$

3 Result and Discussion

3.1 Mathematical Thin-Layer Drying Modeling

To standardize the drying curves, information of moisture content at each interval of experimentation was transformed to mainly useful MR expressions and then curve fitting computation with time has been carried on selected drying models.

Table 2 demonstrates the values of drying coefficients and constant for the selected models, which were obtained by the regression analysis of the natural logarithm of MR on drying time. For validation of models, statistical analysis and graphical presentation were used. From the table, it is observed that the R² values for all models are bigger than 0.95, indicating a good fit and varied between 0.9684–0.9958 while RMSE values stuck between 0.0116–0.1342.

These values confirm that all selected thin-layer drying models envisage the drying kinetics of tomato effectively. Result shows that Wang and Singh model has the highest value of R², hence found to be more precise in forecasting the thin-layer

Table 2 Statistical parameters of drying models

Sn.	Drying model	Drying constant	R ²	RSME
1	Newton’s model	k = 0.1773	0.9927	0.0253
2	Page model	k = 0.228; n = 0.825	0.9684	0.0414
3	Modified page model	k = 0.2163; n = 0.8253	0.9838	0.0511
4	Henderson and Pabis model	k = 0.2264; a = 1.143	0.9823	0.0299
5	Wang and Singh model	a = -0.149; b = 0.006	0.9958	0.0116
6	Thompson model	a = -6.144; b = -0.685	0.9946	0.1342

drying characteristics of tomato. Figures 2, 3, 4, 5, 6 and 7 demonstrate plotting of experimental data with predicted ones for the models showing better fit for experimental data. In these diagrams, the experimental values are concentrated around

Fig. 2 Newton model

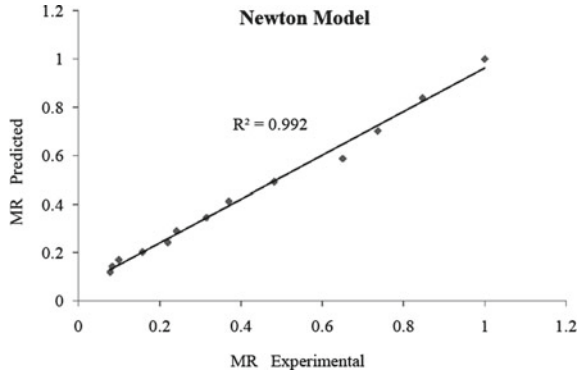


Fig. 3 Page model

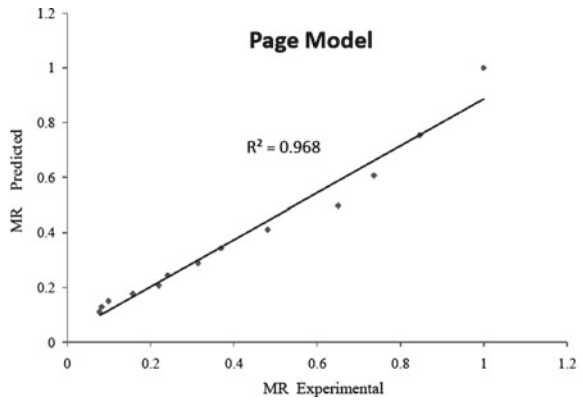


Fig. 4 Modified page model

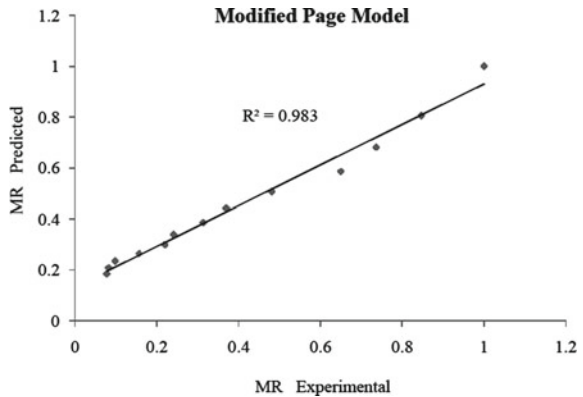


Fig. 5 Henderson and Pabis model

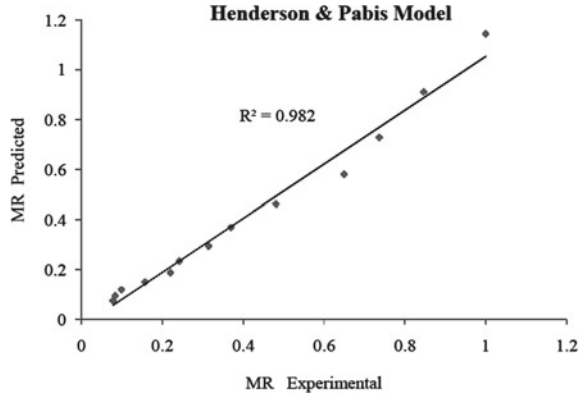


Fig. 6 Wang and Singh model

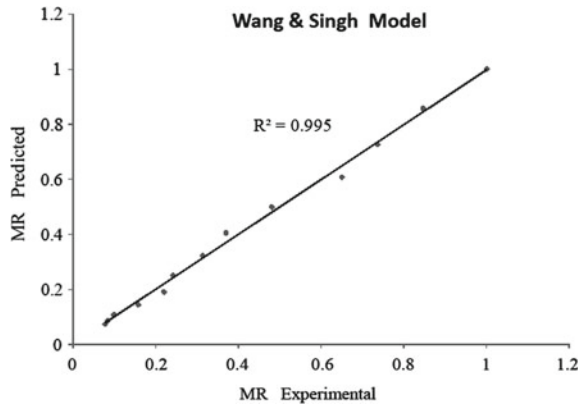
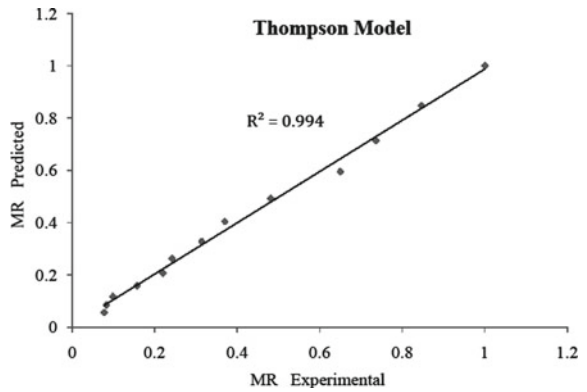


Fig. 7 Thompson model



a straight line representing the values found by computation, which indicates the exactness of thin-layer drying model for drying of tomato.

3.2 Numerical Computation of Heat and Mass Transfer

In this study, the authors focus on forced convection only due to faster drying with better quality of produce as compared to natural convection mode of drying. Table 3 illustrates experimental data as well as results of convection heat and mass transfer coefficients. The product of Re and Pr has been experiential as $(RePr) < 10^5$, which shows that whole heat transport for tomato slices drying falls inside a laminar regime. Result showed that with increase in drying time (no. of observations), Nu starts to decline as a result of reduction in the rate of moisture evaporation. Also, the fluctuation in constant C as well as coefficient n can be observed as 0.76, 0.94, 0.444 and 0.247 respectively, for the consecutive drying days. It is experiential that convective heat and mass transfer coefficient in dryer are very high during commencement of drying. This is mostly due to high moisture content of products as well as high rate of moisture evaporation in the beginning.

In other words, product surface behaves like wetted surface. This verifies that h_c is a sturdy function of moisture evaporated. The behavior of convective heat and mass transfer coefficient is shown in Figs. 8 and 9.

The value of convective heat and mass transfer coefficient for tomato slices varies from 2.17 to 13.51 W/m²K and 91 to 707 W/m²K, respectively. In other words, the value of heat along with mass transfer coefficient decreases with drying days due to decrease in moisture content.

Table 3 Experimental data for thermal modeling

Day	T _i °C	RePr	m _v kg	Nu	h _c	h _m
1	48	22,738	0.292	65.34	13.51	658.58
1	49	17,876	0.21	58.72	12.156	707.46
1	49	16,240	0.165	56.27	11.661	552
1	47	15,361	0.322	54.90	11.31	526.87
1	42	14,734	0.131	53.89	10.94	611.21
1	39	13,276	0.151	51.45	10.365	584.62
2	46	21,725	0.241	11.12	2.283	94.29
2	51	18,992	0.125	10.75	2.239	91.19
2	54	117,924	0.100	10.60	2.224	236.93
2	56	17,433	0.095	10.53	2.223	130.86
2	55	16,025	0.09	10.31	2.168	100.63

Fig. 8 Variation of Nu versus RePr

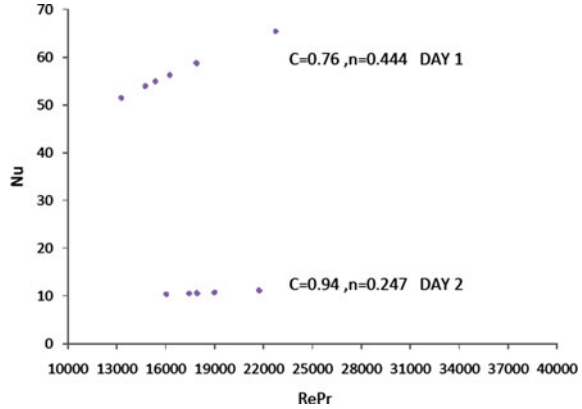
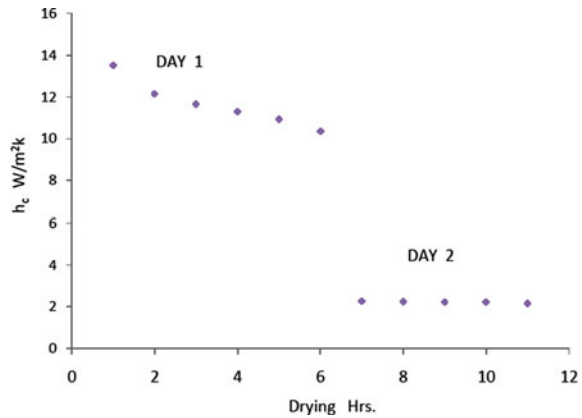


Fig. 9 Variation of convection heat transfer with drying time



4 Uncertainty Analysis

Errors and uncertainties in the experimentation can take place from instrument selection, condition, calibration, observation, ambiance, reading, and trial scheduling. In this work, different observations like temperatures, RH, speed of drying air, moisture content of produce, solar radiation, and weight loss were measured by appropriate utensil. Throughout the measurement of above parameters, the experimental errors, i.e., the uncertainties that take place, are shown in Table 4.

Let X_R be the uncertainty in result and $X_1, X_2 \dots X_n$ be the errors in the individual variables.

Table 4 Uncertainty analysis

Sn.	Uncertainty	Solar dryer	Sun drying
1	Ambient air temperature	± 0.381	± 0.381
2	Drying air temperature in tunnel 1	± 0.381	–
3	Drying air temperature in tunnel 2	± 0.381	–
4	Drying air outgoing temperature from greenhouse	± 0.381	–
5	Weight loss	± 0.500	± 0.500
6	Relative humidity (RH)	± 0.141	± 0.141
7	Air speed at inlet	± 0.173	± 0.173
8	Solar radiation (I)	± 0.141	± 0.141

5 Conclusions

The conclusions drawn from the present study have been summarized as follows:

1. The drying behavior of tomato slices was experimentally examined by regression analysis. Six thin-layer drying models were compared with two statistical parameters R^2 and RMSE. According to the outcome, the Wang and Singh model gave outstanding fit for all data with higher R^2 (0.9958) and lower RMSE (0.0116).
2. It is inferred that the convection heat and mass transfer coefficient are sturdy functions of relative humidity, temperature as well as mass of product for a specific size of tunnel greenhouse. Result showed that h_c and h_m varied from 2.17 to 13.51 W/m²K and 91 to 707 W/m²K, respectively, and experiential to lessen with the succession of drying time owing to decrease in moisture removal with an increase in drying time in every day of drying.
3. The moisture content of tomato was reduced from 90 to 11% w.b. in 18 h for the open sun drying, whereas the solar tunnel dryer took only 13 h.
4. The drying air is heated by the tunnel greenhouse satisfactorily with the purpose of increasing its capacity in favor of taking up moisture from the product.

From the above discussions, a novel proposed design of solar tunnel greenhouse dryer is the best option for end user. The dryer is exceptional for mass fabrication, superb transportability, effortless tracking, and easy assembly at site makes it a Do It Yourself (DIY) kit; thus helpful notably to get better agricultural returns for farmers in appreciation of the hard efforts they have devoted in crop cultivation. Therefore, commercial application looks to be feasible.

References

1. R. Patil, R. Gawande, Comparative analysis of cabinet solar dryer in natural and forced convection mode for tomatoes. *Int. J. Res. Sci. Innov.* **3**(7), 49–52 (2016)
2. R. Patil, R. Gawande, A review on solar tunnel greenhouse drying system. *Int. J. Renew. Sustain. Energy Rev.* **56**, 196–214 (2016)
3. E. Akpınar, Determination of suitable thin layer drying curve model for some vegetables and fruits. *J. Food Eng.* **73**, 75–84 (2006)
4. R. Patil, R. Gawande, Mathematical modeling of solar drying system in solar drying technology-concept, design, testing, modeling, economics, and environment, by ed. O. Prakash, A. Kumar, Eds. (Springer Nature, Singapore, 2017), pp. 265–316
5. R. Patil, R. Gawande, Drying characteristics of Amla candy in solar tunnel greenhouse dryer. *Int. J. Food Process Eng.* **41**(6), 1–11 (2018)
6. O. Badaoui, S. Hanini, A. Djebli, B. Haddad, A. Benhamou, Experimental and modeling study of tomato pomace waste drying in a new solar greenhouse: evaluation of new drying models. *J. Renew. Energy* **133**, 144–155 (2019)
7. D. Ahmed, H. Salah, B. Ouassila, H. Brahim, B. Amina, Modeling and comparative analysis of solar drying behavior of potatoes. *J. Renew. Energy* **145**, 1494–1506 (2020)
8. M. Kumar, O. Prakash, K. Kasana, Experimental investigation on natural convective heating of milk. *J. Food Process Eng.* **35**(5), 715–726 (2012)
9. M. Kumar, Effect of size on the convective heat and mass transfer coefficients during natural convection greenhouse drying of khoa-a heat desiccated milk product. *Int. J. Renew. Energy Biofuels* **2014**, 1–11 (2014)

Efficiency Improvement of Concentrated Photovoltaic (CPV) System by Way of Various Active and Passive Cooling Techniques—A Review



Yogesh Nandurkar, Vivek Korde, and Narendra Giradkar

Nomenclature

A	Area (m ²)
CR	Concentration ratio (-)
G(λ)	Spectral DNI (W/m ² /nm)
q _{heat}	Heat power (W)
P _m	Maximum power output (W)
P _{in}	Incident Power (W)
V _{oc}	Open circuit Voltage
MJT	Multi Junction Tandem
CPV	Concentrated photovoltaic

Greek Letters

λ	Wavelength (nm)
η_{opt}	Optical Efficiency (-)
η_{cell}	Cell Efficiency (-)

Y. Nandurkar · V. Korde (✉) · N. Giradkar
Department of Mechanical Engineering, Yeshwantrao Chavan College of Engineering, Hingna
Road, Wanadongri, Nagpur 441110, India
e-mail: vmkorde@gmail.com

Abbreviations

InGaAs	Indium Gallium Arsenide
InGaP	Indium Gallium Phosphide
Ge	Germanium

1 Introduction

Solar energy is the world’s largest remaining source of untapped renewable energy. Majority of the world population are away from the power grid and do not have proper access to the electricity. Extending power lines from power grid to remote areas is often not yet economically feasible and so decentralized power sources, such as the CPV system, are a promising alternative. Multijunction cells consist of more than one pair of p-n junctions. It is designed in such a way that solar energy of different wavelengths can be converted into electricity through different layers of cell as shown in Fig. 1. Typically layers are stacked on top of each other, with light incident on the largest-band gap layer, which transmits longer wavelengths to smaller-band gap layers underneath.

MJTs are categorized as Concentrated Photovoltaic CPV, immense heat is generated through concentration. However, efficiency of MJT is reported around 46% according to National Renewable Energy Laboratory (NREL 2020). Such solar cells can be economically viable if sunlight is concentrated by a factor greater than 300x [1]. Even though the amount of light not converted into electricity is converted into heat, this waste heat deteriorates both the performance and codal life of the cell.

The solar cell’s efficiency is defined as the proportion of the maximum power output of the cell to the DNI which is incident on the cell.

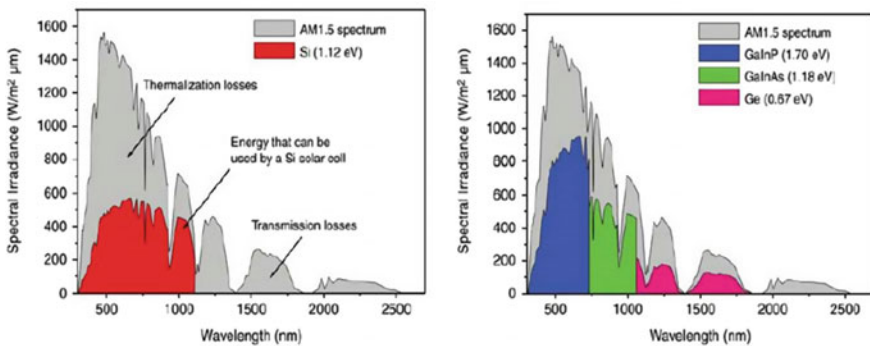


Fig. 1 Spectrum utilization through Conventional PV and MJT solar cell (NREL, 2020)

$$\eta_{cell} = \frac{P_{out}}{P_{in}} = \frac{P_{in}}{\int CR * A * \lambda * G(\lambda) * \eta_{opt}(\lambda) * d\lambda} \tag{1}$$

Therefore, the heat power produced on the cell is

$$q_{heat} = P_{in} * (1 - \eta_{cell}) \tag{2}$$

the electrical conversion efficiency because of the temperature dependence of the open – circuit voltage

High concentrations result in high heat flux on the solar cell’s surface and a rapid increase in the cell’s temperature. High temperature reduces (V_{oc}) and the maximum power voltage (V_{mp}) [2]. It has been observed that under $500 \times$ concentration and without any cooling arrangements, the solar cell can exceed $1000 \text{ }^\circ\text{C}$ [1]. This emphasizes the need for proper cooling technology to maintain the temperature within safe operation limits as well as to avoid suboptimal performance and risk of system failure [3].

2 Literature Review

Exhaustive efforts are being made worldwide to reduce the operating temperature of CPV module to increase overall performance in terms of electrical efficiency, power output and codal life of the module. A number of researchers have worked on cooling the CPV/PV module with various active and passive cooling techniques. Some of these techniques are discussed in the following section.

2.1 Peltier Effect (Active Cooling Medium)

Figure 2 shows the schematic of the combined PV-TEC system, the TEC module is installed in the back side of the PV cell and there is an aluminum sheet in between in order to spread the cooling effect in the back surface of the PV cell. Solar radiation

Fig. 2 Schematic of the thermoelectric cooling system [4]

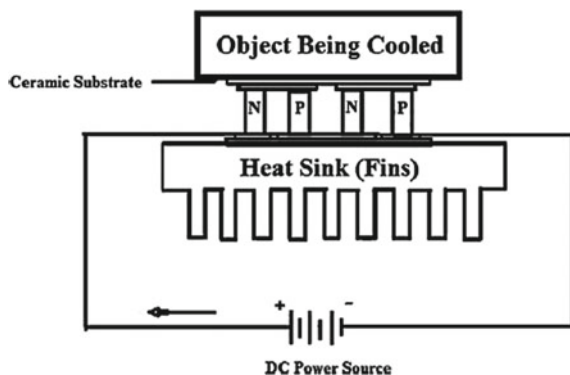


Fig. 3 Pulsating Cooling Pipe Arrangement on the Rear Side of PV Panel [5]



falls on the top surface of the encapsulated PV cell. A small portion of the sunlight energy is converted to electricity by PV cell and rest of it is wasted as heat through the top and bottom surfaces of the encapsulated cell. A fraction of the generated electricity by the PV cell is used to feed the TEC module in order to provide the cooling effect for the PV cell.

It can be observed that for a fixed solar radiation, higher cell temperature leads to less output power. At 3200 W/m^2 , the generated power for a cell temperature of 298 K is about 80% more than the generated power by the PV cell when the cell temperature is 360 K, which shows the importance of using an appropriate cooling system, especially at higher solar radiation levels which occurs in the CPV system [4].

2.2 Forced Cooling (Active Cooling Medium)

Forced cooling is another alternative way of cooling PV module. Figure 3 shows schematic of pulsating cooling pipe arrangement on the rear side of PV panel. 12 V DC fans are placed to dissipate the heat from the heat pipe at the top as shown in Fig. 3.

It has been found that the electrical output of water-cooled CPV is 4.7–5.2 times more than that of PV module (without concentration and cooling) [5].

2.3 Natural Cooling (Passive Cooling Medium)

Micro-fins have been identified as one of the most promising solution for CPV cooling. It can improve the thermal performance and at the same time lowers the weight of the system. Figure 4 shows cross-sectional view of the micro-finned silicon wafer and zooms on the fins. The CPV model is tested under concentrator standard

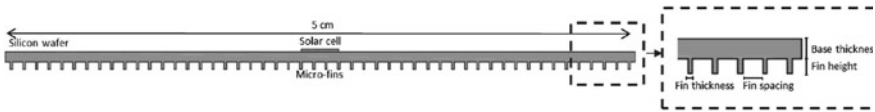


Fig. 4 Cross-Sectional view of the micro-finned silicon water and zoom on the fins [6]

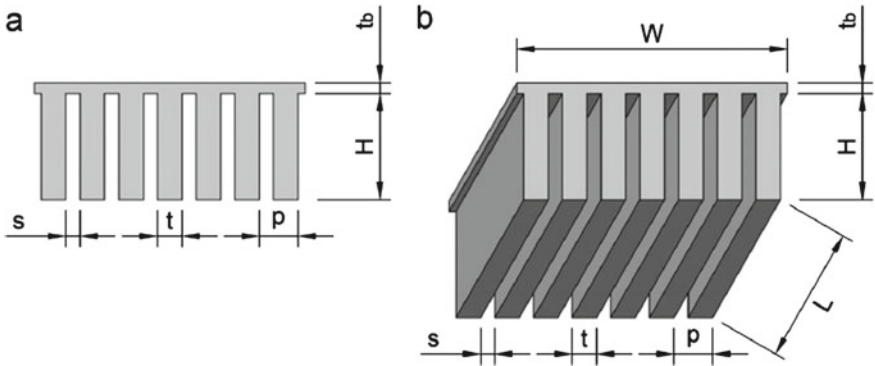


Fig. 5 Schematics of a finned heat sink a front view and b 3D rendering [7]

test conditions: 1000 W/m^2 for direct normal irradiance, an ambient temperature of $20 \text{ }^\circ\text{C}$ and cell electrical efficiency of 42.5%. The cell produces 2.20 W of waste heat. Worst case conditions: 1000 W/m^2 for direct normal irradiance, an ambient temperature of $20 \text{ }^\circ\text{C}$ and cell efficiency of 0%. In these conditions, the heat produced by the cell rises to 3.83 W [6].

2.4 Extended Surface Cooling (Passive Cooling Medium)

Extended surfaces are commonly used to extend transfer area to enhance conventional heat transfer passively. Fins are widely used in multiple fields where cooling is required from industrial to electronics applications. Figure 5 shows schematic of finned heat sink is attached at the back side of CPV module; and result shows that in Fig. 6, cell temperature goes upto $120 \text{ }^\circ\text{C}$ without fins; and in Fig. 7, cell temperature decreases upto $80 \text{ }^\circ\text{C}$ with fins under standard testing condition [7].

2.5 Heat Pipe (Passive Cooling Medium)

Heat pipe cooling is suitable for single cell arrays at high concentration ratio, e.g., 1000 suns, and linear concentrator at lower concentrator ratios, in the order of 30 suns. Roynes et al. [8] used a copper heat pipe with soldered longitudinal copper fins

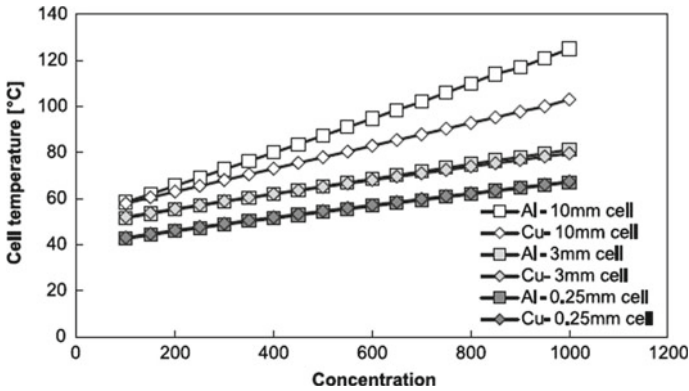


Fig. 6 Cell temperatures for different substrates and cell dimensions, depending on the geometric concentration without fins [7]

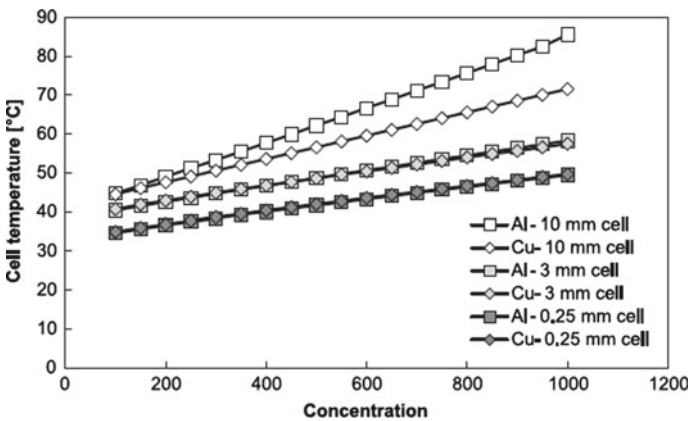


Fig. 7 Cell temperatures for different substrates and cell dimensions, depending on the geometric concentration with fins [7]

to remove heat at roughly 700 suns, using water or acetone as the working fluid. Heat removal was by natural convection. The temperature difference between the cell and the ambient air was roughly 30 °C. Beach and White [9] conducted a study comparing heat pipe and forced convection water cooling for single cell system and concluded that the heat pipe cooling system was superior. Farahat [10] examined heat pipe cooling for a linear concentrator with about 24 suns incident on the cell. The heat pipe was a kite-shaped thermosyphon, with benzene as the working fluid. Heat was rejected from two aluminum plates with perpendicular extruded fins. The evaporator temperature exceeded the design temperature of 140 °C for wind speed of less than 1 m/s. Feldman et al. [11] cooled a linear concentrator with a copper thermosyphon, with 20 suns incident on the cell. The working fluid was refrigerant R-11, due to the relatively low operating temperature of 40 °C. Heat removal was by

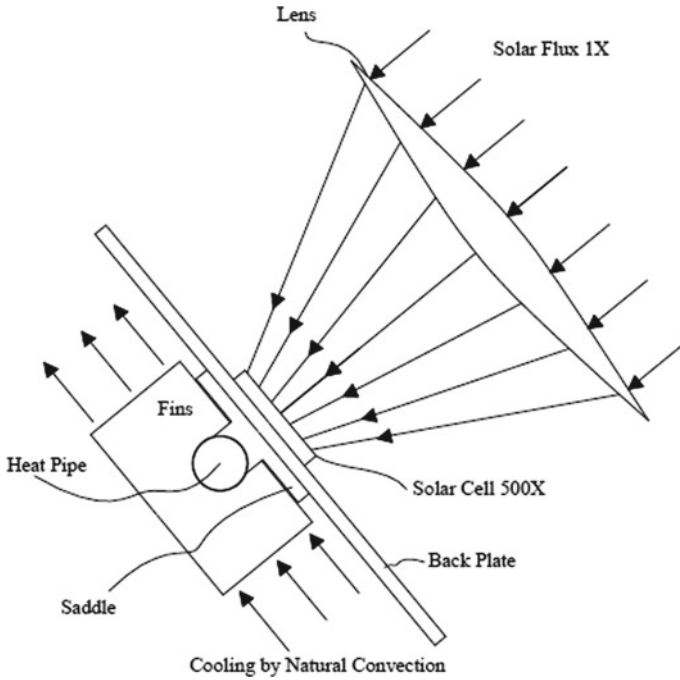


Fig. 8 Passive cooling by using Heat Pipe, Fins and Fresnel lens [13]

natural convection [12]. A schematic of the concentrated photovoltaic module with a heat pipe heat sink is shown in Fig. 8. The solar cell is mounted on a back plate. The incoming solar flux (1X) is concentrated roughly 500 times by a Fresnel lens. The concentrated flux strikes the solar cell, producing electricity. The waste thermal energy passes from the cell through the saddle and into the heat pipe rejecting the heat to the atmosphere by passive cooling, with a temperature difference of only 43 °C. In contrast, the temperature difference between the cell and ambient would be over 110 °C using passive cooling from the back plate [13].

3 Smart Solar Power Plant Managing Through Scada

One such system designer is Staer Sistemi, an automation and control company based in Italy, which tackled the design of the first PV automated management system in late 2009 and has since revised it over the last 4 years. The initial design included a simple data acquisition system (DAS), but the company quickly identified that due to the volatility of solar radiation at ground level, mainly due to atmospheric turbulence, it would require a pretty fast sampling pace (5 s or less). Due to this requirement, the company decided the best approach would be to develop the final application in an industrial established Supervisory Control and Data Acquisition

(SCADA) Environment. This way it would allow designers to manage data streams in the range of several thousand measures per second.

3.1 Monitoring PV Plants

Designed for the monitoring of the performance, the system logs any problem and triggers alarms so that the engineering staff can fix or change components or fine-tune the process of plant operation. The system monitors the performance by means of a sophisticated mathematical model initialized once at installation time with some plant design data: PV panels peak power, inverters, manufacturer-provided electric parameters, number of strings, strings length, etc. The automatic comparison between the calculated and the real production figures (supplied by the already mentioned data logger) will give a precise indication of the plant performance or plant health every minute or less. Today, monitoring and performance analysis of solar PV plants has become extremely critical due to the increasing cost of operation and maintenance as well as reducing yield due to performance degradation during the lifecycle of the plant equipment. This means that the use of a monitoring system can become essential to ensure high performance, low downtime and fault detection of a solar PV power plant during the entire lifecycle.

3.2 Scada System Increases Solar PV Plant Performance

When contemplating the use of a solar electric photovoltaic system, it is important to assess how much energy in theory the system can produce according to location, orientation and plant conversion efficiency. Solar PV installations effectively reduce the customer load and, during minimum loading conditions, may export energy back to the utility in a net energy metering (NEM) transaction. The Institute of Electrical and Electronic Engineers (IEEE) recommended a set of guidelines (IEEE P1547.6) to PV system integrators to help them design systems that are operable with utility systems. SCADA provided flexibility in monitoring and controlling the various plant component and operations, including trackers, inverters, substations and meters. Figure 9 shows the schematic of Supervisory Control and Data Acquisition. The system has proven capable of managing PV plants exceeding 5 MW individually, as well as some larger multi-tenant, multi-site systems.

4 Conclusion

The operating temperature of CPV module pronouncing its effect upon its overall performance is well documented. As the temperature increases linearly it deteriorates

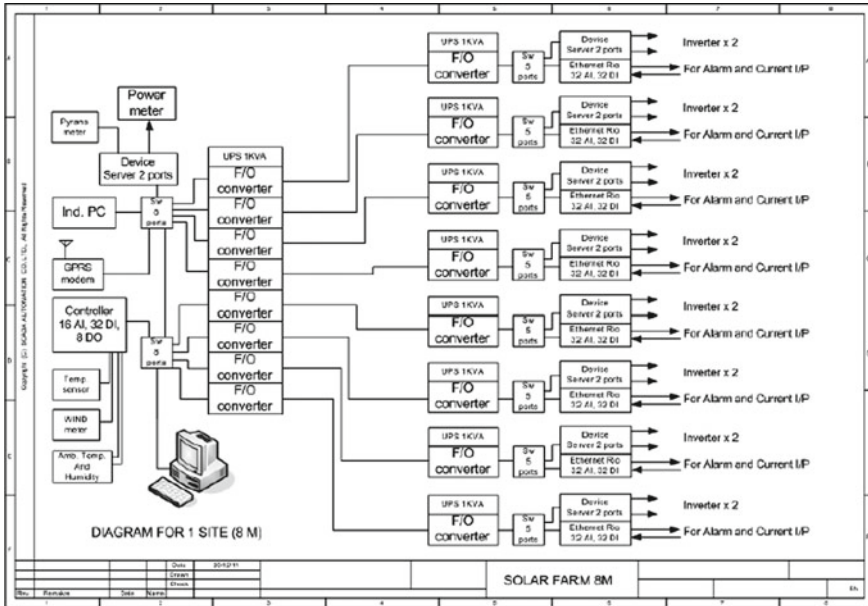


Fig. 9 Schematic of supervisory control and data acquisition

the performance in terms of power output, efficiency and codal life of cell. Therefore, decreasing the operating temperature of CPV module can boost the electrical efficiency. This paper describes various active and passive cooling techniques for improving the performance of CPV module. In passive cooling, fins are commonly used to enhance conventional heat transfer from back of CPV module. Heat pipe is another widely used medium for passive cooling of CPV module. Micro-fins on the back side of CPV module with certain time interval reduces the CPV module temperature significantly. However, active cooling medium required additional power for maintaining cell operating temperature within optimum range. Introducing Peltier cooling device at back of CPV module and force cooling with the help of compressed air is used for controlling the operating temperature of module. All these techniques have significant effect on minimizing the CPV module operating temperature resulting in overall performance improvement in terms of power output, electrical efficiency and codal life of cell.

5 Future Scope

A number of researches show that various active and passive cooling techniques were utilized and all are effective, but these techniques were performed on different CPV/PV module material and configuration in different geographical condition. So,

it's very complicated to compare between them which one is more effective. So, there is a scope of performing a research with all these various cooling techniques on one setup and to study which technique is more optimum among them.

References

1. H. Cotal, J. Frost, Heat transfer modeling of concentrator multijunction solar cell assemblies using finite difference techniques, in *35th IEEE PVSC*, Honolulu, HI, USA (2010)
2. H. Cotal, R. Sherif, Temperature dependence of the IV parameters from triple junction GaInP/InGaAs/Ge concentrator solar cell, in *4th World Conference on photovoltaic Energy Conversion*, (IEEE, 2006), pp. 845–848
3. M. Theristis, T. Odonovan, Electrical-thermal analysis of III-V triple-junction solar cells under variable spectra and ambient temperatures. *Sol. Energy* **118**(2015), 533–546 (2015)
4. H. Najafi, K. Woodbury, Optimization of a cooling system based on Peltier effect for photovoltaic cells. *Sol. Energy* **91**(2013), 152–160 (2013)
5. A. Raj, S. Kumar, G. Manikandan, P. Titus, An experimental study on the performance of concentrated photovoltaic system with cooling system for domestic applications. *Int. J. Eng. Adv. Technol.* (2014). ISSN: 2249-8975
6. L. Micheli, K. Reddy, T. Mallick, Plate micro-fins in natural convection: an opportunity for passive concentrating photovoltaic cooling. *Energy Procedia* **82**(2015), 301–308 (2015)
7. L. Micheli, E. Fernandez, F. Almonacid, T. Mallick, Performance, limits and economics perspectives for passive cooling of High Concentrator Photovoltaics. *Sol. Energy Mater. Sol. Cells* **153**(2016), 164–178 (2016)
8. A. Royne, C. Dey, D. Mils, Cooling Photovoltaic cells under concentrated illumination: a critical review. *Sol. Energy Mater. Sol. Cells* **86**(2005), 451–483 (2005)
9. T. Beach, M. White, Heat pipe for passive cooling of concentrator solar cells, in *IEEE@1981 Proceedings of the 15TH Photovoltaic Specialists Conference* (1981), pp. 75–85
10. A. Farahat, Improvement in the thermal electric performance of a photovoltaic cells by cooling and concentration techniques, in *IEEE@2004 39th International Universities Power Engineering Conference*, Newyork (2004), pp. 623–628. ISBN: 1-86043-365-0
11. T. Feldman, D. Kenney, W. Edenburn, A passive heat pipe cooled photovoltaic receiver, in *IEEE@1981 Proceedings of the 15TH Photovoltaic Specialists Conference* (1981), pp.165–172
12. A. Akbarzadeh, T. Wadowski, Heat piped-based cooling system for photovoltaic cells under concentrated solar radiation. *Appl. Thermal Eng.* **16**(1), 81–87 (1996)
13. W. Aderson, S. Tamanna, D. Sarrat, P. Dussinger, *Heat pipe cooling of concentrating photovoltaic (CPV) systems*. American Institute of Aeronautics and Astronautics, Advanced Cooling Technologies, Inc., Lancaster, PA, 17601 (2007)

Experimental Study of Vacuum Tube Heat Pipe-Based Solar Collector for Cooking Application



Asim Kumar Joshi, Sachin Gupta, Arunendra Kumar Tiwari, Falgun Raval, and Milan Sojitra

1 Introduction

Cooking is an energy-intensive process. In developing countries like India, people below the poverty line still use biomass as primary cooking fuel. Most people use conventional fuel sources like LPG/PNG or electricity for household cooking in urban areas. In both cases, the resulting fuel demand contributes to deforestation and a rise in greenhouse gas emissions. In the case of biomass, indoor pollution often happens, which seriously affects the user's health. This pollution causes around 7,80,000 premature deaths a year in India [1]. Still, biomass usage as cooking fuel is about 80 and 18% in rural and urban India [2] because biomass is readily available and inexpensive.

To overcome these issues and for sustainability, green cooking fuels are being explored and studied. Solar energy is one of them, which is freely and abundantly available. In India, round the year (300–330 days), solar energy received is around 5–7 kWh/m² [3], high enough to be utilized for cooking. Solar cookers, in general, are classified as concentrating and non-concentrating. Concentrating cooker gives higher temperatures but requires tracking, which makes it complicated and costly. Under the non-concentrating category, box-type solar cookers are the simplest, cheapest having a maximum achievable temperature of around 120–130 °C [4]. The box-type solar cookers provide slow cooking. In the non-concentrating category, the potential of a flat plate solar collector and solar evacuated tube is for medium temperature application [5, 6].

The first study on using a vacuum tube with heat pipe for solar cooking was reported by Balzar et al. in 1996. They tested a solar collector system with six tubes mounted in parallel to heat 5 l of edible oil up to 252 °C [7]. Garg et al. [8] developed

A. K. Joshi (✉) · S. Gupta · A. K. Tiwari · F. Raval · M. Sojitra
Solar Energy Division, Sardar Patel Renewable Energy Research Institute (SPRERI), Vallabh Vidya Nagar, Anand 388120, Gujarat, India

a heat exchanger-based pressure cooker using a solar collector with 12 vacuum tubes and tested it for boiling water at the different loads of 4, 8, and 14 kg water. They concluded that in the system, full pressure condition establishes at 115 °C and that it is useful for community-level cooking. Esen [9] studied three different refrigerants in heat pipe to vacuum tubes for cooking application. The maximum temperature obtained was 175 °C for heating 7–l edible oil. The time required for cooking 250 g rice and 500 g potato was 50–63 min and 57–70 min for the three refrigerants. Sharma et al. [10] tested solar vacuum tube collector with erythritol phase change material for different 5, 7, 8, and 10 kg loads of water and concluded that the system cooked successfully twice in a day.

Not much work has been reported on testing such solar vacuum tube systems with loads other than water. In this paper, the performance of a solar collector with heat pipe for water boiling and cooking rice and split pigeon pea is evaluated and discussed for entire day operation in Indian climatic conditions. Heat-up time taken and detailed temperature distributions were measured and examined.

2 Experimentation and Methodology

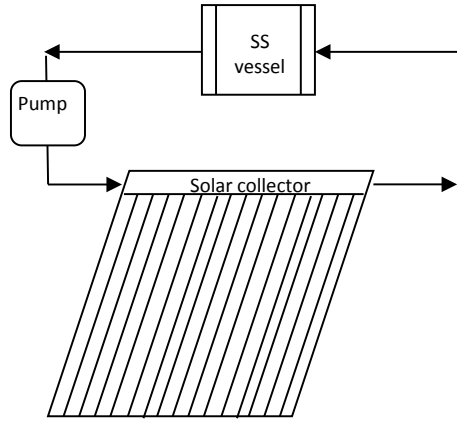
The test setup is fabricated in-house, installed, and tested in Solar Energy Division at SPRERI. The test setup's schematic and photographs are shown in Fig. 1a, b. It consists of a single vacuum tube solar collector (SVTC) having 20 tubes with heat pipes connected in series. The SVTC is manufactured and supplied by M/s WesTech Solar Technology Wuxi Co. Ltd., China. A gear pump is connected in line to circulate the HTF. The HTF used was SK Supertherm 300 brand synthetic oil. The oil was circulated through the collector's header and in the cooking vessel's jacket in a closed loop-cycle, as shown in Fig 1a. The cooking vessel is made of food-grade stainless steel. The vessel is provided with a jacket of 10 mm to circulate HTF in it for indirect heating. The vessel is of 3 l capacity having inner diameter 119 mm and height 110 mm.

The instantaneous values of solar irradiance (W/m^2) at the tilted angle 26° of solar collector, temperature ($^\circ\text{C}$) of HTF at the inlet and outlet collector, and water in the vessel were recorded at an interval of 2 min.

The system is tested in three phases.

2.1 Water Boiling Test

Initially, the stainless-steel jacket vessel (SSV) was filled with 3.0 kg ambient temperature water before beginning the test. The vessel has been insulated from all sides except the top. The vessel top was kept covered during experimentation with a stainless-steel plate without any insulation. The water was allowed to heat up to



(a)



(b)

Fig. 1 a Schematic SVTC with heat pipe cooking system, b SVTC heat pipe-based cooking test setup

$\geq 85\text{ }^\circ\text{C}$. After boiling, water is replaced with fresh water. The experiment has been performed on December 30, 2019, from 9:00 am to 5:00 pm.

The system efficiency has been evaluated during this test using the following equation.

$$\eta = \frac{(M \times C_p \times \Delta T \times N)}{(A \times G)} \tag{1}$$

where

M = mass of water = 3 kg;

C_p = specific heat of water = 4.18 kJ/kg °C;

ΔT = difference of initial and final water temperature = (avg. 90 °C – 25 °C) = 65 °C;

A = gross area of the collector = 3.21 m²;

G = total radiance = 5.01 kWh/m².day; and

N = the number of batches, i.e., frequency of water replacement = 09.

2.2 Stagnation Test

In this test, the thermic fluid was allowed to get heated up to maximum achievable temperature without any load/heat sink. During this experiment, the entire system has been kept insulated, and the pump is operated during the entire test period at 4 l per minute (LPM) flow rate. This test is performed on January 09, 2020, from 9:00 am to 5:00 pm.

2.3 Cooking/Load Test

The system was tested for cooking by boiling. Rice and split pigeon peas lentil are cooked alternately. The dry weight of rice and lentil taken in each slot is 500 g. Before cooking, lentils are soaked in water for 1 h, while rice is directly cooked. This experiment has been performed on February 01, 2020, from 9:00 am to 5:00 pm.

3 Results and Discussions

3.1 Water Boiling Tests

During the test, nine batches of the water (3 l each), i.e., 27 l of water, got heated up to ≥ 85 °C in the whole day from 9:00 am to 5:00 pm. The variations in temperature and radiation values during water boiling tests are shown in Fig 2. In the graph, the temperature of water in the vessel is represented by ‘Water in SSV’. The HTC temperature at collector inlet and outlet is represented by ‘Collector in’ and ‘Collector out’. The ambient temperature and radiation recorded are represented as

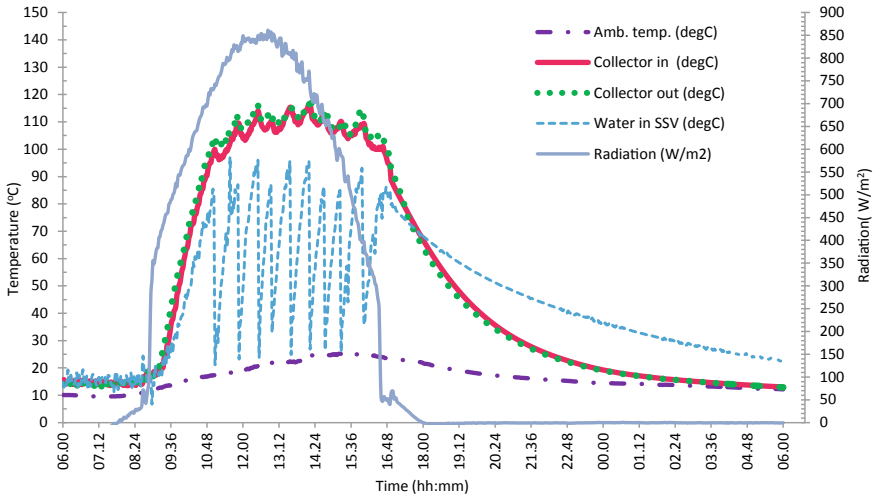


Fig. 2 Temperature profile during water boil test

‘Amb. Temp.’ and ‘Radiation’. Drops in water temperature indicate replacing hot water with ambient temperature as a new load. Initially, from 9:00 am to 11:00 am, it took approximately 2 h to reach water temperature up to 95 °C due to the preheating of thermic fluid and low radiation. After that, it took around 30–40 min for heating to reach a water temperature ≥ 85 °C. The radiation received during the experiment period is 5.01 kWh/m².day. The overall efficiency of the system is estimated using Eq. (1) and found to be 12.66 % based on the total water boiled in the entire day against solar energy input on the collector area.

3.2 Stagnation Temperature Test

In this test, the temperature of the inner plate top surface of the jacketed SS vessel is measured without any load to observe the possible maximum achievable temperature. The thermic fluid flow line and vessel are kept insulated during this test. The results are shown in Fig. 3, which indicates that the collector outlet temperature is around 173 °C while the stagnation temperature achieved is 164 °C. With an increase in radiation, the temperature of HTF at collector inlet and outlet and SS vessel surface increases. The collector outlet reached 152 °C at 12:52 pm and remained above 150 °C till 4:36 pm, i.e., for 3 h and 44 min. The maximum radiation observed was 869 W/m² observed at 12:52 pm, and the average radiation for the testing period was 635 W/m². The SS vessel surface temperature reached 100°C at 11.30 am, i.e., in 2.5 h and a maximum of 164 °C at 2.00 pm. Overall, the surface temperature remained above 100 °C till 6.00 pm, i.e., for around 6.5 h.

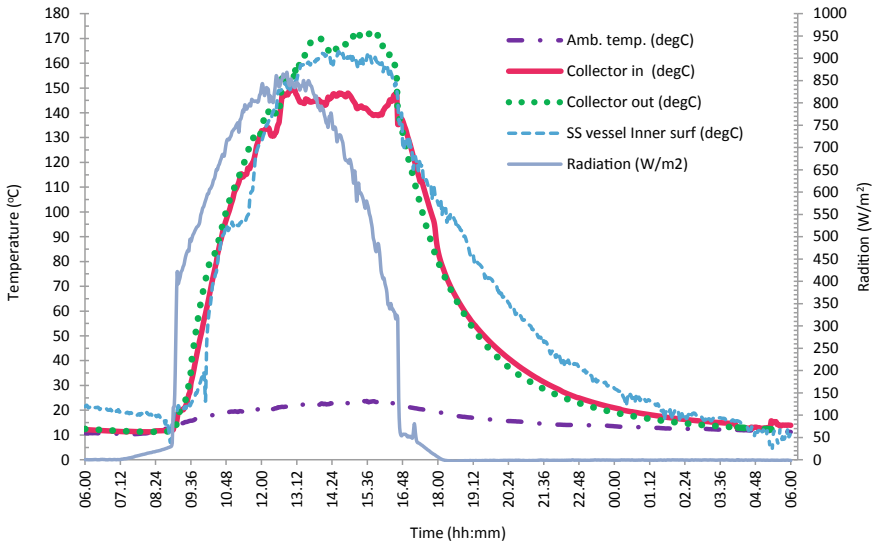


Fig. 3 Temperature profile and radiation during stagnation test

3.3 Cooking/load Test

In the beginning, the preheating of HTF up to temperature suitable for boiling water took more time as radiation was low in the morning. The average radiation observed from 9:00 am to 10:00 am is 393.2 W/m^2 . The first batch of 500 g rice and 1.8 kg water has been filled at 9.00 am with the start of the system. The first batch of rice cooked in 2 h. After that, it took 40–50 min for cooking every batch of dry 500 gm rice or lentil. Per 500 gm of the dry item, 1.8 l of water is added. During the experiment, from 9:00 am to 5:00 pm, the system cooks a total of 2.0 kg of each dry rice and 1.5 kg split pigeon peas lentil. The wet weight of cooked rice and split pigeon peas lentil is 7.8 and 4.1 kg, respectively. After getting heated, the thermic fluid temperature remained in the range of 120–140 °C. The maximum temperature of HTF at the collector inlet and outlet has been observed as 136 and 140 °C, respectively, at $4.42 \text{ kWh/m}^2/\text{day}$ of solar energy input. The variations in temperature and radiation values during cooking tests are shown in Fig 4. Figure 5 shows the cooked rice and lentils in the stainless-steel vessel.

System testing is under progress. It will be tested for other flow rates to optimize the flow rate for the maximum efficiency of the collector. Other identified HTF will be used and tested. Cooking tests for other items like boiling potato, egg, etc., will be carried out.

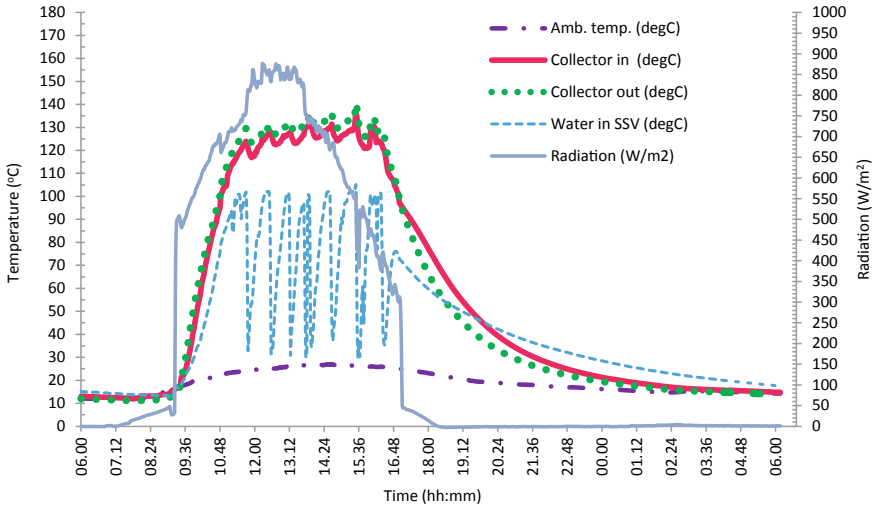


Fig. 4 Temperature profile observed in the system during rice and slit pigeon pea cooking

Fig. 5 Photographs of Rice and Lentils being cooked in the SVTC cooking device



4 Conclusion

The developed prototype of a solar collector with a heat pipe was found suitable for cooking by boiling. The total amount of rice and split pigeon peas lentils used was 2.0 and 1.5 kg on dry basis. The total weight of rice and lentils after cooking was 7.8 kg and 4.1 kg, which is sufficient for a family of four people. The overall efficiency of the system has been estimated at 12.66% for boiling water. From the results, it is concluded that the SVTC with heat pipe has the potential to be used for moderate temperature (150–170 °C) cooking applications.

Acknowledgements This research project was supported by the Indian Council of Agricultural Research (ICAR), India, under the All India Coordinated Research Project program, and the authors are also thankful to Dr. Gaurav Mishra, Director, SPRERI, for continuous guidance and support during the execution of the project.

References

1. A. Pillarisetti, M. Ghorpade, S. Madhav, A. Dhongade, S. Roy, K. Balakrishnan, S. Sankar, R. Patil, D. Levine, S. Juvekar, K. Smith, Promoting LPG usage during pregnancy: a pilot study in rural Maharashtra, India. *Environ. Int.* **127**, 540–549 (2019)
2. M. Sehgal, S.A. Rizwan, A. Krishnan, Disease burden due to biomass cooking-fuel related household air pollution among women in India. *Glob. Health Action* **7**(25236), 1–11 (2014)
3. S. Mohanty, P. Patra, S. Sahoo, A. Mohanty, Forecasting of solar energy with application for a growing economy like India: survey and implication. *Renew. Sustain. Energy Rev.* **78**, 539–553 (2017)
4. S.Z. Farooqui, A review of vacuum tube based solar cookers with the experimental determination of energy and exergy efficiencies of a single vacuum tube based prototype. *Renew. Sustain. Energy Rev.* **31**, 439–445 (2014)
5. A.K. Tiwari, S. Gupta, A.K. Joshi, F. Raval, M. Sojitra, TRNSYS simulation of flat plate solar collector based water heating system in Indian climatic condition. *Mater. Today Proc.* (2020). <https://doi.org/10.1016/j.matpr.2020.08.794>
6. S. Gupta, S. Rajale, F. Raval, M. Sojitra, A.K. Tiwari, A. Joshi, R. Singh, Comparative performance analysis of flat plate solar collectors with and without aluminium oxide-based nano-fluid. *Mater. Today Proc.* (2020). <https://doi.org/10.1016/j.matpr.2020.08.797>
7. A. Balzar, P. Stumpf, S. Eckhoff, H. Ackermann, M. Grupp, A solar cooker using vacuum-tube collectors with integrated heat pipes. *Sol. Energy* **58**(1–3), 63–68 (1996)
8. R. Kumar, R.S. Adhikari, H.P. Garg, A. Kumar, Thermal performance of a solar pressure cooker based on evacuated tube solar collector. *Appl. Thermal Eng.* **21**(16), 1699–1706 (2001).
9. M. Esen, Thermal performance of a solar cooker integrated vacuum-tube collector with heat pipes containing different refrigerants. *Sol. Energy* **76**(6), 751–757 (2004)
10. S.D. Sharma, T. Iwata, H. Kitano, K. Sagara, Thermal performance of a solar cooker based on an evacuated tube solar collector with a PCM storage unit. *Sol. Energy* **78**(3), 416–426 (2005)

Reliability Assessment of Smart Grid with Renewable Energy Sources, Storage Devices, and Cyber Intrusion



Lalit Tak, Atul Kumar Yadav, Neeraj Kumar Singh,
and Vasundhara Mahajan

1 Introduction

Development in the world economy and population, combined with rapid urbanization, has increased fuel energy consumption and energy demand on a daily basis. In order to maintain a healthy eco-system, in addition to the challenges of meeting rising demand, greater reliability, security, productivity, and a safe environment are also important. Technological change and innovation, in order to make the grid process smarter and smarter smart grids, the strides into digital technology were introduced [1].

The smart grid provides an unparalleled opportunity for the energy industry to step into the new age of reliability, availability, and efficiency, adding to the power infrastructure that enables electricity to be stored and generated by consumers, enabling faster electricity restoration after disconnection from the utility.

In recent decades, the advent of many technical advances as well as environmental and economic issues have made conventional electricity systems redundant and not well suited to meet the requirements of reliability, performance, and sustainability, not just because the complexities of the electricity grid also pose a challenge to the production and distribution of electricity [1, 2].

The implementation of a new smart grid concept or the automation of the grid to make it smarter through the use of various types of equipment and controls that interact and function together deliver power more effectively and efficiently to restore services more quickly when outages occur [2].

The smart grid technology encompasses various new technologies and applications that interact to create a more secure and reliable system. Electricity distribution systems are undergoing a revamp; moving towards smarter utilities with innovations such as electric vehicles, home appliances, etc. The modern grid allows electricity

L. Tak (✉) · A. K. Yadav · N. K. Singh · V. Mahajan
SVNIT, Surat, Gujarat, India

and data to flow in two forms, consisting of two distinctive and complex networks, cyber and power. Each network has its own set of rules and standards defined and is regulated exclusively by physical and logical laws belonging to that network. There is a security issue with the emergence of cybercrime, especially where communication is concerned.

Which is critical in fault detection, isolation and restoration from the reliability point of view and not only should recognize and isolate the faulty region. It's automatically reenergize the non-faulty component and boost reliability metrics [3].

Architecture of smart grid has been shown in Fig. 1. It visualizes each component, i.e., bulk generation, energy storage, a two-way communication system, transmission, distribution, and customer sections.

From a cybersecurity viewpoint, the implications of malicious commands can be modeled for risk management and early mitigation. Steps that are taken when a cyberattack takes place in a network component are that the affected area is isolated and measures are taken to restore supplies, such as closing points usually open. At higher loading speeds, reliability becomes more critical because supply restoration can be unfeasible or limited when failure occurs. In order to have more practical reliability, network limitations, e.g., line capacity and voltage limits, and various other steps need to be taken into account [4].

The design and technologies used for transmission and distribution grids and their device interactions would need to be modified. The demands of this transition will increase over the next 10–15 years as a result of energy efficiency initiatives

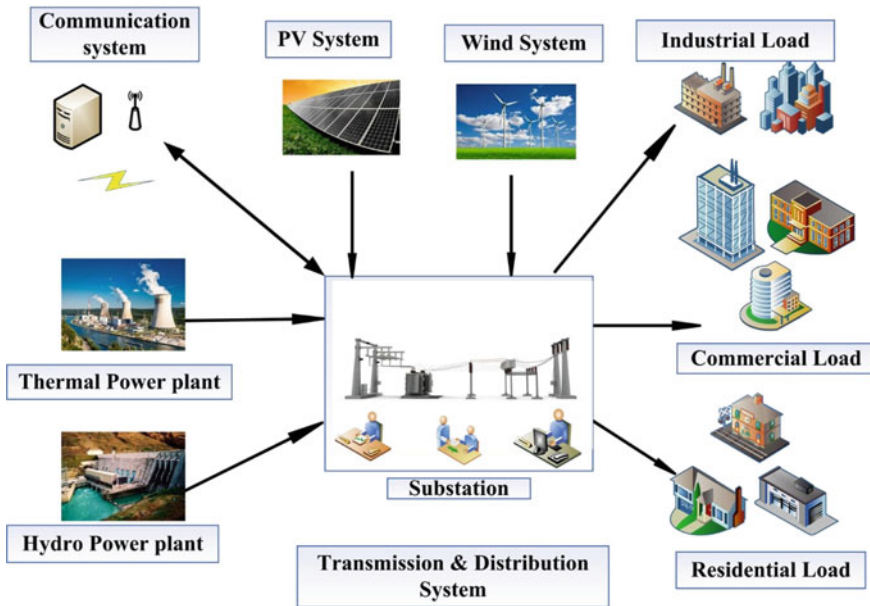


Fig. 1 An example of architecture of smart grid

in buildings with an increased presence of zero or positive energy buildings, i.e., equipped with their own energy sources for self-consumption or for selling part of their excess output to electricity operators and the complete integration of renewable energy sources (RES) which, by their very nature, display fluctuations in availability and productivity [5]. Energy storage would be needed in order to effectively cover the mismatch between energy needs and the generation of RES and the use of electric vehicles and their need for both to be sluggish.

This paper deals with the reliability of a smart grid based on a different mix of power grid systems such as traditional power grids, renewable energy grids, power grids connected with storage devices and cyber intrusions (CIs). The MATLAB software program is used for the simulation and study of electrical power systems. Results show that more efficient and sustainable electricity can be supplied to end-users when the power grid is combined with traditional, renewable energy sources and storage devices.

This paper is structured as follows. Section 2 briefly describes the smart grid and cyber threats. Section 3 describes basic principles for the evaluation of reliability indices. Section 4 addresses the case analysis of four incidents. The findings for these cases are compared in Sect. 5. Finally, the inference drawn from the discussions in this paper is set out in Sect. 6.

2 Smart Grid with Cyber Intrusion

Electrical grids power our day-to-day life, but it's time to smarten up!

“A self healing grid” or “smart grid” is an electrical grid based on the design idea of “Demand Follows Supply.” It is the digital technology that helps in meeting the complex power demand by providing two-way communication between the customer and utilities with the increased flow of information and energy.

A smart grid is a developing network of communication control, computers, automation, and new technologies and tools working together to make the grid more efficient, more reliable, more secure, and greener. With more advancement in this field, the smart grid will replace today's grid's aging infrastructure, and utilities can better communicate with us to help manage our electricity needs [6].

The benefits associated with the smart grid include:

1. Helps in the identification and to monitor any glitches or problems that may arise, i.e., real-time availability status.
2. Improving outage management: restore power in less time.
3. Actively manage energy consumption.
4. A small electrical device, i.e., in-home display, is paired up with a smart meter to give you all kinds of data about your energy use.
5. The dynamic pricing of power in the smart grid enables the user to adjust their demand according to time-varying pricing.

Separating myths from reality allows us to benefit from all the benefits that a smarter, efficient, secure, and more modernized electric grid (smart grid) offers. It's essential to stay acquainted and learn about your utility's different ways to deploy a smart grid to improve their electric service [5, 6].

The smart grid permits the authority to connect/disconnect the consumers remotely for not paying bills, without going to their houses/industries. A smart meter in the smart grid context records the consumer's power usage and communicates this data on time to the utility center, which enables them to generate the electricity bills with that data. It can be inferred that the smart meters replaced the meter readers in this new era of power generation [7]. Analytics platforms are built, which enables to control or monitor the peak load of the grid. Monitoring structure of smart grid is shown in Fig. 2. In grid monitoring, it will monitor the storage available in energy storage devices and it will also communicate with the advanced metering infrastructure.

The SCADA-OMS (outage management system) method allows for the rapid identification of faults and their position directly on the portal. This reduces the time required to clear the fault (tree collapse, transformer burst, etc.). The demand response system allows the utility to run a load-reduction program (automated). Say, if the consumer consumes more power than the prescribed value, he or she will be physically removed from power, and this will happen 2–3 times to remind the consumer of his or her consumption so that the consumer decreases his or her load at specific intervals. If it still does not reduce its load, the power supply would be limited for the entire load limitation duration. Provision may be temporarily disconnected by the user using the portal if the supply is not needed for a few months. The entire electrical grid is superimposed on the “geographic information system,” which monitors feeders, transformers, and houses. Supervising the violation of the sanctioned load by the consumers helps in generating revenues to the utility [5–7].

The smart grid can solve many problems, but it also poses many challenges. These problems are related to a lack of understanding and adaptation to emerging technologies among citizens, electrical infrastructure at the distribution level. Significant

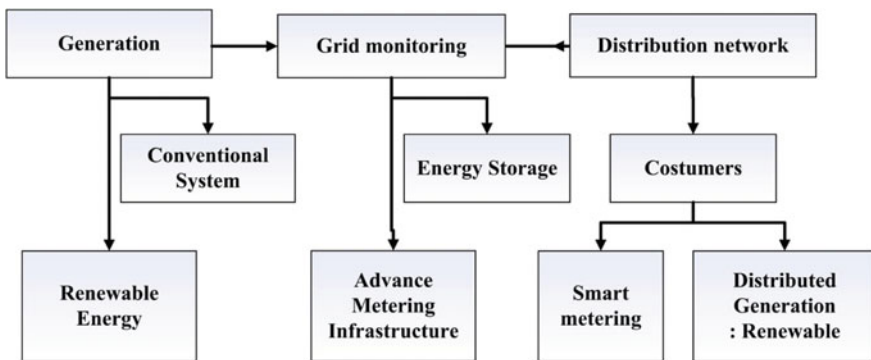


Fig. 2 Monitoring structure of smart grid

investment is required in the rehabilitation of the infrastructure or in the implementation of remote monitoring (PMU) technology. The smart grid faces a variety of challenges, but also offers excellent opportunities [8]. Cyber intrusion in power grid and control center is shown in Fig. 3.

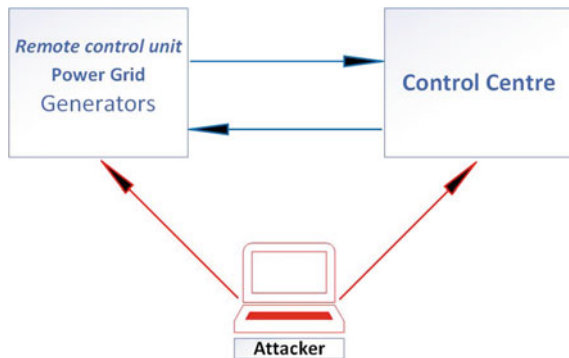
Owing to high penetration of the Internet, cyber protection is one of the most critical needs in the world, as cybersecurity threats are perilous. In the smart grid system, the vulnerability of the system renders it vulnerable to cyberattacks. Cyberattacks in the smart grid system rely on a number of factors that enable the attacker to reduce the information security of the system [9]. In the smart grid system, cyberattacks target sensitive information to unauthorized users, who exploit the information to hurt others and take advantage of it. Cyberattacks often target the unauthorized deletion or alteration of information in the network system and the transmission of false information to the customer. Most cybersecurity experts agree that malware is a key weapon option for malicious intent to infringe cybersecurity efforts in cyberspace [9].

Malware may be distributed to utility center servers or the organization to extract certain sensitive pieces of information by inserting those functions by malware. The aim of the attacker could also be to conduct a denial-of-service attack, which puts the power supply at a standstill—creating outages and difficulties in restoring the power supply [10–12].

Researchers in the field of power systems have recently increased their emphasis on power interruption by malware attacks, which is the leading cause of device unreliability. If the alarm is not activated immediately after the malicious data has been detected, the device will be exposed to the risk of unauthorized access to the data [10–12].

A comprehensive study of sources of threat helps in achieving smart grid security. Smart grid security threats classification by sources is as follows [13].

Fig. 3 Cyber intrusion in power system



2.1 Technical Sources of Threat

The three salient points of the technical sources of threat are identified and these are.

2.1.1 Infrastructural Security

The smart grid system, a very complex system that is geographically and economically distributed, interconnecting users, utilities, power stations, substations, ICT devices, etc., needs protection, because bypassing any of these by unauthorized users makes the system prone to cyberattack and weakens the system making it unreliable.

2.1.2 Technical and Operational Security

It covers the infrastructural installations and operation procedures. It also ensures that routine check occurs because the identification and diagnosis of the problem beforehand makes the system reliable, secure, efficient, and with uninterrupted operations.

2.1.3 Systems' Data Management Security

This aspect covers real-time supervision and monitoring of the data and storing the necessary information and data. It also provides security against cyberattacks by injection of false information, malware attacks, terrorism, etc. The main concern is the customer's privacy breach by access to their personal information. Various protocols and guiding policies are made against this to provide customer satisfaction in terms of privacy assurance.

2.2 Non-technical Sources of Threat

This includes.

2.2.1 Environmental Security

The environmental hazards such as earthquakes, floods, falling of trees, bush burning, etc., are factors that can prevent the smart grid's deployment. So, while installing the smart grid, various environmental factors of that location should be a matter of concern. Furthermore, a smart response system should be set up to tackle the situation as soon as possible to restore the power supply.

2.2.2 Government Regulatory Policies and Implementation

The government should introduce various policies to create awareness among the peoples about the new technologies that are emerging for the country’s socio-economic development. The various organizations should raise funds under the government to set up the smart grid system’s infrastructure by replacing the aging electric power system. Investment should also be made in the research and development sector by the government.

3 Reliability Assessment of Smart Grid with Consideration of Cyber Intrusion

Reliability is the possibility that the system can perform its task in an acceptable manner for the period of time intended under the operating conditions encountered. The description of reliability is broken down into the following sections as shown in Fig. 4.

The Block one, probability, provides the numerical input for the reliability evaluation as well as the first device adequacy index. The remaining three blocks are all engineering parameters, and probability theory is not helpful in this part of the assessment [14].

Generally, only the engineer responsible for a particular system can satisfactorily supply information relating to these. For reliability evaluation, the steps involved are as follows:

- a. Recognize the way of system operation
- b. Analyze the ways in which system can fail
- c. Reduce the consequences of the failures
- d. Obtain models to exemplify these characteristics.

After that, select the reliability evaluation technique. Reliability evaluation can be done with these two techniques: analytical and simulation.

Analytical techniques exemplify the system by a mathematical model and evaluate the reliability indices from this model using mathematical solutions. Monte Carlo

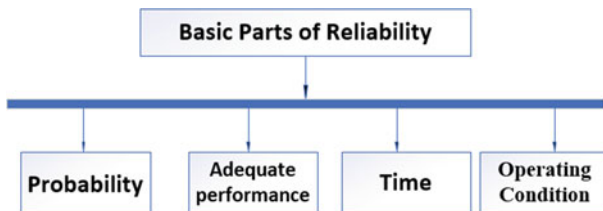


Fig. 4 Basic parts of reliability

simulation methods, however, estimate the reliability indices by simulating the actual process and random behavior of the system [14].

3.1 Reliability Evaluation at Generation Side

Availability means the percentage of time that the system remains operational under normal circumstances in order to serve its intended purpose.

$$\text{Mean time to repair(MTTR)} = \frac{1}{\mu} \quad (1)$$

$$\text{Mean time to failure(MTTF)} = \frac{1}{\lambda} \quad (2)$$

$$\text{Forced outage rate(FOR)} = \frac{\lambda}{\lambda + \mu} \quad (3)$$

Here, forced outage rate (FOR) is also called “Unavailability” of the system.

$$\text{Availability of the System} = 1 - \text{FOR} \quad (4)$$

$$\text{Availability} = \frac{\mu}{\lambda + \mu}; \quad (5)$$

where λ is expected failure rate, μ is expected repair rate, mean time between failures can be calculated as

$$\text{MTBF} = \text{MTTF} + \text{MTTR} \quad (6)$$

Availability can also be determined in terms of MTTF and MTTR.

$$\text{Availability} = \frac{\text{MTTF}}{\text{MTTF} + \text{MTTR}} \quad (7)$$

3.2 Reliability Evaluation at Distribution Side

When a customer is connected at load point, he requires all system components in between supply side and himself. For evaluation of reliability indices for such a situation, we are using a classical concept that includes three basic parameters such

as average failure rate, average repair duration, and average annual unavailability or average annual outage time [15]. Here, we can evaluate the following values as shown below:

$$\text{Failure rate } \lambda = \sum_{i=0}^n \lambda_i \tag{8}$$

$$\text{Annual unavailability } U = \sum_{i=0}^n \lambda_i r_i \tag{9}$$

$$\text{Repair time } r = \frac{U}{\lambda} = \frac{\sum_{i=0}^n \lambda_i r_i}{\sum_{i=0}^n \lambda_i} \tag{10}$$

$$\text{Annual Customer Interruptions} = \sum N_i \lambda_i \tag{11}$$

$$\text{Customer Interruption Duration} = \sum N_i U_i \tag{12}$$

3.2.1 Customer-Orientated Indices

The customer indices are calculated by the following expressions:

$$\text{SAIFI} = \sum N_i \lambda_i / \sum N_i \tag{13}$$

$$\text{SAIDI} = \sum N_i U_i / \sum N_i \tag{14}$$

$$\text{CAIDI} = \sum N_i U_i / \sum N_i \lambda_i \tag{15}$$

$$\text{ASAI} = (\sum N_i * 8760 - \sum N_i U_i) / \sum N_i \lambda_i \tag{16}$$

$$\text{ASUI} = 1 - \text{ASAI} \tag{17}$$

where λ_i is the failure rate, N_i is the total number of customers at load point i , and U_i is the annual outage duration at load point i .

3.2.2 Load-Orientated Indices

The load indices are calculated by the following expressions:



Fig. 5 Two-state model of cyber intrusion

$$ENS = \sum LiUi \tag{18}$$

$$AENS = ENS / \sum Ni \tag{19}$$

where Li is average load at load point i .

3.3 Cyber Intrusion Modeling and Calculation

For cyber intrusion, two-state model is used as shown in Fig. 5.

$$\text{Mean time to cyber intrusion} = 1/\alpha \tag{20}$$

Whenever cyber intrusion occurs in the system, the operator will follow two steps:

Step 1: Identify and block the intrusion.

Step 2: Introduce a new method to handle the blockage when any other intrusion came in the future.

$$\text{Repair time to recover cyber intrusion } \beta = 1/2\alpha \tag{21}$$

4 Case Studies

The performance evaluation conducted based on the IEEE 14 bus system. Average load data taken from Appendix A [16] and number of customers assumed are given in Table 1.

Case 1: A system with conventional sources

Data sheet for case 1 is shown in Table 2. Customer- and load-orientated indices evaluated for case 1 are as follows:

Table 1 Details of the distribution system

S. no.	Bus no.	Load point	No of costumers, N	Avg. load demand, L (kW)
1	2	Lp1	2000	21,700
2	3	Lp2	7000	94,200
3	4	Lp3	4000	47,800
4	5	Lp4	700	7600
5	6	Lp5	900	11,200
6	9	Lp6	3000	29,500
7	10	Lp7	800	9000
8	11	Lp8	400	3500
9	12	Lp9	600	6100
10	13	Lp10	1000	13,800
11	14	Lp11	600	14,900
Total			21,000	259,300

Table 2 Reliability indices for case 1

Load point	λ (failures/year)	r (h/failure)
Lp1	1.98	2.58
Lp2	1.84	3.63
Lp3	1.69	2.77
Lp4	1.44	2.46
Lp5	1.69	3.13
Lp6	1.58	2.54
Lp7	1.99	2.75
Lp8	1.75	3.20
Lp9	1.69	2.48
Lp10	1.48	3.10
Lp11	1.86	2.89

Annual Customer Interruptions = 36, 771
 Customer Interruption Duration = 111, 922.4
 SAIFI = 1.751interruption/customer
 SAIDI = 5.329637h/customer
 = 319.7782min/customer
 CAIDI = 3.043767h/customer interruption
 = 182.62600min/customer interruption
 ASAI = 0.9993916
 ASUI = 0.0006084060

Table 3 Reliability indices for case 2

Load point	λ (failures/year)	r (h/failure)
Lp1	1.70	2.61
Lp2	1.82	1.76
Lp3	1.42	1.82
Lp4	1.62	1.92
Lp5	1.21	1.73
Lp6	1.39	1.54
Lp7	1.46	1.96
Lp8	1.11	2.60
Lp9	1.32	2.28
Lp10	1.16	2.20
Lp11	1.21	1.90

$$ENS = 1,406,182.02 \text{ kWh}$$

$$AENS = 66.96105 \text{ kWh/customer.}$$

Case 2: A system with renewable energy sources

Data sheet for case 2 is shown in Table 3. Customer- and load-orientated indices evaluated for case 2 are as follows:

$$\text{Annual Customer Interruptions} = 32,503$$

$$\text{Customer Interruption Duration} = 60,494.55$$

$$SAIFI = 1.547762 \text{ interruption/customer}$$

$$SAIDI = 2.880693\text{h/customer}$$

$$= 172.8416\text{min/customer}$$

$$CAIDI = 1.861199\text{h/customer interruption}$$

$$= 111.6719\text{min/customer interruption}$$

$$ASAI = 0.9996712$$

$$ASUI = 0.0003288462$$

$$ENS = 747,301.9 \text{ kWh}$$

$$AENS = 35.58580 \text{ kWh/customer.}$$

Case 3: A system with conventional, renewable energy sources, and storage devices

Data sheet for case 3 is shown in Table 4. Customer- and load-orientated indices evaluated for case 3 are as follows:

Table 4 Reliability indices for case 3

Load point	λ (failures/year)	r (h/failure)
Lp1	1.40	1.11
Lp2	1.32	1.70
Lp3	1.22	1.85
Lp4	1.42	1.64
Lp5	1.11	1.18
Lp6	1.50	1.69
Lp7	1.46	1.76
Lp8	1.21	2.30
Lp9	1.32	1.98
Lp10	1.36	2.60
Lp11	1.11	2.10

Annual Customer Interruptions = 27, 883
 Customer Interruption Duration = 47, 929.62
 SAIFI = 1.327762 interruption/customer
 SAIDI = 2.282363 h/customer
 = 136.9418 min/customer
 CAIDI = 1.718955 h/customer interruption
 = 103.1373 min/customer interruption
 ASAI = 0.9997395
 ASUI = 0.0002605437
 ENS = 592, 480.9 kWh
 AENS = 28.21338 kWh/customer

Case 4: A system with conventional, renewable sources, and storage devices, including cyber intrusion

Data for the cyber interruption in terms of intrusion time of the system α and recovery time of the system β is shown in Table 6. Reliabilities indices for this case calculated using failure and repair rate of the systems with intrusion and recovery time of the system are shown in Table 5.

Customer- and load-orientated indices evaluated for case 4 are as follows:

Annual Customer Interruptions = 45, 382
 Customer Interruption Duration = 43, 475.04
 SAIFI = 2.161048 interruption/customer

Table 5 Reliability indices for case 4

Load point	λ (failures/year)	r (h/failure)
Lp1	1.70	0.68
Lp2	2.16	0.93
Lp3	2.61	0.98
Lp4	1.21	1.07
Lp5	1.55	1.07
Lp6	2.25	0.92
Lp7	2.73	0.94
Lp8	1.60	1.27
Lp9	1.16	1.24
Lp10	2.68	1.36
Lp11	2.05	1.13

Table 6 Data sheet of cyber interruption

Load point	α (failures/year)	β (h/failure)
Lp1	2	0.250
Lp2	3	0.166
Lp3	4	0.125
Lp4	1	0.500
Lp5	2	0.250
Lp6	3	0.166
Lp7	4	0.125
Lp8	2	0.250
Lp9	1	0.500
Lp10	4	0.125
Lp11	3	0.166

$$\begin{aligned}
 \text{SAIDI} &= 2.070240 \text{ h/customer} \\
 &= 124.2144 \text{ min/customer} \\
 \text{CAIDI} &= 0.957979 \text{ h/customer interruption} \\
 &= 57.47879 \text{ min/customer interruption} \\
 \text{ASAI} &= 0.9997637 \\
 \text{ASUI} &= 0.0002363288 \\
 \text{ENS} &= 543,603.4 \text{ kWh} \\
 \text{AENS} &= 25.88588 \text{ kWh/customer.}
 \end{aligned}$$

5 Result and Discussion

Since innovation and technology have ushered in a new era of energy, healthier, smarter, and greener, while this transformation offers opportunities, it also poses challenges to “meet the customer”. The electric utility industry defines various reliability indices to measure the system performance and distribution system reliability. In Fig. 6, the performance evaluation is done on IEEE 14 bus system, and the comparison is performed among various indices, i.e., customer-oriented indices and load-oriented indices.

System average interruption duration index (SAIDI): the most often used performance measurement indices. On comparing the data of SAIDI from all the four cases mentioned above and from the bar chart (Fig. 6), it can be analyzed that the reduction in the value of SAIDI took place by 45.94% on switching to the system with renewable energy source from the conventional energy source. Further, it is reduced by 57.14% for the system which includes conventional with renewable energy sources and storage devices. In comparison with case 1, a decrease of 61.15% in the SAIDI value is seen for the system, including cyber intrusion.

System average interruption frequency index (SAIFI): These customer-oriented indices give the average number of times a customer experiences an outage during the time under study.

From the comparison of data and the bar chart (Fig. 6), it can be seen that a decrease of 11.67% in the outage value is obtained in a system with a renewable energy source (compared to case 1). When conventional with renewable energy sources and storage devices are considered, a higher decrease of 24.17% is seen in

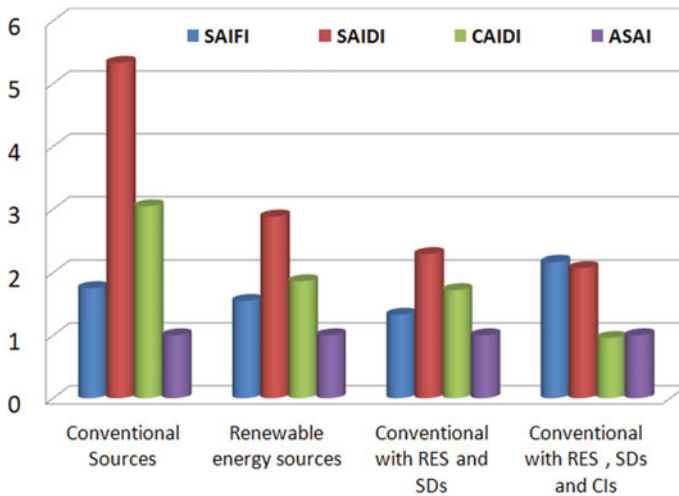


Fig. 6 Reliability assessment of power grid system

the outage that customer experiences. But the trend shows an increase of 23.41% in the number of outages on the system, including cyber intrusion.

Customer average interruption duration index (CAIDI): Once an outage occurs, the average time to restore service is found by CAIDI. In case 2, the value of CAIDI is enhanced by 38.85% compared to case 1. Moreover, a 43.52% improvement was noticed in the value of CAIDI in case 3 when storage devices are integrated.

Average service availability index (ASAI): ASAI is the total number of customer hours that service was available during a given time to the total customer hours demanded. No appreciable change is observed in ASAI's value while making a comparison among all the four systems.

From the comparison of data of the annual customer interruption and customer interruption duration, it can be inferred that a decrease of 11.60% is seen in annual customer interruption between conventional sources and renewable sources. In comparison, a reduction of 24.17% is observed in conventional with renewable energy sources and storage devices. But on cyber intrusion, the interruption value rises by 23.41%. On calculating the percentage decrease in customer interruption duration, a decrease of 45.94% is seen between conventional sources and renewable sources, and the trend shows that the percentage goes on decreasing for both 2 and 3 cases as shown in Fig. 7. In comparison, an increase of 61.15% in customer interruption duration is seen in conventional with renewable energy sources and storage devices, including cyber intrusion.

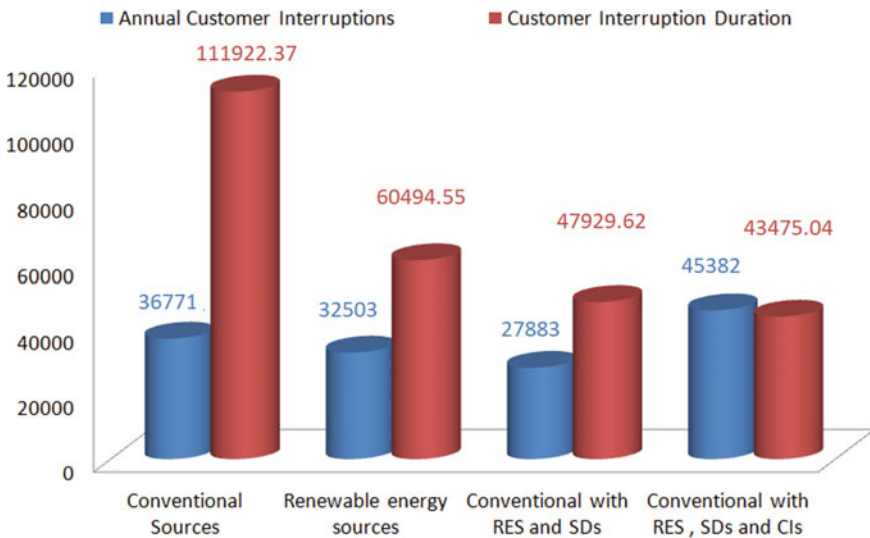


Fig. 7 Customer interruption for different cases

6 Conclusion

This paper has analyzed the reliability indices of smart grid taking four different systems: a conventional energy source, renewable energy source, conventional with renewable energy source and storage devices, and conventional with renewable energy source and storage devices, including cyber intrusion. The performance evaluation is carried out on IEEE 14 bus system, and simulation is done on MATLAB software. According to the results, as stated above, it can be inferred that the most efficient system is “conventional with renewable energy sources and storage devices.” But on cyber intrusion, the system’s efficiency decreases, it becomes less secure and unreliable, resulting in unexpected outages and difficulty in the restoration of power supply. Cyberattacks are becoming more sophisticated and thereby presenting challenges to the electric utility industry. As future work, the performance evaluation will be conducted on a large scale to detect cyber intrusion and for the implementation of secure architecture to recover faster.

References

1. K. Moslehi, R. Kumar, A reliability perspective of the smart grid. *IEEE Trans. Smart Grid* **1**, 57–64 (2010)
2. B. Falahati, Y. Fu, Reliability assessment of smart grids considering indirect cyber-power interdependencies. *IEEE Trans. Smart Grid* **5**, 1677–1685 (2014)
3. A. Escalera, B. Hayes, M. Prodanovic, Reliability assessment of active distribution networks considering distributed energy resources and operational limits, in *CIREN Workshop 2016*, pp. 1–4 (2016)
4. G. Celli, E. Ghiani, F. Pilo, G.G. Soma, Reliability assessment in smart distribution networks. *Electr. Power Syst. Res.* **104**, 164–175 (2013)
5. M.L. Tuballa, M.L. Abundo, A review of the development of Smart Grid technologies. *Renew. Sustain. Energy Rev.* **59**, 710–725 (2016)
6. M. Fadaeenejad, A.M. Saberian, M. Fadaee, M.A.M. Radzi, H. Hizam, M.Z.A. AbKadir, The present and future of smart power grid in developing countries. *Renew. Sustain. Energy Rev.* **29**, 828–834 (2014)
7. M.E. El-Hawary, The smart grid” state-of-the-art and future trends. *Electr. Power Compon. Syst.* **42**, 239–250 (2014)
8. A. Bari, J. Jiang, W. Saad, A. Jaekel, Challenges in the smart grid applications: an overview. *Int. J. Distrib. Sens. Netw.* **10**, 974682 (2014)
9. D.B. Rawat, C. Bajracharya, Cyber security for smart grid systems: Status, challenges and perspectives, in *SoutheastCon 2015* (2015), pp. 1–6
10. Y. Liu, P. Ning, M.K. Reiter, False data injection attacks against state estimation in electric power grids. *ACM Trans. Inf. Syst. Secur. (TISSEC)*, **14**, 1–33 (2011)
11. A. Abur, A.G. Exposito, *Power System State Estimation: Theory and Implementation* (CRC Press, 2004)
12. E. Handschin, F.C. Schweppe, J. Kohlas, A. Fiechter, Bad data analysis for power system state estimation. *IEEE Trans. Power Appar. Syst.* **94**, 329–337 (1975)
13. A.O. Otuoze, M.W. Mustafa, R.M. Larik, Smart grids security challenges: classification by sources of threats. *J. Electr. Syst. Inf. Technol.* **5**, 468–483 (2018)
14. R. Billinton, R.N. Allan, *Reliability Evaluation of Engineering Systems* (Springer, 1992)

15. T.L. Laubst, Reliability evaluation of power systems, R. Billington, R.N. Allan (Plenum Press, New York and London, 1984). *Qual. Reliability Eng. Int.* **1**, 141–141 (1985)
16. J. Rajathy, Data sheets for IEEE 14 bus system (2003)

Distance Relaying with Power Swing Detection in the Presence of Distributed Resources



Pankaj Ramtekkar, Suraj Dudhe, Ankur Gupta, and Munishwar Meshram

1 Introduction

Distributed resources are widely used because of their advantages like lower capital cost and potential for reduced emissions [1]. Distribution generation helps to reduce the transmission loss and thereby transmission cost. This will help to improve the transmission efficiency of a line. The protection of distribution generation has very much influence due to the parameters such as technologies used for generation purpose, operating conditions, rated power, and fault location [2]. The penetration of distributed generation will be more challengeable in the protection systems [3].

The relay performance ensures that the system will work properly and the power is fed continuously and protects the systems from damage [4]. Whenever there is addition of DG to the distribution feeder for feeder end fault, the effective reach of relay decreases when there is an increase in value of impedance measured and then its actual impedance and this may affect the effective reach of the relay which may further decrease its value [5].

2 Adaptive Distance Protection

To protect transmission line from different types of faults which are under its reach, the distance relay is used [6]. In the adaptive form, there will be a change in trip

P. Ramtekkar (✉) · S. Dudhe · A. Gupta
G. H. Rasoni College of Engineering, Nagpur, India
e-mail: pankaj.ramtekkar@raisoni.net

M. Meshram
Mahatransco, Ahmednagar, India

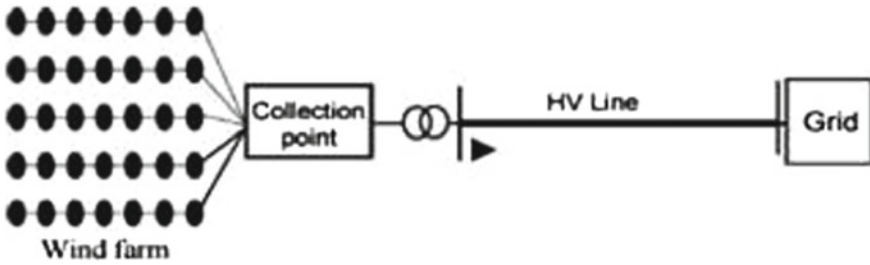


Fig. 1 Interconnection of wind farm to grid

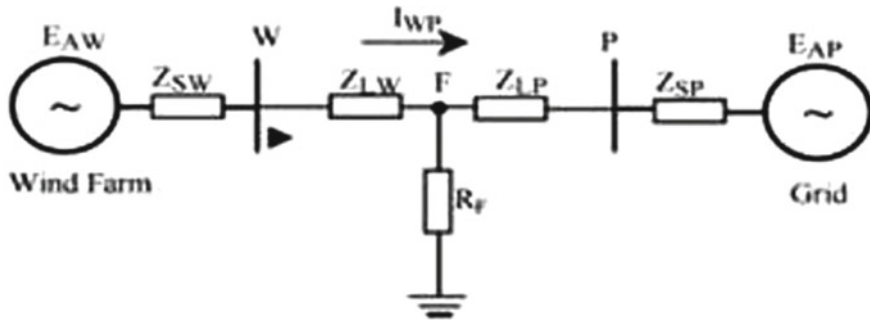


Fig. 2 Line diagram of phase-a ground fault

boundary as the system conditions are changed. Here, we have considered line-to-ground fault, and boundary for other remaining faults can be find out similarly. The trip boundary taken here is of mho relay characteristic on an impedance plane [7]. This trip boundary can be obtained by changing the fault location and resistance of fault which comes under within their limit, and trip boundary can be found out which is a mho characteristic on impedance plane [8, 9]. The error term is inserted due to the fault resistance, whenever there is a fault on system [10, 11] (Figs. 1, 2, 3 and Table 1).

3 Power Swing

The relay performance has adversely affected the power swing and must be handled by a relay assigned to it very carefully [12]. For undesirable effects due to power swing, the relay must not respond [13, 14]. The impedance trajectory for a power swing and a fault during power swing are shown in Figs. 4 and 5. From Figs. 4 and 5, it is observed that both the power swings, i.e., with fault and without fault, are easily differentiate as this relay performance is improved and its reliability is improved [15].

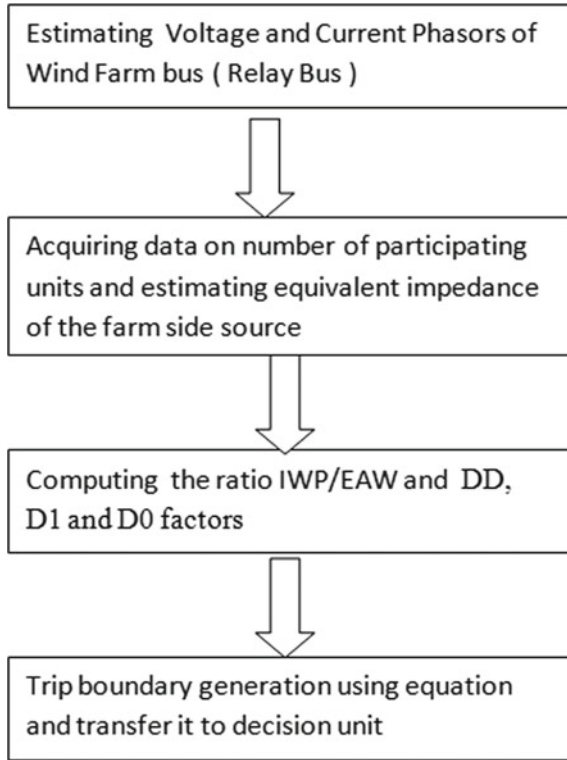


Fig. 3 Flowchart

Table 1 Parameters of wind turbine generator

Generator rated MVA	1.5 [MVA]
Machine angular mechanical speed	60 [Hz]
Rotor radius	40[m]
Rotor area	5026 [m ²]
Air density	1.225 [Kg/m ³]
Gear box efficiency	0.979
Gear ratio	90.5
Equation for power coefficient	MOD 2

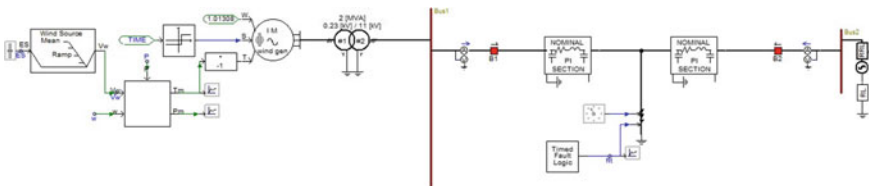


Fig. 4 Simulation

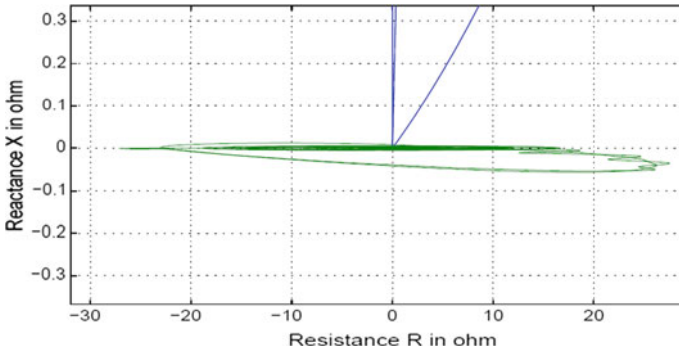


Fig. 5 Impedance trajectory during power swing

4 Simulation and Results

The wind unit is connected to the grid through the transmission line. At point F, an L-G fault is created. The equivalent simplified models of wind farm and grid are considered here. Shunt capacitance is neglected here. The integration of wind with grid through transmission line simulated in PSCAD is shown in Figs. 3 and 6 and Tables 2, 3.

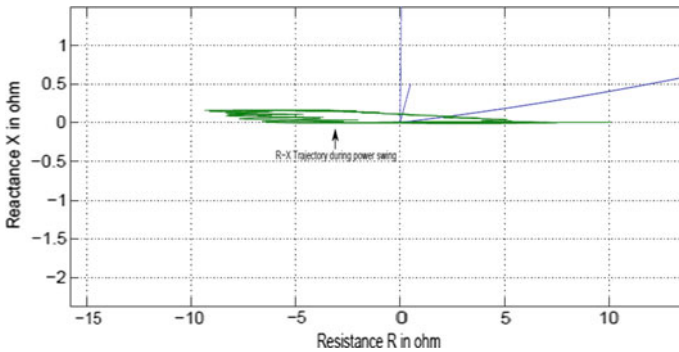


Fig. 6 Impedance trajectory for fault during power swing

Table 2 Source impedances of wind farm for different cases

Sequence impedance	Case 1	Case 2
Positive sequence impedance	$20e^{85j}\Omega$	$30e^{85j}\Omega$
Zero sequence impedance	$200e^{85j}\Omega$	$300e^{85j}\Omega$

Table 3 Grid side source impedances of wind farm for different cases

Sequence impedance	Case 1	Case 2
Positive sequence impedance	$1e85j \Omega$	$2e85j \Omega$
Zero sequence impedance	$1.5e85j \Omega$	$3e85j \Omega$

5 Conclusion

The adaptive nature of distance relay has been found out for different changing conditions. The conditions are wind farm impedance, grid side impedance, voltage amplitude ratio, and power transfer angle for line-to-ground fault. The adaptive distance relay along with power swing effect is studied. It will be helpful to increase the reliability of system protection in the presence of power swing issues.

References

1. J. Ma, J. Li, Z. Wang, An adaptive distance protection scheme for distribution system with distributed generation. *Critical Infrastructure (CRIS), 2010 5th International Conference on*, pp. 1–4 (2010)
2. S. De Rijcke, P. Peerez, J. Driesen, Impact of wind turbines equipped with doubly-fed induction generators on distance relaying
3. U.D.O. Erdinc, B. Vural, N. Chau, Green power—wind generated protection and control considerations
4. A. Sinclair, D. Finney, D. Martin, P. Sharma, Distance protection in distribution systems: how it assists with integrating distributed resources. *Industry Applications, IEEE Transactions on*, pp. 2186–2196 (2014)
5. S. Brahma, A. Girgis, Development of adaptive protection scheme for distribution systems with high penetration of distributed generation. *Power Delivery, IEEE Transactions on*, pp. 56–63 (2004)
6. Y. Zhao, J. de Palma, J. Mosesian, R. Lyons, B. Lehman, Line 2013: line fault analysis and protection challenges in solar photovoltaic arrays
7. D. Uthitsunthorn, T. Kulworawanichpong, Distance protection of a renewable energy plant in electric power distribution systems. *Power System Technology (POWERCON), 2010 International Conference on*, pp. 1–6 (2010)
8. R.B. Hewitson, L.G. Mark Brown, *Practical Power System Protection*. Ltd (2009)
9. I. Chilvers, N. Jenkins, C.P, Distance relaying of 11 kv circuits to increase the installed capacity of distributed generation. *Generation, Transmission and Distribution, IEE Proceedings*, pp. 40–46 (2005)
10. S. Jang, J. Choi, J. Kim, D. Choi, An adaptive relaying for the protection of a wind farm interconnected with distribution networks
11. F. Calero, Distance elements: linking theory with testing. *Protective Relay Engineers, 2009 62nd Annual Conference for*
12. Y. Paithankar, S. Bhide, *Fundamentals of Power System Protection*. PHI Learning Pvt. Ltd (2013)

13. T. Sidhu, D. Baltazar, R. Palomino, M. Sachdev, A new approach for calculating zone-2 setting of distance relays and its use in an adaptive protection system
14. A. Pradhan, G. Joos, Adaptive distance relay setting for lines connecting wind farms *Energy Conversion, IEEE Transactions on*, pp. 206–213 (2007)
15. P. Ramtekkar, S. Dudhe, Distance protection scheme in the presence of distributed resources. *International Conference on Advances in Mechanical and Electrical Engineering [ICAMEE-2019]*

Modeling and Simulation of FPGA-Based Vector-Controlled Induction Motor Drive Using Simulink



Sumit Kumar Gupta 

1 Introduction

Variable-speed drives are the machines for varying the rotating speed of adjustable speed drives by varying frequency of electrical power system to the machine. Drive system on the whole is a combination of power converter, electrical machine, and controller [1]. Induction motors have many advantages over DC motors. Induction motors do not have commutators involved in their operation which gives less control over power and speed of the machine. But due to the advancement in the field of efficient semiconductor switches, it becomes much easier to control the speed and power in induction motor to keep them in the upper side [2]. Variable frequency drive controllers are solid-state electronic power conversion devices. If the refined control algorithm is to be realized, simulation and implementation phases are to be performed on two different stages, first the parameters and control strategy are validated using high-level simulation of controller and drive system then second HDL test bench will verify the response of HDL controller and Simulink simulation but writing the HDL code is not an easy task and it is really required to have a tool that can emulate the hardware directly so that the process of design and implementation could be completed in same high level. So it seems very useful if a tool performing high-level simulation, i.e., Simulink could be able to generate the code necessary for FPGA implementation so that the cumbersome task of writing HDL code or writing the algorithm in other machine languages like in embedded C, Fortran, or any other binary level language could be avoided.

One fundamental issue is to choose type of implementation platform. DSP functions can be implemented in two programmable platforms: digital signal processors

S. K. Gupta (✉)

Department of ECE, School of Studies of Engineering and Technology Guru Ghasidas Vishwavidyalaya, Bilaspur, India

e-mail: sgupta@ggu.ac.in

and FPGAs. In the past, use of DSP was obvious, but many applications need more processing capabilities of DSPs which leads to the use of FPGA for implementation. The primary reason for choosing FPGA over DSPs by the application is their MIPS (millions of instructions per second) requirement and second advantage is product reliability and maintainability [3]. FPGA is very much similar to programmable logic devices which contains only limited number of switches nearly in hundreds while FPGA supports thousands of programmable switches. Therefore, FPGA is becoming more popular these days for designing integrated circuit prototypes. Once the design is ready, hardware chips can be produced for faster performance. The flexibility in programming the status of PLDs allows the user to increase parallelism and hence to increase the performance which further increases the utilization of logic gates. The advantage of increasing the parallel processing makes FPGA to be the answer for most of the complex control system implementation algorithms.

FPGAs are already used successfully in many areas which utilizes the power semiconductor. The control of the switching status of those switches is most important, for example, in the cases of power factor correction algorithms, PWM inverters control, non-linear control algorithms implementations, speed measurement algorithms, etc. The use of FPGA in such wide areas which is not limited to these only makes FPGA a powerful and efficient solution or answer to all the problems associated with hardware implementation and for the challenges that are going to come in future [4].

If FPGA implementation is to be done it needs VHDL code for test bench verification of the algorithm for the control adopted. A new simulation tool, i.e., Xilinx System Generator integrated with MATLAB Simulink can simulate directly hardware along with the high-level simulation and can automatically generate VHDL codes which is to be used in later stages of implementation. This new tool Xilinx System Generator works with MATLAB Simulink as a toolbox, and it is having library of blocks like addition, subtraction, multiplication, etc. for general operations. It also has CORDIC functions like division arctan, sqrt, etc. which uses complex algorithms for calculations as given in [5] for different operations and the system made up of these library of blocks can be implemented in FPGA. For simulating power electronics drive control, user must have own power circuit which is made with Simulink library, i.e., power system block set while the controller part is made with Xilinx System Generator library of blocks, and all the blocks are simulated in MATLAB Simulink environment simultaneously [6].

This paper uses a new tool Xilinx System Generator along with MATLAB Simulink for simulation for control algorithm of variable-speed drive. The implementation using System Generator has two advantages over traditional methods. First, the implemented algorithm is assured to behave exactly as in the simulation and the other, and further system-level modeling is not required. An example of vector control of an induction motor is presented and discussed. To develop all the tasks involved, MATLAB Simulink, System Generator, and ISE tools are utilized for implementation [7–9].

2 Vector Control Principal

In vector control, induction motor drive is considered analogous to separately excited DC machine. In separately excited DC machine, the developed torque is

$$T_e = K_t' I_a I_f \tag{1}$$

Neglecting armature reaction and field saturation, i_{qs} is torque component and I_f is field component.

In vector-controlled induction motor drive,

$$T_e = K_t \hat{\psi}_r i_{qs} = K_t' i_{qs} i_{ds} \tag{2}$$

where i_{qs} is torque component and i_{ds} is field component.

In Fig. 1, the machine model is shown in synchronously rotating reference frame, and inverter is omitted as having current gain of unity. The machine terminal phase currents $i_a, i_b,$ and i_c are converted to i_{ds}^s and i_{qs}^s components by using abc to dq transformation, and then they are transformed to synchronously rotating frame using unity vector $\cos \theta_e$ and $\sin \theta_e$ before given to machine model as shown in Fig. 2. Unit vector assures correct alignment of i_{ds} vector with flux $\bar{\psi}_r$ and i_{qs} perpendicular to it [4].

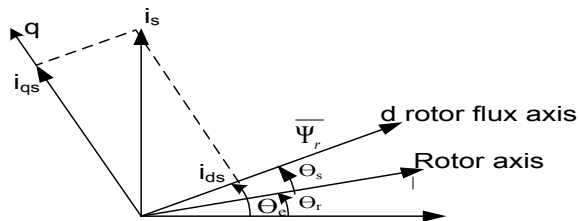
$$T_e = \frac{3}{2} n_p \frac{L_m}{L_r} (\psi_{dr} i_{qs} - \psi_{qr} i_{ds}) \tag{3}$$

where n_p is number of pole pairs, L_m shows magnetizing inductances, and L_r is rotor inductance. Also ψ_{qr} and ψ_{dr} represent the rotor flux linkage to the quadrature axis and direct axis. Considering direct axial flux to be vanished, torque equation is

$$T_e = \frac{3}{2} n_p \frac{L_m}{L_r} (\psi_{dr} i_{qs}) \tag{4}$$

Considering i_{ds} to be constant for the time being, torque expression comes out to be linearly depending upon i_{qs} and hence torque response becomes faster as i_{qs} response was.

Fig. 1 Principles of vector control



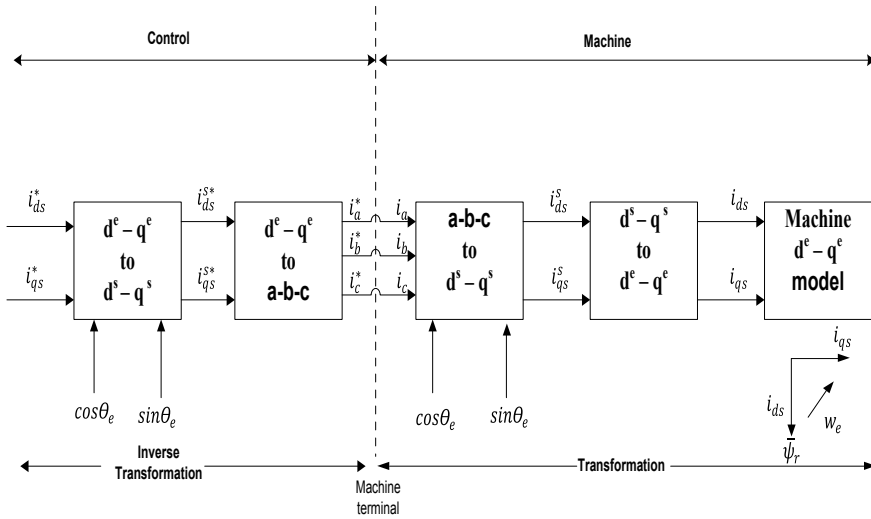


Fig. 2 Representation of vector control principal using machine d-q model

3 Simulation Tool

3.1 Power System Block Set

In MATLAB tools, electrical power system toolbox is comprised of electrical circuit components and electromechanical devices like motors, generators, inverters, etc. Requirement for increased efficiency forced system engineers to use power electronic devices and sophisticated control system concepts. The libraries contain model of transformers, lines, machines, and power electronics.

3.2 System Generator Block Set

Xilinx System Generator block set is developed by Xilinx and it can be used as toolbox in MALTAB Simulink. System Generator proved system-level support for bit true modeling which enables to create floating- and fixed-point models in same environment. To connect the control system algorithm implemented in system generator to the power blocks, i.e., drive part of the Simulink, some special blocks are utilized which are named as GatewayIn and GatewayOut. “GatewayIn” block is used to convert floating-type signal to a fixed-type signal with selected fixed time step. “GatewayOut” is utilized to provide the output in the prescribed and needed format for further utilization. For modeling a system, SG blocks are used which are FPGA blocks and represent hardware blocks. The responses of these blocks are

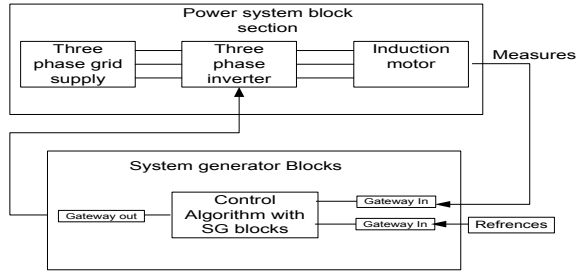
exactly same as hardware. The system modeled with these blocks can directly go for FPGA implementation as Xilinx System Generator can generate VHDL (VHSIC high description language). The VHDL code generated is synthesized in synthesizer and schematic circuit is made which can generate configuration file that can be used for FPGA implementation. The system generator blocks are similar to Simulink blocks and it can replace Simulink blocks easily but it works with fixed time step. It has some problem with specific functions like square root, division, sine, cosine, inverse trigonometry, etc. but these functions can also be implemented with iterative procedure of finding solution like CORDIC algorithms for sine, cosine, division, square root, inverse trigonometric, etc. The latest version of system generator has these blocks but with some limitations like sine and cosine can only be calculated for $-\pi/2$ to $\pi/2$, so it needs some calibration for angle calculation.

3.3 Simulation and Modeling of Vector Control of AC Drives

An application example of vector control of an induction motor is taken to show the capability of Xilinx System Generator. To simulate the complete circuit, first, the power circuit requirement is determined and parameters are calculated according to the options available and then power system block set of Simulink is used to simulate it and second the vector control technique is chosen and implemented using only SG block set which are simply addition subtraction multiplication and logic blocks. All simple arithmetic operations can be implemented using these blocks but for some of the operations like division sine, cosine, arctan, sqrt and implementing a transfer function for filters it needs some extra effort like, for example, implementation of a transfer function is done by first converting it from s domain to z domain with system sampling time and then discrete domain transfer function is made using delay blocks. Similarly, for calculating sine and cosine of an angle in abc-dq conversion block, concept of angular rotation is used. The use of SG blocks makes the system simulation time larger compared to model with only PS block set because SG blocks behaves exactly same as hardware so comparatively it needs more number of operations for addition, subtractions, etc. Each block made with SG block contains system generator token which has options for type of device to be used for implementation, code to be generated having option of VHDL or Verilog, FPGA clock period, Simulink system period, and the most important option of generate core which is used to generate code for targeted FPGA. The power system block set can be simulated with continuous time step and discrete step both but SG blocks can only use discrete time step, now both the power circuit and control circuit are connected using interfacing blocks which are GatewayIn and GatewayOut and simulation of power circuit and control circuit is done simultaneously (Fig. 3).

The vector control algorithm is simulated first in MATLAB Simulink which uses dq to abc conversion, abc to dq conversion, and current regulator which generates firing pulses for three-phase inverters. Figure 8 shows vector control algorithm modeled in MATLAB Simulink which uses induction motor with specifications given

Fig. 3 Interconnection of controller and power system section



in Table 1. Figures 10, 11, and 12 show the outputs of simulations which are speed, three-phase current, and torque with a speed reference of $w_{ref}=120$ and flux reference $Phir^* = 0.96$, and these outputs are to be verified by a system which has a controller made up of only system generator blocks and rest of the block from MATLAB Simulink as shown in Fig. 9 (Figs. 4, 5, 6 and 7).

Fig. 4 Concept used for angle range conversion

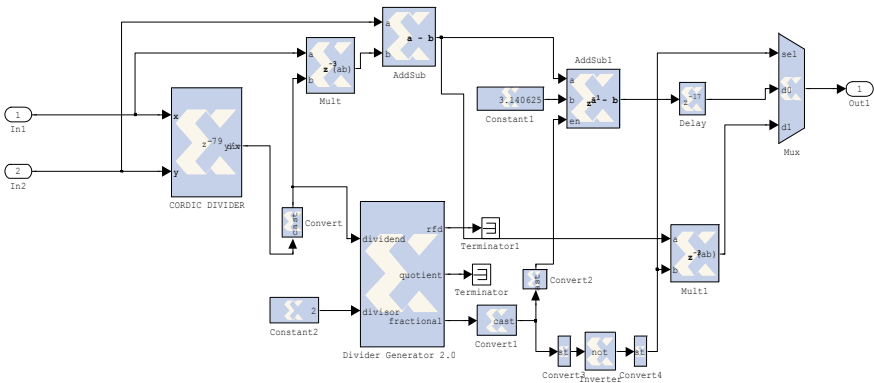
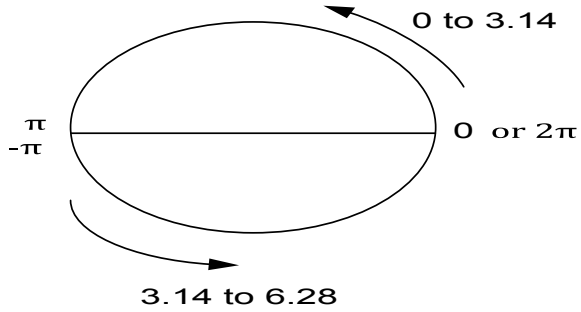


Fig. 5 Angle conversion block

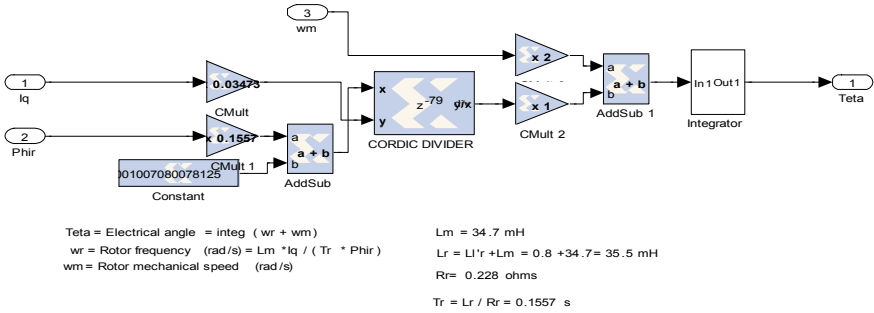


Fig. 6 Theta calculation block using only system generator block set

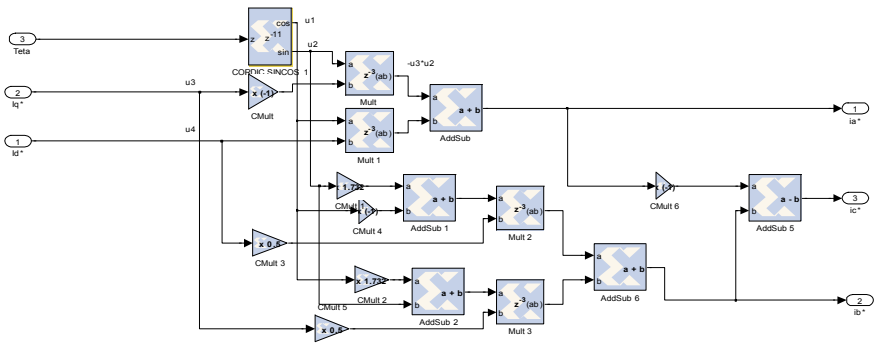


Fig. 7 dq-abc conversion block using system generator CORDIC block and commonly used block

The algorithm model creation in Xilinx System Generator was simple as most of the blocks can be created by using general blocks like addition, subtraction, multiplication, etc. Some of the blocks have critical design like the theta calculation block as it uses CORDIC function which has limitation within its input range. We have flux angle variation from 0 to 360 in radian in vector control which is out of range of CORDIC function so we have to convert it to range between pi and -pi. To convert the angle from 0 to 360 to -pi to pi, concept of arc geometry is used as shown in Fig. 4. On the first, rotation angle varies between 0-3.14(0-π), and on second rotation angle varies between 3.14-6.28(π-(-π)). This conversion of 3.14-6.28 to (π-(-π)) is needed and is implemented using above concept shown in Fig. 4 in Xilinx System Generator using general blocks and CORDIC divider block. Other than that the transfer function block which converts id to Phir uses sampling time of $T_s = 2e-5$ which is downsampled by 10 as system sampling period is $T_s = 2e-6$. Motor parameters are again as per the parameters given in Table 1. Figures 6 and 7 show the important blocks of abc to dq conversion and theta calculation block with system generator library of blocks. Figure 9 presents the simulated model of the control system algorithm entirely made up of SG blocks. Each input and output needs a “Gateway” block to connect to standard Simulink blocks. The outputs of

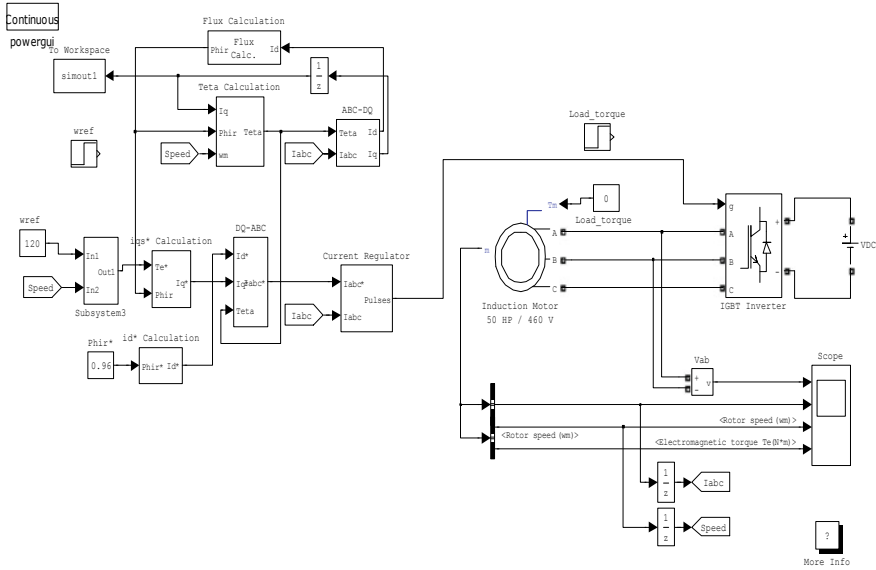


Fig. 8 Vector control of induction motor drive using Simulink

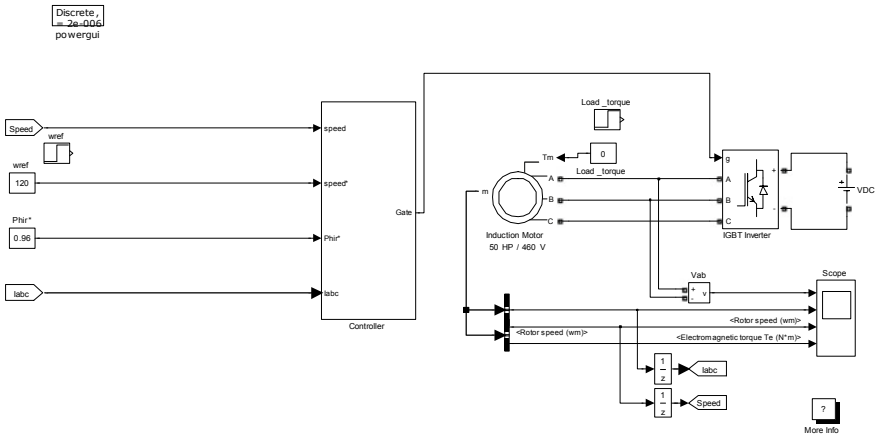


Fig. 9 Vector control of induction motor drive using Simulink

system simulated with Xilinx System Generator are given in Figs. 13, 14, and 15 which are speed, three-phase current, and torque with reference speed and reference same as system simulated with Simulink.

After doing simulation in Simulink, the next milestone is VHDL code generation, which can further be utilized in Xilinx software for further operation for converting it into a configuration file which is used for programming FPGA, and these are

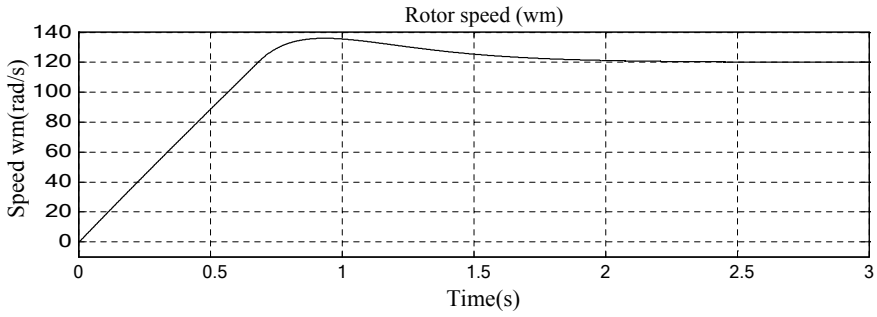


Fig. 10 Rotor speed with $\omega_{ref} = 120$ using only power system block set

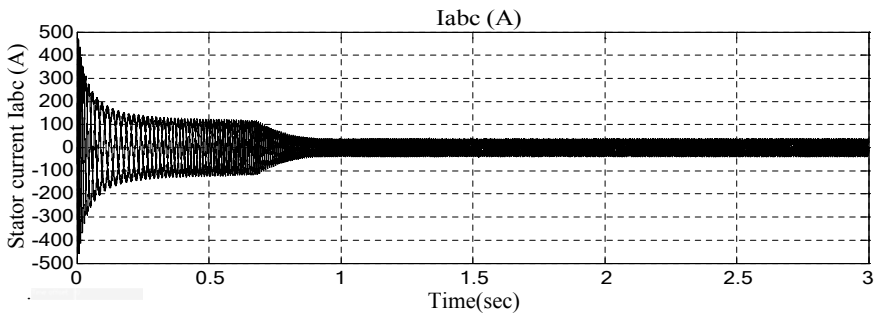


Fig. 11 Three-phase current using only power system block set

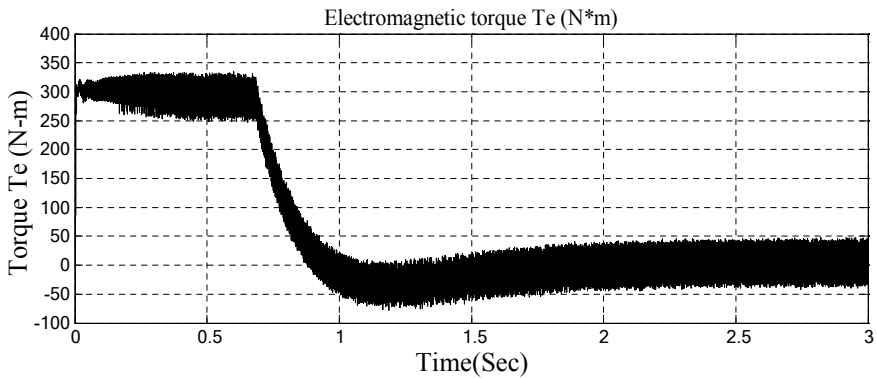


Fig. 12 Electromagnetic torque using only power system block set

very simple steps. If the system performance is to be changed, all these steps are not required, so the process is much faster. The advantage of using Xilinx System Generator is VHDL code generated which is guaranteed to be implemented and requires

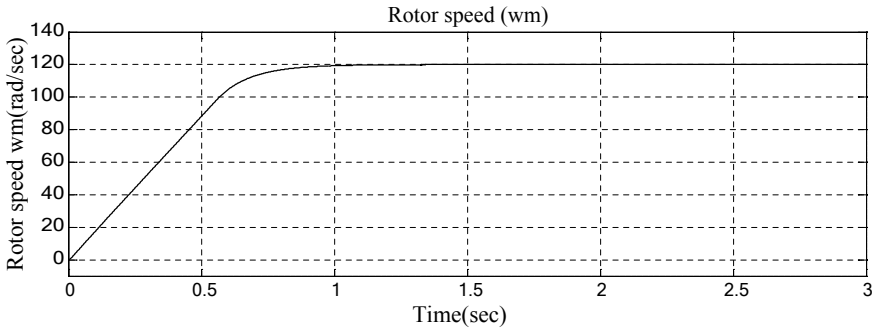


Fig. 13 Rotor speed with $w_{ref} = 120$ using power system and XSG

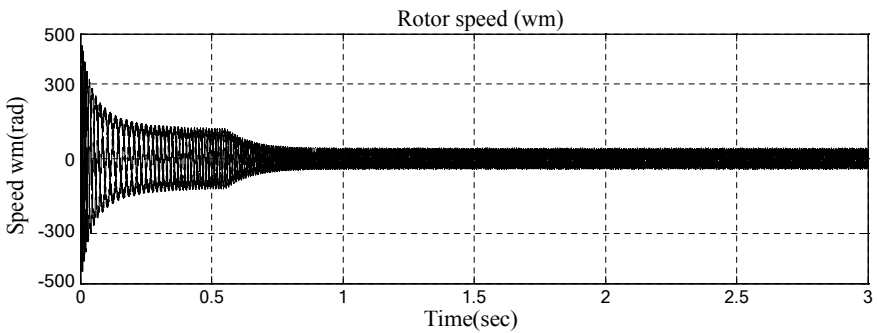


Fig. 14 Three-phase current using power system and XSG

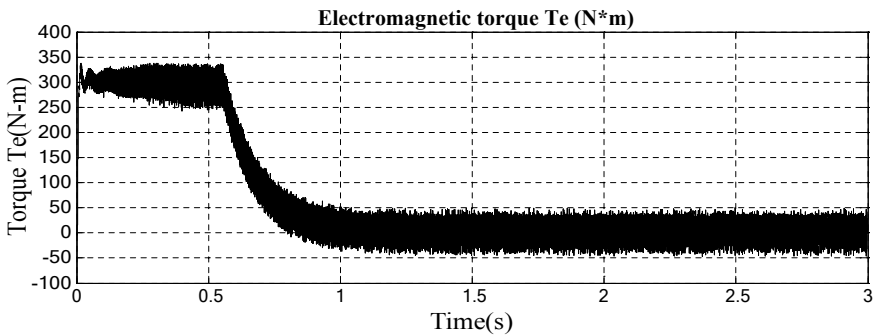


Fig. 15 Electromagnetic torque using power system and Xilinx System Generator block set

lesser time because of only one step for both software and hardware simulation testing.

4 Conclusion

An approach for FPGA implementation of vector control algorithm for variable-speed drive control is simulated and results are verified. In simulation using Xilinx System Generator, we observe the improvement in speed tracking where a reduction in steady-state error and torque ripples was observed. The advantage of procedure adopted is that it saves lot of time because the simulation using only system generator blocks represents exactly the hardware, so further testing for implementation is not needed. Also, there is no need of writing complex codes in VHDL or in “C” language, as Xilinx System Generator tool itself generates VHDL code for the controller which is made up of only system generator blocks. The advantage of code generated by Xilinx System Generator itself is that it is guaranteed to be implemented.

Appendix

Symbol	Parameters	Values
P_n (VA)	Nominal power	50*746
V_n	Voltage (line-line)	460
f_n (Hz)	Frequency	60
R_s (ohm)	Stator resistance	0.087
L_{ls} (H)	Stator inductance	0.8e-3
R_r' (ohm)	Rotor resistance	0.228
L_{lr}' (H)	Rotor inductance	0.8e-3
L_m (H)	Mutual inductance	34.7e-3
J (Kg.m ²)	Inertia	1.662
F (N.m.s)	Friction factor	0.1
pO		2
Ts		2e-6

References

1. B.K. Bose, *Modern Power Electronics and AC Drives* (Prentice-Hall, N.J., 2002)
2. P.C. Sen, Electric motor drives and control-past, present and future. *IEEE Trans. Ind. Electron.* **37**(6), 562–575 (Dec. 1990)
3. ALTERA “FPGA vs. DSP Design Reliability and Maintenance,” White paper 01023, May 2007, ver 1.1
4. E. Monmasson, M.N. Cirstea, FPGA design methodology for industrial control systems—a review. *IEEE Trans. Ind. Electron.* **54**(4), 1824–1842 (Aug. 2007)

5. G. Buja, D. Casadei, G. Serra, Direct stator flux and torque control of an induction motor: Theoretical analysis and experimental results, in *Proceedings IEEE IECON'98*, vol. 1, pp. T50–T64 (1998)
6. F. Ricci, H. Le-Huy, Modeling and simulation of FPGA-based variable-speed drives using Simulink. *Math. Comput. Simul.* **63**, 183–195 (2003)
7. R. Andraka, A survey of CORDIC algorithms for FPGAs, in *Proceedings ACM/SIGDA Conference*, pp. 191–200 (1998)
8. *Matlab User Guide*, Mathworks, Natick, MA (2005)
9. *System Generator User Guide*, Xilinx, San Jose, release 10.1 March, 2008

Design of Sine Filter for GTO-Based Auxiliary Converter for Electric Locomotive Using MATLAB Simulink



Rutuja S. Hiware, Shradha K. Umathe, and Shridhika Bire

1 Introduction

Generally, in locomotives for auxiliary circuits, the 3- ϕ squirrel cage IM is used as the maintenance cost is low. In this, three-phase, 415 V supply runs 12 auxiliaries, further three-phase auxiliaries, and one battery charger are fed by this AC supply. When required oil cooling blowers and traction motors are run. Depending upon the operating temperatures and speed, the blowers speed can be adjusted by the control electronics. Whenever the auxiliary converters are operating, the transformer and traction converter work continuously. Auxiliary winding of main transformer provides one-phase 1000 V supply to auxiliary converter. Further, this AC supply is fed to rectifier module auxiliary converter where it converts into DC and then it is forwarded to DC link. From the DC link, pure DC will be obtained which is further fed to inverter module auxiliary converter. From this, 415 V, three-phase AC supply with variable amplitude of voltage and frequency will be obtained and again it is fed to different three-phase auxiliaries. In this system, there are three auxiliary converters which work together to obtain the one-phase 1000 V AC input supply and provide three-phase 415 V output to run battery charger and 12 different auxiliaries (Fig. 1).

R. S. Hiware (✉) · S. K. Umathe
G. H. Raisoni College of Engineering, Nagpur, India
e-mail: rutuja.hiware@raisoni.net

S. K. Umathe
e-mail: shradha.umathe@raisoni.net

S. Bire
ABB India limited, Aundh, Pune, India

2 Methodology

2.1 Overview of Single-Phase AC to Three-Phase AC System

The single-phase to three-phase auxiliary converter topology for traction drives. The operation of the converter is analyzed using the separation and link approach. The control is built by using the sinusoidal pulse width modulation (SPWM) for the bi-directional switches in this converter. This single-phase to three-phase converter has advantage as this replaces the conventional AC-DC-AC stages so the effective energy conversion is efficient and the control is conventional carrier-based SPWM (Fig. 2).

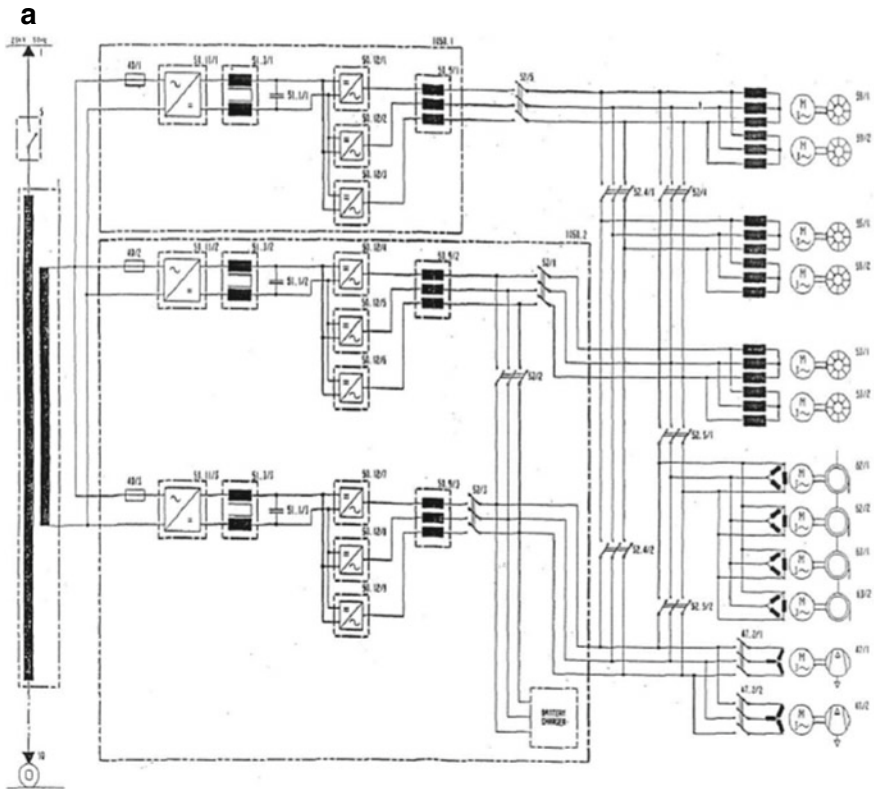


Fig. 1 a Circuit diagram of auxiliary circuit equipment. b Flowchart of locomotive operation

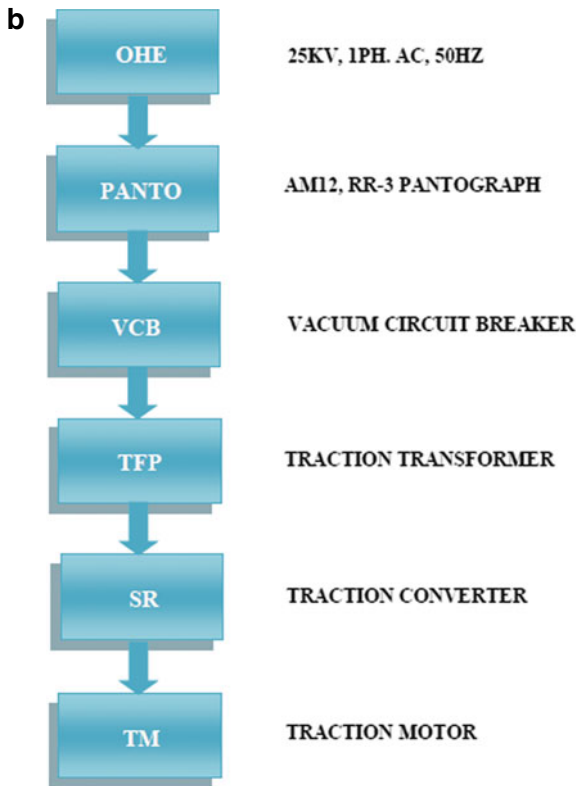


Fig. 1 (continued)

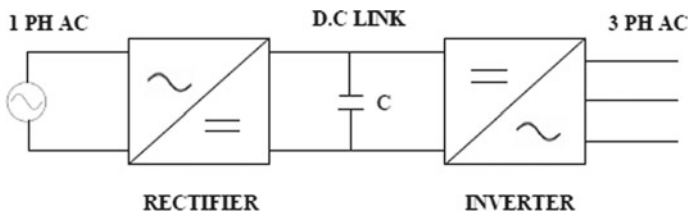


Fig. 2 Circuit diagram of single-phase to three-phase AC Conversion

2.2 Single-Phase Half Controlled Bridge Converter

See Figs. 3, 4, 5 and 6.

Fig. 3 Fully controlled converter with load side freewheeling diode

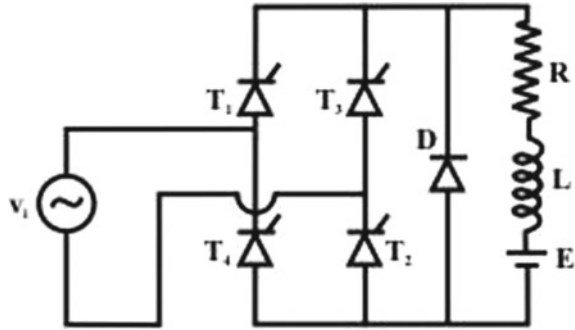


Fig. 4 Half controlled converter—alternative-1

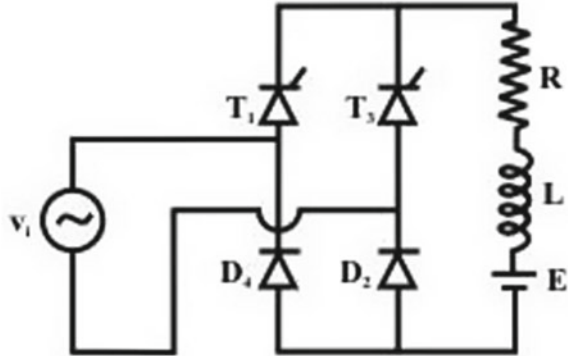
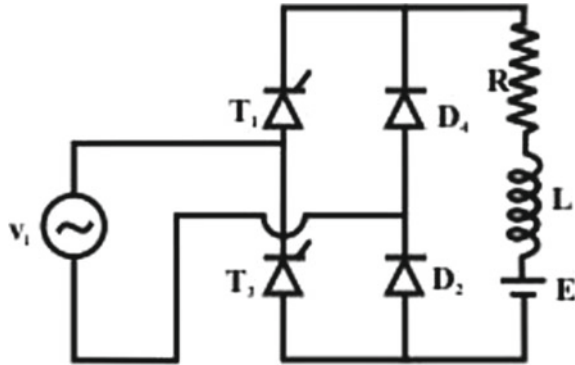


Fig. 5 Half controlled converter—alternative-2



2.3 Three-Phase Bridge Inverter

See Figs. 7 and 8.

Device / Mode	VT1	VT3	VD2	VD4	V0
T1D2	0	-V1	0	-V1	V1
T1D4	0	-V1	V1	0	0
T3D4	V1	0	V1	0	-V1
T3D2	V1	0	0	V1	0
NONE	$\frac{V1 - E}{2}$	$-\frac{V1 + E}{2}$	$\frac{V1 - E}{2}$	$-\frac{V1 + E}{2}$	E

Fig. 6 Conduction table of single-phase half controlled converter

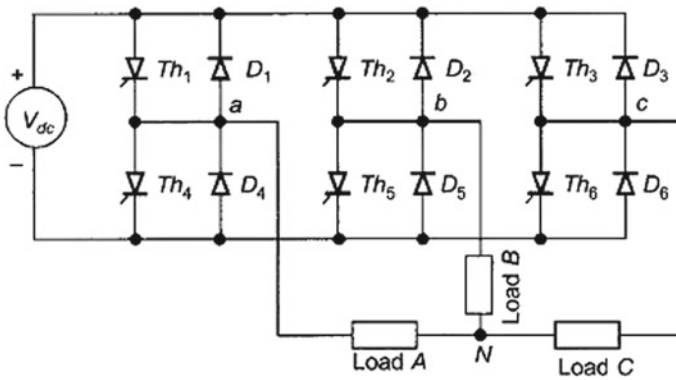


Fig. 7 Circuit diagram of three-phase bridge inverter

Th ₁		Th ₄		Th ₁		Th ₄					
Th ₅		Th ₂		Th ₅		Th ₂		Th ₅			
Th ₃	Th ₆		Th ₃		Th ₆		Th ₃				
I	II	III	IV	V	VI	I	II	III	IV	V	VI
Th ₁	Th ₁	Th ₁	Th ₄	Th ₄	Th ₄	Th ₁	Th ₁	Th ₁	Th ₄	Th ₄	Th ₄
Th ₅	Th ₅	Th ₂	Th ₂	Th ₂	Th ₅	Th ₅	Th ₅	Th ₂	Th ₂	Th ₂	Th ₅
Th ₃	Th ₆	Th ₆	Th ₆	Th ₃	Th ₃	Th ₃	Th ₆	Th ₆	Th ₆	Th ₃	Th ₃

Fig. 8 Sequence of conducting thyristors in three-phase bridge inverter

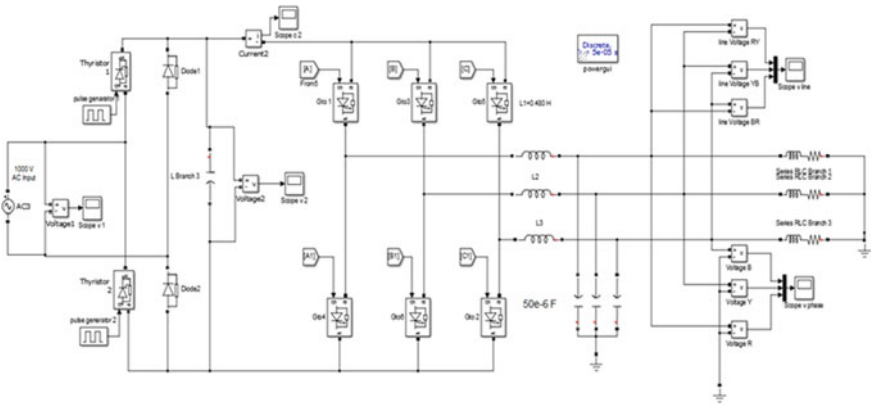


Fig. 9 Power circuit of auxiliary converter

3 Design and Implementation

See Fig. 9.

4 Result

See Figs. 10, 11, 12, 13 and 14.

Fig. 10 Output of inverter without sine filter: line voltage

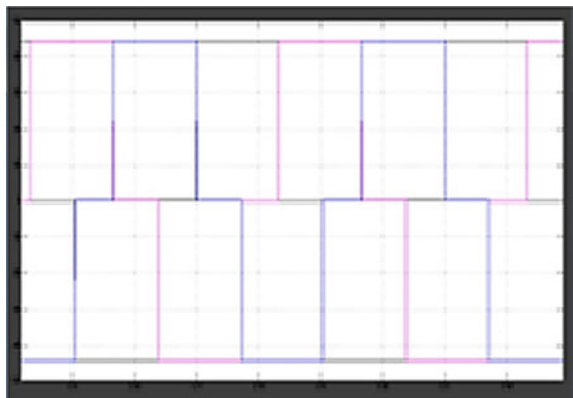


Fig. 11 Output of inverter without sine filter: phase voltage

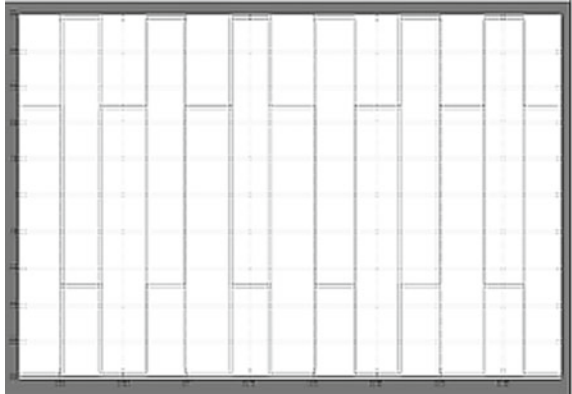


Fig. 12 Output of inverter with sine filter: line voltage

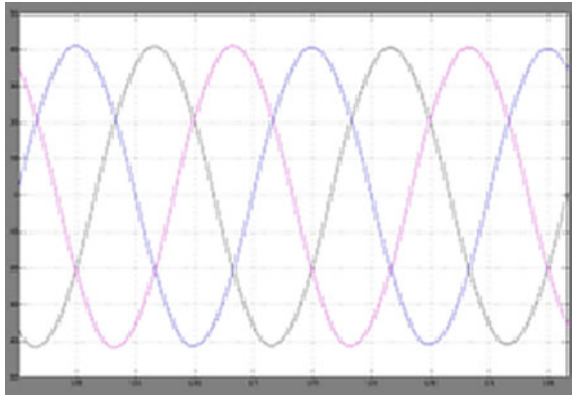


Fig. 13 Output of inverter with sine filter: phase voltage

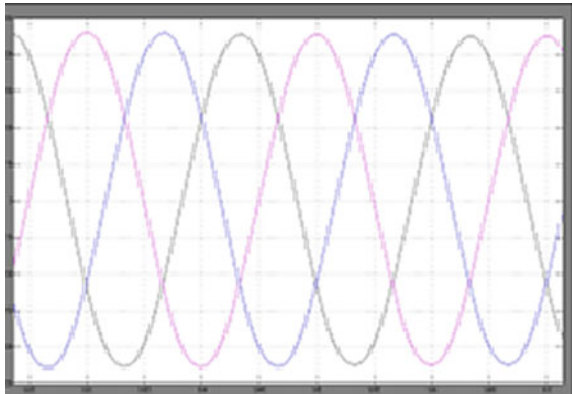
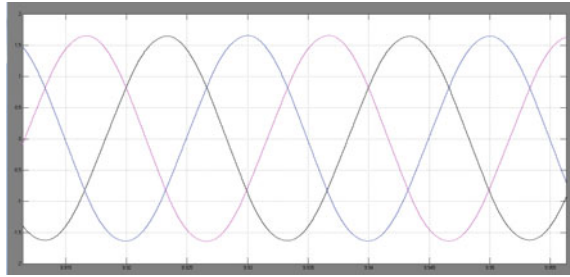


Fig. 14 Output current waveform of inverter



5 Conclusion

The single-phase to three-phase auxiliary converter topology for traction drives. The operation of the converter is analyzed using the separation and link approach. The control is built by using the sinusoidal pulse width modulation (SPWM) for the bi-directional switches in this converter. This replaces the conventional AC-DC-AC stages so the effective energy conversion is efficient. The control is conventional carrier-based SPWM. By using the filter circuit we can reduce the harmonics in the system and we can obtain the smooth sinusoidal waveform.

References

1. I. Kahn, P.D. Ziogas, M.H. Rashid, A Novel single to three phase static converter. *IEEE Trans. Ind. Appl.* **25**(1), 143–152 (1989)
2. J. Xiao, W. Zhang, H. Omori, K. Matsui, A novel operation strategy for single-to three-phase matrix converter, in *Electrical Machines and systems, ICMES-2009/5382800*, (2009), pp. 1–6
3. P. Wheeler, J. Rodriguez, J. Clare, L. Empringham, A. Weinstein, Matrix converters: a technology review. *IEEE Trans. Ind. Electron.* **49**(2), 276–288 (2002)
4. R.S. Hiware, J.G. Chaudhari, Indirect field oriented control for induction motor drive using space vector modulation technique. in *International Conference on Emerging Trends in Engineering & Technology (ICETET)*, (IEEE, 2011)
5. G. Milan, M. Mohamadian, S.M. Dehghan, E. Seifi, A. Yazdian, A Novel SPWM strategy for single to three-phase matrix converter, in *2nd PEDSTC-2011 (IEEE)*, pp. 495–500
6. M. Macan, N. Težak, Integrated traction and auxiliary power supply converters for diesel-electric rail vehicles, in *15th International Power Electronics and Motion Control Conference, EPE-PEMC 2012 ECCE Europe*, (Novi Sad, Serbia, 2012)
7. M. Macan, I. Bahun, Ž. Jakopović, Output DC voltage elimination in PWM converters for railway applications, in *Conference on Electrical Drives and Power Electronics, EDPE2011 The High Tatras*, 2011
8. S.K. Deshmukh, R.S. Hiware, Speed control of DC motor using chopper. *Int. J. Sci. Res.* **6**(3), 1751–1753 (2017)
9. A. Coccia, A. Del Pizzo, R. Rizzo, Auxiliary winding of a multibody traction transformer for filtering psophometric currents produced by interlaced modulation of PWM rectifiers. *IEEE, PEDS* **1**, 665–670 (2003)
10. S. Sabbanwar, R.S. Hiware, Battery Super capacitor Hybrid Energy Storage System, in *International research conference on recent advances in engineering & technology (IRCRAET)* ISBN NO-978–3–642–24819–4 (2014)

11. P.K. Steimer, H.E. Grüning, J. Werninger, E. Carroll, S. Klaka, S. Lindner, IGCT—a new emerging technology for high power, low cost inverters, in *Conf. Rec. IAS*, (1997), pp. 1592–1599
12. N. Khan, S. Umathe, Three level inverter : design and fabrication, in *3rd International Conference on Quality Up gradation in Engineering, Science & Technology, IC-QUEST 2014*, (2014)
13. J. Rodríguez, B. Wu, S. Bernet, J. Pontt, S. Kouro, Multilevel voltage source converter topologies for industrial medium voltage drives. *IEEE Trans. Ind. Electron. Spec. Sect. High Power Drives* **54**(6), 2930–2945 (2007)
14. L.G. Franquelo, J. Rodríguez, J.I. Leon, S. Kouro, R. Portillo, M.A.M. Prats, The age of multilevel converters arrives. *IEEE Ind. Electron. Magaz.* 28–39 (2008)
15. S.A. Gonzalez, M.I. Valla, C.F. Christiansen, Analysis of a cascade asymmetric topology for multilevel converters, in *IEEE International Symposium on Industrial Electronics (ISIE'07)*, (Vigo, Spain, 2007) pp. 1027–1032
16. M.P. Kazmierkowski, M. Jasinski, G. Wrona, DSP based control of grid-connected power converters operating under grid distortions. *IEEE Trans. Ind. Inform.* **7**(2), 204–211 (2011)

Analysis of Control Techniques and Filter Design of Multilevel Inverter



Vaidehi Korde, Neha Sute, V. B. Borghate, and V. M. Korde

1 Introduction

A multilevel inverter generates a staircase output which resembles close to a sinusoidal waveform. The basic circuit diagram of cascaded H-bridge multilevel inverter and its output voltage waveform can be visualized as shown in Fig. 1. The closeness of this output waveform to sine wave is indicated by %THD parameter. The multilevel converter has several advantages such as production of lesser common mode voltage, drawing low distortion current, which can be handled at both lower and higher switching frequencies, and with the selective harmonic distortion technique the harmonic content at the output can be reduced, has lower dv/dt , etc.

The conventional topologies of symmetric multilevel inverters are categorized as

- (a) Diode clamped-type multilevel inverter.
- (b) Flying capacitor-type multilevel inverter.
- (c) Cascaded H-bridge (CHB)-type multilevel inverter.

Cascaded H-bridge (CHB)-type multilevel inverter is preferred (and chosen for further analysis in this work) over the other two topologies (diode-clamped and flying capacitor topologies) because.

- (1) The output levels in the voltage obtained are more than twice the number of DC sources used.
- (2) Because of modularity, faulty section can be easily identified and replaced.
- (3) Easy packaging and manufacturing because of modular structure.

V. Korde (✉) · N. Sute · V. B. Borghate
Department of Electrical and Electronics Engineering, Visvesvaraya National Institute of Technology (VNIT), Nagpur, India

V. M. Korde
Department of Mechanical Engineering, Yeshwantrao Chavan College of Engineering (YCCE), Nagpur, India

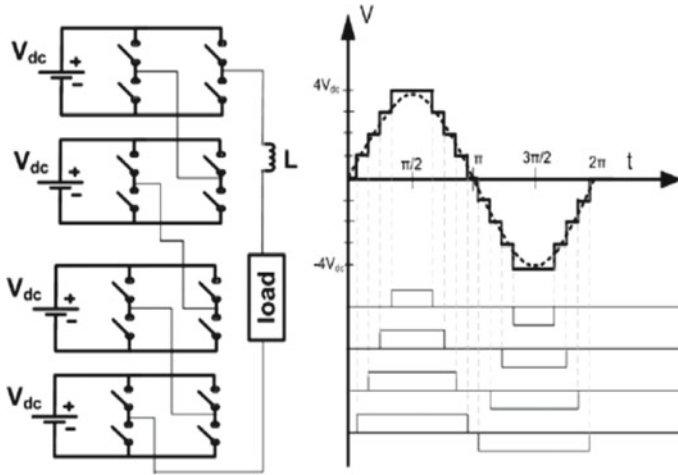


Fig. 1 Basic cascaded H-bridge topology

- (4) As more output voltage is obtained it is used in the high-power applications.
- (5) No requirement of any clamping diodes and capacitors.

The objective of this paper is to conduct a detailed analysis of level-shifted PWM control techniques and various filter designs used for multilevel inverters.

2 Control Techniques of Multilevel Inverters

In many industrial applications, the output voltage of inverter is required to be controlled to overcome the changes in input voltage and to meet the need of v/f control. The various methods for the control of output voltage of inverters can be enumerated as follows:

- (1) External control of the AC output voltage.
- (2) External control of the DC input voltage.
- (3) Internal control of the inverter output voltage (PWM control).

PWM method is referred to as the internal control method. In the first two methods, extra circuits for the control of either DC input or AC output become necessary. The third method, however, does not require such circuits. The first two methods require the use of peripheral components whereas the third method requires no external components. Hence, the most efficient method of controlling the output voltage is to include Pulse Width Modulation (PWM) control within the inverters. So, this method of control is discussed in great detail in the following section. The advantage of Sine PWM is that it concentrates all the dominant harmonics at carrier frequency and they can be eliminated by properly designing a filter for the inverter and the filter size gets reduced too.

2.1 Sine Pulse Width Modulation (SPWM)

In this method, the reference signal is taken as sinusoidal waveform and the carrier signal is taken as triangular waveform. The frequency of inverter output voltage depends on frequency of reference signal (f_R) and amplitude of reference signal (V_R) controls the modulation index (M_a). We can control the amplitude of output voltage by varying the modulation index (M_a). The modulation index (M_a) is V_R/V_C .

Sine PWM is further classified as.

1. Level shifted
 - (a) In Phase Disposition (IPD).
 - (b) Alternate Phase Opposite Disposition (APOD).
 - (c) Phase Opposite Disposition (POD).
2. Phase Shifted

Level-shifted PWM techniques will be discussed in this paper.

2.2 Level-Shifted Sine PWM Scheme

In level-shifted SPWM technique, we use carrier waves which are shifted by certain amplitude. The sinusoidal reference signal is compared with a triangular carrier wave to obtain the gating signals.

For N number of levels in output phase voltage, $(N - 1)$ carrier signals of same frequency and amplitude are required. The switching frequency of the inverter is equal to the carrier frequency, that is, (device switching frequency) $f_C = f_{cr}$, where f_C is switching frequency of inverter. Average device switching frequency is $f_C = f_{cr}/(N-1)$. The conduction time distribution of the devices is uneven. The switching pattern is generated by comparing the carrier waves with the modulating wave. The carrier waves above zero reference are compared with modulating wave to generate positive half output voltage, whereas carrier waves below zero reference are responsible for negative half output voltage.

In Phase Disposition (IPD)

The carrier waves have same amplitude and frequency and there is no phase shift between them. But these carriers are at different offset values. These modulations are carried at unity modulation index. Switching pattern produced by using this scheme is shown in Fig. 2.

Alternative Phase Opposite Disposition (APOD)

In this technique, all the carrier waves are alternatively in phase opposition with each other. The simulation of modulation signal and carrier waveforms of a five-level inverter using this scheme is shown in Fig. 3.

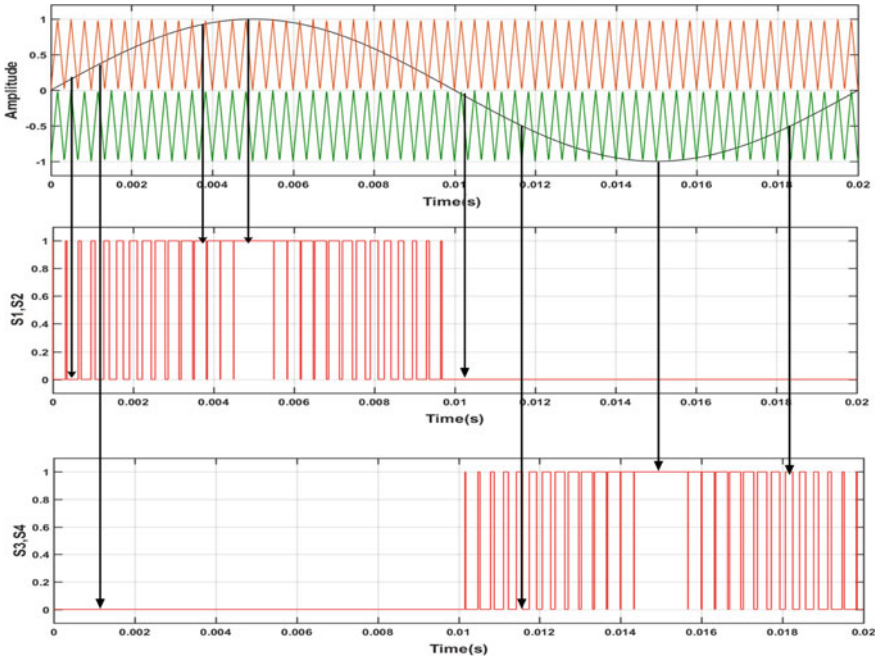


Fig. 2 Switching pattern produced by using the IPD carrier-based PWM scheme

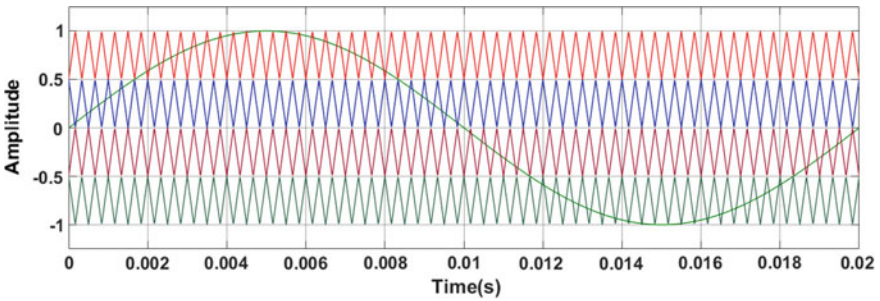


Fig. 3 Simulation of modulation signal and carrier waveforms of a five-level inverter using APOD as carrier-based PWM scheme

Phase Opposite Disposition (POD)

In this, the carrier waves above the zero reference are in same phase and the carrier waves below the zero reference are in same phase. The simulation of modulation signal and carrier waveforms of a five-level inverter using this scheme is shown in Fig. 4.

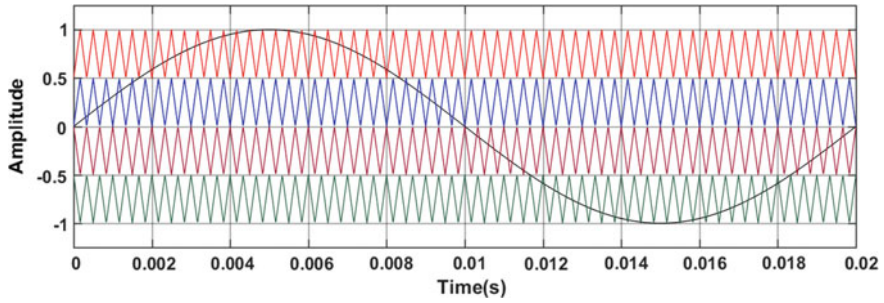


Fig. 4 Simulation of modulation signal and carrier waveforms of a five-level inverter using POD as carrier-based PWM scheme

2.3 Simulations of Five-Level CHB

Similarly, the simulations were done for three-level, asymmetric seven-level, and asymmetric nine-level multilevel inverters too and were used for further analysis (Figs. 5, 6 and 7).

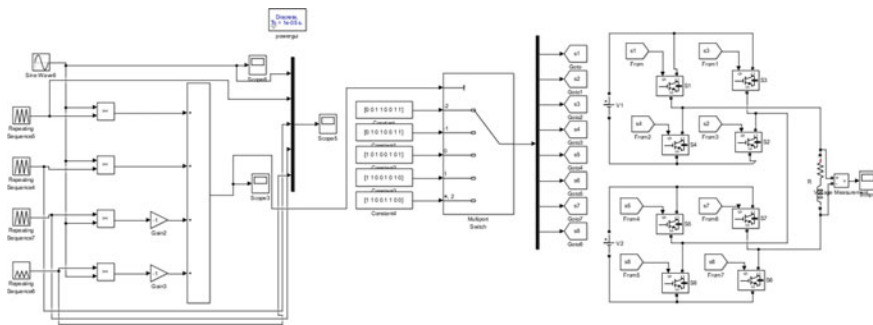


Fig. 5 Simulation circuit of single-phase five-level CHB

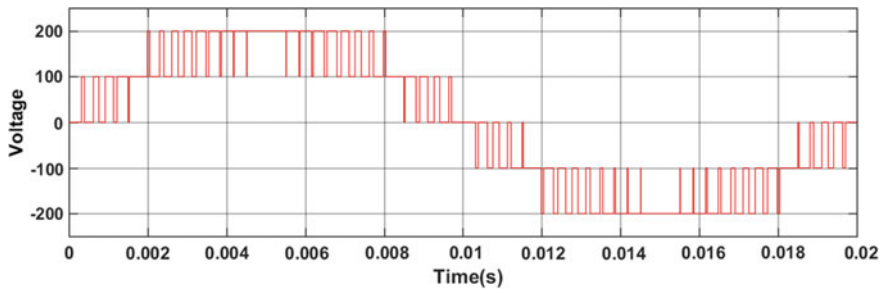


Fig. 6 Five-level output phase voltage

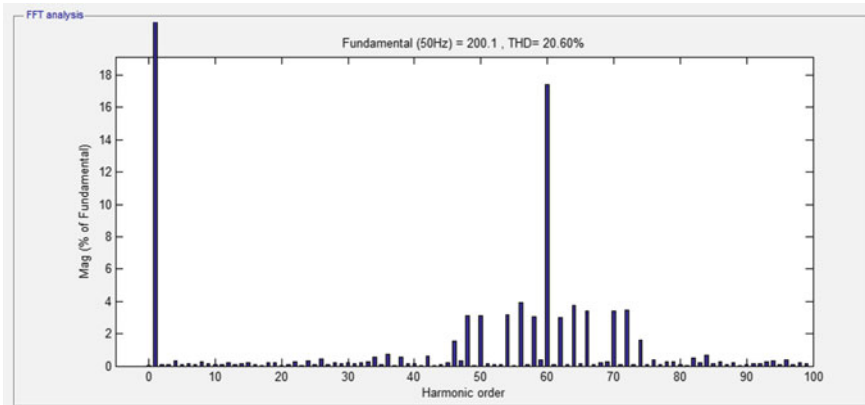


Fig. 7 FFT window for five-level CHB

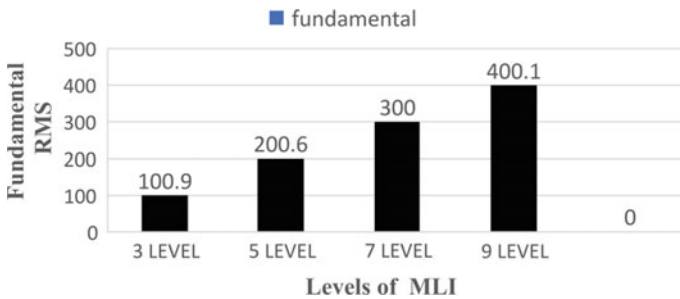


Fig. 8 Levels versus fundamental voltage

2.4 Effect of Increase in Levels

As levels in multilevel inverter go on increasing, the number of steps in phase voltage increases and hence will provide more fundamental voltage which is shown in Fig. 8. The %THD will be reduced with increase in levels as shown in Fig. 9 and the waveform will be closer to a sinusoid.

2.5 Comparative Analysis of Carrier-Based PWM Schemes

The comparative analysis of fundamental voltage and %THD of all the three carrier-based PWM schemes (IPD, APOD, POD) is carried out on symmetrical five-level CHB with $V_{dc} = 100\text{ V}$ and $M_a = 1$.

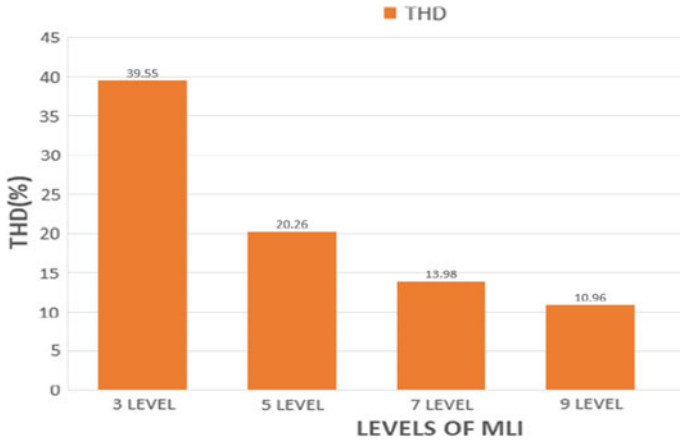
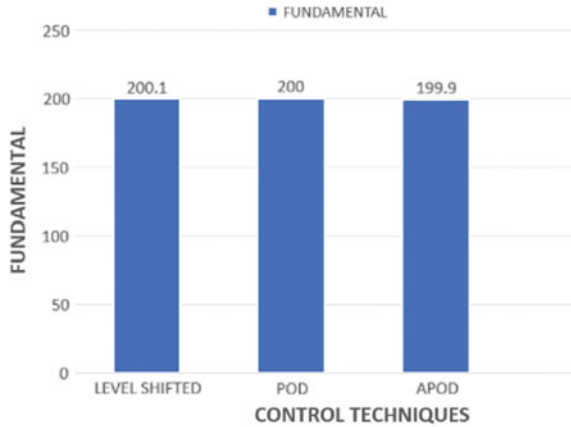


Fig. 9 Levels vs. %THD

Fig. 10 Variation in fundamental voltage with PWM technique



By observing the results, it can be clearly concluded that from Fig. 10, there is no significant variation in fundamental output voltage when any of the three techniques are used and the POD technique provides better %THD performance as seen in Fig. 11.

Hence, further analysis is carried out based on POD carrier-based PWM scheme.

2.6 Effect of Change in Carrier Frequency

This is observed on symmetrical five-level cascaded H-bridge with $V_{dc} = 100\text{ V}$ and $M_a = 1$ with POD technique.

Fig. 11 Variation in %THD with PWM technique

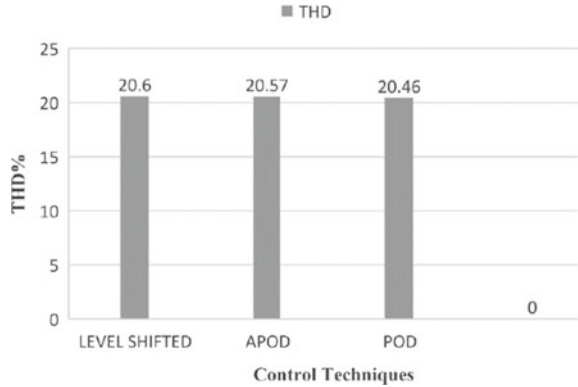


Table 1 Variation of %THD and fundamental voltage with carrier frequency (f_c)

F_c (KHz)	THD%	Fundamental (V)
1	23.11	200.5
1.5	21.86	201
2	20.77	199.8
2.5	20.51	199.8
3	14.20	200
3.5	3.18	199.7
4	2.11	200.7
4.5	1.84	200.2
5	1.79	198.6
5.5	1.37	200.2
6	1.11	200

- (a) The effect of increase in the carrier frequency is observed in the simulation, and from Table 1 and Fig. 12, it can be seen that %THD decreases with increase in frequency.
- (b) This is because the dominant harmonics get concentrated at switching frequency in case of multicarrier SPWM techniques.
- (c) There is not much variation in fundamental voltage.

2.7 Effect of Change in Modulation Index (M_a)

This is observed on symmetric seven-level cascaded H-bridge with $V_{dc} = 100$ V and $f_c = 3$ kHz.

- (a) As Modulation Index (M_a) reduces from unity, there is reduction in levels of output voltage.

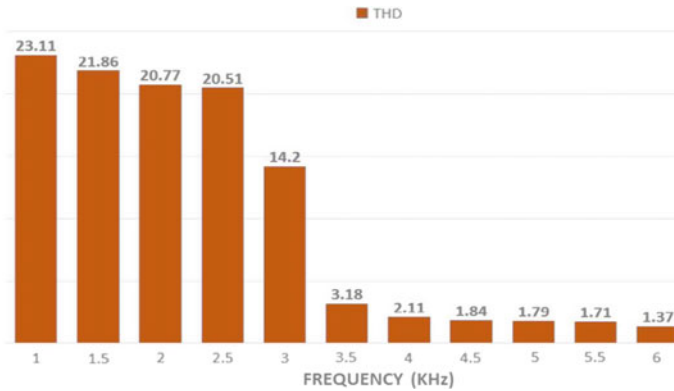


Fig. 12 Variation in %THD with carrier frequency (f_c)

Table 2 Effect of change in Modulation Index (M_a) on %THD and fundamental voltage

M_a	THD%	Fundamental (V)
1	14.1	296.7
0.9	17.22	265.2
0.8	16.45	240.6
0.7	16.84	207.6
0.6	19.72	175.6
0.5	24.77	149.9
0.4	27.79	162
0.3	35.46	90.46

- (b) In seven-level voltage, three steps are available in positive half cycle. If M_a reduces by one-third the seven-level voltage will be reduced to 5. Similarly, if it reduces by two-third, five level is reduced to three levels.
- (c) As we decrease the M_a , the fundamental decreases and THD increases and is shown in Table 2. The increase in THD is due to the decrease in the number of levels.

3 Filter Design

The filter for multilevel inverter should be designed such that the output voltage and current harmonics stay within the limits even for the worst condition. The filters used for the analysis are L filter, LC filter, LCL filter, and LCL filter with damping resistor (R_d).

3.1 Analysis of L, LC, and LCL Filters

L Filter

The application of this filter is suitable for high switching frequency inverters [1]. Figure 13 shows the diagram for L filter.

The inductance value should be chosen such that it should be less than 20% so as to limit the voltage drop during the normal conditions [2]. The ripple current can be found as [3]

$$I_{ripple} = \frac{0.2\sqrt{2}P}{3\left(\frac{V_L}{\sqrt{3}}\right)}$$

The filter inductance is given by

$$L_i = \frac{0.5 \cdot \left(V_{dc} - \frac{V_{dc}}{2}\right)}{2 \cdot I_{ripple} \cdot f_{sw}}$$

LC Filter

It is second-order filter which has better damping behavior than L filter. Figure 14 shows the diagram for LC filter.

The attenuation of second-order filter is after the cutoff frequency and it has no gain before the cutoff frequency, but it gives a peak at the resonant frequency, which is given by

$$f_r = \frac{1}{2\pi\sqrt{L_i \cdot C_f}}$$

Inverter-side inductance is as calculated previously in “L” filter. For the design of the filter capacitance, it is considered that the maximum power factor variation seen

Fig. 13 L filter

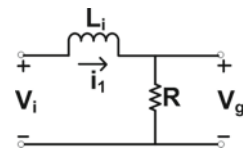


Fig. 14 LC filter

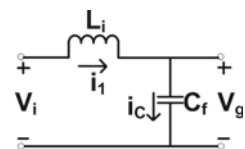
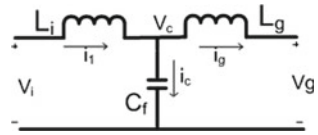


Fig. 15 LCL filter



by the grid is 5%, so x is taken as 0.05. A design factor higher than 5% can be used, whenever necessary to compensate the inductive reactance of the filter [3].

Base impedance is $Z_b = \frac{V^2}{P}$, Capacitance is $C_b = \frac{1}{Z_b \cdot 2\pi f}$, and

Filter Capacitance is $C_f = x \cdot C_b$.

LCL Filter

The attenuation of the LCL filter is for frequencies above resonant frequency. Figure 15 shows the diagram for LCL filter.

The carrier frequency must be twice compared to the cutoff. There should be sufficient distance between cutoff frequency and the grid frequency [1]. The cutoff frequency of the LCL filter can be calculated as

$$f_{res} = \frac{1}{2\pi} \sqrt{\frac{L_i + L_g}{L_i \cdot L_g \cdot C_f}}$$

In order to design an LCL filter, the following constraints are to be followed [3]:

- (a) The value of capacitor for which power factor decrease is bearable is considered. It is generally below 5%.
- (b) The inductance value should be such that it should be less than 10% so that the voltage drop at the normal conditions is limited.
- (c) In order to avoid the resonance problems with higher harmonic spectrum and the lower harmonic spectrum, the line frequency should be one-tenth of resonant frequency and the carrier frequency should be twice the resonant frequency.
- (d) For calculation of inductor on the grid side, we use the following equation:

$$L_g = r \cdot L_i$$

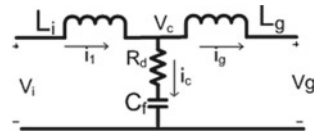
where “ r ” is ripple attenuation constant and it can be defined as the relation between the grid-side inductance and the inverter-side inductance. When r is 30%, the voltage drop across L_g is minimum.

LCL Filter with Damping Resistor

Figure 16 shows the diagram for LCL filter with damping resistor. Oscillations can occur in the LCL filter and it will magnify frequencies around its cutoff frequency. Therefore, the damping resistor is added to the filter. The damping resistor is connected in series with the filter capacitor [1].

The value of the damping resistor is calculated as

Fig. 16 LCL filter with damping resistor R_d



$$R_d = \frac{1}{3 \cdot 2\pi \cdot f_{res} \cdot C_f}$$

4 Analysis of Filter Design Using Simulations

Simulations are done in MATLAB-Simulink. From simulations, we have observed the output waveforms, the Total harmonic Distortion (THD), and the dominant harmonics created have performed FFT analysis and have derived conclusions accordingly. According to our previous analysis, we have found that Phase Opposite Disposition (POD) gives better performance compared to other SPWM techniques.

4.1 Analysis of Three-Phase Three-Level CHB

With switching frequency as 3 kHz and system frequency as 50 Hz and giving input DC input voltage to the CHB as 350 V, following analysis of phase voltage and phase current is studied. The load power is consuming 1 KW. The FFT window showing dominant harmonics as well as THD is observed.

Without Filter

The output voltage and current waveforms and FFT window of three-phase three-level CHB inverter without filter are shown in Figs. 17 and 18, respectively, and %THD content in Fig. 19.

From the figures, we can see that without filter, the stepped phase voltage is obtained and there are ripples in the current waveform. Hence, the THD of phase voltage is found to be 36.26%. The dominant harmonics are situated at 56th harmonic. The fundamental peak value of fundamental is found out as 350.8 V while total phase voltage rms as 279.7 V. To get a pure sinusoid, we need to use filters.

With LCL Filter and damping resistor

After the use of LCL filter with damping resistor, the current waveform gets smooth as shown in the phase current waveform (Figs. 20 and 21) and the %THD decreases (Fig. 22).

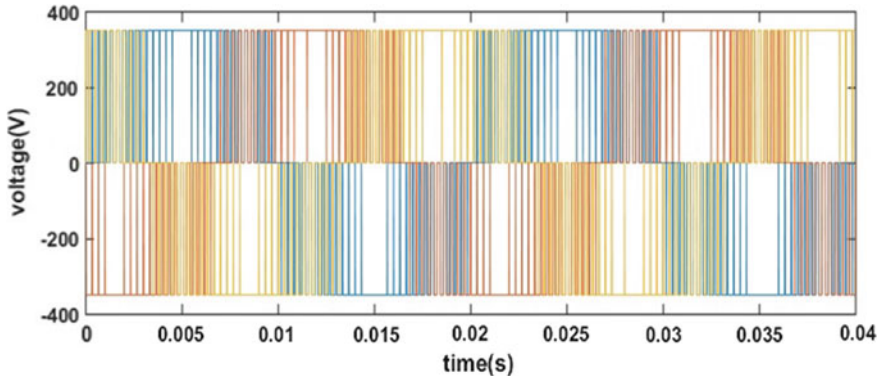


Fig. 17 Output voltage waveform of three-phase three-level CHB inverter without filter

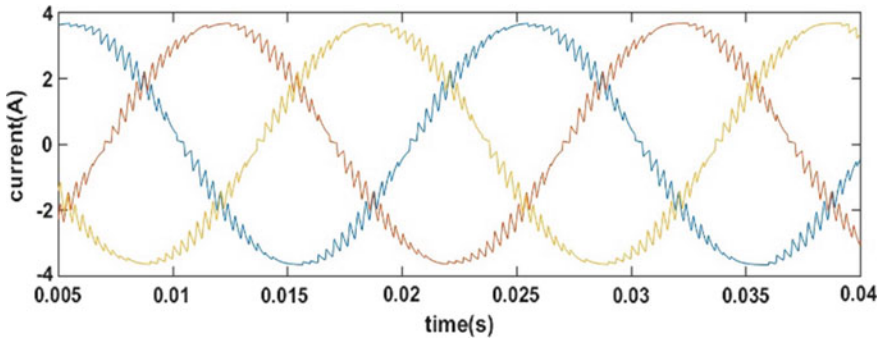


Fig. 18 Output current waveform of three-phase three-level CHB inverter without filter

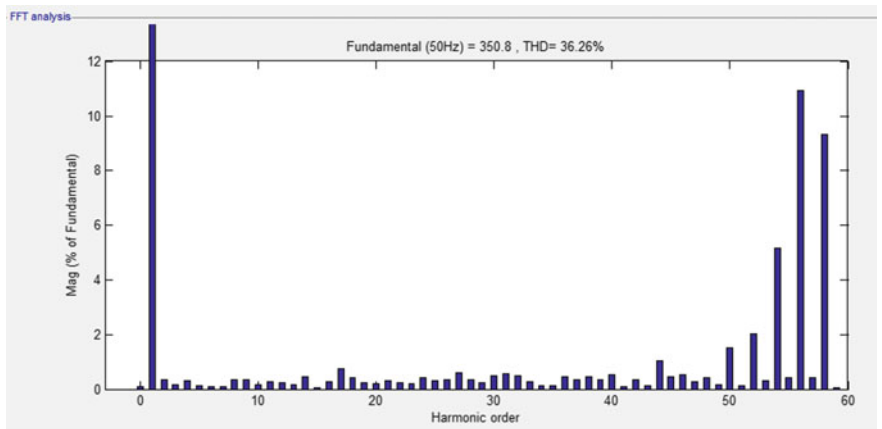


Fig. 19 FFT window of three-phase three-level CHB inverter without filter

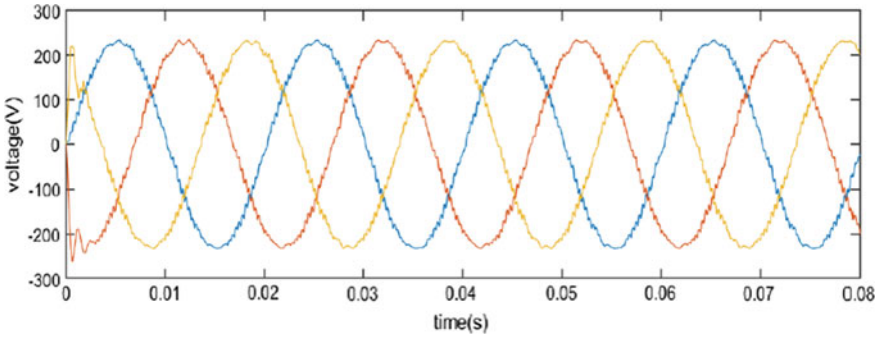


Fig. 20 Output voltage waveform of three-phase three-level CHB inverter with LCL filter and damping resistor

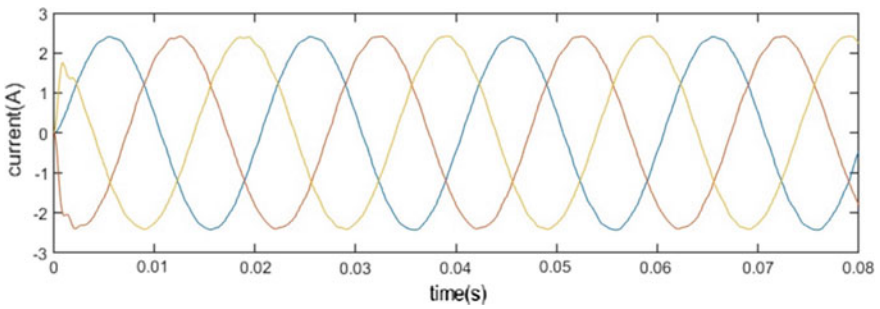


Fig. 21 Output current waveform of three-phase three-level CHB inverter with LCL filter and damping resistor

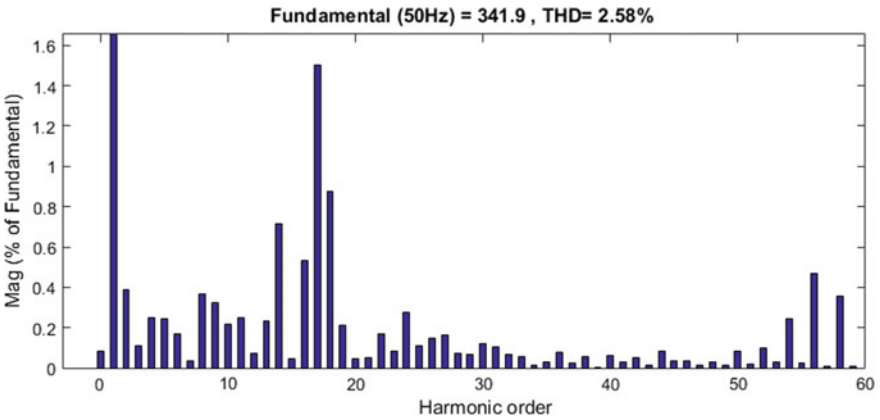


Fig. 22 FFT window of three-phase three-level CHB inverter with LCL filter and damping resistor

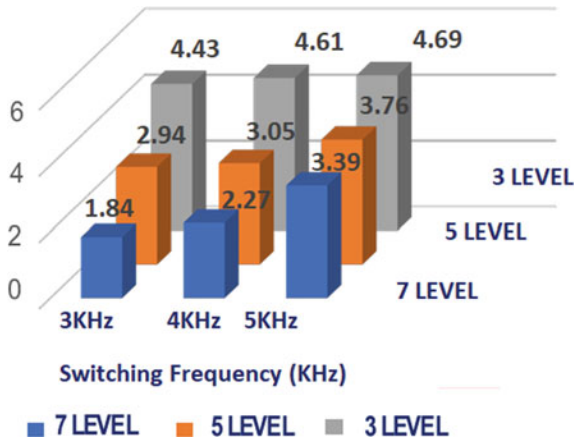


Fig. 23 %THD values of various levels at various switching frequencies (or carrier frequencies)

4.2 Effect on %THD by Variation of Levels and f_c of Three-Phase CHB

By using LCL filter design, the analysis is carried out at different levels and at various switching frequencies. The effect on %THD of filter parameters at various carrier or switching frequencies (f_c) for various levels can be seen in Fig. 23.

4.3 Comparison of Filter Sizes According to IEEE Standards

For grid-tied mode, converters require L or LCL filters for output current filtering and reducing the number of harmonics injected to the grid below limits stipulated by the IEEE Std. 512–1992 and IEEE Std. P1547-2003 IEEE Std. 519–1992: Recommended Practices and Requirements for Harmonic Control in Electrical Power Systems [4]. According to the standards, the tolerable ripple (THD) should be within 5%.

Arbitrarily chosen LCL filter parameters to maintain IEEE standards.

The LCL filter design parameters are shown in Table 3 for different levels and at various f_c .

Table 3 LCL filter design parameters for different levels and carrier frequencies

Level	Switching frequency fc								
	3 kHz			4 kHz			5 kHz		
	Li (mH)	Cf (uF)	Lg (mH)	Li (mH)	Cf (uF)	Lg (mH)	Li (mH)	Cf (uF)	Lg (mH)
3	19.54	1.66	5.86	14.65	1.66	4.395	11.7	1.66	3.51
5	12	1.66	3.6	10.5	1.66	3.15	9.25	1.66	2.775
7	10	1.66	3.325	9.18	1.66	2.75	4.8	1.66	1.44

4.4 Stability Analysis of LCL Filter Without and with Damping Resistance

Without Damping Resistor

Open-loop transfer function of LCL filter is given as

$$G_d(s) = \frac{I_g}{V_i} = \frac{1}{L_i C_f L_g s^3 + (L_i + L_g) \cdot s}$$

where I_g = grid-side current and V_i = inverter output.

With Damping Resistor

Open-loop transfer function of LCL filter with damping resistance is given as

$$G_d(s) = \frac{I_g}{V_i} = \frac{C_f R_d \cdot s + 1}{L_i C_f L_g s^3 + C_f (L_i + L_g) R_d s^2 + (L_i + L_g) s}$$

where I_g = grid-side current, V_i = inverter output voltage, and R_d = damping resistor.

In magnitude plot of LCL filter without R_d (Fig. 24), a peak is occurring at resonant frequency which causes the abrupt increase in gain margin of system causing oscillations and makes system unstable. Also, both gain margin (G_m) and phase margin (P_m) are having opposite signs, which indicates the instability of the system. While, in magnitude plot of LCL filter with R_d (Fig. 25), the peak at resonant frequency is diminished by the addition of damping resistor. Addition of series damping resistor with capacitor improves stability of the system by attenuating the ripples at resonant frequency and both the gain margin (G_m) and phase margin (P_m) are having same signs, which means that the system is stable.

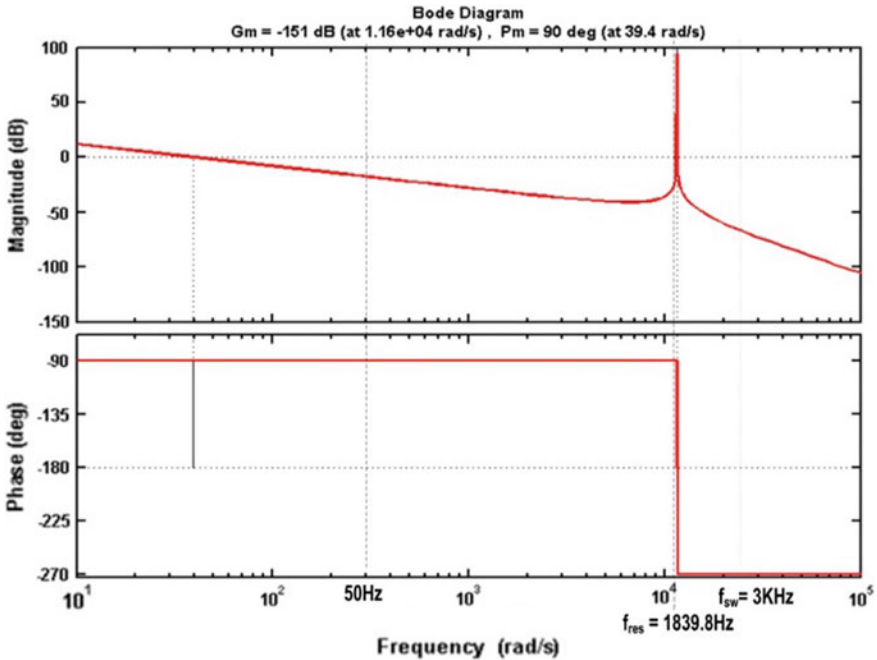


Fig. 24 Bode plot for LCL filter without damping resistor

5 Conclusions

Among the three carrier wave-based PWM schemes, Phase Opposite Disposition (POD) is found to have lesser %THD from our analysis. So, we have done our further analysis based on POD technique. On a particular level, if switching frequency is increased, the %THD decreases. As Modulation Index (M_a) reduces from unity there is reduction in levels of output voltage. As we decrease M_a , the fundamental decreases and %THD increases due to decrease in number of levels.

LCL filter is more preferable for multilevel inverters. It can also be concluded that as we go on increasing the levels of multilevel inverter, filter requirements have been reduced so with respect to its size and cost. But there is a limitation in increasing levels as the circuit complexity increases with levels as well as size and cost increases. Also, with increase in switching frequency, there is a decrement in %THD with levels, but still the limitations of increasing the switching frequency are dominant owing to the switching losses and EMI interference.

Pure LCL filter makes the system unstable and causes oscillations and this has been inferred from the bode plots. Addition of series damping resistor with capacitor improves stability of the system by attenuating the ripples at resonant frequency. Hence, it can be concluded that the designed LCL filter is stable.

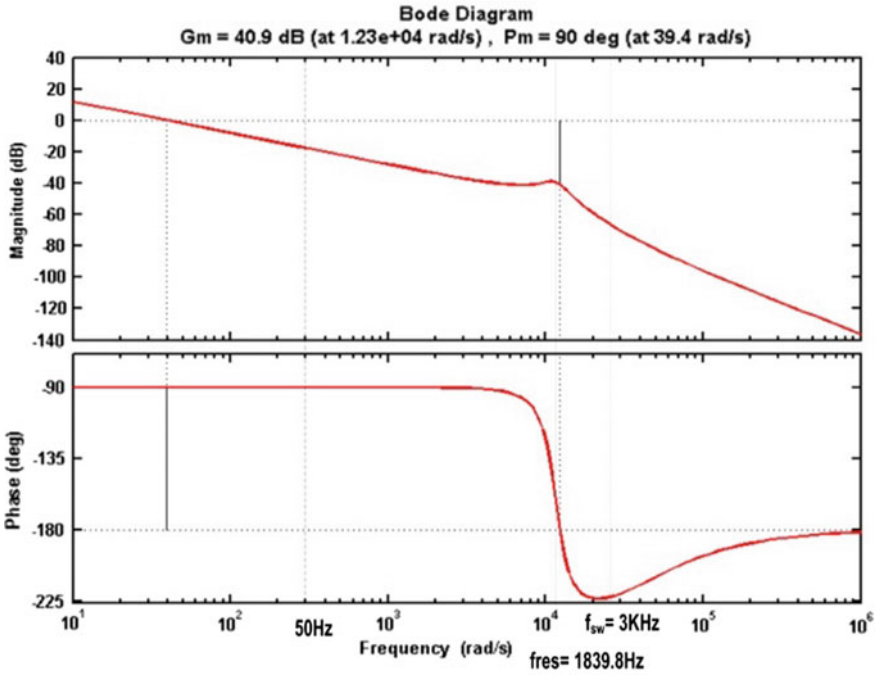


Fig. 25 Bode plot for LCL filter with damping resistor

References

1. A.E.W.H. Kahlane, L. Hassaine, M. Kherchi, LCL filter design for photovoltaic grid connected systems, in *IREC2015 The Sixth International Renewable Energy Congress, Conference Paper* (IEEE, 2015)
2. A. Reznik, M.G. Simões, A. Al-Durra, S.M. Muyeen, LCL filter design and performance analysis for grid interconnected systems. *IEEE Trans. Ind. Appl.* **50**(2) (2014)
3. K. Vamsi Krishna, H.M. Suryawanshi, Comparison between 2-level and 3- level grid connected inverters implemented using SRF PLL technique, in *Conference Paper IEEE* (2015)
4. M. Hojabri, M. Hojabri, Design, application and comparison of passive filters for three-phase grid-connected renewable energy systems. *ARNP J. Eng. Appl. Sci.* **10**(22) ISSN 1819-6608 (2015)

Increasing the Accuracy and Reducing the Installation Cost of Automatic Power Factor Correction System Using TRIAC



Mohammad Khalid Saifullah, Md. Sajedul Rahman, Md. Masum Miah, Md. Rubaiyat Rahman Shibly, Nasim Mia, Md. Salman Rahman, Saikat Das, and K. M. Ahsan-uz-Zaman

1 Introduction

Power factor can be defined as the ratio of KW to KVA of any electrical load where KVA is denoted for apparent power of that load and KW is denoted for actual power of that same load. The power factor indicates, how the load current affects the efficiency of any power system, i.e., power factor is calculated to understand how efficiently the supply current is being converted to useful work output. Different kinds of modern domestic loads were used generally in the electrical system like air conditioners, fans, refrigerators, washing machines, lamps, television, water pumps, etc. which are inductive in nature. These inductive loads cause very poor power factor that unsettles AC voltages which therefore decrease the performance of other components that is connected in the same system. Also having poor power factors these components require a huge current which increases the cost. Poor power factor enables copper losses, reduces systems handling capacity, draws low-voltage regulation, and therefore results in a very poor, lessened overall efficiency of that distribution system. As power factor is related to the efficiency of the power system, it is important to electric utilities used over the world. So, in order to minimize financial losses, to reduce system and copper losses, to decrease the amount of extra current that is required for inductive load, to boost the reliability and efficiency of the system, poor power factor should be improved or corrected. A series of static capacitor banks are used worldwide to meet these losses. But this project discussed in this paper is based on

M. K. Saifullah (✉) · Md. M. Miah · Md. R. R. Shibly · N. Mia · Md. S. Rahman · S. Das · K. M. Ahsan-uz-Zaman

Department of EEE, Mymensingh Engineering College, Mymensingh, Bangladesh

Md. S. Rahman

Department of EEE, Rajshahi University of Engineering and Technology, Rajshahi, Bangladesh

using only a single capacitor which is connected with a TRIAC which is controlled by a microcontroller that enables the system to control capacitive currents to get the desired value of power factor.

2 Literature Survey

2.1 *Previous Works and Their Limitation*

A lot of works have been done on various PFC circuit topologies [1]. Some work has been done earlier on reactive power compensation, usually fixed value capacitors are used in the first stage in power factor controllers. Capacitors are added to individual loads or motors in a parallel way. The most used technique of improving power factor is through setting one capacitor bank with the incoming switchgear bus or transformer [2, 3]. If the load increases the more capacitor is being connected across the load to balance the inductive load. This convention power factor control comprises a power factor sensing relay and several values of capacitors that are discrete are switched ON and switched OFF to the required value via a set of contactors [4–7]. This system has some serious disadvantages, such as sometimes it can't provide perfect indemnification to the power (reactive) as the steps are only a near about recompense to the available power factor. Moreover, when the capacitors work at the full-rated voltage for a long time and at a definite switching specimen with relay, the peak voltage is increased far off the rated peak voltage of capacitors that can demolish or decrease the lifetime of those elements. In some systems, the relay has been replaced by TRIAC [8, 9]. But still, the multi-number of capacitor or capacitor bank has been used. Therefore, the compensation error cannot be removed.

2.2 *Proposed System to Overcoming the Limitation*

The main aim of all the above works has been to reduce cost, optimize the performance of active PFC circuits, and make the scheme automatic. In this paper, the power factor has been improved through controlling the reactive power compensation. In a low load period, the reactive power compensation will be less than compared to the high load period. To obtain this task automatically there need some devices which are used for sensing, controlling, recovering power factor, and protecting the whole system. In the proposed system, only one capacitor (capacitor bank can be used also if necessary) has been used with TRIAC. The required reactive power or I_c has been controlled by controlling the firing angle of the TRIAC that controls the input power to the capacitor. Therefore, the capacitor is being used for multiple value of compensation. The firing angle has been controlled by microcontroller using the method given in Eqs. 1, 2, and 3.

$$P = V.I. \cos \Phi \quad (1)$$

$$S = P + jQ \quad (2)$$

$$\text{Power Factor} = P/S = P/\sqrt{(P^2 + Q^2)} \quad (3)$$

In proposed system, the supply voltage is constant, so for a given quantity of real power the load current will be less at high power factor or vice versa. Therefore, we can determine the desired power factor by observing the line current. In this project, we used a Hall-effect-type current sensor to measure current. The applied current flowing through this copper conduction path generates a magnetic field in which the Hall IC converts into a proportional voltage.

3 Proposed System of Control Scheme

3.1 Block Diagram of Proposed System

In this paper, the power factor has been improved through controlling the reactive power compensation. In a low load period, the reactive power compensation will be less than compared to the high load period. To obtain this task, automatically there need some devices which are used to sensing, controlling, recovering power factor, and protecting the whole system. Block diagram of automatic power factor control unit is shown in Fig. 1. Some important parts of the block diagram are discussed in next section.

3.2 Zero-Crossing Detector

Among different forms of comparator, applied form is known as zero-crossing detector. The fundamental comparator circuits of op-amp can be applied as zero-crossing detector which has been given zero reference voltage (V_{ref}). A zero-crossing detector is illustrated in Fig. 2i by making use of an inverting op-amp comparator. In Fig. 2ii the waveform of output voltage is depicted which specify the time and direction of crossing zero volt by input signal voltage V_{in} . The input signal may be a slowly changing waveform that may be a low-frequency one in some applications. In such kind of case, the quick switch of output voltage V_{out} from one state of saturation to other state may not happen as there may be output voltage fluctuation between two saturation states where the voltage fluctuations are mainly endangered for noise that

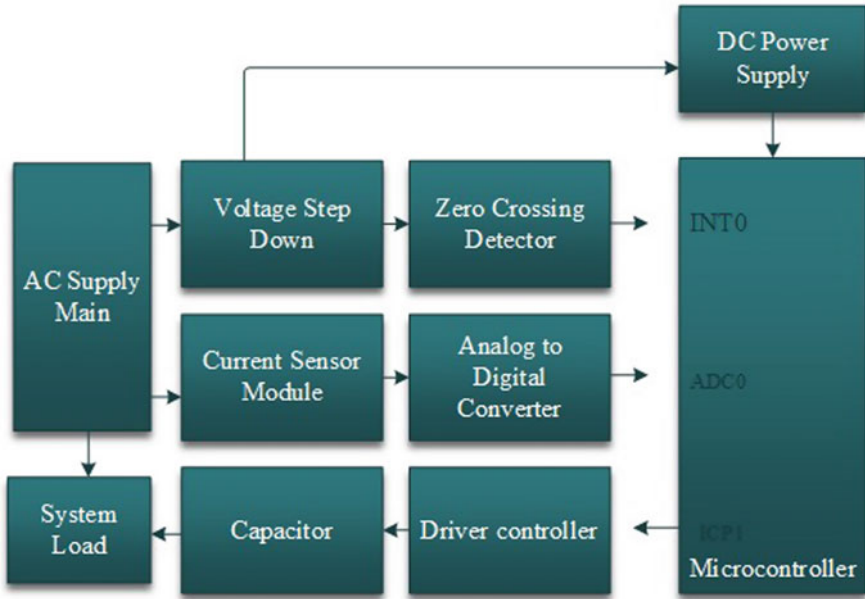


Fig. 1 Block diagram of automatic power factor control unit

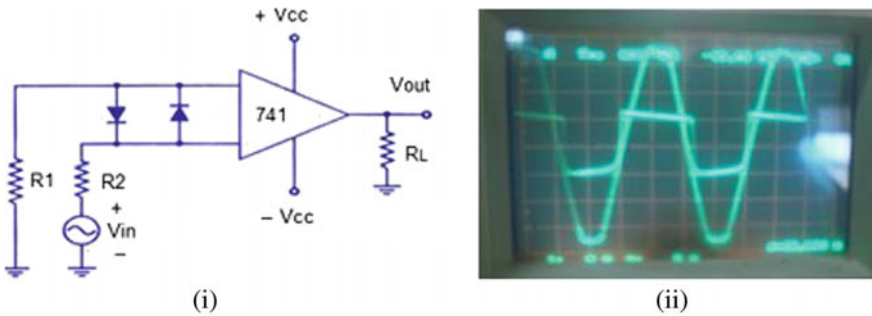


Fig. 2 (i) Circuit diagram of zero-crossing detector and (ii) input and output waveforms of zero-crossing detector

is produced from input terminals of op-amp. Therefore, to overcome these problems positive feeding or regenerative can be used as these causes the output voltage to alter faster. Also, false output transitions may get eliminated that may be caused by the noise at the input of op-amp.

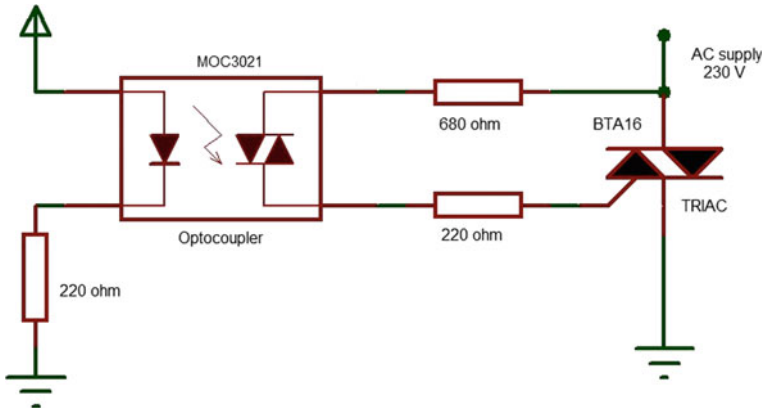


Fig. 3 Circuit diagram for controlling and driver

3.3 Driver and Controller Circuit

The driver and control circuit consists of an optocoupler and a TRIAC. The optocoupler is used as a TRIAC driver and the TRIAC is used as controlling device which controls the line current. The optical isolator or optocoupler is a component that can transfer electrical signals by using light between two isolated circuits. Optoisolator prevents high voltages from affecting the system that is receiving the signal. Input signal of optocoupler is fed from microcontroller pin ICP1, the input signal is 5 V, and 2 ms duration pulse. The optocoupler is coupled with TRIAC for controlling capacitive current. The following circuit showed in Fig. 3 has been used for controlling the output current.

TRIACs are bidirectional, therefore current can flow in either direction. The RMS value of current depends on the position of firing pulse of TRIAC. TRIACs are very convenient switches for alternating current circuits for the bi-directionality properties. When a current flowing into or out of its gate is sufficient to turn on the relevant junctions in the quadrant of operation the TRIAC starts conducting. The output waveforms of TRIAC are given in Fig. 4 for different firing angles.

3.4 Flowchart of Microcontroller Program

The flowchart of the microcontroller program is depicted in Fig. 5. In the start, a default firing angle of TRIAC has been set, and then the line current value has been taken as default value of current. After that the firing angle has been increased and decreased by 5 ° and for those firing angle the current reading has been taken. The three value is compared and the lowest value has been taken as new default value. This process continues until finding out the lowest line current for the particular TRIAC firing angle.

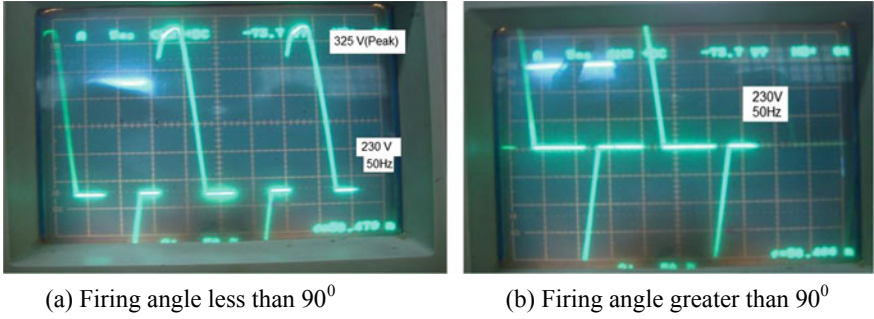


Fig. 4 Output waveforms of TRIAC for the case of resistive load only

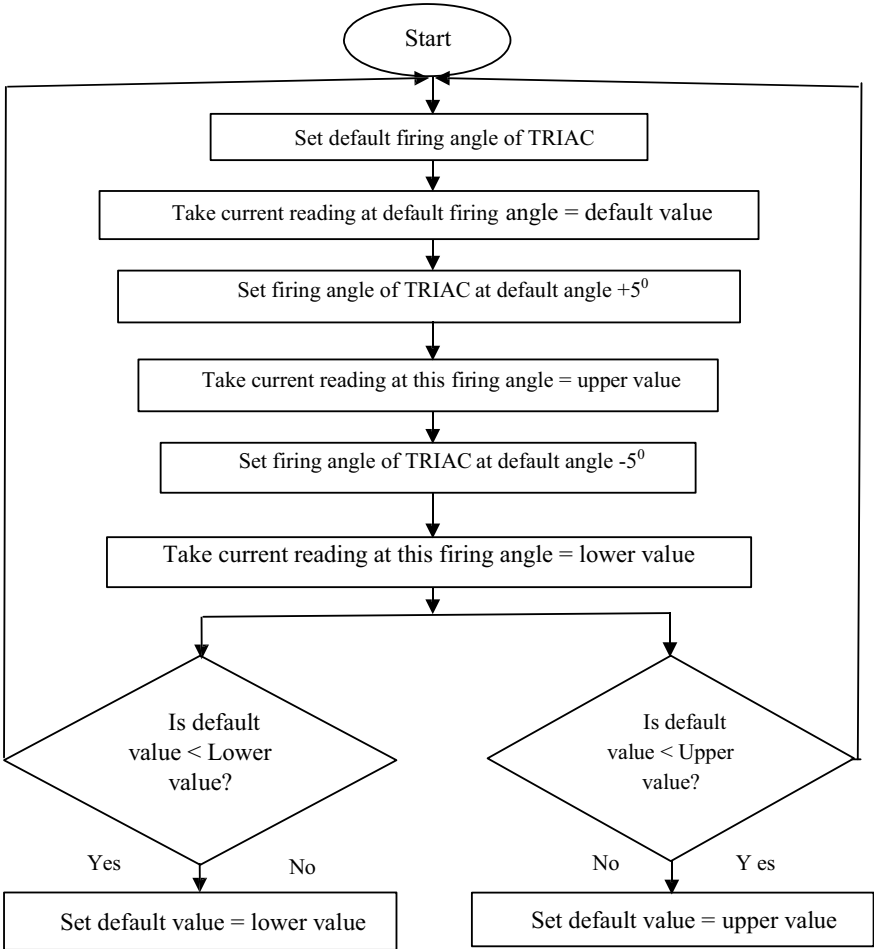


Fig. 5 Flowchart of microcontroller program

4 Experimental Studies

In this project, the main idea is to control firing angle of the TRIAC for controlling the current through the capacitor that is connected in series. Several experiments have been done before doing the final experiment. Some of the experiment are discussed as follows.

4.1 Current Controlling Through the Capacitor

The current through the capacitor can be controlled by connecting the capacitor in series with TRIAC. The firing angle of the TRIAC is changed by the control circuit as a result the current through capacitor also changed. Due to the system voltage is constant so that the reactive power of the capacitor is a function of capacitive current. To observe the change of current through static capacitor by TRIAC and control driver a circuit has been made. The result has been shown in Fig. 6. It is observed from the figure that, when the firing angle is increased the current through the capacitor decreased. The relation between firing angle and capacitor current is graphically shown in Fig. 6.

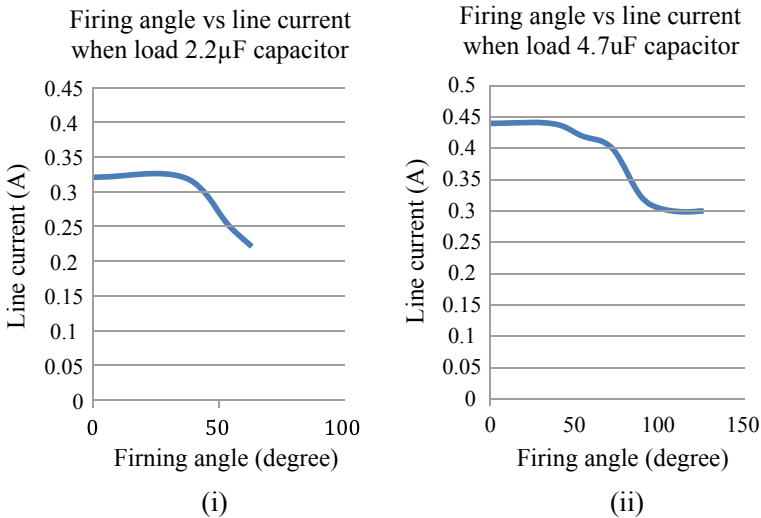


Fig. 6 Firing angle versus load current when the load is capacitors with capacitance (i) 2.2 μF and (ii) 4.7 μF

Table 1 The result of manual power factor correction

Part No	Firing angle adjustment	Voltage (Volt)	Current (A)	Power (Watt)	Power factor
1	Without capacitance	248	0.58	125	0.86
2	Full capacitance	248	0.80	130	0.66
3	Adjusting firing angle	248	0.51	130	~1

4.2 Manual Power Factor Correction

To observe the power factor correction manually by reactive power compensation at various inductive loads, an inductive load table fan of 50 W has been used in this experiment of manual power factor correction. In the case of power factor correction of table fan, the line current increases when no capacitance is connected and full capacitance connected, and the line current is reduced when the firing angle is 450° . There is significant change of line current after adjusting the firing angle as the power factor of the table fan is sufficiently improved. The result of manual power factor correction is given in Table 1.

4.3 Final Experiment and Results

The circuit diagram of this project consists of various types of active elements and passive elements as shown in Fig. 7. The project has an integrated current sensor IC Allegro™ACS712 that offers several advantages over other current sensor solutions. These Allegro sensors are incredibly small and offered a standard automotive-qualified surface-mount packages. There is also a power supply point to power the circuit and operational amplifier to amplify necessary signals. This is also used as a regulating IC (7805, 7812). Voltage sources in a circuit cannot provide fixed voltage outputs because there may be fluctuations. The constant value of output voltage is maintained by a voltage regulator IC. 7805 IC, a member of 78xx series of fixed linear voltage regulators, is used to reduce such fluctuations and it is a popular voltage regulator integrated circuit (IC). A step-down transformer as well as optocoupler is also in the system circuit that performs individual's operations. A TRIAC is also connected along with a capacitive load and with the optocoupler. The MOC3021 comes in an internal light-emitting diode and a TRIAC-based light activating-based transistor. This optocoupler protects high resistive and inductive loads. It can make the current to flow up to 1A. MOC3021 optocoupler work is to keep any kind of current to flow toward the circuit. Several resistors and capacitors are also used in this circuit. All of these are depicted in Fig. 7 as shown.

The results of the proposed model of this power factor improvement technique are shown in Table 2. It is seen from the table that without using capacitor current taken by the system is 1.20 A when voltage is 240 V, power is 185 W, and power factor is 0.65. Then a capacitor is connected with this microcontroller -based system

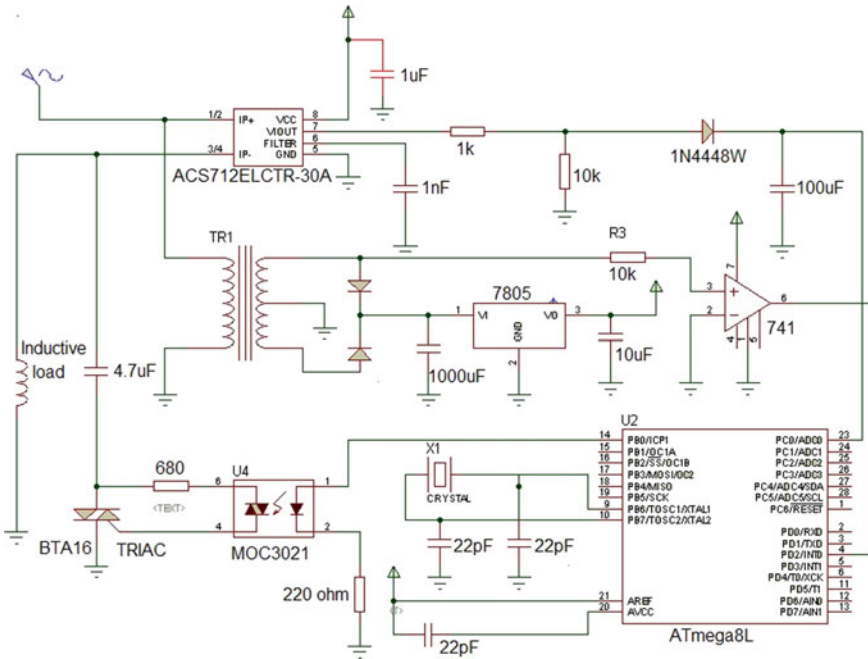


Fig. 7 Circuit diagram of automatic power factor correction unit

Table 2 Wattmeter reading automatic power factor correction when load is in series connection with inductor (1.16 H) and resistor (216 ohms variable)

Part No	Firing angle	Voltage (Volt)	Current (A)	Power (Watt)	Power factor
1	Without capacitance	240	1.20	185	0.65
2	At stable position	240	0.80	190	~1.0
3	Peak current	240	1.80	185	0.67

and while it was adjusting with the system, there was the peak current of 1.8 A, power taken by load was 185 W, and the power factor was near about 0.67. After a while, the attachments reached a stable position and the line current significantly de- creased to the lowest value 0.65 A. Power factor was almost unity in this stable position and power taken by the load was 190 W that means power loss has been decreased also. Thus, the proposed system runs successfully.

5 Conclusion

In the final designed scheme, the power factor correcting capacitor is connected across the inductive load. When the power factor of the load is reduced or more inductive loads are connected to the system then the firing angle of TRIAC is reduced and thus the reactive leading power compensation increases which improved the power factor of load and vice versa. Therefore, the only TRIAC is being used for several values of capacitance. As a result, we don't need several collections of capacitors. An experiment has been performed in the lab, where the line current, the power, and the power factor of the load before connecting the capacitor were 1.20 A, 185 W, and 0.65, respectively, and after the connection of the PFC unit, the line current, the power, and the power factor became 0.80 A, 190 W, and 0.99, respectively. The statistical result shows the schemes improve power factor also considering some negligible power loss. Though there were some minor limitations like slow starting, TRIAC triggering that create oscillation that reduces the lifetime of the system, it is found that this proposed system can get a desirable amount of power factor that is almost near unity. It can be said that if this proposed system is implemented in large aspects, it can bring a revolutionary change in the power factor improvement systems.

References

1. H. Wolfgang, S. Jurgen, J. Wolfgang, *Reactive Power Compensation*. (A John Wiley & Sons Ltd., India, 2012)
2. B.L. Theraja, A.K. Theraja, *A Textbook of Electrical Technology*. (S. Ch and & Company Ltd, India, 1959)
3. V.K. Mehta, M. Rohit, *Principles of Power System* (S. Chand & Company Ltd., India, 2005)
4. S.R. Smruti, Microcontroller based automatic power factor correction in mines. Ph.D. thesis, National institute of technology Rourkela, Odisha, India, 2015
5. B. Satyasuranjeet, M. Sibasis, B. Monalisa, Automatic power factor correction by microcontroller 8051. Ph.D. thesis, National Institute of Technology, Rourkela, 2007
6. S.B. Reetam, M. Satadal, Automatic power factor improvement using microcontroller, in *Proceedings of the 2015 International Conference and Workshop on Computing and Communication (IEMCON)*, C. Satyajit, N.H. Himadri (IEEE Systems, Man, and Cybernetics Society) <https://doi.org/10.1109/IEMCON34776.2015>
7. R.S. Biswas, S. Mal, Automatic Power Factor Improvement by using Microcontroller. *Global J. Res. Eng. Electr. Electron. Eng.* **13**(6) (2015)
8. R.M. Shobha, A.K. Ashwini, M.M. Maithili, V.P. Sadhana, Arduino based power factor correction. *Int. J. Electr. Electron. Data Commun.* **4**(4) ISSN: 2320–2084 (2016)
9. A. Waqas, F. Haroon, U.R. Ata, T. Rana, A. Monib, Automatic power factor correction for single phase domestic loads by means of arduino based TRIAC control of capacitor banks, in *Proceedings of the 2nd International Conference on Energy Conservation and Efficiency (ICECE)* (IEEE, 2018), <https://doi.org/10.1109/ICECE45411.2018>

Testing Topologies to Overcome Fault in Micro-Grid Connected System



Ankur Kumar Gupta, Rishi Kumar Singh, and Shradha Umathe

1 Introduction

In the switchgear portfolio, there are two types of products—powergear and controlgear. Powergear products are located at the upstream level and provide all the necessary protection features in addition to isolation. However, controlgear products are downstream devices used for switching the motors and other operating equipment. Along with that they can also sense fault and provide a tripping mechanism. They are not meant for isolation. The controlgear products can be widely categorized into two types—contactors and relays.

Contactors are devices with very high operating life meant for switching the motors on and off, even at very high frequencies. A relay is a fault-sensing unit, which provides a tripping command to the contactor in the event of any overload, short circuit, single phasing, locked rotor, or ground fault [1-3]. The project undertaken provides an in-depth study of the control gear product—“Relay.” The main aim of this project is “Yield Improvement of Overload Relay.”

The ideology of the project is to improve the existing overload relay (rating: 25A-37A) with design changes in existing mechanism which will improve the accuracy, reliability, and first testing yield of the product. Basically the existing product was verified by performing product tests and by finding various parameters regarding the mechanism and the quality of material used to manufacture the existing product [5-7]. As the power system, resources, and energy saving continue to progress, the demand of reducing their size and improvement of energy efficiency also increases. There is

A. K. Gupta (✉) · R. K. Singh
Maulana Azad National Institute of Technology, Bhopal, Madhya Pradesh, India

A. K. Gupta · S. Umathe
Department of Electrical Engineering, G. H. Raisoni College of Engineering, Nagpur, India
e-mail: shradha.umathe@raisoni.net

also a high demand of reducing the size and improvement of power consumption of thermal overload relays, which increases the competition between the industries.

Microcontrollers and electronic-based overload relays use comparators to compare the flowing current to a predetermined value, when the current value increases the predetermined value, the relay asserts an auxiliary output which opens the protected circuit, and thus the relay gets tripped protecting the circuit.

Relays are also installed in huge amount in railway signaling, since railway signal circuits must be highly protected electrically and there comes the need of installing relays. Railway signaling relays protect the system from false feeds, double switching contacts, and also used so that no false feed can cause a false signal [8]. MN-type thermal overload relays are specially manufactured for MNX-type contactors, and they work on the same principle as thermal overload relay. MN relays are also available in three frame sizes from 0.2A to 570A; they are directly mounted on MNX contactors and are modified for ambient temperature compensation.

2 Thermal Overload Relay (RTO Relay) and Its Classification

A relay can be defined as a switch; switches are generally used to close or open the circuit manually, and a relay is also a switch that uses electric signals to connect or disconnect two circuits instead of manual operation, which in turn connects or disconnects other circuits [9].

Thermal overload relay is an inverse time-delay overload relay which for its operation depends on a bimetal for producing differential thermal expansion due to the current flow thereby tripping a lever. Thermal overload relays are economic electromechanical protection devices for the main circuit. L&T's thermal overload relays are manufactured mainly to complete the MO series of contactors.

3 Main Benefits

- a. Isolated alarm circuit contact.
- b. Ambient to temperature.
- c. Optimized match to MO contactors.
- d. Mounting kit is available separately.

4 Main Features

- a. Tripped/non-tripped indication from front.
- b. Sensitive to phase failure.

- c. Auto/manual functions at front.
- d. Easy access to START and STOP/ RESET buttons.
- e. Sealable transparent top cover.
- f. Easy to mount on MO contactors.

5 Principle of Operation

Above figure shows the circuit diagram of overload relay, various components are as follows:

- A = Heated bimetal strips.
- B = Trip slide.
- C = Trip lever.
- D = Contact lever.
- E = RepARATION bimetal strip.

The bimetal strips (heater) might be warmed legitimately or in a roundabout way. In the primary case, current directly flows through heater and in the second case current courses through a protection warming the heater. The protecting material causes some deferral of the heat stream so the inactivity of heat transfers that are heated is more noteworthy than with their privilege warmed partners.

The cooling time consistent of warm transfers is no longer than that of typical engines. This also prompts an expanding distinction between the real temperature and that reproduced by the warm hand-off in discontinuous technique.

6 Construction of Thermal Overload Relay

The construction of thermal overload relay is quite simple. Three bimetals are mounted on the housing of the relay. The three terminals of bimetal (heater element) act as an input for the relay. The three bimetal strips are assigned as R-pole terminal, Y-pole terminal, and B-pole terminal whose distance from the vertical wall of relay must be ideally 4 mm, 3 mm, and 3 mm, respectively. Two metals are attached on the bimetal strips, namely, metal A having low coefficient of expansion and metal B having high coefficient of expansion. Also one heating strip or wire is wound on every bimetallic strip. One end of the bimetal strips acts as an input and the other end acts as an output which goes to any contactor or motor.

On the bimetal strips a tripping lever is attached with a mechanism which is located exactly above the bimetal strips. This lever can move freely which is then attached to the tripping mechanism. This mechanism as a whole acts as a main tripping mechanism of thermal overload relay.

The front part of the relay has one START (green) and one STOP/RESET (red) button and along with that it has one knob (blue) for changing the range from maximum to minimum and also one knob which is for the setting of AUTO and MANUAL (yellow) mode. It also has one knob which can lock and unlock the STOP/RESET button.

7 Working of Thermal Overload Relay

When a relay is connected with a contactor of specified range and if the current is passed through it in the range of relay then the current will flow from relay to contactor without any disturbance but if an over current flows through the heating coil of relay, it heats up the bimetallic strips.

If the current flow in the circuit exceeds the specified range of relay, heat is generated in the coil, thus both the metals start to expand due to the heat generated by the coil. But metal B expands more than that of metal A. Thus, the bimetallic strip bends toward metal A because of this dissimilar expansion. This bending of bimetal will cause the tripping lever to displace from its position and it will apply force on the above tripping mechanism [11-13]. Thus, the tripping mechanism will trip the relay which will disconnect the circuit and the current will stop flowing. Thus, the contactor will be protected from getting damaged due to over current flow.

8 Contactor and Its Classification

A contactor is an exchanging device having just one situation very still and when worked, it is fit for making, conveying, and breaking electric flow under ordinary circuit conditions remembering working for over-burden conditions. Contactors are employed in control and power circuits, with load currents on the main contacts varying from a fraction of an ampere to hundreds of amperes, depending on the particular application.

Although the construction of a contactor is similar to that of a circuit breaker, its action is the exact opposite. A circuit breaker usually employs an electromagnet for its opening when a fault occurs, whereas a contactor employs an electromagnet for opening or closing a circuit under normal operating conditions. However, a contactor can withstand short-circuit conditions when used with a suitable S.C.P.D (short-circuit protective device).

9 Main Benefits

- a. Motor starters (direct online starter and star-delta starter).
- b. Furnace.
- c. Lighting.
- d. For switching of small resistive loads.
- e. For switching of solid devices.
- f. In domestic applications.

10 Principle of Operation

The electromagnetic contactors take a shot at Faraday's first law of electromagnetic enlistment. A current conveying conductor creates an attractive field around it. At whatever point the electromagnetic loop is invigorated, an electromagnetic field is delivered. This electromagnetic field pulls in the metallic bar (armature) toward the empty barrel-shaped magnet. In contactors with split electromagnets, the mobile half piece of the electromagnet is pulled in toward the fixed piece of the electromagnet.

11 Working of Contactor

In normal condition when the contactor is connected in an assembly, the bridge is balanced by two return springs keeping the bridge and the contacts at the original position. Initially, at rest, the moving and fixed magnets are apart from each other.

When coil current is switched OFF, the electromagnetic force is reduced to zero and compressed return springs come back to the original position bringing the bridge assembly to the normal position. Thus, the magnets and contacts are separated. This is OFF position of the contactor.

12 Tests Performed on Relays

- a. IS (Indian Standard) test.
- b. Temperature rise test.
- c. Deflection test.

13 Conclusion

While testing the sample of RTO-1 (25A-37A) relay for IS test and deflection test, it was observed that the relay was tripping under 5 min at 1.25In on maximum current setting in IS test, but at minimum current setting it was not tripping in 1.2In as well as in 1.3In.

For this problem, some changes were made in the sample as follows:

- a. The distance between the wall and pip was decreased.
- b. The distance between the wall and pip was increased.
- c. The gap between the lever and wall was reduced by sticking paper in the gap.
- d. The strip-type heater was replaced with the wire-type heater.
- e. The heaters were replaced according to their resistance value.

When the distance between the wall and pip was decreased, 1.05In current is passed through the relay.

When the heaters were replaced some parameters were checked and kept constant like the resistance of the heaters in both strip type and wire type were kept constant. The strip or wire which is wound on the bimetal is made up of copper and has its specific resistance which causes the heating of bimetal resulting in tripping of relay.

Thus, the conclusion was made that the relay with all the parameters remaining same except the relay with strip-type heater will not trip in the rating 25A to 35A unless the heaters are replaced with wire-type heaters.

References

1. Y. Chung, D.-J. Won, S.-Y. Park, S.-Il Moon, J.-K. Park, The DC link energy control method in dynamic voltage restorer system. *Electric. Power Energy Syst.* (25), 525–531 (2003)
2. D.-M. Lee, T. G. Habetler, R. G. Harley, J. Rostron, T. Keister, A voltage sag supporter utilizing a PWM switched autotransformer. *IEEE Power Electronics Specialists Conference, Aachen, Germany*, pp. 4244–4250 (2004)
3. A. K. Ramasamy, R. K. Iyer, R.N. Mukerjee, V. K. Ramachandramurthy, Dynamic voltage restorer for voltage sag compensation. *IEEE PEDS*, pp. 1289–1293 (2005)
4. C. Fitzer, M. Barnes, P. Green, Voltage sag detection technique for a dynamic voltage restorer. *IEEE Trans. Industry Appl.* 40(1), 203–212 (2004)
5. P. Daehler, R. Affolter, Requirements and solutions for dynamic voltage restorer, a case study (the summary of the presentation for the panel session “Method for voltage sag mitigation”) *Power Winter Meeting, Singapore, January 23–27, 2000*
6. D. Mahimda Vilathgamuwa, H. M. Wijekoon, Control and analysis of a new dynamic voltage restorer circuit topology for mitigation long duration voltage sags. *IEEE Trans. Power Electron.* 1105–1112 (2002)
7. P.T. Nguyen, T. K. Saha, Dynamic voltage restorer against balanced and unbalanced voltage sags: modelling and simulation. *IEEE Trans. Power Deliv.* 1–6 (2004)
8. X. Xingning, X. Yonghai, L. Lianguang, Simulation and analysis of voltage sag mitigation using active series voltage injection. *IEEE Trans. Power Electron.* 1317–1322 (2000)
9. L. Ahou, K. M. Smedley, *Unified Constant Frequency Integration Control of Active Power Filters* (IEEE, pp. 406–412, 2000)

10. D. Hongfa, G. J. Xianzhong, *New Concepts of Dynamic Voltage Restoration for Three Phase Distribution Systems* (IEEE, pp. 1427–1432, 2000)
11. N. Mohan, T. M. Undeland, W. P. Robbins, *Power Electronics—Converters, Applications and Design. Switch Mode DC–AC Inverters* (Wiley, pp. 200–248, 2003)
12. A. K. Gupta, A. Gupta, A novel design of smart train. In: 2018 International Conference on Smart Electric Drives and Power System (ICSEDPS), Nagpur, pp. 69–74 (2018). <https://doi.org/10.1109/ICSEDPS.2018.8536053>
13. A. K. Gupta, P. Gupta, A novel control scheme for single and three phase dynamic voltage restorer using PSCAD/EMTDC. In: 2018 International Conference on Smart Electric Drives and Ower System (ICSEDPS), Nagpur, pp. 44–49 (2018). <https://doi.org/10.1109/ICSEDPS.2018.8536000>

Improving Reactive Power Compensation by Using Hybrid-STATCOM



Ramchandra Adware and V. K. Chandrakar

1 Introduction

It has long been known that it is possible to increase the steady-state power flow and control of voltage profile over a wide range by using a shunt compensating device. The reactive compensation is aimed to enhance the transmission lines' fundamental electrical parameters to make them more compliant with the prevailing demand for loads. In order to suppress line overvoltage during light load, shunt compensator with fixed and switched mechanical reactors whereas, for higher load conditions, shunt compensator with switched mechanical condensers are used. This paper is focused on some specific power quality issues to improve transmission capability by improving reactive power compensation and providing a basis for compensation and control strategies based on power electronics and obtaining specific compensation objectives. In a transmission system, the ultimate purpose of applying reactive shunt compensation is to increase the transmittable power. In order to improve the steady-state transmission characteristics as well as the reliability of the system, this may be necessary. In order to improve transient stability and the damp power system oscillations, Var compensation is, thus, used for voltage regulations, as well as for dynamic voltage control.

If we look at the Indian situation, an order of approximately EUR 78 million has been released by the Power Grid Corporation of India (PGCIL). Supply of planning and engineering facilities, as well as construction and installation of equipment in four substations at Indian Energy suppliers. In the Indian states of Bihar, Jharkhand and Odisha, Ranchi, Raurkela, Kishenganj and Jeypore substations are located:

R. Adware (✉) · V. K. Chandrakar
Department of Electrical Engineering, G. H. Raisoni College of Engineering, Nagpur, India
e-mail: ramchandra.adware@raisoni.net

V. K. Chandrakar
e-mail: vinod.chandrakar@raisoni.net

Table 1 Characteristics of different compensators for transmission system

Compensator	Response time	Resonance problem	DC-link voltage	Compensation range	Cost
SVCs	Slow	Yes	–	Wide	Low
STATCOMs	Very Fast	No	High	Wide	High
C-STATCOMs	Fast	No	Low	Narrow	Low
PPF STATCOMs	Fast	Yes	High	Narrow	Medium
SVC/APF	Fast	Yes	High	Wide	High
Hybrid-STATCOM	Fast	No	Low	Wide	Medium

where static compensation systems can help regulate the supply of power in these regions. A subsection of Flexible AC transmission systems (FACTS) is the reactive power compensation technology. The parameters that define the function of the power supply grid and account for the transmission quality can be controlled by these systems. Transmission impedances, currents, voltages and phase angles between the various nodes are included in such parameters.

The compensation for reactive power is split into parallel compensation and serial compensation. Parallel compensation systems, such as those to be used in India, mainly control the contact point voltage and thus promote the safe and efficient operation of the grid. SVCs (Static Var Compensators) were the most traditionally used compensating device or system used, but they suffered from many problems, such as sluggish response, harmonic current injection and resonance problems [1, 2]. In order to overcome these drawbacks and improve compensation efficiency, a combined system of active power filter and a static compensator was further developed [3–8].

But those systems were very complicated and expensive. In order to resolve this, capacitor-coupled static compensator (C-STATCOM) [9] and traction power systems [10–12] have been applied to several series-based systems consisting of different forms of passive power filters. But these devices failed to have low dc-link voltages and had a very limited range of compensations (Table 1).

In order to achieve these above benefits and to boost the operational efficiency of passive power STATCOM, various control strategies have been suggested in the past to capacitive coupled STATCOM and other STATCOMS.

The instantaneous p-q principle is one of the suggested techniques. Negative control of the sequences, zero control of the sequence [7], nonlinear control [13], control method of back propagation (BP) [8], control theory based on Lyapunov [14], instantaneous d-q theory, the theory of instantaneous symmetrical control [15] and the theory of hybrid voltage and current control. A hybrid combination of passive filters was also implemented in [16, 17] considering the reduction of the existing level of the active power filters and STATCOMS.

2 Circuit Configuration of Proposed System

The following circuit configuration is shown in the figure with Hybrid, traditional and Capacitor-coupled STATCOM. This device (STATCOM with TCLC filter) consists of an LC component powered by a thyristor and an active part of an inverter.

The high voltage drop between system voltage and inverter voltage can be generated by the TCLC component here from Hybrid-STATCOM. This enables the system's active inverter part to work at the voltage level at the DC bus. Due to the above reasons, the system can gain a very wide compensation for reactive power. A low-rated inverter is taken as a system part because a small rating filter enhances the output of the TCLC component by absorbing unwanted frequency signals of current produced by the TCLC. As a consequence, the mistuning of the firing angle is also avoided, which further results into the problem of voltage resonance being avoided by the system.

Figure 1 displays the hybrid-STATCOM configuration, and this is the circuit where L_s is the impedance of the transmission line and the x means the respective phase of the system, e.g. phase a, b and c.

The voltage V_{sx} stands for system voltage or source voltage at the respective phase and V_x means the voltage at the load with respect to phases. i_{sx} , i_{Lx} and i_{cx} are the currents of source, load and compensating current.

Hybrid-STATCOM has two parts one is a low rating inverter and another one is thyristor-controlled LC filter. First one is responsible for the tuning of the TCLC part to reduce harmonic currents whereas the second part is responsible for the reactive power compensation by tuning the firing angle of the thyristor.

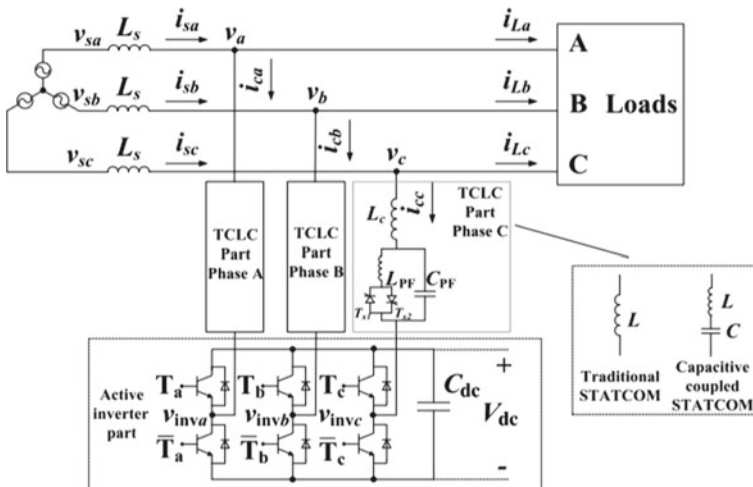


Fig. 1 3-phase system with STATCOM circuits

The low rating inverter component consists of a voltage source converter with a dc-link capacitor, and the active inverter part with a small rating is used to increase the output of the LC component operated by the thyristor.

3 V-I Characteristics

The V-I characteristics of the different types of STATCOM are observed, compared and discussed on the basis proposed system.

As shown in above Fig. 2, the inverter voltage V_{invx} is the voltage produced by the active inverter part and V_x is the reference coupling voltage. Also, loading currents show from extreme left to extreme right that inductive current is compensated from capacitive loading to inductive loading under various conditions. In conventional or traditional STATCOM, the inverter voltage required for the compensation is very high though it is providing a wide range but it requires high-rated inverter for the smooth Var compensation.

In Fig. 3 V-I characteristics of Coupled capacitor STATCOM have been drawn with respect to loading capability. Also, inverter voltage and coupling voltage are shown where it is seen that a inverter voltage is providing a wide range of magnitude of voltage from very low voltage to high but the inductive current loading capability is very narrow, which means if we go with the wide range of compensation, STATCOM may lose its control and will not able to compensate the required power.

From Fig. 4, the proposed system gives the same amount of reactive power as demanded by the load. This implies that the compensating mechanism can have the same amount of reactive power with the opposite polarity as the load. The summation

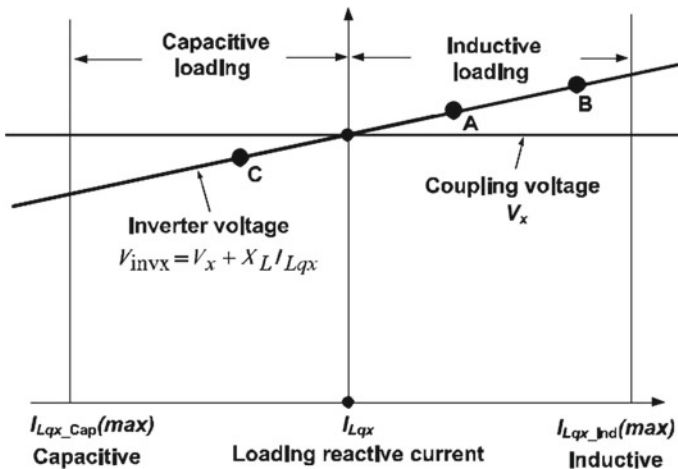


Fig. 2 Conventional STATCOM- V-I characteristics

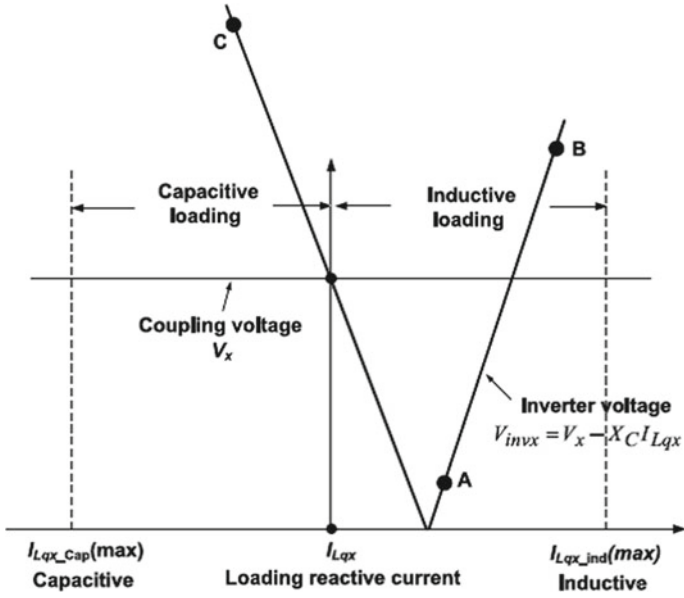


Fig. 3 C-STATCOM V-I characteristics

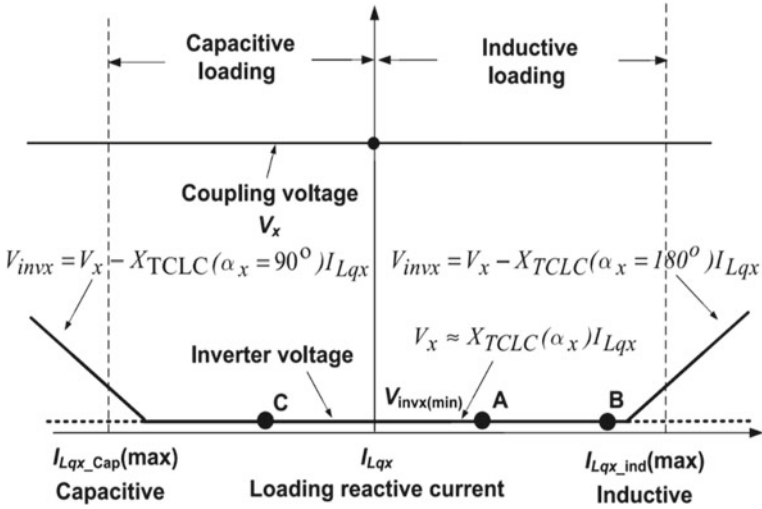


Fig. 4 Hybrid-STATCOM V-I characteristics

of the reactive power of the thyristor control LC filter part and the low-rated inverter component will, therefore, be the reactive power that will be provided.

It can be expressed as follows.

$$Q_{Lx} = -Q_{cx} = -(Q_{TCLC} + Q_{invx}) \tag{1}$$

In the above expression, QLx is inductive reactive power, Qcx capacitive reactive power, QTCLC is reactive power of TCLC part of the system and Qinvx is reactive power of the inverter. If the above expression (1) is expressed in voltage, then it will be as follows.

$$Q_{Lx} = V_x I_{Lq_x} = -X_{TCLC}(\alpha_x) I_{cq_x}^2 + V_{invx} I_{cq_x} \tag{2}$$

where $X_{TCLC(\alpha_x)}$ is the impedance and α_x is the respective firing angle. V_x and V_{invx} are the coupling point and inverter voltages root mean squared values. I_{Lq_x} and I_{cq_x} are the load RMS and reactive currents compensating value, where $I_{Lq_x} = -I_{cq_x}$. Therefore, (2) can be simplified further as.

$$V_{invx} = V_x + X_{TCLC}(\alpha_x) I_{Lq_x} \tag{3}$$

Thus, from the above expression, the impedance of TCLC will be as follows:

$$\begin{aligned} X_{TCLC}(\alpha_x) &= (X_{TCR}(\alpha_x) X_{CPF}) / (X_{CPF} - X_{TCR}(\alpha_x)) + X_{Lc} \\ &= [(\pi X_{LPF} \cdot X_{CPF}) / (X_{CPF}(2\pi - 2\alpha_x + \sin 2\alpha_x) - \pi X_{LPF})] + X_{Lc} \end{aligned} \tag{4}$$

On the basis of the circuit and above equations, the minimum inductance and capacitance of the system can be expressed as follows:

At $(\alpha_x = 90^\circ)$,

$$X_{Ind (min)} = [X_{LPF} X_{CPF} / (X_{CPF} - X_{LPF})] + X_{Lc} \tag{5}$$

Similarly.

At $(\alpha_x = 180^\circ)$.

$$X_{Cap(min)(\alpha_x = 180^\circ)} = -X_{CPF} + X_{Lc} \tag{6}$$

As shown in Fig. 4, the proposed system help to maintain minimum voltage at the inverter terminal and ensure maximum inductive and capacitive reactive current compensation.

If the reactive current required is more than the thyristor-controlled LC part, then the inverter part will increase its voltage marginally to compensate for the power. Thus, it is concluded that this proposed system can provide a wide range of compensation with low inverter voltage as shown in Fig. 4.

4 Control Scheme for the Proposed System

The control scheme for the proposed system is implemented by integrating and organizing the control of the active inverter part and the LC part of thyristor control. This is achieved with the intention that both parts of the proposed system balance each other’s performance (Fig. 5).

1. TCLC filter Component: This part of the proposed system is controlled on the basis of instantaneous p-q theory and implemented to improve the system performance in terms of compensation range as well as to reduce harmonics.

$$X(TCLC) = (x)/(I(Lqx)) \tag{7}$$

Therefore, by acquiring the necessary impedance value of TCLC, the necessary value of alpha is obtained by calculation.

2. Low rating inverter component: Its control is based on instantaneous active and reactive current id-iq model for calculating harmonic component. This part helps TCLC to improve the power compensation under various load conditions by decreasing harmonic current and continuously monitoring and compensating ref. current and measured current.

$$\begin{bmatrix} i_{ca}^* \\ i_{cb}^* \\ i_{cc}^* \end{bmatrix} = \sqrt{\frac{2}{3}} \cdot \begin{bmatrix} 1 & 0 \\ -1/2 & \sqrt{3}/2 \\ -1/2 & -\sqrt{3}/2 \end{bmatrix} \cdot \begin{bmatrix} \cos \theta_a & -\sin \theta_a \\ \sin \theta_a & \cos \theta_a \end{bmatrix} \cdot \begin{bmatrix} i_d \\ i_q \end{bmatrix} \tag{8}$$

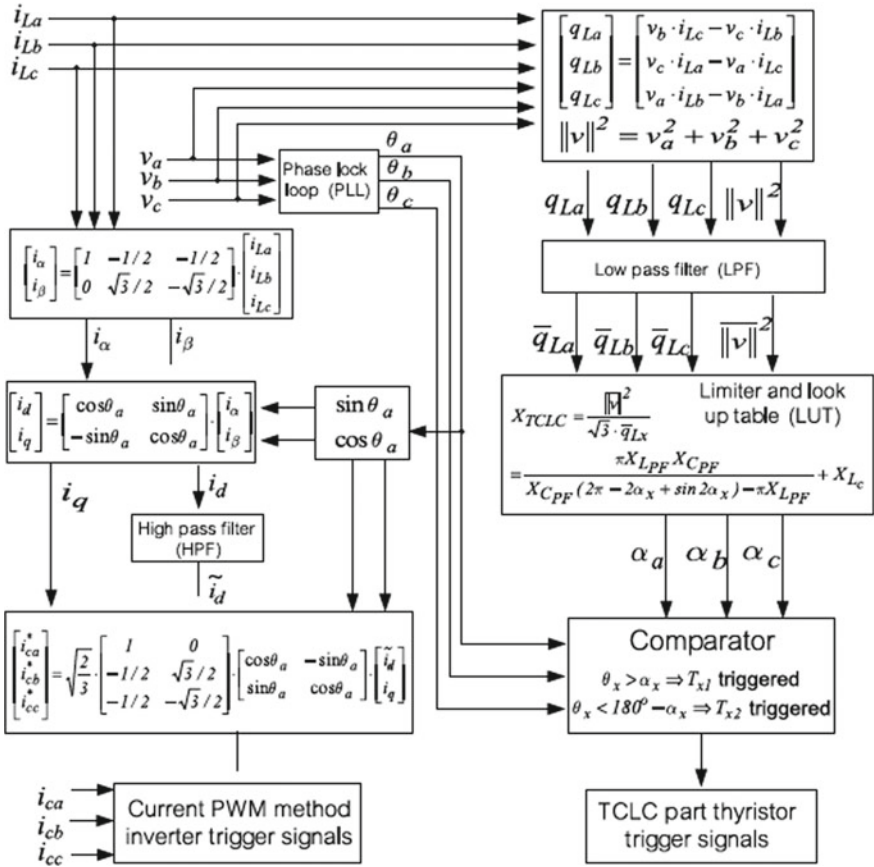


Fig. 5 Control scheme

5 Simulations and Results

In the simulation and results, four different cases are considered for the system simulation. The following table illustrates the different values considered under different situations (Table 2).

5.1 System with Light Inductive Load

In this case, system simulation is done with different types of STATCOM under light inductive load on three-phase source system and static load as shown in Fig. 1. Simulation results are obtained on MATLAB Simulink and interpreted on the basis of Var power compensation with respect to time as shown below.

Table 2 Performance parameters of STATCOM under different conditions

	Parameters	Physical values
System parameters	V_s, f, U	110 V, 50 Hz, 0.1 mH
Traditional STATCOM	L	5 mH
C-STATCOM	L, C	5 mH, 80 uF
Hybrid-STATCOM	L_c, L_{PF}, C_{PF}	5 mH, 30 mH, 160 uF
Case A: inductive and light loading	L_{L1}, R_{L1}	30 mH, 14 Ω
Case B: inductive and heavy loading	L_{L2}, R_{L2}	30 mH, 9 Ω
Case C: capacitive loading	C_u, R_u	200 uF, 20 Ω

There are three results shown in the Simulink results, and it shows reactive power. The upper graph shows load reactive power, the middle one is compensation reactive power and the lower graph shows source reactive power demand (Figs. 6, 7 and 8).

From the above graphs, it is observed that load reactive power demand is 1200 Var, and therefore, the overall compensation reactive power to be delivered by compensating device is -1300 Var and source reactive power is Var. Thus, the percentage of compensation is above 90%. Without compensating device, the source has to deliver about 90% of reactive power.

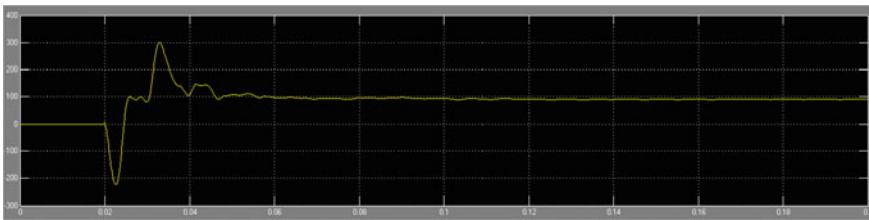


Fig. 6 Source reactive power of the lightly inductive load

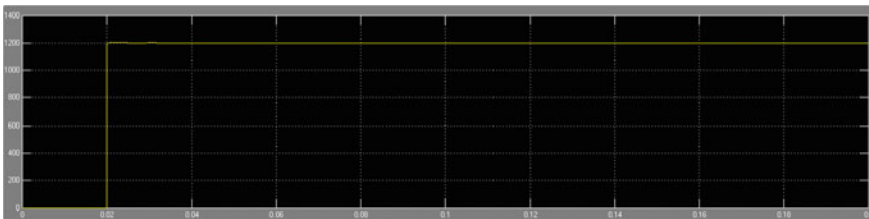


Fig. 7 Load reactive power of the lightly inductive load

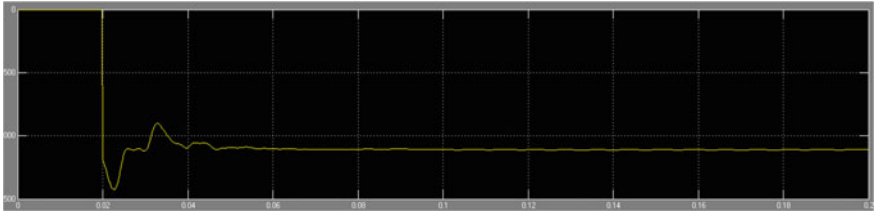


Fig. 8 Compensating reactive power of the lightly inductive load

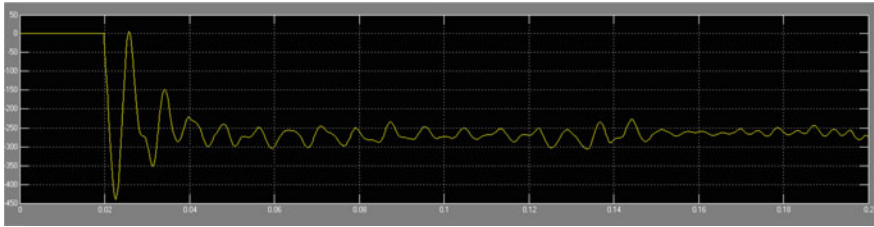


Fig. 9 Source reactive power of the heavily inductive load

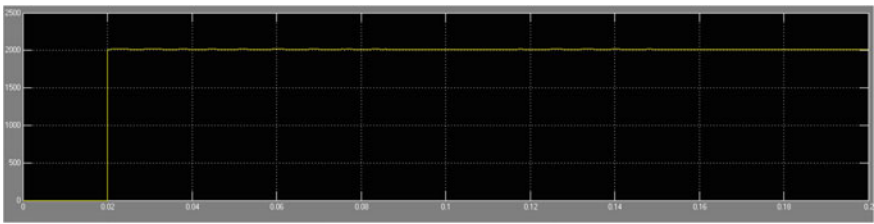


Fig. 10 Load reactive power of the heavily inductive load

5.2 System with High Inductive Load

From the following figures, a System with high inductive load shows reactive power demand of about 2000Var, compensation Var is 2250 and source reactive power 250 Var. Thus source has to bear 250 Var. Thus, the percentage of compensation is above 90% for high inductive load also (Figs. 9, 10 and 11).

5.3 System with Capacitive Load

The following figure shows the Simulink results of a system with hybrid-STATCOM with capacitive load. From the above waveforms, it is observed that load reactive

power is -890 , compensation reactive power is 600 and source reactive power is -290 Var. Thus, the source has to bear -290 extra. Therefore, the percentage of compensation is above 90% (Figs. 12, 13 and 14; Table 3).

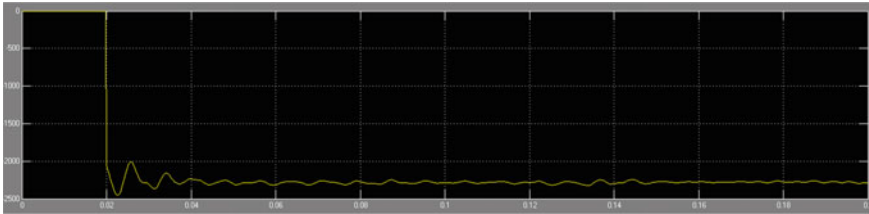


Fig. 11 Compensating reactive power of the heavily inductive load

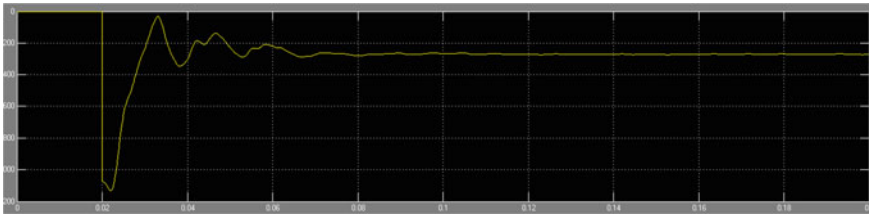


Fig. 12 Source reactive power of the capacitive load

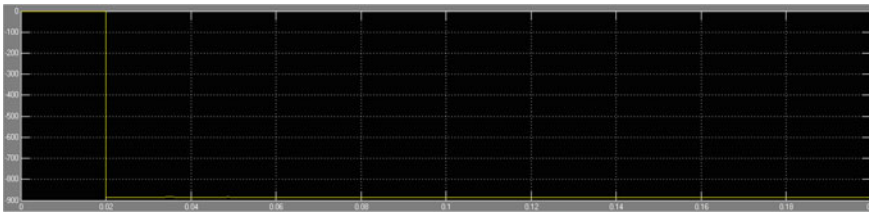


Fig. 13 Load reactive power of the capacitive load

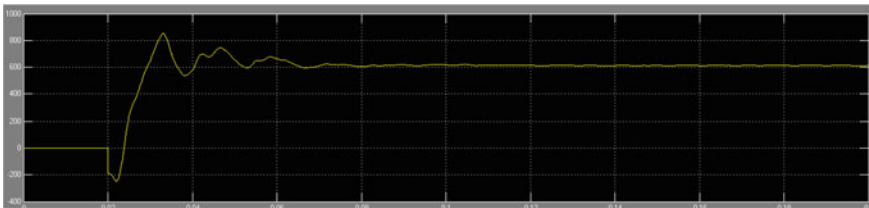


Fig. 14 Compensating reactive power of the capacitive load

Table 3 Simulation results with different types of loading conditions

Type of load	Source reactive power	Load reactive power	Compensator reactive power
Lightly inductive	100	1200	-1300
Heavily inductive	-250	2000	-2250
Capacitive	-270	-890	600

6 Conclusion

A three-phase system with different types of loads has been studied with hybrid-STATCOM and it is found to be low cost and robust in nature due to low dc bus voltage at inverter part and improved power quality and increase range in reactive power compensation with the help of TCLC filter in conjunction with the STATCOM. Performance is analysed on the basis of V-I characteristics and concluded that hybrid-STATCOM is having better performance than the traditional and coupled C-STATCOM. Control techniques are also studied and found that it is complicated than other types of STATCOM as there is a need to control both the components of the proposed system but it has been found that in terms of its performance, it is worth to do simultaneous control over the inverter and TCLC part.

References

1. J. Dixon, L. Moran, J. Rodriguez, R. Domke, Reactive power compensation technologies: State-of-the-art review. *Proc. IEEE* **93**(12), 2144–2164 (2005)
2. L. Gyugyi, R. A. Otto, T. H. Putman, Principles and applications of static thyristor-controlled shunt compensators. *IEEE Trans. Power App. Syst.* **PAS-97**(5), 1935–1945 (1978)
3. T. J. Dionise, Assessing the performance of a static VAR compensator for an electric arc furnace. *IEEE Trans. Ind. Appl.* **50**(3), 1619–1629 (2014)
4. F.Z. Peng, J.S. Lai, Generalized instantaneous reactive power theory for three-phase power systems. *IEEE Trans. Instrum. Meas.* **45**(1), 293–297 (1996)
5. L.K. Haw, M.S. Dahidah, H.A.F. Almurib, A new reactive current reference algorithm for the STATCOM system based on cas-caded multilevel inverters. *IEEE Trans. Power Electron.* **30**(7), 3577–3588 (2015)
6. J.A. Munoz, J.R. Espinoza, C.R. Baier, L.A. Moran, J.I. Guzman, V.M. Cardenas, Decoupled and modular harmonic compensation for multilevel STATCOMs. *IEEE Trans. Ind. Electron.* **61**(6), 2743–2753 (2014)
7. V. Soares, P. Verdelho, An instantaneous active and reactive current component method for active filters. *IEEE Trans. Power Electron.* **15**(4), 660–669 (2000)
8. M. Hagiwara, R. Maeda, H. Akagi, Negative-sequence reactive-power control by a PWM STATCOM based on a modular multilevel cascade converter (MMCC-SDBC). *IEEE Trans. Ind. Appl.* **48**(2), 720–729 (2012)
9. C. Kumar, M. Mishra, An improved hybrid DSATCOM topology to compensate reactive and nonlinear loads. *IEEE Trans. Ind. Electron.* **61**(12), 6517–6527 (2014)
10. J. He, Y.W. Li, F. Blaabjerg, Flexible microgrid power quality enhancement using adaptive hybrid voltage and current controller. *IEEE Trans. Ind. Electron.* **61**(6), 2784–2794 (2014)

11. S. Hu, Z. Zhang, Y. Chen et al., A new integrated hybrid power quality control system for electrical railway. *IEEE Trans. Ind. Electron.* **62**(10), 6222–6232 (2015)
12. M.-C. Wong, C.-S. Lam, N.-Y. Dai, Capacitive-coupling STATCOM and its control. Chinese Patent 200710196710.6, May 2011
13. C.-S. Lam, M.-C. Wong, W.-H. Choi, X.-X. Cui, H.-M. Mei, J.-Z. Liu, Design and performance of an adaptive low-dc-voltage-controlled LC-Hybrid active power filter with a neutral inductor in three-phase four-wire power systems. *IEEE Trans. Ind. Electron.* **61**(6), 2635–2647 (2014)
14. S. Rahmani, A. Hamadi, K. Al-Haddad, A Lyapunov-function-based control for a three-phase shunt hybrid active filter. *IEEE Trans. Ind. Electron.* **59**(3), 1418–1429 (2012)
15. K.-W. Lao, N. Dai, W.-G. Liu, M.-C. Wong, Hybrid power quality compensator with minimum dc operation voltage design for high-speed traction power systems. *IEEE Trans. Power Electron.* **28**(4), 2024–2036 (2013)
16. A. Varschavsky, J. Dixon, M. Rotella, L. Moran, Cascaded nine-level inverter for hybrid-series active power filter, using industrial controller. *IEEE Trans. Ind. Electron.* **57**(8), 2761–2767 (2010)
17. L. Wang, C.-S. Lam, M.-C. Wong, A hybrid-STATCOM with wide compensation range and low DC-link voltage. *IEEE Trans. Indus. Electron.* **63**(6) (2016)
18. B. Singh, S.R. Arya, Back-propagation control algorithm for power quality improvement using DSTATCOM. *IEEE Trans. Ind. Electron.* **61**(3), 1204–1212 (2014)
19. S. Rahmani, A. Hamadi, N. Mendalek, K. Al-Haddad, A new control technique for three-phase shunt hybrid power filter. *IEEE Trans. Ind. Electron.* **56**(8), 2904–2915 (2009)
20. H. Akagi, K. Isozaki, A hybrid active filter for a three-phase 12-pulse diode rectifier used as the front end of a medium-voltage motor drive. *IEEE Trans. Power Electron.* **27**(1), 69–77 (2012)
21. S.P. Litran, P. Salmeron, Reference voltage optimization of a hybrid filter for nonlinear load reference. *IEEE Trans. Ind. Electron.* **61**(6), 2648–2654 (2014)
22. J. Dixon, Y. del Valle, M. Orchard, M. Ortuzar, L. Moran, C. Maffrand, A full compensating system for general loads, based on a combination of thyristor binary compensator, and a PWM-IGBT active power filter. *IEEE Trans. Ind. Electron.* **50**(5), 982–989 (2003)
23. W. Y. Dong, Research on control of comprehensive compensation for traction substations based on the STATCOM technology. Ph.D. dissertation, Tsinghua University, Beijing, China (2009)

Electric Vehicle Technology: Trends and Challenges



Nadeem Akhtar and Vijay Patil

1 Introduction

The popularity of electric vehicles (EV) has steadily increased over the recent years. These vehicles act as an alternate solution in reducing greenhouse gas (GHG) emissions. The GHG emission causes rise in carbon dioxide (CO₂) level, which in turn increases the heating effect and global warming of the earth. Global warming effect such as rise of temperature every year has severe effects on many lives on the earth. There are various reports in this regards which reveals severe impacts of climate change on lives. The man made developments and industrialization that uses the fossil fuel burning have contributed to the rise in pollution of earth. Similarly the exhaust emissions of automotive vehicles are the key contributor to the GHG, which leads to different types of cancers and other serious diseases [1]. EV uses the electric power for running and zero emission; hence, use of EVs on road will reduce the emissions in metro cities of India such Delhi, where cleaner air is much important during November and December months of the year. EVs have many advantages over the internal combustion engine (ICE) based vehicle such as high starting torque at startup as well as at low speed, good acceleration, easy to operate, zero emission during idle condition, and capable of frequent start-stop driving in traffic conditions. The cost of electricity is cheaper than the fossil fuels for same power extraction, and maintenance cost is very less as compared to the ICE based engines.

N. Akhtar (✉) · V. Patil

Department of Electrical Engineering, R. C. Patel Institute of Technology, Shirpur, Maharashtra, India

e-mail: nadeem.riyaz@rcpit.ac.in

V. Patil

e-mail: vijay.patil@rcpit.ac.in

According to author [2], it is estimated that the oil resources will be exhausted by 2038 and transportation industry requires around 49% [1]. EV are an alternative resource over ICE vehicle for reducing the effect of global warming [3]. The different types of EVs are ground vehicle, airborne, electrical powered space craft, and seaborne vehicles. The airborne vehicle is manned as well as unmanned. The ground vehicles can be classified as battery electric vehicle (BEV), hybrid electric vehicle, plug-in hybrid electric vehicle (PHEV), fuel cell electric vehicle (FCEV), Rail borne Electric Vehicles, and Space Rover Vehicles. The BEV is operated by battery-powered electric motors, while HEV and PHEV are driven by ICE alone, assisted by electric motors. FCEV is also powered by electric motors but powered by a stack of fuel cells. The term BEV is abbreviated as EV in subsequent sections. This paper addresses the issues in EV adoption in society based on technical and socio-economics challenges.

2 Technical Issues with EV

EV offers numerous advantages over ICE vehicle, but EV adoption in society faces various challenges. The popularization of EV is mainly affected with numerous technical issues. Technical issues are related with the designing and operating parameters of EV. It directly impacts on the social acceptance of EV in the society.

2.1 Powering Batteries

The powering batteries are major source to EV propulsion system and main contributor to the overall load of the car. The EV driving range and refueling time are mainly dependent on the powering capacity of the battery; hence, battery technology development leads to attain the desired performance of battery life, and its ampere hour rating. The overall EV price is reduced by reducing the battery price which carries an important share in total cost of EV. The different types of batteries available in the market are lead-acid, Ni-Cd, Ni-Zn, Zn/air, Ni-MH, Na/S, Li polymer, and Li-ion batteries. Yong et al. [4] described the advantages, structural model, and applications of graphene based batteries used in EVs. These batteries are selected on the basis of numerous parameters like energy density, the power density, the cycle life, calendar life, and the cost per kWh, safety, energy efficiency, and self-discharge [5]. The battery selection is the tradeoff between the energy, power density, and vehicle range [5]. The relationship between the car range and battery capacity is not linear [5]. According to International Energy Agency (IEA), the battery prices should be under USD 300/kWh. Another important parameter while selecting the battery is cycle and calendar lives. It should not be inferior to the EV life, which ultimately increases the ownership cost of vehicle. It is mainly affected by how battery is used (e.g., rate of discharge, charge, and temperature of operation). The use of battery

management system boosts the battery life by properly utilizing it. The battery life is affected by operating temperature that reduces its life by 20–30%. Slow charging batteries have more life span than the fast charging batteries.

The different batteries used in the EV technology are lead acid, Nickel Metal Hydride battery (Ni-MH), Lithium-ion batteries (Li-Ion), Nickel-Zinc (Ni-Zn), and Nickel–Cadmium (Ni–Cd). The lead (Pb) acid batteries have low specific energy, but cheaper, easily available in market, and its technology mature enough but potential for improvement is very low. It has limited calendar life as compared to others such as Ni-MH battery. It has low energy, low power density, and requires maintenance. The Ni-MH battery is used in hybrid vehicle (Toyota Prius) and cheaper than Li-ion battery. Its energy density is two times the lead acid battery, long calendar life, safe at higher voltage, high specific energy, and long operating temperature range. The energy density is lies 60–80 Wh/kg, hence not suitable for battery operated EVs [6]. It suffers with self-discharge, short life time of 200–300 cycles if discharged with high load currents and memory effects due to reduced reusable power. Figure 1 shows the comparison of batteries with different parameters.

The energy density of Li-ion batteries is two times of Ni-MH as lithium has highest electrochemical potential and low equivalent mass [6]. It has high efficiency, long calendar life, recyclable, and offers improved performance at high temperature. It is more expensive than other batteries and has elongated charging time. The over-charging effect causes the fires and hence raises the safety issues. The other lithium ion batteries include lithium cobalt oxide (LiCoO₂), Lithium Polymer (LiMnO₄), and Lithium ion phosphate (LiFePO₄). The LiFePO₄ is smaller, light weight, and has good thermal stability while suffers with low energy density [8]. LiCoO₂ has high power and energy density, but has safety issue and costly. LiMnO₄ has good thermal stability, high power density, but suffers with moderate calendar life and lower energy. The sodium Nickel Chloride (Na/NiCl₂) battery is considered as safe and low cost battery. Its cost is around one third of Li-ion batteries. It has longer calendar life and

Fig. 1 Power and energy capabilities of battery type [7]

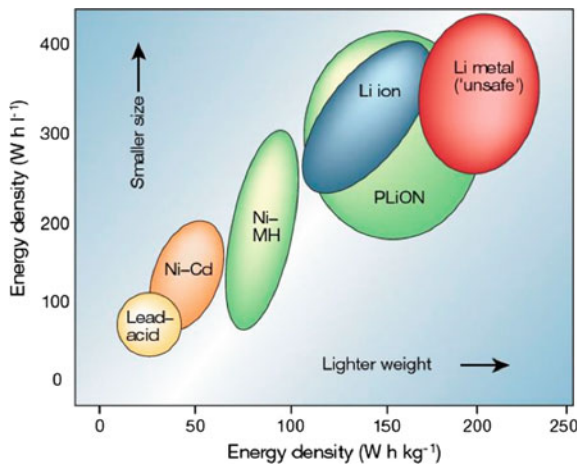


Table 1 Battery comparison [9]

Parameter	Comparison
Price	Pb << Ni << Li ion
Safety	Li << Ni << Pb
Capability	Pb << Ni << Li
Calendar life	Pb << Li = Ni
Refueling time	Li << Ni << Pb
Heaviness	Li << Ni << Pb

discharges completely without degrading its life expectancy. However it suffers with low specific power due to which it is not considered to power battery operated EVs. It is used in association with power sources such as super capacitors [6]. The other batteries Ni-Zn have high power density, ecofriendly but suffers with fast growth of dendrite. Ni-Cd has longer life, recyclable and full discharge that would not damage it. It is costly and can cause pollution if cadmium is not properly disposed. Ni-cadmium batteries have maximum life but suffers with heavy use of cadmium which affects the environment. The battery weight of EV should be light with large storage capacity so that EVs runs larger distance. Table 1 compares the performance of Li-ion, Ni, and lead acid battery on the basis of five parameters.

The refueling of EV is done through the battery recharging that requires the supply conversion. This conversion may lead to harmonics introduction that ultimately degrades the power quality. The poor power quality directly affects charging process and battery life. The battery contains numerous poisonous materials like lead, cadmium, nickel, etc.; hence, its disposal should be permitted under specific regulations. Recycling of the battery is a better option to shrink the life cycle price. Table 4 shows the batteries used by the EV manufacturers with their model names.

Battery Management System (BMS) monitors the battery health and keeps the battery in safe and non-damaging mode. BMS monitors voltage, currents, and temperature of each battery cell and keeps them within the operating range. This leads to a longer calendar, cycle life, improved protection, and increased power capabilities for a relatively small increase in costs.

2.2 Battery Charging and Infrastructure

The refueling of EV batteries is often required for drained battery. The battery refueling takes longer time as compared to the gasoline vehicle. Further each charging (refueling) station is not suitable for EV, due to different capacity and type of battery used. Total number of charging points at refueling center limits and number of EV at a time. This refueling is either conductive or inductive in nature. The conductive charging uses the cable plugged to the electrical grid [12]. This is light, compact, efficient method that allows bi-directional power flows. The inductive charging is

Table 2 Batteries used in EV Models [10]

Battery Technology	EV Model (Company)
Li-ion	Escape PHEV, Ford Focus Electric (Ford), Mini E-2012 (BMW), iMiEV-2010 (Mitsubishi), Audi e-tron (Audi), Leaf EV-2010 (Nissan), Kona (Hyundai), Fiat 500e (Fiat), Zoe, Fluence Z.E (Renault), I-Pace (Jaguar Land Rover), Roadster-2009, Tesla Model X, S, 3 (Tesla) Mercedes-Benz EQC (Mercedes-Benz)
NiMH	Saturn Vue Hybrid (GM) Escape, Fusion, MKZ HEV (Ford) Prius, Lexus (Toyota) Civic, Insight (Honda) Altima (Nissan) X6 (BMW) ML450, S400 (Daimler Benz)
LiFePO ₄	E6 (BYD)
Lithium Polymer Kokam	Micro Vett (Fiat)
Lithium-ion Polymer	Ioniq Electric (Hyundai) Kia e-Soul (Kia Motors)
Nickel-Metal Hydride	RAV4 L V EV (BEA11) (Toyota)
Lithium Nickel Manganese Cobalt Oxide (LiNiMnCoO ₂)	Rimac C Two (Rimac Automobili)

Table 3 SAE AC charging characteristics [11]

AC Charging Scheme	Supply Voltage (V)	Maximum Current (A)	Output Power (kW)
Level 1	120 V, 1-phase	12	1.08
	120 V, 1-phase	16	1.44
Level 2	208 to 240 V, 1-phase	16	3.3
	208 to 240 V, 1-phase	32	6.6
	208 to 240 V, 1-phase	≤ 80	≤ 14.4
Level 3	208/480/600 V	150–400	3

Table 4 SAE DC charging features [11]

DC charging scheme	DC voltage range (V)	Maximum current (A)	Power (kW)
Level 1	200–450	≤80	≤36
Level 2	200–450	≤200	≤90
Level 3	200–600	≤400	≤240

achieved through Constant current (CC), constant voltage (CV), and constant power (CP) method [8]. The faster battery charging process uses combination such as CC/CV. Authors [13, 14] used pulse and negative pulse-charging to achieve faster battery charging. The CC method uses variable voltage, CV uses variable current, and CP uses constant power for battery charging process [14]. These charging methods are preferred in nickel–cadmium and nickel-metal hydride batteries [13].

The combination of CC-CV method is ideal for quick charging of lithium-ion batteries, in two modes. Initially CC is used until it reaches to a predefined voltage, followed by CV until current drops nearly zero value. It prevents over-voltages and thermal stress [8]. The pulse charging method uses current pulses, but precise control of the pulses is crucial. Wireless charging is another name for inductive charging which is more versatile and easier charging process. The wireless connection eliminates the spark issue due to plugging and unplugging. The inductive charging is also possible while driving the EV car. The wireless power is either inductive or capacitive power transfer. AC charging requires the conversion of AC to DC, which needs converter [11]. Table 3 shows different charging levels defined by Society of Automotive Engineers (SAE) for AC charging.

DC charging systems are faster than AC system, which requires dedicated wiring and installations at garages or charging stations. The different levels of DC charging station are shown in Table 4.

Battery charger should monitor the battery chemistry to avoid any harm to it; further it should withstand fast charging conditions during the charging process. The individual charging point at home facilitates the charging in residential areas. A public charging spots should facilitate the EV charging for the residents in urban areas and commercial areas who suffers with private parking space. Schneider electric has developed the RFID based charging points for EV users (Table 5).

The charging time of EV should be optimized by using new technology. The older EV battery requires full night charging. The different models such Mahindra’s model e2o EV hatchback and Hero Electric E Sprint electric scooter charges in 5 h and 8 h [9]. The lead acid battery requires 70% in first 40% charging time while rest period top ups the charging process. The new batteries used EVs charges faster than the old one. A single standardized connector technology at charging station will reduce battery charging time. The charging should not affect the power quality of the system as well

Table 5 Charging time requirement of EV models [15]

Vehicle		Charging time (h) from empty to full				
Model	Battery	3.7 kW	7 kW	22 kW	50 kW	150 kW
Jaguar I-Pace	90 kW	30	13	13	1.5 (0–80%)	0.75 (0–80%)
Tesla Model S	75 kW	21	11	5	2	1
Audi e-tron	95 kW	31	13.5	4	1.5 (0–80%)	0.5 (0–80%)
BMW i3	33 kW	11	4.5	3	0.6 (0–80%)	NA
Nissan LEAF	40 kW	11	6	6	1	NA

Table 6 Power comparison of same size motors [16]

Motor	Power (kW)	Base speed	Maximum speed
IM	93	3000	12,000
SRM	77	2000	12,000
BLDC	110	4000	9,000

as avoid harmonic to be injected. Further the components life of charging station should not be affected by the fluctuations in the output load conditions (Table 6).

Battery swapping at Battery Switching Station (BSS) will achieve the fast battery charging. BSS replaces discharged battery with fully charged battery; hence, EV refueling is as like refueling of gasoline vehicles. This solution confronts another major challenges that opening of high electric energy connection may lead to spark and discharge [17]. The development of such BSS for monitoring and storing the number of batteries requires as additional safety requirements [18]. BSS needs to store each types of battery with rating, which further increases the investment of BSS [19, 20]. According to [21], there are currently about 320,000 publicly accessible charging stations in the worldwide. China has the highest number of fast-chargers that represent one third of all chargers operating worldwide. Table 7 shows the time requirement for numerous EV models from empty battery to full charging at different power levels adopted from [15].

2.3 Electric Motors in EV

The electric motor is most essential component in EV drive system. There are many advantages of electric motors over ICE. Electric motors performance decides the performance of EV in terms of maximum speed, acceleration, and climbing performance. Moreover electric motors can be used as generators in braking mode to recover the electrical energy. Electric motors used for EV must satisfy the basic requirements for effective functioning. These requirement includes high starting torque, low speed during hill climbing; high power density for acceleration and high speed cruising for highway; and high efficiency over wide torque and speed range. It should be suitable for regenerative braking; overload capability during certain period of time; controllability, high reliability and robustness at affordable costs, with good thermal and cooling systems. However, their efficacy fluctuates with torque and speed, being higher at high torque and low speed. The two tests associated with motor are the acceleration and gradeability test.

The acceleration performance of EV is evaluated by the time required to accelerate the vehicle to achieve the desired or high speed from null or low speed. Accelerating the vehicle from null speed tests starting acceleration while low to high speed test passing ability of the vehicle [22]. The gradeability of vehicle is tested by the maximum road grade an automobile can overcome at a specified speed, and the highest speed that the vehicle can reach. The electric motors are acted as propulsion

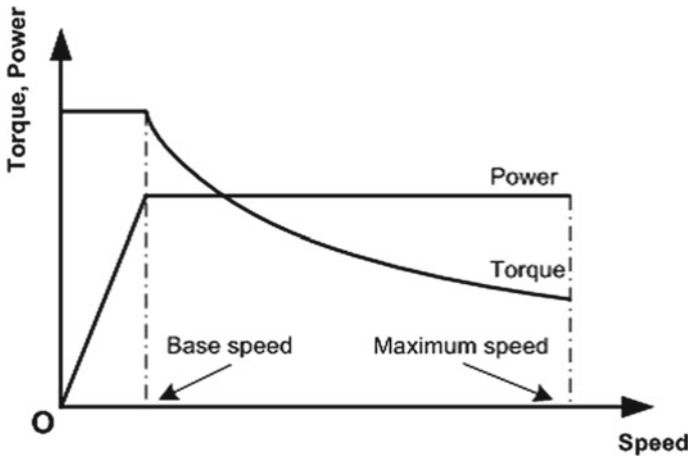


Fig. 2 Output characteristic of motor desired for EV [22]

system in EV; hence, torque speed characteristic of electric motor plays a vital role in EV propulsion system. The desired output characteristics are shown in Fig. 2. From this characteristic, motor drive should be able to deliver high torque at low speed for EV acceleration and high power at high speed of EV. It is also desired that constant power range of the characteristics should be wide.

Figure 3 shows the typical output performance of electric motor in numerous industrial applications. During the normal mode of operation, motor provides the constant rated torque up to base speed. Beyond base speed is the constant power region up to the maximum speed limit. The constant power range depends on the type of motor and employed control scheme employed. The above characteristics

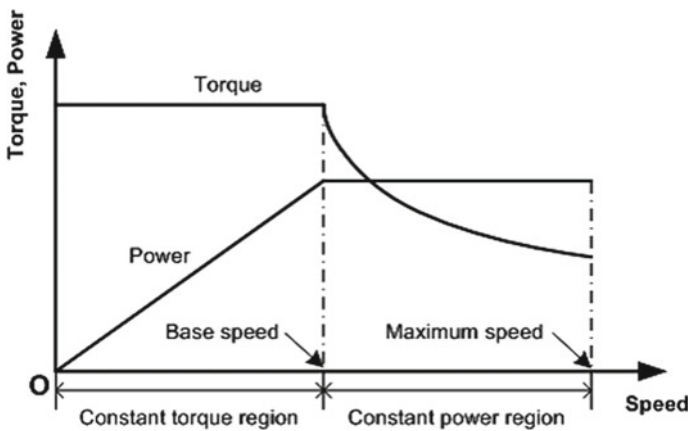


Fig. 3 Typical performances of electric motor drives in industrial [22]

(Fig. 3) shows that for acceleration performance, power requirement declines as constant power region ratio increases. Torque requirement increases with increase in constant power region ratio that results in bulkiness of the motor. The passing time and distance suffers with increase in constant power region ratio. The motor power decreases with maximum speed of the motor. This will decrease the converter power requirement for increasing the constant power range and cost. The low speed motors with stretched constant power speed range and high torque needs added iron and copper to support this higher flux and torque. Motor selection for EV is very important since it directly affects the EV propulsion system. Therefore selecting a motor for EV is a major challenge in EV industry. The motor for EV should have low electromagnetic interface, cost, and weight and should be fault tolerant. The motor should have high instant power, torque for EV starting and climbing, as well as high power during high speed operation. It should have wide speed range over the constant power section of characteristics.

The advancement in power electronics field allows the use of different electric motors such as brushless DC motor, asynchronous motor, permanent magnet synchronous motor, and switched reluctance motor. EVs can have different numbers of motors, depending on their requirements, for example Toyota Prius has one and Acura NSX has three. Author [23] uses two electric motors combined via planetary gear train mechanism. This choice is based on the type of vehicle and its functionality. The DC motors were employed during the initial phase development of EVs. The development in power electronics field promoted the use of different motors. DC motors are the simplest motor considered for EV application, since it is least complicated and inexpensive but suffers with brush deterioration and rotor heat losses, hence not suitable. The other motors reported in EV literature are DC series motor [24], Brushless DC Motor, Permanent Magnet Synchronous Motor (PMSM) [16, 25], Three Phase AC Induction Motors [26], Switched Reluctance Motors (SRM) [27], and synchronous Reluctance Motors [28].

The high torque at low velocity makes the DC brushed motors ideal for the EVs. However brushed DC motor suffers with poor power density. The brushed DC motor are smaller, light weight and has no copper losses. It is more reliable with enhanced heat dissipation capability and has more torque density and specific power. It suffers with short constant power range, decrease in torque with increased speed due back emf generation in stator, and high cost due to permanent magnet. The permanent magnet brushless DC (PMBLDC) motor has greater torque, high-power density, and efficiency. It has zero rotor copper losses [11] due to absence of rotor, wide speed characteristics (see Fig. 4), high efficiency, controllability, and safety. The BLDC commutation uses electronic switches for current supply to the motor winding with the rotor position. Hall sensors, resolvers, or optical encoders are used for detecting the rotor position. The presence of position sensor makes the motor more expensive and raises control issues. Author [29] proposed a sensor less scheme for BLDC motor in which lower speed commutation moments are identified by H functions.

Induction motor (IM) is most commonly used that can operate on alternating current (AC). It is widely preferred for constant-speed applications. The different

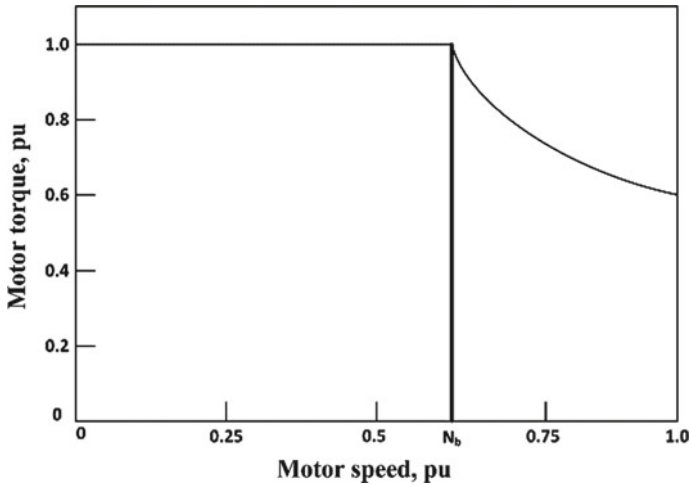
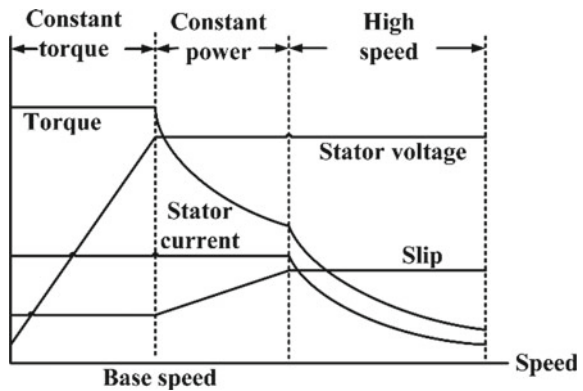


Fig. 4 Permanent Magnet Brushless DC Motor Characteristics [11]

features of IM includes robust construction, excellent peak torque, and low maintenance and makes it most competent candidate for EV propulsion system. It has improved speed limit due to the absence of commutator and brush, hence free from brush friction. This extends the constant power speed range on the characteristic. The speed variation of IM can be achieved by varying the frequency of the excited voltage. The IMs suffers with high copper loss, low efficiency, low power factor, and limited constant power range. IM controllers are costlier than the DC motor. The constant power range of IM can be increased by 2–3 times the base speed, but EV needs 4–5 times more expansion. Figure 5 shows the IM characteristics. Vector control makes the IM drives suitable for EV system’s needs. Author [30] demonstrated minimization in loss at any load condition.

Fig. 5 Induction motor drive characteristics [11]



The switched reluctance motors (SRM) are gaining much popularity for EV application. SRM have advantages such as simple and rugged construction, simple control, fault-tolerant operation, wide constant power range, high power density, and outstanding torque–speed characteristics. The high starting torque, high torque-inertia ratio, and torque-speed characteristics make suitable candidate for gearless operation in EV application. The rotor structure does not have any windings, magnets, commutator, or brushes. The range can be extended up to 2–3 times the base speed using proper control strategy [22]. The SRM are noisy due to variable torque and are less efficient, bulkier than the permanent magnet machines. SRM are affected by the design and control strategy due to slot fringe effect and poles and high saturation of the pole-tips [11]. These drawback limits the advancement in SRM as compared to IM and permanent magnet machines.

Synchronous Reluctance Motor offers the combine advantage of permanent magnet and IM. It is fault tolerant like an IM, effective and small size with similar control strategy of permanent magnet machines. The controllability, manufacturing, and low power factor obstruct its use in EVs [11]. The increase in saliency improves the power factor that can be attained by laminated rotor in axial or transverse direction. The power factor can be improved by integrating the permanent magnet in rotor of Synchronous Reluctance Motor that creates the permanent magnet assisted Synchronous Reluctance Motor [11]. According to [31] Axial Flux Ironless Permanent Magnet Motor is more suitable and advanced one to be used for EV. The absence of stator core and radial field air gap proves better power density. It has the advantages that machines rotors can be mounted on lateral wheel ends, centering the stator windings on the axle. Table 6 shows the power comparison of three motors in terms of power and speed of the motor. Table 7 shows the electric motor used with EV models.

Table 7 Motors in EV models [32]

Motor type	EV model name
Brushed DC motor	Fiat Panda Elettra (Series), Conceptor G-Van (Separately excited), Mazda Bongo (Shunt)
Permanent magnet brushless DC motor	Honda EV Plus, Toyota RAV 4, Toyota Prius (2005), Nissan Altra, Suzuki Senior Tricycle
Permanent magnet synchronous motor	Toyota Prius, Nissan Leaf, Soul EV
Induction motor	Tesla Model S, Tesla Model X, Toyota RAV4, GM EV1, Ford Think City, Fiat Seicento Elettra
Switched reluctance motor	Chloride Luca
PM assisted synchronous reluctance motor	BMW i3
Axial flux ironless permanent magnet motor	Renovo Coupe

3 Social and Economic Issues with EV

This section discusses the numerous issues of social and economics related issues with EV. The issues discussed are EV range, environmental impacts, charging period, safety concerns lack of number of charging station, and EV price.

3.1 *Impact on Environment*

The use of ICE based vehicles burns the fuel and emits the various gases like CO₂. In addition to CO₂ (76%) the other emission includes 2% in carbon mono oxide (CO), 56% in nitrogen oxides (NO_x), and 9% in hydrocarbon (HC) [32] and thus polluting the air. The use of EVs benefits the environment by reducing the emission of air polluting particles in the environment and noise level with zero toxic element. The gasoline powered vehicles emits air polluting elements with noise and have sensible vibration noise. In contrast to this EV is quiet and almost vibration-free. EVs are powered and controlled by environmentally friendly electric motors. The CO₂ emission level of EV is dependent on many factor such as vehicle miles traveled (VMT) and fuel economy. The use of EV will also give rise to the CHG, if EV charging is done through conventional energy sources. This will add extra load on the generating power plant. Further CHG will be increased during the peak hours for EV charging, since the conventional power plant are ICE based which uses either coal or gasses for power generation, and hence rises CO₂ emission. This effects will be minimized if EV charging is integrated properly with renewable energy resources. Thus EVs emissions are null during its life and further charging emission is minimized through the use of renewable energy resources. The country like Denmark reduces the CO₂ emission by 85% from transportation using EVs [11].

EVs use different types of battery such as Li-ion for powering the motors. It will increase the demand for lithium and hence the lithium based batteries. This increased demand of lithium will increase the lithium mining because less than 1% of lithium is recycled today [33, 34]. The non-recyclable lithium has to be properly disposed, since it has harmful effects on environment. The manufacturing of Li-ion batteries causes the pollution at the production sites of these batteries. Thus in future less polluting battery process has to be invented for cleaner environment.

The emission of toxic elements builds the air pollution. The air polluting elements includes CO, sulfur dioxide (SO_x), NO_x, HC, and CO₂ that affects the general human health. The presence of CO₂ in the environment causes the rise in temperature and hence the global warming. The presence of hydrocarbon causes the cancer and could irritate mucous membranes [32]. The presence of NO_x in the environment produces the yellowish-brown haze and becomes a toxic gas that affects the lung tissue if united with oxygen. The presence of carbon mono oxide reduces the blood's ability to transport oxygen that affects the lungs and heart [32]. The presence of SO_x with water vapor may lead to acid rain [32].

Table 8 EV and conventional vehicle cost comparison [28]

EV Model	Model price	Equivalent ICE Model	Model price	Hikes price (%)
Volkswagen e-Golf	₹20,38,694	Volkswagen Golf	₹6,50,000	214
Mitsubishi i-MiEV	₹14,95,261	Chevy Beat	₹5,40,000	177
Fiat 500e	₹22,10,879	Fiat 500	₹10,40,000	113
Tata Nexon EV	₹16,07,000	Tata Nexon	₹7,98,000	101
Tata Tigor EV	₹11,09,000	Tata Tigor	₹7,49,000	48
Mahindra e Verito	₹9,75,000	Mahindra Verito	₹7,65,000	27

3.2 EV Prices

There are various challenges of EVs in India which includes the cost, speed, and its efficiency for mileage. The initial cost of EV is high as compared to conventional fuel vehicle. Table 1 compares the EV and equivalent conventional vehicle cost in India [28]. The higher initial cost of EV limits the number of purchases by the customer and still lack with government subsidies (Table 8).

3.3 Driving Range

In EVs battery is the only source to power the motor; hence, battery is most important component in EV to decide the range. Therefore drivers always suffer from short driving range of EV. It is estimated that the driving range of EV is five times lesser than the conventional vehicles [9]. The EVs on average provide 120 km run for full charge of batteries, hence not suitable for long distance drives. These range depend on numerous factors such as vehicle configurations, road conditions, battery type, battery age, number of passengers, driving condition, driving style, and climate condition. Table 2 shows the range for different EVs. Tesla Model S has highest range in single range among the EVs, while Renault Twizy has lowest range. The Indian EVs offer maximum speed of 85 km/h [35]. The range of EV can be increased by continuing the charging of batteries during EV running condition with solar photovoltaic cells in the form of window glasses of vehicle (Table 9).

EV has several risk factors that include the risk of fire, vehicle safety. EV can easily catch the fire after a crash or mechanical failure. The weight of EV is mainly dependent on the battery weight. The impact of collision time will be severe on light vehicle as compare to the heavy vehicle. The battery location affects the center of gravity, increases the driving stability, and lowers the accident risk. The EV technology adoption to the society will take some time to change certain habits [36]. The EV changes the driver’s style of refueling and driving style habits. Further a better quality EV will win the trust of the peoples for its regular use.

Table 9 Electric vehicle model with range (in km) [10]

EV	Range (Km)	EV	Range (Km)
Tesla Model S	610	BYD e6	300
Tesla Model X	528	Skoda CITIGOe IV	260
Hyundai Kona	470	BMW i3	246
Renault Zoe	400	Fluence Z.E	213
Chevrolet Bolt EV	383	Ford Focus Electric	185
Jaguar I-Pace	350	Fiat 500e	140
Audi e-tron (2018)	328	Renault Twizy	100

The refueling of EV requires longer time as compared to the refueling of conventional ICE vehicle. The performance of short range EVs can be improved by increasing the number of charging stations, fast charging batteries, high density batteries, etc. Refueling time on the charger outline, its infrastructure and operating power level. EV range is maximized by reducing the weight of vehicle, since heavy weight vehicle demands higher energy and hence results in battery draining faster. The light weight like aluminum, plastic, and composites should replace the steel to reduce the vehicle weight. This will further increase the EV price and raise the safety issues.

4 Discussion

The increasing demands of energy day by day is not fulfilled by the natural resources like coal, oil, and natural gas. These resources are finite, and discovery of new energy resources is decreasing day by day. Further the fuel prices for gasoline vehicle is increasing, hence need of an alternative resource for vehicle is urged in global community. The sale of gasoline vehicle is almost doubled in last 25 years that are the main contributors to CHG emission. The CHG emission by gasoline vehicle is also dependent on VMT and fuel economy. The fuel economy is affected vehicle practices and operating conditions. The CHG emission leads to global warming effect on earth planet. The electric vehicle is an alternate solution to gasoline vehicle in order to reduce the temperature rise effect. EVs are battery powered vehicle and require electricity for refueling of battery. The use of renewable energy resources for battery charging will reduce the global warming effect. The electricity prices are much cheaper than the petrol or diesel, since it is generated locally and its price is not changed drastically. The use of EV has many benefits but it faces many challenges

for its implementation in India. The designed EV should be safer in order to win the trust of citizens. EV should be safe against collision, vibrations, shocks and fire, short circuit protection, overcharge protection, over-discharge protection, and over current protection. EV should be tested for above protection test by opening the testing centers for EV users. Advanced technology use for protection will be the probable solution for this issue. The use of better management and battery technology makes the improvement in driving range of EV. The new technology always suffers with servicing and repairing, increasing the number of service station and charging station at cheaper rate is the key solution. The mass production of EVs using advanced technology with government subsidies on the EV purchase will bring down the cost. The batteries are the heart of EV, since the range of EV is mainly dependent on its powering capacity. EV batteries should power EV for longer range with fast charging time. The batteries cost around 35% of total EV cost, hence reducing the battery cost will reduce EV cost. The light weight material should be used for EV manufacturing, since it affects the battery draining. The increased number of charging station suitable for every type of EV will reduce the wait for refueling. For keeping the global temperature under two and gaining larger market share, the stronger government policies will support the transport electrification. The EV uses on Indian road is going to be increased under India's Vision of 2030. NITI AAYOG (India), declared charging points for EVs is mandatory for multi-store apartments. It is declared that public place like shopping malls, residential areas, commercial buildings and offices must reserve the 10% parking space for EV.

5 Conclusion

EVs have great potential to become the future of transportation industry, with less impact on environmental conditions. The use of EV on Indian roads will reduce numerous CHG emission and keep the global temperature growth under two degrees. This deployment will depend on various factors such as EV performance, battery cost, efficiency, development of EV model with cheaper cost, acceptance of EV by society with implied driving behaviors. Standard development for safety and environment will further boost the EV adoption in urban and suburban zones. The increase number of renewable energy integrated charging station and service station will boost the adoption of EV on Indian roads. The success of EV makes it road transporter for the society. The environment education programs will promote the use of EVs among the peoples, further the government policies will enhance the promotion of EV on road and hence helps in reducing the pollution. The EV has to overcome the different technical issues to win the trust of society. The technical issues are long lasting batteries, battery charging, charging infrastructure development, and lack of options for high performance EVs.

Conflicts of Interest The authors declare no conflict of interest.

References

1. N. Ding, K. Prasad, T.T. Lie, The electric vehicle: a review. *Int. J. Electr. Hybrid Veh.* **9**(1), 49–66 (2017)
2. M. Ehsani, Y. Gao, A. Emadi, *Modern electric, hybrid electric and fuel cell vehicles—fundamentals, theory, and design* second edition (2010)
3. G. A. Chandak, A. A. Bhole, A review on regenerative braking in electric vehicle. In *2017 Innovations in Power and Advanced Computing Technologies (i-PACT)* 1–5 (2017)
4. Y. Li, J. Yang, J. Song, Nano energy system model and nanoscale effect of graphene battery in renewable energy electric vehicle. *Renew. Sustain. Energy Rev.* **69**, 652–663 (2017)
5. A. Burke, B. Jungers, C. Yang, J. Ogden, Battery electric vehicles: an assessment of the technology and factors influencing market readiness. *Public Interest Energy Research (PIER) Program California Energy Commission*, 1–24 (2007)
6. A.M. Andwari, A. Pesiridis, S. Rajoo, R. Martinez-Botas, V. Esfahanian, A review of battery electric vehicle technology and readiness levels. *Renew. Sustain. Energy Rev.* **78**, 414–430 (2017)
7. Y. Miao, P. Hynan, A. von Jouanne, A. Yokochi, Current Li-ion battery technologies in electric vehicles and opportunities for advancements. *Energies* **12**(6), 1074 (2019)
8. X. Sun, Z. Li, X. Wang, C. Li, Technology development of electric vehicles: a review. *Energies*, **13**(1), 90 (2020)
9. G. Aswani, V.S. Bhadoria, J. Singh, Electric vehicles In India: opportunities and challenges. In: *2018 International Conference on Automation and Computational Engineering (ICACE)*, 65–71 (2018)
10. https://en.wikipedia.org/wiki/Electric_vehicle
11. F. Un-Noor, S. Padmanaban, L. Mihet-Popa, M.N. Mollah, E. Hossain, A comprehensive study of key electric vehicle (EV) components, technologies, challenges, impacts, and future direction of development. *Energies* **10**(8), 1217 (2017)
12. R.C. Green II., L. Wang, M. Alam, The impact of plug-in hybrid electric vehicles on distribution networks: a review and outlook. *Renew. Sustain. Energy Rev.* **15**(1), 544–553 (2011)
13. I. Rahman, P.M. Vasant, B.S.M. Singh, M. Abdullah-Al-Wadud, N. Adnan, Review of recent trends in optimization techniques for plug-in hybrid, and electric vehicle charging infrastructures. *Renew. Sustain. Energy Rev.* **58**, 1039–1047 (2016)
14. X. Muneret, M. Coux, P. Lenain, Analysis of the partial charge reactions within a standby VRLA battery leading to an understanding of intermittent charging techniques. In *INTELEC. Twenty-Second International Telecommunications Energy Conference (Cat. No. 00CH37131)*, 293–298 (2000)
15. <https://insideevs.com/news/378363/charging-time-electric-car/>. Accessed on 22 March 2020
16. A. Loganayaki, R. Bharani Kumar, Permanent magnet synchronous motor for electric vehicle applications. In: *2019 5th International Conference on Advanced Computing & Communication Systems (ICACCS)* 1064–1069 (2019)
17. J. Yang, H. Sun, Battery swap station location-routing problem with capacitated electric vehicles. *Comput. Oper. Res.* **55**, 217–232 (2015)
18. R. Rao, X. Zhang, J. Xie, L. Ju, Optimizing electric vehicle users' charging behavior in battery swapping mode. *Appl. Energy* **155**, 547–559 (2015)
19. J.D. Adler, P.B. Mirchandani, Online routing and battery reservations for electric vehicles with swappable batteries. *Transp. Res. Part B Methodologic.* **70**, 285–302 (2014)
20. M. Armstrong, C.E.H. Moussa, J. Adnot, A. Galli, P. Rivière, Optimal recharging strategy for battery-switch stations for electric vehicles in France. *Energy Policy* **60**, 569–582 (2013)
21. E. Macioszek, in *Smart and Green Solutions for Transport Systems*, ed. by G. Sierpiński. *Electric vehicles—problems and issues. TSTP 2019. Advances in Intelligent Systems and Computing*, vol 1091 (Springer, Cham, 2020)
22. X.D. Xue, K.W.E. Cheng, N.C. Cheung, Selection of electric motor drives for electric vehicles. In: *2008 Australasian Universities Power Engineering Conference*, 1–6 (2008)

23. M. De Carlo, G. Mantriota, Electric vehicles with two motors combined via planetary gear train. *Mech. Mach. Theory* **148**, 103789 (2020)
24. Z. Bitar, A. Sandouk, S.A. Jabi, Testing the performances of DC series motor used in electric car. *Energy Proc.* **74**, 148–159 (2015)
25. T.A. Huynh, M.F. Hsieh, Performance analysis of permanent magnet motors for electric vehicles (EV) traction considering driving cycles. *Energies* **11**(6), 1385 (2018)
26. Z. Bitar, S.A. Jabi, Studying the performances of induction motor used in electric car. *Energy Proc.* **50**, 342–351 (2014)
27. S. R. Patel, N. Gandhi, N. Chaithanya, B. N. Chaudhari, A. Nirgude, Design and development of Switched Reluctance Motor for electric vehicle application. *International Conference on Power Electronics, Drives and Energy Systems*, 1–6 (2016)
28. Y. Somayaji, N. K. Mutthu, H. Rajan, S. Ampolu, N. Manickam, Challenges of electric vehicles from lab to road. In *2017 IEEE Transportation Electrification Conference (ITEC-India)* 1–5 (2017)
29. S. Sundeeep, B. Singh, Robust position sensor less technique for a PMBLDC motor. *IEEE Trans. Power Electron.* **33**(8), 6936–6945 (2017). <https://doi.org/10.1109/TPEL.2017.2759761>
30. K. Yamada, K. Watanabe, T. Kodama, I. Matsuda, T. Kobayashi, An efficiency maximizing induction motor drive system for transmission less electric vehicle. *Proceedings of 13th International Electric Vehicle Symposium*, 2, 529–536 (1996)
31. C. P. Jose, S. Meikandasivam, in *Innovative Design and Development Practices in Aerospace and Automotive Engineering*. A review on the trends and developments in hybrid electric vehicles, pp. 211–229 (Springer, Singapore, 2017)
32. W.A. Salah, B. Alsayid, M.A.M. Albreem, B.A. Zneid, M. Alkhasawneh, A.A. Mofleh, A.A. Sneineh, A.A.A. Aish, Electric vehicle technology impacts on energy. *Int. J. Power Electron. Drive Syst. (IJPEDS)* **10**(1), 1–9 (2019)
33. R. Vidhi, P. Shrivastava, A review of electric vehicle lifecycle emissions and policy recommendations to increase EV penetration in India. *Energies* **11**(3), 483 (2018)
34. S.H. Mohr, G.M. Mudd, D. Giurco, Lithium resources and production: critical assessment and global projections. *Minerals* **2**(1), 65–84 (2012)
35. M. Mohamed, G. Tamil Arasan, G. Sivakumar, Study on electric vehicles in india opportunities and challenges. *Int. J. Sci. Res. Environ. Sci. Toxicol.* **3**(1), 1–5 (2018)
36. M. Wolsink, The research agenda on social acceptance of distributed generation in smart grids: Renewable as common pool resources. *Renew. Sustain. Energy Rev.* **16**(1), 822–835 (2012)
37. A.M. Lulhe, T.N. Date, A technology review paper for drives used in electrical vehicle (EV) & hybrid electrical vehicles (HEV). In *2015 International Conference on Control, Instrumentation, Communication and Computational Technologies (ICCICCT)*, 632–636 (2015)
38. C. Huang, F. Lei, X. Han, Z. Zhang, Determination of modeling parameters for a brushless DC motor that satisfies the power performance of an electric vehicle. *Meas. Control* **52**(7–8), 765–774 (2019)
39. P. Bhatt, H. Mehar, M. Sahajwani, *Electrical Motors for Electric Vehicle—A Comparative Study*. Available at SSRN 3364887 (2019)
40. A. P. Goncalves, S. M. A. Cruz, F. J. T. E. Ferreira, A. M. S. Mendes, A. T. De Almeida, Synchronous reluctance motor drive for electric vehicles including cross-magnetic saturation. In *2014 IEEE Vehicle Power and Propulsion Conference (VPPC)*, 1–6 (2014)
41. Young, K., Wang, C., & Strunz, K. (2013). Electric vehicle battery technologies. In *Electric vehicle integration into modern power networks* (pp. 15–56). Springer, New York, NY.
42. K. V. Vidyandandan, *Batteries for electric vehicles*
43. J. Larminie, J. Lowry, *Electric Vehicle Technology Explained* (Wiley, 2012)

Solar Micro-Inverter with Phase Shift Power Modulation and Half Wave Cyclo-Converter



Amit L. Nehete, Gururaj Talewad, and Chetan B. Khadse

1 Introduction

The energy is the major and universal measure of all kind of work by human beings and nature. The per capita energy consumption decides the standard of living of a given country. The energy is the part and parcel of the countries' economy. The renewable energy sources have upper hand to the conventional energy sources in the area of availability. The conventional energy sources are going to dry up in further time, and renewable energy sources will be the only option available to human kind [1]. In renewable energy, solar energy is inexhaustible and can be available in abundant. The solar photovoltaic technology (PV) converts solar energy into electricity and fed into a grid or used separately for power lighting, heating, and cooling system devices [2]. DC power produced by the solar cells needs to be converted in AC form or may be required to be used in DC depending on the applications. Power converters in the solar PV system brings the generated power into the suitable form for the end consumer. Thereby, there is a lot of scope or several types of power converters in the solar PV configuration. Power optimizer, string inverter, central inverter and module or micro inverter are some popular types of the converters [3]. Out of which micro converter is recommended to be the best by many researchers. The optimization of the energy harvest, reduced installation cost, improved system reliability, soft switching, and standardized design are some of the benefits of the micro inverter.

The multilevel inverter is implemented for harmonic reduction in solar pv application in [4]. DC microgrid PV architecture using microinverter is proposed in [5]. A quasi z-source matrix microinverter is proposed for grid connected pv applications in [6]. A case study on microinverter used for 2.24 kW pv system is done in [7]. This paper will present a design of micro inverter that can convert from a 25 to 40

A. L. Nehete (✉) · G. Talewad · C. B. Khadse
Dr. Vishwanath Karad MIT World Peace University, Maharashtra, Pune, India
e-mail: amit.nehete@mitwpu.edu.in

V low voltage DC input to single phase 240 V AC at high efficiency. Conceptual design of this topology was developed by A.K. Hayman. However, the proposed work has different focus. Primarily the goal was to design a working model having descent efficiency with less attention on the optimization. Here, in this paper, while designing, the various aspects of exploiting the high efficiency are explored.

2 System Description

The inverter is developed keeping commercial view in front thereby the market largely governs the design goals. Input, output, and operational requirements are given in Table 1, and notations used are given in Table 2. Galvanic isolation between input and output ensures safety standards necessary for commercial inverters.

The focus of control strategy is to reduce the amount of r.m.s currents in the circuit that will reduce the conduction loss. The resonant inverter controls power throughout a line cycle, and cyclo converter acts as a rectifier supplying all of its power to the line.

Due to this, resonant inverter supplies the least excess current thereby, minimum excess energy consumption at the resonant tank.

Table 1 Design specifications

Parameter	Value
Input voltage (minimum)	25 V DC
Input voltage (maximum)	40 V DC
Voltage at the output terminals	Single phase 240 V AC, 50 Hz
Power (average)	0–175 W
Efficiency (%)	96
Power factor	1
Switching frequency	Desirable to be = >50 kHz for size considerations

Table 2 Notations for frequencies and time of interest

Parameter	Symbol	Value
Frequency of switching	f_{SW}	≥ 50 kHz
Frequency of switching angular	ω_{SW}	$2\pi f_{SW}$ rad/s
Period of switching	T_{SW}	$1/f_{SW}$ s
Frequency of line	f_{line}	50 Hz
Frequency of line angular	ω_{line}	$2\pi f_{line}$ rad/s
Period of line	T_{line}	$1/f_{line}$ s
Instantaneous time	T_{line}	S

3 MATLAB Simulation and Results

The controller part of the micro inverter consists of two separate loops. These loops regulate the output power and voltage of the photo voltaic link.

In the current control loop, the output current of the micro inverter is effectively regulated by controlling inverter phase shift φ in the grid connected mode. The grid current i_o and the reference grid current $i_{o,peak}$ determine the permissible working range for value of φ . The required φ value is calculated by phase-shift controller of the ac-ac converter. The output γ of the phase locked loop is used as input for the same (Fig. 1). Use of modulation method or correspond a look up table are the two alternatives that can be followed for developing the phase-shift controller. A look up table method of φ control is used quite often for such circuits. However, in this work, γ is used to adjust φ to calculate the required output current. And the full-bridge phase shift θ controls the Photo Voltaic-link voltage of the inverter.

The proposed micro inverter is simulated with MATLAB/Simulink. The intent while designing the inverter was to achieve high-efficiency of the operation with minimal size for the resonant components as well as improve the performance of power switches with soft switching. Selection of a proper resonant component size that is essential to have switching with reduced noise and less losses throughout operation which becomes difficult due to continuously varying output power. To overcome this, equivalent load resistance of the inverter is calculated by the average power of the inverter.

Q (quality factor) of the series resonant circuit is assumed to be 4. Soft switching of all power switches operation is obtained by considering the ratio of switching frequency to resonant frequency $f 1.1$. φ (phase shift) essential to attain change in power between the load range (from full to zero) is observed to be restricted and not more than 45° . The parameters for the simulation are mentioned in Table 3.

The Resistive load of 175W is connected across output terminals of micro-inverter in simulation circuit. Figure 2 shows simulink input voltage and current waveforms. The Fig. 3 shows the switching pulses for the switches.

Figure 4 shows simulink output voltage and resonant current of bridge inverter. The output waveform of 25 kHz is generated by bridge inverter. Figure 5 shows simulink output current and voltage of high frequency transformer. The high

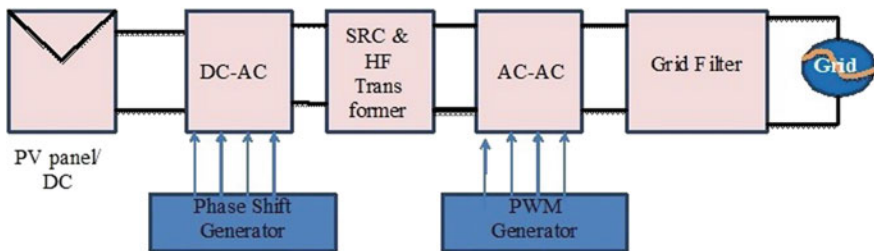


Fig. 1 Structure of micro-inverter

Table 3 Micro-inverter simulation parameters

Parameter	Symbol	Value
Resonant inductor	L_{res}	84.60 μ H
Resonant capacitor	C_{res}	120.9nF
Switching frequency	f_{sw}	>50 kHz
Quality factor	Q	4
Input voltage	V_{in}	25 V
RMS output voltage	V_{out}/N_{line}	240 V
Transformer turns ratio	N	8

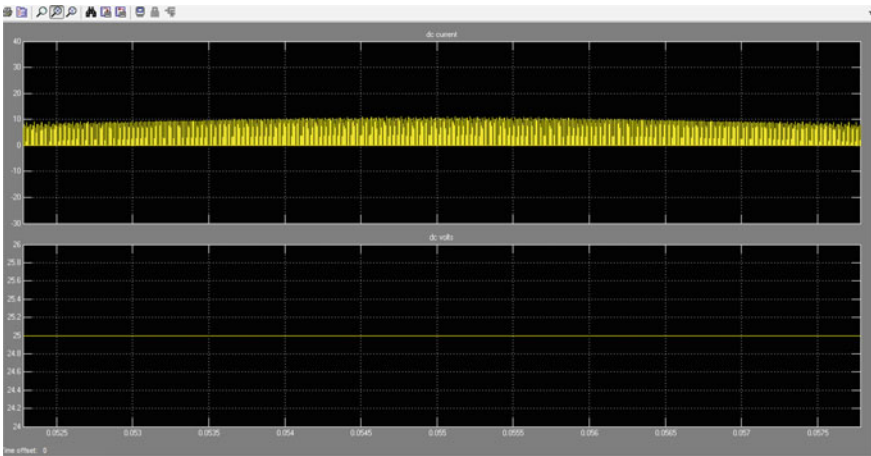


Fig. 2 Input voltage and current



Fig. 3 Switching pulses for switches S1, S2, S3, S4

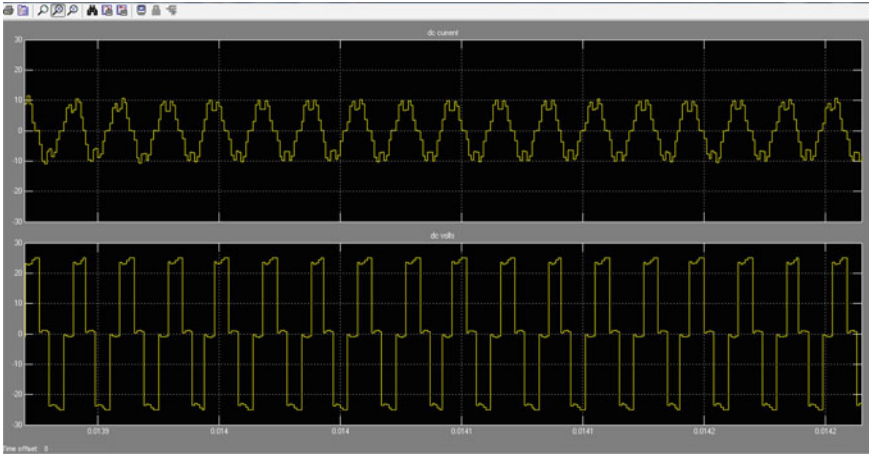


Fig. 4 Bridge inverter output current and voltage

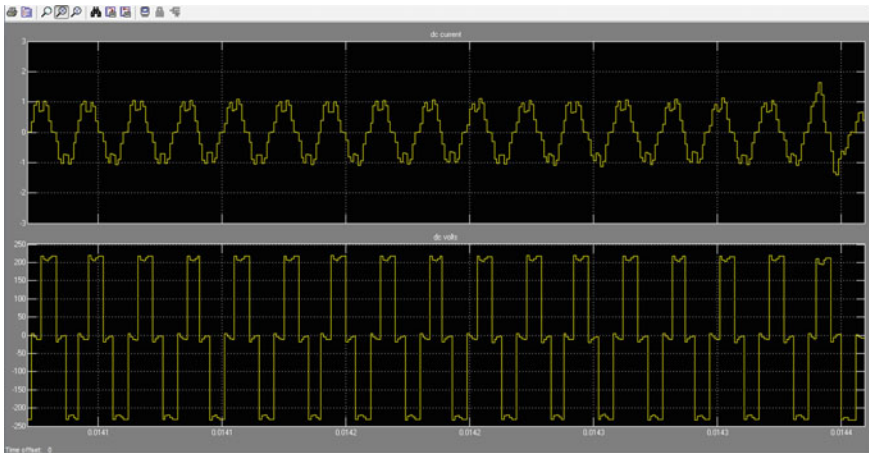


Fig. 5 High frequency transformer output current and voltage

frequency 25 V is stepped up to high frequency 230 V. Figure 6 shows that zero voltage switching takes place at all the power switches as I_{res} (resonant current) is observed lagging to the V_{FB} (voltage full-bridge terminals) and seen leading to the V_{cc} (voltage input terminals of cycloconverter). Waveform shown in Fig. 7 indicates the maximum voltage of grid at negative side. Also, the occurrence of zero voltage switching is observed at all switches of the cycloconverter as in this figure it can be observed that the.

I_{res} (resonant current) is observed lagging to the V_{FB} (voltage full-bridge terminals) and seen leading to the V_{cc} (voltage input terminals of cycloconverter).

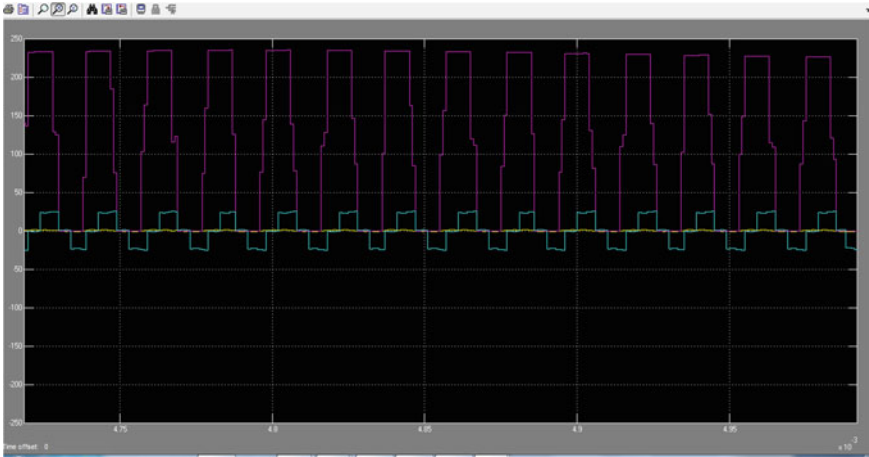


Fig. 6 Simulated I_{res} (resonant current), V_{FB} (voltage at full-bridge terminals) and V_{cc} (voltage at input terminals of cycloconverter) at maximum grid voltage at positive side

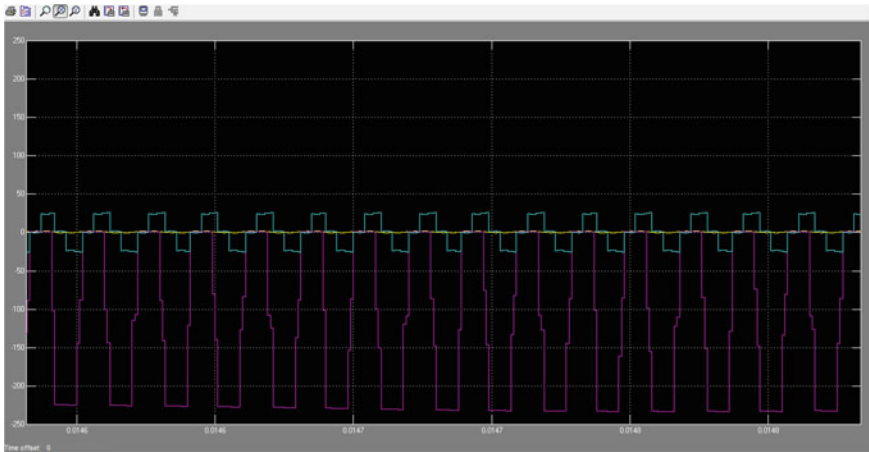


Fig. 7 Simulated I_{res} (resonant current), V_{FB} (voltage at full-bridge terminals) and V_{cc} (voltage at input terminals of cycloconverter) at maximum grid voltage at negative side

Waveform showing voltage of the grid is observed in Fig. 8 which underlines that the simulated configuration of micro inverter along with phase-shift control can be feasibly implemented.

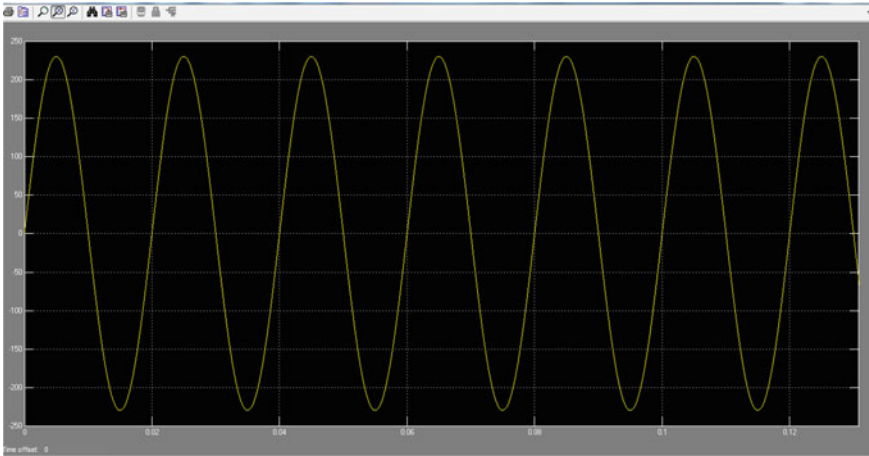


Fig. 8 Output voltage of micro-inverter

4 Conclusions

This work aims the contribution towards development of solar inverters with better efficiencies to enable more and more energy extraction from solar panels. A micro-inverter topology that includes half-wave cyclo-converter and a full-bridge inverter is put forth here. Single power stage of power conversion makes use of lesser number of power switches. Thereby, substantial decrease in losses caused due to switching and conduction is observed. Soft switching at the time of turning the power switches on and off is a feature of the use of series-resonant tank. It implies to minimal losses that occur in switching because of increased frequency of switching. Analysis of soft-switching operation is done by using derived resonant current equation for the three stepped full bridge output voltage and the half-wave cyclo-converter input voltage. Results of the simulation corroborate the design and operation of the proposed inverter.

References

1. R. A. Dunlap, R. Energy, Requirements and sources, vol 1
2. J. Yuan, F. Blaabjerg, Y. Yang, A. Sangwongwanich, Y. Shen, An overview of photovoltaic microinverters: topology, efficiency, and reliability. In: 2019 IEEE 13th International Conference on Compatibility, Power Electronics and Power Engineering, pp. 1–6 (2019)
3. Hossam, A., Gabbar: Microinverter Systems For Energy Conservation In Infrastructures. Energy Conservation in Residential, Commercial, and Industrial Facilities pp. 125–202 (2018)
4. S. A. Yadav, C. B. Khadse, Implementation of multilevel inverter for harmonic reduction in solar PV application. In: 2019 2nd International Conference on Intelligent Computing, Instrumentation and Control Technologies (ICICT), pp. 665–669 (2019)

5. E. Marafante, L. Mackay, T. G. Hailu, G. R. C. Mouli, L. Ramirez-Elizondo, P. Bauer, PV architectures for DC microgrids using buck or boost exclusive microconverters. *IEEE Eindhoven PowerTech*, 1–6 (2015)
6. L. Palma, A quasi Z-source matrix microinverter for grid connected PV applications. In: 2020 International Symposium on Power Electronics, Electrical Drives, Automation and Motion (SPEEDAM), pp. 526–531 (2020)
7. N. A. Matchanov, K. O. Seok, A. A. Mirzaev, M. A. Malikov, D. S. Saidov, Study of energy yield on grid connected micro-inverter type 2.24 kW PV system using PVsyst simulation software. *Appl. Solar Energy* **56**(4), 263–269 (2020). <https://doi.org/10.3103/s0003701x20040076>

Load Flow Analysis of 5 Bus Power System for Three Phase Symmetrical Fault Using MATLAB



Prajakta Vikas Dhole and Sahebrao Narsingrao Patil

1 Introduction

The load flow studies are a very important part of power system analysis. It helps in planning, economic scheduling, and control of an existing power system. In the solution of power flow, the system is assumed to operate under balanced conditions. The system is represented in form of single line diagram. The solution is obtained in terms of the magnitudes and phase angle of voltages at each bus, real, and reactive power flowing through the lines [1].

Power flow calculations are done with the help of various iterative methods such as Gauss-Seidel method, Newton-Raphson method [2, 3], and Fast Decoupled method. The Gauss-Seidel method is the modification of the Gauss-iteration method. This modification reduces the number of iterations. In this method the value of unknown immediately reduces the number of iterations, the calculated value replace the earlier value only at the end of the iteration. Because of it, the Gauss-Seidel methods converge much faster than the Gauss methods. In Gauss Seidel method the number of iterations required to obtain the solution is much less as compared to Gauss method [4].

In this study, power flow analysis is performed for 5-bus system under three phase fault conditions. The results are obtained with the help of MATLAB. Three phase fault is applied at the load bus. Obtained results are compared with normal operating conditions. This gives system behavior under fault conditions [5] and most effective fault point of the system.

P. V. Dhole (✉)

Chhatrapati Shivaji Maharaj University, Navi Mumbai 410206, India

S. N. Patil

Bhivrabai Sawant Institute of Technology and Research, Pune 412207, India

2 Power Flow Analysis

The current at the bus i is given by [4]

$$I_i = V_i \sum_{j=0}^n y_i - \sum_{j=1}^n y_{ij} V_j \quad j \neq i \quad (1)$$

y_{ij} is actual admittance per unit.

The above current, in terms of real and reactive power, is given by

$$\frac{P_i - jQ_i}{V_i^*} = V_i \sum_{j=0}^n y_{ij} - \sum_{j=1}^n y_{ij} V_j \quad j \neq i \quad (2)$$

Equation (2) is solved for V_i by Gauss–Seidel method, and the iterative sequence becomes

$$V_i^{(k+1)} = \frac{\frac{P_i^{sch} - jQ_i^{sch}}{V_i^{*(k)}} + \sum y_{ij} V_j^{(k)}}{\sum y_{ij}} \quad j \neq i \quad (3)$$

P_i^{sch} and Q_i^{sch} are the net real and reactive powers in per unit.

Since for the bus admittance matrix Y_{bus} , off-diagonal elements are $Y_{ij} = -y_{ij}$, Eq. (3) becomes

$$V_i^{(k+1)} = \frac{\frac{P_i^{sch} - jQ_i^{sch}}{V_i^{*(k)}} - \sum_{j \neq i} Y_{ij} V_j^{(k)}}{Y_{ii}} \quad (4)$$

Net real and reactive powers at slack bus are given as below

$$P_i^{(k+1)} = \text{Re} \left\{ V_i^{*(k)} \left[V_i^{(k)} Y_{ii} + \sum_{j=1, j \neq i}^n Y_{ij} V_j^{(k)} \right] \right\} \quad J \neq 1 \quad (5)$$

$$Q_i^{(k+1)} = -\text{Im} \{ V_i^{*(k)} [V_i^{(k)} Y_{ii} + \sum_{j=1, j \neq i}^n Y_{ij} V_j^{(k)}] \} \quad j \neq i \quad (6)$$

3 Power System Under Consideration

Figure 1 shows the one-line diagram of 5-bus power system. The generators are connected to buses 1 and 4. At bus 1 the voltage magnitude is adjusted to 1.06 pu and is taken as slack bus. The system comprises of four load buses, and it has one generator bus. Bus 4 acts as both load and generator bus. Voltage magnitude and real power generation at bus 4 is fixed to 1.047 pu and 45 MW respectively. Line impedances in per unit are marked on a 100 MVA base. The line charging substances are neglected (Fig. 2; Tables 1, 2 and 3).

Fig. 1 A typical bus of the power system

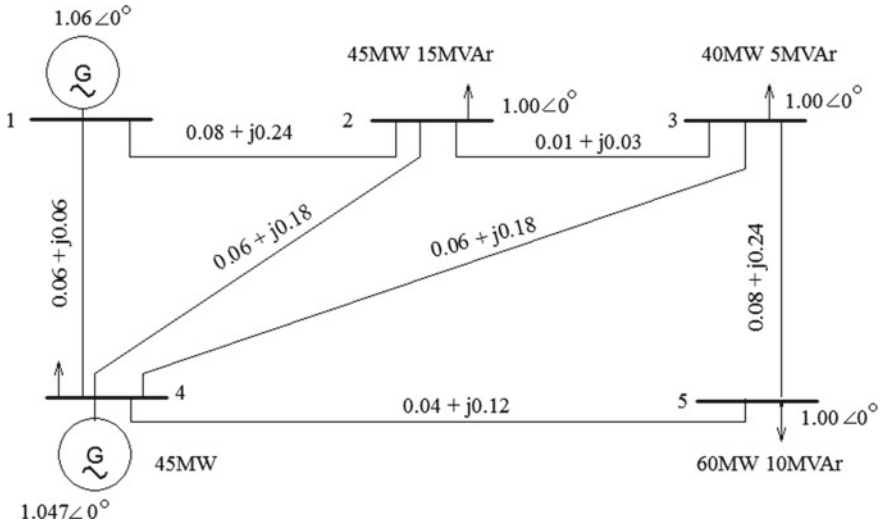
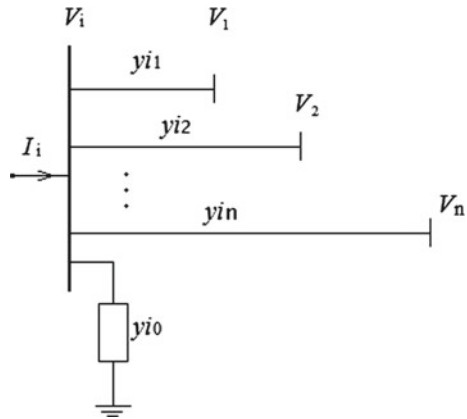


Fig. 2 One line diagram of 5 bus power system

Table 1 Operating conditions of 5 bus system

Bus no	Voltage (pu)	Angle δ (degree)	Generation active power (MW)	Load	
				MW	MVA _r
1	1.06	0	0	0	0
2	1.00	0	0	45	15
3	1.00	0	0	40	5
4	1.047	0	45	0	0
5	1.00	0	0	60	10

Table 2 Line data of power system

Bus-to-bus	Resistance (pu)	Reactance (pu)
1 to 2	0.08	0.24
1 to 4	0.06	0.06
2 to 3	0.01	0.03
2 to 4	0.06	0.18
3 to 4	0.06	0.18
3 to 5	0.08	0.24
4 to 5	0.04	0.12

Table 3 Synchronous Machine data of power system

Bus	Machine subtransient reactance X_d'' (pu)
1	0.2
4	0.15

4 Procedure

- (1) Load flow analysis is carried out for the pre-fault condition on the given five bus power system. Results were obtained using MATLAB. This gives voltage, phase angle, real, and reactive power.
- (2) Fault analysis is done for three phase symmetrical fault at bus no. 5. This results in change of voltage, phase angle, real, and reactive power at the buses.
- (3) Load flow analysis is performed considering the post-fault conditions.

5 Results

5.1 Load Flow Analysis Under Normal Operating Conditions

Maximum Power Mismatch = 0.000837173.

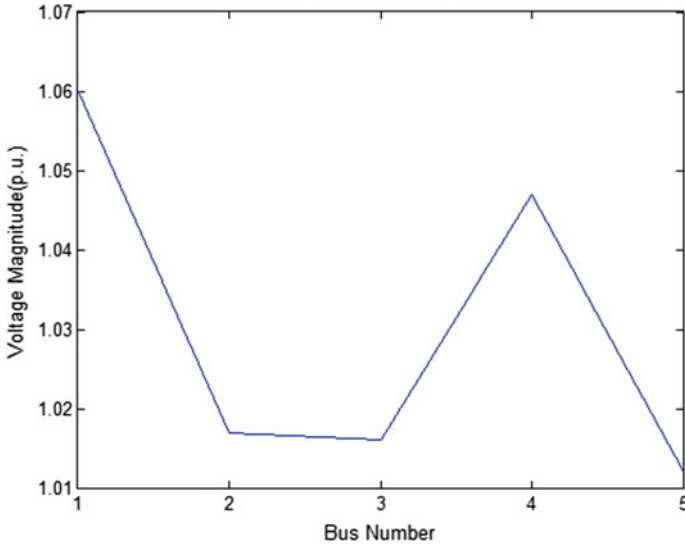


Fig. 3 Voltage magnitude versus bus number for load flow analysis in normal operating conditions

Table 4 Load flow solution under normal operating condition

Bus no	Voltage(pu)	Angle (degrees)	Load		Generation	
			MW	MVAr	MW	MVAr
1	1.060	0.00	0.00	0.00	106.423	-31.312
2	1.017	-5.148	45.00	15.00	0.00	0.00
3	1.016	-5.496	40.00	5.00	0.00	0.00
4	1.047	-3.156	0.00	0.00	45.00	74.834
5	1.012	-6.398	60.00	10.00	0.00	0.00
Total	-	-	145.00	30.00	151.423	43.522

No. of Iterations = 20.

The magnitude of voltages range between 1.06 and 1.012 p.u. The total active and reactive line losses are 6.327 MW and 13.092 MVAr respectively. Total load on system is 145 MW and 30 MVAr respectively. The voltage profile is shown in Fig. 3 (Tables 4 and 5).

5.2 Three Phase Fault at Bus Number Five

Three phase balanced fault at bus no. 5 through a fault impedance of 0.16 Ω.

Total fault current = 3.7941 per unit (Table 6).

Table 5 Line flow and losses

Line		Power at bus and Line flow			Line loss	
From	To	MW	MVA _r	MVA	MW	MVA _r
1	–	106.423	–31.312	110.934	–	–
	2	42.558	6.819	43.101	1.323	3.968
	4	63.786	–38.04	74.268	2.945	2.945
2	–	–45.000	–15.00	47.434	–	–
	1	–41.235	–2.85	41.334	1.323	3.968
	3	19.736	–3.45	20.036	0.039	0.117
	4	–23.556	–9.0	25.217	0.369	1.108
3	–	–40.000	–5.000	40.311	–	–
	2	19.697	3.569	20.018	0.039	0.117
	4	–26.872	–8.254	28.111	0.460	1.379
	5	6.571	–0.506	6.590	0.034	0.101
4	–	45.000	74.834	87.322	–	–
	1	–60.840	40.986	73.358	2.945	2.945
	2	23.925	10.108	25.973	0.369	1.108
	3	27.332	9.633	28.980	0.460	1.379
	5	54.577	13.961	56.334	1.158	3.474
5	–	–60.000	–10.000	60.828	–	–
	3	–6.537	0.607	6.565	0.034	0.101
	4	–53.419	–10.487	54.439	1.158	3.474
Total Loss		–	–	–	6.327	13.092

Table 6 Bus voltages during fault in per unit

Bus no	Voltage magnitude(pu)	Angle
1	0.8550	–15.4301
2	0.7589	–21.0948
3	0.7434	–22.3948
4	0.7847	–18.3262
5	0.6071	–42.8323

5.3 Load Flow Analysis Under Three-Phase Balanced Fault

Maximum Power Mismatch = 0.000878504.

No. of Iterations = 26.

The magnitude of voltages range between 0.86 and 0.734 p.u. The total active and reactive line losses are 12.134 MW and 24.778 MVA_r respectively, which are almost

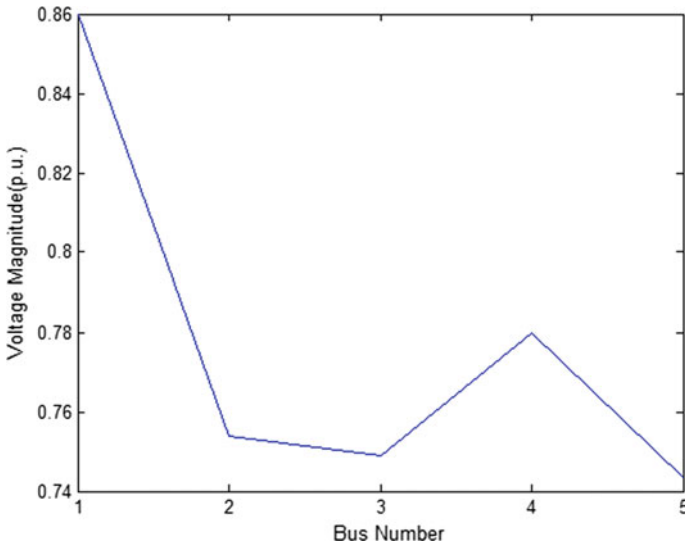


Fig. 4 Voltage magnitude versus bus number for load flow analysis after occurrence of three phase symmetrical fault at bus number 5

Table 7 Load flow solution under three phase fault condition

Bus no	Voltage(pu)	Angle (degrees)	Load		Generation	
			MW	MVAr	MW	MVAr
1	0.860	-15.40	0.00	0.00	112.11	68.141
2	0.754	-21.606	45.00	15.00	0.00	0.00
3	0.749	-22.064	40.00	5.00	0.00	0.00
4	0.780	-17.079	0.00	0.00	-13.344	0.00
5	0.734	-23.295	60.00	10.00	0.00	0.00
Total	-	-	145.00	30.00	157.117	54.797

doubled following the three phase symmetrical fault at bus number 5. The voltage profile is shown in Fig. 4 (Tables 7 and 8).

6 Conclusion

The successful operation of power system requires the monitoring of various parameters like voltage magnitude and angles, real, and reactive power flows and the losses. In this study, load flow analysis is done under normal operating conditions. This gives the line loadings which further changes the voltage magnitudes and angles.

Table 8 Line flow and losses

Line		Power at bus and Line flow			Line loss	
From	To	MW	MVA _r	MVA	MW	MVA _r
1	–	112.117	68.141	131.200	–	–
	2	38.181	26.958	46.739	2.363	7.089
	4	73.947	41.193	84.647	5.813	5.813
2	–	–45.000	–15.00	47.434	–	–
	1	–35.818	–19.869	40.960	2.363	7.089
	3	17.044	5.986	18.065	0.057	0.172
	4	–26.203	–1.274	26.234	0.727	2.181
3	–	–40.000	–5.000	40.311	–	–
	2	–16.987	–5.813	17.954	0.057	0.172
	4	–28.883	–2.027	28.954	0.896	2.689
	5	5.874	2.864	6.535	0.061	0.183
4	–	45.00	–13.344	46.937	–	–
	1	–68.135	–35.380	76.773	5.813	5.813
	2	26.930	3.455	27.150	0.727	2.181
	3	29.779	4.716	30.150	0.896	2.689
	5	56.337	14.080	58.070	2.217	6.651
5	–	–60.00	–10.000	60.828	–	–
	3	–5.813	–2.681	6.402	0.061	0.183
	4	–54.120	–7.429	54.628	2.217	6.651
Total loss		–	–	–	12.134	24.778

These values can be used for further fault study. The bus voltage magnitude and phase angles, line flows, and line losses are computed using MATLAB. Further the effect of fault on power flow analysis is investigated.

Three phase symmetrical fault is placed at bus number five that gives complete system behavior during fault occurrence. The result obtained is used for planning, scheduling, and control of existing system. The losses are almost doubled under the three phase symmetrical fault. To overcome the losses, we can adjust the power output at the slack bus. Also more power can be generated when the losses are quite high.

References

1. I. Nagrath, J. Kothari, *Modern power system analysis*, 2nd edn. (Tata McGraw-Hill, New Delhi, 1989)
2. H. Abaali, T. Talbi, R. Skouri, Comparison of Newton Raphson and Gauss Seidel methods for power flow analysis. *World Acad Sci Eng Technol* **12**(9), 627–633 (2018)

3. Vidyasagar S, Christober S (2012) Improved power flow simulation for distribution system. In: IEEE international conference on advances in engineering, science and management. IEEE, New York
4. H. Saadat, *Power system analysis*, 2nd edn. (Tata McGraw-Hill, New Delhi, 2002)
5. Kadam S, Bhosale Y, Kulkarni S (2013) Fault level analysis of power distribution system. In: International conference on energy efficient technologies for sustainability. IEEE, New York
6. Jun L (2013) Power flow and power flow calculation research in power system. *intelligence computation and evolutionary computation*, vol 180. Springer, Heidelberg, pp 439–445
7. Foong T, Tay L, Nanda J (2014) Some new findings on gauss-Seidel technique for load flow analysis. In: International conference on robotic, vision, signal processing & power applications, vol. 1. Springer, Singapore, pp 529–535
8. O. Elgerd, *Electric energy systems theory: an introduction*, 2nd edn. (Tata McGraw-Hill, New Delhi, 1983)
9. M. Saha, J. Izykowski, E. Rosolowski, *Fault location on power networks* (Springer, Berlin, 2010)
10. MathWorks Homepage. <https://www.mathworks.com/>. Accessed 05 Oct 2020.

MIL, SIL, and PIL Simulations of a Grid-Tied Inverter



Piyush Pandey, Saurabh Mani Tripathi , Utkrisht Goswami, Hemant Kumar Verma, and Aman Kumar Sriwastava

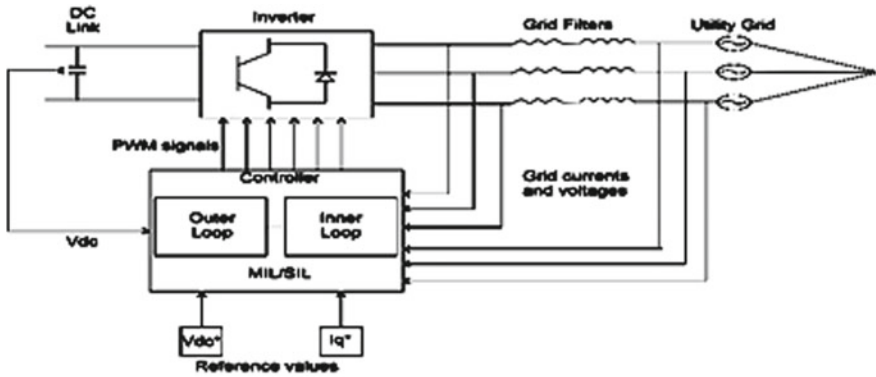
1 Introduction

Distributed renewable energy generation systems are becoming more and more popular in today's time. The output of these systems is irregular in nature which makes the power generated by these sources unfit for supplying directly into the utility grid. The generated electricity is, therefore, conditioned using power electronic devices before supplying it to the grid [1, 2]. Maintaining the DC link voltage, synchronization with the grid, and ensuring power quality are the most important tasks of the inverter system [3, 4]. Some commonly used control strategies for controlling grid-tied inverters have been discussed in [1, 2, 5, 6]. Before the actual implementation of such systems, they have to be thoroughly tested for satisfactory performance. This can be done in the laboratory conditions to reduce implementation cost, debugging time, and reduce the risk of damage of the inverter systems. For such purposes, tests like model-in-the-loop (MIL), software-in-the-loop (SIL), and processor-in-the-loop (PIL) simulations are being used in the development process [7]. In this paper, the voltage control method has been presented which is used to ensure the unity power factor operation by controlling the d - q axes currents. The proposed scheme results in good transient performance. The performance of the proposed control strategy has been tested in MATLAB/SIMULINK environment by way of MIL, SIL, and PIL simulation techniques. The C-code used in SIL and PIL simulation tests has been generated using the embedded coder. The paper is organized in following sections—Sect. 2 describes the grid-tied inverter control schematics and modeling equations. The control scheme for the grid-tied inverter has been discussed in Sect. 3. The MIL, SIL, and PIL test results have been discussed in Sect. 4. The conclusions from the work have been brought out in Sect. 5.

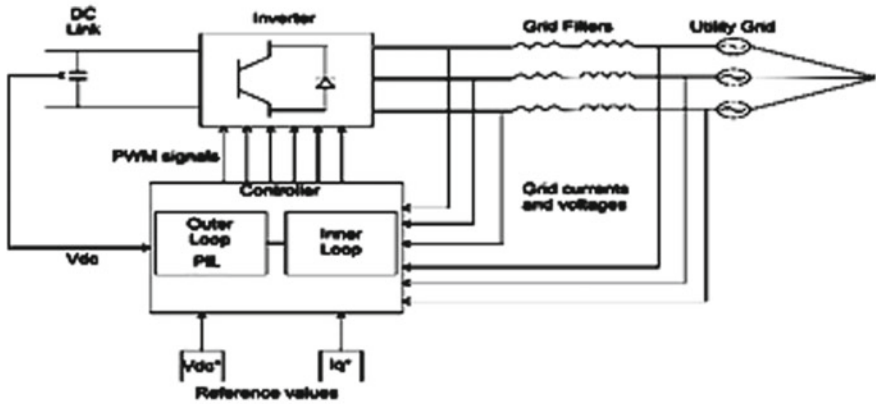
P. Pandey (✉) · S. M. Tripathi · U. Goswami · H. K. Verma · A. K. Sriwastava
Electrical Engineering Department, Kamla Nehru Institute of Technology, Sultanpur, India

2 Schematics for Grid-Tied Inverter Control

The generated power from the DG source is required to be controlled and conditioned, before feeding to the grid using a grid-tied inverter as illustrated in Fig. 1. The schematic arrangement of the grid-tied inverter control for MIL and SIL simulation tests is shown in Fig. 1a, and the schematic arrangement for PIL simulation test is shown in Fig. 1b.



(a)



(b)

Fig. 1 Schematic arrangement of the grid-tied inverter control for (a) MIL/SIL simulation tests (b) PIL simulation test

2.1 Grid Voltage Equations

The d - q axes grid voltages can be expressed using the following equations:

$$e_{dg} = v_{dg} + L_g \times \frac{di_{dg}}{dt} + R_g \times i_{dg} - \omega_g \times L_g \times i_{qg}, \quad (1)$$

$$e_{qg} = v_{qg} + L_g \times \frac{di_{qg}}{dt} + R_g \times i_{qg} + \omega_g \times L_g \times i_{dg}, \quad (2)$$

where e_{dg} , e_{qg} are d -axis and the q -axis grid voltages; R_g is the coupling resistance; L_g is the coupling inductance; v_{dg} , v_{qg} are d -axis and the q -axis inverter voltage, and ω_g is the grid (angular) frequency.

2.2 DC-Link

The DC link capacitor voltage can be represented as follows:

$$\frac{d}{dt}(V_{DC}) = \frac{P_s - P_g}{CV_{DC}}, \quad (3)$$

where P_s is the generated DG power and P_g is the supplied power to the grid.

The real power P_g can be calculated using the equation given as follows:

$$P_g = \frac{3}{2} \times (e_{dg} \times i_{dg} + e_{qg} \times i_{qg}) \quad (4)$$

3 Control of the Grid-Tied Inverter

Figure 2 depicts the schematic diagram of the controller which has been used in the grid-tied inverter control at power factor equal to unity wherein the DC-link capacitor voltage V_{DC} is being compared to reference DC voltage V_{DC}^* and the error signal generated is given to the outer loop PI controller to give the d -axis grid current as follows:

$$i_{dg}^* = K_{pv} \times \left(\frac{1 + pT_{iv}}{pT_{iv}} \right) \times (V_{DC}^* - V_{DC}), \quad (5)$$

where K_{pv} , T_{iv} are the proportional gain and integral time constant of the outer loop PI controller.

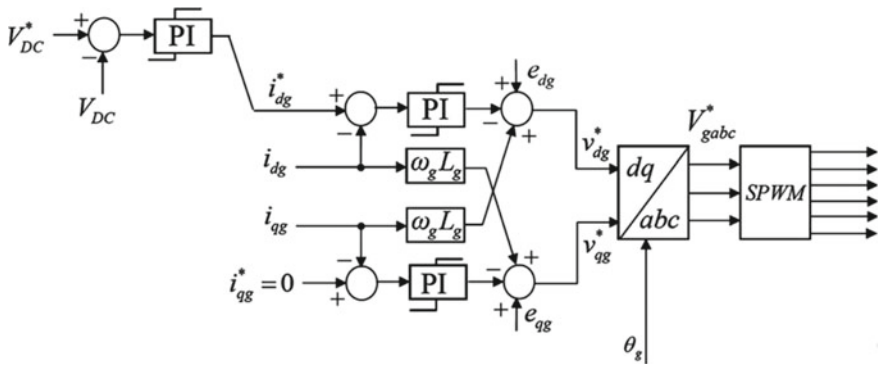


Fig. 2 Voltage oriented control schematic for grid-tied inverter [1]

The q -axis reference grid current i_{qg}^* is commanded to be zero to achieve unity power factor operation. These reference d - q axes currents being compared to actual d - q axes currents, and the error is given to the inner loop PI controllers to generate the d - q axes inverter voltages v_{dg}^* and v_{qg}^* given as follows:

$$v_{dg}^* = K_{pc} \times \left(\frac{1 + pT_{ic}}{pT_{ic}} \right) \times (i_{dg}^* - i_{dg}) \tag{6}$$

$$v_{qg}^* = K_{pc} \times \left(\frac{1 + pT_{ic}}{pT_{ic}} \right) \times (i_{qg}^* - i_{qg}) \tag{7}$$

where K_{pc}, T_{ic} are the proportional gain and integral time constant of the inner PI controllers (Fig. 2).

The inverse transformation of d -axis and q -axis inverter voltages gives 3-phase reference inverter voltages which are then utilized to generate the gate pulses for the grid-tied inverter using a PWM modulator.

Table 1 System parameters [1]

Coupling grid resistance	1.85 Ω
Coupling inductance	12.8 mH
DC capacitor value	1000 μ F
DC link voltage (Reference value)	800 V
Grid frequency and voltage	50 Hz and 415 V (r.m.s.)
Proportional-gain (outer loop PI)	0.69
Integral-time constant (outer loop PI)	0.0055
Proportional-gain (inner loop PI)	70.69
Integral-time constant (inner loop PI)	0.00044

4 Mil, Sil, and Pil Simulation Tests

The controller has been tested using MIL, SIL, and PIL simulation techniques to demonstrate the performance of the grid-tied inverter. PIL simulation test has been done for the outer loop of the controller using the Arduino Uno microcontroller board. The simulation test parameters are listed in Table 1.

4.1 Mil Simulation Test

Figure 3 shows the performance results against a variation in the input DC current from 8 to 10A so as to demonstrate the success of the control scheme of the grid-tied inverter by way of MIL simulation.

The step input DC current variation from 8 to 10A is depicted in Fig. 3a. With the sudden increase in the DC current, the DC link voltage tends to increase which is then taken care of by the outer loop PI controller (see Fig. 3b).

The results of the MIL test show that the outer loop PI controller keeps the DC-link capacitor voltage at its reference value even after the input DC current is varied. Figure 3d–e depicts that the grid voltage vectors are aligned to the d -axis. The variation in the d -axis grid current is in line with the varying input DC current (see Fig. 3f–g). The inner current PI controller maintains the q -axis grid current at zero value to make certain the unity power factor, which can also be verified from the waveforms shown in Fig. 3c. The three-phase grid voltage remains at its nominal value; however, the variation in the three-phase grid current can also be seen according to the varying input DC current. Here, it is worth mentioning that the grid current has been scaled by a factor of 15 so as to clearly demonstrate the variation in the same in Fig. 3c with respect to the varying input DC current. Thus, the MIL simulation results clearly reveal that a fast transient response and good steady-state performance can be guaranteed while adopting the voltage oriented control scheme for the grid-tied inverter.

4.2 Sil Simulation Test

The performance results of SIL simulation test with identical DC current input are shown in Fig. 4. In SIL simulation test, the performance results have been obtained after replacing the controller block developed in the MATLAB/SIMULINK environment by a SIL block containing the embedded C-code for the control action. The result of SIL simulation test depicted in Fig. 4 demonstrate almost similar performance of the grid-tied inverter system to that obtained using MIL simulation test.

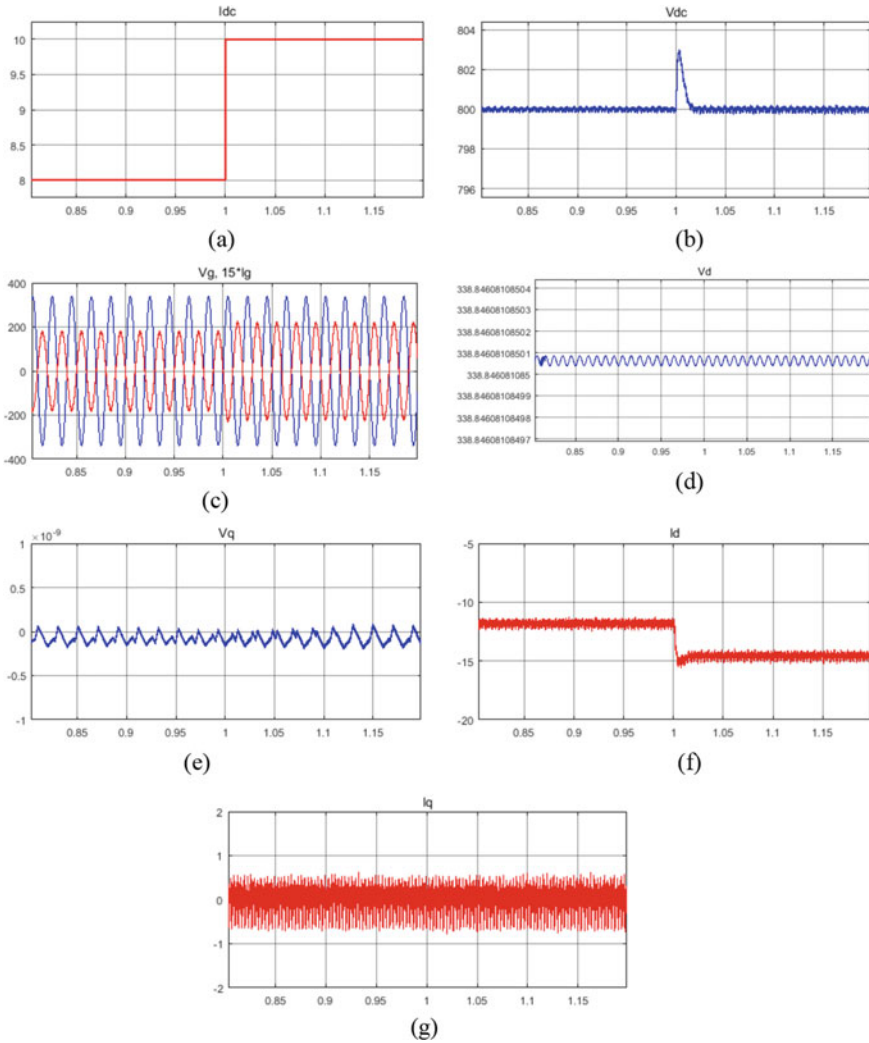


Fig. 3 Grid-tied inverter performance with varying input DC current under MIL simulation test. **a** Input DC current. **b** DC capacitor voltage. **c** Grid voltage and grid current (scaled by 15) for Phase-‘a’. **d** Grid voltage: d -axis. **e** Grid voltage: q -axis. **f** Grid current: d -axis. **g** Grid current: q -axis

4.3 Pil Simulation Test for Low Cost Experimental Validation

The PIL simulation is a low cost experimental test setup wherein the embedded C-code of the controller block is run in an external processor [7]. In PIL simulation test arrangement, an Arduino Uno microcontroller has been employed as shown in Fig. 5 and the corresponding performance results are shown in Fig. 6. For PIL simulation

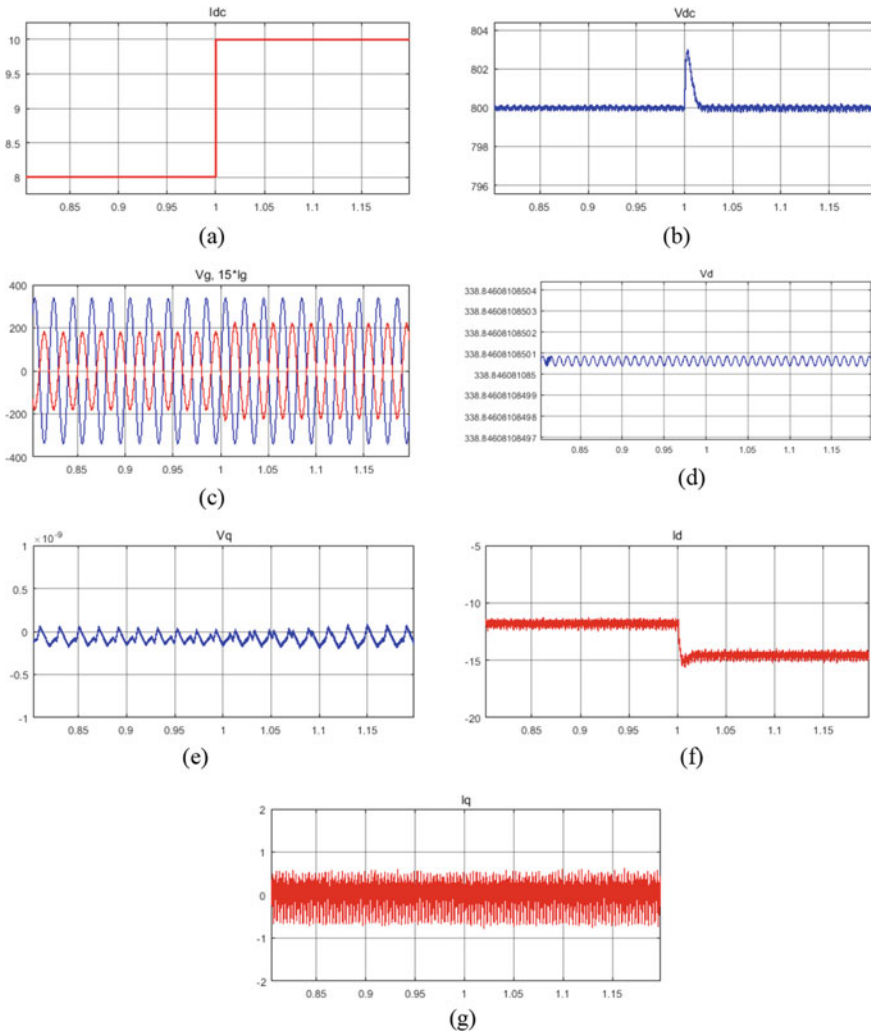


Fig. 4 Grid-tied inverter performance with varying input DC current under SIL simulation test. **a** Input DC current. **b** DC capacitor voltage. **c** Grid voltage and grid current (scaled by 15) for Phase-‘a’. **d** Grid voltage: d -axis. **e** Grid voltage: q -axis. **f** Grid current: d -axis. **g** Grid current: q -axis

test, the outer control loop has been replaced with a PIL block which interacts with the external Arduino Uno microcontroller board so as to execute the embedded C-code which is generated for the outer loop of the controller.

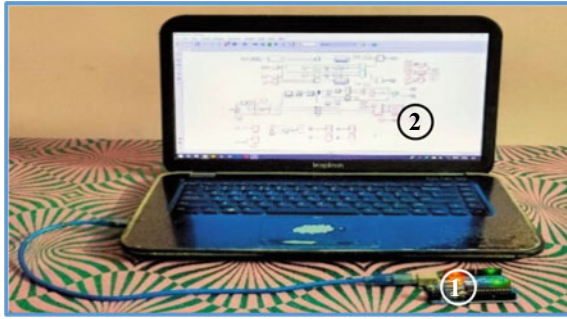


Fig. 5 PIL simulation test setup—(1) Arduino Uno microcontroller board executing the outer loop of controller. (2) Laptop PC simulating the grid-tied inverter control in MATLAB/SIMULINK environment

The result of PIL simulation test also reveals a comparable performance as that obtained via MIL and SIL simulation tests. This way the controller performance has been validated experimentally by way of the PIL simulation test making use of a low cost controller hardware.

5 Conclusion

The voltage-oriented control schematic for grid-tied inverter was presented. The performance of the control scheme for grid-tied inverter was tested through developed MIL, SIL, and PIL simulation models in MATLAB/SIMULINK environment. The performance results of MIL simulation test confirmed that the control scheme is effective in feeding the power grid while maintaining the unity power factor. The control scheme was also tested using SIL simulation wherein the embedded C-code was generated to perform the control action. Performance results from the SIL simulation test confirmed that the embedded C-code for the controller was executing as desired. Further, for a low cost experimental validation, the embedded C-code for the outer loop of the controller was executed on an Arduino Uno microcontroller board by way of PIL simulation test setup which validated that the control scheme can be implemented in a physical controller so as to achieve a satisfactory operation of the grid-tied inverter.

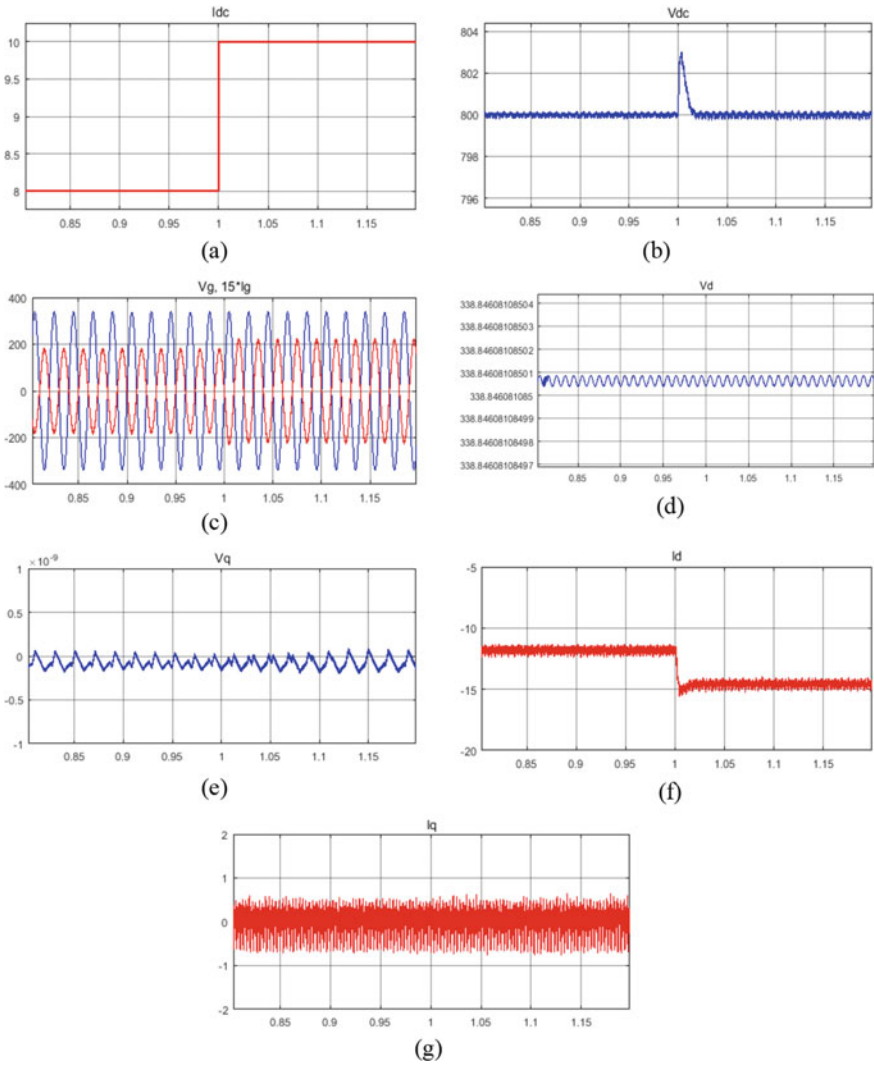


Fig. 6 Grid-tied inverter performance with varying input DC current under PIL simulation test. **a** Input DC current. **b** DC capacitor voltage. **c** Grid voltage and grid current (scaled by 15) for Phase-‘a’. **d** Grid voltage: d -axis. **e** Grid voltage: q -axis. **f** Grid current: d -axis. **g** Grid current: q -axis

Acknowledgements The authors sincerely acknowledge the support received from the Technical Education Quality Improvement Program (TEQIP)–III at KNIT, Sultanpur, for carrying out this UG Project.

References

1. S.M. Tripathi, A.N. Tiwari, D. Singh, Optimum design of proportional-integral controllers in a grid-integrated PMSG-based wind energy conversion system. *Int Trans Electr Energy Syst* **26**(5), 1006–1031 (2016)
2. R. Marouani, A. Mami, Voltage oriented control applied to a grid-connected photovoltaic system with maximum power point tracking technique. *Am J Appl Sci* **7**(8), 1168–1173 (2010)
3. S.M. Tripathi, A.N. Tiwari, D. Singh, Controller design for a variable-speed direct-drive permanent magnet synchronous generator based grid-interfaced wind energy conversion system using D-partition technique. *IEEE Access* **5**, 27297–27310 (2017)
4. Prakash S, Sahoo S, Mishra S (2018) A linear quadratic regulator for small signal stability improvement of grid connected PMSG. In: 2018 IEEMA engineer infinite conference (eTechNXT), pp 1–6
5. F. Blaabjerg, R. Teodorescu, M. Liserre, A.V. Timbus, Overview of control and grid synchronization for distributed power generation system. *IEEE Trans Ind Electr* **53**(5), 1398–1409 (2006)
6. Tripathi SM, Singh S (2020) Hardware-in-the-loop simulation of grid-tied converter for unity power factor operation. In: 2020 international conference on contemporary computing and applications (IC3A), pp 250–253
7. S. Motahhir, A.E. Ghzizal, S. Sebti, A. Derouich, MIL and SIL and PIL tests for MPPT algorithm. *Cogent Eng* **4**(1), 1–18 (2017)

Performance Investigation on Vector Controlled IPMSM Drive Using MIL, SIL, and PIL Simulations



Utkrisht Goswami, Saurabh Mani Tripathi , Piyush Pandey, Saumya Jain, and Govind Saroj

1 Introduction

Permanent magnet synchronous motors (PMSM) are being progressively utilized nowadays because of their advantages over other machines [1–3]. In PMSM, the field is created by permanent magnets [4]. PMSMs have received vast acceptance in industries due to their fast dynamic responses. The PMSMs can further be classified as surface-mount permanent magnet synchronous motor (SPMSM) and interior permanent magnet synchronous motor (IPMSM) [2]. The work presented in this paper makes use of IPMSM for transient performance analysis. The IPMSM has an asymmetrical magnetic system, and hence it is essentially a salient pole motor. The d -axis inductance and the q -axis inductance are not equal due to the asymmetrical pole orientation ($L_d \neq L_q$) [5]. In order to ensure the best performance of the PMSM drives, control schemes such as minimal loss scheme and maximum torque schemes have been suggested in the past researches [6]. As far as this paper is concerned, a vector control method for IPMSM drive is suggested in order to guarantee maximum torque per ampere (MTPA) via controlling the d - q axes currents against a given reference speed command (see Fig. 1). The error in the rotor speed is processed by a PI controller to generate the reference torque command which is then used to generate the reference q -axis and d -axis currents. A hysteresis current controller is employed in the inner loop in order to minimize the current error [7]. In order to reduce the implementation cost and to avoid the possibility of damage of actual machine, the simulation techniques such as model-in-the-loop (MIL), software-in-the-loop (SIL), and processor-in-the-loop (PIL) are used [8]. In this work, the IPMSM drive control has been implemented in MATLAB/Simulink environment and the efficacy of the drive control has been demonstrated by way of MIL, SIL, and PIL simulation techniques.

U. Goswami (✉) · S. M. Tripathi · P. Pandey · S. Jain · G. Saroj
Department of Electrical Engineering, Kamla Nehru Institute of Technology, Sultanpur, India

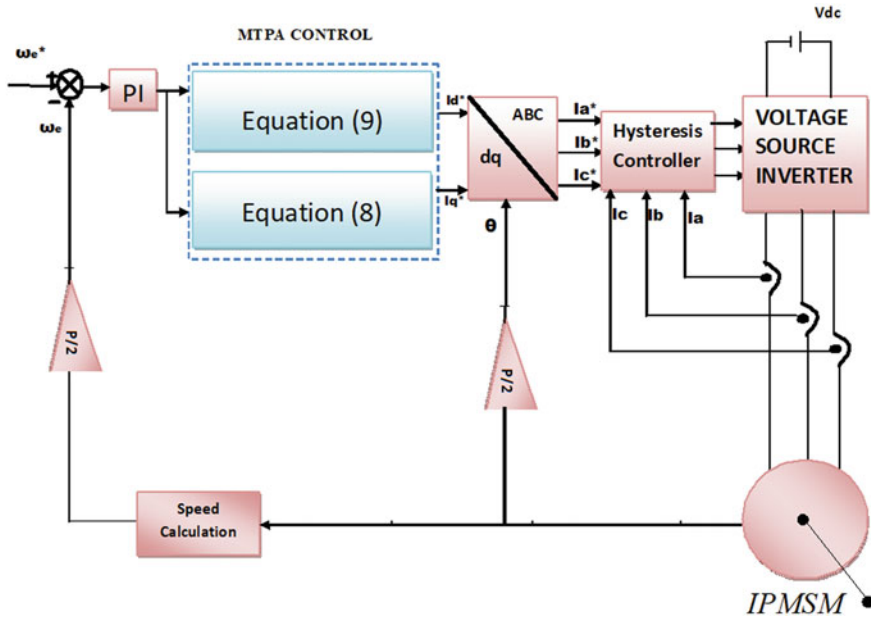


Fig. 1 Vector controlled IPMSM drive

2 Modeling of IPMSM

The d - q axes stator voltage equations are given by

$$V_d = I_d \cdot R_s + L_d \frac{dI_d}{dt} - \omega_e \cdot L_q \cdot I_q, \tag{1}$$

$$V_q = I_q \cdot R_s + L_q \frac{dI_q}{dt} + \omega_e L_d \cdot I_d + \omega_e \lambda_{pm}, \tag{2}$$

where λ_{pm} is the rotor flux; L_d and L_q are the direct and quadrature axes inductances, respectively; I_d and I_q are the direct and quadrature axes stator currents; ω_e is the angular electrical speed.

The electromagnetic torque equation of IPMSM is expressed as follows:

$$T_e = (3P/4) \times (\lambda_{pm} I_q + (L_d - L_q) I_d I_q), \tag{3}$$

where P is the number of poles of the motor.

The mechanical torque equation is given by

$$T_e = T_l + B\omega_m + J \frac{d\omega_m}{dt}, \tag{4}$$

where T_l is the load torque; ω_m is the angular mechanical speed; B and J are the friction coefficient and rotational inertia of the motor, respectively,

$$\omega_e = (P/2)\omega_m. \quad (6)$$

3 Control Scheme for the IPMSM Drive

The outer speed control loop consists of a PI controller which compares the motor speed with the reference speed command. The PI controller generates the electromagnetic torque reference as output

$$T_e^* = K_{ps} \left(\frac{1 + pT_{is}}{pT_{is}} \right) \cdot (\omega_r^* - \omega_r), \quad (7)$$

where K_{ps} is the proportional gain and T_{is} is the integral time constant of the speed PI controller.

The reference torque generated is used to calculate the reference q -axis and d -axis stator currents as follows:

$$I_q^* = \frac{T_e^*}{(3P/4) \times (\lambda_{pm} + (L_d - L_q)I_d^*)} \quad (8)$$

$$I_d^* = -\frac{\lambda_{pm}}{2(L_d - L_q)} - \sqrt{I_q^{*2} + \left[\frac{\lambda_{pm}}{2(L_d - L_q)} \right]^2} \quad (9)$$

The d -axis and q -axis reference stator currents are converted to a–b–c reference frame by using inverse Clark and Park transformations. The reference a–b–c stator currents thus generated are compared with measured a–b–c stator currents, and the errors are passed through hysteresis controller. The hysteresis controller generates the gate pulses for the inverter.

4 MIL, SIL, and PIL Simulation Tests

The controller has been tested using MIL, SIL, and PIL simulation techniques to demonstrate the transient performance of the vector controlled IPMSM drive. PIL simulation test has been carried out for the outer speed control loop using the Arduino Uno microcontroller board. The drive system parameters are listed in Table 1.

Table 1 System parameters

Stator resistance	0.9585Ω
<i>d</i> -axis inductance	0.004987H
<i>q</i> -axis inductance	0.005513H
Rotor flux	0.1827Wb
DC voltage (<i>V_{dc}</i>)	300 V
Proportional-gain (speed PI)	0.1196
Integral-time constant (speed PI)	41.0323
Motor inertia (<i>J</i>)	0.0006329 kg-m ²
Number of poles (<i>P</i>)	8
Output power	900 W
Rated torque	8 N-m
Rated speed	2000 rpm

4.1 MIL Simulation Test

The performance of the drive has been tested for (1) start-up at rated load, (2) decrement of load torque to half value, (3) increment of load torque to rated value, and (4) speed reversal in order to demonstrate the effectiveness of the control scheme for IPMSM drive. Figure 2 shows the performance of the IPMSM drive control during start-up at rated load condition. The waveforms have been obtained by way of MIL simulation. The speed command is given for 2000 rpm. The torque is at rated value. It can be seen that there is a small overshoot in speed response, but it settles at the reference value in about 0.2 s. The *q*-axis current is proportional to the load torque.

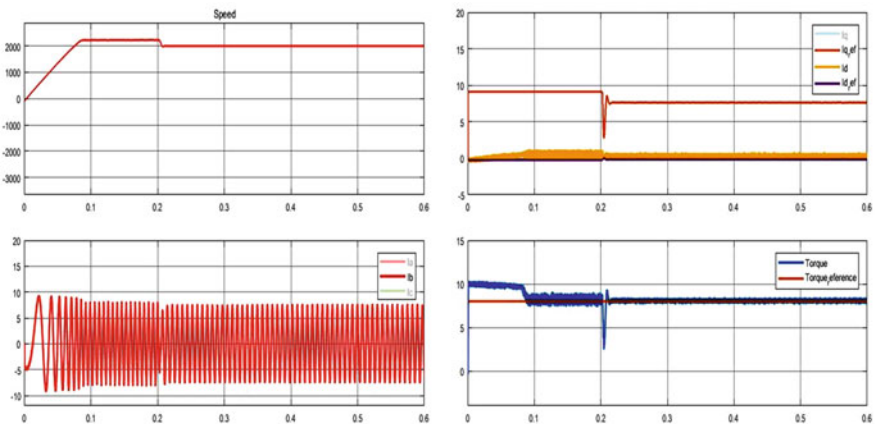


Fig. 2 MIL simulation: Performance of the IPMSM drive control during start-up at rated load—Rotor speed, *d-q* axes stator currents, three-phase stator current and electromagnetic torque responses (from left to right)

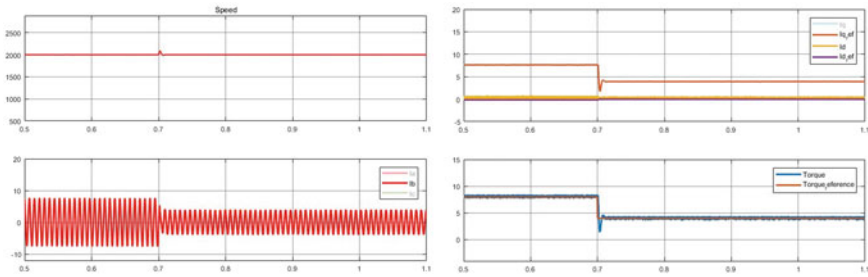


Fig. 3 MIL simulation: Performance of the IPMSM drive control during decrease in load torque to half value at rated speed—Rotor speed, d - q axes stator currents, three-phase stator current and electromagnetic torque responses (from left to right)

Figure 3 shows the performance of the IPMSM drive control during decrease in load torque to half value at rated speed condition. When load torque is changed to half of the rated value, the speed increases but settles again to its original value. The stator current also reduces with the reduction of the load torque. The decrement in q -axis current is proportional to the decrease in load torque. Figure 4 shows the performance of the IPMSM drive control during increase in load torque to the rated value at rated speed condition. When load torque is changed again to the rated value, the speed decreases slightly but settles again to its original value. The stator current also increases with the increase of the load torque. The increment in q -axis current is proportional to the increase in load torque.

Figure 5 shows the performance of the IPMSM drive control during speed reversal at rated load condition. The speed command is given for -2000 rpm. The torque is at rated value. It can be seen that the rotor settles at the reference value very quickly but comparatively with higher undershoot. Still, the current remains within the permissible value. This way the drive performance has been found satisfactory in all transient conditions considered above.

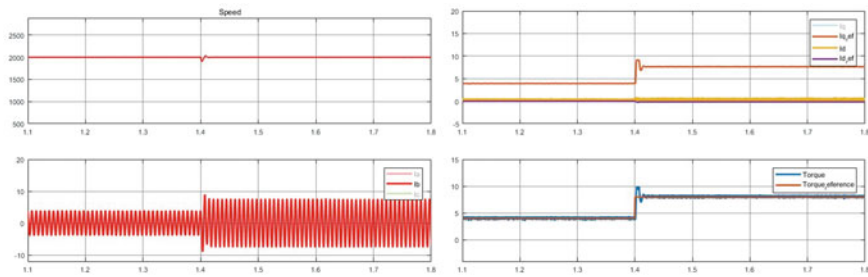


Fig. 4 MIL simulation: Performance of the IPMSM drive control during increase in load torque to the rated value at rated speed—Rotor speed, d - q axes stator currents, three-phase stator current and electromagnetic torque responses (from left to right)

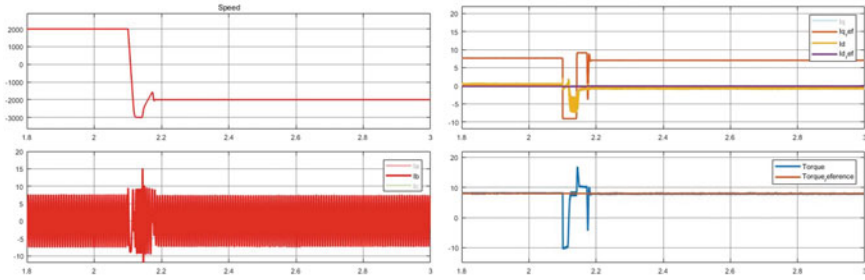


Fig. 5 MIL simulation: Performance of the IPMSM drive control during speed reversal at rated load—Rotor speed, d - q axes stator currents, three-phase stator current and electromagnetic torque responses (from left to right)

4.2 SIL Simulation Test

The performance results of SIL simulation test with identical transient conditions are shown in Figs. 6, 7, 8, and 9. In SIL simulation test, the performance results have been obtained after replacing the controller block developed in the MATLAB/SIMULINK environment by a SIL block containing the embedded C-code for the drive control.

The results of SIL simulation test as illustrated in Figs. 6, 7, 8, and 9 demonstrate almost similar performance of the IPMSM drive system to those obtained using MIL simulation. The IPMSM drive operation is found satisfactory in all transient conditions under SIL simulation test. When load torque decreases the speed increases and then settles at the reference value. When load torque is increased the speed decreases, but later settles at the reference value. On speed reversal, large overshoots are observed; however, the drive performance is acceptable in all transient conditions.

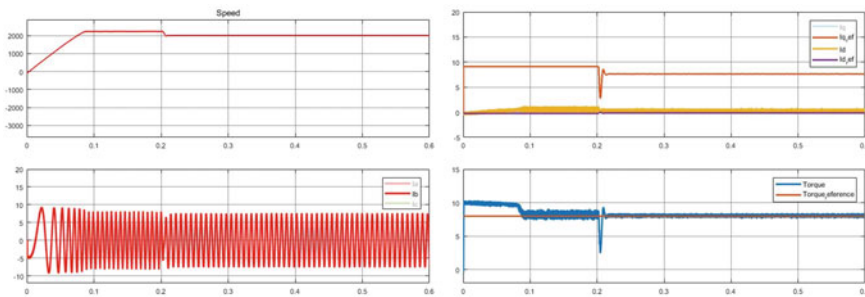


Fig. 6 SIL simulation: Performance of the IPMSM drive control during start-up at rated load—Rotor speed, d - q axes stator currents, three-phase stator current and electromagnetic torque responses (from left to right)

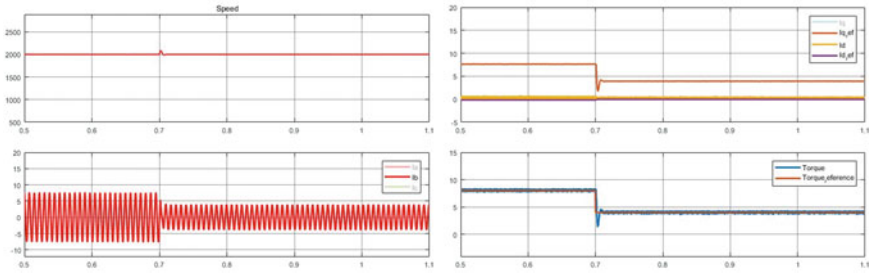


Fig. 7 SIL simulation: Performance of the IPMSM drive control during decrease in load torque to half value at rated speed—Rotor speed, d - q axes stator currents, three-phase stator current, and electromagnetic torque responses (from left to right)

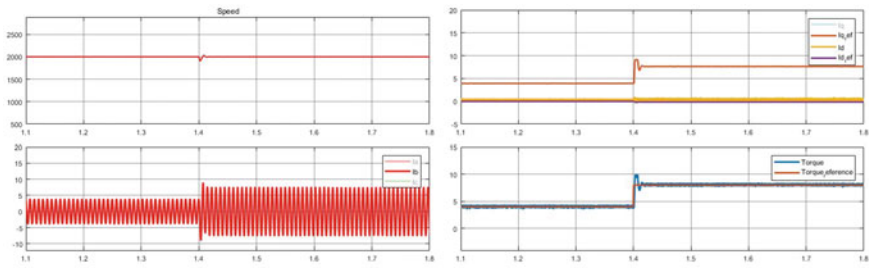


Fig. 8 SIL simulation: Performance of the IPMSM drive control during increase in load torque to the rated value at rated speed—Rotor speed, d - q axes stator currents, three-phase stator current, and electromagnetic torque responses (from left to right)

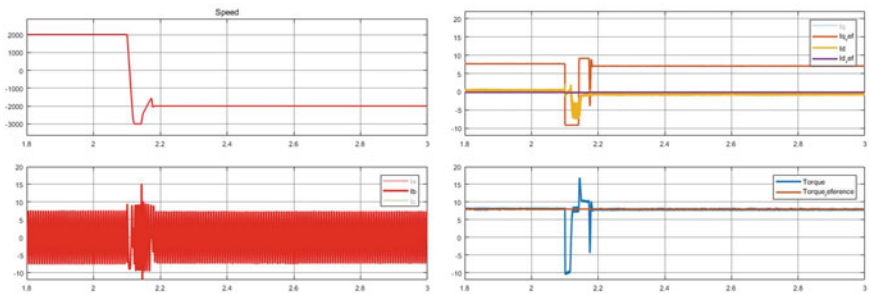


Fig. 9 SIL simulation: Performance of the IPMSM drive control during speed reversal at rated load—Rotor speed, d - q axes stator currents, three-phase stator current, and electromagnetic torque responses (from left to right)

4.3 PIL Simulation Test for Low Cost Experimental Validation

The PIL simulation has also been carried out which is a low cost experimental test setup for performance validation. In PIL simulation test, the embedded C-code of the controller block is executed in an external processor. In this work, for PIL simulation test, an Arduino Uno microcontroller has been used as illustrated in Fig. 10 and the corresponding performance results are presented in Figs. 11, 12, 13, 14.

For PIL simulation test, the outer control loop has been replaced with a PIL block which interacts with the external Arduino Uno microcontroller in order to execute the embedded C-code for the outer loop of the drive controller.

As can be seen in PIL simulation results shown in Figs. 11–14, the performance of the IPMSM drive is very close to those obtained via MIL and SIL simulation tests. Only a slight deviation can be observed. This way the efficacy of the drive controller

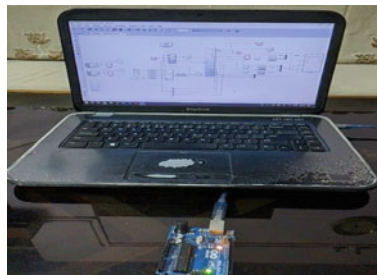


Fig. 10 PIL simulation test setup employing an Arduino Uno microcontroller board executing the outer loop of controller and a Laptop PC simulating the IPMSM drive control in MATLAB/Simulink environment

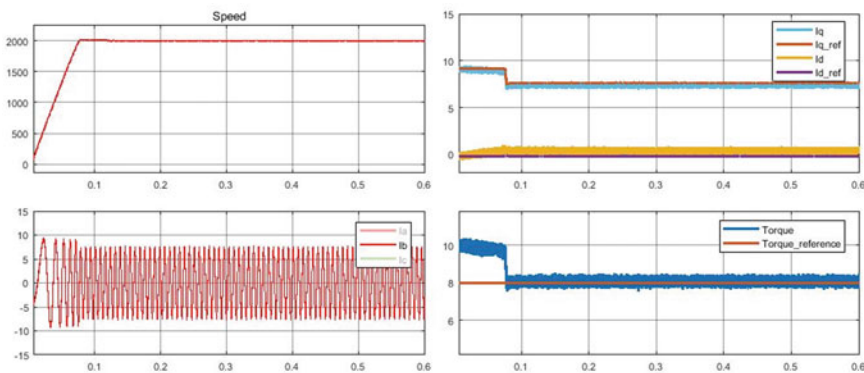


Fig. 11 PIL simulation: Performance of the IPMSM drive control during start-up at rated load—Rotor speed, d - q axes stator currents, three-phase stator current, and electromagnetic torque responses (from left to right)

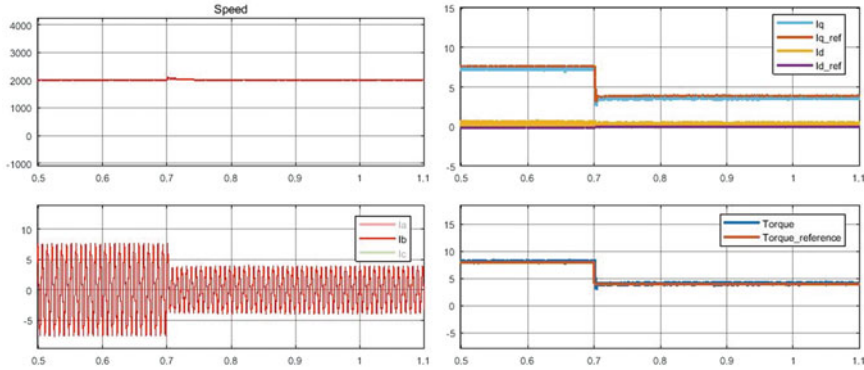


Fig. 12 PIL simulation: Performance of the IPMSM drive control during decrease in load torque to half value at rated speed—Rotor speed, d - q axes stator currents, three-phase stator current, and electromagnetic torque responses (from left to right)

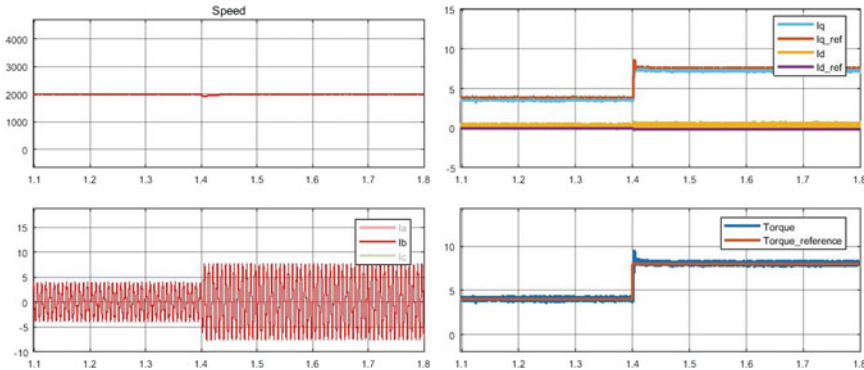


Fig. 13 PIL simulation: Performance of the IPMSM drive control during increase in load torque to the rated value at rated speed—Rotor speed, d - q axes stator currents, three-phase stator current, and electromagnetic torque responses (from left to right)

has been experimentally validated by way of the low cost PIL simulation test using Arduino Uno microcontroller.

5 Conclusions

The vector control scheme for IPMSM drive was presented. The performance of the control scheme for IPMSM drive was tested using developed MIL, SIL, and PIL simulation models in MATLAB/Simulink environment. The performance results of MIL simulation test demonstrated that the vector control scheme is effective in

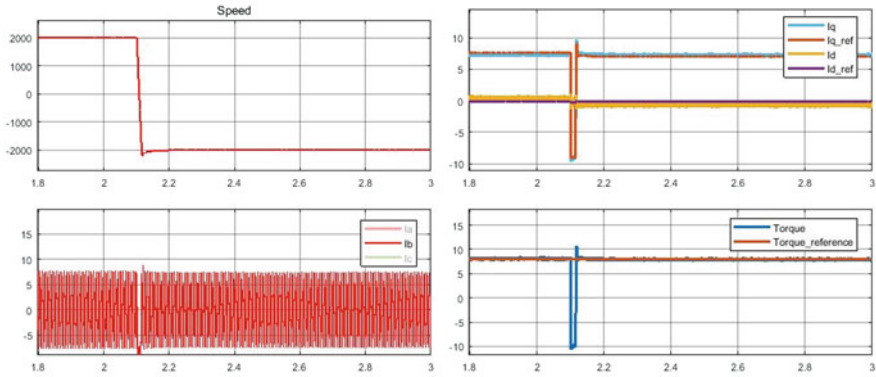


Fig. 14 PIL simulation: Performance of the IPMSM drive control during speed reversal at rated load—Rotor speed, d - q axes stator currents, three-phase stator current, and electromagnetic torque responses (from left to right)

handling all the transient conditions which includes startup, increase/decrease of load torque and speed reversal. The vector control scheme was also tested using SIL simulation technique wherein the embedded C-code was generated to perform the drive control. Transient performance results from the SIL simulation test revealed that the embedded C-code generated for the controller was executing well. Furthermore, the embedded C-code for the outer speed loop of the drive control system was executed on an Arduino Uno microcontroller board by way of PIL simulation test which experimentally validated the satisfactory control performance of the IPMSM drive for all transient conditions.

Acknowledgements The authors sincerely acknowledge the support received from the Technical Education Quality Improvement Program (TEQIP)–III at Kamla Nehru Institute of Technology, Sultanpur, for carrying out this U.G. Project.

References

1. A. Mishra, P. Agarwal, S.P. Srivastava, A comprehensive analysis and implementation of vector control of permanent magnet synchronous motor. *Int J Power Energy Conversion* **5**(1), 1–23 (2014)
2. Nan Z, Dejun Y (2020) Research on MTPA control of IPMSM drive using online parameter identification method. In: 2020 5th Asia conference on power and electrical engineering (ACPEE), pp 689–693
3. Q. Yin, H. Li, H. Luo, Q. Wang, C. Xu, An improved sensorless vector control method for IPMSM drive with small DC-link capacitors. *Energies* **13**(3), 1–26 (2020)
4. H. Tuna, O. Bilgin, Design and implementation of permanent magnet synchronous motor speed control for variable flowrate moto-pump application. *Int J Comput Sci Electron Eng* **4**(2), 104–107 (2016)

5. Jerkan DG, Gecić MA, Marčetić DP (2014) IPMSM inductances calculation using FEA. In: X international symposium on industrial electronics INDEL 2014, pp 134–138
6. S.M. Tripathi, C. Dutta, Enhanced efficiency in vector control of a surface-mounted PMSM drive. *J Franklin Inst* **355**, 2392–2423 (2018)
7. A. Naik, A.K. Panda, S.K. Kar, Improving the dynamic response during field weakening control of IPMSM drive system using adaptive hysteresis current control technique. *Int J Emerg Electr Power Syst* **17**(3), 235–249 (2016)
8. S. Motahhir, A.E. Ghzizal, S. Sebt, A. Derouich, MIL and SIL and PIL tests for MPPT algorithm. *Cogent Eng* **4**(1), 1–18 (2017)

Artificial Intelligence Based State of Charge Estimation of Electric Vehicle Battery



S. P. Nangrani and Ishaan S. Nangrani

1 Introduction

The term artificial intelligence (modern AI) was coined formally in 1956 at a conference at Dartmouth College, in Hanover, New Hampshire. MIT Scientist, Marvin Minsky, was very optimistic about and foreseen the future of AI [1]. In 1997 computer intelligence defeated world chess champion Garry Kasparov at that time, thus opening up a challenge to human intelligence.

AI has wide applications, and it almost covered all field of engineering involving data computation based on input output mathematical correlation and decision making for controlling system response. Several applications related to AI have been reported by eminent authors. To list a few, circuit breaker, flashover voltage of insulation, partial discharges in current transformers, substation risk management, power quality, fuzzy logic based power system stabilizer, voltage control, protection system, static security assessment, condition monitoring, demand forecasting, etc. The list is endless [2–6]. This paper throws light on all such applications and introduces several features of AI to a novice as well as high end researcher. Electric vehicles are futuristic upcoming area where one can use AI for several condition monitoring issues of charging, battery life, dynamic risk, and chaotic behavior.

Needless to say that core knowledge of electrical power system differs a lot from biological and artificial intelligence domain understanding. But usage is eminent and needs better mapping of objectives in modern era. This feature of AI makes it exciting and as well as challenging.

S. P. Nangrani (✉)

Department of Electrical Engineering, G. H. Raisoni College of Engineering, Nagpur, India
e-mail: Sunil.nangrani@raisoni.net

I. S. Nangrani

Department of Computer Engineering, Vivekanand Education Society's Institute of Technology (VESIT), Mumbai, India

Man-made consciousness has given extraordinary potential and space to the streamlining of electrical designing, and it will achieve extraordinary improvement in monetary perspective, yet additionally in security what's more, genuine activity control. Since the coming of computerized reasoning, it has been generally applied in all fields of life, and accomplished outstanding application impact, its rise has even brought up the course for the advancement of numerous fields, the field of electrical computerization control is no special case. As a general rule, the utilization of man-made brainpower innovation has enormously advanced the advancement of the solid practice of electrical computerization, and ought to be given full consideration to by related undertakings and staff.

Different sections in paper will highlight step by step understanding of integration of core knowledge and its alternate decision making using AI and machine learning algorithms.

This paper intends to abridge the rise and advancement of recent computer gadgets and adding one more dimension to the field on control in electrical power system [7–18].

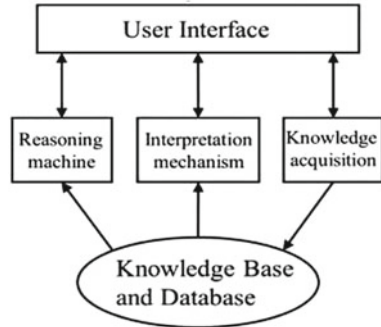
2 The Research Direction of Artificial Intelligence

One of the good features of AI approach is less rigorous in implementation as compared to use of core knowledge of electrical engineering related to differential equations and their numerical solution, fourier transform, laplace transform, and complex mathematical approach [19–32]. Intelligence is closely associated with knowledge in human beings. Similarly in machines, knowledge base systems are called as expert systems.

2.1 *Expert Systems*

A specialist framework i.e. Expert System (ES) is a product framework that catches human ability for supporting basic leadership; this is helpful for managing issues including fragmented data or a lot of complex information. Master frameworks are especially valuable for on-line tasks in the control field since they fuse emblematic and decide based information that relate circumstance and activities, and they additionally can clarify and legitimize a line of thinking. The ES fundamentally comprises of information base, database, thinking machine, translation system, information securing and UI, which is appeared in Fig. 1. Fault location and detection in electrical system usually makes effective use of expert system. The miniature version of implementing AI for decision making keeping in view the experts experience, knowledge, and inference engine.

Fig.1 Schematic of expert system



2.2 Machine Learning

Machine learning is subset of modern AI techniques. Machines and programs are designed in such a way so as to have learning based on memory, statistics, and errors made in past. It is a process by which machines mimic human decision. However the decisions by human beings are more intelligent, but machines have also progressed tremendously to showcase their power when machine defeated world chess champion Garry Kasparov. It basically centers around how the software platforms recreates human learning conduct, redesigns the current information structure with the information and aptitudes learned, and persistently improves its exhibition. Information updating and reconfiguration of mathematical architecture is beauty of AI designs. AI procedures are regularly embraced for tending to the information procurement bottleneck in executing master frameworks. In utilizing machine insight procedures to handle this bottleneck, information is consequently extricated from information. It possess several features such as minimal human intervention, identifying patterns in data and information, learning, reconfiguration, adjustments of weight in model, self-driven and effective data mining.

2.3 Neural Networks

The artificial neural system (ANN) approach is used to mimic the decision making of human beings using central nervous system controlled by human brain. Biological neurons and its structure as existing in body are beyond the reach of human being. Still use of supercomputing facilities focused solution of machines for specific challenge is beating human champions and experts in a surprising way.

Artificial implementation of the intelligence machine is nothing but non-linear mapping of input output relation with better accuracy using different architectures and learning algorithms using multilayer perceptron computational models.

2.4 Deep Learning

Deep learning is related to algorithms which extract high level features from data with the use of multiple layers. For this foundation of artificial neural network needs to be understood well. They differ from task-specific algorithms in many ways. Based on application use of different types of learning such as supervised or unsupervised learning. Deep learning is upper layer of a broader family of machine learning methods. Artificial neural network is at the core of deep learning. It works similar to our nervous system and brain. It has a similarity to biological natural intelligence. However it is limited and not touched the full dimension of intellectuality as that of human brain. However it is able to take complex decision based on huge data in a very short time which is suitable and resembles human intelligence.

However core technologies are little bit reluctant to apply this new science due to question of reliability. But certainly few areas of core engineering can be ascertained with the use of such technology. Benefits of deep learning will be evident when used more frequently. It will open up a new dimension of looking into existing methodologies. For example in electrical engineering, power flows on transmission line is dependent on classical methods of load flow analysis using Gauss Seidal and Runge–Kutta methods. But researchers have used AI to predict power flows correctly on transmission line without any core engineering mathematics.

3 Benefits of Artificial Intelligence in High Voltage Engineering

3.1 A Subsection Sample

Following are some applications where use of AI has been researched in depth and it is found that it is easy and simple when compared to complex mathematical engineering equations. Like once upon a time, Laplace Transform and Fourier Transform simplified the solution of differential equation similarly, we can coin a term AI Transform which will simplify the task of computation and decision making will be based on intelligent approach.

- (1) Design of Controllers: The classical PID controller design has been replaced by memory based input output data control patterns.
- (2) Fault detection: There are technical ways of analyzing fault location and detection but use of image processing and decision making by AI enabled expert system can pin point the faults, and it has replaced earlier approach of electrical engineering analysis.
- (3) Performance upgrade: Adaptive AI techniques take care of memory and learning in a coordinated way as human intelligence hence performance upgrade is quite obvious.

- (4) More helpful to utilize. The implementation is quite helpful and concepts of AI can be utilized wherever required with proper integration of existing tools and platforms.
- (5) Good consistency: When compared with expert decision, results of AI based designs are quite consistent.

4 Application of Artificial Intelligence in Electrical Power System

Architecture of Prolog based Expert System for relay setting [33] is shown in Fig. 2. A novice user can input system parameters related to network configurations and associated relay parameters will be set which will protect the system using short circuit analysis software. Use of object oriented programming in such architecture is not related to core knowledge of electrical engineering. Various classes for transmission lines, isolators, circuit breakers and transformers can be defined as object and functionality of each object can be defined.

Supervised neural networks have been applied in power system analysis in [33]

- planning (long-term load forecasting)
- operation (optimal power flow, unit commitment, generator shedding, state estimation, static and dynamic security assessment, dynamic contingency analysis, fault detection, fault location, daily load forecasting, substation maintenance, system voltage stability assessment)

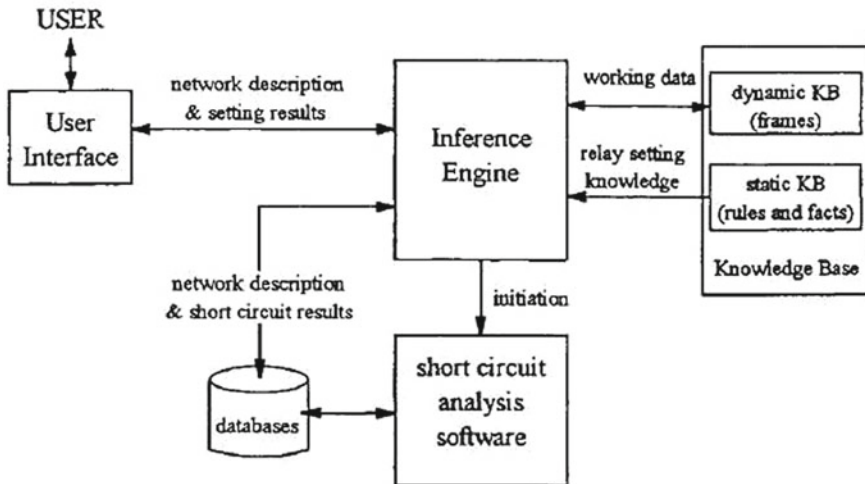


Fig.2 Relay setting based expert system

- analysis (dynamic stability assessment, generator voltage and speed control system design both analogue and digital, identification of coherent dynamic equivalents, signal processing in harmonic analysis, bad data detection, monitoring and protection).

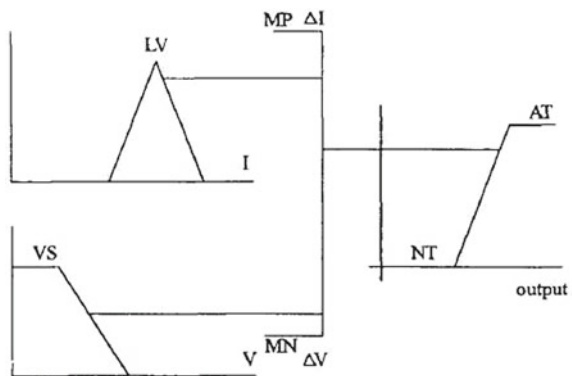
Unsupervised applications include condition monitoring. Conditions of existing networks are function of daily operational experiences hence its classification to known target cannot be ascertained. Hence unsupervised learning networks are more popular for such issues in electrical power system. Transformer DGA analysis represents infinite sets of gas concentration pointing to different conditions of health of transformer. Classification of such health parameters require support of AI techniques.

Artificial intelligence is effectively used in electrical system to identify faults with the support of Fuzzy Logic based design. Even the advanced form of Fuzzy design i.e. Adaptive Neuro Fuzzy Inference System is effectively used for the same purpose with better accuracy. Hence various researchers have reported successful results related to fault and failures of electrical systems under uncertain parameters. Type-2 fuzzy systems were another addition which takes care of uncertainties in engineering parameters.

Figure 3 describes membership function of fuzzy based relay [33]. VS is a linguistic variable for VERY SMALL, LV is used for Large Value, AT for Absolute Trip, NT for No Trip.

Expert systems make use of various layers before arriving at a decision. The layer involves fuzzy, expert knowledge, input–output correlation and weightage of parameters in output decision. Most of earlier approaches were platform dependent. Machine learning is successful in implementing them on platform independent and ready to use class and functions. This reduces the burden on design engineer for understanding intricacies of mathematics behind the intelligence.

Fig.3 Fuzzy relay



5 Conclusion

Based on discussions in previous sections, the focus of this paper successfully advocates the use of AI techniques. Various areas of AI can be utilized such as ANN, fuzzy, neuro fuzzy, hybrid models, evolutionary approaches for applying to core application. This will ease out the burden of technical computation for high voltage electrical power system and its issues. Areas such as partial discharge data can be handled very well by AI techniques to predict fault in advance. Condition monitoring is also picking up based on usage of AI techniques. Demand side forecasting is based on big data analytic concepts. This requires data analytics along with machine learning algorithms and concepts. With the advancement of architecture of modern electrical systems with UHV technology, behavior of electrical system is additionally confronting new difficulties. The customary control has been hard to adjust to the present complex dynamic conditions. Various trends in data are falsely understood by power system operators. AI usage is expanding, but it needs to be applied in a justified way by understanding various tools and techniques of programming platforms. This paper will benefit the power system operators and utilities in nutshell.

References

1. Crevier D (1993) AI: the tumultuous history of the search for artificial intelligence. Basic Books, New York
2. Ai-min L, Xin L, Xiang-dong L (2005) Fault diagnosis method of high voltage circuit breaker based on (RBF) artificial neural network. In: 2005 IEEE/PES transmission & distribution conference & exposition: Asia and Pacific. IEEE, New York, pp 1–4
3. M. Belkheiri, B. Zegnini, D. Mahi, Modeling the critical flashover voltage of high voltage insulators using artificial intelligence. *J Intell Comput Appl (JICA)* **2**(2), 137–154 (2009)
4. M.-H. Wang, C.-Y. Ho, Application of extension theory to PD pattern recognition in high-voltage current transformers. *IEEE Trans Power Delivery* **20**(3), 1939–1946 (2005)
5. M. Žarković, Z. Stojković, Artificial intelligence based thermographic approach for high voltage substations risk assessment. *IET Gener Transm Distrib* **9**(14), 1935–1945 (2015)
6. WR Anis, Ibrahim, M.M. Morcos, Artificial intelligence and advanced mathematical tools for power quality applications: a survey. *IEEE Trans Power Delivery* **17**(2), 668–673 (2002)
7. S.P. Nanrani, S.S. Bhat, Fractional order controller for controlling power system dynamic behavior. *Asian J Control* **20**(1), 403–414 (2018)
8. S.P. Nanrani, S.S. Bhat, Numerical study of optimized fractional-order controller for chaos control of nonlinear dynamical power system. *Int Trans Electr Energy Syst* **27**(8), e2336 (2017)
9. Nanrani SP, Bhat SS (2015) Power system security assessment using ranking based on combined MW-chaotic performance index. In: TENCON 2015: 2015 IEEE region 10 conference. IEEE, New York, pp 1–6
10. S.P. Nanrani, A.R. Singh, A. Chandan, Chaos driven instability control using interval type-2 fuzzy logic controller for better performance. *J Intell Fuzzy Syst* **34**(3), 1491–1501 (2018)
11. Naik KR, Nanrani SP, Bhat SS (2016) Modeling of operation of loss of excitation relay in presence of shunt FACTS devices. In: 2016 IEEE 6th international conference on power systems (ICPS). IEEE, New York, pp 1–6
12. Nanran SP, Bhat SS (2015) Chaotic behavior of single machine infinite bus power system subjected to turbine torque ripple. In: 2015 modern electric power systems (MEPS). IEEE, New York, pp 1–5.

13. S.P. Nangrani, S.S. Bhat, Smart grid security assessment using intelligent technique based on novel chaotic performance index. *J Intell Fuzzy Syst* **34**(3), 1301–1310 (2018)
14. S.P. Nangrani, Real time point to point discrete MPPT simulation for wind energy system. *Int J Adv Electr Electron Eng* **1**, 352–361 (2011)
15. Nangrani SP, Bhat SS (2015) Identification of most vulnerable line for divergent trend of power flow using Lyapunov Exponent. In: 2015 International conference on power, instrumentation, control and computing (PICCC). IEEE, New York, pp 1–5
16. S.P. Nangrani, State of art fractional order controller for power system stabilizer. *J Intell Fuzzy Syst* **36**(3), 2165–2173 (2019)
17. S.P. Nangrani, S.S. Bhat, Instability, chaos and bifurcation control in nonlinear dynamical system behavior using perturb-boost fuzzy logic controller. *J Intell Fuzzy Syst* **32**(4), 3017–3029 (2017)
18. S.P. Nangrani, K.D. Joshi, Trends in chaos and instability for understanding system complexity. *J Intell Fuzzy Syst* **38**(5), 6727–6737 (2020)
19. V. Uraikul, C.W. Chan, P. Tontiwachwuthikul, Artificial intelligence for monitoring and supervisory control of process systems. *Eng Appl Artif Intell* **20**(2), 115–131 (2007)
20. D.E. Goldberg, J.H. Holland, Genetic algorithms and machine learning. *Mach Learn* **3**(2), 95–99 (1988)
21. A.K.C. Wong, Y. Wang, Pattern discovery: a data driven approach to decision support. *IEEE Press* **33**(1), 114–124 (2003)
22. B.R. Bakshi, G. Stephanopoulos, Representation of process trends-III: Multiscale extraction of trends from process data. *Comput Chem Eng* **18**(4), 267–302 (1994)
23. M.H. Hassoun, Fundamentals of artificial neural networks. *Proc IEEE* **84**(6), 906 (1996)
24. F.A. Cubillos, E.L. Lima, Adaptive hybrid neural models for process control. *Comput Chem Eng* **22**(12), S989–S992 (1998)
25. P.F. Tsai, J.Z. Chu, S.S. Jang, S.S. Shieh, Developing a robust model predictive control architecture through regional knowledge analysis of artificial neural networks. *J Process Control* **13**(5), 423–435 (2003)
26. Y. Power, P.A. Bahri, Integration techniques in intelligent operational management: a review. *Knowl-Based Syst* **18**(2), 89–97 (2005)
27. Y. Lecun, Y. Bengio, G. Hinton, Deep learning. *Nature* **521**(7553), 436–444 (2015)
28. W.G. Ji, Application of artificial intelligence technology in the analysis of electrical automatic control. *Electron Test* **3**, 137–138 (2014)
29. S.Q. Xiao, J.C. Peng, The application of artificial intelligence technology in electrical automation control. *Autom Instrument* **530**, 1049–1052 (2013)
30. H Yang, J Mathew, L Ma (2002) Intelligent diagnosis of rotating machinery faults: a review. In: Proceedings of the 3rd Asia-Pacific conference on systems integrity and maintenance. Queensland University of Technology Press, Brisbane
31. L.B. Jack, A.K. Nandi, Fault detection using support vector machines and artificial neural networks, augmented by genetic algorithms. *Mech Syst Signal Process* **16**(2–3), 373–390 (2002)
32. A. Siddique, G.S. Yadava, B. Singh, Applications of artificial intelligence techniques for induction machine stator fault diagnostics: review. *IEEE Int Symp Diagnos Electr Mach* **49**(3), 29–34 (2003)
33. Laughton MA (1997) Artificial intelligence techniques in power systems. In: IEE colloquium on artificial intelligence techniques in power systems (Digest No: 1997/354). IET

Accelerometer-Based Hand Gesture Control Robot Using Arduino and 3-Axis Accelerometer



Ankit and Shweta Agarwal

1 Introduction

For the past few decades, robots are only controlled by buttons, controllers. But as the robotics is evolved now, we can control the robot using data glove, voice and also by gestures [1, 2]. In this system, gestures are captured using an ADXL335 accelerometer sensor and the particular tilt of the hand is in analog value [3–5]. That value is converted into input and input is wirelessly transferred using RF receiver and transmitter module and input is sent to the L293D motor driver and the robot will move according to gesture. Arduino is used as an interface that will allow different sensors to communicate with each other and call as a hub of both transmitter and receiver parts [6–8]. This technology can be used for military purposes where conditions are not favorable for humans. The whole concept of VR gaming works upon gesture control. The medical field uses this technology where doctors are not able to treat any patient [9, 10].

2 Block Diagram

The model is divided into transmitter module and receiver module (Figs. 1 and 2).

Ankit · S. Agarwal (✉)
CSE-UIE, Chandigarh University, Mohali, Punjab, India

© The Author(s), under exclusive license to Springer Nature Singapore Pte Ltd. 2022
M. L. Kolhe et al. (eds.), *Smart Technologies for Energy, Environment and Sustainable Development, Vol 2*, Springer Proceedings in Energy,
https://doi.org/10.1007/978-981-16-6879-1_66

687

Fig. 1 Block diagram of the transmitter part

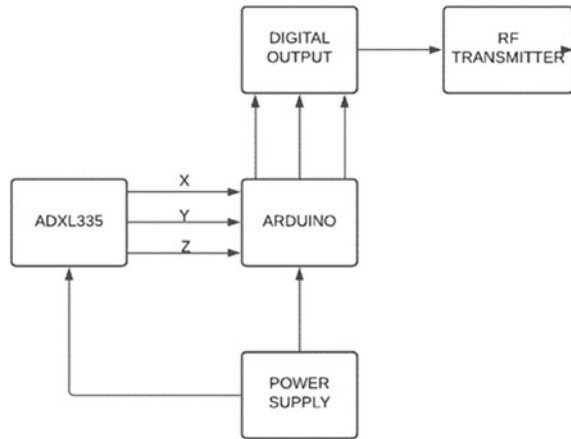
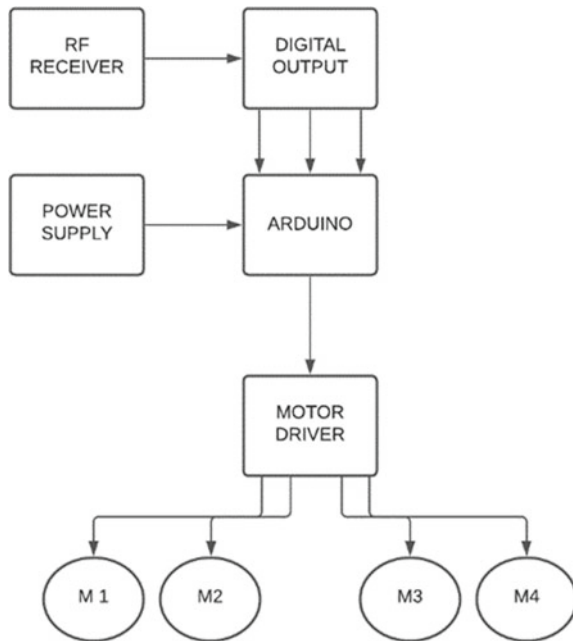
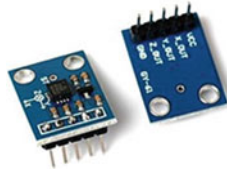


Fig. 2 Block diagram of the receiver part



3 Hardware Description

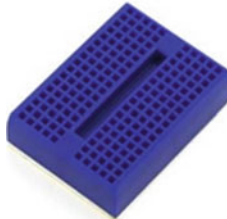
- (i) **ADXL335 Accelerometer sensor:** This sensor is used to detect tilt, ADLX335 sensor can check tilt along the x-, y- and z-axis. This sensor has five pins VCC, x-input, y-input, z-input and ground [11].



- (ii) **Transmitting RF module:** It is a part of the RF pair module. This transmitter part is used to send the digital output of the ADXL335 sensor to the receiver part. This sensor has four pins VCC, DATA, GND and ANT. ANT pin is used as an antenna, and we can attach an antenna with it for good connection [12].



- (iii) **Bread Board:** A breadboard is a rectangular board with a lot of holes that are used to make circuits and connections. Bread boards are used when we have limited pins for giving input and output.



- (iv) **Arduino Board:** Arduino is like a brain of all sensors. In simple words, it helps to establish communication between all the sensors. Arduino is used to make various models and is applicable to attach all types of sensors. It consists of Micro Processor, 2 VCC and 2 GND pins, and we have different analog and digital pins so we can use specific pins for input and output. We can even give power using DC and by using USB [13, 14].



- (v) **L293D Motor Driver:** When we are talking about robots and motors, L293D motor driver is the most important part. As motors work on 9v power and Arduino work on 5v input. We even need to change the polarity of motors to moving forward and backward so L293D motors driver is used to give 9 V input and change polarity according to the user input [15].



- (vi) **Battery:** For giving power to the receiver Arduino and motors, we need 9v batteries or even we can use 12v batteries for a good backup.



- (vii) **Motors and chassis:** We need 2 BO motors to move the robot and chassis to support all the components on it.



4 Hardware Design

Hardware part is divided into two parts as follows:

Fig. 3 Circuit diagram of transmitter module

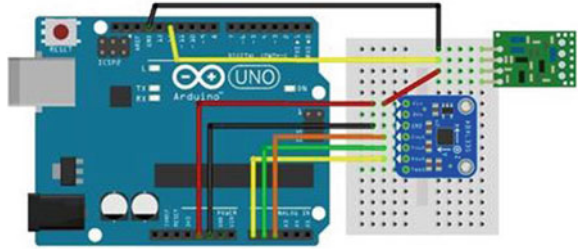
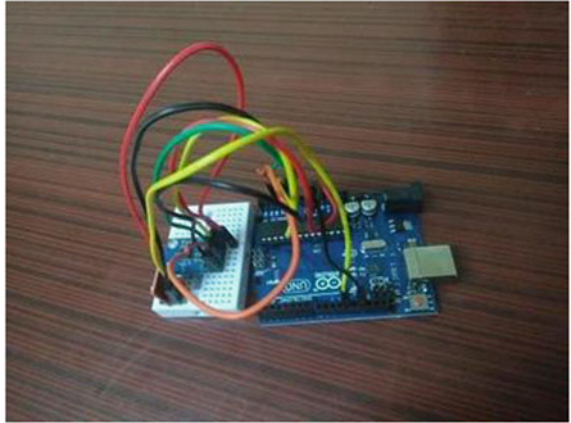


Fig. 4 Implemented Module



4.1 Transmitter Module

- The whole functioning of the Transmitter end is as the input of ADXL355 accelerometer sensor X, Y and Z is connected with an analog input of Arduino, and for giving power to sensor, VCC and GND of Arduino are connected with VIN and GND of ADX335 sensor [16, 17].
- In the RF transmitter module, VCC is connected to the VIN of the ADXL335 sensor.
- The input of the RF module is connected with pin 11 digital input of Arduino board and ground with gnd of digital input of Arduino board.
- For giving power to the Arduino board, we can directly connect it with USB [18, 19] (Figs. 3 and 4).

4.2 Receiver Module

- In the receiver module, motors are connected with a motor driver; IN1, IN2, IN3 and IN4 of the motor driver are connected with digital input 3, 4 and 5 pins of Arduino board. For giving power to motors and L293D sensor batteries, the

Fig. 5 Circuit diagram of receiver module

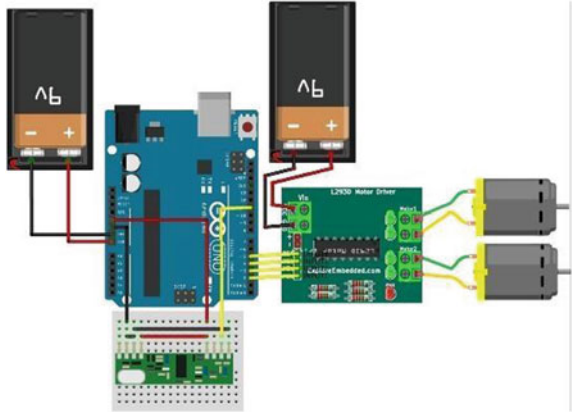
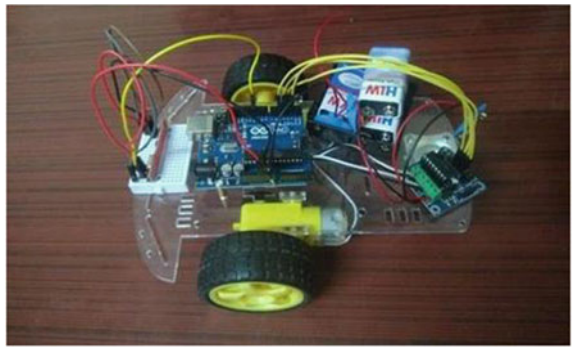


Fig. 6 Implemented Module



positive end of the battery is connected with Vin and the negative end with the GND of the motor driver [20, 21]

- For giving power to RF receiver module, 5v input of Arduino board is connected with + 5v of RF sensor, GND of Arduino with GND of RF sensor and DATA pin of RF is connected with digital input pin 11 of Arduino.
- To give power to the Arduino battery, the positive end of the battery is attached with Vin and the negative end with GND of Arduino board [22] (Figs. 5 and 6).

5 Working Principle

ADXL335 accelerometer sensor is a sensor that works on the principle of acceleration due to gravity. This sensor detects the tilt and gives a particular analog value. The robot will move according to the particular tilt [23, 24] (Table 1).

Table 1 Movement of the robot on hand tilt

Hand movement	Movement of robot
Tilting hand downward	Robot will move forward
Tilting hand upward	Robot will move backward
Tilting hand right	Robot will move right
Tilting hand left	Robot will move left
No tilt	Robot will not move

For checking the analog value of tilt, we need to write a basic program in Arduino IDE. Arduino IDE is open source and free and this software is easy to use and user-friendly (Fig. 7 and Table 2).

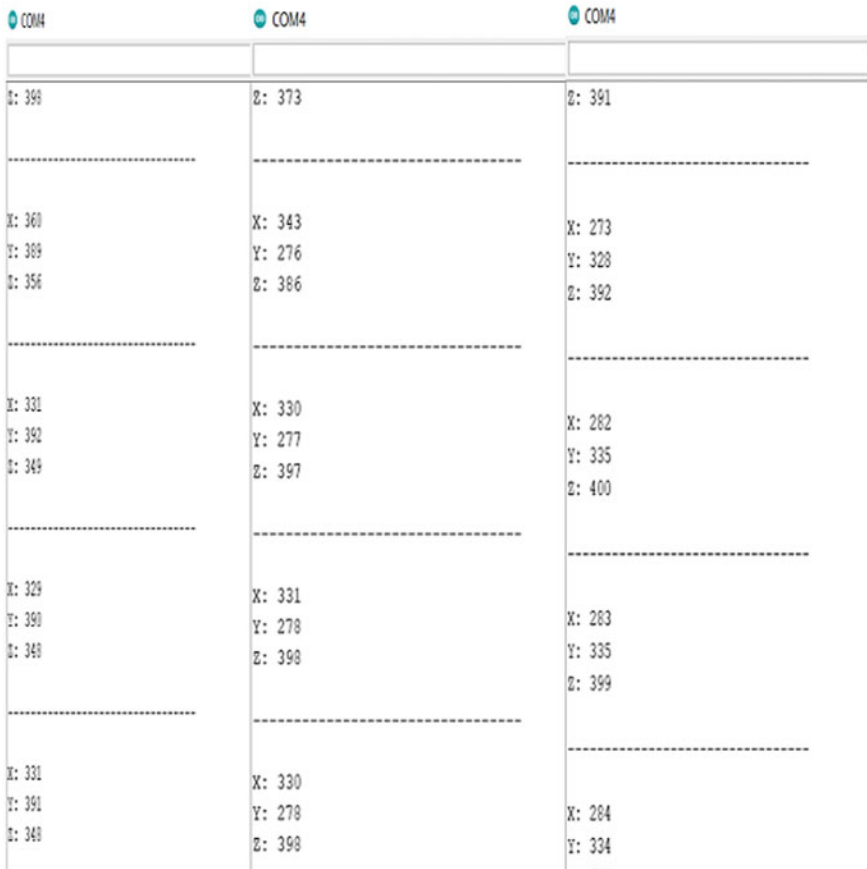


Fig. 7 Analog value on every tilt of ADX1335 sensor

Table 2 Analog value along 3-axis using ADXL335 sensor

Direction	X-axis analog value	Y-axis analog value	Z-axis analog value
Stable	329	326	416
Upward tilt	329	280 (-50) approx	410
Left tilt	378 (+50) approx	365	395
Right tilt	279 (-50) approx	324	401
Downward tilt	329	370 (+50) approx	411

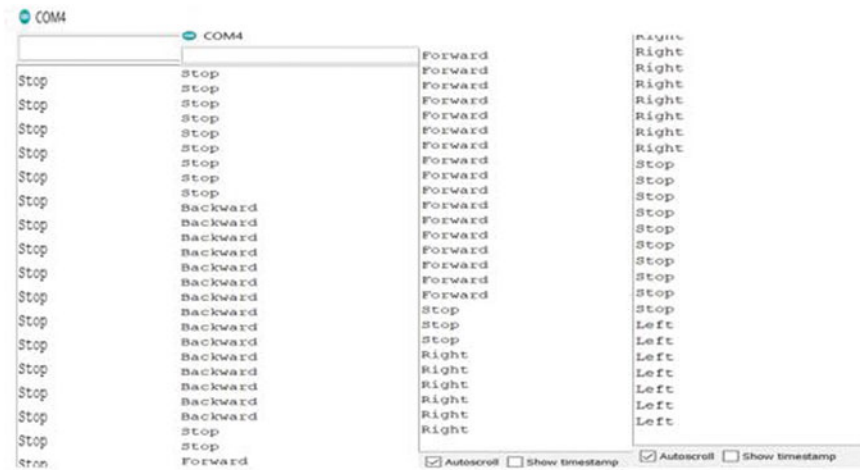


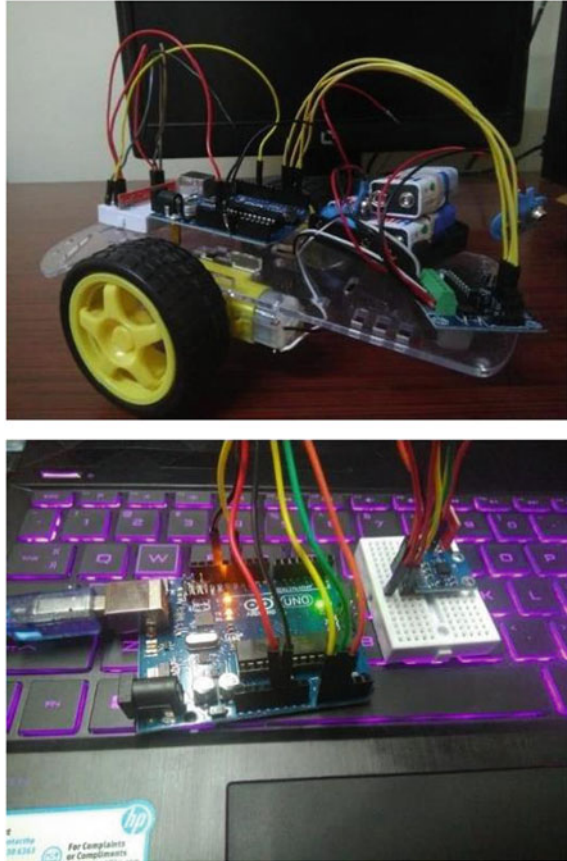
Fig. 8 Tilt detection in every direction

So, we need to write another program to send a digital output to the Receiver RF module. For sending signal wirelessly, we need to add a header file (VirtualWire.h) [25, 26] (Fig. 8).

6 Result

We successfully built a hand gesture-controlled robot using Arduino. The device is working correctly in all directions with negligible error. The ADXL335 sensor is also working well as giving accurate analog value and showing tilt direction. The communication between both RF modules (receiver and transmitter) is good and they are working for quite a range and communication is good even when there is

Fig. 9 Final module



an obstruction between them. For giving power to Motor driver and BO motors, we need good batteries. 9v batteries can work only for 60 min. RF sensor is good than IR sensor as the range of RF sensor is more than 5 m and range of IR sensor is up to 5 m (Fig. 9).

7 Advantages

- (i) Easy to operate.
- (ii) Not so expensive.
- (iii) Reliable.
- (iv) All the parts are easily available.
- (v) User-Friendly.
- (vi) The range is good.
- (vii) Rigid Hardware.

8 Applications

- (i) Controlled robots can be used as Surgical robots.
- (ii) These robots can be used at pandemics where humans are not safe for traveling.
- (iii) These robots can be used as surveillance robots.
- (iv) These robots can be used for military purposes where human lives are in danger.
- (v) These types of robots can be used for persons who are physically challenged people to navigate their robot around space.
- (vi) Gesture-controlled robots can be used at heavy construction places.

9 Future Scope

This technology can be used in smart cars to control them without steering. Controlling any type of robot using this technology like controlling drones can be used at places where doctors cannot directly treat the patient. This technology can be used to make robots that can work in the home and care take babies and old people. By adding more features to the robot, this technology can be used in vulnerable places like rescuing people. It can be used for military purposes as guard robots [27].

10 Conclusion

In this paper, we have developed a hand gesture control robot using an ADXL335 sensor and Arduino. RF pair module is working on 433 MHz and had a range of more than 10 m. The device is working correctly with no errors. The cost is low. This technology can be upgraded and used in fields like medical, security and automobiles. We can make a robot that works just using face gestures and a robot for daily help at home and offices.

References

1. P. Chanda, P. Mukherjee, S. Modak, A. Nath, Gesture controlled robot using Arduino and android. *Int. J. Adv. Res. Comput. Sci. Softw. Eng. (IJRCSSE)* **6**, 227–234 (2016)
2. S. Nayak, J. Nalini, B.B.V.L. Deepak, *Int. J. Adv. Technol. Eng. Sci.* **02(05)** (2014)
3. Millmen, Halkias, in *Electronic Circuit & Device*
4. J.L. Raheja, et al., in *Real-Time Robotic Hand Control Using Hand Gestures*
5. M.R. Bahubalendruni, B.B. Biswal, M. Kumar, et al., A note on mechanical feasibility predicate for robotic assembly sequence generation, in *CAD/CAM, Robotics and Factories of the Future* (Springer, India, 2016), pp. 397–404

6. B.B.V.L. Deepak, C.A. Rao, B.M.V.A. Raju, Weld seam tracking and simulation of 3-axis robotic arm for performing welding operation in CAD environment, in *CAD/CAM, Robotics and Factories of the Future* (Springer, India, 2016), pp 405–415
7. B.B. Biswal, B.B. Deepak, Y. Rao, Optimization of robotic assembly sequences using immune based technique. *J. Manuf. Technol. Manag. (JMTM)* **24**(3), 384–396 (2013)
8. S. Lenman, L. Bretzner, B. Thuresson, Using marking menus to develop command sets for computer vision based hand gesture interfaces, in *Proceedings of the Second Nordic Conference on Human-Computer Interaction* (ACM, 2002), pp. 239–242
9. N.S. Pollard, J.K. Hodgins, M.J. Riley, et al., Adapting human motion for the control of a humanoid robot, in *IEEE International Conference on Robotics and Automation, 2002 Proceedings, ICRA'02*, vol. 2, pp. 1390–1397 (2002)
10. G.R.S. Murthy, R.S. Jadon, A review of vision based hand gestures recognition. *Int. J. Inf. Technol. Knowl. Manag. (IJITKM)* **2**(2):405–410 (2009)
11. P. Garg, N. Aggarwal, S. Sofat, Vision based hand gesture recognition. *World Acad. Sci. Eng. Technol.* **49**(1):972–977 (2009)
12. A. Pradhan, B.B.V.L. Deepak, Obtaining hand gesture parameters using image processing, in *IEEE 2015 International Conference on Smart Technologies and Management for Computing, Communication, Controls, Energy and Materials (ICSTM)*, pp. 168–170 (2015)
13. P. Jia, H.H. Hu, T. Lu, et al., Head gesture recognition for hands-free control of an intelligent wheelchair. *Ind. Robot. Int. J.* **34**(1):60–68 (2007)
14. B.B.V.L. Deepak, D. Parhi, Intelligent adaptive immune-based motion planner of a mobile robot in cluttered environment. *Intell. Serv. Robot. (ISR)* **6**(3), 155–162 (2013)
15. S.S. Rautaray, A. Agrawal, Vision based hand gesture recognition for human computer interaction: a survey. *Artif. Intell. Rev.* **43**(1), 1–54 (2015)
16. S. Biswas, U. Rahman, A. Nath, A new approach to control a robot using android phone and colour detection technique. *Int. J. Comput. Sci. Inf. Technol. (IJCSIT)* **6**(3):2985–2989 (2015)
17. M. Barr, Embedded systems glossary. Neutrino Technical Library. Retrieved 03 June 2016
18. M. Rehm, N. Bee, E. André, *Wave Like an Egyptian - Accelerometer Based Gesture Recognition for Culture Specific Interactions* (British Computer Society, 2007)
19. R. Cipolla, A. Pentland, *Computer Vision for Human-Machine Interaction* (Cambridge University Press, 1998). ISBN 978-0-521-62253-0
20. Y. Wu, T.S. Huang, Vision-based gesture recognition: a review, in *Gesture-Based Communication in Human-Computer Interaction*. Springer Lecture Notes in Computer Science, vol 1739, pp 103–115 (1999). ISBN 978-3-540-66935-7. <https://doi.org/10.1007/3-540-46616-9>
21. *Int. J. Innov. Technol. Explor. Eng. (IJITEE)* **9**(2) (2019). ISSN: 2278-3075
22. D.G.S. Rao, D.D. Bhattacharya, A. Pandey, A. Tiwari, Dual sensor based gesture robot control using minimal hardware system. *Int. J. Sci. Res. Publ.* **3**(5) (2013). ISSN 2250-3153
23. P. Somaiya, V. Panchal, D. Mehta, R. Advirkar, Gesture controlled robot. Department of Extc, K.J. Somaiya Institute of Engineering and Information Technology, Mumbai (2013)
24. *Int. J. Technol. Res. Eng.* **2**(7) (2015)
25. J.L. Raheja, R. Shyam, U. Kumar, P.B. Prasad, Real-time robotic hand control using hand gestures. In: *Second International Conference on Machine Learning and Computing* (2010)
26. S. Waldherr, S. Thrun, R. Romero, *A Gesture Based Interface for Human-Robot Interaction* (Kluwer Academic Publishers, Netherland, 2000)
27. C.H.X. Wang, M.K. Mandal, M. Meng, D. Li, Efficient face and gesture recognition techniques for robot control. In: *CCECE*, pp 1757–1762 (2003)
28. V.I. Pavlovic, R. Sharma, T.S. Huang, Visual interpretation of hand gestures for human-computer interaction: a review. *IEEE Trans. Pattern Anal. Machine Intell.* **19**(7):677–695 (1997)
29. T.G. Zimmerman, J. Lanier, C. Blanchard, S. Bryson, Y. Harvill, *A Hand Gesture Interface Device*, pp. 189–192 (1989)
30. A. Malima, E. Ozgur, M. Cetin, A fast algorithm for vision-based hand gesture recognition for robot control, in *IEEE International Conference on Computer Vision* (2006)

31. A. Malima, E. Ozgur, M. Cetin, A fast algorithm for vision-based hand gesture recognition for robot control, in *Signal Processing and Communications Applications, 2006 IEEE*, 14th April 2006, pp. 1–4 (2006)
32. T.G. Zimmerman, J. Lanier, C. Blanchard, S. Bryson, Y. Harvill, A hand gesture interface device, in *Proceedings of the SIGCHI/GI Conference on Human Factors in Computing Systems and Graphics Interface, ser. CHI '87* (ACM, New York, NY, USA, 1987), pp. 189–192. <http://doi.acm.org/10.1145/29933.275628>
33. J.L. Raheja, R. Shyam, U. Kumar, P.B. Prasad, Real-time robotic hand control using hand gestures, in *Proceedings of the 2010 Second International Conference on Machine Learning and Computing, ser. ICMLC '10* (IEEE Computer Society, Washington, DC, USA, 2010), pp. 12–16
34. B. Ma, W. Xu, S. Wang, A robot control system based on gesture recognition using kinect. *TELKOMNIKA Indonesian J. Electr. Eng.* **11**(5), 2605–2611 (2013)
35. R.O. Duda, P.E. Hart, D.G. Stork, *Pattern Classification*, 2nd edn. (Wiley, New York, 2001)
36. T. Liu, H. Guo, Y. Wang, A new approach for color-based object recognition with fusion of color models, in *Congress on Image and Signal Processing Conference Sanya-China*, vol. 3, pp. 456–460 (2008)

Artificial Intelligence-Based State of Charge Estimation of Electric Vehicle Battery



Samruddhi Dewalkar and S. P. Nangrani

1 Introduction

Electric Vehicles are going to be very popular due to the depletion of conventional fuels. The most important component of the electric vehicle is its battery. The state of the battery is a decisive factor for the performance and efficiency of the electric vehicle. Internal aspects of the battery include a clear understanding of its charge mechanism and its state during the running of the electric vehicle. State of Charge (SoC) is an important parameter for examining battery performance. It is a measure of battery capacity. The accurate state of charge cannot be determined due to several factors and assumptions based on the complexity of physics and chemistry of the battery. Estimation of SoC is one of the challenging tasks but near to accurate estimation of it protects the battery from overcharging and improves the life of the battery which ultimately saves energy. There are different types of methods that ensure accurate SoC calculation but still none of the methods can get accurate results. Conventional methods of SoC estimation are equation based with several parameters which defer from battery to battery, according to size and manufacturer of the battery. All batteries function in a different manner. Hence, Artificial Intelligence (AI)-based techniques are effective in the prediction of SoC as per ongoing research reported for different applications. Artificial Intelligence provides different models through which SoC can be calculated. SoC depends on voltage, current, temperature and ampere capacity as major parameters. There is no straight mathematical relation between these parameters. Hence, non-linear mapping of a vast amount of data to SoC estimation requires the use of AI-based data-driven techniques. Comparing

S. Dewalkar (✉) · S. P. Nangrani
G. H. Raison College of Engineering, Nagpur, India
e-mail: dewalkar_samruddhi.mtechips@ghrce.raisoni.net

S. P. Nangrani
e-mail: sunil.nangrani@raisoni.net

these models, we can get the best model through which near to accurate SoC calculation can be done. The conventional fundamental equation of current is the rate of change of charge. Hence, mathematical relation for SoC as a function of time is given as follows [1]:

$$\text{SoC}(t + 1) = \text{SoC}(t) + \frac{\int_t^{t+\tau} Idt}{Q_{rated}}$$

AI having excellent learning capabilities makes industries catchier towards it. Nowadays, different types of traditional techniques are replaced by artificial intelligence to ease the work. For SoC estimation, artificial intelligence models Artificial Neural Network (ANN) model and Support Vector Machine (SVM) model are used. This helps to determine adaptive, near to accurate, best suited and which makes it more capable of estimating SoC. Although artificial intelligence-based techniques don't depend on battery physics as these models are totally dependent on data-driven approach. Lithium-ion batteries are a better choice for electric vehicles as compared to lead-acid batteries. Hence, plug-in and full-battery electric vehicles (PHEVs and BEVs) use Lithium-ion (lithium-ion) batteries. They are preferred due to their high energy density and compact size over other batteries. Mathematical models of the battery give deep insight into the differential performance of batteries. These models are basically based on the charging and discharging of the capacitor with respect to time. However, practical batteries have an effect on temperature as well as on SoC.

There are a lot of models analysed by researchers, some of them are simple and complex as well. One such popular model is Electrochemistry-based model and the other is the electrical circuit model. Other types of models are generally derived from these two basic models. Another type of classification is a mathematical model and an analytical model where the mathematical model is the electrochemical model and the analytical model is based on empirical data.

Ageing equations of batteries are related to the life estimation of batteries. The selection of the battery model is very crucial for the analysis purpose. If we are interested in battery SoC, there may be many options but one has to use the model with more details if the target is accuracy.

2 Literature Review

Support Vector Machine (SVM): To change non-linear model from the linear model, the SVM model algorithm needs both regression or classification challenges but the complexity of the SVM system is higher because of its complex quadratic programming [2].

Genetic Algorithm (GA):- Zheng Chen used this method for EV applications for the calculation of the state of health [3]. GA is used to estimate the battery model parameters and also the diffusion capacitance in real using measurement of current and voltage of the battery.

Artificial Neural Network (ANN):-This has self-adaptability and self-learning abilities. To improve the performance, backpropagation neural network can be used [4]. Artificial Neural Network (ANN) can be described as processing devices that are loosely modelled after the neural structure of a brain.

Particle Swarm Optimization (PSO):- This is a nature-inspired nature approach of different types of species of birds or fishes. The advantage of this method is that data can be shared in a group where the individual bird does not know the exact location of food. However, food sites can be tracked through the information sharing method [5].

Bacterial Foraging Algorithm (BFA):- This is another nature-based method. It has high efficiency and simplicity [6].

Recurrent Neural Network (RNN):- This method has current has input to model. This adds additional weight to create the feedback loop to maintain internal neurons [7].

Fuzzy Logic (FL):-This method consists of fuzzification, fuzzy rule base, inference engine and defuzzification. FL method is time-consuming and needs large memory.

Adaptive Neuro Fuzzy Inference System (ANFIS):- This method is more advanced than artificial NN and Fuzzy Logic (FL) [8].

Review on some AI-based techniques for SoC estimation is discussed above and comparative analysis can be done through this study of artificial-based techniques on State of Charge estimation with traditional techniques. Every method discussed above is unique and has its own advantages and disadvantages.

3 Methodology

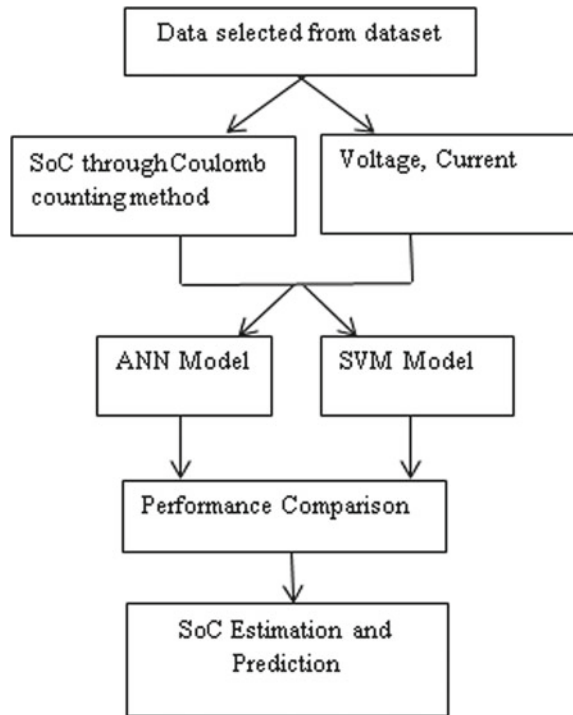
AI techniques need large data samples for learning. Relevant and appropriate data can only produce predictions accurately. The datasets chosen don't consist of the SoC parameter. SoC is mathematically calculated based on time interval, battery state and current. Dataset consists of time series data of Current, voltage and initial storage conditions. As the dataset is analysed, inputs are given to AI models for testing, validation and training. Both the models' performance is evaluated and the best model is selected.

AI techniques need training of models which are required to calculate the state of charge. Data samples collected are closely studied and corrupt data is neglected.

The Coulomb counting method is used for reference to compare the results of the traditional method and results from these two models. Models are created with the use of data in MTLAB software since MATLAB software is usually used in educational institutes and can be easily learned.

Performance comparison can be done by analysing the graphs obtained through these models. The data collected may consist of some incorrect or duplicate or corrupt data so these kinds of data need to be sorted out to get the most suitable result.

Fig. 1 Flowchart for estimation of accurate SoC



Ageing tests of batteries involve different types of tests named as pulse current discharge, static capacity and charge-discharge cycle. Few tests are indirect measurements of SoC (like the Coulomb Counting) while there are direct methods also to measure SoC such as using a battery tester.

MATLAB-based ANN model helps in handling huge data, analysing data easily and predicting SoC. The data fed to these models must be related to the testing of the battery. Detailed excel sheet can store time-based samples of voltage, current, temperature and SoC as measured by measuring instruments. The excel file data will be fed as a pattern to ANN models programmed on the software tool MATLAB (Fig. 1).

4 Result

Data samples consist of some corrupt or duplicate samples so such samples are excluded.

The following graphs shows the relationship of voltage and current with SoC.

From the dataset, it is observed that during its life cycle, battery goes from different stress environments. From Fig. 2, the voltage Vs SoC graph is linear up to 30% of SoC, stable up to 80% of SoC and increases thereafter as observed. Current is inversely

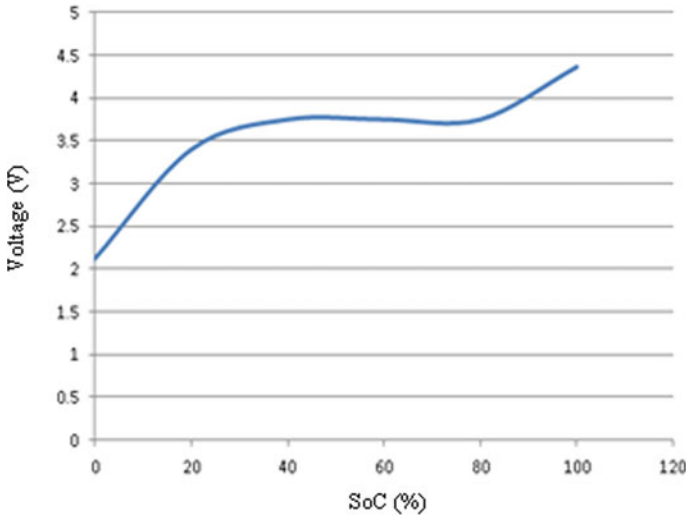


Fig. 2 Voltage versus SoC graph

proportional to SoC percentage as shown in Fig. 3. Data points from these graphs are used as input patterns for training purposes in ANN models and output will be SoC. Batteries from different manufacturers are tested and the collection of similar capacity batteries from the same manufacturer helps in better training and a part of data points can be used for testing. SoC can be measured by measuring instruments in a lab and results of software-based ANN models are then compared with measured test results. If they reveal closeness to SoC estimated by analytical equation, then the model is acceptable else it requires tuning of ANN models so as to give output as predicted and measured by the test.

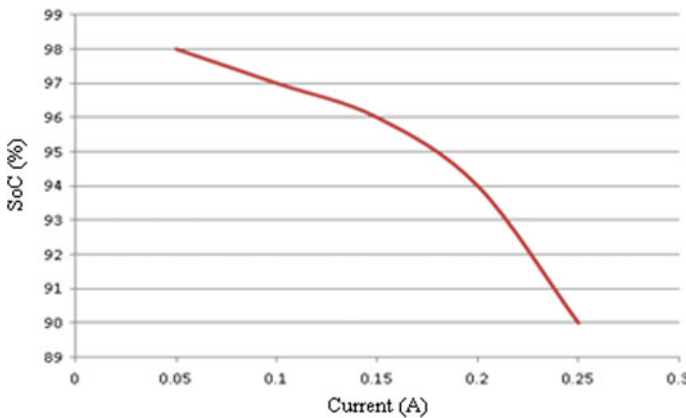


Fig. 3 Current versus SoC graph

5 Conclusion

The above paper indicates that using AI techniques minimizes error in calculating SoC. So using artificial intelligence models, one can get near to accurate SoC than using traditional techniques. The study shown in the literature review shows how the use of AI for estimation of SoC is helpful as AI-based techniques are simpler and have higher accuracy. AI-based estimation takes care of uncertain parameters such as temperature which cannot be correlated through straight mathematical relations. Test results when fed as input to ANN-based software models give an estimation of SoC which can be measured by SoC Tester as well. ANN models are also adaptive in the sense that one can tune the model for better accuracy. All the models when cleverly put together helps to compute tasks that were previously thought to be reserved for humans. More and more techniques are being introduced to make the calculation simpler and make the method user-friendly. Measured SoC was in close agreement with AI-predicted SoC values which proves the efficacy of intelligent methods.

References

1. Z. Li, J. Huang, B.Y. Liaw, J. Zhang, On state-of-charge determination for lithium-ion batteries. *J. Power Sources* **348**, 281–301 (2017)
2. J.A. Anton, P.G. Nieto, C.B. Viejo, J.V. Vilan, Support vector machines used to estimate the battery state of charge. *IEEE Trans. Power Electron.* **28**, 5919–5926 (2013)
3. Z. Chen, C.C. Mi, Y. Fu, J. Xu, X. Gong, Online battery state of Health estimation of Genetic Algorithm for electric and hybrid Vehicle applications. *J. Power Sources* **240**, 184–192 (2013)
4. M.A. Hannan, M.S.H. Lipu, A. Hussain, M.H. Saad, A. Ayob, Neural network approach for estimating state of charge of lithium-ion battery using backtracking search algorithm. *IEEE Access* **6**, 10069–10079 (2018)
5. M.U. Ali, B. Habib, M. Iqbal, Fixed head short term hydro Thermal scheduling using improved particle swarm optimization. *Nucleus (Islamabad)* **52**, 107–114 (2015)
6. Y. Ma, J. Ru, M. Yin, H. Chen, W. Zheng, Electrochemical Modelling and parameter identification based on bacterial foraging optimization algorithm for lithium-ion batteries. *J. Appl. Electrochem.* **46**, 1119–1131 (2016)
7. Y. Zhang, R. Xiong, H. He, M.G. Pecht, Long short-term Memory recurrent neural network for remaining useful life prediction of lithium-ion batteries. *IEEE Trans. Veh. Technol.* **67**, 5695–5705 (2018)
8. H. Dai, P. Guo, X. Wei, Z. Sun, J. Wang, Anfis (adaptive neuro- fuzzy inference system) based online soc (state of charge) correction considering cell divergence EV (electric vehicle) traction batteries. *Energy* **80**, 350–360 (2015)
9. B.J. Landi, M.J. Ganter, C.D. Cress, R.A. DiLeo, R.P. Raffaele, Carbon nanotubes for lithium ion batteries. *Energy Environ. Sci.* **2**(6), 638–654 (2009)
10. J. Li, H. Cheng, H. Guo, S. Qiu, Survey on artificial intelligence for vehicles. *Automot. Innov* **1**(1), 2–14 (2018)
11. D.J. Lim, J.H. Ahn, D.H. Kim, B.K. Lee, A mixed SOC estimation algorithm with high accuracy in various driving patterns of EVs. *J. Power Electron.* **16**(1), 27–37 (2016)
12. R. Xiong, J. Cao, Q. Yu, H. He, F. Sun, Critical review on the battery state of charge estimation methods for electric vehicles. *IEEE Access* **6**, 1832–1843 (2017)
13. Y. Wang, C. Zhang, Z. Chen, A method for state of health Charge estimation of Li-ion batteries based on multi-model switching. *Appl. Energy* **137**, 427–434 (2015)

14. P. Singh, R. Vinjamuri, X. Wang, D. Reisner, Design and implementation of a fuzzy logic-based state of charge meter for li-ion batteries used in portable defibrillators. *J. Power Sources* **2162**, 829–836 (2006)
15. S. Pai, M.R. Sindhu, Intelligent driving range predictor for green transport, in *IOP Conference Series: Materials Science and Engineering*, vol. 561, no. 1 (IOP Publishing, 2019, October), p. 012110
16. A. Hammouche, E. Karden, R.W. De Doncker, Monitoring state-of-charge of Ni–MH and Ni–Cd batteries using impedance spectroscopy. *J. Power Sources* **127**(1–2), 105–111 (2004)
17. Nangrani, S.P. and Bhat, S.S., 2015, November. Power system security assessment using ranking based on combined MW-chaotic performance index. In *TENCON 2015-2015 IEEE Region 10 Conference* (pp. 1-6). IEEE.
18. Nangrani, S.P. and Bhat, S.S., 2017. Numerical study of optimized fractional-order controller for chaos control of nonlinear dynamical power system. *International Transactions on Electrical Energy Systems*, 27(8), p.e2336.
19. Naik, K.R., Nangrani, S.P. and Bhat, S.S., 2016, March. Modeling of operation of loss of excitation relay in presence of shunt FACTS devices. In *2016 IEEE 6th International Conference on Power Systems (ICPS)* (pp. 1-6). IEEE.

Wattages Optimization of Small Hydro Power Station to Build up Energy



Prachi Dashrath Mohite , Shweta Abhay Khalatkar,
and Abhay M. Khalatkar

1 Introduction

There are many techniques to solve a model that too in this case a small hydro model which keeps an eye on the head of water for increasing values. Similarly, we can monitor the different other values such as head pressure with the help of turbines usage. Also, the other conditions such as the alternators, governors and turbines also play a vital role in contributing to the optimization of small hydro power plants.

2 Classification of Small Hydro II

Classification of small hydro according to wattages is shown in following Fig. 1 and used for further study and evaluation of the model of power plant with other factors keeping in mind.

Small-hydro	1,500,000 Watts
Mini-hydro	1,000,000 Watts
Micro-hydro	100,000 Watts
Pico-hydro	5000 Watts

P. D. Mohite

Electrical Department P.E.S College of Engineering Aurangabad, Aurangabad, Maharashtra, India

S. A. Khalatkar (✉)

Computer Science Engineering Department, G H Rasoni University, Amravati Amravati, Maharashtra, India

A. M. Khalatkar

Mechanical Department, G. H. Rasoni College of Engineering, Nagpur, India

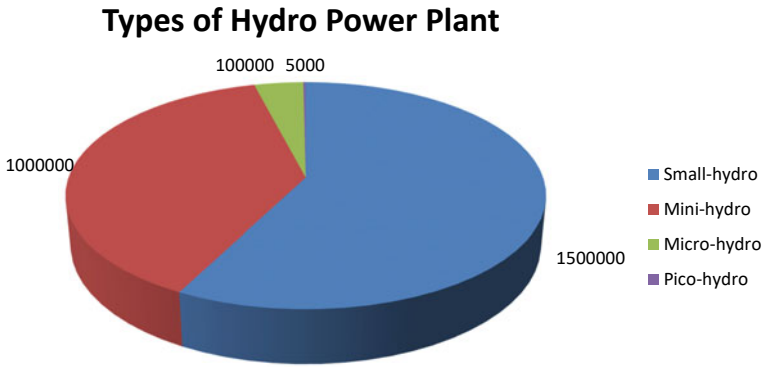


Fig. 1 Classification of small hydro power plant

The classification can be seen from the chart for different percentages of values.

3 Watts Optimization III

We can find the power according to the potential of water and depending upon the height of the head if we achieve the flow rate constant. We are calculating the head as vertical height in metres from turbine house to the penstock.

The following parameters are accounted for calculations [1].

$$\text{Power in kW (P)} = P = g * Q * H * f_{\text{eff}}$$

Gravity constant 9.81 m/s^2 (g).

Flow rate in m^3 / s (Q).

H head in m (H).

The power will be calculated for all the values and it shows that the power will increase with the increasing head; also, if other values may vary or be kept constant, the energy maximization is possible and may also contribute to energy factors with head pressure and period of turbine operation [2]. The following table shows the values to be tabulated and verified on simulation [3] (Table 1).

4 Results and Discussion IV

The graphical representation is shown in Fig. 2. The increasing nature of parameter of the head with increasing power values and hence optimization of the plant.

Table 1 Readings of small hydro plant

n	P	g	Q	H	Feff = 0.5
1	15000 W	9.81 m/s ²	0.3 m ³ /s	10	0.5
2	18,000 KW	9.81 m/s ²	0.3 m ³ /s	12	0.5
3	21,000 KW	9.81 m/s ²	0.3 m ³ /s	14	0.5
4	24,000 KW	9.81 m/s ²	0.3 m ³ /s	16	0.5
5	27,000 KW	9.81 m/s ²	0.3 m ³ /s	18	0.5
6	30,000 KW	9.81 m/s ²	0.3 m ³ /s	20	0.5
7	33,000 KW	9.81 m/s ²	0.3 m ³ /s	22	0.5

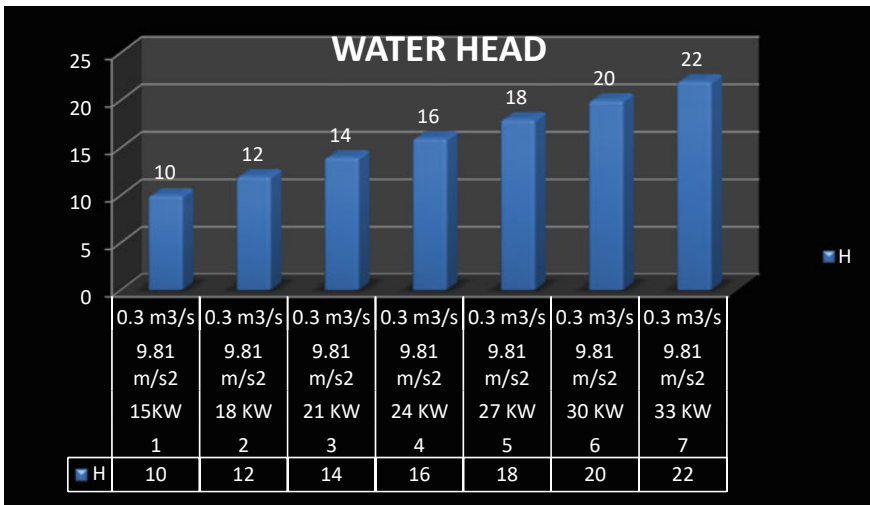


Fig. 2 Water head

The graph for current point and evaluations is shown which shows direct iteration made with initial point set correct and fit in the equation [4]. The output is for the head of 10 m value [5] (Fig. 3).

The graph for best function value and current function value point set correct and fit in the equation. The output is for the head of 10 m value [6] (Fig. 4).

The graph for violation zero value, step size and optimality value point set correct and fit in the equation. The output is for the head of 10 m value [7] (Fig. 5).

The graph for current point and evaluations is shown which shows direct iteration made with the initial point set correct and fit in the equation [8]. The output is for the head of 22 m value (Fig. 6).

The graph for best function value and current function value point set correct and fit in the equation [9]. The output is for the head of 22 m value (Fig. 7).

The graph for violation zero value, step size and optimality value point set correct and fit in the equation [10]. The output is for the head of 22 m value (Fig. 8).

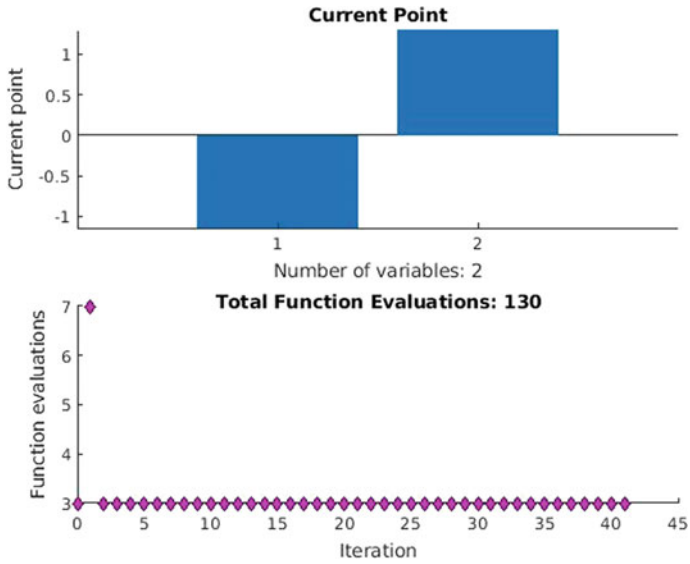


Fig. 3 Current point and evaluations

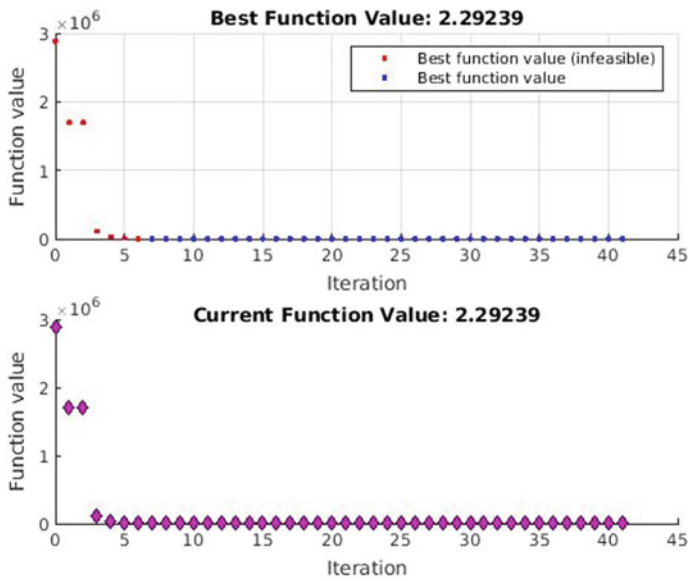


Fig. 4 Best value and current function value

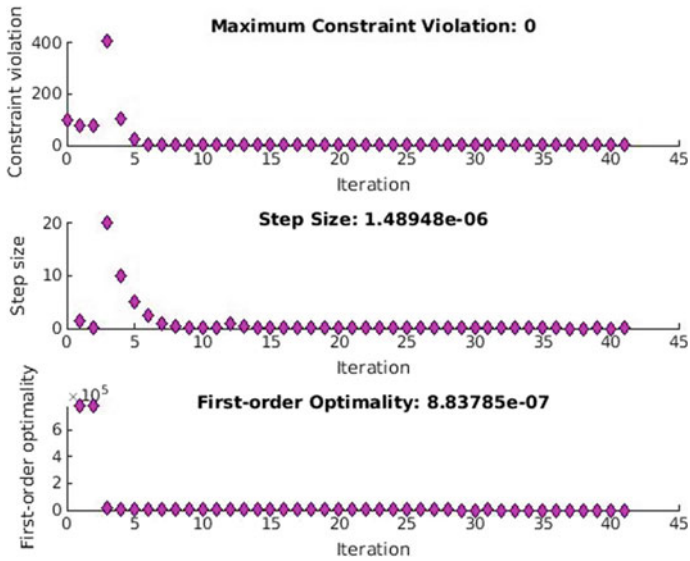


Fig. 5 Violation, step size and optimality

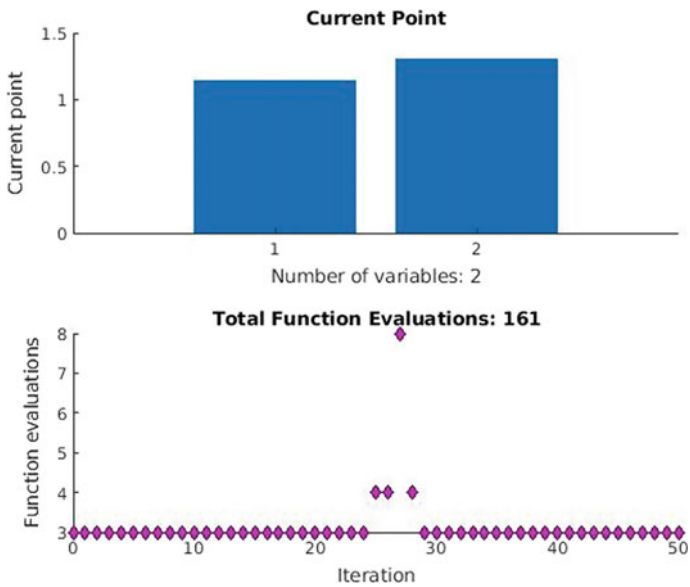


Fig. 6 Current point and evaluations

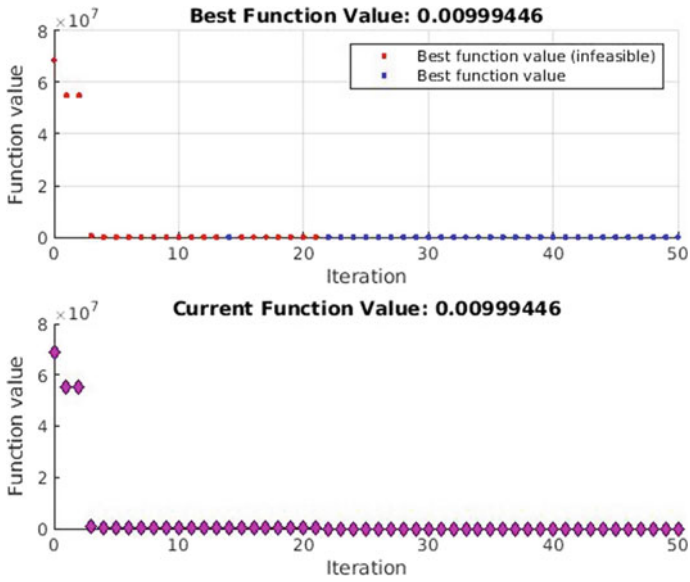


Fig. 7 Best value and current function value

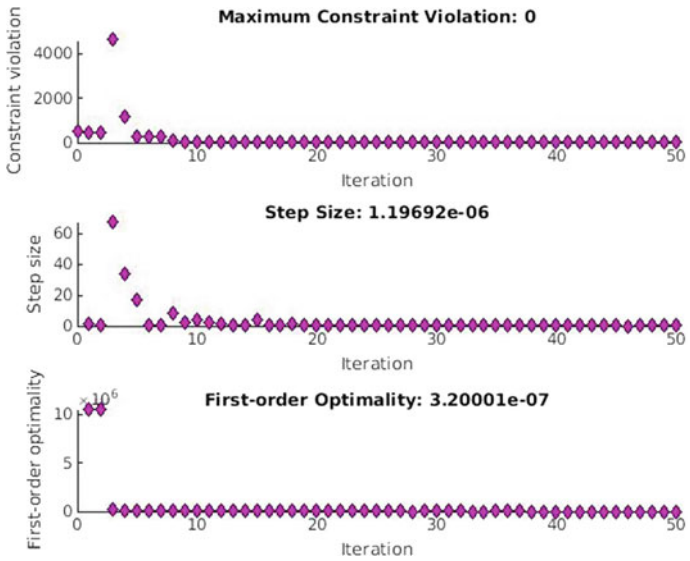


Fig. 8 Violation, step size and optimality

The graph for violation zero value, step size and optimality value point set correct and fit in the equation [11]. The output is for the head of 22 m value.

5 Conclusion

The model has a type of small hydro power plant and the points considered are power, head, Gravity, water discharge, etc. [12]. Also, the other factors can be noted, and similarly, the power calculation can be done [13]. And hence optimization can be performed by other factors also.

References

1. Modelling and Controlling Hydropower Plants by German Ardul Munoz-Hernandez & Sa'ad Petrous Mansoor & Dewi Ieuan Jones
2. Hydro power—the design, use, and function of hydromechanical, hydraulic, and electrical equipment by Raabe J
3. Hydro Plant Electrical Systems by Clemen & David M
4. Optimizing Optimization: The Next Generation of Optimization by Stephen Satchell
5. Engineering Optimization: Theory and Practice, Fourth Edition by Singiresu S. Rao
6. Optimization Theory and Methods: Nonlinear Programming (Springer Optimization and Its Application) by Wenyu Sun Ya-xiang Yuan
7. An Introduction to Optimization by Stanislaw H. Zak
8. Numerical Analysis and Optimization: An Introduction to Mathematical Modelling and Numerical Simulation (Numerical Mathematics and Scientific Computation) by Gregoire Allaire & Alan Craig
9. Modeling and Econometrics in Economics and Finance) by Bruce D. Craven
10. Search and Optimization by Metaheuristics: Techniques and Algorithms Inspired by Nature by Ke-Lin Du & M. N. S. Swamy (auth.)
11. Evaluation and Optimization of Electoral Systems by Pietro Grilli di Cortona & Cecilia Manzi & Aline Pennisi & Federica ca & Bruno Simeone
12. UX Optimization: Combining Behavioral UX and Usability Testing Data to Optimize Websites by W. Craig Tomlin
13. Optimization in Economics and Finance: Some Advances in Non-Linear, Dynamic, Multi-Criteria and Stochastic Models (Dynamic)

A Review on the Development of Solar Power Automatic Biodegradable Waste Sorter and Composter



Amit S. Borole and A. R. Phadke

1 Introduction

India is said to be the country of Farmers. Fertilizer is one of the basic needs for farming and to improve the fertility of land required for farming. Nowadays, due to the decrease in the efficiency of land and soil properties, it becomes immensely important to put a step forward and try to improve the quality of the soil. This can be done by good quality of Composting [1].

Composting is a technique which is very less in operation cost and also it does not create pollution. Hence, it can be widely used to create a nutrient for the plants and it will improve the fertility of the soil. This creates a naturally created fertilizer, as it's an acceleration of nature's process in itself, with the assumption that each material decomposed with time.

Compost creates organic material which is obtained by recycling the various natural materials which can be declared as waste materials. Compost is rich in nutrients. Compost is a value-added package for the soil to improve its fertility and it can be used as a conditioner for soil. The compost requires a green waste heap which is converted into humus after a period of time. However, compost can be a complex monitored process as well to obtain fast and efficient results.

The problem with compost is that many of the farmers don't know the exact process of its manufacturing. Also, it takes 45–60 days to produce good quality of Compost. With the help of technology, we can improve the quality as well as the speed of the Composting. The model will be completely automatic and the process can be done faster by providing adequate heat to the grinded mixture of biodegradable

A. S. Borole (✉)
SSBT's COET, KBC NMU, Jalgaon, Maharashtra, India

A. R. Phadke
College of Engineering Pune, Pune, India
e-mail: arp.elec@coep.ac.in

waste. This model will have a solar panel to provide the required amount of electricity for the crusher and composter. This will also give supply to the automated process of sorting between degradable and non-degradable waste.

Hence, a system can be developed which will automatically monitor the process of composting and will also sort waste into two different categories.

2 System Description

Figure 1 represents the block diagram of the complete model. The process can be justified in four steps as Collection of waste, Sorting of degradable waste, Crushing in small pieces and Composting. As shown, solar panels will charge the battery and hence will supply power to the crusher mainly and to the complete process also.

The smart Bio sorter has to segregate degradable waste from non-degradable waste. In this sorter, the important aspect is to identify distinguishing properties of degradable materials, and then with the help of these properties, these materials will be sorted out from each other.

Degradable waste is generally consisting of garden waste and kitchen waste. These wastes have their own unique shapes such as banana or apple or leaves. These can be identified on the basis of shape and color, which is quite different from non-degradable waste like plastic, glass or paper boxes. This shape and color of different samples can be provided to the robot and it can be trained to such a level that it can identify degradable and non-degradable waste up to a certain extent. Further, the material sorted as degradable waste by the robot can be processed from a humidity

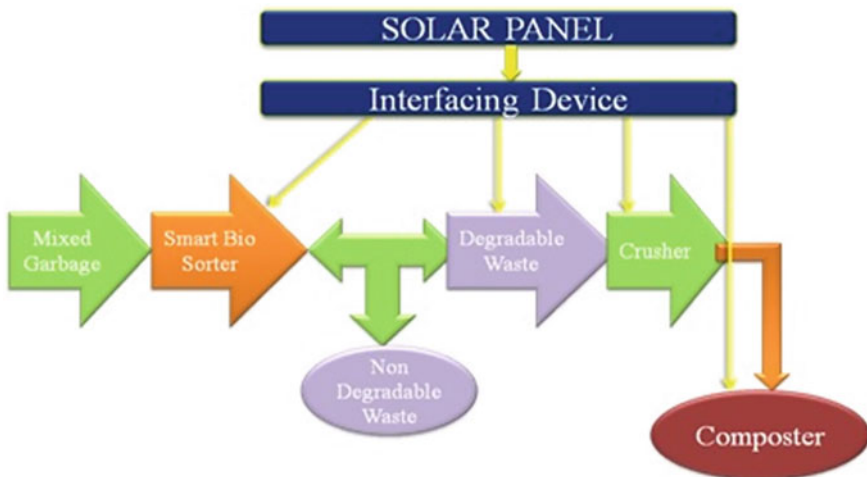


Fig. 1 Block diagram of model

sensor which will detect moisture present in the waste material. This can be done by a method called image processing.

Crusher will operate as ON command is given to it based on capacity of the solar system. Crusher will convert waste degradable material into small pieces and then the output of the crusher will be fed to the composter. Now composter will require some mechanical and chemical processes according to the composting process. For the fast composting process, extra adequate heat will be provided by solar panels.

3 Literature Review

There are several articles explaining the types of compost and the process to enhance the quality of compost. Also, there are several publications listed below having brief details about the crusher and its blade design. There are numerous papers justifying solar interfacing systems but it was tough to get literature on the combination of all these articles. The literature found and studied is in separate categories are as follows.

3.1 *Smart Bio Sorter*

Joshi et al. [2] have explained about sorting of metal, glass and paper from the waste materials. In this paper, they have not focused on sorting of degradable waste but they proposed sorting of the above-mentioned materials which generally occur in the category of degradable materials. The robotic arm works with the help of a metal proximity sensor which is an electronic instrument that detects the presence of metal nearby.

Ranjani and Chockalingam [3] proposed a sorter based on both sensors and image processing techniques, in which they explained an overview of their proposed system. The system includes a robotic arm that will work on the inputs given by the MATLAB image processing tool. The database is already stored in MATLAB and with the help of a camera, objects can be identified.

In Saravana kanaan et al. [4], explained about three stages of image processing for waste separation as follows:

1. Color feature extraction
2. Size feature extraction
3. Texture feature extraction.

This can be achieved by pictures taken from a web cam or RGB camera and a robot having an arm and gripper. The robot movement is based on the function of the camera and what it detects completely depends on the input provided by the camera with the image processing technique of shape, pattern and shade.

Rokade et al. [5] mentioned a robot having a dustbin mounted on it. The waste collection done in the bin is sorted out by the robot having the following components:

- PIC 18F452 microcontroller.
- Motor driver L293D.
- DC motor –30 rpm, 12v.
- Obstacle sensor.
- USB to TTL.
- Camera.
- MATLAB image processing algorithm.

It can be determined that image processing technique can be a primary filter for waste sorting and then some sensors can be applied for more accuracy.

3.2 Crusher

In paper Wang et al. [6], explained their contribution in the field of proximity switch in crushers used to crush garbage. In this paper, the author provided a new low power switch that can be replaced by a mechanical switch. This made the automatic process of crusher whenever the required amount of garbage is collected in the kitchen sink. In this paper, the APDS-9960 device is used which adopts digital RGB of single 8 pin package, ambient light and short-range hand gesture sensors.

In Li et al. [7], wrote their experimental fault analysis on garbage crushers. The authors stated eight different categories of faults which can occur in garbage crushers such as a crack in rotor blades and they also stated symptoms for the particular fault. In this paper, the author stated diagnosis of faults based on ant colony algorithm. ACA gives better results to improve training efficiency which is shown in the case study given below (Table 1).

Table 1 Fault diagnosis of crusher

Sr. No	Fault type	Fault symptom
1	Blade crack of rotating cutter	Spindle temperature
2	Spindle wearing	Rotor speed
3	Sieve jamming	Motor bearing temperature
4	Garbage wrapping	Crushing throat size
5	Crushing throat locked	Temperature of crusher case
6	Motor bearing burnt out	Spindle speed
7	Overloading	Vibration
8	Crusher is overheating	Differential pressure of filter

Huang et al. [8] wrote about improvements done in crusher design to have better performance. They did this research for coal crushers but their study can be used to design garbage crushers.

3.3 Composter

Taumi [1] gave a detailed analysis about composting process. The author developed model of compost tumbler which is operated on solar energy for rotation of heap. The paper gives a brief idea about organic and non-organic materials, the process of composting and precautions taken for good quality of compost. This process can be automated by solar energy.

To prepare better compost, the following process should be conducted:

- I. Prepare the composter based on the material size that needs to be composted.
- II. Select a sunny area where this composter can be placed.
- III. Create layers while placing materials in the composter. Place the twigs at the bottom and allow air to pass through it. Above it, place the leaves and soft green material over the first layers.
- IV. There must be some water content in the material so that composting will become faster.

3.4 Solar System and Interfacing

In Sivaprasad et al. [9], stated the DC-DC converter technique used for dual input solar interfacing system. The author describes the converters for DC micro grid connected with the solar photovoltaic system. The proper study of insolation and temperature is to be done for the installation of the solar system. For this purpose, a DC-DC converter can be used to make stable voltage. Paper describes the SPY generation, MPPT algorithm and mathematical modeling of solar cell and analysis of DC-DC converter and implementation of MPPT algorithm.

The DC-Dc converter is specially designed to meet the load demand of DC load. There are many converters depending upon the application like buck converter which steps down the supply voltage, boost converter which boosts the supply voltage, SEPIC converter and flyback converter. These converters regulate the unregulated DC supply using the PWM switching at a fixed frequency. This individual converter requires the individual switching for each operation to turn on and turn off it. Because it's used in power applications, so it requires power devices such as switch, like Power MOSFET, IGBT, BJT and Thyristor. These power switches require an additional control circuit to operate them, which is known as the gate driver circuit. These techniques used the pulse width modulation to control the converter voltage, frequency and phase delay. The general types are as follows:

DC-DC Boost Converter.
 DC-DC Buck Converter.
 DC-DC Buck-Boost Converter.

After reviewing various aspects, there seems a chance of improvements in the current available composters and sorter. The sorting of waste is becoming an important issue that is yet to be solved. This problem is identified and the system is proposed for sorting of waste and its decomposing. There are several problems in designing this system such as the design of robotic arms, design of sorter, design of crusher and solar power required for it [10].

Assume the following:

Radius of motor blades = 20 cm = 0.2 m

Total waste handling at a time = 10 kg

Total Degradable waste at a time = 6–7 kg

For 3 cycles of operation in a day, waste handling in crusher = 2 kg

$$\begin{aligned}\text{Torque (T)} &= \text{Force} * \text{radius} \\ &= \text{Weight} * \text{gravity} * \text{radius} \\ &= 2 * 9.81 * 0.2 \\ &= 3.924 \text{ Nm}\end{aligned}$$

$$\begin{aligned}\text{Torque (T)} &= \text{Force} * \text{radius} \\ &= \text{Weight} * \text{gravity} * \text{radius} \\ &= 2 * 9.81 * 0.2 \\ &= 3.924 \text{ Nm}\end{aligned}$$

$$\begin{aligned}\text{Input Power} &= \text{Output Power} / \text{efficiency} \\ &= 41 / 0.8 \\ &= 50 \text{ W (approx)}\end{aligned}$$

4 Comparative Analysis

The paper covers multidisciplinary articles and papers relevant to the proposed system. As a similar system is not yet designed, exact comparison can't be done between two models but the effectiveness of different topologies used for various phases of the proposed system can be done. The DC-DC converter Boost topology will be a handful due to its simple design and high-end output. The crusher design is suitable from [7] is a handy one where several faults are detected and eliminated.

5 Conclusion

The proposed system is analyzed with a thoughtful process and every aspect of the proposed system is feasible to design and develop. The system consists of solar panels installed in its outermost top and the use of a battery can be avoided by analyzing day-to-day insolation of sun rays in the area it is desired to be installed. Especially, in the rainy season, when a backup or storage system is essential, it can be provided with an external source to plug in.

References

1. R. Toumi, *Design of a composting bin to convert AUI's biomass to an organic fertilizer*
2. V.V. Joshi, R. Ghugikar, B. Bhise, P. Bhawar, S. Kakade, Waste segregation using smart robotic arm. *Int. Res. J. Eng. Technol. (IRJET)* **04**(05), 2017
3. P. Ranjani, A.L. Chockalingam, Solid non-biodegradable waste segregation using Matlab and Robotic ARM. *JCHPS* (8) 2016. (December 2016)
4. G. Saravana kannan, S. Sasi kumar, R. Ragavan, M. Balakrishnan, Automatic garbage separation robot using image processing technique. *IJSRP*, **6**(4) 2016
5. R. Rokade, A. Maurya, V. Khade, S. Tandel, J. Mali, Smart garbage separation robot with image processing technique, in *ICIATE-2018 Conference Proceedings*
6. S. Wang, J. Guo, D. Xu, Non-contact low-power proximity switch based on kitchen garbage crusher, in *2018 International Conference on Intelligent Transportation, Big Data & Smart City (ICITBS)*, Xiamen, 2018, pp. 101–104. <https://doi.org/10.1109/ICITBS.2018.00034>
7. X. Li, C. Li, M. Huang, H. Jing, The fault diagnosis of garbage crusher based on ant colony algorithm and neural network, in *2009 Third International Conference on Genetic and Evolutionary Computing*, Guilin, (2009), pp. 515–519. <https://doi.org/10.1109/WGEC.2009.165>
8. M. Huang, Z. Li, B. Kuang, An improving design of solid garbage crusher for garbage coal production line, in *2010 Asia-Pacific Power and Energy Engineering Conference (Chengdu, 2010)*, pp. 1–4. <https://doi.org/10.1109/APPEEC.2010.5449102>
9. A. Sivaprasad, S. Kumaravel, S. Ashok, Integration of solar PV/battery hybrid system using dual input DC-DC converter, in *2016 Biennial International Conference on Power and Energy Systems: Towards Sustainable Energy (PESTSE)* (Bangalore, 2016), pp. 1–5. <https://doi.org/10.1109/PESTSE.2016.7516473>
10. N.H. Baharudin, T.M. Nizar, F.A. Hamid, R. Ali, M.I. Misrun, Topologies of DC-DC converter in solar PV applications. *Indones. J. Electric. Eng. Comput. Sci.* **8**(2), 368–374 (2017). <https://doi.org/10.11591/ijeecs.v8.i2.pp368-374>

Correction to: **Spiritual Elixir: Application of Ganga Water in Treatment of Wastewater**



Monika Negi, Ayushi Maithani, and Sakshi Gupta

Correction to:
**Chapter “Spiritual Elixir: Application of Ganga Water
in Treatment of Wastewater” in: M. L. Kolhe et al. (eds.),
*Smart Technologies for Energy, Environment and Sustainable
Development, Vol 2, Springer Proceedings in Energy,*
https://doi.org/10.1007/978-981-16-6879-1_5**

The original version of the book was inadvertently published with incorrect author names in chapters 5. Chapter authors group has been changed from “Sakshi Gupta, Deepak Khare, Nitin Mishra” to “Monika Negi, Ayushi Maithani, Sakshi Gupta”.

The correction chapter and the book have been updated with the changes.

The updated original version of this chapter can be found at
https://doi.org/10.1007/978-981-16-6879-1_5

© The Author(s), under exclusive license to Springer Nature Singapore Pte Ltd. 2023
M. L. Kolhe et al. (eds.), *Smart Technologies for Energy, Environment and Sustainable
Development, Vol 2*, Springer Proceedings in Energy,
https://doi.org/10.1007/978-981-16-6879-1_70

C1